

Indonesian Journal of Chemistry

Vol. 23, No. 5, October 2023



Approved by WoS/ISI/Scopus
No. 055/M/PT/2020

Effect of Sintering Temperature on the Microstructure Behavior of Gelcasted Porous Ceramics Using Cassava Starch as Pore Template

Suriati Eka Putri¹, Diana Eka Pratiwi¹, Rachmat Triandi Tjahjanto², Nita Magfirah Ilyas¹, Dahlang Tahir³, Abd Rahman⁴, and Heryanto Heryanto^{3*}

¹Department of Chemistry, Faculty of Mathematics and Natural Sciences, Universitas Negeri Makassar, Jl. Daeng Tata, Makassar 90244, Indonesia

²Department of Chemistry, Faculty of Mathematics and Natural Sciences, Brawijaya University, Jl. Veteran, Malang 65145, Indonesia

³Department of Physics, Faculty of Mathematics and Natural Sciences, Hasanuddin University, Jl. Perintis Kemerdekaan Km. 20, Makassar 90245, Indonesia

⁴Inorganic Chemistry, King Fahd University of Petroleum & Minerals, Academic Belt Road, Dhahran 31261, Saudi Arabia

* **Corresponding author:**

email: heryanto@science.unhas.ac.id

Received: November 3, 2022

Accepted: May 4, 2023

DOI: 10.22146/ijc.78875

Abstract: The gelcasting technique was employed to fabricate porous ceramics utilizing kaolinite clay as the base material with a combination of 20 wt.% cassava starch. The utilization of cassava starch as a pore-template material is a sustainable and eco-friendly approach. The dry mixture compacted pellets underwent calcination for 2 h at three distinct sintering temperatures, namely 900, 1000, and 1100 °C. The present study investigated the impact of sintering temperatures on various ceramic properties, including but not limited to porosity, hardness, crystallinity, lattice strain, and morphology. Furthermore, an increase in sintering temperature led to a reduction in crystallinity of the ceramic material from 81.71 to 78.06%, while the lattice strain increased, as determined by the full width at half maximum peak diffraction calculation. The study determined that the pore size remained microporous (21 Å) across all temperature treatments. Ultimately, a porous ceramic material was fabricated, exhibiting a porosity of 39.44% by volume and a desirable hardness of 94 HB. The optimal sintering temperature for this material was found to be 900 °C. The anticipated application of the porous ceramic, which has taken on a pellet shape, is as a catalyst support for wastewater filtration in the future.

Keywords: cassava starch; kaolinite clay; sintering

■ INTRODUCTION

Customized porosity of materials gives unique qualities and features, which are difficult to be obtained and achieved in conventional materials. Porous materials are being used in many end products and technologies presently. Furthermore, porous materials are also used in many different ways and forms in everyday human life. For example, polymer foams are used for packaging. Lightweight aluminum structures are used in buildings and airplanes while porous ceramics are used to clean water. Porous ceramics provide the opportunity to

combine high porosity with crucial properties such as high thermal conductivity, high strength, and chemical stability, which are essential for industrial applications and development. The implementation of the materials includes catalytic support [1-2], removal of heavy metal ions or azo dyes from wastewater [3-4], thermal insulators [5], combustion analyzers [6], and membrane for microfiltration [7]. However, due to pricey raw materials and production techniques, the usage of porous ceramics in more widespread applications is restricted [8]. Therefore, the development of porous

materials made from natural resource materials and the fabrication route using low temperatures are of interest and goal in this study.

Several methods have been employed to fabricate porous ceramics, including the direct consolidation method [9], fused deposition [10], freeze casting [11], gelcasting [12], foam gelcasting [13], and sol-gel [14]. Among these methods, gelcasting is a simple low-cost method because the fabrication process does not require high temperatures and pressures [15]. Gelcasting is one method of shaping process that is entirely developed with basic principles of *in-situ* polymerization of monomers in a ceramic slurry, creating a strong, cross-linked polymer-solvent gel that acts as a pore template [16]. Our previous research produced porous ceramic by the gelcasting method, and the material has good properties (high porosity with high ceramic body strength) as adsorbent for azo dyes [2]. In addition, Han et al. [17] also produced a porous ceramic body with good thermal conductivity for heat insulation applications. As a result, gelcasting will unquestionably become a crucial technique for producing ceramic parts in various shapes.

The most often used gel, acrylamide (AM), is a neurotoxic, and the raw materials employed are synthetic metal oxide powders such alumina, nitride, and zirconia [18-19], which is expensive. As a result, the industry is hesitant to use the gelcasting technology. Therefore, it is necessary to discover alternative natural polymers and raw materials. Several natural polymers, such as chitosan [18], rice flour [20], cassava starch [21], and egg white [22], have been developed as pore templates by several researchers. The raw material that has attracted the attention of researchers is clay [23]. Besides being quite abundant, this natural mineral also has good chemical resistance, good thermal stability, and good mechanical properties.

Liu et al. [24] have successfully used natural clay as a raw material in the gelcasting process to fabricate porous ceramics and reported that porosity could be controlled by adjusting sintering temperatures. In addition, low-cost porous ceramics by gelcasting method using clay have also been successfully carried out with a sintering temperature of 1100–1500 °C, reporting that by adjusting

sintering temperatures, pore size distribution and gas permeability can be controlled [25]. However, both of these studies still use AM as a gelling agent. As for the use of cassava starch as a pore template, we have observed previously. The resulting porous ceramics can be used as catalyst support [26]. In addition, Barros Calado et al. [27] using a combination of sunflower oil as a gelling agent and starch consolidation, reported that the manufacturing methods were effective in the production of cellular porous ceramics with low energy, low amounts of gelling agent and low environmental costs. However, the raw material used is synthetic metal oxide powder, i.e., alumina. Based on these perspectives, the challenge to investigate how the sintering temperature affects the microstructure behavior of porous ceramics is necessary for this field. As an improvement, the base material made of clay and cassava starch is applied, which is certainly more environmentally friendly and can be suggested for the industry. To the best of our knowledge, no previous studies have investigated the combination of clay as raw material and cassava starch as a pore template. In addition, quantitative analyses to illustrate the relationship between crystallinity and crystallite size to the porosity response of ceramics are also reported in detail.

■ EXPERIMENTAL SECTION

Materials

Natural clay was taken from South Sulawesi (was slightly ground and sieved to pass 60 mesh, containing 71.12 wt.% SiO₂, 11.98 wt.% Al₂O₃, 5.68 wt.% Fe₂O₃, and less than 0.80 wt.% of TiO₂, CuO, K₂O, ZnO by XRD analysis). The cassava starch (containing 59.97% of starch) and carboxy methyl cellulose (CMC) were used as the dispersant.

Instrumentation

Determination of thermal treatment

Thermal analysis using the thermogravimetric (TG) and differential thermal analysis (DTA) Hitachi STA7300 was used to determine the thermal treatment. On an alumina crucible, 5.947 mg of gelcasted green

body ceramic was weighed. It was isothermally heated at 30 °C for 10 min under airflow (8 L/min) and then heated to 1100 °C in a static air environment. The reference material was alumina, and the heating rate was 30 °C/min.

Mechanical stability

Mechanical stability was measured using Galdabini's Universal Testing Machine (UTM) type PM 100, with a cross-sectional area of 20 × 20 mm.

Chemical stability

Chemical stability is determined by acid and alkali resistance, which is calculated by the weight loss after acid and alkali treatment. The acid solution used is 50% H₂SO₄, while the alkali solution is NaOH is 35% aqueous solution, porous ceramics soaked with chemical reagents for a day.

Procedure

As much as 5 g of natural clay and 0.1 g of CMC were added to distilled water in a ratio of 50:1 (50% vol). Then, the aqueous suspension was added to cassava starch of 9 wt.% [27]. The suspension was moulded, aerated to dry, and heated at 70 °C for 2 h, resulting in gelcasted green body ceramics. After that, the body ceramic was sintered at 900, 1000, and 1100 °C with a heating rate is 50 °C/30 min and thermal treatment based on TGA/DTA results. The fabrication scheme of porous ceramic by gelcasting method in the study as shown in Fig. 1.

Sample characterization

The phase of the specimen was characterized by X-ray diffraction (XRD, Shimadzu 7000) with CuK α radiation ($\lambda = 1.5405 \text{ \AA}$). The average crystallite size was determined by the Debye-Scherrer equation. The microstructures of the specimen were observed by scanning electron microscopy (SEM, JEOL-6000PL), which qualitatively indicated a grain size of 60 mesh. The quantitative analysis was also examined with energy dispersive analysis (EDX), and phase quantification was obtained from SEM-EDX maps by processing EDX area maps using Image JED-2300 software.

Mass shrinkage is determined by calculating the ratio of the difference between the mass of the specimen before and after sintering to the mass before sintering. The bulk density and apparent porosity were measured by the Archimedes principle according to the ASTM C373-88. The hardness test (Hardness Brinell/HB) of porous ceramic samples is made using a microhardness tester. Ceramics are smoothed using Ipolising and sandpaper. Ceramics are placed on the stand and then pressed by a steel ball with a diameter of 10 mm and a load of 5 kg in order to determine the magnitude of hardness.

The pore characteristic of the specimen, including surface area, pore volume, and pore distribution, was determined by adsorption N₂ using a surface area analyzer (SAA, type Quantachrome Nova 4200e) with outgas time

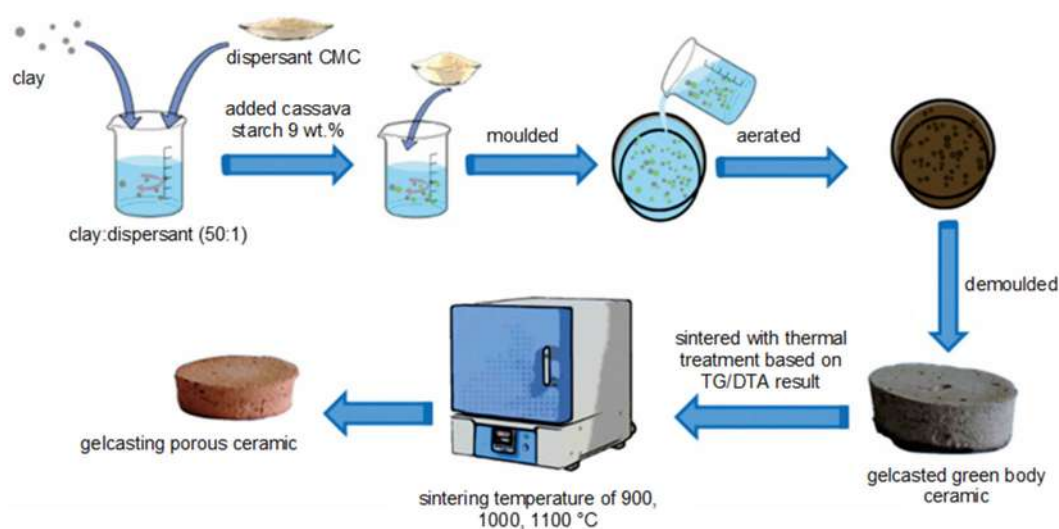


Fig 1. Schematic illustration of fabrication porous ceramic by gel casting method

of 3 h at a temperature of 250 °C. The textural characteristics, such as surface area and pore volume, were determined through the application of the Brunauer-Emmet-Teller (BET) method. The total pore volume was estimated by measuring the amount of adsorbed gas at a relative pressure of $P/P_0 = 0.99$. Additionally, the pore distribution was analyzed using the Barret-Joyner-Halenda (BJH) method.

■ RESULTS AND DISCUSSION

Thermal Cycling

Thermal treatment is an extremely important step in the porous ceramic manufacturing process. In this study, the stages of thermal treatment based on TGA/DTA analysis of gelcasted green body ceramics are shown in Fig. 2. The results showed there are three stages of weight loss during heating. The first stage, noted by the elimination of free and physically adsorbed water from the piece's surface as well as in the starch consolidation, occurs between 25 and 130 °C with a weight loss of 31.66%. This phenomenon agreed with Barros Calado et al. [27]. The second stage corresponds to 23.33% of weight loss at a temperature between 150 and 390 °C possibly due to the thermal decomposition of starch beginning and continuing in the third step with oxidative decomposition. This phenomenon is followed by the exothermic peak at 385 °C on the DTA curve. It is estimated that at this stage, the formation of pores on the green body ceramic has started to occur. The third stage occurs between 400 and 600 °C with a weight loss of 12.80%, possibly due to carbon dioxide released by the degradation of the starch polymer and the release of the hydroxide group from aluminum hydroxide to alumina, respectively [28]. It is also supported by Nie and Lin [29], which reported that the crucial temperature range for burning starch out before ceramic sintering is from 300 to 600 °C.

In addition, the DTA thermogram showed, at 460 °C, an exothermic peak, as shown by the formation of a down peak, indicating the rearrangement of metal oxides to become denser; hence, an exothermic peak develops after 500 °C. Additionally, at temperatures between 600 and 1000 °C associated with the phase transformation from

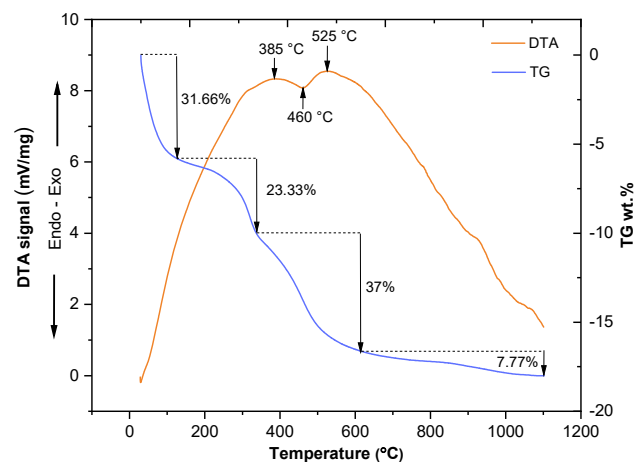


Fig 2. Thermal analysis of gelcasted green body ceramic using TGA/DTA

meta kaolinite to Al-Si spinel [30]. Thus, thermal treatment is carried out by holding temperatures at 100, 400, and 600 °C for 1 h followed by sintering with temperature variations of 900, 1000, and 1100 °C for 2 h.

Mineralogy and Crystallinity

The XRD patterns of the samples sintered at 900, 1000, and 1100 °C are shown in Fig. 3. The crystalline phases are identified as quartz (SiO_2) PDF# 00-046-1045 as a main phase existing in clay [31], mullite ($3\text{SiO}_2 \cdot 2\text{Al}_2\text{O}_3$) PDF# 00-002-0452, and hematite (Fe_2O_3) PDF# 00-002-0919. As the sintering temperature is raised to 1100 °C, the orthoclase ($(\text{Na,K})(\text{Si}_3\text{Al})\text{O}_8$) PDF# 00-009-0478 reflection intensities increase while the quartz reflection starts to decrease as a result of consumption by the ongoing mineral processes. This agrees with Lu et al. [32] who reported the partial dissolution of quartz in glass melts facilitating the nucleation and crystallization of the anorthite phase. The formation of anorthoclase indicates that the Si sites in the clay are retaining the K released at a temperature over 1000 °C [33]. As a result, the produced porous ceramic's mineralogical phases are considerably influenced by the sintering temperature.

In addition, the sintering temperature also affects the crystallinity, crystallite size, and microstrain of samples, as shown in Fig. 4. Crystallinity increased with increasing temperature to 1000 °C and decreased significantly when the sintering temperature was increased to 1100 °C.

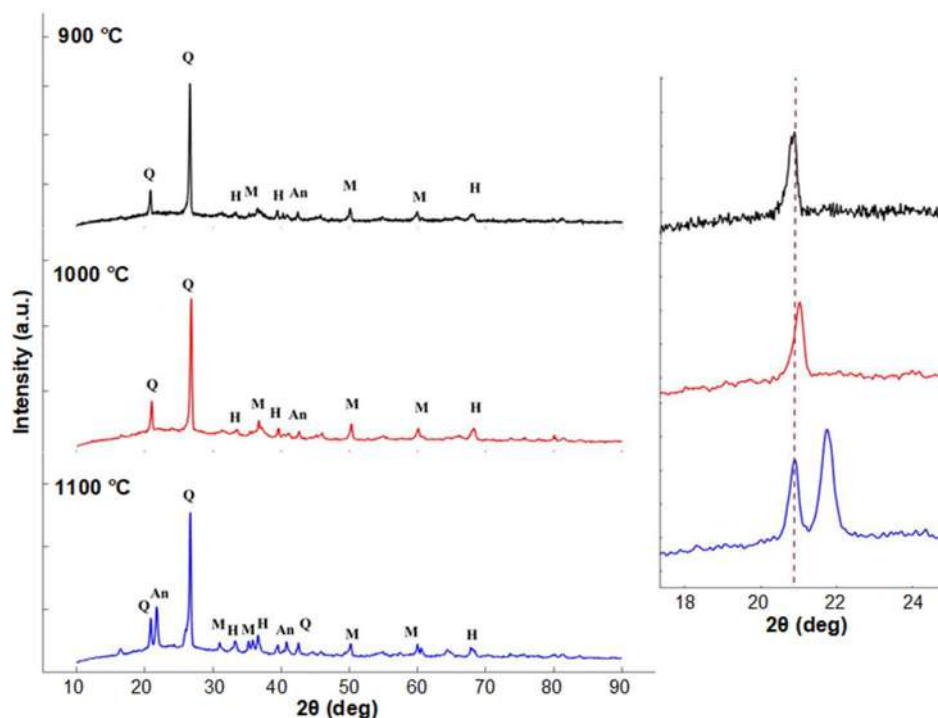
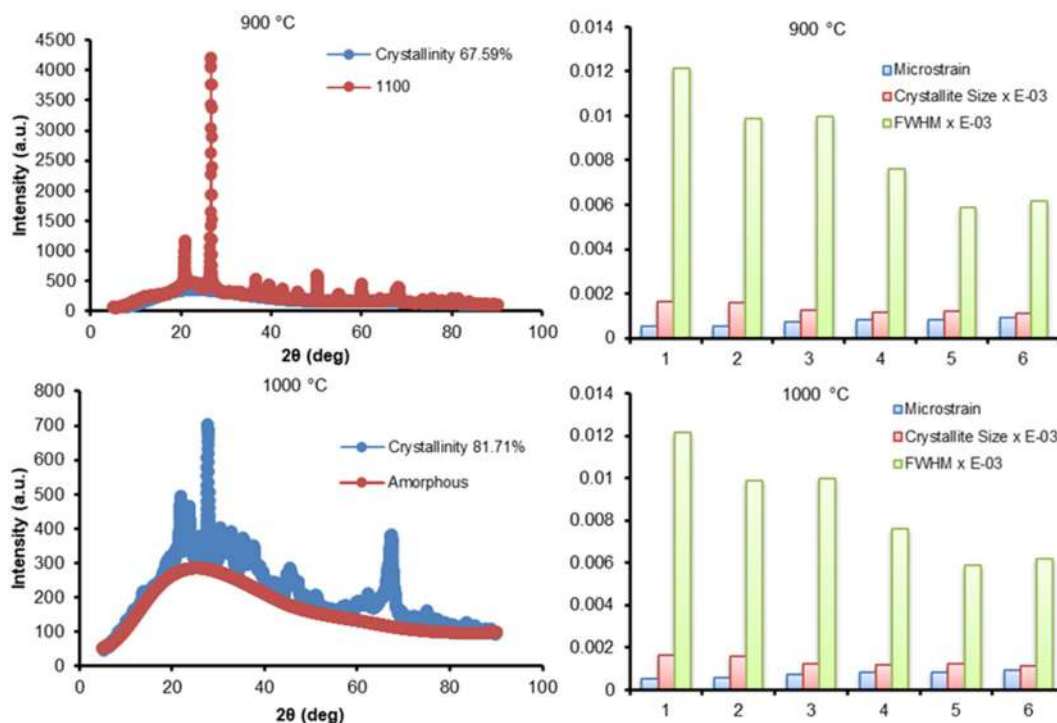


Fig 3. XRD patterns of gelcasted porous ceramics, and the enlarged of spectrum to shows the phase shift as the result of with various sintering temperatures. Q: Quartz, An: Anorthoclase, M: Mullite, H: Hematite



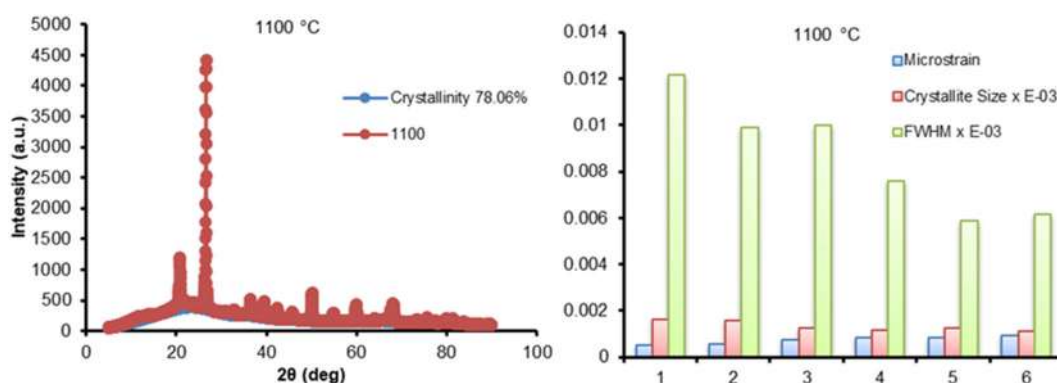


Fig 4. The evaluation of crystallinity, the crystallite size, and microstrain vs full-width half maximum

This is due to the melting of the microstructure typical of the sintering liquid phase and can be attributed to the decrease in mullite intensity (Fig. 3) with increasing sintering temperature. The increase in crystallinity up to 1100 °C was observed with full width at half maxima (FWHM) and did not change with increasing sintering temperature. Sintering temperature up to 1100 °C does not change the crystal phase but only causes an increase in the intensity of the diffraction peak [34].

From the maximum peak FWHM amount, the crystallite size of specimens calculated using the Debye-Scherrer equation as Eq. (1) [35-36],

$$D = \frac{0.9\lambda}{\beta \cos \theta} \quad (1)$$

where λ (1.5406 Å) is the x-ray wavelength radiation of $\text{CuK}\alpha$, β is the full width at FWHM of the diffraction peak, and θ is the Bragg angle. Based on Fig. 4, the crystallite size increased with the increasing sintering temperature of 1000 °C and increased at 1100 °C. It is well known that the higher sintering temperature promotes grain growth, and consequently, crystallite size increases as a function of sintering temperature [37]. The present investigation reveals that the samples' crystallite size exhibited a decreasing trend with an increase in sintering temperature up to 1100 °C. The observed anomalous behavior may be accounted for by positing a significant increase in defect concentration resulting from densification at a temperature of 1000 °C. This phenomenon may be attributed to the relatively low degree of crystallinity exhibited by the specimen at the sintering temperature of 1000 °C, as evidenced by Fig. 4, and the consequent rapid deformation of particles. The

utilization of the Williamson-Hall method was employed to verify the structural parameters of the specimens, whereby the strain was determined through the application of Eq. (2).

$$B_{hkl} \cos \theta = \frac{k\alpha}{D} + (4\epsilon \sin \theta) \quad (2)$$

When using the Williamson-Hall calculation method, it is presumed that the strain is constant throughout crystallographic space and that the material's characteristics are independent of space [38]. Fig. 4 shows the correlation between crystallite size and microstrain; the smaller crystallite size, the microstructure increases. This is corresponded by Venkatesh et al. [39], reported that the decrease in the FWHM of the diffraction peaks with sintering temperature, indicating an improvement in the crystallization process by elimination of defects such as voids or vacancies, crystallite growth, and crystallite coalescence.

Surface Morphology

The SEM images of the samples sintered at 900, 1000, and 1100 °C are shown in Fig. 5. The surface morphology shows heterogeneous microstructures with large pores in the sample sintered at 900 °C. The high porosity is responsible for the thermal degradation of starch. The sample is more microstructurally dense when sintered at 1000 °C, but the porosity is still significant, which can be attributed to a lack of vitreous phase to completely fill all the narrow pores. In contrast, the number of narrow pores decreases at a sintering temperature of 1100 °C, due to the fluxing effects of these

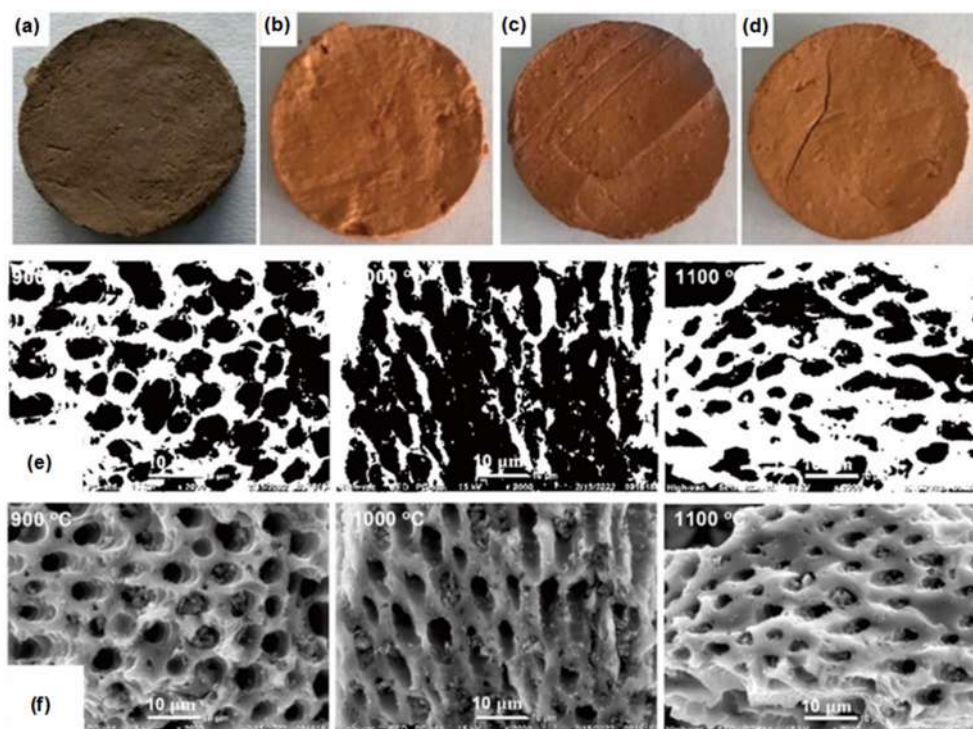


Fig 5. Digital photos of (a) green body porous ceramic, sintered porous ceramic at temperatures (b) 900 °C, (c) 1000 °C, (d) 1100 °C, (e) grayscale of SEM image for more visibility of porosity boundary, (f) SEM images of samples with various sintering temperature with 2000× magnification

oxides. The presence of alkaline-rich phases in the sample speeds up the vitrification process [40]. A vitreous phase may also be induced by the amorphous silica produced during the breakdown of metakaolin [33]. As the temperatures increase, the number of narrow pores is decreased by this phase's binds the particles strong.

Apparent Porosity, Density, and Hardness

The sintering temperatures have a significant effect on the apparent porosity, density, and hardness of gelcasted porous ceramics, as shown in Table 1. Porosity decreases as the sintering temperature increases, which parallels the increase in mass shrinkage and density. It can be explained by body densification, which promotes partial removal of porosity at high temperatures. This result is supported by the results obtained by SEM (Fig. 5), where the formation of the vitreous phase increases with the highest sintering temperature [33]. When the sintering temperature was increased to 1100 °C the porosity decreased, and the mass shrinkage and density increased. This is due to the driving force of densification increased.

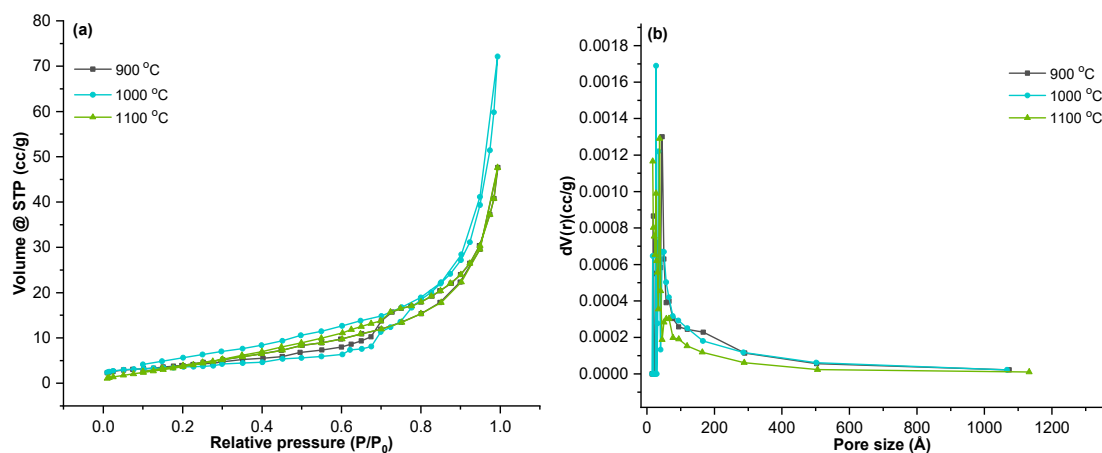
Thus, when excessive sintering temperature leads to the collapse of the ceramic structure, and therefore, cracks in the ceramic body are observed (Fig. 6). These results imply that there is an upper limit for sintering.

Based on the result of chemical stability, the porosity of ceramic has a significant impact on the chemical stability of specimens. Based on Fig. 5(e) and (f), the increase in porosity will deteriorate the chemical resistance of the specimen. It can be attributed to the increasing porosity of a material, the easier it is for acids and bases to be adsorbed [15], which can be associated with a decrease in the hardness of the specimen. The porous ceramic is least resistant in sulfuric acid solution than in sodium hydroxide solution. Chemical stability results were carried out with two different solvents, such as acid and alkali solutions. The stability results can be written as follows: (1) in acid solution are presented 0.0350 ± 0.002 , 0.0027 ± 0.019 , and $0.0110 \pm 0.006\%$ for 900, 1000, and 1100 °C, respectively; (2) in alkali solution are presented 0.022 ± 0.015 , 0.009 ± 0.013 , and $0.008 \pm 0.008\%$ for 900, 1000, and 1100 °C, respectively. These

Table 1. Effect of sintering temperature on mass shrinkage, apparent porosity, density, and hardness of gelcasted porous ceramics

Sintering temperature (°C)	Mass shrinkage (%)	Apparent porosity (%)	Density (g/cm ³)	Hardness (HB)	Ref.
900	12.93 ± 0.20	39.44 ± 0.30	10.54 ± 0.02	94.00	This study
1000	16.37 ± 0.10	37.88 ± 0.20	18.56 ± 0.02	101.00	This study
1100	20.48 ± 0.20	29.19 ± 0.20	46.88 ± 0.01	108.00	This study
500	18.70	0.00	-	25.27 ± 1.00	
600	18.60	0.20	-	22.74 ± 1.50	[41]
700	9.15	26.80	-	6.87 ± 1.20	
1350	17.42	11.17	-	5.80	
1400	20.79	4.42	-	7.70	[42]
1450	21.73	1.19	-	11.10	
1500	22.66	0.29	-	13.20	
1550	22.33	0.42	-	12.50	
1250	0.48 ± 0.17	50.56 ± 0.30	1.37 ± 0.01	25.95 ± 3.46	[43]
1550	2.38 ± 0.62	48.05 ± 1.45	1.44 ± 0.04	36.00 ± 9.28	[43]
1270	15.30	49.90	0.97	-	[44]
1100	-	50.00	1.05	-	[45]
800	-	50.20	1.26	-	[46]

Note for (-) is not reported

**Fig 6.** (a) Isotherm of adsorption-desorption curves and (b) pore size distribution of samples

results are associated with the presence of iron compounds in the ceramic body according to the results of the XRD analysis in Fig. 3, which then react with acids to form water-soluble iron sulfate compounds and exchange alkaline ions contained in the ceramic body with hydrogen ions from the acid. The results of the XRD analysis also indicated the presence of silica in the form of quartz. The low acid resistance is also caused by the hydrolysis of the Si-O bond, which is known as the breakdown of the silica framework.

The hardness of samples increases when the sintering temperature increases and is inversely proportional to porosity. The increase of hardness properties at the sintering temperature of 1100 °C was due to the progressive formation of anorthoclase (a vitreous phase that fills the narrow pores) and mullite (strong crystalline phase) (as shown in Fig. 3), which increases the mechanical strength [47]. However, in order to obtain porous ceramic with high porosity (39.44%) and sufficient hardness property (94.00 HB),

Table 2. Pore characteristics of samples

Sintering temperatures (°C)	S_{BET} (m^2/g)	V_t (cm^3/g)	Average pore diameter (Å)
900	16.58	0.14	21.26
1000	17.83	0.09	21.19
1100	16.61	0.13	21.41

the optimal temperature suitable for sintering is 900 °C. The resulting hardness is almost the same as the results of our previous study using acrylamide polymer as a pore template [48]. For the result of mechanical stability, the effect of sintering temperature shows linear results on compression strength. Specimen dimensions were used as a benchmark in determining sample mechanics, where the 1100, 1000, and 900 °C have pressure results with 10.90, 10.27, and 9.56 MPa, respectively. This difference in pressure resistance can be influenced by changes in microstructure and d-spacing properties at the unit crystal scale [49-51].

Pore Characteristics

Pore characteristics consist of specific surface area (S_{BET}), volume total (V_t), and average pore diameter are shown in Fig. 6 and the corresponding in Table 2. There are no obvious hysteresis loops, as can be seen in the N_2 adsorption-desorption isotherms curves of the samples (Fig. 5(a-d)). According to the Brunauer-Deming-Deming-Teller classification, the adsorption isotherms for all samples are close to type III, indicating the interaction of the adsorbate with the adsorbed layer is greater than the interaction with the adsorbent surface [52].

Based on Table 2, the pore characteristics of gelcasted porous ceramic are not affected by sintering temperatures. The specific surface area in this study is higher when compared to our previous study, which used polyacrylamide as the pore template [53]. The specific area observed by Salomão and Brandi [54] which used chitosan as a pore template of 7 m^2/g , is lower than in this study. The average pore size of all samples was microporous, indicating the material suitable as a support catalyst and wastewater filter [55]. The specific surface area increases at the sintering temperature of 900 to 1000 °C, and decreases at 1100 °C. This is related to the formation of the molten phase at temperatures above

1000 °C, which promotes sintering of the liquid phase [8]. However, this contradicts the apparent porosity of the sample (Table 1), which shows a decrease in porosity with increasing sintering temperature. This anomalous behavior is thought to be related to the defects produced during densification which are associated with sample crystallinity and rapid particle deformation [32].

CONCLUSION

Porous ceramics were formed by the gelcasting method using clay and cassava starch. Pore formation was largely caused by the thermal degradation of starch so a thermal study was carried out using TGA/DTA to determine thermal cycling. The crystalline phase is identified as quartz, mullite, and hematite for the samples sintered at 900, 1000, and 1100 °C. Based on the XRD results, the crystallinity of the ceramic decreased while the lattice strain increased when the sintering temperature increased. Then, the porosity of the ceramic decreased with increasing sintering temperatures. The hardness properties were significantly improved as the sintering temperatures were increased from 900 to 1100 °C. The pore characteristics are not affected by sintering temperatures, and the average pore size for all samples was microporous. The findings imply that the sintering temperature can be used to continually regulate the microstructure properties of porous ceramics based on clay.

ACKNOWLEDGMENTS

This work was supported by DRTPM Ministry of Education, Culture, Research, and Technology Republic of Indonesia in the scheme of *Penelitian Dasar Unggulan Perguruan Tinggi* (PDUPT) contract number 109/UN36.11/LP2M/2021 and *Lembaga Penelitian dan Pengabdian Masyarakat* (LP2M) Universitas Negeri Makassar that has held writing workshops of scientific

articles in reputable international journals as a forum for the creation of this research article.

■ AUTHOR CONTRIBUTIONS

Suriati Eka Putri conducted the experiment and wrote the manuscript, Diana Eka Pratiwi revised the manuscript, Rachmat Triandi Tjahjanto and Dahlang Tahir did proofreading the manuscript, Nita Magfirah Ilyas conducted the TGA/DTA analysis, Abd Rahman conducted the BET and BJH calculations, and Heryanto conducted the XRD analysis and finalization. All authors agreed to the final version of this manuscript.

■ REFERENCES

- [1] Guo, W., Hu, T., Qin, H., Gao, P., and Xiao, H., 2021, Preparation and *in situ* reduction of Ni/SiC_xO_y catalysts supported on porous SiC ceramic for ethanol steam reforming, *Ceram. Int.*, 47 (10, Part A), 13738–13744.
- [2] Putri, S.E., Pratiwi, D.E., Tjahjanto, R.T., Hasri, H., Andi, I., Rahman, A., Ramadhani, A.I.W.S., Ramadhani, A.N., Subaer, S., and Fudholi, A., 2022, The renewable of low toxicity gelcasting porous ceramic as Fe₂O₃ catalyst support on phenol photodegradation, *Int. J. Des. Nat. Ecodyn.*, 17 (4), 503–511.
- [3] Putri, S.E., Pratiwi, D.E., Triandi, R., Mardiana, D., and Side, S., 2018, Performance test of gelcasted porous ceramic as adsorbent of azo dyes, *J. Phys.: Conf. Ser.*, 1028, 012039.
- [4] Kim, I.J., Park, J.G., Han, Y.H., Kim, S.Y., and Shackelford, J.F., 2019, Wet foam stability from colloidal suspension to porous ceramics: A review, *J. Korean Ceram. Soc.*, 56 (3), 211–232.
- [5] Chen, Y., Wang, N., Ola, O., Xia, Y., and Zhu, Y., 2021, Porous ceramics: Light in weight but heavy in energy and environment technologies, *Mater. Sci. Eng.: R: Rep.*, 143, 100589.
- [6] Ismail, A.K., Abdullah, M.Z., Zubair, M., Jamaludin, A.R., and Ahmad, Z.A., 2016, Effect of ceramic coating in combustion and cogeneration performance of Al₂O₃ porous medium, *J. Energy Inst.*, 89 (1), 81–93.
- [7] Fontão, N.C., Ferrari, L.N., Sapatieri, J.C., Rezwan, K., and Wilhelm, M., 2022, Influence of the pyrolysis temperature and TiO₂-incorporation on the properties of SiOC/SiC composites for efficient wastewater treatment applications, *Membranes*, 12 (2), 175.
- [8] Akhtar, F., Rehman, Y., and Bergström, L., 2010, A study of the sintering of diatomaceous earth to produce porous ceramic monoliths with bimodal porosity and high strength, *Powder Technol.*, 201 (3), 253–257.
- [9] Nepomuceno, M.C.S., Bernardo, L.F.A., Pereira-de-Oliveira, L.A., and Timóteo, R.O., 2021, Cement-based grouts for masonry consolidation with high content of limestone filler, metakaolin, glass powder and ceramic waste, *Constr. Build. Mater.*, 306, 124947.
- [10] Liu, K., Zhou, C., Chen, F., Sun, H., and Zhang, K., 2020, Fabrication of complicated ceramic parts by gelcasting based on additive manufactured acetone-soluble plastic mold, *Ceram. Int.*, 46 (16, Part A), 25220–25229.
- [11] de Moraes Santos, L.N.R., de Melo Cartaxo, J., Silva, J.R.S., Rodrigues, A.M., de Andrade Dantas, E.L., de Sousa, F.B., de Araújo Neves, G., and Menezes, R.R., 2021, High porous ceramics with isometric pores by a novel saponification/gelation/freeze-casting combined route, *J. Eur. Ceram. Soc.*, 41 (14), 7111–7118.
- [12] Shahbazi, H., and Tataei, M., 2019, A novel technique of gel-casting for producing dense ceramics of spinel (MgAl₂O₄), *Ceram. Int.*, 45 (7, Part A), 8727–8733.
- [13] Hooshmand, S., Nordin, J., and Akhtar, F., 2019, Porous alumina ceramics by gel casting: Effect of type of sacrificial template on the properties, *Int. J. Ceram. Eng. Sci.*, 1 (2), 77–84.
- [14] Jesus, M.A.M.L., Ferreira, A.M., Lima, L.F.S., Batista, G.F., Mambrini, R.V., and Mohallem, N.D.S., 2021, Micro-mesoporous TiO₂/SiO₂ nanocomposites: Sol-gel synthesis, characterization, and enhanced photodegradation of quinoline, *Ceram. Int.*, 47 (17), 23844–23850.

- [15] Han, L., Li, F., Zhang, H., Dong, L., Pei, Y., Zhu, Q., Wu, W., Jia, Q., and Zhang, S., 2019, Low-temperature preparation of porous diatomite ceramics via direct-gelcasting using melamine and boric acid as cross-linker and sintering agent, *Ceram. Int.*, 45 (18, Part A), 24469–24473.
- [16] Jana, D.C., Sundararajan, G., and Chattopadhyay, K., 2017, Effect of monomers content in enhancing solid-state densification of silicon carbide ceramics by aqueous gelcasting and pressureless sintering, *Ceram. Int.*, 43 (6), 4852–4857.
- [17] Han, L., Li, F., Huang, L., Zhang, H., Pei, Y., Dong, L., Zhang, J., and Zhang, S., 2018, Preparation of Si₃N₄ porous ceramics via foam-gelcasting and microwave-nitridation method, *Ceram. Int.*, 44 (15), 17675–17680.
- [18] Bengisu, M., and Yilmaz, E., 2002, Gelcasting of alumina and zirconia using chitosan gels, *Ceram. Int.*, 28 (4), 431–438.
- [19] Kandi, K.K., Thallapalli, N., Kumar, M.S., and Raod, C.S.P., 2019, Fabrication and parametric optimization of SiO₂-BN gelcast ceramic composites using response surface methodology, *Mater. Today: Proc.*, 18, 2298–2307.
- [20] Wan, W., Huang, C., Yang, J., and Qiu, T., 2014, Study on gelcasting of fused silica glass using glutinous rice flour as binder, *Int. J. Appl. Glass Sci.*, 5 (4), 401–409.
- [21] Luchese, C.L., Spada, J.C., and Tessaro, I.C., 2017, Starch content affects physicochemical properties of corn and cassava starch-based films, *Ind. Crops Prod.*, 109, 619–626.
- [22] He, X., Su, B., Zhou, X., Yang, J., Zhao, B., Wang, X., Yang, G., Tang, Z., and Qiu, H., 2011, Gelcasting of alumina ceramics using an egg white protein binder system, *Ceram.-Silik.*, 55 (1), 1–7.
- [23] Mohammed, M.N., Yusoh, K., and Haji Shariffuddin, J.H., 2020, Thermal and structure analysis based on exfoliation of clay in thermosensitive polymer by *in-situ* polymerization, *Indones. J. Chem.*, 20 (1), 88–95.
- [24] Liu, Y.F., Liu, X.Q., Wei, H., and Meng, G.Y., 2001, Porous mullite ceramics from national clay produced by gelcasting, *Ceram. Int.*, 27 (1), 1–7.
- [25] Liu, Y.F., Liu, X.Q., Li, G., and Meng, G.Y., 2001, Low cost porous mullite-corundum ceramics by gelcasting, *J. Mater. Sci.*, 36 (15), 3687–3692.
- [26] Putri, S.E., Pratiwi, D.E., Tjahjanto, R.T., and Rahman, A., 2022, The effect of binder concentration on the ability of gelcasting porous ceramics as TiO₂ support catalyst, *Indones. J. Fundam. Sci.*, 8 (1), 51–60.
- [27] Barros Calado, C.M., Iturri, M.S., Colonetti, V.C., Constantino de Souza, V., Fernandes, C.P., Hotza, D., and Novy Quadri, M.G., 2021, Green production of cellular ceramics by emulsification of sunflower oil followed by gelcasting and starch consolidation, *J. Cleaner Prod.*, 282, 124468.
- [28] Offner, A., Bach, A., and Sauvart, D., 2003, Quantitative review of *in situ* starch degradation in the rumen, *Anim. Feed Sci. Technol.*, 106 (1-4), 81–93.
- [29] Nie, Z., and Lin, Y., 2015, Fabrication of porous alumina ceramics with corn starch in an easy and low-cost way, *Ceram.-Silik.*, 50 (4), 348–352.
- [30] Low, I.M., and McPherson, I.M., 1988, The structure and composition of Al-Si spinel, *J. Mater. Sci. Lett.*, 7 (11), 1196–1198.
- [31] Kagonbé, B.P., Tsozué, D., Nzeukou, A.N., and Ngos, S., 2021, Mineralogical, physico-chemical and ceramic properties of clay materials from Sekandé and Gashiga (North, Cameroon) and their suitability in earthenware production, *Heliyon*, 7 (7), e07608.
- [32] Lu, J., Li, Y., Zou, C., Liu, Z., and Wang, C., 2018, Effect of sintering additives on the densification, crystallization and flexural strength of sintered glass-ceramics from waste granite powder, *Mater. Chem. Phys.*, 216, 1–7.
- [33] Mouiya, M., Bouazizi, A., Abourriche, A., Benhammou, A., El Hafiane, Y., Ouammou, M., Abouliatim, Y., Younssi, S.A., Smith, A., and Hannache, H., 2019, Fabrication and characterization of a ceramic membrane from clay and banana peel powder: Application to industrial wastewater treatment, *Mater. Chem. Phys.*, 227, 291–301.

- [34] Almasri, K.A., Sidek, H.A.A., Matori, K.A., and Mohd Zaid, M.H., 2017, Effect of sintering temperature on physical, structural and optical properties of wollastonite based glass-ceramic derived from waste soda lime silica glasses, *Results Phys.*, 7, 2242–2247.
- [35] Jangong, O.S., Heryanto, H., Rahmat, R., Mutmainna, I., Gareso, P.L., and Tahir, D., 2021, Effect of sugar palm fiber (SPF) to the structural and optical properties of bioplastics (SPF/starch/chitosan/polypropylene) in supporting mechanical properties and degradation performance, *J. Polym. Environ.*, 29 (6), 1694–1705.
- [36] Suryani, S., Heryanto, H., Rusdaeni, R., Fahri, A.N., and Tahir, D., 2020, Quantitative analysis of diffraction and infra-red spectra of composite cement/BaSO₄/Fe₃O₄ for determining correlation between attenuation coefficient, structural and optical properties, *Ceram. Int.*, 46 (11, Part B), 18601–18607.
- [37] Singh, L.K., Bhadauria, A., Jana, S., and Laha, T., 2018, Effect of sintering temperature and heating rate on crystallite size, densification behaviour and mechanical properties of Al-MWCNT nanocomposite consolidated via spark plasma sintering, *Acta Metall. Sin. (Engl. Lett.)*, 31 (10), 1019–1030.
- [38] Reddy, M.P., Shakoor, R.A., Mohamed, A.M.A., Gupta, M., and Huang, Q., 2016, Effect of sintering temperature on the structural and magnetic properties of MgFe₂O₄ ceramics prepared by spark plasma sintering, *Ceram. Int.*, 42 (3), 4221–4227.
- [39] Venkatesh, D., Siva Ram Prasad, M., Rajesh Babu, B., Ramesh, K.V., and Trinath, K., 2015, Effect of sintering temperature on the micro strain and magnetic properties of Ni-Zn nanoferrites, *J. Magn.*, 20 (3), 229–240.
- [40] Mouiya, M., Bouazizi, A., Abourriche, A., El Khessaimi, Y., Benhammou, A., El hafiane, Y., Taha, Y., Oumam, M., Abouliatim, Y., Smith, A., and Hannache, H., 2019, Effect of sintering temperature on the microstructure and mechanical behavior of porous ceramics made from clay and banana peel powder, *Results Mater.*, 4, 100028.
- [41] Feng, D., Ren, Q., Ru, H., Wang, W., Jiang, Y., Ren, S., and Zhang, C., 2019, Effect of oxygen content on the sintering behaviour and mechanical properties of SiC ceramics, *Ceram. Int.*, 45 (18, Part A), 23984–23992.
- [42] Liu, P., Li, Z., Xiao, P., Luo, H., and Jiang, T., 2018, Microstructure and mechanical properties of *in-situ* grown mullite toughened 3Y-TZP zirconia ceramics fabricated by gelcasting, *Ceram. Int.*, 44 (2), 1394–1403.
- [43] Mohamed Ariff, A.H., Mohamad Najib, M.A., Mohd Tahir, S., As'Arry, A., and Mazlan, N., 2021, Effect of sintering temperature on the properties of porous Al₂O₃-10 wt% RHA/10 wt% Al composite, *Adv. Mater. Process. Technol.*, 7 (3), 417–428.
- [44] Lin, K.L., Chang, J.C., Shie, J.L., Chen, H.J., and Ma, C.M., 2012, Characteristics of porous ceramics produced from waste diatomite and water purification sludge, *Environ. Eng. Sci.*, 29 (6), 436–446.
- [45] Bahrami, A., Simon, U., Soltani, N., Zavareh, S., Schmidt, J., Pech-Canul, M.I., and Gurlo, A., 2017, Eco-fabrication of hierarchical porous silica monoliths by ice-templating of rice husk ash, *Green Chem.*, 19 (1), 188–195.
- [46] Hao, L., Gao, W., Yan, S., Niu, M., Liu, G., and Hao, H., 2019, Preparation and characterization of porous ceramics with low-grade diatomite and oyster shell, *Mater. Chem. Phys.*, 235, 121741.
- [47] Aksel, C., 2003, The effect of mullite on the mechanical properties and thermal shock behaviour of alumina–mullite refractory materials, *Ceram. Int.*, 29 (2), 183–188.
- [48] Putri, S.E., and Pratiwi, D.E., 2016, The Effect of Mole Ratio of Acrylamide (AM) Monomer and Methylene-bis-acrylamide (MBAM) Crosslinker Toward the Hardness of Gelcasting Porous Ceramics, *Proceeding of ICMSTEA 2016: International Conference on Mathematics, Science, Technology, Education and their Applications*,

- Makassar, Indonesia, 3rd–4th October 2016, 412–415.
- [49] Amir, N., Tahir, D., and Heryanto, H., 2023, Synthesis, structural and optical characteristics of activated carbon photocatalysts to adsorb pesticide waste, *J. Mater. Sci.: Mater. Electron.*, 34 (5), 445–458.
- [50] Ilyas, S., Heryanto, H., and Tahir, D., 2021, Correlation between structural and optical properties of CuO/carbon nanoparticle in supports the photocatalytic performance and attenuate the electromagnetic wave, *J. Environ. Chem. Eng.*, 9 (1), 104670.
- [51] Heryanto, H., and Tahir, D., 2021, The correlations between structural and optical properties of magnetite nanoparticles synthesised from natural iron sand, *Ceram. Int.*, 47 (12), 16820–16827.
- [52] Brunauer, S., Deming, L.S., Deming, W.E., and Teller, E., 1940, On a theory of the van der Waals adsorption of gases, *J. Am. Chem. Soc.*, 62 (7), 1723–1732.
- [53] Putri, S.E., Pratiwi, D.E., Tjahjanto, R.T., Mardiana, D., and Subaer, S., 2018, On the effect of acrylamide and methylenebicacrylamid ratio on gelcasted ceramic pore character, *J. Chem. Technol. Metall.*, 53 (5), 841–844.
- [54] Salomão, R., and Brandi, J., 2013, Macrostructures with hierarchical porosity produced from alumina-aluminum hydroxide-chitosan wet-spun fibers, *Ceram. Int.*, 39 (7), 8227–8235.
- [55] Wang, W., Wang, M., Feng, X., Zhao, W., Luan, C., and Ma, J., 2018, Effects of deposition temperature on the structural and optical properties of single crystalline rutile TiO₂ films, *Mater. Chem. Phys.*, 211, 172–176.

Spectrophotometric Determination of Trace Quantities of Pure Atropine and Pharmaceutical Preparations with SbI_4^{2-} Ion

Riyadh Hasan Mohammed Ali*, Bashar Mudhaffar Abdullah, and Rasha Ismail Ahmed

Department of Medical Laboratories Techniques, Al-Rafidain University College, Baghdad 00964, Iraq

* Corresponding author:

email: ryadhhasan1@ruc.edu.iq

Received: November 8, 2022

Accepted: May 27, 2023

DOI: 10.22146/ijc.79010

Abstract: This study aims to estimate a simple, rapid and sensitive method for a trace amount of atropine (ATR) in medicinal compounds. Two approaches were followed to accomplish this aim, i.e., spectrophotometric determination of pure ATR and pharmaceutical preparations using SbI_4^{2-} ion as a new reagent. The procedure involves the implementation of an ion-association complex with this alkaloid. The resulting complex was extracted and detected spectrophotometrically at 492 nm. Appropriate parameters were investigated, including the ion SbI_4^{2-} concentration and the pH value of the complex formation. Using chloroform to extract the complex, taking into consideration extraction time and volume of solvent used. The calibration graph is linear in the ranges of $0.5-5.0 \times 10^{-3}$ M. Precision, accuracy, detection limit, and RSD %, as well as relative standard deviation ($n = 5$), were calculated. The test sensitivity was $0.013 \mu\text{g cm}^{-2}$. Several interference additives were studied by investigating the effect of equal and duplicate quantities of some common excipients on selectivity, such as starch, glucose, lactose, glycerin, and talc. The molar ratio of the SbI_4^{2-} -ATR was determined. The amount of ATR in the pharmaceutical tablets and eye drop preparation was calculated using E_{rel} at ratios of 2.24 and 2.75%, respectively.

Keywords: atropine; spectrophotometer; SbI_4^{2-} -atropine complex; solvent extraction; pharmaceutical compounds

■ INTRODUCTION

Numerous effects of atropine (ATR), such as treating slow heart rate or lowering secretions or intraocular pressure, are irreplaceable without this substance at specific concentrations when urgently needed and for a variety of objectives. For this reason, a number of research groups and scientists, including chemists and pharmacists, are working together to establish a valid procedure to estimate a trace amount of ATR, which leads to learning more about ATR, as well as the numerous analytical methods for determining trace amounts, following simple and rapid steps, and understanding its features. As a result, the concept of research was born [1-5].

Many analytical techniques are competing in research and focus on this important medicinal substance, its locations in the parts of plants and their concentration sites. We outline here some of the important results and

key findings in this field. Optimization of parameters for conventional heated solid-liquid extraction of ATR from *Datura stramonium* seeds was obtained by the particle size, temperature, and ethanol concentration [6].

Electrochemiluminescence sensors are used for forensic analysis to detect and quantify ATR with linearity across a concentration range of 0.75 to 100 μM [7]. To measure ATR in belladonna leaves, an HPLC method was designed and validated. Analysis of the analytical curves of atropine revealed linearity 50–200 $\mu\text{g mL}^{-1}$ with $R^2 = 0.9996$, LOD and LOQ of 3.75 and 11.4 $\mu\text{g mL}^{-1}$, respectively. The approach was precise, repeatable, and accurate, with a recovery rate of 103% [8].

Two methods have been applied for the spectrophotometric determination of ATR in bulk sample and in dosage form. The first with bromphenolblue (BPB). The calibration graph is linear

in the ranges of 0.5–40 $\mu\text{g mL}^{-1}$. The second method with 2,3-dichloro-5,6-dicyano-*p*-benzoquinone (DDQ) with a linearity range of 2.5–50.0 $\mu\text{g mL}^{-1}$ [9]. A planar electrochemical cell was used for the first time for the voltammetric determination of ATR with a LOD reaching 0.08 μM [10].

Methods for determining pharmaceuticals using extractive, sensitive spectrophotometers, and spectrofluorometric preparations such as tablets and suppositories have been carried out. Meralazine and 2,6-dihydroxybenzoic acid were found to yield colored products where oxidative coupling reaction with other reagents shows the highest absorption, Beer's rule was consistent at concentrations ranging from 1.25–30 and 0.5–12.5 $\mu\text{g mL}^{-1}$ when measured at 640 and 515 nm alternately [11-14]. The utilization of ion pair production allows multiple analytical techniques, like as extraction, spectrophotometry, and their combination [15-16].

In this regard, the new research falls within the scope of competition for the speed and simplicity of the innovative scientific method, as well as minor quantities in the concentration found. Using the SbI_4^{2-} ion reagent, a new procedure for determining a pure alkaloid in pharmaceutical preparations was described. The goal of the method involves producing a simple, rapid, and sensitive, involve extracting an ion pair complex between the organic base ATR and the inorganic ion and measuring the intensity of the color complex in the organic phase using spectrophotometric analysis at 492 nm. In this procedure, the ideal experimental settings were investigated, including SbI_4^{2-} concentration, pH value, types of extraction solvents, volume and shaking time, phase ratio, and the number of extractions. In addition, to study the expected interactions of such compounds, we conducted stoichiometric studies on the molar ratio and compared the results with previous studies.

■ EXPERIMENTAL SECTION

Materials

The materials used in this study were eye-drop atropine sulfate 1% cooper (S.A Pharmaceuticals) ($\text{C}_{17}\text{H}_{23}\text{NO}_3$) $_2 \cdot \text{H}_2\text{SO}_4 \cdot \text{H}_2\text{O}$). L-Ascorbic acid (Alpha chemika, Batch No.LA503). Different organic solvents

were used, such as dichloromethane, chloroform, 1,2-dichloroethane, xylene and toluene. Sb(II) stock standard solution (BDH) and ATR sulfate analar from Fluka (Mr. 694.63) were purchased. The drugs used in this work were taken from the local market.

Instrumentation

The instrumentations used in this study were a Shimadzu UV-1800 UV/visible scanning spectrophotometer; 115 VAC, was used to measure the absorbance of all samples in this work. Operational spectrum was 190 to 1100 nm. The instrument was equipped with a quartz cell. The pH of samples was measured using Eutech Instruments/pH 700/pH/mV $^{\circ}\text{C}/^{\circ}\text{F}$ meter.

Procedure

In this study, each 1 mL of eye-drop ATR sulfate contains 10 mg ATR sulfate. Alkaloid stock standard solutions were prepared. Lower concentrations of the stock solutions were prepared by dilution of 0.0600 g of ATR sulfate in a 50 mL volumetric flask. ATR 1000 $\mu\text{g mL}^{-1}$ was prepared by dissolving 0.0600 g of atropine sulfate in a 50 mL volumetric flask. The working solution of SbI_4^{2-} was prepared by adding 1.0 mL of antimony stock solution to 50 mL volumetric flask with 10 mL of 1:1 H_2SO_4 , 5 mL of 2% (wt/v) ascorbic acid, and 10 mL of 40% (wt/v) KI, stand for 10 min and proceed with deionized water (DIW) to the mark and shake for homogeneity and reading the maximum absorbance against H_2O as a blank [17]. A 1,000 $\mu\text{g mL}^{-1}$ of Sb(II) stock standard solution was used. Intermediate standard solution concentrations were freshly generated by dilution ten times. Pharmaceutical grade ATR tablets SDI, Entro-stop, ATR sulfate (0.025 mg) were used in this work. All other chemicals and reagents were of analytical grade. DIW was used throughout this work.

Optimization of experimental parameters

The influence of varying parameters on the color intensity was studied to attain maximal sensitivity. A number of preparatory experiments were established for the fast and quantitative synthesis of colored complexes,

such as concentration of SbI_4^{2-} , pH-value, reaction time, kinds of extracting solvents, number of extractions, and shaking time.

Effect concentration of SbI_4^{2-} . The effect of SbI_4^{2-} concentration was studied by using a fixed quantity each time of ATR with different amounts of prepared SbI_4^{2-} (from 0.5 to 3.5 mL) of 2.0×10^{-4} M and extracting the colored complex with 4 mL of chloroform and measure the absorbance, at 492 nm (Table 2). It was concluded that 2.0 mL of the prepared concentration of SbI_4^{2-} is required to obtain maximum absorbance and remains constant by increasing the volume of the reagent, and it has no effect on the determination of the alkaloid. The influence of pH on the development of the SbI_4^{2-} -ATR complex has been investigated also. This is performed by changing the pH by 0.1 M of HCl or NaOH from pH 1 to 8 and measuring the absorbance. This is performed after fixing all the other conditions. Then the complex formed was extracted with 4 mL chloroform and the absorbance at 492 nm was measured against the blank; the highest absorbance was obtained at pH 2.0–3.0 (Table 1).

Influence of the reaction time. The reaction was carried out at different times (2–20 min) while keeping other conditions constant. It was estimated that 5 min is sufficient for a complete reaction to reach maximum absorbance.

Quantity of extractions, types of extraction solvents, and shaking duration. Different organic solvents were used to get better efficiency of extraction, such as dichloromethane, chloroform, 1,2-dichloroethane, xylene, and toluene. Extraction time and the number of extractions were studied to reach the maximum absorbance. Chloroform was found to be a sufficient solvent, and 1 min with one batch extraction is enough to complete extraction.

A spectrum of the SbI_4^{2-} -ATR

The maximum absorption of the complex was studied by scanning the spectrum of the extracted colored ion-association complex of SbI_4^{2-} -ATR from 200–600 nm, and it indicates that the maximum absorbance is at 492 nm.

Interferences sample preparation

Stock solutions of 1,000 ppm of the common excipients such as starch, glucose, lactose, glycerin, and

talk were prepared by dissolving 0.025 g each with suitable solvents and continued to 25 mL of the solvent.

M/L ratio

An aliquot of the ATR standard solution (0.5 to 4.0 mL) was transferred to 10 mL test tubes, each containing 1.0 mL of SbI_4^{2-} standard solution at the greatest wavelength.

Analytical procedure

Calibration graph. The calibration graph was managed using standard solutions at the optimum conditions of the experiment. A series of 10 mL graduated cylinders are added aliquots of stock solution of 2.0×10^{-5} M ATR concentration. A stock solution of 2.0 mL of SbI_4^{2-} was then added to the mixtures. After shaking the mixture, it was left to stand for 5 min. The volume was subsequently increased to 5.0 mL with DIW and extracted with 4.0 mL chloroform. The absorbance of the purple-colored ion-pair complex was measured at 492 nm using a 1 cm path cell against a blank constructed in the same way but without the addition of medication.

To calculate the phase ratio, the volume of the aqueous layer was fixed by increasing the organic layer volume from 4.0 to 8.0 mL after stabilizing other optimum conditions. The volume of the organic layer was then fixed at 4.0 mL, with an increase in the aqueous layer from 4.0 to 8.0 mL. The complex was extracted, and the absorbance was measured. To determine the adequacy of the extraction, this factor was determined after completely removing the organic layer for the first time. This is followed by withdrawing the aqueous layer to another separating funnel. Finally, an equal volume of the organic solvent used in the first time was added. This process was repeated again to find the second absorbance. After observing the adequacy of the solvents used in extracting the formed complex and determining the appropriate ones, it was used to experiment on a blank solution containing the same concentration of SbI_4^{2-} ion solution with the application of optimal conditions and absorbance measurement.

Analytical characteristics. Standard solutions were prepared and analyzed in triplicates to study the linearity, Sandell sensitivity, slope (b), correlation coefficient (R^2), and LOD values.

Stoichiometry between ATR and SbI_4^{2-} . This was investigated using the mole ratio method, equimolar from the reagent and the ATR 2.0×10^{-4} M, to a series of 10 mL graduated cylinder, volume from a stock solution of the ligand ATR with exceeding volumes of the reagent and applied the optimum conditions and read the absorbance at λ_{max} against the mole ratio, and plot the curve [18].

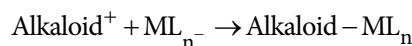
Interferences. The selectivity of the present method was tested by examining the effect of equal and duplicate quantities of some common excipients (starch, glucose, lactose, glycerin, and talk) on selectivity. Stock solution for these excipients was prepared by dissolving 0.0250 g in a 25 mL volumetric flask, from each one in an appropriate solvent and continue to the mark to get $1,000 \mu\text{g mL}^{-1}$. The results indicated that excipients do not affect or interfere with the determination of ATR in pharmaceutical preparations or dosage forms.

Analytical applications. The standard addition method procedure was used to determine the content of ATR in tablets and eye drop preparations; the contents of 10 tablets (entro-stop) were grounded and mixed well. A 0.05 g of this powder was dissolved in ethanol:water solvent and then filtered and poured into a 10 mL volumetric flask and continue with solvent to the mark. Then, we took 500 μL to several test tubes containing a series increasing amount of ATR and continued with all optimum conditions and extraction with 4 mL chloroform, and established the standard calibration curve. The same procedure for eye drops was used after preparing the suitable sample by taking 1 mL from the content and diluting it to 25 mL in a volumetric flask.

■ RESULTS AND DISCUSSION

The ion-pair complex's absorbance was measured in the region of 200–600 nm in comparison to a blank solution. Fig. 1 illustrates the maximum absorbance peak which was found to λ_{max} equal to 492 nm. Fig. 2 depicts the influence of SbI_4^{2-} ion concentration on the formation of the $[\text{ATR-SbI}_4^{2-}]$ complex. There was an increase in absorbance as we added the reagent. It was anticipated that the reaction would be concluded with the addition of 2 mL of the reagent. Fig. 3 depicts the influence of pH values on the absorbance of the alkaloid complex in

question. It was discovered that a pH range of 2–3 was the best setting for the reaction; alkaloids do not ionize at pH above 7, therefore, no ion-association complex formation is expected [19]. In an acidic media, the alkaloid's nitrogen atom is protonated.



ML_n^- symbolizes the SbI_4^{2-} and Alkaloid^+ is the protonated ATR [17]. The interaction of two oppositely

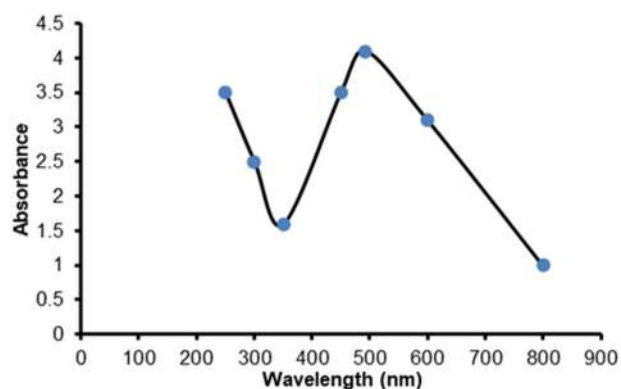


Fig 1. Absorption spectra of the complex SbI_4^{2-} -ATR formed against reagent blank

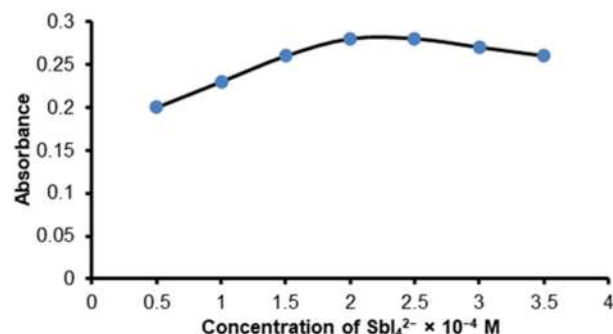


Fig 2. The absorbance of the complex produced is influenced by the concentration of SbI_4^{2-}

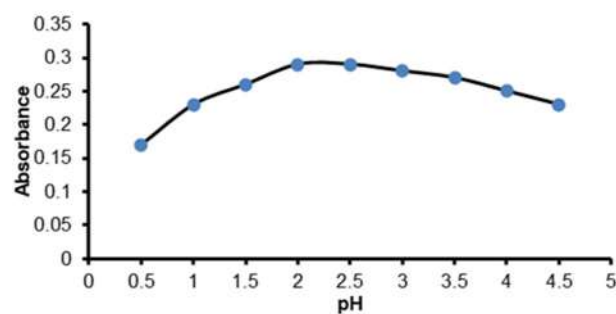


Fig 3. The effect of pH on the development of the SbI_4^{2-} -ATR complex

charged species under optimal conditions results in the production of an ion-pair complex in an aqueous medium when ATR combines with the SbI_4^{2-} ion in an acidic medium. The outcomes demonstrated that an ion pair complex was produced in a 1:1 ratio (Scheme 1) via electrostatic attraction between the positive protonated ATR and the SbI_4^{2-} reagent's anion.

The interaction of two oppositely charged species under suitable conditions results in the production of an ion-pair complex in an aqueous medium when ATR combines with the SbI_4^{2-} ion in an acidic medium. The outcomes demonstrated that an ion pair complex was produced in a 1:1 ratio via electrostatic attraction between the positive protonated ATR and the SbI_4^{2-} reagent's anion.

Experiments have demonstrated that 4 mL of the organic phase is sufficient for the complete depletion of the organic- SbI_4^{2-} complex in the aqueous phase as well as reading the absorbance. The extraction of the ATR complex required only 1 min of shaking time.

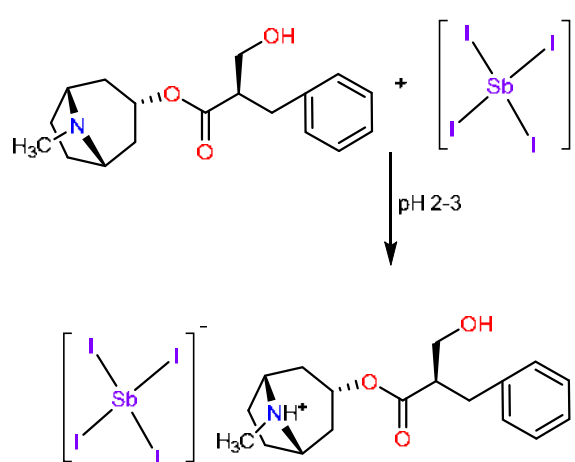
Table 1 shows the appropriate concentration of the SbI_4^{2-} reagent, as well as the optimal pH range and absorbance for one (A1) and two (A2) batch extractions, also with the comparison with the blank extraction (A). It can be concluded that the former is the most suitable. The complex formed is slightly soluble in aqueous media but freely soluble in organic solvent, and a 5 min interval is sufficient. One extraction was shown to be sufficient for achieving a quantitative recovery of the complex in the minimum amount of time.

The results indicate that satisfactory accuracy and precision could be attained by the current method (Table 2). The E_{rel} % value was 2.38, which appeared a high value

of accuracy with the RSD% of 3.76. The maximum color intensity was attained almost instantly, and 5 min was enough to complete the formation of the ion-association complex between the reagent SbI_4^{2-} and ATR, and the color intensity was stable for more than 10 h.

Table 3 shows regression value, slope, and correlation coefficient of the procedure, and it appears interesting results. Linear regression was used to derive a linear equation for the standard curve. Fig. 4 illustrates the linearity from the range $0.5\text{--}5.0 \times 10^{-5}$ M. After this concentration the line start to be little bit bending to apposite deviation.

The present method has been effective for the evaluation of ATR in pharmaceutical preparations. The obtained results are shown in Tables 4 and 5. It refers to the ATR content measured by the proposed method being in good agreement with those results by manual reference British pharmacopeia method [20], and these



Scheme 1. Proposed reaction pathway between atropine- SbI_4^{2-} ion pair complex under recommended procedure

Table 1. Effect of SbI_4^{2-} concentration and pH-values

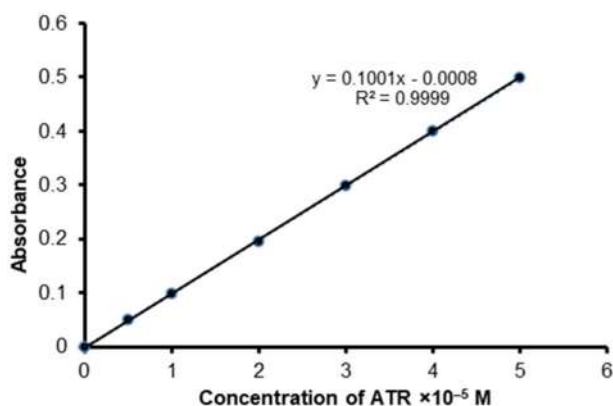
Alkaloid conc. ($\times 10^{-5}$ M)	SbI_4^{2-} conc. (M)	pH	Absorbance		
			Extr. 1 A1	Extr. 2 A2	Extr. blank A
ATR (2.0)	2.0×10^{-4}	2-3	0.280	0.025	0.012

Table 2. Linearity, precision, accuracy, limit of detection (LOD), sensitivity, and confidence limit are all analytical parameters

Comp.	Linearity ($\times 10^{-5}$ M)	RSD% (n = 5)	E_{rel} %	D.L (μM)	Sensitivity ($\mu\text{g cm}^{-2}$)	Confidence limit
ATR	0.5-5.0	3.76	2.38	1.13	0.013	0.420 ± 0.018

Table 3. Regression value, slope, and correlation coefficient

Sample	Regression $Y = BX + A$	Slope	Corr. coeff. (R^2)
ATR	$Y = 0.1001X + 0.0008$	0.1001	0.9999

**Fig 4.** The linearity of the determination of the ATR

experiments are used easily and rapidly on pharmaceutical preparations.

Table 6 demonstrates that a comparison with an earlier technique for the determination of Quinidine (QND) using another reagent (PdI_4^{2-}) was made [17], and it was discovered that the treatment is competitive in these areas. This demonstrates that a more sensitive LOD allows the linearity to reach the lowest concentration.

Table 4. Comparison between the concentrations found against the stated one (Entro-stop) using the standard addition method

Alkaloid	Preparation sample	Manufacture	Stated concentration (mg)	Concentration found (mg)	% E_{rel}
ATR tablet	Entro-stop	SDI/IRAQ	0.0250	0.0255	2.24

Table 5. Comparison between the concentrations found against the stated ATR using the standard addition method

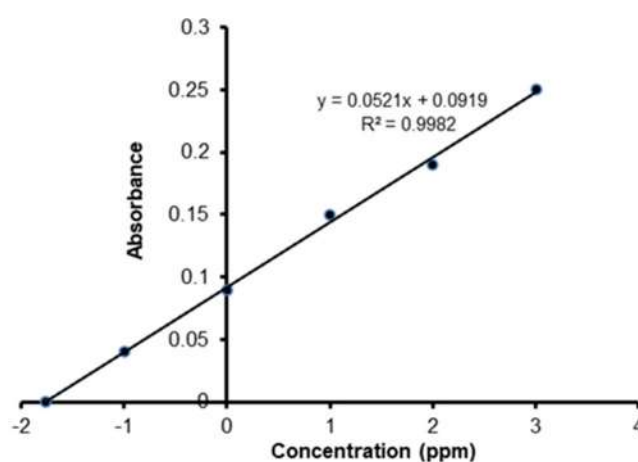
Alkaloid	Preparation sample	Manufacture	Stated concentration (mg mL^{-1})	Concentration found (mg mL^{-1})	% E_{rel}
ATR eye-drop	Atropine sulfate/cooper	Cooper pharmaceutical	1.0	1.027	2.75

Table 6. A comparison of the novel method to the prior one that used the SbI_4^{2-} reagent

Alkaloid	Inorganic complex	Linearity ($\times 10^{-5}$ M)	D.L (μm)	RSD%
ATR	SbI_4^{2-}	0.5–5.0	1.13	3.76
QND	PdI_4^{2-}	2.0–6.0	1.50	2.84

Fig. 5 and 6 demonstrate the results obtained using the standard addition method to find the exact concentrations in the pharmaceutical preparations, and these results prove that the method of standard additions is appropriate and compatible with this method and can be used in a simple and accurate manner in this line of work.

Fig. 7 shows the molar ratio method used in estimating the rate of the ligand to the reagent used at 492 nm, and it is clear from the obtained figure that the

**Fig 5.** The standard addition method for the determination of ATR in the Entro-stop tablet pharmaceutical preparations

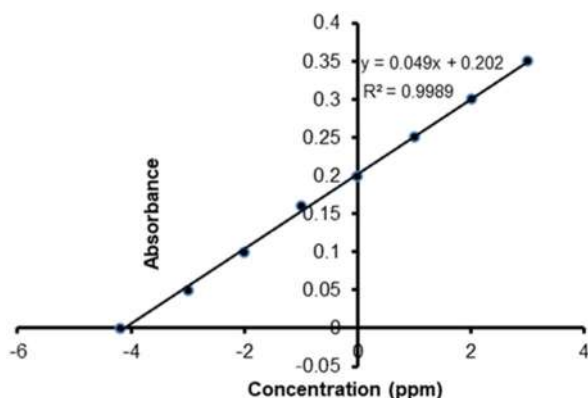


Fig 6. The standard addition method for the determination of ATR in the eye-drop pharmaceutical preparation

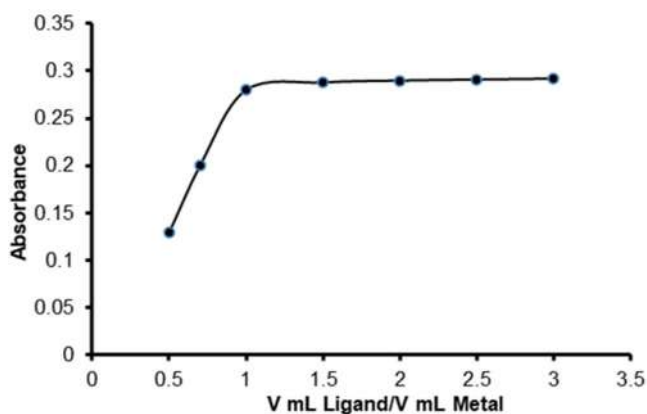


Fig 7. Molar ratio method for SbI_4^{2-} -ATR complex

results are proven after reaching the result 1:1, the curve begins to take the form of a straight line parallel to the x-axis, which indicates the sufficiency of the interaction.

■ CONCLUSION

The proposed method was new, simple, and proved to be sensitive for the spectrophotometric determination of Atropine (ATR) drugs in pure and pharmaceutical preparations by the formation of the ion association complex using a new reagent SbI_4^{2-} . It is evident from the data presented in this work that we can use the SbI_4^{2-} ion in analytical technique as a suitable one when we need to analyze trace or ultra-trace quantities of ATR in pharmaceutical samples. When compared to previous methods that used different techniques and metals, the detection limits for the three alkaloids detected were found to be between 0.006–0.011 ppm, Precision RSD =

0.73–2.69%, and Accuracy E_{rel} 0.45–1.11%, for three alkaloids detected. The proposed method was a simple one and did not contain any difficult reaction conditions and can be used as a new method for determining the presence of ATR in pharmaceutical tablets and eye drop preparations. For future research, we recommend combining different hybridization techniques with other techniques to improve sensitivity.

■ ACKNOWLEDGMENTS

The authors would like to thank Al-Rafidain University College for providing the the excellent support and facilities throughout this research.

■ REFERENCES

- [1] World Health Organization, 2019, *The International Pharmacopoeia*, 9th Ed., Department of Essential Medicines and Health Products, World Health Organization, Geneva.
- [2] Zhao, C., Cai, C., Ding, Q., and Dai, H., 2020, Efficacy and safety of atropine to control myopia progression: A systematic review and meta-analysis, *BMC Ophthalmol.*, 20 (1), 478.
- [3] Moriyama, K., Takami, Y., Uozumi, N., Okuda, A., Yamashita, M., Yokomizo, R., Shimada, K., Egawa, T., Kamei, T., and Takayanagi, K., 2016, Assessment of drug content uniformity of atropine sulfate triturate by liquid chromatography-tandem mass spectrometry, X-ray powder diffraction, and Raman chemical imaging, *J. Pharm. Health Care Sci.*, 2 (1), 4.
- [4] Saito, J., Imazumi, H., and Yamatani, A., 2019, Physical, chemical, and microbiological stability study of diluted atropine eye drops, *J. Pharm. Health Care Sci.*, 5 (1), 25.
- [5] Afsar, A., and Bajwa, J.A., 2017, Determination of best regime for administration of atropine eye drops for cycloplegia, *Adv. Ophthalmol. Visual Syst.*, 6 (1), 42–45.
- [6] Pejić, M., Janković, M., Djordjević, S., and Koturević, B., 2020, Extraction and identification of atropine from 'legal high' plant species, *Int. Sci. Conf. "Archibald Reiss Days"*, 10, 713–720.

- [7] Brown, K., McMenemy, M., Palmer, M., Baker, M.J., Robinson, D.W., Allan, P., and Dennany, L., 2019, Utilization of an electrochemiluminescence sensor for atropine determination in complex matrices, *Anal. Chem.*, 91 (19), 12369–12376.
- [8] Koetz, M., Santos, T. G., Rayane, M., and Henriques, A.T., 2017, Quantification of atropine in leaves of *Atropa belladonna*: Development and validation of method by high-performance liquid chromatography (HPLC), *Drug Anal. Res.*, 1 (1), 44–49.
- [9] Mahmood, A.K., 2017, Development of two different spectrophotometric methods for the determination of atropine drug in pure form and pharmaceutical preparations, *Ibn Al-Haitham J. Pure Appl. Sci.*, 25 (3), 226–241.
- [10] Dushna, O., Dubenska, L., Vojs, M., Marton, M., Patsay, I., Ivakh, S., and Plotycya, S., 2022, Highly sensitive determination of atropine in pharmaceuticals, biological fluids beverage on planar electrochemical cell with working boron-doped diamond electrode, *Electrochim. Acta*, 432, 141182.
- [11] Nair, S.G., Shah, J.V., Shah, P.A., Sanyal, M., and Shrivastav, P.S. 2015, Extractive spectrophotometric determination of five selected drugs by ion-pair complex formation with bromothymol blue in pure form and pharmaceutical preparations, *Cogent Chem.*, 1 (1), 1075852.
- [12] Aziz, A.T., and Sultan, S.H., 2019, Spectrophotometric determination of mesalazine in pharmaceutical preparation by oxidative coupling reactions with m-aminophenol and 2,6-dihydroxybenzoic acid, *Baghdad Sci. J.*, 16 (4), 1010–1016.
- [13] Wedian, F., Lataifeh, A., and Mohammed, M.S., 2020, Simultaneous spectrofluorometric analysis of tablets containing hydrochlorothiazide combined with timolol maleate or amiloride hydrochloride, *Acta Pharm.*, 70 (3), 373–385.
- [14] El-Didamony, A.M., Hafeez, S.M., and Saad, A.A., 2015, Extraction-spectrophotometric determination of some antihypertensive drugs in pharmaceutical and biological fluids using two sulphonphthalein dyes, *Int. J. Appl. Pharm.*, 7 (1), 10–17.
- [15] Ammar, R.A., 2015, Determination of doxazosinmesylate by ion-pair complex formation with bismuth(III) tetraiodide using spectrophotometric and atomic absorption spectroscopic, *Orient. J. Chem.*, 31 (4), 2487–2497.
- [16] Khawla, S.A., Qutaiba, A.Q., Falah, H.S., Al-Salman, H.N.K., and Hussein, H.H., 2020, The spectrophotometric determination of antiepileptic drug in standard and pharmaceutical formulations by diazotization coupling reaction and some metals complexes, *Syst. Rev. Pharm.*, 11 (3), 247–260.
- [17] Ali, R.H.M., and Fadhil, J., 1999, Determination of some biologically active alkaloids using ion-association palladium complexes and indirect electrothermal atomization atomic absorption spectrophotometry, *Iraqi J. Sci.*, 40 (4), 1–20.
- [18] Abd Alrassol, K.S., Qasim, Q.A., Ahmed, G.S., and Al-Salman, H.N.K., 2019, A modified and credible method to estimate nitrofurantoin in the standard of substances and pharmaceutical dosage, *Int. J. Pharm. Res.*, 11 (4), 1057–1071.
- [19] Ali, R.H.M., 2021, Using the platinum as an ion-association complex in indirect determination of microgram quantities of some alkaloids and pharmaceutical compounds by GET-AAS, *Ann. Rom. Soc. Cell Biol.*, 25 (4), 8974–8981.
- [20] Skoog, D.A., Holler, F.J., and Crouch, S.R., 2017, *Principles of Instrumental Analysis*, 7th Ed., Cengage Learning, Boston, MA, USA.

Simple Thermal Analysis as a Green Method for the Detection of Meat Adulteration

Ilma Nugrahani¹ and Aditya Aditya^{2,3*}

¹School of Pharmacy and Halal Center Study, Bandung Institute of Technology, Jl. Ganesha No. 10, Bandung 40132, Indonesia

²Master's Program School of Pharmacy, Bandung Institute of Technology, Jl. Ganesha No. 10, Bandung 40132, Indonesia

³Study Program of Pharmacy, Faculty of Health Sciences and Pharmacy, University of Gunadarma, Jl. Margonda Raya No. 100, Depok 16424, Indonesia

* **Corresponding author:**

tel: +62-8979757524

email: aditya@staff.gunadarma.ac.id

Received: November 16, 2022

Accepted: July 20, 2023

DOI: 10.22146/ijc.79201

Abstract: Differential scanning calorimetry (DSC) is one of the most widely developed thermal analysis methods for meat samples for halal authentication of food or processed products. Research on adulteration detection for various types of meat and its derivatives has been developed before and still requires organic solvents. Therefore, the concept of the "green method" is being tried to develop in this research. DSC analyses are performed in the same experimental conditions for all sample powder: sample mass 2 mg, temperature range 30–400 °C, and heating rate 20 °C min⁻¹. The results showed there is a characteristic minor endothermic peak for each meat. Chemometric analysis was carried out using the principal component analysis (PCA) method to ensure that the thermal characteristics of each meat were utterly different in both pure and mixed meat. The results of this analysis indicate that each pure meat has a different score plot. Therefore, the developed thermal analysis method is quite reliable in determining the different types of meat based on the characteristic minor endothermic peak in the thermogram and the score plot from PCA analysis.

Keywords: DSC; chemometric analysis; method development; minor endothermic peak; pork

■ INTRODUCTION

Adulterating beef with pork or other meats is still common in many countries, such as China and Indonesia. That was done for economic concerns or to obtain greater profits [1]. Adulterating meat has not been a significant problem for a long time if consumed fresh or because it is available in small quantities. However, with improved technology and modern storage facilities, meat adulteration has become a significant problem. In this case, a food product that does not list or mention the ingredients used on the final product label is considered a food adulteration. Food fraud or adulteration has huge economic potential, believed to be worth several billion dollars annually [2]. For example, it was reported in the Guardian newspaper that 900 people were imprisoned in China for meat fraud involving 20,000 tons of unsuitable meat, including mink, rat, and fox. In addition, 4% of

lamb is sold for takeaway dishes containing other types of meat [1].

Research on adulteration detection for various types of meat and its derivatives has been carried out using various methods such as high-pressure liquid chromatography (HPLC), gas chromatography (GC), electronic nose (EN), polymerase chain reaction (PCR), enzyme-linked immunosorbent assay (ELISA), nuclear magnetic resonance (NMR), near-infrared (NIR) spectroscopy, laser-induced breakdown spectroscopy (LIBS), fluorescent light spectroscopy, Fourier transform infrared (FTIR) spectroscopy, mass spectrometry (MS), Raman spectroscopy (RS), and thermal analysis such as differential scanning calorimetry (DSC) for the detection of fat in meat at low temperatures [2]. Naturally, the analytical methods that have been developed have advantages and disadvantages, including the complexity of sample

preparation, measurement, and data processing. In addition, the detection method that has been developed still requires organic solvents.

Real-time PCR is one standard method for analyzing non-halal meat [3]. In recent years PCR has been widely developed for DNA analysis of non-halal meat in processed products containing halal meat [4-5]. DNA-based identification is a reliable technique with high speed and sensitivity [6]. However, one of the drawbacks of this method is that it requires sophisticated instruments and trained operators, making it unsuitable for field-based analysis [7]. In addition, the use of organic solvents used during sample preparation and analysis induces that this method can pollute the environment if the waste is not handled correctly, which can cause a reduction in the number of wild animals, a decrease in ecosystem function, and threaten human health [8]. Thus, the development of environmentally friendly analytical methods can be an option to prevent negative impacts on the environment and living things. One of the solid analysis methods, such as thermal analysis, can be a prospective environmentally friendly method for the future [9]. Several modern thermal analysis methods, such as DSC, DTA, and TGA, have been used to determine the ingredients' characteristics to see the safety and quality of these foods. DSC is one of the most widely developed methods, especially for food samples, namely meat or its derivatives, for halal authentication of food or processed products. DSC makes analysis can be simple and fast. In addition, the small sample requirement for analysis is one of the advantages of this method [2].

Therefore, the development of an analytical method with the concept of the "green method" [9], using a combination of thermal analysis with DSC as a confirmation tool and electrothermal for the routine analysis carried out at high temperatures by looking at the decomposition temperature of the sample makes this method more efficient because it does not use organic solvents and the steps of measuring and processing data are shorter and easier. This study aims to develop a reliable and environmentally friendly thermal analysis method, especially for determining various types and

assessing the halal-ness of meat products using DSC instruments and electrothermal semi-manual tools.

■ EXPERIMENTAL SECTION

Materials

The materials used in this study were beef, pork, rabbit, and chicken obtained from the Yogya Junction 8 Toserba (Bandung, Indonesia) and traditional markets in the Bandung area. In addition, Indium (Merck, Bandung, Indonesia) was used for DSC analysis.

Instrumentation

The tools used were a 5" kitchen knife (Qian Jin, Singapore), 245 mL small jar (Yoshikawa SW TX07, Japan) vial, spatula, tweezers, capillary tube, watch glass, alcohol thermometer, analytical glass scale (Fujitsu FSR-A220, Japan), 9 L toaster oven (KLAZ, Ace Hardware, Indonesia), blender & chopper (Homu, China) electrothermal (Electrothermal AZ 9003 IA9000, UK), DSC (Rigaku Thermo Plus EVO2 DSC8231, Japan), aluminum pans & plate, and hydraulic presses for DSC analysis obtained from Rigaku (Rigaku, Tokyo, Japan).

Procedure

Meat powder manufacturing

The manufacture of meat powder begins with collecting each meat by choosing the same part, namely the breast of meat. Furthermore, meat powder was made by a convective drying method using an oven at 40 °C [10-11]. The meat is first separated from the fat that looks white using a kitchen knife, then sliced thinly 1–2 mm thick, and then placed in a container lined with aluminum foil. Drying was carried out using an oven for 22 h, then the dry weight of the meat was weighed. If it has been constant for weighing several times, the drying is considered complete [11]. An alcohol thermometer inserted into the oven at the same time as the meat drying is used to control the temperature stable at ± 40 °C. The following process is smoothing dried meat using a blender and filtering using a 200-mesh sieve to produce a fine powder with uniform particle size. Determination of drying shrinkage can be done by looking at the difference between wet weight and dry

weight, which is expressed as a percentage of drying shrinkage in the meat [10-12].

Sample preparation

The sample for electrothermal observation was prepared by weighing 2 mg of meat powder with an analytical balance. The sample was inserted into the mouth of the capillary tube and gently tapped until it reached the bottom of the tube. In addition, for the sample analysis of DSC, into an aluminum pan that had been previously tare, as much as 2 mg of meat powder was added and then weighed with an analytical balance. Furthermore, the sample is evenly spread as thin as possible to cover the container's bottom. Then the pan is covered with a cover plate and compressed until it is tightly closed. Pans that have been closed can be directly analyzed by DSC [13].

Method validation

The specificity of a method can be determined by analyzing the thermogram of an empty aluminum pan and ensuring that there is no pan interference in the qualifying sample. In this case, the ability to choose between compounds of closely related structures must be demonstrated. This ability should be confirmed by obtaining a positive result by comparing the characteristic thermogram profile of pork with a negative result of a sample that does not contain analytes, i.e., beef powder. Furthermore, the results were confirmed by ensuring that a positive response was not obtained from beef powder. In this study, the resulting thermogram must show that the procedure is not affected by impurities or adding other substances to the sample. It can be done by spiking or adding the beef powder to pork powder in a ratio (1:1), or 1 mg each is mixed into a mortar, homogenized, put into a pan, and weighed with an analytical balance. A good thermogram from the spiking results will show that the test results are not affected by the presence of foreign materials [14-15].

Accuracy and precision are not needed in the validation of qualitative analytical methods, but to ensure good repeatability in measurement and recovery of analytical results that are close to the actual value. In this study, accuracy and precision tests are still carried out [14-

15]. The accuracy and precision tests were carried out on one sample concentration with three measurements on each meat sample. The accuracy test that is carried out to assess the measure of accuracy or proximity of the analysis results to the average can use the recovery parameter by the difference between the obtained analysis results and the average measurement results, which is expressed as a percentage of the recovery. The precision test is determined by the Relative Standard Deviation (RSD) parameter by the difference between the calculation result of the standard deviation and the average measurement result [14].

Sample analysis

Electrothermal observations were carried out by entering a capillary tube filled with samples into a semi-manual electrothermal furnace, then heated in the range of 30–350 °C with a heating rate of 10 °C min⁻¹. Observations were assisted with a smartphone camera, and the reading was carried out three times. In addition, the DSC analysis was carried out to study the thermal profiles of various types of meat. The meat powder sample that has been put in an aluminum pan and tightly closed is heated at a temperature of 30–400 °C with a heating rate of 20 °C min⁻¹ [16]. An empty aluminum pan is used as a reference.

Data analysis

DSC thermogram data is analyzed with the help of software related to various available programming. Thermogram data analysis was performed using the ThermoPlus software. The resulting data is stored in Excel, then processed by making an overlay of the sample thermogram profile to see the difference in thermal characteristics of both pure and mixed samples. Chemometric analysis for multivariate data classification using the PCA technique was performed using Minitab software version 19 (Minitab, LLC).

RESULTS AND DISCUSSION

Meat Drying

Meat drying is the first step to obtaining meat powder samples that will be used to analyze various types of meat using the thermal analysis method (Table

1). The most abundant component in meat is water, followed by protein and fat, while carbohydrates, minerals, and vitamins are contained in much smaller amounts [17]. The great water content makes the meat unable to last long at room temperature, so it must be stored in a cold refrigerator to extend its shelf life of the meat.

In this study, the meat was made into powder by conventional drying methods using an oven at 40 °C to prevent protein denaturation, which began at around 40 °C [11,18]. Drying time was carried out for 22 h because it is the optimal time for drying meat so it can be mashed into powder [11]. Meat that has been in powder form, as shown in Table 1, can be stored at room temperature for an extended period so it could be used for the thermal analysis method which is one of the solids analysis methods to measure the heat profile of a sample [9].

From the results of weighing the meat before and after drying, the drying shrinkage from the largest to beef, followed by pork, chicken, and rabbit. The drying shrinkage plays an essential role in water transport during heating [19]. In this case, the drying process can cause a

loss of water content in the meat. Based on the research by Bampi et al. [11], showing that the maximum temperature reached inside the samples while using the convective drying method was 40 °C, and 22 h were necessary to reduce the meat moisture from 2.50 to 1.25 g g⁻¹ (dry basis), it means that during drying there is a drying shrinkage of 50%. However, in this research that has been done on meat that also uses an oven at a temperature of 40 °C, the percentage of drying shrinkage shows almost the same results, even exceeding the average water content of meat in general. That means the meat's water content can evaporate completely at that temperature. Naturally, the water content of meat is approximately 75% and 20% protein, with the remaining 5% representing a combination of fat, carbohydrate, and minerals. Still, the percentage of water can vary depending on the type of meat [20]. Based on the research from Li et al. [21], fresh beef has 65–80% water content, which is highly perishable, while dehydrated beef is more suitable for transport and storage due to its longer shelf life and lower mass and volume. Furthermore, Table 2 shows that the drying residue data for each meat can be representative to explain that the

Table 1. Pictures of meat before and after dried to powder













Meat Types	Beef	Pork	Rabbit	Chicken
Raw meat				
Dry meat				
Meat powder				

Table 2. Drying shrinkage of meat

Meat types	Wet weight (g)	Dry weight (g)	Drying shrinkage (%)	Drying residue (%)
Beef	20.255	3.950	$\frac{20.255 - 3.950}{20.255} \times 100 = 80.5$	19.5
Pork	33.885	8.018	$\frac{33.885 - 8.018}{33.885} \times 100 = 76.3$	23.7
Rabbit	48.481	13.249	$\frac{48.481 - 13.249}{48.481} \times 100 = 72.7$	27.3
Chicken	28.476	7.514	$\frac{28.476 - 7.514}{28.476} \times 100 = 73.6$	26.4

drying carried out has wholly evaporated the water and left only other content of the meat such as protein.

Specificity Test

Method validation is carried out to provide sufficient evidence that the analytical method can fulfill its objectives [15]. In this case, the validation process is determined through laboratory testing, which shows that the performance characteristics of the procedure have met the requirements following its intended use [14]. The development of the analytical method carried out in this study is qualitative analysis or identification so that the specificity test is selected as a characteristic of analytical performance in method validation [14].

The results of the pork specificity test showed that at a temperature of 186.9 °C, the pork sample obtained an actual positive result (True Positive), and the beef obtained an actual negative result (True Negative). That can be seen in Fig. 1, where a minor endothermic peak appears in the pork sample's thermogram profile with a peak temperature of 186.9 °C, while in the beef sample, there is no peak at that temperature. To ensure that the analytical procedure is not affected by the presence of impurities or the addition of other substances to the sample, spiking or addition of beef to pork is carried out in a ratio (1:1). The test results on the mixed sample showed that the minor endothermic peak which was the characteristic thermal characteristic of the pork sample

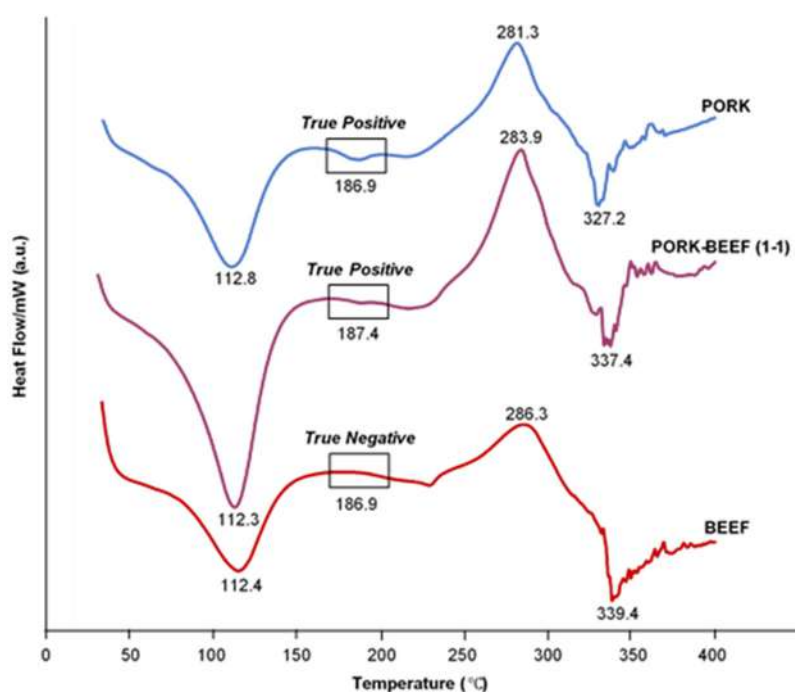


Fig 1. DSC thermogram of pork specificity test results

still appeared at the peak temperature of 187.4 °C. In this case, a peak temperature shift of 0.5 °C and a reduction in enthalpy occurred in the pork sample after adding beef. A previous study by Talik et al. [22] showed a significant effect on the composition of the mixture or analyte concentration on enthalpy, where the analyte concentration was directly proportional to the enthalpy. The smaller the analyte concentration, the smaller the enthalpy. In another study, a sample adulterated showed a peak temperature shift from the initial position [23].

Accuracy and Precision Test

The method has good precision, determined for one concentration level of 2 mg of meat sample. The results were expressed as the RSD with the condition that the value is < 1.3% [24]. Based on Table 3, the RSD value for various types of meat has met the requirements, and the smaller the RSD value from a series of measurements, the more precise the method used. In addition, the recovery of various types of meat is in the range of 99.99–100.02%. These results are still included in the recovery requirements, namely 98–102%, according to the level of analyte concentration [24].

Meat Powder Analysis

In its development, the DSC method was used to observe the behavior of the denaturation process in the muscle tissue of halal and non-halal animals without being dried into a powder. The thermogram results clearly

show each sample's thermal characteristics of the denaturation process [25]. The development of the DSC method in this study was carried out for the halal authentication of food ingredients in the form of meat. This method was developed for the identification of non-halal meat or qualitative analysis. In Islamic law, if a food has been contaminated with ingredients that are forbidden, then the food becomes haram [26]. In this case, there is no tolerance for haram ingredients in a food, so regardless of the concentration of haram ingredients detected, the food will still have haram status. Therefore, this research focuses on developing an environmentally friendly qualitative analysis method for identifying non-halal meat as an effort for halal authentication.

The DSC signal is presented in the form of a thermogram, with the x-axis representing temperature and the y-axis representing heat flow. To carefully compare the results of the thermograms of each meat sample before and after mixing, the unit of heat flow on the y-axis is made an arbitrary unit while the temperature on the x-axis is fixed with the unit °C. This is done to see in detail the differences in thermal characteristics, especially the characteristic minor endothermic peaks of each sample, through an overlay of a thermogram profile made using Excel. To create the overlay, the raw data from the ThermoPlus software integrated with DSC is exported in the form of an Excel file. Furthermore, temperature (°C) and heat flow (mW)

Table 3. Validation of the DSC method based on the characteristic minor endothermic peak of meat

Sample	Repeatability of measurements (n=3) (°C)	Average minor endothermic peak (°C)	Mean recovery (%)	% RSD
Beef	228.1	229.1	99.99	0.48
	228.9			
	230.3			
Pork	186.9	186.9	99.99	0.09
	186.9			
	186.7			
Rabbit	193.4	192.5	99.99	0.68
	193.1			
	191.0			
Chicken	177.9	178.9	100.02	0.65
	178.7			
	180.2			

data from each sample are collected to be overlaid by changing the heat flow value either by adding or subtracting values so that the resulting thermogram profile can be seen clearly when you want to compare differences between samples.

The DSC thermogram profile from Fig. 2 contains major endothermic peaks that appear in the temperature range of 103–113 °C in the beef, pork, rabbit, and chicken samples, with peak temperatures being at 112.4, 112.8, 109.5, and 103.4 °C. In addition, minor endothermic peaks that are characteristic of both beef, pork, rabbit, and chicken and only appear in samples are at peak temperatures of 229.1, 186.9, 192.5, and 178.9 °C, respectively. Another endothermic peak in the temperature range of 320–340 °C was only found in the beef, pork, and rabbit samples with peak temperatures at 339.4, 327.2, and 324.7 °C, respectively. Meanwhile, the DSC thermogram profile did not show any endothermic peaks in that temperature range in the chicken sample. The DSC thermogram profile also indicates the presence of exothermic peaks in the beef, pork, rabbit, and chicken

samples in the temperature range of 280–300 °C with peak temperatures being at 286.3, 281.3, 284.5, and 297.9 °C.

Furthermore, Table 4 shows that the first major endothermic peak in the temperature range of 103–113 °C in the DSC thermogram profile Fig. 2 in each sample is the release temperature of water molecules. That can be observed by electrothermal, where the sample looks drier than the initial before heating. In addition, the top of the capillary tube looks dewy after the heating is complete. This is caused by the sample releasing water molecules in the form of gas at that temperature range so that the sample looks dry and there is dew on the top of the capillary tube.

The other endothermic peak in the temperature range of 170–230 °C is a characteristic minor peak of every meat because it appears consistently in three measurements using DSC. On direct electrothermal observation and from the results of video recording with a smartphone camera, it can be seen that a small portion of the sample undergoes a physical transformation, and a big portion does not undergo physical transformation.

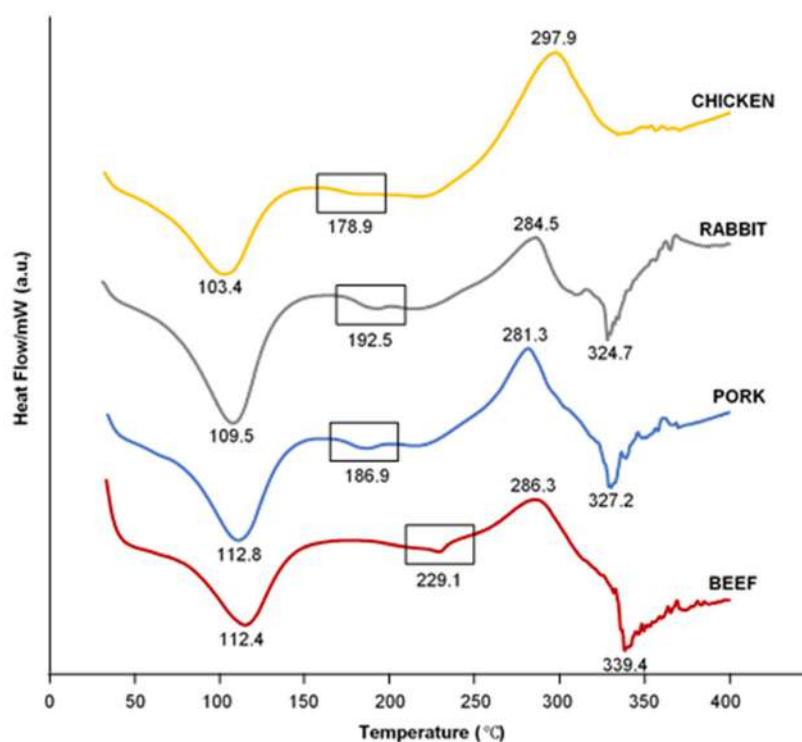






















Fig 2. DSC thermogram profile of various types of meat

Table 4. Results of observing various types of meat with electrothermal

Sample	Results of observing					
Chicken	30 °C	103.4 °C	178.9 °C	297.9 °C	350 °C	
						
	Rabbit	30 °C	109.5 °C	192.5 °C	284.5 °C	324.7 °C
						
		Pork	30 °C	112.8 °C	186.9 °C	281.3 °C
						
Beef			30 °C	112.4 °C	229.1 °C	286.3 °C
						

That can be caused by the small concentration of components in the sample and still in the multi-component sample, not in pure form, so it is more difficult to observe.

In addition, the exothermic peak that appears on the DSC thermogram profile of each sample in the temperature range of 280–300 °C is the decomposition temperature where, if observed by electrothermal, each sample undergoes a carbonation process or only leaves carbon as a residue. In the temperature range of 320–

340 °C, it can be seen in the DSC thermogram profile that there is an endothermic peak when observed by electrothermal. Each sample undergoes a melting process or phase change from solid to liquid. However, in the chicken sample in this temperature range, there is no endothermic peak in the DSC thermogram profile, and observations made by electrothermal up to 350 °C in the sample do not show that there is no melting process.

Based on research conducted by Weiss et al. [27] regarding the thermal stability tested on eight standard

amino acids, including glycine, cysteine, aspartic acid, asparagine, glutamic acid, glutamine, arginine, and histidine, shows that several processes can occur on heating, such as chemical decomposition or sublimation without decomposition.

This is in line with research that has been carried out on samples of meat powder which is known to contain amino acids where information on thermal characteristics starts from the temperature of the release of water molecules, which is indicated by the sample appearing dry, then the decomposition temperature which is indicated by a change in color to black in the sample, and the point at which the sample turns black. Melting can be observed by electrothermal so that the purpose of determining the type of meat using the thermal analysis method can be achieved.

Mixing pork and beef with several comparisons was carried out to study the thermal characteristics of pork before and after being mixed. In addition, the research design based on cases that occurred in the field related to contaminated meat or adulteration of beef with pork is expected to make an analytical method developed that reliably detects the presence of pork in beef which can be seen with the DSC thermogram, profile.

Several previous studies related to the detection of the presence of pork in food products have been successfully carried out using DSC with the research design of mixing pork content in food products intentionally to study the thermogram profile before and after mixing [23,28-30]. However, the research focuses on detecting lard instead of protein or muscular tissue from pork [2]. Azir et al. [23] conducted a study on fatty acid composition, triacylglycerol profile, and thermal properties of lard in cocoa butter showed a real difference between lard and cocoa butter in their thermal characteristics. In another study, lard was intentionally mixed into butter with various concentrations; qualitatively, the thermogram profile analysis showed subtle differences between butter, lard, and their mixtures [28].

Based on the experiments, the characteristic minor endothermic peak at pork up to a concentration of 33.3% in the mixed sample can still be detected with a very small

enthalpy. In addition, there is a shift in the peak temperature at a concentration ratio of 1:2, which seems to decrease by 0.6 °C (Fig. 3). Meanwhile, at a concentration ratio of 1:1, the peak shift was seen to increase by 0.5 °C. A shift in peak temperature due to the adulteration of pork content in food samples has been reported by Azir et al. [23]. In this study, a sample of butter adulterated with lard showed a peak temperature shift after adding lard.

In the experimental results, the mixed sample not only produces a shift in peak temperature, but the enthalpy also affects the ratio of the pork concentration in the mixed sample. The enthalpy of the unmixed pork sample at its characteristic endothermic peak is 1.275 J/g. In contrast, the mixed pork-beef sample with a concentration ratio of 2:1, 1:1, and 1:2 each has an enthalpy of 0.705, 0.445, and 0.114 J/g. In this case, the enthalpy at pork's characteristic minor endothermic peak is directly proportional to the concentration. This result is in line with the research of Nurrulhidayah et al. [28], where the enthalpy at the characteristic endothermic peak of the butter sample appears to decrease along with the decrease in sample concentration due to adulteration of lard added intentionally.

Mixing beef with other meat powders, such as chicken and rabbit, was carried out to ensure that each meat powder's characteristic minor endothermic peak would still appear in the peak temperature region after being mixed. The ratio of 2:1 was chosen so that the characteristic peak of each meat powder still appears with a peak that can still be seen so that it can be considered in distinguishing the beef mixture from each meat powder. In addition, the design of this study was also carried out to see the purity of beef, which can be observed from the DSC thermogram profile. Fig. 4 shows that the characteristic endothermic peak in beef at 229.1 °C is not visible in the DSC thermogram profile when mixed with other meat powders, even at the largest beef concentration (66.67%) in the beef-pork mixture (2:1) seen in Fig. 3 still does not show the characteristic endothermic peak of beef. This thing can be a marker of the presence of a mixture in the beef.

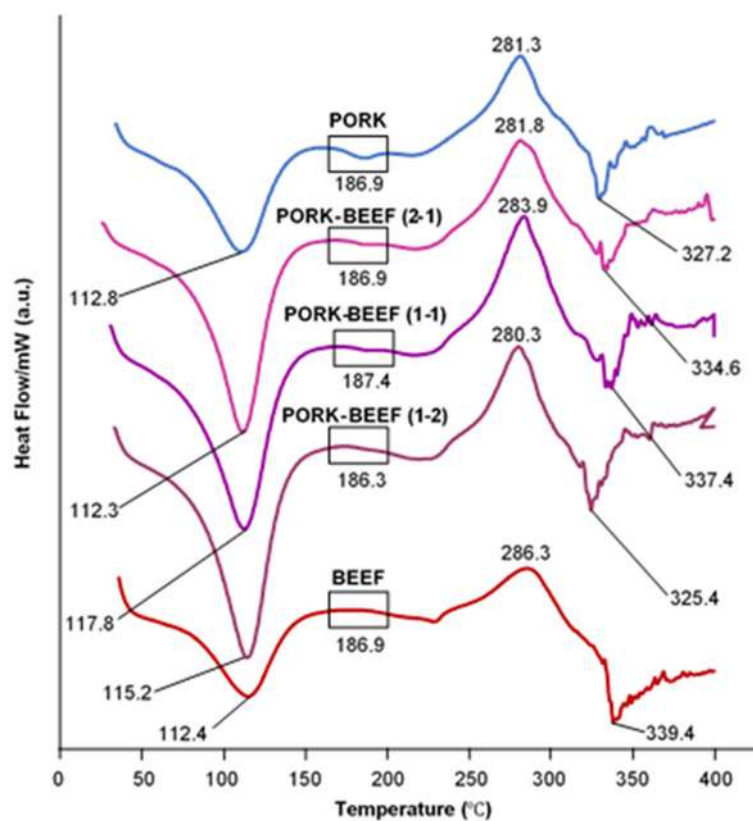


Fig 3. DSC thermogram profile of beef and pork mixing with comparison of 2:1, 1:1, and 1:2

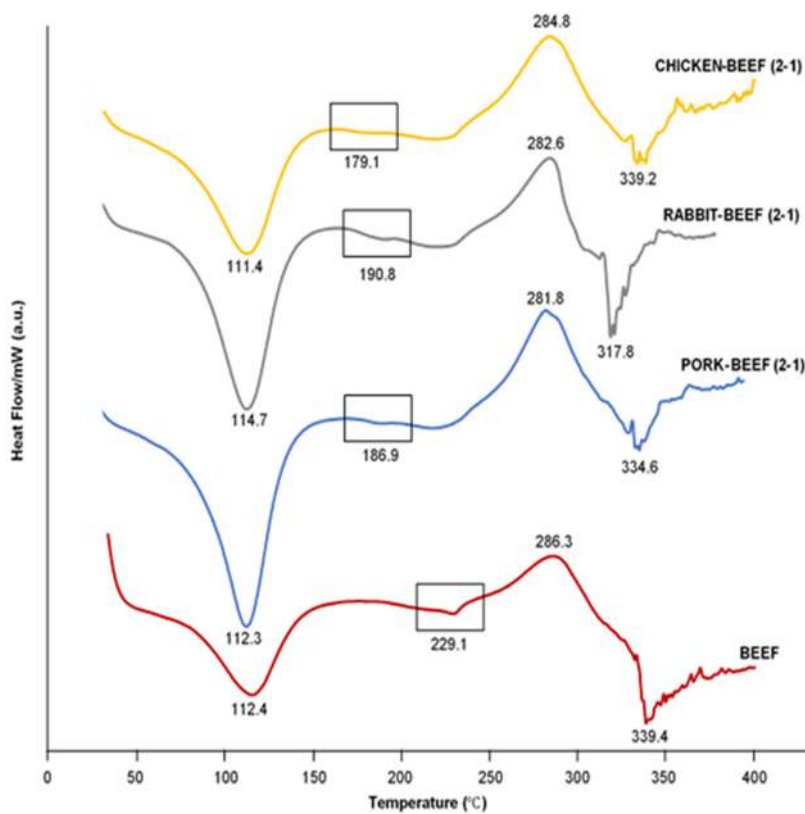


Fig 4. DSC thermogram profile of beef mixing with various meat in 2:1 comparison

From the experimental results, the characteristic minor endothermic peak in the peak temperature area of each meat powder still appears after being mixed. However, there is a shift in peak temperature and a reduction in enthalpy in each mixed sample. Fig. 4 shows that the characteristic peak temperature of chicken in the mixed sample is 179.1 °C, while the rabbit and pork are at 190.8 and 186.9 °C, respectively. The peak shift in characteristic endothermic peaks significantly occurred in the mixed sample containing rabbits, which experienced a peak decrease of 1.7 °C. In contrast, in the mixed sample containing chicken, the peak shift only occurred by 0.2 °C. However, the peak temperature does not change in the sample mixture of pork. The characteristic peak enthalpies of the pork, rabbit, and chicken samples before mixing were 1.275, 2.189, and 1.044 J/g, but after mixing, the enthalpies of pork, rabbit, and chicken were reduced to each of 0.705, 1.510, and 0.590 J/g.

Peak shifts and a decrease in enthalpy at the characteristic endothermic peak of a food sample due to adulteration of pork content have also been reported by Azir et al. [23]. In this study, a sample of butter added intentionally with lard showed a decrease in enthalpy along with a reduction in the concentration of butter due to the addition of concentration. Adulteration of lard, in addition to impurity carried out, can cause a shift in butter's characteristic minor endothermic peak [23].

DSC parameter data starting from Ton, Tp, Tof, and enthalpy were obtained from the processing of the thermogram profile of each sample using the ThermoPlus software integrated with DSC (Table 5). At the same time, the data range is the distance between Ton and Tof. Three peaks that appeared below 300 °C were chosen for chemometric analysis because they were peaks that could still be observed when electrothermal observations were carried out.

Table 5. DSC parameters obtained from thermograms of pure and mixed samples

Sample	Peak	DSC Parameters				
		Ton (°C)	Tp (°C)	Tof (°C)	Enthalpy (J g ⁻¹)	Range (°C)
Beef	1	83.1	112.4	141.1	-126.047	58.0
	2	223.5	229.1	234.4	-1.575	10.9
	3	231.0	286.3	312.7	76.548	81.7
Pork	1	81.1	112.8	136.5	-143.363	55.4
	2	170.9	186.9	195.3	-1.275	24.4
	3	248.2	281.3	299.2	145.267	51.0
Rabbit	1	79.5	109.5	133.2	-185.652	53.7
	2	175.1	192.5	199.6	-2.189	24.5
	3	244.5	284.5	298.7	77.295	54.2
Chicken	1	70.4	103.4	130.2	-129.579	59.8
	2	166.2	178.9	191.1	-1.044	24.9
	3	245.8	297.9	324.7	162.412	78.9
Pork-Beef (1:2)	1	92.5	115.2	136.4	-196.271	43.9
	2	180.3	186.3	193.4	-0.114	13.1
	3	247.9	280.3	321.4	116.892	73.5
Pork-Beef (1:1)	1	94.4	117.8	137.5	-229.405	43.2
	2	177.7	187.4	193.6	-0.445	13.9
	3	250.9	283.9	324.8	148.625	73.9
Pork-Beef (2:1)	1	86.5	112.3	134.7	-185.647	48.3
	2	176.7	186.9	194.8	-0.705	19.1
	3	245.7	281.8	325.4	139.132	79.7
Rabbit-Beef (2:1)	1	84.9	114.7	137.6	-182.283	52.7
	2	172.3	190.8	196.7	-1.510	24.4
	3	242.7	282.6	313.8	93.281	71.1

Sample	Peak	DSC Parameters				
		Ton (°C)	Tp (°C)	Tof (°C)	Enthalpy (J g ⁻¹)	Range (°C)
Chicken-Beef (2:1)	1	83.0	111.4	136.5	-129.711	53.5
	2	168.7	179.1	190.3	-0.590	21.6
	3	245.7	284.8	314.1	136.162	68.4

Ton: Temperature onset; Tp: Temperature peak; Tof: Temperature offset

Nine samples of pure and mixed meat powder were subjected to chemometric analysis using the PCA technique to see the differences in each sample based on the closeness of the score plots and the similarity of physicochemical properties. PCA is a technique for reducing the amount of data when there is a correlation present, and it is not helpful if the variables are uncorrelated [31].

To construct a validation model in adulteration studies, pork and beef mixtures were used as adulteration in the 0–100% w/w range. All DSC parameters in the thermogram, including onset, peak, offset, enthalpy, and range, are subjected to Partial Least Square (PLS)

regression (Fig. 5). Table 6 shows the R², RMSE, and SE values obtained during cross-validation using the leave-one technique for validating chemometric models. The R² value for the actual value of pork is 0.9982, while the DSC prediction value (y-axis) is 0.9967; the results showing > 0.99 on both values illustrate the match between the predicted value and the actual value [29]. Furthermore, the RMSE and SE values for the calibration sample were lower than the validation sample, but the difference in values for the two samples was not too significant. The smaller the RMSE and SE values in the calibration and validation samples, the lower the error model will be developed [29].

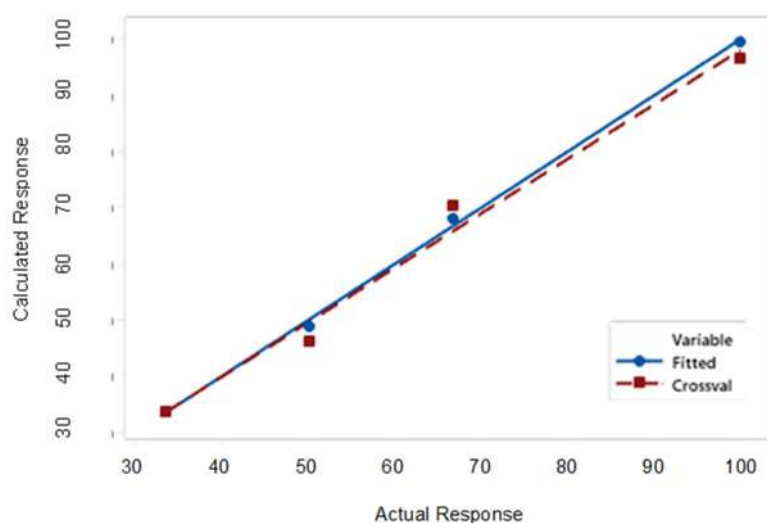


Fig 5. Scatterplot of actual vs predicted values of pork powder as an adulterant in beef powder using Partial Least Square Regression (PLSR)

Table 6. Multivariate statistical summary from DSC-PLSR calibration for characteristic minor endothermic peak thermograms of pork, and their admixtures with beef

Calibration models	Factor	Calibration			Validation		
		R ²	RMSEC	SEC	R ²	RMSEP	SEP
Characteristic minor endothermic peak PLS	2	0.9982	1.0248	4.2012	0.9967	3.0948	7.8516

RMSEC, root mean square error for calibration; RMSEP, root mean square error for prediction; SEC, standard error for calibration; SEP, standard error for prediction

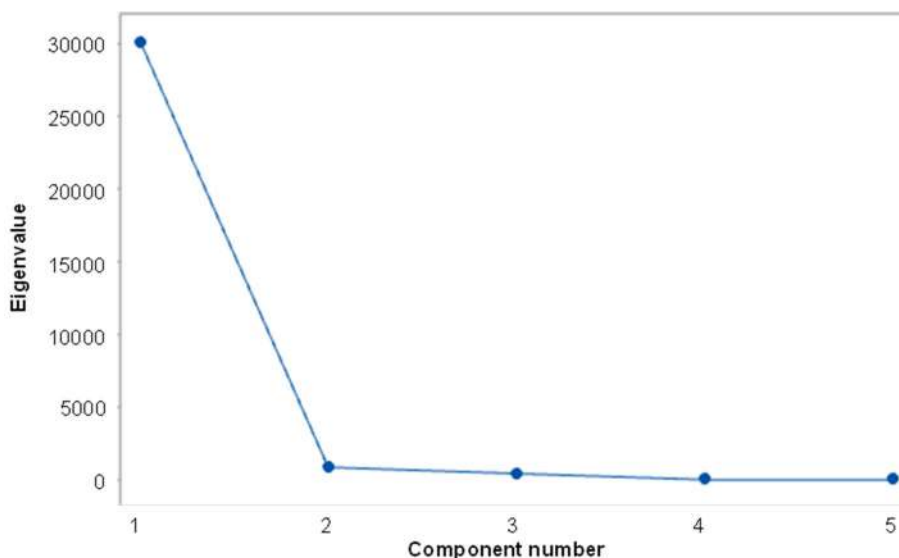


Fig 6. The results of the scree plot sample using PCA analysis

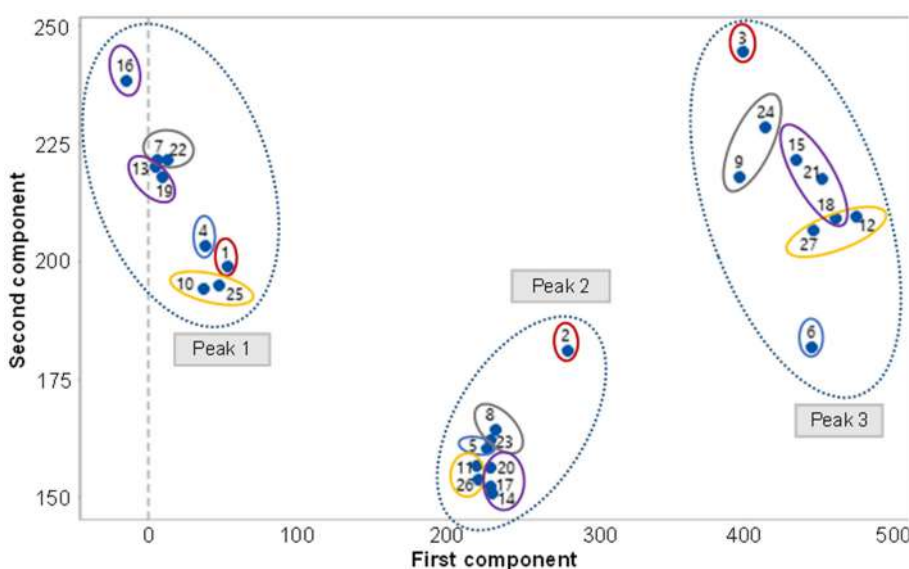


Fig 7. Score plot of pure and mixed samples. A peak of pure beef (red); A peak of pure pork (blue); A peak of beef and pork mix (violet); A peak of pure and mixed rabbit (grey); A peak of pure and mixed chicken (yellow)

The PCA score plot of the sample was described by the first and second principal components (PC1 and PC2). PC1 and PC2 explain the maximum variance of the entire sample with a value of 98.5% consisting of 95.8% PC1 and 2.7% PC2.

The result of PCA is referred to as PC and two or more samples with the same PC may be considered similar. The closest score plot between PC1 and PC2 shows the similarity of characteristics between the samples [32]. Fig. 7 shows three peaks of samples

observed based on the closeness of the score plots and the similarity of the thermal characteristics. In pure samples of meat powder the score plot between PC1 and PC2 for each meat showed different results or there were differences in the thermal characteristics of each sample. This classification explains that the samples are divided into four different groups a fact that is not easy to see from the original data [31]. PCA is not only used for the classification of pure samples being analyzed but also to detect sample adulteration which in this study was

intentionally mixed between samples of meat powder to see differences in the thermal characteristics of pure and mixed meat. The shift in the score plot of the pure sample for each meat powder after being mixed with other meat (beef) can be a consideration in determining the purity of a sample, meaning that there are differences in the thermal characteristics of the pure sample and the mixed sample.

Previously the potential use of DSC in combination with multivariate calibration was reported to verify boar meat adulteration in processed food products, namely meatballs; these data support the effectiveness of DSC in analyzing and detecting wild boar meat adulteration. Which was successfully classified in meatball samples using the chemometric method of PCA [29]. In another study, the DSC and PCA methods successfully detected differences in samples of lard forgery into beef and chicken fat up to a concentration of 0.5%, as seen in the heating thermogram profile [30].

Based on the results of the research that has been carried out. It is hoped that the analytical method that has been developed can be used routinely for testing the halalness of food products, especially those made from meat. Suppose the sample has been appropriately classified. Halal authentication should only be sufficient until qualitative analysis. Still, to see the quantitative relationship between the sample and the emerging thermal characteristics. Further research is needed to see the sensitivity of the thermal analysis method that has been developed.

■ CONCLUSION

Developing a thermal analysis method with an environmentally friendly concept has succeeded in identifying differences in beef, pork, rabbit, and chicken. This method can determine the type of meat that is analyzed through the DSC thermogram profile, which is a thermal characteristic of each meat. The PCA technique has successfully classified meat samples based on their thermal characteristics. The difference in thermal characteristics between pure and mixed meat samples can also be seen clearly after chemometric analysis.

■ ACKNOWLEDGMENTS

The authors are grateful to the Ministry of Education Culture Research and Technology of the Republic of Indonesia. This research was funded by The Research and Technology - High Education Directorate, Education Ministry of Republic Indonesia. 083/E5/PG.02.00.PT/2022.

■ AUTHOR CONTRIBUTIONS

Conception and design, I.N.; acquisition of data, A.; analysis and interpretation of data, I.N. and A.; took part in drafting the article or revising it critically for important intellectual content, I.N. and A.; agreed to submit to the current journal, A.; gave final approval of the version to be published, I.N. and A.; and agree to be accountable for all aspects of the work, I.N. and A.

■ REFERENCES

- [1] Pointing, J., Al-Teinaz, Y.R., Lever, J., Critchley, M., and Spear, S., 2020, "Food Fraud" in *The Halal Food Handbook*, Eds. Al-Teinaz, Y.R., Spear, S., and Abd El-Rahim, I.H.A., Wiley-Blackwell, Hoboken, New Jersey, US, 321–329.
- [2] Mortas, M., Awad, N., and Ayvaz, H., 2022, Adulteration detection technologies used for halal/kosher food products: An overview, *Discover Food*, 2 (1), 15.
- [3] Ballin, N.Z., Vogensen, F.K., and Karlsson, A.H., 2009, Species determination - Can we detect and quantify meat adulteration?, *Meat Sci.*, 83 (2), 165–174.
- [4] Rahman, M.M., Ali, M.E., Abd Hamid, S.B., Mustafa, S., Hashim, U., and Hanapi, U.K., 2014, Polymerase chain reaction assay targeting cytochrome b gene for the detection of dog meat adulteration in meatball formulation, *Meat Sci.*, 97 (4), 404–409.
- [5] Rohman, A., Rahayu, W.S., Sudjadi, S., and Martono, S., 2021, The Use of real-time polymerase chain reaction combined with specific-species primer for analysis of dog meat DNA in meatball, *Indones. J. Chem.*, 21 (1), 225–233.

- [6] Chen, X., Lu, L., Xiong, X., Xiong, X., and Liu, Y., 2020, Development of a real-time PCR assay for the identification and quantification of bovine ingredient in processed meat products, *Sci. Rep.*, 10 (1), 2052.
- [7] Tao, D., Xiao, X., Lan, X., Xu, B., Wang, Y., and Khazalwa, E.M., 2022, An inexpensive CRISPR-based point-of-care test for the identification of meat species and meat products, *Genes*, 13 (5), 912.
- [8] Babu, N.S., and Reddy, S.M., 2014, Impact of solvents leading to environmental pollution, *J. Chem. Pharm. Sci.*, Special Issue 3, 49–52.
- [9] Nugrahani, I., 2021, Sustainable pharmaceutical preparation methods and solid-state analysis supporting green pharmacy, *Curr. Pharm. Anal.*, 17 (8), 969–982.
- [10] Wu, D., Wang, S., Wang, N., Nie, P., He, Y., Sun, D.W., and Yao, J., 2013, Application of time series hyperspectral imaging (TS-HSI) for determining water distribution within beef and spectral kinetic analysis during dehydration, *Food Bioprocess Technol.*, 6 (11), 2943–2958.
- [11] Bampi, M., Schmidt, F.C., and Laurindo, J.B., 2019, A fast drying method for the production of salted-and-dried meat, *Food Sci. Technol.*, 39 (Suppl. 2), 526–534.
- [12] Ren, Y., and Sun, D.W., 2022, Monitoring of moisture contents and rehydration rates of microwave vacuum and hot air dehydrated beef slices and splits using hyperspectral imaging, *Food Chem.*, 382, 132346.
- [13] Gill, P., Moghadam, T.T., and Ranjbar, B., 2010, Differential scanning calorimetry techniques: Applications in biology and nanoscience, *J. Biomol. Tech.*, 21 (4), 167–193.
- [14] USP, 2021, <1225> *Validation of Compendial Procedures*, USP 35, 877–882.
- [15] ICH, 2022, *Validation of Analytical Procedures Q2(R2)*, European Medicines Agency, Amsterdam, Netherlands, 1–34.
- [16] Savanović, D., Grujić, R., Rakita, S., Torbica, A., and Božičković, R., 2017, Melting and crystallization DSC profiles of different types of meat, *Chem. Ind. Chem. Eng. Q.*, 23 (4), 473–481.
- [17] Cobos, A., and Diaz, O., 2015, “Chemical Composition of Meat and Meat Products” in *Handbook of Food Chemistry*, Eds. Cheung, P.C.K., and Mehta, B.M., Springer, Heidelberg, Germany, 471–510.
- [18] Kovácsné Oroszvári, B., Bayod, E., Sjöholm, I., and Tornberg, E., 2006, The mechanisms controlling heat and mass transfer on frying of beefburgers. III. Mass transfer evolution during frying, *J. Food Eng.*, 76 (2), 169–178.
- [19] Pathare, P.B., and Roskilly, A.P., 2016, Quality and energy evaluation in meat cooking, *Food Eng. Rev.*, 8 (4), 435–447.
- [20] U.S. Department of Agriculture (USDA), 2013, *Water in Meat & Poultry*, Food Safety and Inspection Service, <https://www.fsis.usda.gov/food-safety/safe-food-handling-and-preparation/food-safety-basics/water-meat-poultry>.
- [21] Li, X., Xie, X., Zhang, C., Zhen, S., and Jia, W., 2017, Role of mid- and far-infrared for improving dehydration efficiency in beef jerky drying, *Drying Technol.*, 36 (3), 283–293.
- [22] Talik, P., Żuromska-Witek, B., Hubicka, U., and Krzek, J., 2017, The use of the DSC method in quantification of active pharmaceutical ingredients in commercially available one component tablets, *Acta Pol. Pharm.*, 74 (4), 1049–1055.
- [23] Azir, M., Abbasiliasi, S., Tengku Ibrahim, T.A., Abdul Manaf, Y.N., Sazili, A.Q., and Mustafa, S., 2017, Detection of lard in cocoa butter—Its fatty acid composition, triacylglycerol profiles, and thermal characteristics, *Foods*, 6 (11), 98.
- [24] AOAC, 2016, *Appendix F: Guidelines for Standard Method Performance Requirements*, AOAC International, Gaithersburg, MD, 1–18.
- [25] Agafonkina, I.V., Korolev, I.A., and Sarantsev, T.A., 2019, The study of thermal denaturation of beef, pork, chicken and turkey muscle proteins using differential scanning calorimetry, *Theory Pract. Meat Process.*, 4 (3), 19–23.
- [26] Pointing, J., 2020, “The Legal Framework of General Food Law and the Stunning of Animals Prior to Slaughter” in *The Halal Food Handbook*,

- Eds. Al-Teinaz, Y.R., Spear, S., and Abd El-Rahim, I.H.A., Wiley-Blackwell, Hoboken, New Jersey, US, 271–281.
- [27] Weiss, I.M., Muth, C., Drumm, R., and Kirchner, H.O.K., 2018, Thermal decomposition of the amino acids glycine, cysteine, aspartic acid, asparagine, glutamic acid, glutamine, arginine and histidine, *BMC Biophys.*, 11 (1), 2.
- [28] Nurrulhidayah, A.F., Arief, S.R., Rohman, A., Amin, I., Shuhaimi, M., and Khatib, A., 2015, Detection of butter adulteration with lard using differential scanning calorimetry, *Int. Food Res. J.*, 22 (2), 832–839.
- [29] Guntarti, A., Rohman, A., Martono, S., and Yuswanto, A., 2017, Authentication of wild boar meat in meatball formulation using differential scanning calorimetry and chemometrics, *J. Food Pharm. Sci.*, 5, 8–12.
- [30] Dahimi, O., Abdul Rahim, A., Abdulkarim, S.M., Hassan, M.S., Zam Hashari, S., Siti Mashitoh, A., and Saadi, S., 2014, Multivariate statistical analysis treatment of DSC thermal properties for animal fat adulteration, *Food Chem.*, 158, 132–138.
- [31] Miller, J.N., and Miller, J.C., 2010, *Statistics and Chemometrics for Analytical Chemistry*, 6th Ed., Prentice Hall, Hoboken, New Jersey, US.
- [32] Sulistiawan, A., Setyaningsih, W., and Rohman, A., 2022, A new FTIR method combined with multivariate data analysis for determining aflatoxins in peanuts (*Arachis hypogaea*), *J. Appl. Pharm. Sci.*, 12 (7), 199–206.

Supplementary Data

This supplementary data is a part of a paper entitled “Protein Modelling Insight to the Poor Sensitivity of Chikungunya Diagnostics on Indonesia’s Chikungunya Virus”.



Fig S1. Sequence alignment of E1-E2 Ind-CHIKV. The mutation points are highlighted in dark color. The CHK-152 antibody binding site are presented in red line and the B-cell epitopes are highlighted in black and blue color, respectively



Fig S1. Sequence alignment of E1-E2 Ind-CHIKV. The mutation points are highlighted in dark color. The CHK-152 antibody binding site are presented in red line and the B-cell epitopes are highlighted in black and blue color, respectively (Continued)

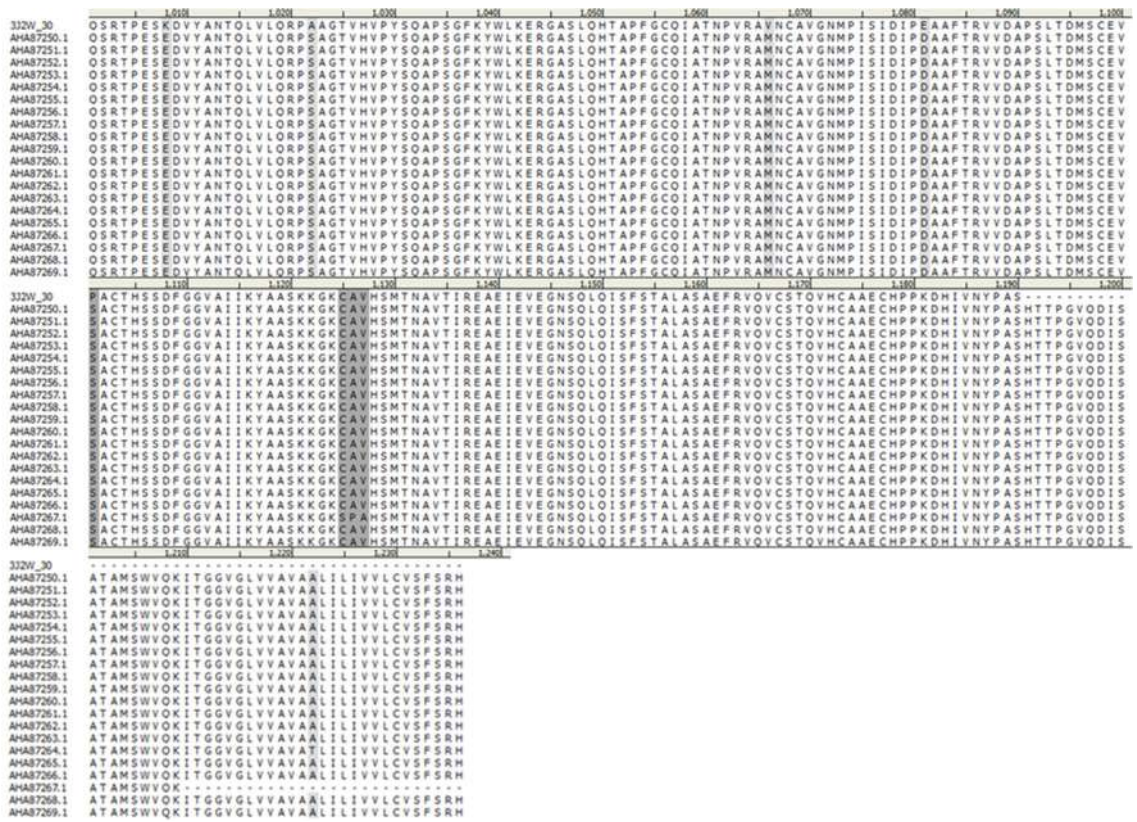


Fig S1. Sequence alignment of E1-E2 Ind-CHIKV. The mutation points are highlighted in dark color. The CHK-152 antibody binding site are presented in red line and the B-cell epitopes are highlighted in black and blue color, respectively (*Continued*)

Protein Modelling Insight to the Poor Sensitivity of Chikungunya Diagnostics on Indonesia's Chikungunya Virus

Bevi Lidya^{1,2}, Muhammad Yusuf^{3,4}, Umi Baroroh⁵, Korry Novitriani⁶, Bacht Alisjahbana⁷, Iman Rahayu³, and Toto Subroto^{3,4*}

¹Doctoral Program of Biotechnology, Postgraduate School, Universitas Padjadjaran, Jl. Dipati Ukur No. 35, Bandung 40132, Indonesia

²Department of Chemical Engineering, Politeknik Negeri Bandung, Jl. Gegerkalong Hilir, Bandung 40559, Indonesia

³Department of Chemistry, Faculty of Mathematics and Natural Sciences, Universitas Padjadjaran, Jl. Raya Bandung-Sumedang Km. 21, Jatinangor, Sumedang 45363, Indonesia

⁴Research Center of Molecular Biotechnology and Bioinformatics, Universitas Padjadjaran, Jl. Singaperbangsa No. 2, Bandung 40132, Indonesia

⁵Department of Biotechnology, Sekolah Tinggi Farmasi Indonesia, Jl. Soekarno Hatta No. 354, Bandung 40266, Indonesia

⁶Department of Medical Laboratory Technology, Faculty of Health Science, Universitas Bakti Tunas Husada, Jl. Cilolohan No. 36, Tasikmalaya 46115, Indonesia

⁷Health Center Unit, Faculty of Medicine, Universitas Padjadjaran, Jl. Prof. Eyckman No.38, Bandung 40161, Indonesia

* **Corresponding author:**

email: t.subroto@unpad.ac.id

Received: November 21, 2022

Accepted: May 27, 2023

DOI: 10.22146/ijc.79301

Abstract: Sensitive detection of infectious diseases is crucial for effective clinical care. However, commercial rapid tests may be limited in their ability to detect pathogen variants across different countries. It was found that the sensitivity of a chikungunya rapid test on local strain was only 20.5% as compared to the East, Central, and South Africa (ECSA) phylogroup. Therefore, the development of geographically specific diagnostics is essential. Investigating the distinctive structural properties of a locally sourced antigenic protein is an important initiative for the development of a specific antibody. This study utilized structural bioinformatics and molecular dynamics simulations to investigate the differences between the E1-E2 antigenic proteins of the Indonesian chikungunya virus (Ind-CHIKV) and that of ECSA. The results showed that some of the mutation points are located at the antibody binding sites of Ind-CHIKV. G194S and V318R mutations were proposed as distinctive features of Ind-CHIKV, leading to weaker antibody binding compared to ECSA. It suggests that modifying the antibody to accommodate bulkier side chains at positions 194 and 318 could improve its effectiveness against Ind-CHIKV. These insights are valuable for developing a highly sensitive immunoassay for Ind-CHIKV and other regional pathogens, ultimately enhancing diagnostic capabilities in Indonesia.

Keywords: chikungunya; bioinformatics; diagnostics; Indonesia; molecular dynamics simulation

■ INTRODUCTION

Sensitive diagnosis of infectious diseases plays an important role in maintaining the quality of health services. Despite the availability of imported rapid tests in

Indonesia, the genetic variation of pathogens amongst different countries has created some causes for concern. Kosasih and colleagues [1] found that the sensitivities of commercial chikungunya rapid tests in detecting the local strains were not satisfying. Two imported products

had sensitivities of only 20.5 and 50.8% on the local samples, as compared to 90.3% when tested on the East, Central, and South Africa (ECSA) phylogroup. A similar result was also reported by the Center for Diseases Control (CDC) in 2016, where at least five commercial chikungunya rapid test performance was unacceptable [2]. The genotype variation between Asian and ECSA strains was suggested as the main source of different results. Therefore, the development of a diagnostic test that is specific to local strains should become a priority. Moreover, chikungunya was recently found to be endemic in Bandung, one of the big cities in Indonesia and some of them belong to acute infection [3-5].

Chikungunya is a disease caused by chikungunya virus (CHIKV). This virus is transmitted to humans by two species of mosquito: *Aedes albopictus* and *Aedes aegypti*. CHIKV causes a range of clinical manifestations, including high fever, headache, erythematous skin rash, and incapacitating arthralgia [6]. CHIKV is an enveloped, positive-stranded RNA virus that belongs to the alphavirus genus of the *Togaviridae* family [7-8]. The genome of CHIKV is ~11.8 kb long and encodes nine viral proteins, five of which are structural proteins, i.e., capsid, E3, E2, E1, and 6K [9-10]. In the mature virion, two surface glycoproteins (E1 and E2) facilitate the viral binding and entry through receptor-mediated endocytosis and low-pH-mediated fusion within the endosomes [11-12]. Proteins E1 and E2 form a heterodimer that covers the viral surface. Kam and colleagues [13] showed that E2 is the primary target for the anti-CHIKV antibody response. Therefore, variations in E1-E2 sequences might lead to the different sensitivity of IgM-based rapid tests. Currently, there are 14 and 6 entries of E1-E2 and E1-only CHIKV sequences of the Bandung strain, respectively found in NCBI [3]. From those sequences, at least six amino acids were found to be different, indicating the polymorphism of CHIKV in Bandung itself. These variabilities also might contribute to the different sensitivity of the IgM-based rapid test.

In recent years, advances in molecular design have contributed to developing "tailored" molecules for diagnostics and therapeutics [14-16]. Recently, Holstein et al. [17] have developed an influenza-specific paper-

based diagnostic test based on the computationally designed protein. The selection of this tailored protein could be an antibody fragment, such as a single-chain variable fragment (ScFv), or the other functional protein that could bind to the antigenic protein. The accessibility of genetic and structural information of pathogenic molecules, in addition to the sophisticated bioinformatics method, has provided a great opportunity to design molecules with desired properties. Structural information on ECSA chikungunya's antigenic protein and its antibody is available in the Protein Data Bank [18].

This study aims to investigate the structural differences between the E1-E2 antigenic protein of Indonesia's CHIKV (Ind-CHIKV) and that of ECSA using a bioinformatics approach. The protein sequence of Ind-CHIKV and the crystal structure of E1-E2 of ECSA CHIKV were used to construct the structural model of local antigens. Then, the behavior of both structures was investigated using molecular dynamics simulation. The affinity of the antibody towards E1-E2 CHIKV was computed using protein docking and molecular mechanics generalized Born surface area (MM/GBSA) methods.

■ EXPERIMENTAL SECTION

Materials

The GenBank number AHA87256.1 which consists of amino acid sequences of E1-E2 antigen of Ind-CHIKV, complex structure of E1-E2 ECSA CHIKV (PDB ID: 3J2W) and its antibody (anti-CHIKV CHK-152, PDB ID: 3J30), and a crystal structure of E1-E2 CHIKV with PDB ID of 3N44 were used in this work.

Instrumentation

This study was carried out on a computer running Ubuntu 20.04.2.0 LTS and equipped with a processor core i7 CPU 920@2.67 GHz, a GPU NVIDIA GeForce RTX 980 4 GB, RAM memory 8 GB, and a hard disk 2 TB.

Procedure

Homology modelling of E1-E2 antigen of Ind-CHIKV

The model structure of the E1-E2 antigen of Ind-CHIKV was constructed by homology modeling method

using MODELLER9.17 in command line mode [19]. The amino acid sequences of the E1-E2 antigen of Ind-CHIKV were retrieved from NCBI (<http://www.ncbi.nlm.nih.gov/>) with GenBank number of AHA87256.1, which consist of E1 and E2 sequences [3]. The template for protein modeling was selected based on the high sequence similarity using BLASTP in NCBI, the quality of template structure, and also the condition of the experimental. The discrete optimized protein energy (DOPE) score, a statistical potential used to assess homology models in protein structure prediction, was calculated for the structure model. The structure with the lowest DOPE score was selected as the best model. The quality of the model was assessed by Ramachandran plot using the PROCHECK server, Z-score using ProSA-web, and VERIFY-3D method [20-22].

Molecular dynamics simulation

All the minimization and molecular dynamics (MD) simulations were performed using pmemd.cuda from AMBER14 [23]. The type of cysteine and protonation states of histidine were adjusted based on their specific chemical environment manually. A box of TIP3P water was added to the system, where the distance between the protein and the edge of the box was set to 10 Å. The system was neutralized by the addition of sodium ions.

The structure was optimized by using 1000 steps of steepest descent, which was followed by 2000 steps of conjugate gradient minimization with 500 kcal mol⁻¹ Å⁻² of harmonic restraints applied to the backbone atoms. A final 5000 steps of unrestrained conjugate gradient minimization were performed in order to remove any steric clashes.

The system was gradually heated to 300 K in the NVT ensemble using harmonic restraints on the backbone atoms under control by the Langevin thermostat. Then, 1000 ps of NPT equilibration was performed with a gradual decrease of harmonic restraints by 1 kcal mol⁻¹ Å⁻² until it reached zero. A 100 ns of the production run in the NPT ensemble was performed with all hydrogen atoms constrained using the SHAKE algorithm. The temperature was controlled with a Langevin thermostat with a collision frequency of 1 ps⁻¹, while pressure was controlled using a Berendsen barostat

with a coupling constant of 1 ps and a target pressure of 1 bar. The time step used during the production stage was set to 2 fs. A non-bonded cut-off value of 10 Å was used, and the long-range electrostatics were treated using the Particle Mesh Ewald method. The MD trajectories were analyzed using the cpptraj module in AmberTools 15.

Evaluation of binding energy

Before computing the binding energy, a cryo-EM resolved the complex structure of E1-E2 ECSA CHIKV and its antibody was shortly minimized *in vacuo* to remove the major sterical clashes at the interface region without affecting the core structure. Each of the 250 steps for steepest descent and conjugate gradient minimization was performed using the sander module in AMBER 14. The minimized complex was submitted to the FireDock server (<http://bioinfo3d.cs.tau.ac.il/FireDock>) as well as Ind-CHIKV with CHK-152 and CHK-152 mutants [24-25].

FireDock is a docking program specifically built for refining and re-scoring the docked protein-protein interactions. In the program options, the type of system was selected for the antibody-antigen complex. One hundred cycles of docking were performed, with a full refinement option activated.

Furthermore, the docked complex by FireDock was minimized in the explicit solvent system. A 100 ns of MD simulation was performed using a similar parameter as described in the previous subsection. Finally, the binding energy and its decomposition analysis were done by the MMPBSA.py module in AmberTools 14.

RESULTS AND DISCUSSION

Structural Model of E1-E2 of Ind-CHIKV

The sequence of E1-E2 of Ind-CHIKV was retrieved from NCBI. This virus was isolated from the human serum of infected patients from Bandung, Indonesia. Twenty entries were found, which were composed of 14 complete sequences of E1-E2 and 6 sequences of E1 only. Six variations within 20 Ind-CHIKV sequences were detected, but they are not located at the antibody binding site (Fig. S1). For this

reason, the sequence with the GenBank number AHA87256.1 was chosen to represent E1-E2 of Ind-CHIKV [3]. Sequence alignment showed that E1 and E2 of Ind-CHIKV shared sequence similarities of 98 and 96%, respectively, with that of the ECSA virus.

The selection of a template is a crucial step in protein modeling [26]. The first attempt in template searching using NCBI resulted in the PDB ID of 2XFC, which is a cryo-electron microscopy (cryo-EM) structure of E1-E2 CHIKV from Semliki Forest (African). However, a cryo-EM structure usually has a low atomic resolution. Hence, it is not suitable to be used as a template for homology modeling. For this reason, further searching was done using sequence similarity with the PDB ID of 2XFC in the PDB server. As a result, a crystal structure of E1-E2 CHIKV with PDB ID of 3N44, with the best resolution of 2.35 Å, was selected as a template. This structure is a mature glycoprotein E1-E2 CHIKV which was soaked in osmium to improve the quality of X-ray structure determination [18,27]. The template covered 729 residues of E1-E2 Ind-CHIKV without any gaps.

After five models of E1-E2 Ind-CHIKV were built using MODELLER, the best model was chosen based on the lowest DOPE score of -74029. Furthermore, the model quality was assessed by the Ramachandran plot (Fig. 1). It is shown that 91.3% of residues were located in the most favored regions, including all mutations in Ind-CHIKV. As many as 8.1 and 0.5% of residues fall into the additional allowed regions and generously allowed regions, respectively. Only one residue falls in the disallowed regions. Upon visual inspection, this residue is located at the backbone of the secondary structure, i.e., beta-sheet. Therefore, a loop optimization step was not required. In general, a protein model with more than 90% residues in the allowed region is categorized as a good model [18,26]. Moreover, model assessment using ProSA-web showed a small difference in Z-score between the model and the template structure (Fig. 2). VERIFY-3D method showed that the score of 94.10% residues of the model is higher than 0.2 (Fig. 3), which considered as a high-quality structure [21,28].

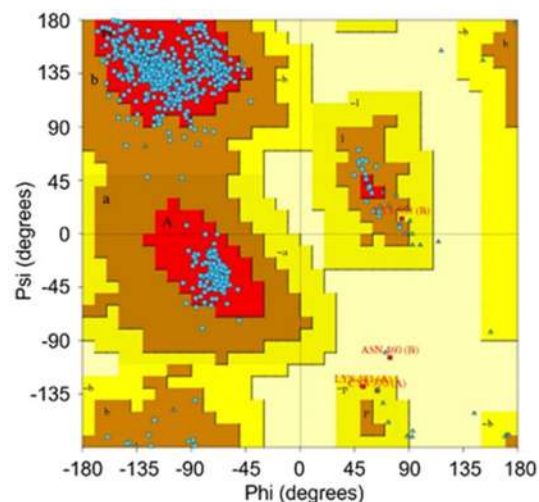


Fig 1. Ramachandran Plot of E1-E2 Ind-CHIKV model

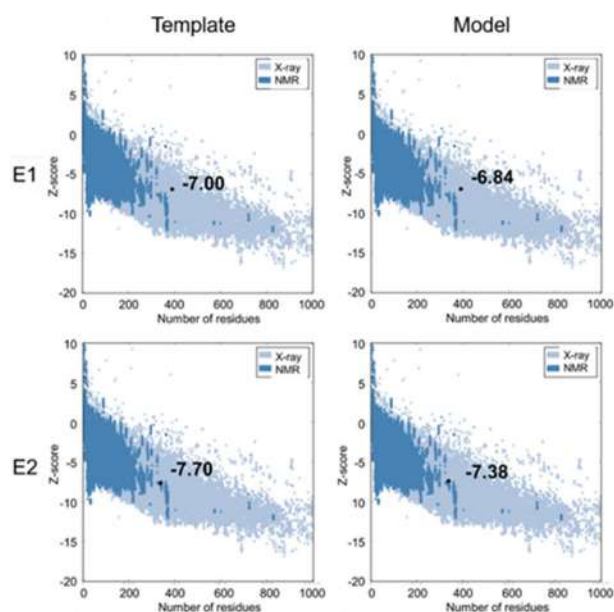


Fig 2. Z-score of E1 and E2 structure of template and model

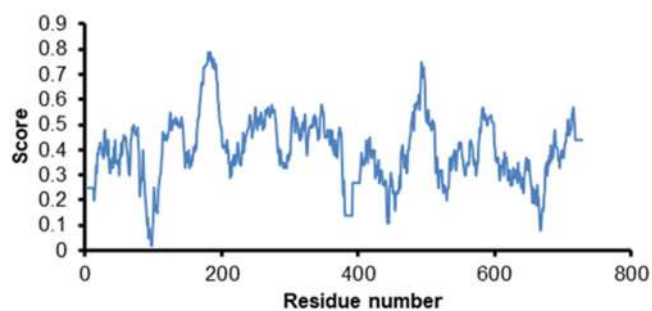


Fig 3. The VERIFY-3D score of E1-E2 Ind-CHIKV model

Mapping of Mutations to the Structure of E1-E2 IndCHIKV

As many as 21 mutations were detected when the sequences of E1-E2 of Ind-CHIKV and ECSA were aligned (Fig. 4). These mutations were found in almost all E1-E2 Ind-CHIKV sequences (Fig. S1). These mutations were visually mapped to the model of E1-E2 Ind-CHIKV. By using a solvent probe with a radius of 1.4 Å, only 2 out of 21 mutations were found to be buried in the solvent, V255 and I317 (Fig. 5).

Due to their location, these 19 residues were predicted to be involved in the interactions with antibodies. Among the 19 mutations, a polymorphism of L248F was detected in 6 out of 14 sequences of E2. This

mutation is known as part of the B-cell epitope [13].

Mutations at the Epitopes

In short, the epitope is part of an antigen (E1-E2 of CHIKV) that is recognized by the immune system, e.g., antibodies, and B-cells. Rapid diagnostic kits that were tested by Kosasih and colleagues [1] were based on the detection of anti-chikungunya IgM. In the serum, IgM was produced as a response to the presence of epitope in CHIKV. Therefore, different epitopes would produce different antibodies. In this study, the structural differences between Ind-CHIKV and ECSA were observed to investigate the possibilities of structural changes at the epitope regions.

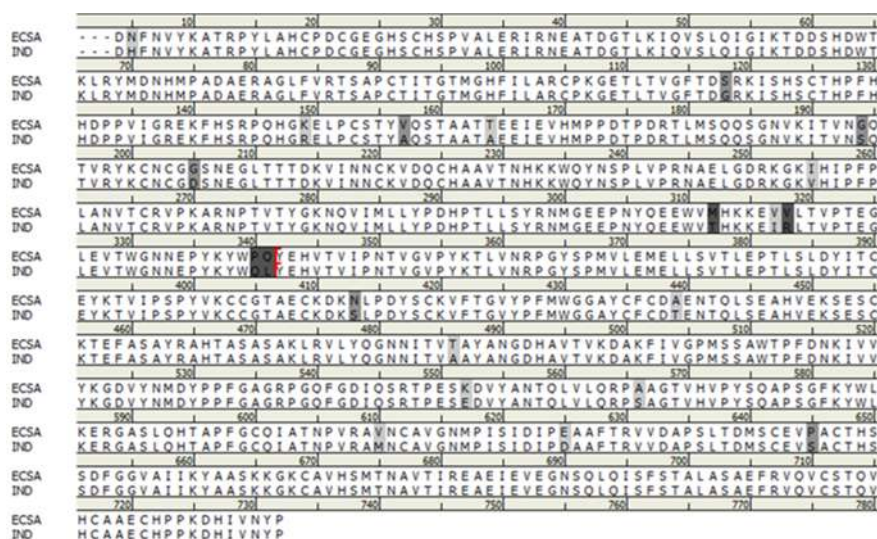


Fig 4. Sequence alignment between E1-E2 of Africa's (PDB ID: 3N44) and Ind-CHIKV virus (based on PDB ID: 3N44 numbering). Mutations are highlighted in dark color

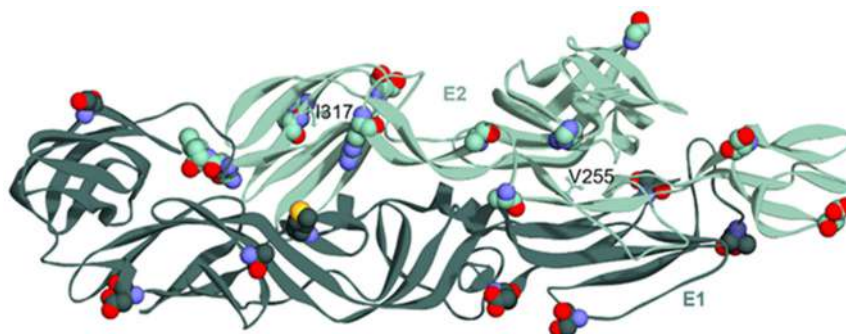


Fig 5. Different residues at E1-E2 Ind-CHIKV as compared to that of African origin. Mutations that are exposed to the solvent are visualized in the space-filling model while the buried in the ball and stick model. E1 and E2 are represented in dark and light green colored ribbons, respectively

In 2014, Kam et al. [13], have identified B-cell epitopes that were recognized by anti-CHIKV antibodies. There were seven linear epitopes located at the E2 protein of CHIKV. Upon comparison with the sequence of E1-E2 Ind-CHIKV, there were five mutations located in the epitope regions of E2, i.e., N5H, G194S, I255V, V318R, and L248F (Fig. 6). In V318R mutation, valine is a relatively small hydrophobic residue, while arginine is a bulky, positively charged amino acid. Therefore, the presence of arginine at position 318 would cause a steric hindrance to the antibodies. Whereas the changes from aliphatic to aromatic residues in N5H and L248F mutations would result in different flexibility to adopt the antibody binding.

Molecular Dynamics Simulation

The deviation and fluctuation of both E1-E2 from ECSA and that of Ind-CHIKV were evaluated by computing root mean square deviation (RMSD) and root mean square fluctuation (RMSF) values with respect to the initial and average conformations, respectively. Fig. 7(a) shows that, in general, both systems have reached equilibrium after 3000 ps. Therefore, fluctuations were calculated from 3000–10000 ps to avoid bias from the unequilibrated motions. It is shown that the deviation of E1-E2 of Ind-CHIKV was higher, especially after 65 ns and reached up to 5.5 Å compared to that of ECSA which showed more stability during the simulation. This slight difference was due to dissimilar residues at positions 248 and 255, as suggested by the higher RMSF around

position 250 in Fig. 7(b). Nevertheless, the residual fluctuation of E1-E2 Ind-CHIKV was generally comparable to that of ECSA. For this reason, it can be suggested that the overall dynamic behavior of both systems was similar.

Furthermore, the observation was more focused on the antibody binding site. Sun et al. [29] have also identified the footprints of a neutralizing antibody using cryo-EM, i.e., CHK-9, CHK-152, m242, and m10. These structures provide an opportunity to explain the mutation effect at the atomic level. All the antibody structures bound to G194 (Fig. 8) thus, it was interesting to be investigated. In addition, the CHK-152 suggests more effective neutralization at a lower concentration than the others [28]. Hence, CHK-152 was used to study the effect of G194S. However, it is noted that the structure should be treated carefully due to the low resolution of cryo-EM structures in general.

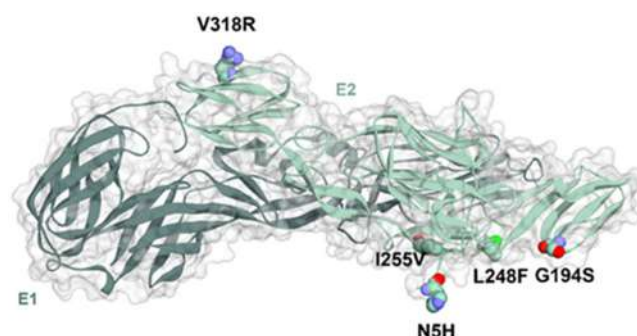


Fig 6. The mutations in the epitope regions of the E2 protein of Ind-CHIKV

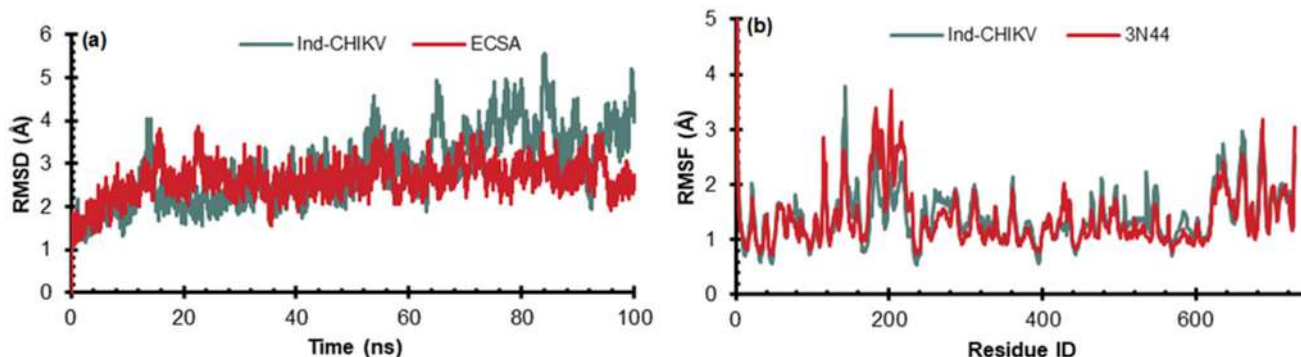


Fig 7. (a) RMSD and (b) RMSF profiles of both ECSA and Ind-CHIKV throughout MD simulation

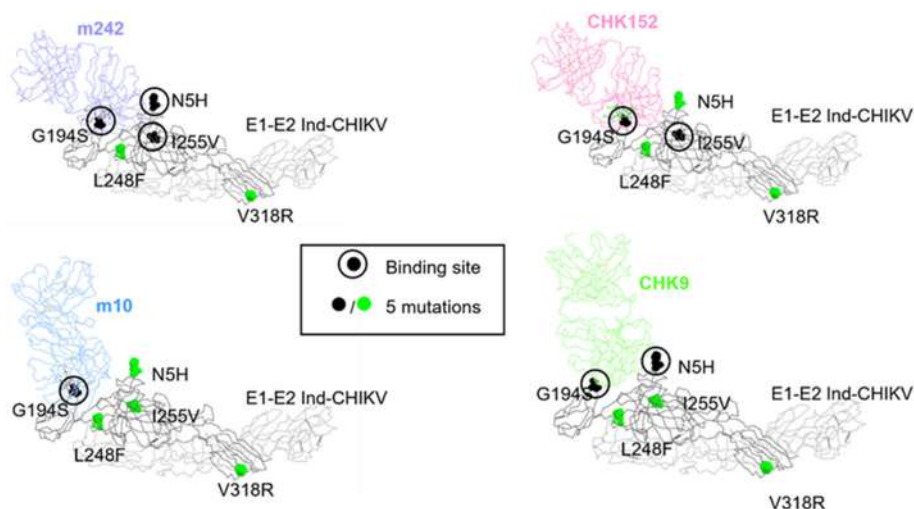


Fig 8. Molecular interactions between E1-E2 Ind-CHIKV and antibody (m242, m10, CHK-152, and CHK-9). The mutations on E1-E2 Ind-CHIKV are drawn in the black and green ball, with the antibody binding site drawn in the black circle. The E1-E2 Ind-CHIKV are colored in black and grey stick, while the antibody of m242, m10, CHK-152, and CHK-9 are colored in purple, blue, pink, and green, respectively

The Effect of G194S in Ind-CHIKV on the Binding of CHK-152

Based on the FireDock calculation, the binding energy of CHK-152 to the ECSA CHIKV was $-81.76 \text{ kcal mol}^{-1}$. Furthermore, a mutant model of G194S (representing Ind-CHIKV) was built to observe the possible impact of this mutation on the binding of CHK-152. Interestingly, the computed affinity of CHK-152 to G194S ($-71.17 \text{ kcal mol}^{-1}$) was predicted to be weaker than the ECSA. At first sight, it can be deduced that the bulkier side chain of serine ($-\text{CH}_2\text{OH}$ group) resulted in an unfavorable binding to the CHK-152. A visual inspection showed that serine 8 was positioned closer to the Y244 of CHK-152, as compared to that of glycine (Fig. 9).

A short distance between S194 and Y244 might result in a repulsive force. This hypothesis was tested by modifying the structure of CHK-152 by Y244G mutation. It is noted that glycine is the smallest residue among 20 amino acids. It was expected that modification of Y244G in the CHK-152 structure would improve its binding to the G194S by removing sterical clashes between S194 and Y244. Table 1 shows that the affinity between G194S and Fab Y244G was increased to $-80.48 \text{ kcal mol}^{-1}$, similar to that of WT (ECSA). This result indicates that the

mutation of G194S in Ind-CHIKV is one of the reasons behind the different affinities with CHK-152. Thus, it can be used as a distinctive feature in developing a specific antibody for Ind-CHIKV.

Since the FireDock refinement was done in the implicit solvent model system, a more realistic 100 ns of the explicit solvent simulation was performed using AMBER. The docked conformation resulting from FireDock was submitted to the MD preparation protocol as described in the method section. The binding energy from the explicit solvent simulation was computed by MM/GBSA method. As a result, a similar trend of binding energy between the two systems is shown in Table 2.

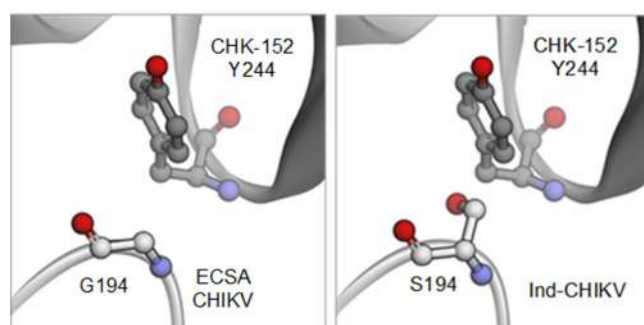


Fig 9. The closer distance between Y244 of the CHK-152 with the bulkier S194 in Ind-CHIKV (right) than to G194 in ECSA CHIKV (left)

Table 1. The calculated binding energy between E1-E2 CHIKV and Fab CHK-152 using Firedock

Energy component	Energy (kcal mol ⁻¹)		
	ECSA and CHK-152	Ind-CHIKV and CHK-152	Ind-CHIKV and CHK-152 (Fab Y244G)
Global energy	-81.76	-71.17	-80.48
Attractive VdW	-55.97	-55.97	-55.44
Repulsive VdW	17.35	35.41	14.83
ACE ^a	11.68	12.33	12.27
H-bond	-10.56	-11.51	-10.04

^aatomic contact energy**Table 2.** The calculated binding energy between E1-E2 of ECSA and Ind-CHIKV with the Fab CHK-152 using the MM/GBSA method

	ECSA	Ind-CHIKV
Binding energy (kcal mol ⁻¹)	-30.62	-24.48
Decomposition of electrostatic energy between residue 194 and Y244 (kcal mol ⁻¹)	-0.08	+0.37

The binding of ECSA to the CHK-152 (-30.62 kcal mol⁻¹) was better than that of Ind-CHIKV (-24.48 kcal mol⁻¹). Furthermore, the decomposition energy between residues at position 194 and the Y244 from the CHK-152 was analyzed. The result showed that S194 has a positive electrostatic energy (+0.37 kcal mol⁻¹) with the Y244, as compared to that of G194 in the ECSA (-0.08 kcal mol⁻¹).

Structural Bioinformatics Study

Similar clinical manifestations between CHIKV, DENV, and Zika virus represent a diagnostic challenge to differentiate itself. Hence a sensitive diagnosis is needed [30-31]. Some diagnostic methods that usually be used to differentiate amongst them are RT-PCR, ELISA, and indirect immunofluorescence (IFA). Unfortunately, these methods require special equipment, need more time, and technical skills from medium to high levels that may not be available in many laboratories, especially in rural areas. Diagnostic using rapid tests has many advantages, such as being highly cost-effective, easy to use, and the results can easily be evaluated and fast. Nevertheless, the commercial rapid test of CHIKV was reported poorly and needs major improvement [2]. This study proposes that the difference in sensitivity of chikungunya rapid tests on the Indonesian strain was due to the genetic variation between ECSA and Ind-CHIKV. Since the rapid tests were based on the detection of IgM anti-CHIKV, then the

differences in sensitivity would derive from the distinctive features of epitopes on the surface of CHIKV. Several mutations were found on the surface of E1-E2 of Ind-CHIKV. Two of them were positioned at the antibody binding sites, i.e., G194S and V318R. In addition, these two mutations were found in all E1-E2 of Ind-CHIKV. These results can be used as a structural basis to develop a more specific molecule to detect antibodies or antigens to develop more sensitive rapid tests. Liu *et al.* [32] proposed that a single chain variable fragment (ScFv) of antibodies can also be engineered to be used for immunoassay. In addition, Holstein *et al.* [17] also suggested that a recombinant antibody fragment could be used as a functional protein for a paper-based diagnostic test. ScFv is widely used for diagnostic purposes in many fields, and there are to detect diseases in humans or plants [33-35].

MD simulation on E1-E2 of Ind-CHIKV and CHK-152 revealed that the binding affinity of this antigen-antibody was low compared to the ECSA. This approach can also be used to design a new antibody, especially ScFv, that has a high affinity to E1-E2 of Ind-CHIKV. Leong *et al.* [36] designed ScFv against *Salmonella typhi* TolC protein using MD simulation. This ScFv was designed de novo by evaluating the shape complementarity and calculating the binding affinity against TolC protein to 74 ScFv designs originating from

five crystal structures. The top five of ScFv designs have high binding affinity against TolC protein, and the top one originated from PDB ID of 3JUY, a variant of b12 antibody targeting HIV-1 gp120 envelope protein. These results can be used to develop the diagnosis for typhoid. Another study of MD simulation reported for evaluating the binding of ScFv against ESAT-6 for TB diagnostic. In this study, two high affinities of ScFv were isolated and built a model structure. MD simulations revealed that the hydrogen bond between amino acid residues of the light chain and residue of ESAT-6 was more in ScFv-7 than in ScFv-3. Hence, joining the heavy chain of ScFv-3 to the light chain of ScFv-7 is good for making new ScFv which may have higher affinity [37,38]. From these cases, MD simulation can be used to design and evaluate the protein-protein interactions, especially antigen-antibody interaction [39-40].

■ CONCLUSION

A possible reason for the low sensitivity of the current diagnostic test to the Ind-CHIKV was due to the genotype variations among strains of viruses. Using a structural bioinformatics approach, this study was able to identify the mutation points at the E1-E2 protein surface of Ind-CHIKV, especially at the antibody binding sites. Furthermore, G194S and V318R mutations were proposed as distinctive features of Ind-CHIKV, different from that of ECSA's. To develop a tailored antibody that would bind to the E1-E2 of Ind-CHIKV, one should accommodate a bulkier side chain at positions 194 and 318. It is expected that the results would provide valuable insight into developing an antibody-based functional protein for the further development of a highly sensitive immunoassay for the Ind-CHIKV or the other regional pathogens.

■ ACKNOWLEDGMENTS

We gratefully acknowledge the INSINAS Research Grant from the Ministry of Research, Technology, and Higher Education Republic of Indonesia with Contract number No. 45/INS-1/PPK/E4/2018 and the PENELITIAN TERAPAN Research Grant from

Politeknik Negeri Bandung No.: 464.10/PL1.R7/LT/2018 to support our research.

■ AUTHOR CONTRIBUTIONS

Conceived and designed the experiments: Bevi Lidya, Muhammad Yusuf, Umi Baroroh, Bacht Alisjahbana, Toto Subroto. Analyzed the data: Muhammad Yusuf, Umi Baroroh, Korry Novitriani, Bevi Lidya. Wrote the first draft of the manuscript: Bevi Lidya, Muhammad Yusuf, Umi Baroroh, Toto Subroto. Contributed to the writing of the manuscript: Bevi Lidya, Muhammad Yusuf, Umi Baroroh, Korry Novitriani, Iman Rahayu, Toto Subroto. Agree with manuscript results and conclusions: Bevi Lidya, Muhammad Yusuf, Umi Baroroh, Korry Novitriani, Bacht Alisjahbana, Iman Rahayu, Toto Subroto. Jointly developed the structure and arguments for the paper: Muhammad Yusuf, Umi Baroroh, Toto Subroto. Made critical revisions and approved final version: Bevi Lidya, Muhammad Yusuf, Umi Baroroh. All authors reviewed and approved the final manuscript.

■ REFERENCES

- [1] Kosasih, H., Widjaja, S., Surya, E., Hadiwijaya, S.H., Butarbutar, D.P.R., Jaya, U.A., and Alisjahbana, B., 2012, Evaluation of two IgM rapid immunochromatographic tests during circulation of Asian lineage chikungunya virus, *Southeast Asian J. Trop. Med. Public Health*, 43 (1), 55–61.
- [2] Burdino, E., Calleri, G., Caramello, P., and Ghisetti V., 2016, Unmet needs for a rapid diagnosis of chikungunya virus infection, *Emerging Infect. Dis.*, 22 (10), 1837–1839.
- [3] Kosasih, H., de Mast, Q., Widjaja, S., Sudjana, P., Antonjaya, U., Ma'roef, C., Riswari, S.F., Porter, K.R., Burgess, T.H., Alisjahbana, B., van der Ven, A., and Williams, M., 2013, Evidence for endemic chikungunya virus infections in Bandung, Indonesia, *PLoS Neglected Trop. Dis.*, 7 (10), e2483.
- [4] Harapan, H., Michie, A., Mudatsir, M., Nusa, R., Yohan, B., Wagner, A.L., Sasmono, R.T., and Imrie, A., 2019, Chikungunya virus infection in Indonesia:

- A systematic review and evolutionary analysis, *BMC Infect. Dis.*, 19 (1), 243.
- [5] Arif, M., Tauran, P., Kosasih, H., Pelupessy, N.M., Sennang, N., Mubin, R.H., Sudarmono, P., Tjitra, E., Murniati, D., Alam, A., Gasem, M.H., Aman, A.T., Lokida, D., Hadi, U., Parwati, K.T.M., Lau, C.Y., Neal, A., and Karyana, M., 2020, Chikungunya in Indonesia: Epidemiology and diagnostic challenges, *PLoS Neglected Trop. Dis.*, 14 (6), e0008355.
- [6] Sahoo, B., and Chowdary, T.K., 2019, Conformational changes in chikungunya virus E2 protein upon heparan sulfate receptor binding explain mechanism of E2-E1 dissociation during viral entry, *Biosci. Rep.*, 39 (6), BSR20191077.
- [7] Bissoyi, A., Pattanayak, S.K., Bit, A., Patel, A., Singh, A.K., Behera, S.S., and Satpathy, D., 2017, "Alphavirus Nonstructural Proteases and Their Inhibitors" in *Viral Proteases and Their Inhibitors*, Eds. Gupta, S.P., Academic Press, Cambridge, US, 77-104.
- [8] Segato-Vendrameto, C.Z., Zanluca, C., Zucoloto, A.Z., Zaninelli, T.H., Bertozzi, M.M., Saraiva-Santos, T., Ferraz, C.R., Staurengo-Ferrari, L., Badaro-Garcia, S., Manchope, M.F., Dionisio, A.M., Pinho-Ribeiro, F.A., Borghi, S.M., Mosimann, A.L.P., Casagrande, R., Bordignon, J., Fattori, V., dos Santos, C.N.D., and Verri, W.A., 2023, Chikungunya virus and its envelope protein E2 induce hyperalgesia in mice: Inhibition by anti-E2 monoclonal antibodies and by targeting TRPV1, *Cells*, 12 (4), 556.
- [9] Chen, R., Mukhopadhyay, S., Merits, A., Bolling, B., Nasar, F., Coffey, L.L., Powers, A., Weaver, S.C., and Consortium, I.R., 2018, ICTV virus taxonomy profile: Togaviridae, *J. Gen. Virol.*, 99 (6), 761-762.
- [10] Rangel, M.V., McAllister, N., Dancel-Manning, K., Noval, M.G., Silva, L.A., and Stapleford, K.A., 2022, Emerging chikungunya virus variants at the E1-E1 interglycoprotein spike interface impact virus attachment and inflammation, *J. Virol.*, 96 (4), e0158621.
- [11] Yap, M.L., Klose, T., Urakami, A., Hasan, S.S., Akahata, W., and Rossmann, M.G., 2017, Structural studies of chikungunya virus maturation, *Proc. Natl. Acad. Sci. U. S. A.*, 114 (52), 13703-13707.
- [12] Xu, X., Zhang, R., and Chen, X., 2017, Application of a single-chain fragment variable (scFv) antibody for the confirmatory diagnosis of hydatid disease in non-endemic areas, *Electron. J. Biotechnol.*, 29, 57-62.
- [13] Kam, Y.W., Lee, W.W.L., Simarmata, D., Le Grand, R., Tolou, H., Merits, A., Roques, P., and Ng, L.F.P., 2014, Unique epitopes recognized by antibodies induced in chikungunya virus-infected non-human primates: Implications for the study of immunopathology and vaccine development, *PLoS One*, 9 (4), e95647.
- [14] Dwivedi, S., Purohit, P., Misra, R., Pareek, P., Goel, A., Khattri, S., Pant, K.K., Misra, S., and Sharma, P., 2017, Diseases and molecular diagnostics: A step closer to precision medicine, *Indian J. Clin. Biochem.*, 32 (4), 374-398.
- [15] Gao, Y.P., Huang, K.J., Wang, F.T., Hou, Y.Y., Xu, J., and Li, G., 2022, Recent advances in biological detection with rolling circle amplification: Design strategy, biosensing mechanism, and practical applications, *Analyst*, 147 (15), 3396-3414.
- [16] Tiller, K.E., and Tessier, P.M., 2015, Advances in antibody design, *Annu. Rev. Biomed. Eng.*, 17 (1), 191-216.
- [17] Holstein, C.A., Chevalier, A., Bennett, S., Anderson, C.E., Keniston, K., Olsen, C., Li, B., Bales, B., Moore, D.R., Fu, E., Baker, D., and Yager, P., 2015, Immobilizing affinity proteins to nitrocellulose: A toolbox for paper-based assay developers, *Anal. Bioanal. Chem.*, 408 (5), 1335-1346.
- [18] Voss, J.E., Vaney, M.C., Duquerroy, S., Vonrhein, C., Girard-Blanc, C., Crublet, E., Thompson, A., Bricogne, G., and Rey, F.A., 2010, Glycoprotein organization of chikungunya virus particles revealed by X-ray crystallography, *Nature*, 468 (7324), 709-714.
- [19] Webb, B., and Sali, A., 2016, Comparative protein structure modeling using MODELLER, *Curr. Protoc. Bioinf.*, 54 (1), 5.6.1-5.6.37.

- [20] Laskowski, R.A., MacArthur, M.W., Moss, D.S., and Thornton, J.M., 1993, PROCHECK: A program to check the stereochemical quality of protein structures, *J. Appl. Crystallogr.*, 26 (2), 283–291.
- [21] Wiederstein, M., and Sippl, M.J., 2007, ProSA-web: Interactive web service for the recognition of errors in three-dimensional structures of proteins, *Nucleic Acids Res.*, 35 (Suppl. 2), W407–W410.
- [22] Ouyang, J., Huang, N., and Jiang, Y., 2020, A single-model quality assessment method for poor quality protein structure, *BMC Bioinf.*, 21 (1), 157.
- [23] Case, D.A., Babin, V., Berryman, J.T., Betz, R.M., Cai, Q., Cerutti, D.S., Cheatham, III, T.E., Darden, T.A., Duke, R.E., Gohlke, H., Goetz, A.W., Gusarov, S., Homeyer, N., Janowski, P., Kaus, J., Kolossváry, I., Kovalenko, A., Lee, T.S., LeGrand, S., Luchko, T., Luo, R., Madej, B., Merz, K.M., Paesani, F., Roe, D.R., Roitberg, A., Sagui, C., Salomon-Ferrer, R., Seabra, G., Simmerling, C.L., Smith, W., Swails, J., Walker, R.C., Wang, J., Wolf, R.M., Wu, X., and Kollman, P.A., 2014, *AMBER 14*, University of California, San Francisco.
- [24] Andrusier, N., Nussinov, R., and Wolfson, H.J., 2007, FireDock: Fast interaction refinement in molecular docking, *Proteins: Struct., Funct., Bioinf.*, 69 (1), 139–159.
- [25] Mashiach, E., Schneidman-Duhovny, D., Andrusier, N., Nussinov, R., and Wolfson, H.J., 2008, FireDock: A web server for fast interaction refinement in molecular docking, *Nucleic Acids Res.*, 36 (Suppl. 2), W229–W232.
- [26] Zhang, H., and Shen, Y., 2020, Template-based prediction of protein structure with deep learning, *BMC Genomics*, 21 (11), 878.
- [27] Wu, F., and Xu, J., 2021, Deep template-based protein structure prediction, *PLoS Comput. Biol.*, 17 (5), e1008954.
- [28] Lüthy, R., Bowie, J.U., and Eisenberg, D., 1992, Assessment of protein models with three-dimensional profiles, *Nature*, 356 (6364), 83–85.
- [29] Sun, S., Xiang, Y., Akahata, W., Holdaway, H., Pal, P., Zhang, X., Diamond, M.S., Nabel, G.J., and Rossmann, M.G., 2013, Structural analyses at pseudo atomic resolution of chikungunya virus and antibodies show mechanisms of neutralization, *eLife*, 2, e00435.
- [30] Sobolev, O.V., Afonine, P.V., Moriarty, N.W., Hekkelman, M.L., Joosten, R.P., Perrakis, A., and Adams, P.D., 2020, A global Ramachandran score identifies protein structures with unlikely stereochemistry, *Structure*, 28 (11), 1249–1258.e2.
- [31] Moulin, E., Selby, K., Cherpillod, P., Kaiser, L., and Boillat-Blanco, N., 2016, Simultaneous outbreaks of dengue, chikungunya and Zika virus infections: Diagnosis challenge in a returning traveller with nonspecific febrile illness, *New Microbes New Infect.*, 11, 6–7.
- [32] Liu, Y., Liu, Y., Mernaugh, R.L., and Zeng, X., 2009, Single chain fragment variable recombinant antibody functionalized gold nanoparticles for a highly sensitive colorimetric immunoassay, *Biosens. Bioelectron.*, 24 (9), 2853–2857.
- [33] Hurwitz, A.M., Huang, W., Kou, B., Estes, M.K., Atmar, R.L., and Palzkill, T., 2017, Identification and characterization of single-chain antibodies that specifically bind GI noroviruses, *PLoS One*, 12 (1), e0170162.
- [34] Shashi Kumar, N., Moger, N., Rabinal, C.A., Krishnaraj, P.U., and Chandrashekara, K.N., 2017, Production of diagnostic kit to detect CRY2B antigen by use of scFv monoclonal antibody, *Int. J. Curr. Microbiol. Appl. Sci.*, 6 (7), 4401–4411.
- [35] Chakraborty, S., Connor, S., and Velagic, M., 2022, Development of a simple, rapid, and sensitive diagnostic assay for enterotoxigenic *E. coli* and *Shigella spp* applicable to endemic countries, *PLoS Neglected Trop. Dis.*, 16 (1), e0010180.
- [36] Leong, S.W., Lim, T.S., Ismail, A., and Choong, Y.S., 2017, Integration of molecular dynamics simulation and hotspot residues grafting for de novo scFv design against *Salmonella typhi* TolC protein, *J. Mol. Recognit.*, 31 (5), e2695.
- [37] Hong, Z., Tian, C., Stewart, T., Aro, P., Soltys, D., Bercow, M., Sheng, L., Borden, K., Khrisat, T., Pan, C., Zabetian, C.P., Peskind, E.R., Quinn, J.F., Montine, T.J., Aasly, J., Shi, M., and Zhang, J., 2021,

- Development of a sensitive diagnostic assay for Parkinson disease quantifying α -synuclein-containing extracellular vesicles, *Neurology*, 96 (18), e2332–e2345.
- [38] Bandehpour, M., Ahangarzadeh, S., Yarian, F., Lari, A., and Farnia, P., 2018, In silico evaluation of the interactions among two selected single chain variable fragments (scFvs) and ESAT-6 antigen of *Mycobacterium tuberculosis*, *J. Theor. Comput. Chem.*, 16 (8), 1750069.
- [39] Rao, V.S., Srinivas, K., Sujini, G.N., and Kumar, G.N.S., 2014, Protein-protein interaction detection: Methods and analysis, *Int. J. Proteomics*, 2014, 147648.
- [40] Sela-Culang, I., Kunik, V., and Ofran, Y., 2013, The structural basis of antibody-antigen recognition, *Front. Immunol.*, 4, 00302.

Titanium Dioxide-Curcumin Composite Materials from Aceh Curcuma Natural Source and Their Evaluation as Antiradical Agents Through *In Vitro* Study

Indriana Kartini^{1,2*}, Tutik Dwi Wahyuningsih^{1,2}, Adhi Dwi Hatmanto^{1,2},
Vina Aida Roza¹, and Yehezkiel Steven Kurniawan¹

¹Department of Chemistry, Faculty of Mathematics and Natural Sciences, Universitas Gadjah Mada, Sekip Utara, Yogyakarta 55281, Indonesia

²Indonesia Natural Dye Institute (INDI), Integrated Research and Testing Laboratory (LPPT), Universitas Gadjah Mada, Sekip Utara, Yogyakarta 55281, Indonesia

* **Corresponding author:**

email: indriana@ugm.ac.id

Received: December 29, 2022

Accepted: July 6, 2023

DOI: 10.22146/ijc.80766

Abstract: The usage of antiradical agents is pivotal for suppressing the negative effects of free radicals on human health. Curcumin, a well-known natural antiradical agent, suffers from its low stability and high price, thus, limiting its potential in real applications. In this work, we carried out the impregnation of encapsulated curcumin from Aceh curcuma source on commercial titanium dioxide. The isolation of curcumin was performed using a simple maceration method, while the encapsulation process was done employing carboxymethylcellulose and maltodextrin to give ethanol-curcumin and triacetin-curcumin powders in 30.35% and 37.21% yield, respectively. The composite materials contained curcumin in a range of 0.016–0.374 mg/g. The characterization data revealed that the curcumin was located on the surface of titanium dioxide through hydrogen bonds. The *in vitro* DPPH assay of the titanium dioxide-curcumin composite material exhibited 39.61 ± 1.36 to $79.70 \pm 1.33\%$ antiradical activity which was higher than titanium dioxide ($31.78 \pm 1.48\%$). Furthermore, the composite material also gave higher antiradical activity than its curcumin sources, i.e., Aceh curcuma ($75.12 \pm 1.79\%$), ethanol-curcumin ($56.66 \pm 0.25\%$), and triacetin-curcumin ($63.58 \pm 0.20\%$) demonstrating a synergistic antiradical effect of titanium dioxide and curcumin as the antiradical agents. These findings demonstrate the importance of the impregnation and encapsulation of curcumin in composite materials for antiradical applications.

Keywords: titanium dioxide; curcumin; Aceh curcuma; antiradical; composite material

■ INTRODUCTION

Free radicals, including reactive oxygen species, generate serious effects on human health, such as inflammation, cancer, and heart diseases [1]. Unfortunately, these free radicals are spontaneously generated from air pollution, ultraviolet irradiation, and modern lifestyles, i.e., smoking, consuming fast food, and doing less exercise, thus cannot be avoided reaching the human body [2]. Therefore, the use of an antiradical agent is highly required. The antiradical agent is a chemical compound that could convert the free radical to the non-radical species, thus protecting biomolecules and cells from a radical chain reaction [3]. From the molecular

point of view, free radical contains at least one unpaired electron; thus, the antiradical agent shall give a hydrogen atom and/or a single electron to deactivate the free radical [4].

Natural sources serve as an abundant source of thousands of chemical compounds that could act as antiradical agents [5]. Among the natural antiradical agents, curcumin is one of the most well-known compounds due to its high antiradical activity, well-established isolation process, and good biocompatibility. The antiradical activity of curcumin is generated from the hydrogen atom donor from its phenolic functional group, in which the formed phenoxy radical is stabilized

through the electron delocalization process [6]. However, curcumin suffers from some serious disadvantages to being applied for commercial purposes, such as low solubility in water, poor stability, and high-cost material [7].

Encapsulation is a useful technique to protect and prevent the degradation of natural compounds. Either carboxymethylcellulose or maltodextrin has been widely employed as the encapsulating agent due to its high efficiency, low toxicity, and low price [8-10]. It was reported by Tomé Constantino and Garcia-Rojas [11] that betanin encapsulation with carboxymethylcellulose could increase the chemical and thermal stabilities of betanin. Furthermore, Negrão-Murakami et al. [12] reported that the encapsulated *Ilex paraguariensis* A St. Hil. extract with maltodextrin increased its physicochemical properties and stability. Furthermore, the antiradical activity of the extract is maintained, as revealed by the *in vitro* 1,1-diphenyl-2-picrylhydrazyl (DPPH) assay.

On the other hand, the encapsulation of curcumin using carboxymethylcellulose and maltodextrin has been reported [13-17]. It was reported that curcumin encapsulation on carboxymethyl cellulose-montmorillonite clay nanocomposite could enhance the stability and solubility of curcumin in water [18]. Taking consideration for antiradical purposes, higher curcumin solubility in water and/or other polar solvents leads to stronger antiradical activity due to less aggregation structure. However, the antiradical activity of encapsulated curcumin is rarely investigated.

Instead of the encapsulation process, the impregnation of natural compounds could suppress the production cost as the expensive natural compounds are homogeneously spread on the surface of the substrate [19]. Among the solid substrates, titanium dioxide gives great benefits due to its excellent stability, low cost, and non-toxic properties [20]. Impregnation of natural compounds using titanium dioxide has been massively reported, including curcumin [21-26]. However, the application of titanium dioxide-curcumin material as the antiradical agent has not been comprehensively studied.

In this work, a series of titanium dioxide-curcumin composite materials were prepared through extraction,

encapsulation, and impregnation of curcumin on the titanium dioxide substrate. The curcumin was isolated from Aceh curcuma through a maceration technique, while the curcumin encapsulation was carried out utilizing carboxymethyl cellulose and maltodextrin as the encapsulated agents. The impregnation of the encapsulated curcumin on the titanium dioxide substrate was conducted by stirring the mixture in a dark condition at room temperature to yield a series of titanium dioxide-curcumin composite materials. The curcumin content in the extracts and composite materials was quantified using a calibration curve from the UV-vis measurement. The antiradical activities of the composite materials, as well as Aceh curcuma and its extracts, were examined using *in vitro* DPPH assay to study the effect of curcumin isolation, encapsulation, and impregnation on the antiradical activity.

■ EXPERIMENTAL SECTION

Materials

The used materials in this work, i.e., titanium dioxide, carboxymethylcellulose, maltodextrin, methanol, ethanol, triacetin, and DPPH were purchased from Merck and employed without further purification. The curcuma powder from Aceh was kindly donated by PT. Bukit Warna Abadi, West Java, Indonesia while the curcumin standard was obtained from Merck with 84% purity based on HPLC analysis.

Instrumentation

The diffuse-reflectance ultraviolet-visible (DR UV-vis) analysis was carried out using a UV-vis spectrophotometer (Jasco V-760). The X-ray diffraction (XRD) data were measured by an XRD diffractometer (Shimadzu XRD 6000) with Cu K α (1.54060 Å) as the radiation source at a voltage of 40 kV and current of 30 mA. The Fourier-transform infrared (FTIR) spectra of the samples were recorded by FTIR spectrophotometer (Shimadzu Prestige-21) while the scanning electron microscope (SEM) micrographs of the composite materials were taken by JEOL JSM-6510 LA. On the other hand, the UV-vis analysis was performed on a double-beam spectrophotometer (Shimadzu UV-

1800) for curcumin quantification on its maximum wavelength, as well as, for evaluation of the antioxidant activity of composite materials.

Procedure

Extraction and encapsulation of curcumin

The extraction and encapsulation of curcumin were carried out following the previous report [27]. The curcuma powder (10 g) from the Aceh region was extracted employing ethanol as the solvent (100 mL) with a mass-to-volume ratio at 1:10 m/v through a stirring technique at 750 rpm stirring speed for 3 h at room temperature. The extract (100 mL) was added to distilled water (100 mL) containing carboxymethylcellulose (0.6 g) and maltodextrin (12 g) for the encapsulation process. The mixture was evaporated at 80 °C to eliminate the ethanol and then sprayed at an inlet temperature of 140 °C to obtain ethanol-curcumin sample. The extraction process using triacetin-ethanol-distilled water (1:3:1 v/v/v) solvent mixture was also carried out to yield triacetin-curcumin sample.

Curcumin quantification

The quantification of curcumin was performed according to the standard method employing a UV-vis spectrophotometer [28]. The curcumin standard was dissolved in ethanol and measured from 300–800 nm to find its maximum wavelength. A series of curcumin standards with different concentrations was prepared to make the calibration curve. The absorbance of the sample solution in ethanol was recorded and then the curcumin purity of the samples was calculated using the calibration curve.

Preparation of composite materials

Titanium dioxide (1.00 g) was added to the sample solution containing curcumin (Aceh curcuma, ethanol-curcumin, and triacetin-curcumin) with various concentrations of 5, 25, and 50 mg/L in ethanol (20 mL). The mixture was stirred in a dark condition at room temperature. After 24 h, the mixture was filtered using Whatman filter paper. The solid residue was washed with cold ethanol until the filtrate became colorless. Afterward, the absorbance of the filtrate was measured to quantify the impregnated curcumin on the titanium dioxide materials.

The composite materials were characterized using DR UV-vis, XRD, and FTIR analyses.

In vitro antiradical activity measurement

The *in vitro* antiradical activity of composite materials was measured following the previous method with slight modification [29]. The composite material (10 mg) was added to methanol (8 mL). Then, DPPH 0.1 mM solution in methanol (2 mL) was added to the mixture. The mixture was shaken in a dark condition for 30 min. The mixture was filtered, and the absorbance of the filtrate was measured using a UV-vis spectrophotometer at 517 nm. The control solution was prepared by mixing methanol (8 mL) and DPPH 0.1 mM solution (2 mL) with the same procedure above. The antiradical activity percentage was determined by calculating the difference between the absorbance of the control and the sample over the absorbance of the control. The antiradical activity of bare titanium dioxide, Aceh curcuma, ethanol-curcumin, and triacetin-curcumin was also measured to evaluate the effect of the impregnation process on the antiradical activity.

■ RESULTS AND DISCUSSION

Extraction and Encapsulation of Curcumin

In this work, the curcumin was isolated from Aceh curcuma powder using a simple maceration method. Ethanol and a mixture of triacetin-ethanol-distilled water were used as the solvent because curcumin is soluble in both media [30]. Carboxymethylcellulose and maltodextrin were employed as the encapsulating agents to enhance the stability of curcumin, as it was known that curcumin could be gradually degraded at room temperature [7]. The curcumin-ethanol sample was obtained as a yellowish orange solid (6.86 g) in 30.35% yield, while curcumin-triacetin was obtained as a yellowish orange solid (8.41 g) in 37.21% yield. The yield of curcumin-triacetin was higher than curcumin-ethanol due to the higher solubility of curcumin in triacetin than in ethanol as previously reported [30]. The curcumin-ethanol sample was checked by thin layer chromatography (TLC) using chloroform:ethanol 97:3 (v/v), yielding retention factor (R_f) values of 0.60, 0.38, and 0.26 for curcumin, demethoxycurcumin, and

bisdemethoxycurcumin, respectively, as reported before [31]. Similar to this, the curcumin-triacetin also yielded three TLC spots at R_f values of 0.60, 0.34, and 0.24 for curcumin, demethoxycurcumin, and bisdemethoxycurcumin, respectively. These results demonstrate the successful isolation and encapsulation of curcumin from Aceh curcuma as the starting material.

Curcumin Quantification

The UV-vis spectrum of the curcumin standard solution at 0.84–8.40 mg/L concentration is shown in Fig. 1. It was found that the maximum wavelength of curcumin in ethanol was observed at 420 nm as previously reported [28]. The absorbance signal at 420 nm originated from $\pi-\pi^*$ electronic transition of curcumin. The absorbance of curcumin standard solutions at 420 nm was plotted against the curcumin concentration (Fig. 1(a)). The calibration curve with a mathematic formula of “Absorbance = 0.1555 [curcumin concentration] + 0.0077” was obtained with a coefficient of determination (R^2) value of 0.9991, demonstrating the validity of the calibration curve (Fig. 1(b)).

By using the equation, it was found that Aceh curcuma contained 4.24% curcumin. On the other hand, curcumin-ethanol and curcumin-triacetin contained 2.43% and 2.56% curcumin, respectively, which were lower than originated Aceh curcuma (4.24%) due to the presence of maltodextrin and carboxymethylcellulose as the encapsulating agents. Compared to the curcumin-ethanol, the curcumin content in curcumin-triacetin sample was higher than curcumin-ethanol due to the

higher solubility of curcumin in triacetin as reported before [30].

Preparation of Composite Materials

The titanium dioxide-curcumin composite materials were prepared to evaluate the effect of encapsulation of curcumin on the antiradical activity. The composite materials were obtained in 91–99% yield based on the initial mass of titanium dioxide (1 g). Fig. 2 shows the photographed image of the composite materials with different curcumin sources and concentrations. The presence of curcumin generated yellow color in the composite material as curcumin powder existed in yellowish orange color [32]. The color intensity was stronger when the initial concentration of curcumin was higher.

The titanium dioxide-Aceh curcuma composite materials were obtained as orange solid, while the titanium dioxide-ethanol-curcumin and titanium dioxide-triacetin-curcumin composite materials were obtained as yellowish color solid. This phenomenon might be caused by the presence of other components besides curcumin in the Aceh curcuma sample. It was reported that crude curcumin powder contains α -phellandrene, β -caryophyllene, turmerone, bisabolone, and sesquiphellandrene [33]. These compounds might be eliminated during the extraction and encapsulation process; thus, the color of titanium dioxide-ethanol-curcumin and titanium dioxide-triacetin-curcumin composite materials originated mainly due to the curcumin color.

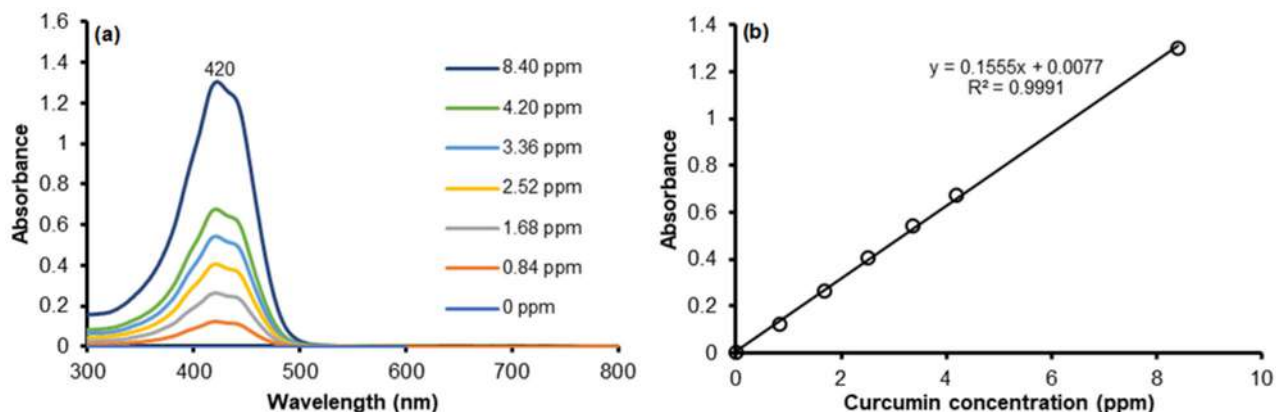


Fig 1. The (a) UV-vis spectra and (b) calibration curve of standard curcumin solution

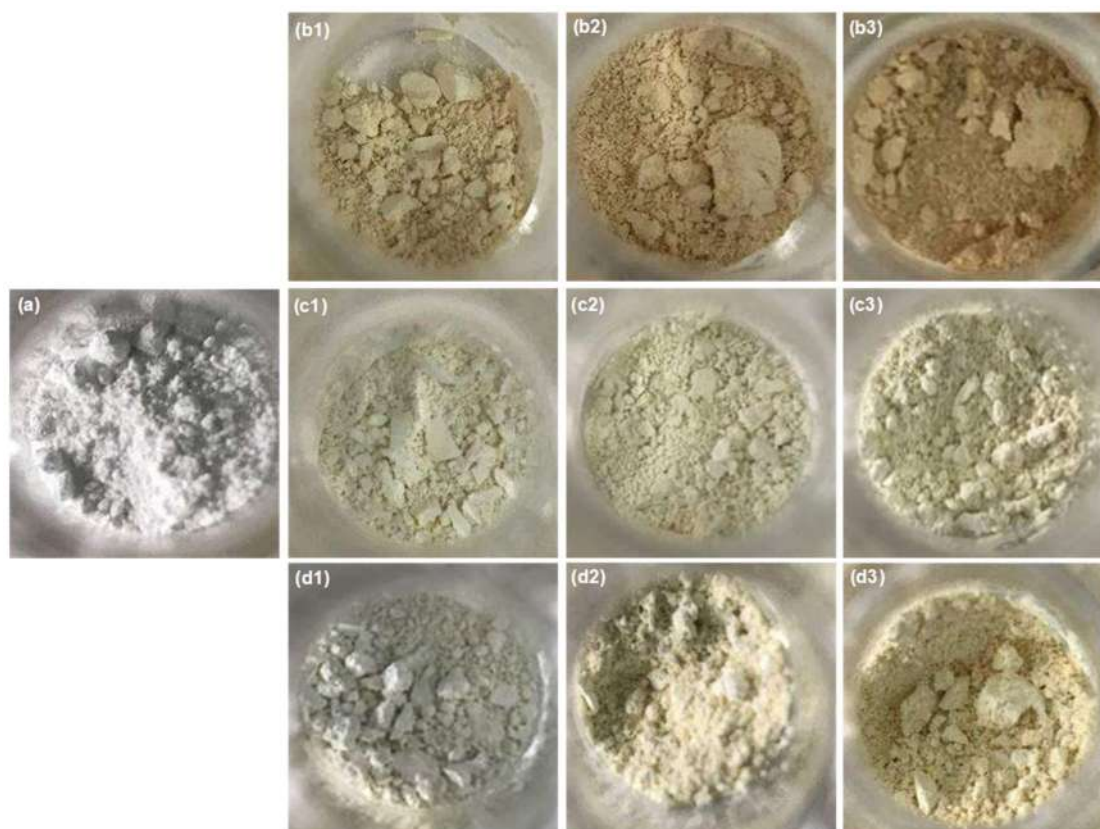


Fig 2. The photographed image of (a) titanium dioxide, (b1–b3) titanium dioxide-Aceh curcuma, (c1–c3) titanium dioxide-ethanol-curcumin, and (d1–d3) titanium dioxide-triacetin-curcumin composite materials. Terms (1), (2), and (3) stand for the initial concentration of curcumin solution of 5, 25, and 50 mg/L, respectively

The composite materials were then characterized using DR UV-vis, XRD, and FTIR instruments. The DR UV-vis spectra of the composite materials are shown in Fig. 3. In accordance with the photographed image of the curcumin samples, Aceh curcuma, curcumin-ethanol, and curcumin-triacetin showed broad absorption signal at 400–550 nm, which corresponded to its orange-yellowish color as previously reported [21]. Meanwhile, bare titanium dioxide had no absorption signal at the visible region (400–800 nm). Consequently, the impregnation of curcumin on the titanium dioxide material showed a weak absorption band at 420 nm. The titanium dioxide-curcumin sample showed the strongest absorption signal at 420 nm among the composite materials, as indicated by its orange color. Meanwhile, the absorption signals of titanium dioxide at 200–380 nm were not significantly influenced, indicating that the curcumins were located on the surface of titanium dioxide as the preparation was

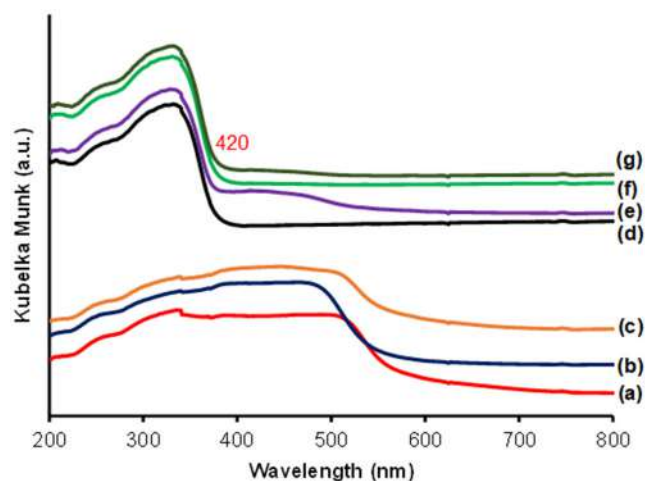


Fig 3. The DR UV-vis spectra of (a) Aceh curcuma, (b) ethanol-curcumin, (c) triacetin-curcumin, (d) titanium dioxide, (e) titanium dioxide-Aceh curcuma 50 mg/L, (f) titanium dioxide-ethanol-curcumin 50 mg/L, and (g) titanium dioxide-triacetin-curcumin 50 mg/L composite materials

performed using a stirring method at room temperature. This phenomenon was also reported for the impregnation of betalain and chlorophyll pigments on the titanium dioxide substrate [22,26].

Fig. 4 shows the XRD data of the titanium dioxide, Aceh curcuma, curcumin-ethanol, curcumin-triacetin, and the titanium dioxide-curcumin composite materials. The Aceh curcuma, curcumin-ethanol and curcumin-triacetin existed as amorphous phases. On the other hand, the unmodified titanium dioxide existed in the anatase crystalline phase of (101), (004), (200), (105), (211), (204), (116), (220), (215), and (224) according to JCPDS No 00-021-1272. Therefore, the XRD data of the composite materials were very similar to the unmodified titanium dioxide. This result strengthened the DR UV-vis data that curcumin was located on the surface of titanium dioxide as no observed changes in the crystalline phase of the titanium dioxide after the impregnation process. A similar result was observed for the *in-situ* synthesis of polyaniline on anatase TiO₂ nanorod [34]. The incorporation of the amorphous phase into the crystalline structure did not change the anatase crystalline structure.

The FTIR spectra of the composite materials are shown in Fig. 5. The FTIR spectrum of Aceh curcuma showed the absorption signals at 3487, 2924, 1627, 1504, 1273, and 1018 cm⁻¹ for ArO-H, C_{sp3}-H, C=O, C=C, C-O-C, and C-O vibrations, respectively, on its FTIR spectrum. This result agreed with other curcuma samples [35-37]. After the encapsulation process, the vibration signals of curcumin-ethanol were shifted from the Aceh curcuma one. The ArO-H signal was shifted from 3487 to 3364 cm⁻¹ due to the encapsulation of curcumin with carboxymethylcellulose and maltodextrin. Meanwhile, the other functional groups of curcumin-ethanol remain, i.e., C_{sp3}-H (2924 cm⁻¹), C=O (1627 cm⁻¹), C=C (1504 cm⁻¹), and C-O (1018 cm⁻¹) vibrations. On the other hand, the FTIR spectrum of curcumin-triacetin showed an additional C=O ester signal of triacetin at 1743 cm⁻¹, while the other signals were not significantly different from the Aceh curcuma sample.

On the other hand, titanium dioxide showed three major peaks at 3433, 678, and 517 cm⁻¹ for the vibration of TiO-H, Ti-O-Ti, and Ti-O functional groups,

respectively [38]. Therefore, the FTIR spectra of titanium dioxide-curcumin composite materials were similar to the FTIR spectrum of bare titanium dioxide sample except for the slight shift of the O-H functional group from 3433 to 3425–3387 cm⁻¹ and the addition of very weak absorption signals at 1627–1018 cm⁻¹ region

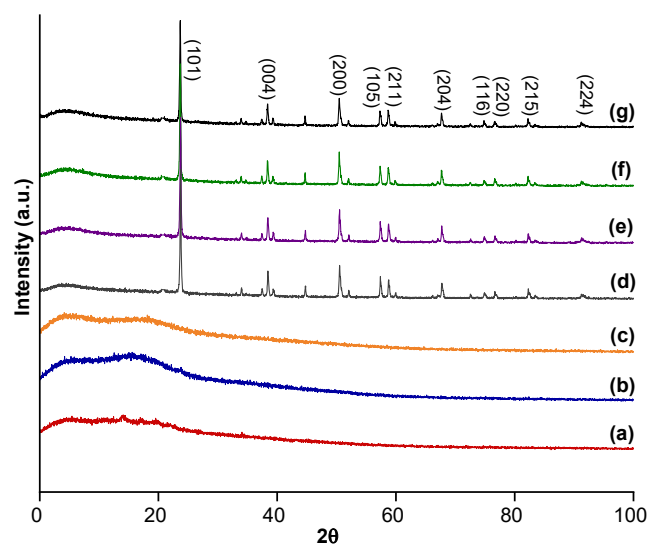


Fig 4. The XRD patterns of (a) Aceh curcuma, (b) ethanol-curcumin, (c) triacetin-curcumin, (d) titanium dioxide, (e) titanium dioxide-Aceh curcuma 50 mg/L, (f) titanium dioxide-ethanol-curcumin 50 mg/L, and (g) titanium dioxide-triacetin-curcumin 50 mg/L composite materials

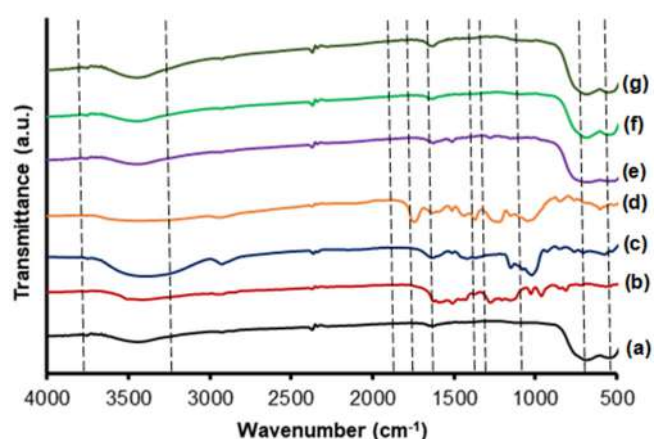


Fig 5. The FTIR spectra of (a) titanium dioxide, (b) Aceh curcuma, (c) ethanol-curcumin, (d) triacetin-curcumin, (e) titanium dioxide-Aceh curcuma 50 mg/L, (f) titanium dioxide-ethanol-curcumin 50 mg/L, and (g) titanium dioxide-triacetin-curcumin 50 mg/L composite materials

due to the presence of impregnated curcumin on the composite materials. In the previous reports, these weak absorption signals indicated the presence of natural compounds in the titanium dioxide [22,26]. Besides, the titanium dioxide signals, i.e., Ti–O–H, Ti–O–Ti, and Ti–O, were not significantly influenced by the presence of curcumin. This result agreed with the DR UV-vis and XRD data indicating that curcumin was impregnated on the surface of titanium dioxide.

The SEM micrographs of titanium dioxide and its composite materials are shown in Fig. 6. It was found that the impregnation of curcumin either from Aceh curcuma or ethanol-curcumin or triacetin-curcumin did not significantly change the surface morphology of the titanium dioxide. This result agreed with the DR UV-vis, XRD, and FTIR data. The distribution of the impregnated curcumin on titanium dioxide was evaluated through the elemental mapping of titanium dioxide and its composite materials shown in Fig. 7. The carbon (C) atoms (red color) appear clustered in several spots for TiO₂-curcuma

samples and tend to be more evenly distributed in the composite materials for curcumin (Fig. 7(c) and 7(d)). This indicates a better particle distribution for curcumin compared to curcuma on TiO₂ surfaces. The better solubility of curcumin in the solvent system also resulted in better curcumin distribution (Fig. 7(d)). This is in line with the previous quantitative fact that the amount of curcumin in the triacetin-curcumin sample (2.56%) is higher than that in the ethanol-curcumin sample (2.43%).

The EDX analysis (Table 1) shows the presence of carbon atoms in the composite materials which come from the impregnated curcumin on the titanium dioxide's surface. The carbon atom percentages in the titanium dioxide-Aceh curcuma-50 mg/L composite material were much higher than titanium dioxide-ethanol-curcumin-50 mg/L and titanium dioxide-triacetin-curcumin-50 mg/L composite materials. This result was reasonable as Aceh curcuma contained not only curcumin but also other organic compounds, such as

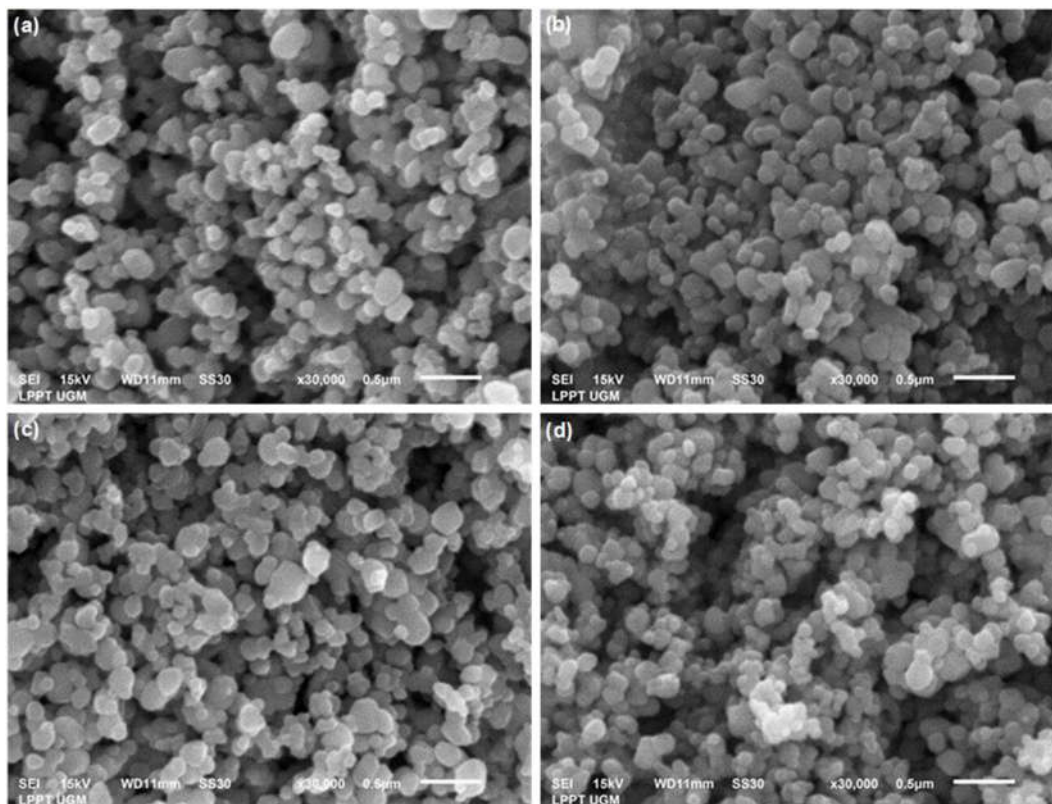


Fig 6. The SEM micrographs of (a) titanium dioxide, (b) titanium dioxide-Aceh curcuma 50 mg/L, (c) titanium dioxide-ethanol-curcumin 50 mg/L, and (d) titanium dioxide-triacetin-curcumin 50 mg/L composite materials

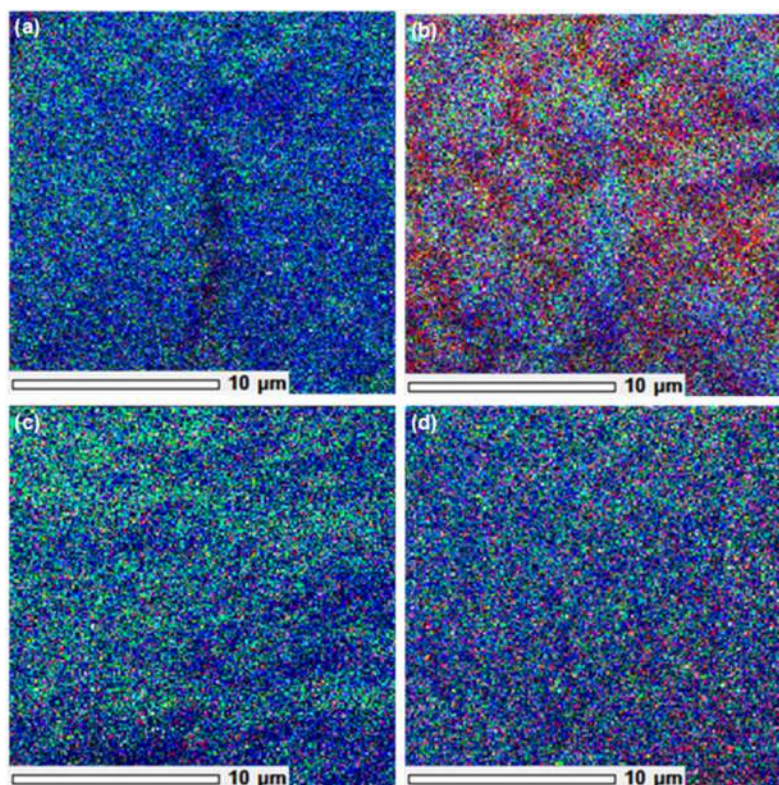


Fig 7. Elemental mapping of (a) titanium dioxide, (b) titanium dioxide-Aceh curcuma 50 mg/L, (c) titanium dioxide-ethanol-curcumin 50 mg/L, and (d) titanium dioxide-triacetin-curcumin 50 mg/L composite materials. Blue, green, and red colors represent titanium, oxygen, and carbon atoms

Table 1. The EDX results of titanium dioxide and its composite materials

Sample	%Atom		
	Ti	O	C
Titanium dioxide	27.16	72.84	-
Titanium dioxide-Aceh curcuma-50 mg/L	12.37	47.20	40.43
Titanium dioxide-ethanol-curcumin-50 mg/L	29.80	63.80	6.41
Titanium dioxide-triacetin-curcumin-50 mg/L	27.46	66.09	6.45

α -phellandrene, β -caryophyllene, turmerone, bisabolone, and sesquiphellandrene, that may be adsorbed on the surface of titanium dioxide. These compounds may result in clustering on the surface of titanium dioxide, as observed in the SEM mapping images.

From the quantitative analysis, it was found that titanium dioxide-Aceh curcuma contains 0.016–0.040 mg curcumin/g composite material. The titanium dioxide-ethanol-curcumin composite materials contain higher curcumin content of 0.093–0.218 mg/g composite material while the titanium dioxide-triacetin-curcumin composite materials contain a much higher curcumin

content of 0.059–0.374 mg/g composite material. The highest content of curcumin in the titanium dioxide-triacetin-curcumin composite materials supports the deduction drawn from the SEM mapping data. Even though both ethanol-curcumin (2.43%) and triacetin-curcumin (2.56%) samples contain lower curcumin content compared to the Aceh curcuma sample (4.24%), the impregnated curcumin on titanium dioxide-ethanol-curcumin and titanium dioxide-triacetin-curcumin composite materials is higher due to the encapsulation process. The encapsulation of curcumin with carboxymethylcellulose and maltodextrin changes

the hydrophilicity of curcumin through host-guest complexation. Therefore, the curcumin complex could be impregnated onto the titanium dioxide surface through hydrogen bonds. The presence of hydrogen bond interactions was supported by the shift O–H signal at the FTIR data of the composite materials ($3425\text{--}3387\text{ cm}^{-1}$) compared to the bare titanium dioxide (3433 cm^{-1}). The plausible interaction of curcumin complex with carboxymethylcellulose and maltodextrin on the surface of titanium dioxide is displayed in Fig. 8.

In Vitro Antiradical Activity Measurement

The antiradical activity of the composite material was evaluated through an *in vitro* assay using DPPH as the artificial free radical. The antiradical activity of titanium

dioxide, Aceh curcuma, curcumin-ethanol, curcumin-triacetin, and the composite materials is listed in Table 2. When the DPPH radical attracts a hydrogen atom and/or receives an electron from the antiradical agent, the color change occurs from purple to yellow. Because of that, DPPH has become the most common artificial free radical used in the *in vitro* antiradical activity assay due to its simple colorimetric quantification using a spectrophotometer [29]. The qualitative observation of the DPPH assay for the determination of the antiradical activity of the composite materials is shown in Fig. 9.

Aceh curcuma, ethanol-curcumin, and triacetin-curcumin gave antiradical activity of $75.12 \pm 1.79\%$, $56.66 \pm 0.25\%$, and $63.58 \pm 0.20\%$, respectively. Aceh curcuma, ethanol-curcumin, and triacetin-curcumin

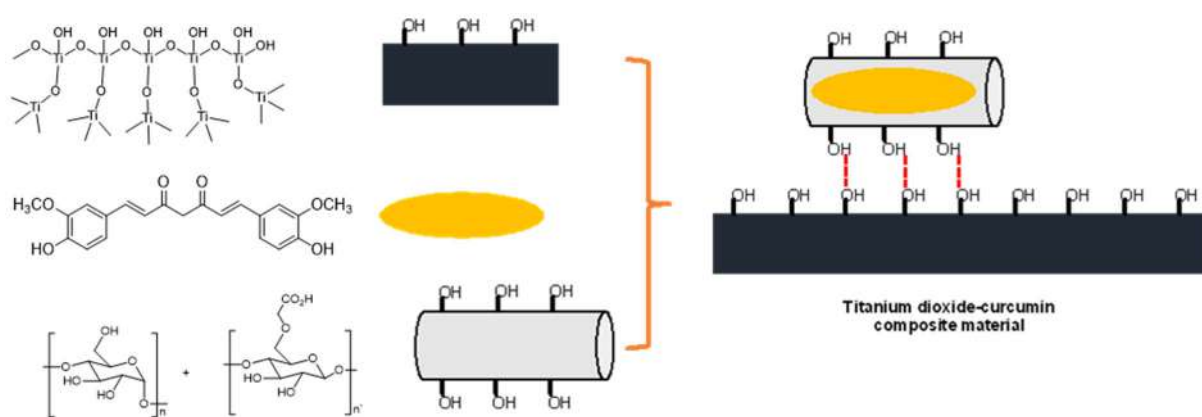


Fig 8. Plausible interaction of curcumin on the surface of titanium dioxide

Table 2. Antiradical activity of titanium dioxide, Aceh curcuma, curcumin-ethanol, curcumin-triacetin, and the composite materials against DPPH radicals

Sample	%Antiradical activity
Aceh curcuma	75.12 ± 1.79
Ethanol-curcumin	56.66 ± 0.25
Triacetin-curcumin	63.58 ± 0.20
Titanium dioxide	31.78 ± 1.48
Titanium dioxide-Aceh curcuma-5 mg/L	55.31 ± 0.63
Titanium dioxide-Aceh curcuma-25 mg/L	58.45 ± 2.03
Titanium dioxide-Aceh curcuma-50 mg/L	76.80 ± 0.65
Titanium dioxide-ethanol-curcumin-5 mg/L	49.66 ± 2.35
Titanium dioxide-ethanol-curcumin-25 mg/L	57.05 ± 2.43
Titanium dioxide-ethanol-curcumin-50 mg/L	73.74 ± 0.20
Titanium dioxide-triacetin-curcumin-5 mg/L	39.61 ± 1.36
Titanium dioxide-triacetin-curcumin-25 mg/L	62.03 ± 1.46
Titanium dioxide-triacetin-curcumin-50 mg/L	79.70 ± 1.33

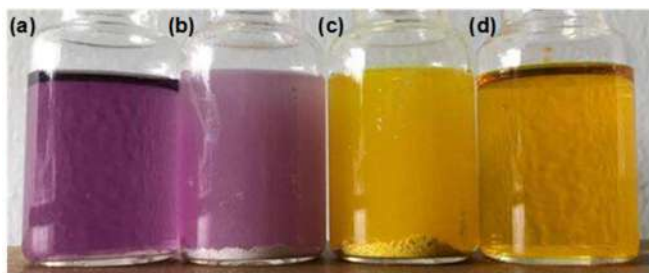


Fig 9. Photographed observation of DPPH solution (a) before and after the addition of (b) titanium dioxide, (c) titanium dioxide-curcumin composite material, and (d) Aceh curcuma as the antiradical agent

contained ArO-H functional group that could also donate its hydrogen atom to scavenge the DPPH radical. High antiradical activity of Aceh curcuma was indicated from the orange color solution composed of yellow color of DPPH and orange color of Aceh curcuma extract as shown in Fig. 9. The antiradical activity of Aceh curcuma was higher than triacetin-curcumin and much higher than ethanol-curcumin. This result was caused by the higher curcumin content in Aceh curcuma (4.24%) than curcumin-triacetin (2.56%) and curcumin-ethanol (2.43%). Furthermore, other bioactive compounds in the Aceh curcuma samples may act as antiradical agents. Even though Aceh curcuma contains curcumin in 1.74–1.66 times higher than the curcumin-ethanol and curcumin triacetin, the antiradical activity of curcumin-ethanol and curcumin triacetin was only 1.18–1.33 times lower than Aceh curcuma. This phenomenon could be caused by the prevention of curcumin aggregation in curcumin-ethanol and curcumin triacetin due to the encapsulation process thus, each impregnated curcumin molecule could serve as a hydrogen atom donor to the DPPH radical as previously reported [39]. A high aggregation tendency for curcuma impregnated onto titanium dioxide has also been detected in SEM mapping results (Fig. 7(b)).

On the other hand, the antiradical activity of unmodified titanium dioxide was $31.78 \pm 1.48\%$. From the FTIR data, titanium dioxide had TiO-H functional groups, which could donate the hydrogen atom to deactivate the DPPH radical. However, since the antiradical activity was low, the color of the DPPH solution remained purple after 30 min incubation period.

The antiradical activity of the composite material was in a range of $39.61 \pm 1.36\%$ to $79.70 \pm 1.33\%$. Fig. 8(d) shows the DPPH solution color after the addition of titanium dioxide-Aceh curcuma-50 mg/L with an incubation period of 30 min. High antiradical activity of the composite material was shown from the disappearance of the purple color of DPPH chemicals. The antiradical activity is enhanced by increasing impregnated curcumin content. Titanium dioxide-Aceh curcuma, titanium dioxide-ethanol-curcumin and titanium dioxide-triacetin-curcumin composite materials contain 0.016–0.040, 0.093–0.218 and 0.059–0.374 mg curcumin/g composite material, respectively. Therefore, it is reasonable if titanium dioxide-Aceh curcuma ($55.31 \pm 0.63\%$ to $76.80 \pm 0.65\%$) and titanium dioxide-ethanol-curcumin ($49.66 \pm 2.35\%$ to $73.74 \pm 0.20\%$) exhibited lower antiradical activity than the titanium dioxide-triacetin-curcumin ($39.61 \pm 1.36\%$ to $79.70 \pm 1.33\%$).

It was also interesting to note that the antiradical activity of the composite material was higher than the antiradical activity of the titanium dioxide and curcumin samples. For example, the antiradical activity of titanium dioxide-Aceh curcuma-50 mg/L ($76.80 \pm 0.65\%$) was higher than titanium dioxide ($31.78 \pm 1.48\%$) and Aceh curcuma ($75.12 \pm 1.79\%$). Additionally, the antiradical activity of titanium dioxide-ethanol-curcumin-50 mg/L ($73.74 \pm 0.20\%$) was higher than titanium dioxide ($31.78 \pm 1.48\%$) and ethanol-curcumin ($56.66 \pm 0.25\%$). The antiradical activity of titanium dioxide-triacetin-curcumin-50 mg/L ($79.70 \pm 1.33\%$) was also higher than titanium dioxide ($31.78 \pm 1.48\%$) and triacetin-curcumin ($63.58 \pm 0.20\%$). These results indicated the synergistic effect of titanium dioxide and curcumin as the antiradical agent. Furthermore, the difference in the antiradical activity of titanium dioxide-ethanol-curcumin-50 mg/L with ethanol-curcumin ($\Delta = 17.08\%$) and titanium dioxide-triacetin-curcumin-50 mg/L with triacetin-curcumin ($\Delta = 16.22\%$) was higher than of titanium dioxide-Aceh curcuma-50 mg/L with Aceh curcuma ($\Delta = 1.68\%$) indicating that encapsulation process is crucial on the stability of curcumin on the composite material on its application as the antiradical agent.

■ CONCLUSION

Titanium dioxide-curcumin composite materials derived from Aceh curcuma and its extracts have been successfully prepared. The isolation and encapsulation of curcumin using ethanol and triacetin-ethanol-distilled water yielded orange-yellowish solids in 30.35% and 37.21% yield, respectively. TLC analysis revealed that the extracts contained curcumin, demethoxycurcumin, and bisdemethoxycurcumin. The curcumin content was quantified using a calibration method employing a UV-vis spectrophotometer at a fixed maximum wavelength of 420 nm. The Aceh curcuma contains 4.24% curcumin while the curcumin-ethanol and curcumin-triacetin contains 2.43% and 2.56% curcumin, respectively. These materials were further employed for the preparation of titanium dioxide-curcumin composite materials in 91–99% yield with curcumin content in a range of 0.016–0.374 mg/g composite material. The composite materials have been characterized by DR UV-vis, XRD, FTIR, and SEM-EDX-mapping analyses, which indicated that the curcumin complex with carboxymethylcellulose and maltodextrin was impregnated on the surface of titanium dioxide through hydrogen bonds. The *in vitro* antiradical activity assay of the composite material exhibited $39.61 \pm 1.36\%$ to $79.70 \pm 1.33\%$, which could be higher than that of titanium dioxide ($31.78 \pm 1.48\%$), Aceh curcuma ($75.12 \pm 1.79\%$), ethanol-curcumin ($56.66 \pm 0.25\%$), and triacetin-curcumin ($63.58 \pm 0.20\%$) due to the synergistic effect of titanium dioxide and curcumin as the antiradical agents. It meant that both impregnation and encapsulation processes are critical for the antiradical activity and stability of curcumin on the surface of titanium dioxide.

■ ACKNOWLEDGMENTS

The authors thank Matching Fund Kedai Reka grant 2022 with contract number of 180/E1/KS.06.02/2022 and 5974/UN1.P/Dit-PUI/HK.08.00/2022 from the Ministry of Education, Culture, Research and Technology of Indonesia.

■ REFERENCES

- [1] Kupaeva, N.V., and Kotenkova, E.A., 2021, Current view on the assessment of antioxidant and antiradical activities: A mini review, *IOP Conf. Ser.: Earth Environ. Sci.*, 854, 012048.
- [2] Liguori, I., Russo, G., Curcio, F., Bulli, G., Aran, L., Della-Morte, D., Gargiulo, G., Testa, G., Cacciatore, F., Bonaduce, D., and Abete, P., 2018, Oxidative stress, aging, and diseases, *Clin. Interventions Aging*, 13, 757–772.
- [3] Tirzitis, G., and Bartosz, G., 2010, Determination of antiradical and antioxidant activity: Basic principles and new insights, *Acta Biochim. Pol.*, 57 (2), 139–142.
- [4] Gulcin, I., 2020, Antioxidants and antioxidant methods: An updated overview, *Arch. Toxicol.*, 94 (3), 651–715.
- [5] Xu, D.P., Li, Y., Meng, X., Zhou, T., Zhou, Y., Zheng, J., Zhang, J.J., and Li, H.B., 2017, Natural antioxidants in foods and medicinal plants: Extraction, assessment and resources, *Int. J. Mol. Sci.*, 18 (1), 96.
- [6] Hewlings, S.J., and Kalman, D.S., 2017, Curcumin: A review of its effects on human health, *Foods*, 6 (10), 92.
- [7] Fuloria, S., Mehta, J., Chandel, A., Sekar, M., Mat Rani, N.N.I., Begum, M.Y., Subramaniyan, V., Chidambaram, K., Thangavelu, L., Nordin, R., Wu, Y.S., Sathasivam, K.V., Lum, P.T., Meenakshi, D.U., Kumarasamy, V., Azad, A.K., and Fuloria, N.K., 2022, A comprehensive review on the therapeutic potential of *Curcuma longa* Linn. in relation to its major active constituent curcumin, *Front. Pharmacol.*, 13, 820806.
- [8] Rahman, M.S., Hasan, M.S., Nitai, A.S., Nam, S., Karmakar, A.K., Ahsan, M.S., Shiddiky, M.J.A., and Ahmed, M.B., 2021, Recent developments of carboxymethyl cellulose, *Polymers*, 13 (8), 1345.
- [9] Rahman Mazumder, M.A., and Ranganathan, T.V., 2020, Encapsulation of isoflavone with milk, maltodextrin and gum acacia improves its stability, *Curr. Res. Food Sci.*, 2, 77–83.
- [10] Zorzenon, M.R.T., Formigoni, M., da Silva, S.B., Hodas, F., Piovan, S., Ciotta, S.R., Jansen, C.A., Dacome, A.S., Pilau, E.J., Mareze-Costa, C.E., Milani, P.G., and Costa, S.C., 2020, Spray drying encapsulation of stevia extract with maltodextrin

- and evaluation of the physicochemical and functional properties of produced powders, *J. Food Sci.*, 85 (10), 3590–3600.
- [11] Tomé Constantino, A.B., and Garcia-Rojas, E.E., 2022, Microencapsulation of betanin by complex coacervation of carboxymethylcellulose and amaranth protein isolate for application in edible gelatin films, *Food Hydrocolloids*, 133, 107956.
- [12] Negrão-Murakami, A.N., Nunes, G.L., Pinto, S.S., Murakami, F.S., Amante, E.R., Petrus, J.C.C., Prudêncio, E.S., and Amboni, R.D.M.C., 2017, Influence of DE-value of maltodextrin on the physicochemical properties, antioxidant activity, and storage stability of spray dried concentrated mate (*Ilex paraguariensis* A. St. Hil.), *LWT-Food Sci. Technol.*, 79, 561–567.
- [13] Ung, V.Y.L., Foshaug, R.R., MacFarlane, S.M., Churchill, T.A., Doyle, J.S.G., Sydora, B.C., and Fedorak, R.N., 2010, Oral administration of curcumin emulsified in carboxymethyl cellulose has a potent anti-inflammatory effect in the IL-10 gene-deficient mouse model of IBD, *Dig. Dis. Sci.*, 55 (5), 1272–1277.
- [14] Goëlo, V., Chaumun, M., Gonçalves, A., Estevinho, B.N., and Rocha, F., 2020, Polysaccharide-based delivery systems for curcumin and turmeric powder encapsulation using a spray-drying process, *Powder Technol.*, 370, 137–146.
- [15] Bourbon, A.I., Costa, M.J., Maciel, L.C., Pastrana, L., Vicente, A.A., and Cerqueira, M.A., 2021, Active carboxymethylcellulose-based edible films: Influence of free and encapsulated curcumin on films' properties, *Foods*, 10 (7), 1512.
- [16] Rezaei, M., Hassanzadeh Nemati, N., Mehrabani, D., and Komeili, A., 2022, Characterization of sodium carboxymethyl cellulose/calcium alginate scaffold loaded with curcumin in skin tissue engineering, *J. Appl. Polym. Sci.*, 139 (22), 52271.
- [17] Ashraf, H., Butt, M.S., Ul-Haq, I., Nadeem, M., Aadil, R.M., Rusu, A.V., and Trif, M., 2022, Microencapsulated curcumin from *Curcuma longa* modulates diet-induced hypercholesterolemia in Sprague Dawley rats, *Front. Nutr.*, 9, 1026890.
- [18] Madunsaka, N., de Silva, K.M.N., and Amaratunga, G., 2015, A curcumin activated carboxymethyl cellulose–montmorillonite clay nanocomposite having enhanced curcumin release in aqueous media, *Carbohydr. Polym.*, 134, 695–699.
- [19] Basso, A., and Serban, S., 2019, Industrial applications of immobilized enzymes—A review, *Mol. Catal.*, 479, 110607.
- [20] Sanches, P.L., Geaquinto, L.R.O., Cruz, R., Schuck, D.C., Lorencini, M., Granjeiro, J.M., and Ribeiro, A.R.L., 2020, Toxicity evaluation of TiO₂ nanoparticles on the 3D skin model: A systematic review, *Front. Bioeng. Biotechnol.*, 8, 00575.
- [21] Lim, J., Bokare, A.D., and Choi, W., 2017, Visible light sensitization of TiO₂ nanoparticles by a dietary pigment, curcumin, for environmental photochemical transformations, *RSC Adv.*, 7 (52), 32488–32495.
- [22] Kurniawan, Y.S., Anggraeni, K., Indrawati, R., and Yuliati, L., 2019, Selective betalain impregnation from red amaranth extract onto titanium dioxide nanoparticles, *AIP Conf. Proc.*, 2175, 020049.
- [23] Yan, Z., He, Z., Li, M., Zhang, L., Luo, Y., He, J., Chen, Y., and Wang, J., 2020, Curcumin doped SiO₂/TiO₂ nanocomposites for enhanced photocatalytic reduction of Cr(VI) under visible light, *Catalysts*, 10 (8), 942.
- [24] Sherin, S., Balachandran, S., and Abraham, A., 2020, Curcumin incorporated titanium dioxide nanoparticles as MRI contrasting agent for early diagnosis of atherosclerosis- rat model, *Vet. Anim. Sci.*, 10, 100090.
- [25] Mollaei, M., Hashemi, M., Siasi, E., Marndi, S.J., and Entezari, M., 2020, Effect of TiO₂ nanoparticles and curcumin on sperm parameters in response to temperature-induced stress in scrotal hyperthermia rats: Role of miR455, *J. Hum. Genet. Genomics*, 4 (2), e122290.
- [26] Kurniawan, Y.S., Anggraeni, K., Indrawati, R., and Yuliati, L., 2020, Functionalization of titanium dioxide through dye-sensitizing method utilizing red amaranth extract for phenol photodegradation, *IOP Conf. Ser.: Mater. Sci. Eng.*, 902, 012029.

- [27] Surojanametakul, V., Satmalee, P., Saengprakai, J., Siliwan, D., and Wattanasirithamn, L., 2010, Preparation of curcuminoid powder from turmeric root (*Curcuma longa* Linn) for food ingredient use, *Kasetsart J.: Nat. Sci.*, 44 (1), 123–130.
- [28] Jagannathan, R., Abraham, P.M., and Poddar, P., 2012, Temperature-dependent spectroscopic evidences of curcumin in aqueous medium: A mechanistic study of its solubility and stability, *J. Phys. Chem. B*, 116 (50), 14533–14540.
- [29] Kedare, S.B., and Singh, R.P., 2011, Genesis and development of DPPH method of antioxidant assay, *J. Food Sci. Technol.*, 48 (4), 412–422.
- [30] Degot, P., Huber, V., Hofmann, E., Hahn, M., Touraud, D., and Kunz, W., 2021, Solubilization and extraction of curcumin from *Curcuma longa* using green, sustainable, and food-approved surfactant-free microemulsions, *Food Chem.*, 336, 127660.
- [31] Kushwaha, P., Shukla, B., Dwivedi, J., and Saxena, S., 2021, Validated high-performance thin-layer chromatographic analysis of curcumin in the methanolic fraction of *Curcuma longa* L. rhizomes, *Future J. Pharm. Sci.*, 7 (1), 178.
- [32] Hope-Roberts, M., and Horobin, R.W., 2017, A review of curcumin as a biological stain and as a self-visualizing pharmaceutical agent, *Biotech. Histochem.*, 92 (5), 315–323.
- [33] Mottahedin, P., Haghighi Asl, A., and Khajenoori, M., 2016, Extraction of curcumin and essential oil from *Curcuma longa* L. by subcritical water via response surface methodology: SWE of curcumin and essential oil via RSM, *J. Food Process. Preserv.*, 41 (4), e13095.
- [34] Wahyuni, S., Kunarti, E.S., Swasono, R.T., and Kartini, I., 2018, Characterization and photocatalytic activity of TiO₂(rod)-SiO₂-polyaniline nanocomposite, *Indones. J. Chem.*, 18 (2), 321–330.
- [35] Chen, X., Zou, L.Q., Niu, J., Liu, W., Peng, S.F., and Liu, C.M., 2015, The stability, sustained release and cellular antioxidant activity of curcumin nanoliposomes, *Molecules*, 20 (8), 14293–14311.
- [36] Cocean, A., Cocean, I., Cimpoesu, N., Cocean, G., Cimpoesu, R., Postolachi, C., Popescu, V., and Gurlui, S., 2021, Laser induced method to produce curcuminoid-silanol thin films to transdermal patches using irradiation of turmeric target, *Appl. Sci.*, 11 (9), 4030.
- [37] Kho, K., Nugroho, D., and Sugih, A.K., 2018, Preparation and characterization of highly water soluble curcumin – dextrose cocrystal, *J. Pure Appl. Chem. Res.*, 7 (2), 140–148.
- [38] Sethi, D., and Sakthivel, R., 2017, ZnO/TiO₂ composites for photocatalytic inactivation of *Escherichia coli*, *J. Photochem. Photobiol., B*, 168, 117–123.
- [39] Jakubczyk, K., Drużga, A., Katarzyna, J., and Skonieczna-Żydecka, K., 2020, Antioxidant potential of curcumin—A meta-analysis of randomized clinical trials, *Antioxidants*, 9 (11), 1092.

Utilization of Steepest Ascent and Box-Behnken Design for Determination of Gadolinium in Acetonitrile by Differential Pulse Voltammetry

Santhy Wyantuti*, Uji Pratomo, Yeni Wahyuni Hartati, Amelia Shafira, Ari Hardianto, and Husein Hernandi Bahti

Department of Chemistry, Faculty of Mathematics and Natural Sciences, Universitas Padjadjaran, Jl. Raya Bandung-Sumedang Km. 21, Jatinangor, Sumedang 45363, Indonesia

* Corresponding author:

email: santhy.wyantuti@unpad.ac.id

Received: January 5, 2023

Accepted: September 5, 2023

DOI: 10.22146/ijc.80979

Abstract: Gadolinium (Gd) is an important material for advanced technology; hence, the development of a sensitive and efficient alternative for the Gd-detection method to reduce the dependency on complicated and expensive methods has been massively investigated. Furthermore, the combination of differential pulse voltammetry (DPV) and the experimental design to detect Gd provides a simple, effective, and efficient method. In this study, the Steepest Ascent and Box-Behnken designs were chosen to determine the maximum voltammetry responses. The optimum conditions used for this study showed an amplitude modulation of 0.0884 V, potential deposition of 1.4382 V, and deposition time was 60.3615 s with the obtained recovery value, accuracy, and precision values being 98.37, 95.91, and 5.12% in relative standard deviation (RSD), respectively. Meanwhile, the detection and quantization limit values are 3.46 and 11.53 mg/L, respectively. Under optimum conditions, the presence of Gd in acetonitrile is determined in a mixture with Eu and Sm. Based on the results, the DPV method is capable of determining the presence of Gd in acetonitrile.

Keywords: Gadolinium; differential pulse voltammetry; acetonitrile; Box-Behnken; Steepest Ascent

■ INTRODUCTION

Gadolinium (Gd) belongs to the lanthanide group or rare earth elements that have great potential for the preparation of modern materials, specifically medical items [1-5]. Given that Gd has an important role in human welfare development, studies for the determination of its presence have significantly increased [6-7]. Furthermore, sophisticated methods such as inductively coupled plasma-mass spectrometry (ICP-MS) and inductively coupled plasma-atomic emission spectroscopy (ICP-AES) have shown great performance in determining the availability of Gd in samples, but they also have some drawbacks including complicated maintenance and high cost [8-10].

Voltammetry is one of the electrochemical methods used for measuring the current generated against the potential difference applied to the working electrode [11]. Advantages of the voltammetric method include a simple procedure, simultaneous analysis, and better detection

limits [12-14]. An experimental design such as Steepest Ascent is a method used to detect the direction that the factor is moving to get the maximum response, while Box-Behnken design is used to estimate the interactions that occur to obtain an optimal process [15-16]. Determination of Gd using this method with Plackett-Burman and Box-Behnken experimental design has been carried out by using water solvent and NH_4Cl electrolyte solution, but the voltammogram of rare earth elements' mixture is complicated as it has the same standard reduction potential value [17].

The demand for organic solvents for metal electrodeposition is increasing as it provides an alternative pathway for electrochemical processes as they accelerate the dissolution and reaction of metal ions [18-20]. In this study, the determination of Gd by differential pulse voltammetry (DPV) with acetonitrile as an organic solvent has been developed using the

optimum factor determined by Steepest Ascent and Box-Behnken experimental designs to optimize the experiment time and reduce the chemicals used.

■ EXPERIMENTAL SECTION

Materials

The materials used in this study were 65% nitric acid (HNO₃) and acetonitrile (CH₃CN), as well as aquabidest, which were obtained from Merck and aquamiliQ, respectively. The other reagents used were from Sigma Aldrich, which include 99% gadolinium oxide (Gd₂O₃), 99% dysprosium oxide (Dy₂O₃), 99.9% samarium oxide (Sm₂O₃), and 99.9% europium oxide (Eu₂O₃).

Instrumentation

The apparatus and equipment used include scanning electron microscope (SEM) JEOL JSM-7500F, Ag/AgCl electrodes (eDAQ), ANOVA 7.0.0 program, potentiostat (Metrohm® µAutolab), Pt wire for the counter electrode (Antam), Minitab 17.1 program, analytical balance (Sartorius), and Pt working electrodes (Antam).

Procedure

Preparation of Gd₂O₃ stock solution 1000 mg/L

The stock solution was made by dissolving 0.1153 g of Gd₂O₃ in 65% solution of HNO₃, which was stirred and boiled until a homogeneous solution was obtained, mixed with 100 mL of distilled water and stirred again. The solution was diluted with acetonitrile to produce varied amounts of Gd.

Background current measurement

A pipette was used to pour 10.0 mL of acetonitrile into a voltammetric cell. DPV was used to determine the current responsiveness of acetonitrile under the following conditions: a potential range, potential deposition, deposition time, amplitude modulation, and scanning rate of -1.0 to +1.0 V, -1.0 V, 60.0 s, 0.05 V, and 0.05 V/s, respectively.

Gd current measurement

DPV was used to determine the current response of a 30.0 mg/L Gd₂O₃ solution under the following conditions with potential range, deposition potential,

deposition time, amplitude modulation, and scanning rate of -1.0 to +1.0 V, -1.0 V, 60.0 s, 0.05 V, and 0.05 V/s.

Surface morphology analysis of Pt working electrode

The surface morphology of the Pt working electrode (about 1 cm) was examined before and after deposition using SEM.

Measurement of Gd with steepest ascent

The selected upper and lower limit factors were set to measure Gd, namely the deposition potential of -1.0 and -2.0 V, deposition time of 40.0 and 80.0 s, and amplitude modulation of 0.05 and 0.10 V, then adjusted to the first-order model in the RStudio program [21-23] and the equation of the first-order model was used to determine the direction of the steepest ascent. The center was made along the direction of the experiment until the maximum response was generated, and then the experiment was designed. The result of Steepest Ascent optimization is shown in Table 1.

Measurement of Gd with Box-Behnken design experimental design

The current responses of 30 mg/L Gd were analyzed using differential pulse voltammetry for 45 measurements (3 repetitions) while Box-Behnken was used to optimize the selected factors with the lower and upper limits of steepest ascent experimental design results, namely the potential deposition of -1.4384 and

Table 1. Selected factors to be optimized by Steepest Ascent

No	Potential deposition (V)	Deposition time (s)	Amplitude modulation (V)	Current (µA)
1	-1.4380	60.3300	0.0910	8.9326
2	-1.4381	60.3362	0.0905	9.2975
3	-1.4382	60.3462	0.0900	9.5924
4	-1.4382	60.3489	0.0894	9.7140
5	-1.4383	60.3552	0.0889	10.1540
6	-1.4384	60.3615	0.0884	9.5479
7	-1.4385	60.3678	0.0879	9.5768
8	-1.4386	60.3741	0.0873	9.5768
9	-1.4386	60.3804	0.0868	9.5321
10	-1.4387	60.3867	0.0863	9.4800
11	-1.4388	60.3931	0.0858	9.2071

Table 2. Selected factors to be optimized by Box-Behnken

Factors	Level			Optimum condition
	-1	0	+1	
Potential deposition (V)	-1.4384	-1.4383	-1.4382	-1.4382
Deposition time (s)	60.3489	60.3552	60.3615	60.3615
Amplitude modulation (V)	0.0894	0.0889	0.0884	0.0884

-1.4382 V, deposition time of 60.3489 and 60.3615 s, and amplitude modulation of 0.0894 and 0.0884 V. The data obtained were analyzed using the Minitab 19 program; the result of Box-Behnken optimization is shown in Table 2.

Determination of Gd in the REE mixture with Sm, Eu, and Dy

A 10 mL of a combination of Sm, Eu, Gd, and Dy was pipetted in acetonitrile. Subsequently, the quantitative determination of the current was conducted by DPV under the Box-Behnken optimal condition.

Calibration curve of Gd

A solution of 10.0, 20.0, 30.0, 40.0, and 50.0 mg/L Gd in acetonitrile were measured by DPV under the optimum condition obtained from Box-Behnken design.

RESULTS AND DISCUSSION

The Acetonitrile and Gadolinium Current Response

The measurement of the acetonitrile current response was carried out to determine the effect of the solvent on the produced Gd response using the DPV

method. As shown in Fig. 1, the acetonitrile did not produce any current response, while the 30 mg/L Gd in acetonitrile shows a characteristic peak near -0.40 V. From this preliminary result, the acetonitrile solvent does not interfere with the response of Gd.

The Effect of Acetonitrile Concentration on the Gd Deposition on the Pt Electrode

Various concentration of Gd in acetonitrile (25, 75, and 100%) was deposited on the Pt electrode by the cyclic voltammetry method. The surface morphology before and after the electrodeposition was analyzed using SEM instrument, and the results obtained are shown in Fig. 2.

As shown in Fig. 2, the amount of Gd deposited on the Pt working electrode is indicated by the white particle aggregate. Furthermore, by increasing the concentration of acetonitrile, the aggregates were found to be highly distributed, and this indicates that an increase in the concentration of acetonitrile is proportional to the increase of white particle aggregate or deposition process of Gd on the working electrode of Pt.

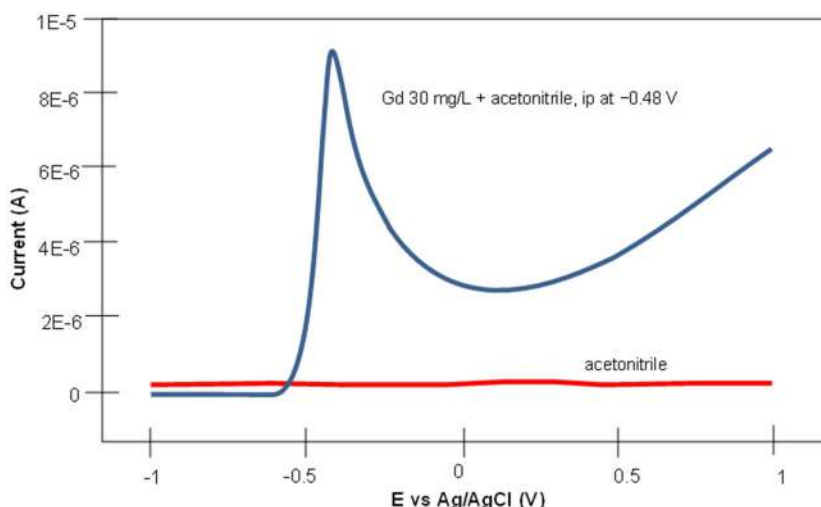


Fig 1. Current response of acetonitrile and Gd 30.0 mg/L in acetonitrile

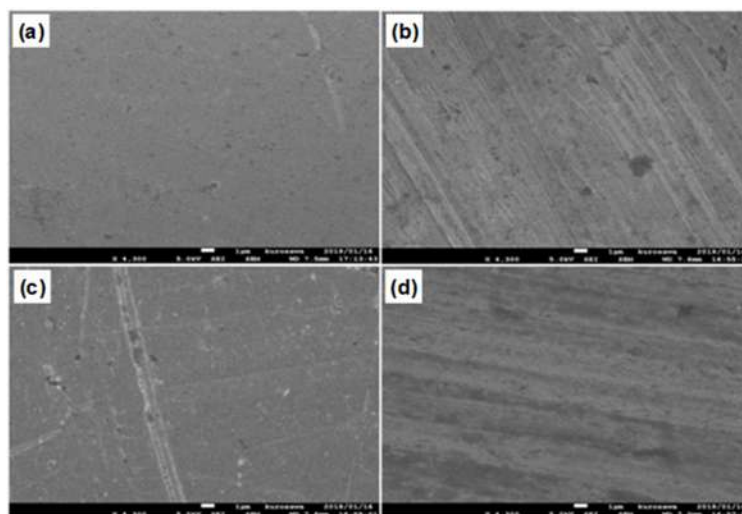


Fig 2. Pt electrode surface images (4300× magnification) after deposition of Gd in (a) 25% acetonitrile, (b) 75% acetonitrile, (c) 100% acetonitrile, and (d) before deposition

Determination of the Optimum Condition with Box-Behnken Design

The main factors that considerably influence the optimum condition for Gd analysis are potential deposition, deposition time and amplitude modulation. They were optimized using Box-Behnken design in the Minitab 19 program. The three factors and three levels were selected, and the obtained current response is presented in Table 3.

The effect of the regression coefficient on the model is presented in Table 4. The p -value of the amplitude modulation factor is 0.0000 and less than 0.05; hence, the factor that significantly influences the measurement of current is amplitude modulation. Additionally, the p -values of deposition time and potential deposition are 0.8059 and 0.3784, and this indicates that deposition time and potential have no effect on the resulting response.

Furthermore, a fit test was carried out to determine

Table 3. The current response of Gd by DPV

Run	Potential deposition (V)	Deposition time (s)	Amplitude modulation (V)	Current (μ A)
1	-1.4384	60.3489	0.0889	11.5100; 11.1740; 11.3900
2	-1.4382	60.3489	0.0889	11.7930; 10.9170; 11.2680
3	-1.4384	60.3615	0.0889	11.7870; 11.3890; 11.3040
4	-1.4382	60.3615	0.0889	11.8800; 11.6610; 11.0830
5	-1.4384	60.3552	0.0884	10.9110; 10.9930; 10.7110
6	-1.4382	60.3552	0.0884	10.4870; 10.8600; 10.9040
7	-1.4384	60.3552	0.0894	10.8400; 10.8880; 10.5150
8	-1.4382	60.3552	0.0894	10.1070; 10.5340; 10.3280
9	-1.4383	60.3489	0.0884	10.7590; 10.1760; 10.4420
10	-1.4383	60.3615	0.0884	10.6810; 10.6340; 10.4950
11	-1.4383	60.3489	0.0894	9.9289; 9.9711; 9.9742
12	-1.4383	60.3615	0.0894	9.8200; 9.7321; 9.6468
13	-1.4383	60.3552	0.0889	9.2721; 9.3852; 9.2754
14	-1.4383	60.3552	0.0889	9.8707; 9.8667; 9.6689
15	-1.4383	60.3552	0.0889	9.5253; 9.6751; 9.3391

Table 4. Effect of the regression coefficient on the model

Term	Coefficient	SE coefficient	<i>p</i>
Constant	95.4210	0.0824	0.0000
Deposition potential	-0.0450	0.0504	0.3784
Deposition time	0.0125	0.0504	0.8059
Amplitude modulation	-0.2403	0.0504	0.0000
Deposition potential*Deposition potential	12.0750	0.0742	0.0000
Deposition time* Deposition time	0.7226	0.0742	0.0000
Amplitude modulation*Amplitude modulation	-0.0764	0.0742	0.3108
Deposition potential*Deposition time	-0.0225	0.0713	0.7543

whether the model agrees with the prediction model. The obtained *p*-value is 0.0413, which was lower than $\alpha = 0.05$ and this indicated that the model is appropriate.

Additionally, it is necessary to test for normality by observing the residual distribution curve. According to the hypothesis for the normality test, when H_0 is accepted at a *p*-value ≥ 0.05 , it shows that the result is normally distributed. Meanwhile, when H_1 is accepted at a *p*-value less than 0.05, it shows that the result is not normally distributed. As illustrated in Fig. 3, the normal distribution curve of the hypothetical residual has a *p*-value above 0.05. Therefore, when H_0 is accepted shows that the residuals were normally distributed and significant. The best conditions for Gd detection include a potential deposition, deposition time, and amplitude modulation of -1.4382 V, 60.3615 s, and 0.0884 V, respectively.

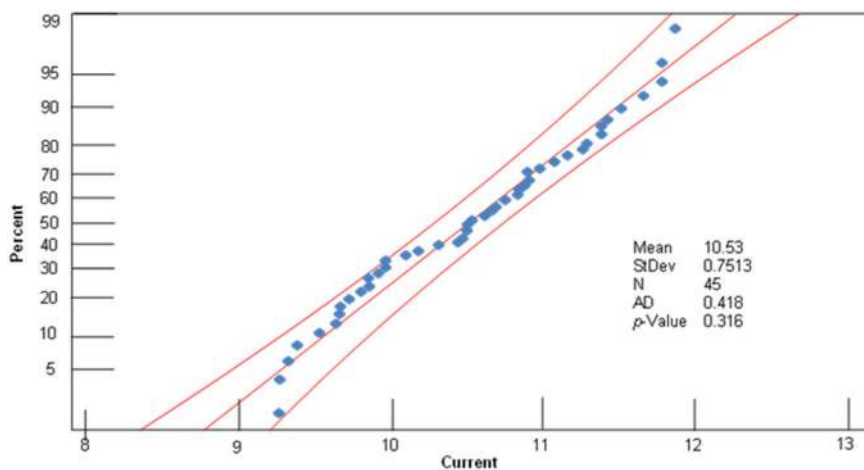
Detection of Gd in a Mixture with Sm, Eu, and Dy under the Optimum Condition

The concentration of Sm, Eu, Gd, and Dy in naturally

occurring monazite on Bangka Belitung Island was 40.21, 0.01, 0.58, and 0.37%, respectively [14,24]. Therefore, various concentrations of Sm, Eu, Gd, and Dy were prepared in this study at 400, 1, 50, and 30 mg/L, respectively. The results are presented in Fig. 4.

Fig. 4 shows that the voltammogram relatively shows no response to the individual Eu and Sm in acetonitrile. Meanwhile, the presence of Gd and Dy produces a high and low current response, respectively. The voltammogram analysis of the mixture of Gd, Eu, Dy, and Sm showed a high current peak at $i_p -0.70$ V, which resembles the peak of Gd at -0.48 V.

In addition, investigation on the mixtures of 50 mg/L Gd with 30 mg/L Dy, 50 mg/L Gd with 1 mg/L Eu, and 50 mg/L Gd with 400 mg/L Sm were carried out, and the result is presented in Fig. 5. Fig. 5(a) shows that a low current response of Dy in acetonitrile is observed while a relatively high current response of Gd is observed. Also, the mixture of Gd and Dy in acetonitrile shows a similar response with a higher response to Gd

**Fig 3.** Normality plot of Box-Behnken design

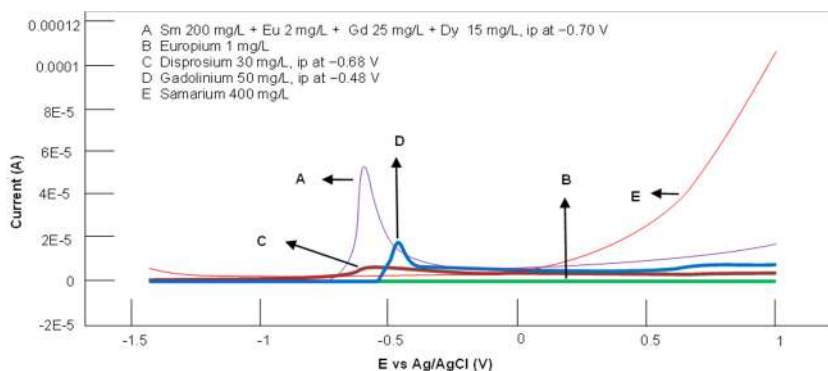


Fig 4. The individual current response of Gd 50 mg/L, Eu 1 mg/L, Dy 30 mg/L, and Sm 400 mg/L, and the mixture of Gd, Dy, Eu and Sm under the optimum conditions by DPV

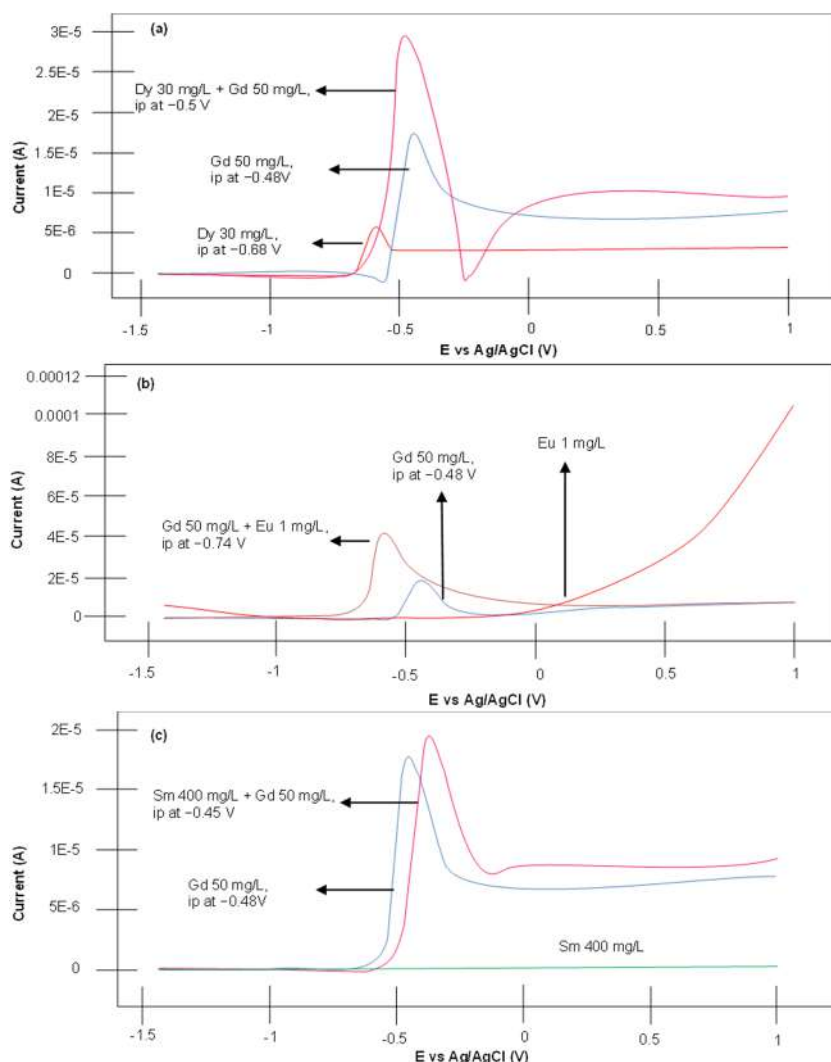


Fig 5. Voltammogram of (a) a mixture of Gd 50 mg/L and Dy 30 mg/L, (b) a mixture of Gd 5 mg/L and Eu 1 mg/L, and (c) a mixture of Gd 50 mg/L and Sm 400 mg/L under the optimum conditions by DPV

peak. In contrast, the voltammogram of individual Eu (Fig. 5(b)) and individual Sm (Fig. 5(c)) in acetonitrile

shows no current response; however, the mixture of Gd-Eu and Gd-Sm shows a similar current response to

individual Gd peak. Conclusively, this result indicates that Gd is determinable in a mixture of Sm and Eu.

The Gd Calibration Curves, Detection Limits, and Quantification Limits

The Gd calibration curve was plotted at several concentrations, including 10, 20, 30, 40, and 50 mg/L. Fig. 6 and 7 depict the current response and the calibration curve, respectively. The differential pulse voltammetry current response demonstrates that the growing current peak is proportionate to the increasing Gd concentration. The graph of current was plotted with a coefficient (R^2) of 0.9995.

The precision, detection, and quantitation limit of the analytical parameters were determined to validate the level of acceptance and significance of the technique in the analysis. The average accuracy and precision were 95.91 and 5.12% (RSD), respectively, while the detection and quantitation limits were 3.46 and 11.53 mg/L, respectively,

and the recovery (%R) calculation was 98.37%. In addition, the comparison between the previous work and this work is shown in Table 5. This research shows better recovery results for the determination of Gd by DPV method.

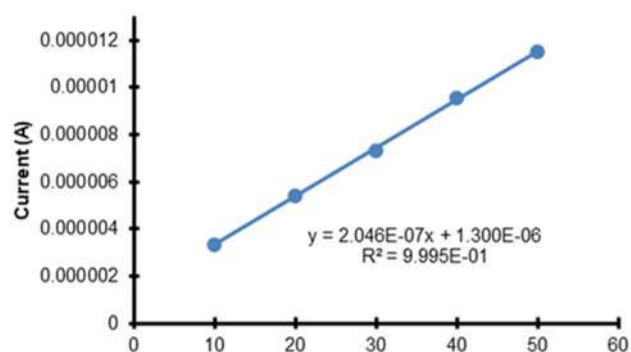


Fig 7. Calibration curve of Gd in acetonitrile under potential range -1.4382 to $+1.0$ V, potential deposition -1.4382 V, deposition time 60.3615 s, amplitude modulation 0.0884 V and scan rate 0, 05 V/s

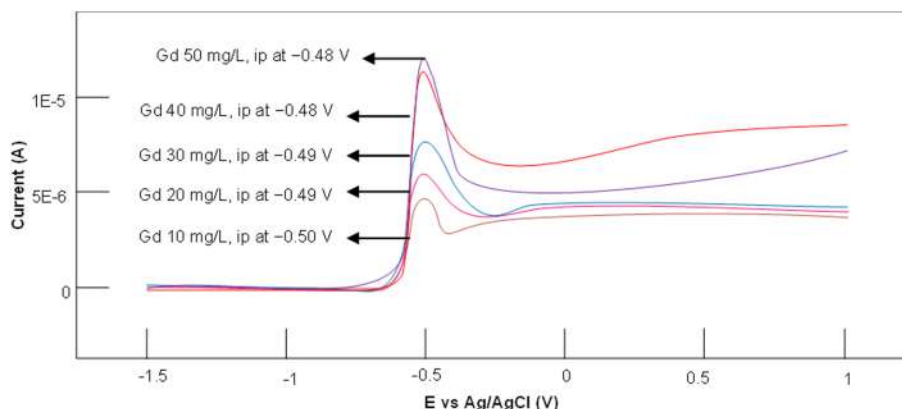


Fig 6. DPV of Gd in acetonitrile 10 to 50 mg/L under the potential range of -1.4382 to $+1.0$ V, deposition potential -1.4382 V, deposition time 60.3615 s, amplitude modulation 0.0884 V and scan rate 0.05 V/s

Table 5. Result comparison with the previous work

Method	Solvent	% Recovery	Reference
Determination of Sm as a complex with DTPA by DPV based on Plackett-Burman experimental design	NH_4Cl	95.754	[11]
Determination of Gd and Tb as complexes with DTPA by DPV based on Plackett-Burman experimental design	NH_4Cl	95.754	[23]
Determination of Dy by DPV based on the Box-Behnken experimental design	CH_3CN	93.620	[14]
Determination of Sm by DPV based on the Box-Behnken experimental design	CH_3CN	98.070	[24]

Method	Solvent	% Recovery	Reference
Determination of Gd by DPV based on the Steepest Ascent and Box-Behnken experimental design	CH ₃ CN	98.375	This research

■ CONCLUSION

The optimum measurement conditions for the detection of Gd in acetonitrile obtained from the Steepest Ascent experimental design and Box-Behnken are potential deposition of -1.4382 V, amplitude modulation of 0.0884 V, and deposition time of 60.3615 s. The recovery value, accuracy and precision were 98.37 , 95.91 , and 5.12% (RSD), respectively, while the LoD and LoQ obtained were 3.46 and 11.53 mg/L. Based on the results, the differential pulse voltammetry is usable in determining the presence of Gd in acetonitrile. Our research provides essential information for the further development of the Gd detection method from rare earth sources like monazite, which has a complex sample matrix potentially interfering with measurement.

■ ACKNOWLEDGMENTS

The author would like to acknowledge the financial support from the Academic Leadership Grant Program, Padjadjaran University, the Directorate of Research and Community Service through *Riset Kompetensi Dosen Unpad* (DRPM-RKDU), Padjadjaran University, Indonesia [1549/UN6.3.1/PT.00/2023].

■ AUTHOR CONTRIBUTIONS

The conceptualization, methodology, supervision, project administration, funding acquisition and resources were prepared by Santhy Wyantuti, Yeni Wahyuni Hartati, Uji Pratomo, and Husein Hernandi Bahti. The software, validation, writing–original draft preparation, and writing–review were done by Santhy Wyantuti, Uji Pratomo, Yeni Wahyuni Hartati, Ari Hardianto, and Husein Hernandi Bahti. The formal analysis, investigation, data curation, and visualization were done by Amelia Shafira, and Ari Hardianto. All authors have read and agreed to the published version of the manuscript.

■ REFERENCES

- [1] Unruh, C., Van Bavel, N., Anikovskiy, M., and Prenner, E.J., 2020, Benefits and detriments of gadolinium from medical advances to health and ecological risks, *Molecules*, 25 (23), 5762.
- [2] Zhou, B., Li, Z., and Chen, C., 2017, Global potential of rare earth resources and rare earth demand from clean technologies, *Minerals*, 7 (11), 203.
- [3] Yan, D., Ro, S., Sunam, O., and Kim, S., 2020, On the global rare earth elements utilization and its supply-demand in the future, *IOP Conf. Ser.: Earth Environ.*, 508, 012084.
- [4] Blomqvist, L., Nordberg, G.F., Nurchi, V.M., and Aaseth, J.O., 2022, Gadolinium in medical imaging-usefulness, toxic reactions and possible countermeasures-A review, *Biomolecules*, 12 (6), 742.
- [5] Kim, H.K., Lee, G.H., and Chang, Y., 2018, Gadolinium as an MRI contrast agent, *Future Med. Chem.*, 10 (6), 639–661.
- [6] Veiga, M., Mattiazzi, P., de Gois, J.S., Nascimento, P.C., Borges, D.L.G., and Bohrer, D., 2020, Presence of other rare earth metals in gadolinium-based contrast agents, *Talanta*, 216, 120940.
- [7] Smoliński, A., Stempin, M., and Howaniec, N., 2016, Determination of rare earth elements in combustion ashes from selected Polish coal mines by wavelength dispersive X-ray fluorescence spectrometry, *Spectrochim. Acta, Part B*, 116, 63–74.
- [8] Zawisza, B., Pytlakowska, K., Feist, B., Polowniak, M., Kita, A., and Sitko, R., 2011, Determination of rare earth elements by spectroscopic techniques: A review, *J. Anal. At. Spectrom.*, 26 (12), 2373–2390.
- [9] Telgmann, L., Lindner, U., Lingott, J., and Jakubowski, N., 2016, Analysis and speciation of lanthanoides by ICP-MS, *Phys. Sci. Rev.*, 1 (11), 20160058.
- [10] Day, P., Erdahl, S., Eckdahl, S., Bornhorst, J., and Jannetto, P.J., 2019, Gadolinium-based contrast agents: A clinically significant analytical interference in inductively coupled plasma mass spectrometry elemental analysis, *Ann. Clin. Biochem.*, 56 (6), 638–645.

- [11] Wyantuti, S., Pratomo, U., Hartati, Y.W., Hendrati, D., and Bahti, H.H., 2018, A study of green electroanalysis conducted by experimental design method for detection of samarium as complex with diethylenetriaminepentaacetic acid (DTPA), *AIP Conf. Proc.*, 2049, 030010.
- [12] Scholz, F., 2015, Voltammetric techniques of analysis: The essentials, *ChemTexts*, 1 (4), 17.
- [13] Han, H., and Pan, D.J., 2021, Voltammetric methods for speciation analysis of trace metals in natural waters, *Trends Environ. Anal. Chem.*, 29, e00119.
- [14] Wyantuti, S., Pratomo, U., Shauvina, S., Hartati, Y.W., and Bahti, H.H., 2021, Differential pulse voltammetry study for quantitative determination of dysprosium(III) in acetonitrile solution, *Int. J. Renewable Energy Dev.*, 10 (2), 191–199.
- [15] Yu, X.L., and He, Y., 2017, Application of Box-Behnken designs in parameters optimization of differential pulse anodic stripping voltammetry for lead(II) determination in two electrolytes, *Sci. Rep.*, 7 (1), 2789.
- [16] Liu, J., Xu, Y., Liu, S., Yu, S., Yu, Z., and Low, S.S., 2022, Application and progress of chemometrics in voltammetric biosensing, *Biosensors*, 12 (7), 494.
- [17] Wyantuti, S., Harahap, F.W., Hartati, Y.W., and Firdaus, M.L., 2021, Application of Plackett-Burman and Box-Behnken experiment design in differential voltammetry analysis for determining gadolinium concentration, *J. Phys.: Conf. Ser.*, 1731, 012017.
- [18] Neuróhr, K., Pogány, L., Tóth, B., Révész, A., Bakonyi, I., and Péter, L., 2017, Electrodeposition of Ni from various non-aqueous media: The case of alcoholic solutions, *J. Electrochem. Soc.*, 162, D256.
- [19] Bourbos, E., Giannopoulou, I., Karantonis, A., Paspaliaris, I., and Pantias, D., 2018, Reduction of light rare earths and a proposed process for Nd electrorecovery based on ionic liquids, *J. Sustainable Metall.*, 4 (3), 395–406.
- [20] Mirzamohammadi, S., Khorsand, H., and Aliofkhaezai, M., 2017, Effect of different organic solvents on electrodeposition and wear behavior of Ni-alumina nanocomposite coatings, *Surf. Coat. Technol.*, 313, 202–213.
- [21] Joyce, A.P., and Leung, S.S., 2013, Use of response surface methods and path of steepest ascent to optimize ligand-binding assay sensitivity, *J. Immunol. Methods*, 392 (1), 12–23.
- [22] Jalalvand, A.R., 2022, Engagement of chemometrics and analytical electrochemistry for clinical purposes: A review, *Chemom. Intell. Lab. Syst.*, 227, 104612.
- [23] Wyantuti, S., Pratomo, U., Hartati, Y.W., Hendrati, D., and Bahti, H.H., 2019, Application of experimental design by differential pulse voltammetry for determination of rare elements as complexes with diethylenetriaminepentaacetic acid (DTPA), *Int. J. Recent Technol. Eng.*, 8 (2S7), 33–37.
- [24] Wyantuti, S., Pratomo, U., Manullang, L.A., Hendrati, D., Hartati, Y.W., and Bahti, H.H., 2021, Development of differential pulse voltammetric method for determining samarium(III) through electroanalytical study of the metal ion in acetonitrile using Box–Behnken design, *Heliyon*, 7 (4), e06602.

Supplementary Data

This supplementary data is a part of a paper entitled “Removal of Methyl Orange Using Nanocomposites Based on Polyaniline/ $\text{Nb}_2\text{O}_5/\text{MnO}_2$ and Polyaniline/ $\text{Nb}_2\text{O}_5/\text{Cr}_2\text{O}_3$ as New Adsorbents”.

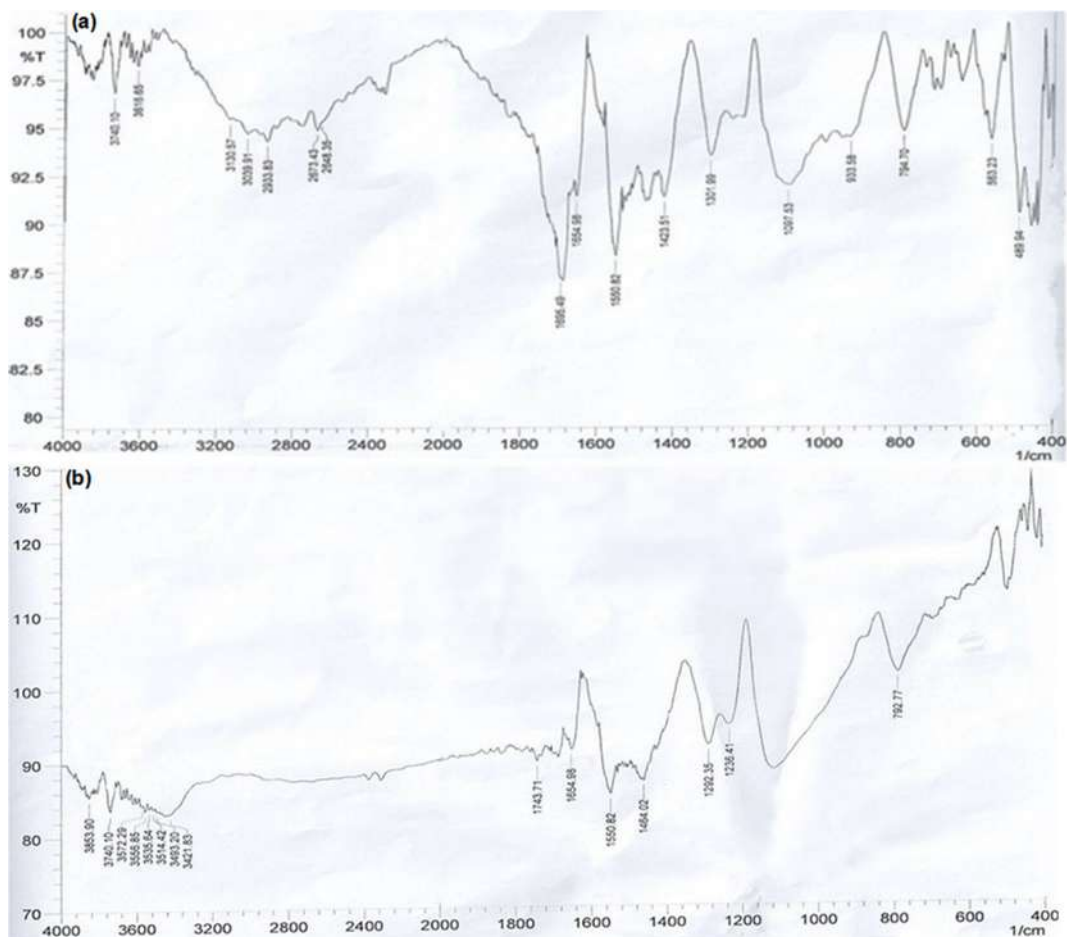


Fig S1. FTIR spectrum of (a) PANI/ $\text{Nb}_2\text{O}_5/\text{MnO}_2$ and (b) PANI/ $\text{Nb}_2\text{O}_5/\text{Cr}_2\text{O}_3$

Removal of Methyl Orange Using Nanocomposites Based on Polyaniline/Nb₂O₅/MnO₂ and Polyaniline/Nb₂O₅/Cr₂O₃ as New Adsorbents

Karrar Majeed Obaid, Ahmed Saadoon Abbas, and Yahya Fahim Al-Khafaji*

Department of Chemistry, College of Science, University of Babylon, Hilla 51002, Iraq

* Corresponding author:

email:

sci.yahya.alkhafaji@uobabylon.edu.iq

Received: February 19, 2023

Accepted: May 17, 2023

DOI: 10.22146/ijc.82417

Abstract: Dyes are the most widely employed materials for coloring applications, especially for industrial purposes; thus, dyes are applied in the textile, cosmetics and foodstuffs. Dyes are very important owing to their applications in all aspects of human life. Accordingly, the production volume of dyes around the world is increasing. In this study, a new type of multifunctional material: polyaniline/Nb₂O₅/MnO₂ and polyaniline/Nb₂O₅/Cr₂O₃ nanocomposites, was prepared by chemical polymerization from aniline monomer in the presence of metal oxides (Nb₂O₅, Cr₂O₃, and MnO₂) and an oxidant (ammonium persulfate) in acidic aqueous solution for the elimination of dye from water. Herein, the nanocomposite was found to be a favorable adsorbent for wastewater treatment due to its high adsorption and efficiency, self-regeneration quality, low cost and easy synthesis. Fourier transform infrared spectroscopy, X-ray diffraction, scanning electron microscopy and UV-visible spectroscopy were used to assess the synthesized nanocomposites' characteristics. From the results, we discovered that polyaniline nanocomposites doped with Nb₂O₅ and MnO₂ nanoparticles had a higher adsorption efficiency (~97.37%) than those found in polyaniline with Cr₂O₃ and MnO₂ (~94.3%). We looked at the adsorption conditions, including the medium's pH, the initial dye concentration, the dosage of the adsorbent, and the adsorption time.

Keywords: adsorption; dye removal; polyaniline; metal oxide

■ INTRODUCTION

Dyes are the most widely employed materials for coloring applications, especially for industrial purposes. Dyes are used for textiles, cosmetics, foodstuffs and anticorrosion [1]. Dyes are very important due to their application in all aspects of human life. Accordingly, their production volume around the world is increasing. Over the last few decades, more attention has been placed on the discharge of about 10–15% of the dyes into the environment. So, there is a major environmental problem arising from the frequent colored wastewater, which is eco-toxic and hazardous in nature. In addition, the quality of water is decreased due to the dyes. Examples of such dye are methyl orange (MO). With this in mind, the treatment of dyes or dyestuffs before their discharge into the environment needs more attention.

Two types of recent treatment techniques could be used: chemical and physical treatment; examples of such

techniques are liquid chromatography, precipitation, ion exchange, and electrochemical [2]. However, the problems with these techniques are that they are expensive, and some of them are not effective. Subsequently, researchers are trying to find other techniques that are not expensive, more active, easy to use and able to be recycled for use multiple times to remove dye from wastewater. Researchers have been investigating several selective adsorbent materials in this area, such as zeolites, chitosan, and clay [3-4]. Owing to the fact that conducting polymer nanomaterials have various chemical and physical possessions, they have been employed in many applications as they are easy to prepare, have a low cost and allow ease of doping polymers polyaniline (PANI) as shown in Fig. 1.

PANI has two functional groups, amine and imine, that facilitate the adsorption of dyes such as MO. Adsorption mechanisms can be affected by many factors

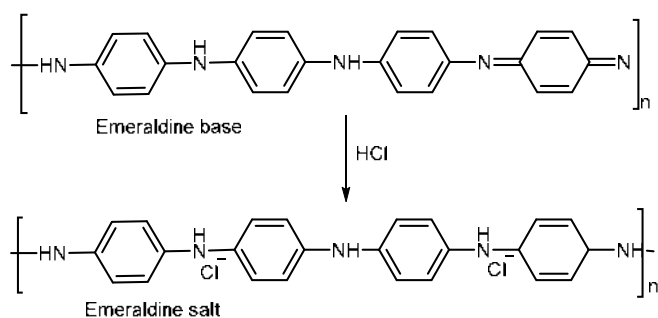


Fig 1. Chemical structure of PANI [13]

related to adsorbent and adsorbate (morphology of the adsorbent and functional group found in both and the porosity of adsorbent). As mentioned in the literature, adsorption capacity can be affected by the interaction of adsorbent and adsorbate, which depend on the pores present on the surface of the adsorbent. To solve this problem, many materials have been employed by mixing them with PANI, for example, carbon nanotubes [5], metal oxides and metals [6].

Through *in situ* chemical oxidation or electrochemical procedures, a number of different noble metal nanoparticle types, such as MnO₂ [7], Co₃O₄ [8], and MWCNTs/Fe₃O₄ [9], have recently been integrated into the PANI framework. Although there has been a lot of research on noble metal nanoparticles combined with conducting polymers, there is not a single study that sufficiently defines their use with increased reactivity, such as Nb₂O₅ and MnO₂, when combined with PANI nanofibers (i.e., PANI/Nb₂O₅/MnO₂ ternary nanocomposites). In this study, aniline monomer was used to polymerize with Nb₂O₅ and MnO₂ nanoparticles in an acidic aqueous media. Ammonium persulfate was used as the oxidant. This study's primary objective is to investigate the effects of pure PANI powder and a novel, highly porous adsorbent material termed as PANI/Nb₂O₅/MnO₂ ternary nanocomposite on the adsorption of MO dyes in the aqueous medium. The 4-dimethylaminoazobenzene-40-sulphonic acid sodium salt, also known as MO, is an anionic dye that is widely used in paper [10-11], pharmaceutical, textile and printing industries [12]. MO is highly soluble in water.

Several methods, including X-ray diffraction (XRD), Fourier transform infrared spectroscopy (FTIR) and

scanning electron microscopy (SEM), were used to characterize the PANI/Nb₂O₅/MnO₂ ternary nanocomposite. The batch equilibrium and UV-vis spectroscopy methods were used to determine the high capacity of this sample in dye adsorption during the following tests: effects of pH solutions, start-up adsorbent dosage, contact time, and dye concentration. The adsorption process's kinetics, isotherms and thermodynamics have all been identified. The information offers hope for several important inferences, such as economic viability and a reusable adsorbent for color removal. Therefore, a unique method is being used to investigate the efficacy of a PANI/Nb₂O₅/MnO₂ ternary nanocomposite as an adsorbent for the removal of MO from wastewater.

■ EXPERIMENTAL SECTION

Materials

Water solutions are used in this study. The materials were utilized exactly as obtained from Sigma-Aldrich and included aniline monomer (99.5%), ammonium persulfate (APS, 98%), and acetone (99.5%). Without further purification, hydrochloric acid (Fisher Chemical, 37%), niobium(V) oxide (Fluka, 99%), chromium(III) oxide, ethanol, sodium hydroxide (99.8%), and manganese(IV) oxide (Panreac, 98%) were utilized.

Instrumentation

FTIR spectroscopy (PerkinElmer), X-ray diffractor (Model: Xrd-6000/Shimadzu, Japan), FE-SEM Thermo Fisher Scientific XL30, a UV-vis spectrophotometer (Shimadzu 1600, Japan), and pH meter (Oakton 550, USA) were used in this work.

Procedure

Synthesis of PANI/Nb₂O₅/MnO₂ adsorbent

Aniline (8 g) dissolved in 100 mL of 1 M HCl solution was then agitated for 1 h before being cooled for a further 30 min. Powder, 1 g of Nb₂O₅ and 1 g of MnO₂, was added straight to the solution by dissolving 14 g of the oxidant solution (APS) in an 80 mL aqueous solution of 1 M HCl; thus, the oxidant solution was synthesized.

So, by using the magnetic stirring method and a thermometer [14-15], aniline and metal oxide were combined. These were then slowly exposed to the APS solution, which was released dropwise from a separating funnel. To keep the temperature of the polymerization solution process at around 1–2 °C, 10 drops of APS were added per minute. The PANI nanocomposite had already been constructed when the polymerization reaction continued for 6 h and the arrangement's color slowly changed from grey to blue to green. The resulting PANI/Nb₂O₅/MnO₂ nanocomposite was washed with acetone, 1 L of 1 M HCl, newly distilled water and a Buchner funnel; lastly, the product was dried in a vacuum oven for 24 h at 70 °C [16]. Similarly, PANI/Nb₂O₅/Cr₂O₃ were synthesized in the same strategy that was used to prepare PANI/Nb₂O₅/MnO₂ described above (Fig. 2).

Batch adsorption experiments and experimental design

Due to their large surface area and superior adsorption capability, the as-synthesized

PANI/Nb₂O₅/Cr₂O₃ and PANI/Nb₂O₅/MnO₂ nanocomposites are useful adsorbents for water and wastewater purification. This study identified MO since it is a typical organic contaminant in industrial sewage. A number of factors, including the pH of the solution, the amount of adsorbent used, the MO dye's starting concentration and the reaction time, were studied in relation to the removal of MO dye's adsorption to PANI/Nb₂O₅/Cr₂O₃ and PANI/Nb₂O₅/MnO₂ nanocomposites. A MO dye adsorption equilibrium experiment was carried out using two 250 mL conical flasks with a constant adsorbent dosage (100 mg) with initial concentrations of 100 mL of MO dye ranging from 10 to 200 mg/L. A pH meter was used to monitor the pH of the setups, which was adjusted to pH 7. To ensure equilibrium conditions, the orbital shakers were shaken at a controlled speed of 300 rpm after 60 min. By making use of a UV-vis spectrophotometer set to its maximum wavelength of 463 nm, a comparison of MO concentrations before and after was determined. Using

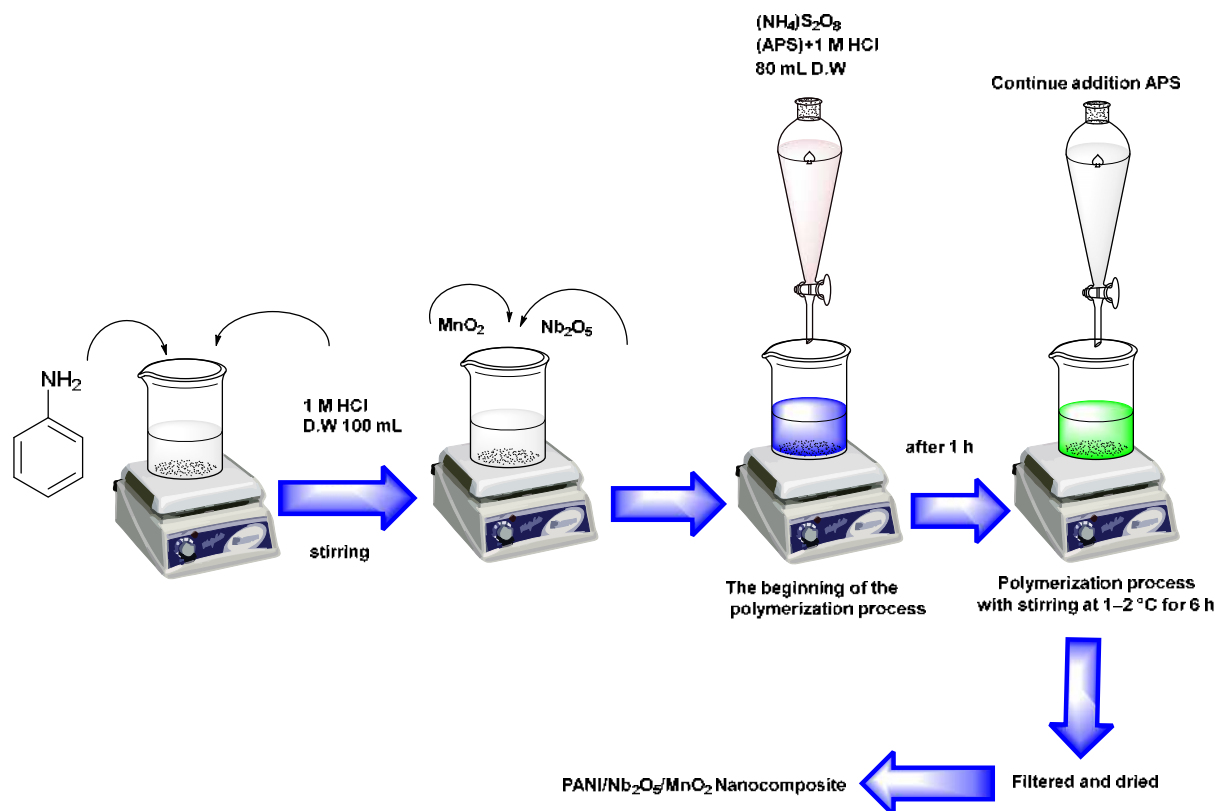


Fig 2. Schematic of the synthesis of PANI/Nb₂O₅/MnO₂ sample by *in situ* oxidative polymerization with its proposed interactions

the following methods, the percentage of dye removal (percent DR) was determined and noted in Eq. (1):

$$\text{Dye removal} = \frac{C_i - C_e}{C_i} \times 100 \quad (1)$$

where C_i is the initial concentration of MO dye (mg/L) and C_e is the equilibrium concentration of MO dye after adsorption (mg/L). The adsorption capacity (q_e) was calculated using Eq. (2):

$$q_e = \frac{(C_i - C_e)V}{M} \quad (2)$$

where: V is the volume of MO dye solution (L) and M is the weight of the adsorbent (g).

■ RESULTS AND DISCUSSION

Characterization of PANI/Nb₂O₅/Cr₂O₃ and PANI/Nb₂O₅/MnO₂

FTIR analysis

Fig. S1(a) and (b) display FTIR peaks for nanocomposites made of PANI/Nb₂O₅/Cr₂O₃ and PANI/Nb₂O₅/MnO₂ in the 400–4000 cm⁻¹ range. It is clear from Fig. S1(a) and (b) that the peak at 3740 cm⁻¹ is observed for all PANI samples, which results from the aromatic amines' N–H stretching [17]. The C–H stretch

of the aromatic ring can be assigned to the range between 2933 and 3039 cm⁻¹. Although the peak at 1423 and 1464 cm⁻¹ refers to the C=C stretching of the benzenoid rings; the peak at 1550 cm⁻¹ is suggestive of the quinoid rings. At 1550 cm⁻¹, the C=N stretch reaches its maximum [16]. The C–H out-of-plane (o/p) bending vibration is maximized between 1097 and 1236 cm⁻¹ [18]. The quinoid and benzenoid rings found in PANI/Nb₂O₅/MnO₂ suggested that the nanoparticles (Nb₂O₅, Cr₂O₃, and MnO₂) were functionalized with PANI, even though peak intensities were seen for PANI/Nb₂O₅/Cr₂O₃ and PANI/Nb₂O₅/MnO₂, and a set of broad bands was discovered between 489 and 792 cm⁻¹, confirming prior research findings that Nb–O, Cr–O and Mn–O interacted on the surface of PANI [19–20]. Tables 1 and 2 present the vibrational assignments for PANI/Nb₂O₅/MnO₂ and PANI/Nb₂O₅/Cr₂O₃ nanocomposites.

XRD analysis

Further attributes of the PANI/Nb₂O₅/Cr₂O₃ and PANI/Nb₂O₅/MnO₂ structures were researched with the means of XRD, as displayed in Fig. 3, to look at the crystallinity and undefined organization present in these

Table 1. FTIR peak assignments for PANI/Nb₂O₅/MnO₂

Assignment	Wavenumber (cm ⁻¹)
N–H stretching from aromatic amines group	3740
O–H stretching of hydroxyl group	3421
C–H stretching of aromatic unit	3039
C=C stretching of quinoid ring	1550
C=C stretching of benzenoid ring	1423
C–H bending	1236
N–H out-of-plan bending	794
Nb–O, Mn–O	563, 489

Table 2. FTIR peak assignments for PANI/Nb₂O₅/Cr₂O₃

Assignment	Wavenumber (cm ⁻¹)
N–H stretching from aromatic amines group	3740
O–H stretching of hydroxyl group	3493
C–H stretching of aromatic unit	2933
C=C stretching of quinoid ring	1550
C=C stretching of benzenoid ring	1464
C–H bending	1097
N–H out-of-plan bending	792
Nb–O, Cr–O	563, 480

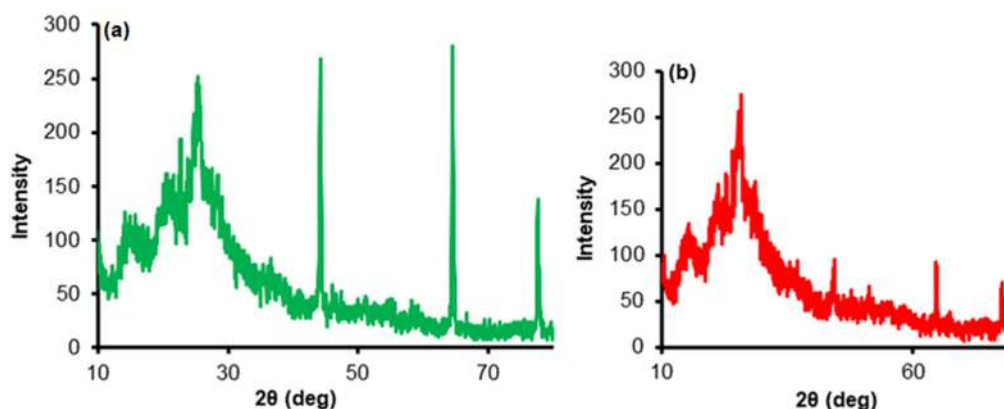


Fig 3. XRD spectra for (a) PANI/Nb₂O₅/MnO₂ and (b) PANI/Nb₂O₅/Cr₂O₃ samples

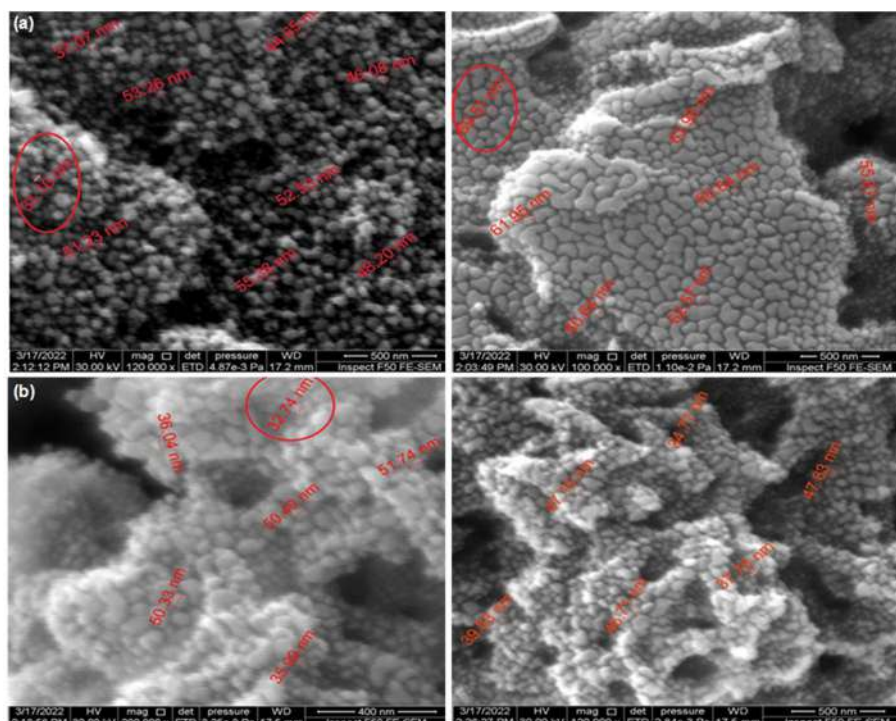


Fig 4. FE-SEM micrographs of (a) PANI/Nb₂O₅/MnO₂ and (b) PANI/Nb₂O₅/Cr₂O₃ nanocomposites

examples [21]. The wide peaks were seen at $2\theta = 9.65^\circ$, 15.65° , 20.6° , 25.35° , 44.2° , 64.55° and 77.65° . These pinnacles confirmed that formless construction was available in PANI/Nb₂O₅/MnO₂ in the lattice [20,22]. While, the PANI/Nb₂O₅/Cr₂O₃ nanocomposite XRD tops were basically indistinguishable from the PANI precious stone planes with $2\theta = 9.2^\circ$, 15.2° , 21.25° and 25.7° , 44.35° , 64.55° and 77.7° separately. The data showed that the metal oxides have adsorption interactions of a nanocrystalline type (Nb₂O₅ and additionally MnO₂, Cr₂O₃) and have a PANI network. This suggests that

PANI was collaborating with Nb₂O₅, Cr₂O₃, and MnO₂ in the great precious stone construction. These outcomes (i.e., XRD) and the close FTIR results have demonstrated that the surface-based polymerization of the aniline monomer of the Nb₂O₅, Cr₂O₃, and MnO₂ nanoparticles [23-24] was successful.

Surface characterization by FE-SEM

The surface morphologies of artificial metal oxides/PANI nanocomposite were investigated via FE-SEM as shown in Fig. 4, where the morphology of Nb₂O₅, Cr₂O₃, and MnO₂ can be seen. The majority of

nanoparticles had spherical shapes and had sizes of around 30–68 nm. The PANI/Nb₂O₅/MnO₂ and the PANI/Nb₂O₅/Cr₂O₃ nanocomposites demonstrated that metal oxide nanoparticles had the same shape and were perfectly coated with thin polymer chains during the aggregation process [25-26]. It was assumed that there was a significant difference in morphology between the composites' surface and size of the PANI/Nb₂O₅/Cr₂O₃ and PANI/Nb₂O₅/MnO₂ nanocomposites. According to the XRD results, the chain diameter of the polymer nanocomposites ranged between 31 and 69 nm, changing the crystal growth's direction during adsorption. The doping of metal oxide nanoparticles in the polyaniline matrix was shown using FE-SEM.

Zeta potential analysis

The pH was 7.4, the zeta potential was 27.66 mV, and mobility was 2.16 V/cm. The addition of 20 mL of

KCl resulted in a reduction in the zeta potential as well as an increase in particle size. At pH 10.2, around the isoelectric point, the biggest size was discovered. In other words, knowing the pH, adjusting and maintaining it at a stable value is required for PANI/Nb₂O₅/MnO₂ suspensions [27]. The electric potential created by a charge on a particle's surface, which can either have a positive or negative polarity depending on the particle's chemistry, is known as the zeta potential. The degree of repulsion between similarly charged particles in a formulation is measured by the zeta potential [28]. A formulation's zeta potential of PANI/Nb₂O₅/Cr₂O₃ indicates its likely physical stability from the changes in the zeta potential along with the particle size (Fig. 5). In the present study, the pH level was 7.4, the value of the zeta potential was 35.22 mV and mobility was 2.75 V/cm. Thus, it does seem to depend on

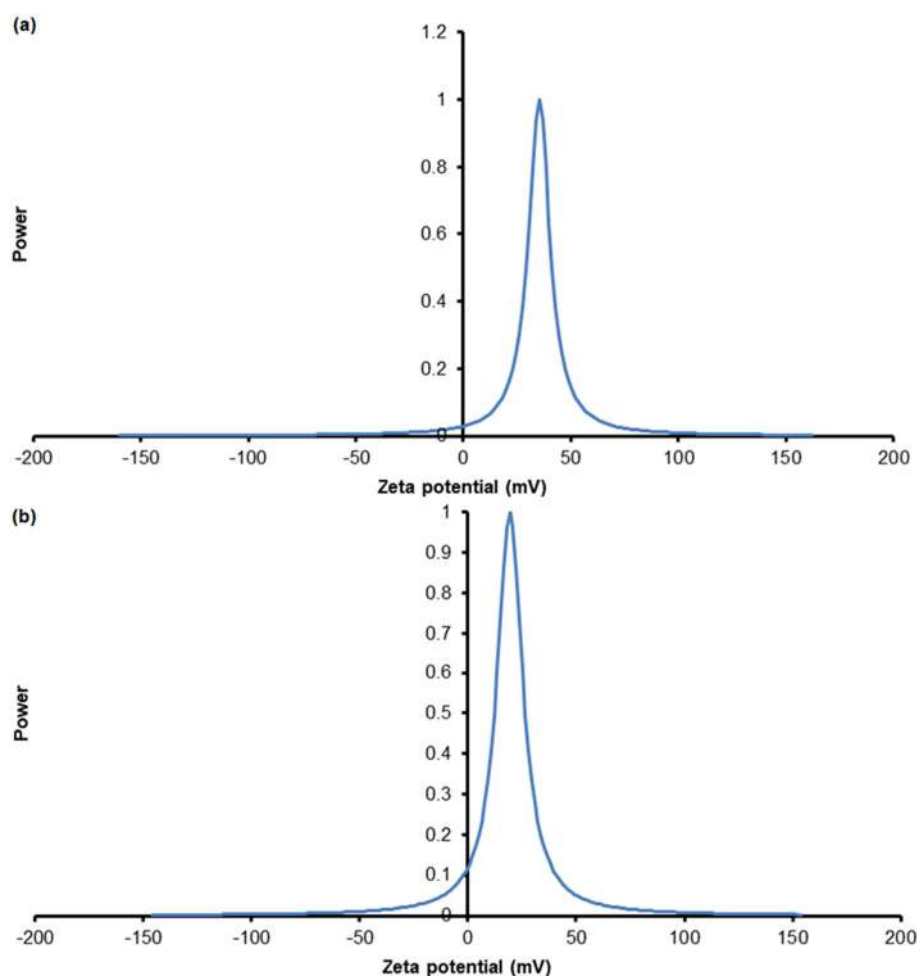


Fig 5. Zeta potential curves for (a) PANI/Nb₂O₅/MnO₂ and (b) PANI/Nb₂O₅/Cr₂O₃

the pH value. Moreover, the zeta potential increases with decreasing value of pH.

Optimization of as-synthesized PANI/Nb₂O₅/Cr₂O₃ and PANI/Nb₂O₅/MnO₂ nanocomposites as adsorbent for MO dye

Influence of adsorbent dosage

Removal tests were conducted using various concentrations of PANI/Nb₂O₅/Cr₂O₃ and PANI/Nb₂O₅/MnO₂, ranging from 10 to 150 mg, to discover the effects of adsorbent dose on MO dye clearance. The impact of the adsorbent dose on removal effectiveness for each dosage is shown in Fig. 6. The removal effectiveness of the MO dye was found to be

greatly increased by increasing the adsorbent dosage from 10 to 50 mg for PANI/Nb₂O₅/Cr₂O₃, from 10 to 100 mg for PANI/Nb₂O₅/MnO₂, from 77.0–87.0% and 70.0–88.5%, respectively. This might be because more active sites became available when the adsorbent dosage was raised; eventually, at a dosage of 50 mg, the associated equilibrium was attained. For subsequent trials, an adsorbent dosage of 50 mg was chosen.

Influence of differences in initial concentration of MO dye on removal process

As shown in Fig. 7, the removal efficiency of PANI/Nb₂O₅/Cr₂O₃ and PANI/Nb₂O₅/MnO₂ was investigated using a variety of initial MO dye

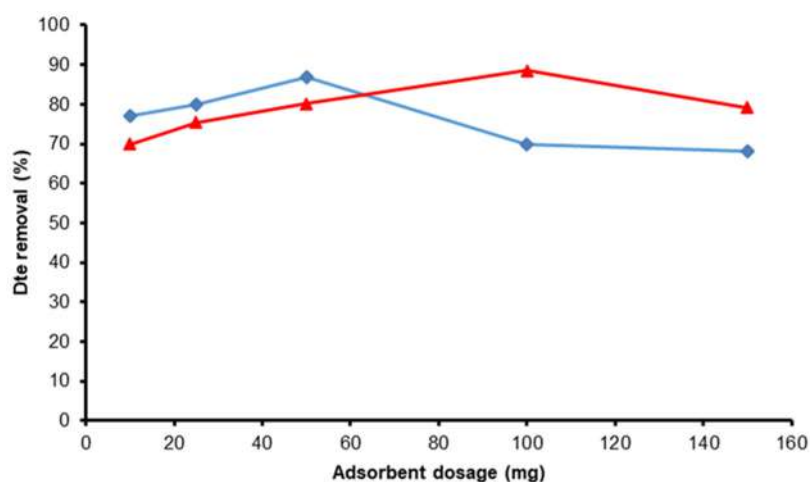


Fig 6. Effect of adsorbent dosage on the removal of MO dye using PANI/Nb₂O₅/MnO₂ (red) and PANI/Nb₂O₅/Cr₂O₃ (blue)

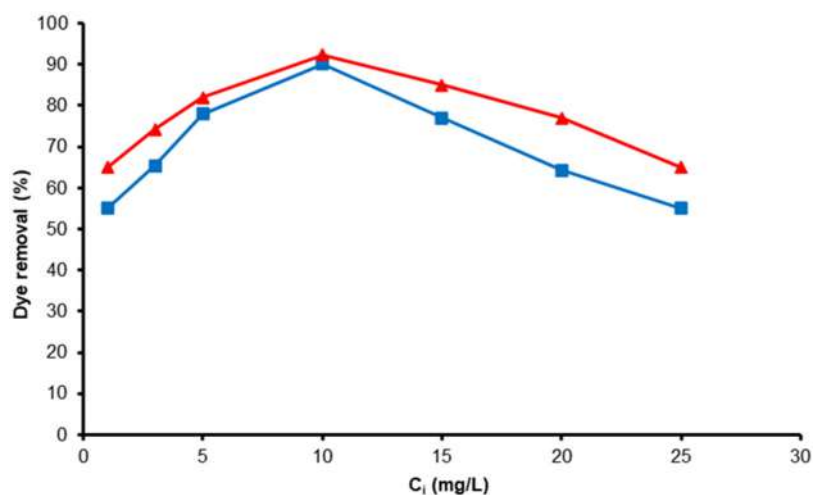


Fig 7. Effect of initial concentration of MO dye on the removal process using PANI/Nb₂O₅/MnO₂ (red) and PANI/Nb₂O₅/Cr₂O₃ (blue)

concentrations ranging from 1 to 25 mg/L at a fixed 50 mg of PANI/Nb₂O₅/Cr₂O₃ and 100 mg of PANI/Nb₂O₅/MnO₂. This graph shows that the original concentration of MO dye was increased. Accordingly, when the original MO dye concentration was increased, the removal effectiveness of the PANI/Nb₂O₅/Cr₂O₃ nanocomposite was high, demonstrating that each of the adsorbents and the MO dye molecules interacted strongly even at low starting concentrations [29]. Additionally, because of the larger surface area and strong electrostatic interactions, PANI/Nb₂O₅/Cr₂O₃ and PANI/Nb₂O₅/MnO₂ nanocomposites are two possible explanations for the effectiveness of these products in the removal of a high percentage of MO dye and the porosity of the adjusted PANI/Nb₂O₅/Cr₂O₃ and PANI/Nb₂O₅/MnO₂ being nanocomposite.

Influence of pH on removal of MO dye

Fig. 8 illustrates how pH affects the proportion of MO dye removed by nanocomposite materials made of PANI/Nb₂O₅/Cr₂O₃ and PANI/Nb₂O₅/MnO₂. Additionally, we investigated the initial and final (equilibrium) pHs. It is clear that at all chosen beginning pHs, the PANI/Nb₂O₅/MnO₂ nanocomposite outperformed PANI/Nb₂O₅/Cr₂O₃ in the removal of MO dye from the aqueous solution (from 2 to 10). To regulate the pH levels during the experiment, 0.1 M HCl or 0.1 M NaOH was used. The orbital shaking speed, quantity of both adsorbents and solution temperature were altered, while the starting MO dye concentration was held constant at 25 mg/L, 300 rpm, 50,100 mg, and 298 K. The findings of

all the best studies pointed to the following: PANI/Nb₂O₅/Cr₂O₃ adsorbents performed better at pH 9 and PANI/Nb₂O₅/MnO₂ adsorbents at pH 7, respectively. Based on an estimated pKa value of MO, as a result, it becomes protonated at the initial pH values of 2 and 3 (pH is less than the pKa of MO), where it is primarily present in anionic form. Additionally, the presence of basic amine groups causes PANI to build a positive charge on its conductive backbone in an acidic media. Consequently, at initial acidic pH values, there was a significant degree of change in the removal rates of adsorbents. This was a result of electrostatic attraction between the positively charged PANI backbone and protonated MO dye molecules. Thus, PANI/Nb₂O₅/Cr₂O₃ nanocomposites for MO dye removal will decline [30-31]. The preferred initial pH range was 2 to 8, with neutral being the best value about 94.20% PANI/Nb₂O₅/Cr₂O₃ and 95.37% for another nanocomposite. This was because, at neutral pH, the MO would primarily take the anionic form, thereby increasing the number of electrostatic interactions between the MO dye and PANI/Nb₂O₅/Cr₂O₃ and PANI/Nb₂O₅/MnO₂ adsorbents [32].

Influence of adsorption time

Another important factor in the color removal process is the adsorption time. Through a series of adsorption experiments with adsorption time ranges between 10 and 120 min, the impact of adsorption duration on MO dye's adhesion to the PANI/Nb₂O₅/Cr₂O₃ and PANI/Nb₂O₅/MnO₂ adsorbents

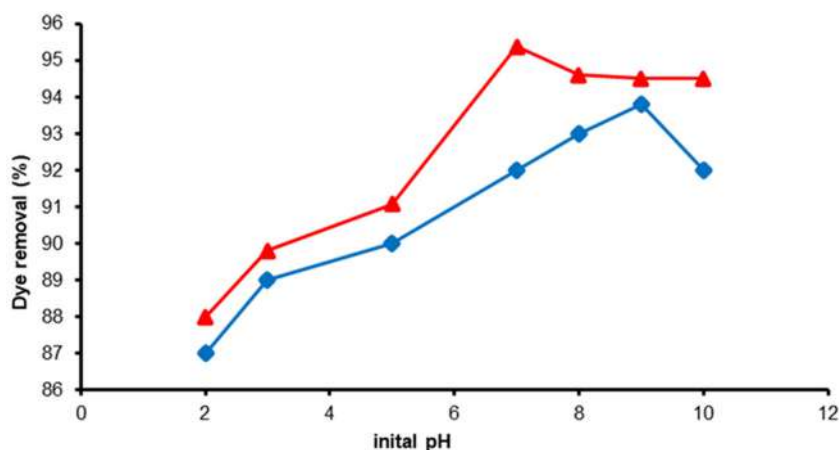


Fig 8. Effect of pH on removal of MO dye using PANI/Nb₂O₅/MnO₂ (red) and PANI/Nb₂O₅/Cr₂O₃ (blue)

was investigated. The results for each of the adsorbents are shown in Fig. 9. It is obvious that the removal rate of MO dye increases from 10 to 60 min and then stays constant from 60 to 120 min. Thus, upon following detour shaking for 60 min, equilibrium is attained in the MO dye adsorption. However, it should be noted that the rate of MO dye removal was extremely rapid during the first 10 min, during which time the MO dye molecules were adsorbent to around 94.2% of the PANI/Nb₂O₅/Cr₂O₃ and 97.8% of the PANI/Nb₂O₅/MnO₂ adsorbents before slowly and gradually increasing until equilibrium was reached at roughly 60 min. Since several active sites were available for MO dye molecules on both adsorbents' surfaces [32], the initial rapid removal of MO dye was explained. The number of active sites that could be removed decreased as the removal time rose; further, the pushing force decreased, resulting in a slow removal rate. As a result, the optimal adsorption time for subsequent research was chosen to be 60 min.

Batch MO Dye Adsorption Studies

Experimentally, it was found that the PANI/Nb₂O₅/Cr₂O₃ and PANI/Nb₂O₅/MnO₂ adsorbents' adsorption capabilities were best at pH 9 and 7, respectively, when used with 100 mL solutions of MO dye with concentrations ranging from 3 to 100 mg/L at room temperature (Fig. 10(a)). As can be seen from this figure, the maximal adsorption capabilities of the PANI/Nb₂O₅/Cr₂O₃ and PANI/Nb₂O₅/MnO₂ with similar

amounts of adsorbents are 148 and 84 mg/g, respectively. Three fundamental isotherm models, specifically the Langmuir, Freundlich, and Temkin models, were used to fit the adsorption data in order to assess the mechanism of adsorption and provide information on the maximum adsorption capacity (q_m) for the relevant adsorbent [32]. The graphs of the isotherm parameters for the linearized equation for MO dye elimination at 298 K are shown in Fig. 10. The three equations for the isotherm models of adsorption at room temperature are listed in Table 3, together with their maximum adsorption capacities (q_m), correlation coefficients (R^2), and other data. Certain presumptions were connected with the Langmuir model, such as the monolayer adsorption of the adsorbate on an even surface of the adsorbent. In addition, chemisorption happens at designated homogenous sites inside the adsorbent to achieve adsorption. The Langmuir equation is given in Eq. (3) [33-34].

$$\frac{C_e}{q_e} = \frac{C_e}{q_m} + \frac{t}{q_m K_L} \quad (3)$$

where: q_m and q_e stand for the MO dye's maximum (mg/g) and empirical (q_e) adsorption capacities, respectively. After the adsorption process, C_e is the amount of MO dye that is still present in the solution, and K_L is the Langmuir constant (L/mg). In order to determine the adsorption capacity, C_e/q_e versus C_e was plotted (Fig. 10(b)).

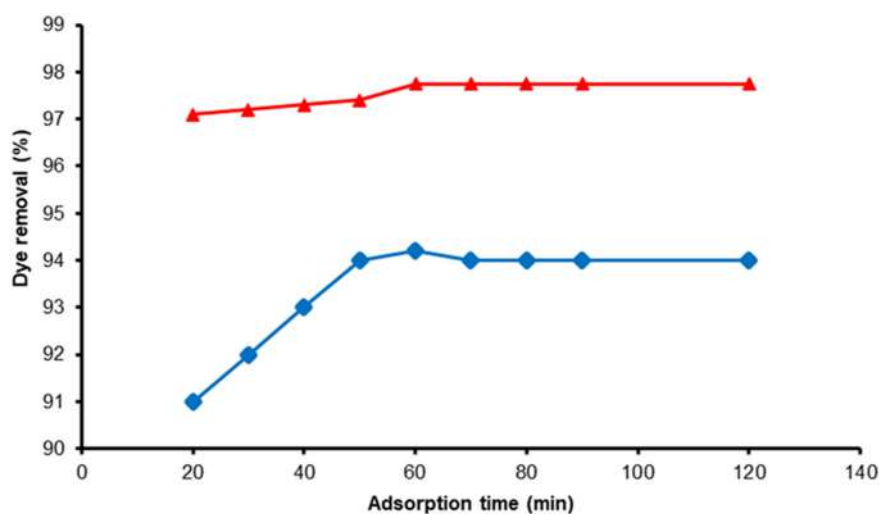


Fig 9. Effect of adsorption time on MO removal using PANI/Nb₂O₅/MnO₂ (red) and PANI/Nb₂O₅/Cr₂O₃ (blue)

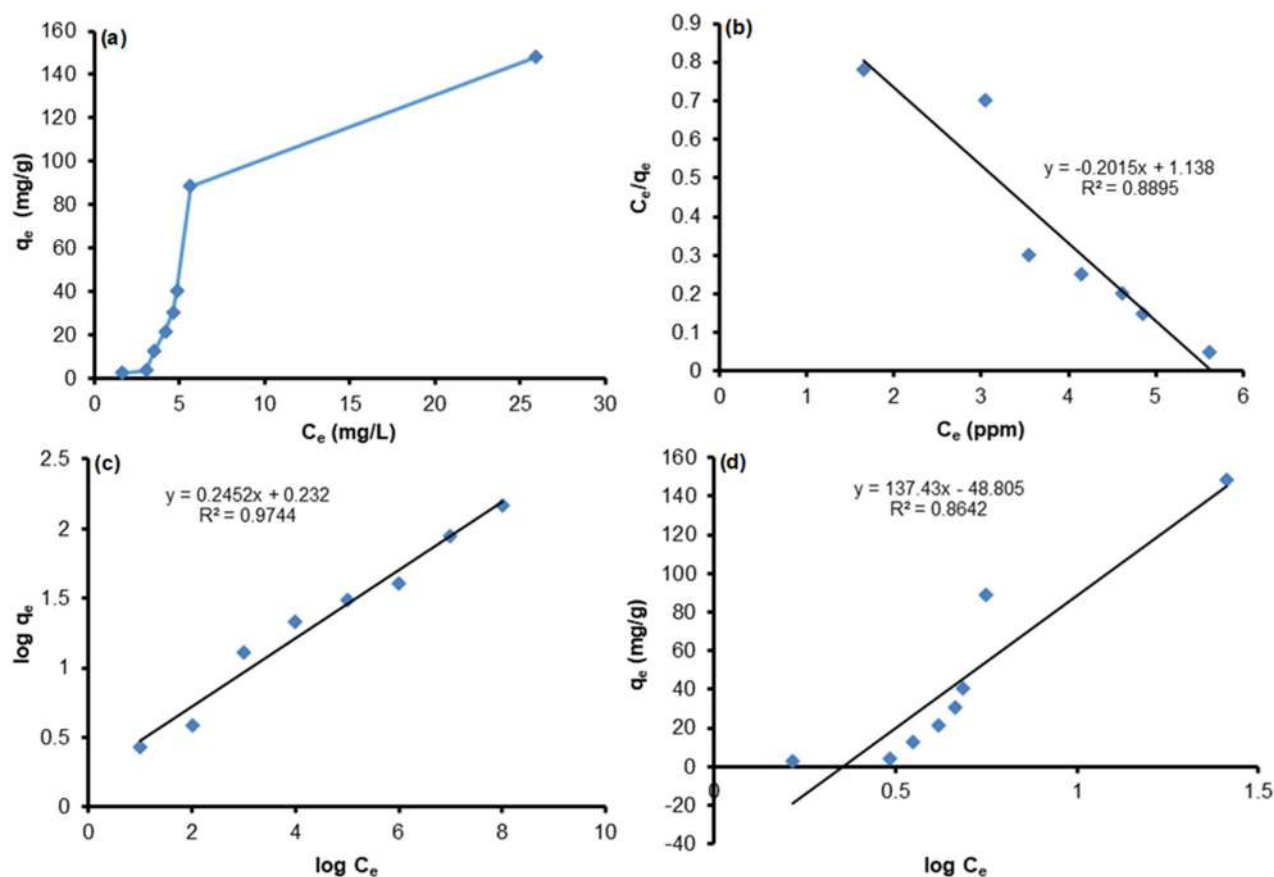


Fig 10. (a) Adsorption isotherms of MO onto PANI/Nb₂O₅/Cr₂O₃ adsorbents (conditions: pH 9; dosage = 50 mg; V = 100 mL; time = 60 min; T = 298 K). Fitting the adsorption isotherm curves of MO dye of adsorbents: (b) Langmuir, (c) Freundlich, and (d) Temkin isotherm models

Table 3. Adsorption Langmuir, Freundlich and Temkin model isotherm parameters for MO dye by PANI/Nb₂O₅/Cr₂O₃ and PANI/Nb₂O₅/MnO₂

Isotherms	Parameters	PNAI/Nb ₂ O ₅ /Cr ₂ O ₃	PNAI/Nb ₂ O ₅ /MnO ₂
Langmuir	q _m (mg/g)	142	115
	K _L (L/mg)	0.18	0.45
	R ²	0.8895	0.9150
Freundlich	K _F (mg/g)(mg/L) ^{1/n}	1.80	3.02
	n	4.00	2.37
	R ²	0.9744	0.9398
Temkin	A	137.0	33.2
	B	48.00	2.38
	R ²	0.8640	0.9660

In Fig. 10 and 11, the gradient and intercept of this (straight) line were used to estimate q_m and K_L, respectively. The Freundlich model is used to fit multilayer adsorption onto a heterogeneous surface, and

the postulated adsorption process is physisorption, which happens as a result of van der Waals interactions. Eq. (4) provides the Freundlich equation [35].

$$\log q_e = \log K_F + \frac{1}{n} \log C_e \tag{4}$$

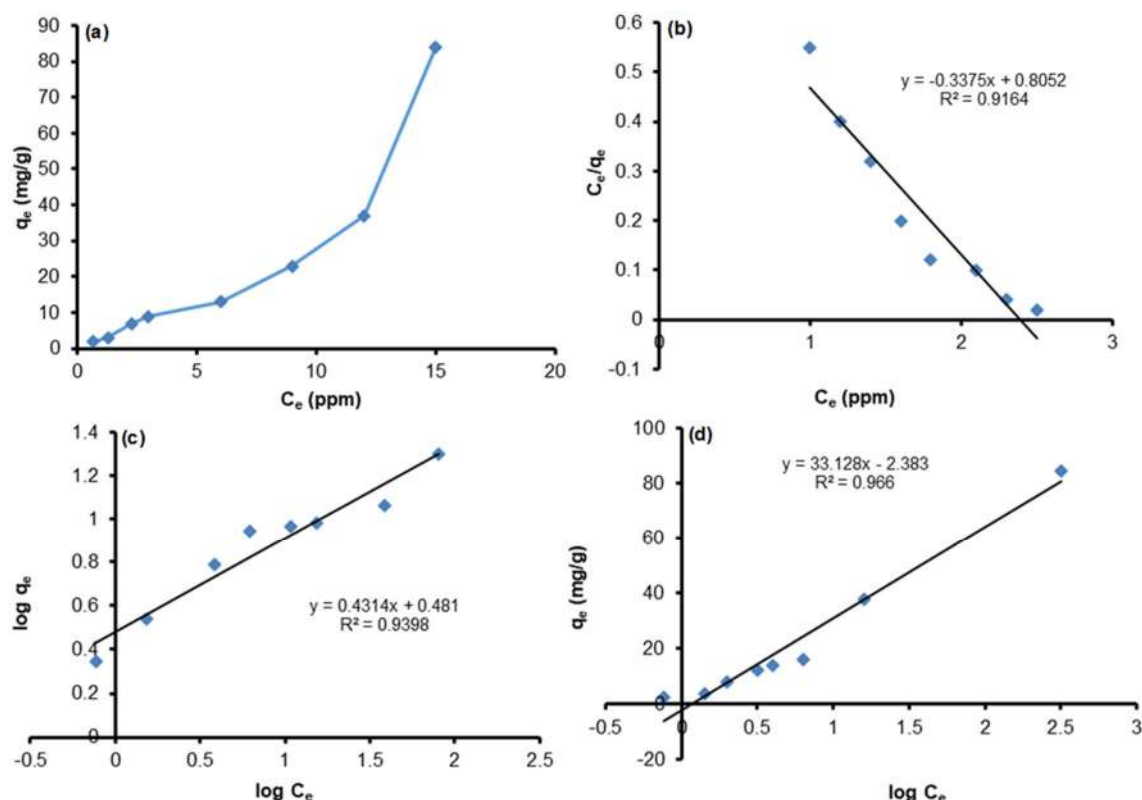


Fig 11. (a) Adsorption isotherms of MO onto PANI/Nb₂O₅/MnO₂ adsorbents (conditions: PH 7; dosage = 100 mg; V = 100 mL; time = 60 min; T = 298 K). Fitting the adsorption isotherm curves of MO dye of adsorbents: (b) Langmuir, (c) Freundlich, and (d) Temkin isotherm models

Table 4. Comparison of the removal efficiency of MO with different adsorbents

Adsorbent	q _m (mg g ⁻¹)	Adsorbent dose (g L ⁻¹)	Equilibrium time (min)	pH	References
PANI-MWCNT	149.25	0.040	60	7.0	[40]
PANI-AC	192.52	0.100	60	6.0	[41]
Co/Fe-MOF	137.60	0.005	60	4.0	[42]
PANI-TiO ₂ /GO	69.23	-----	80	-----	[43]
PANI/Nb ₂ O ₅ /MnO ₂	76.00	0.100	60	7.0	This study
PANI/Nb ₂ O ₅ /Cr ₂ O ₃	118.00	0.050	60	9.0	This study

According to Eq. (3), K_F stands for the Freundlich constant, while adsorption capacity (mg/g) and heterogeneity factor (n) stand for the bond distribution. By graphing $\log q_e$ against $\log C_e$, the Freundlich linear equation was discovered. K_F and n were then accurately calculated from the intercept and slope, respectively, of this linear connection (Fig. 10(c)). Eq. (5) specifies the Temkin equation, where the Temkin isotherm model makes significant assumptions about heterogeneous

surface energy and non-uniform distribution of sorption heat on adsorbents [36]

$$q_e = A + B \log C_e \quad (5)$$

where: A is the Temkin isotherm constant (L/g) and B is a constant related to the heat of adsorption (J/mol). Plots of q_e against $\log C_e$ were used to arrive at the Temkin linear equation (Fig. 10(d)). The gradient and intercept of the straight line provide the values of B and A , respectively. The parameters calculated for the

Langmuir, Freundlich, and Temkin models are listed in Table 3. The Langmuir isotherm appears to best describe the adsorption of MO dye against PANI/Nb₂O₅/Cr₂O₃ and PANI/Nb₂O₅/MnO₂ adsorbents, as evidenced by the coefficients of determination (R²) for the fits of the experimental data of the three isotherms, which showed greater R² (0.9744 and 0.9398) and experimental equilibrium capacities (q_e). This implies that both the PANI/Nb₂O₅/Cr₂O₃ and PANI/Nb₂O₅/MnO₂ adsorbents have strong MO dye adsorption sites, and that the adsorption mechanism is monolayer in nature [37-39]. Table 4 represents the literature review of comparison of the removal efficiency of MO with different adsorbents.

■ CONCLUSION

In the current study, two types of the nanocomposite, PANI/Nb₂O₅/MnO₂ and PANI/Nb₂O₅/Cr₂O₃, were first prepared and characterized as new adsorbents to remove MO dye. The physical and chemical nature of the nanocomposites such as structural, morphological, particle size, and functional groups of the fabricated PANI/Nb₂O₅/MnO₂ and PANI/Nb₂O₅/Cr₂O₃ was established via XRD, FE-SEM, FTIR, UV-vis, and zeta potential, which can be summarized by showing that the adsorptive properties of nanocomposites were more active than pure PANI. The results have shown that the PANI/Nb₂O₅/Cr₂O₃ material has a higher adsorption capacity than PANI/Nb₂O₅/MnO₂ in terms of MO removal. The maximal adsorption capabilities reached 118 and 76 mg/g, respectively. The optimum conditions for the MO removal with PANI/Nb₂O₅/MnO₂ were the dose was 100 mg, the temperature was 298 K, and the pH value was 7. For PANI/Nb₂O₅/Cr₂O₃ nanocomposite, the dose was 50 mg, the temperature was 298 K, and the pH value was 9.

■ ACKNOWLEDGMENTS

The authors thank the University of Babylon for supporting this work.

■ AUTHOR CONTRIBUTIONS

Karrar Majeed Obaid did the laboratory work, Ahmed Saadoun Abbas wrote the experimental part, and Yahya Fahim Al-Khafaji wrote the rest of the paper.

■ REFERENCES

- [1] Merdan, M., Jalal Al-den Fakar Al-den, D., Al-khafaji, Y., and Abbas, A.S., 2019, Theoretical study for chromen azodyes derivative compounds as anti-corrosive, *J. Phys.: Conf. Ser.*, 1234, 012054.
- [2] Xiao, Y., and Hill, J.M., 2018, Benefit of hydrophilicity for adsorption of methyl orange and electro-Fenton regeneration of activated carbon-polytetrafluoroethylene electrodes, *Environ. Sci. Technol.*, 52 (20), 11760–11768.
- [3] Sánchez-Sánchez, Á., Suárez-García, F., Martínez-Alonso, A., and Tascón, J.M.D., 2015, Synthesis, characterization and dye removal capacities of N-doped mesoporous carbons, *J. Colloid Interface Sci.*, 450, 91–100.
- [4] Huang, R., Liu, Q., Huo, J., and Yang, B., 2017, Adsorption of methyl orange onto protonated cross-linked chitosan, *Arabian J. Chem.*, 10 (1), 24–32.
- [5] Serban, G.V., Iancu, V.I., Dinu, C., Tenea, A., Vasilache, N., Cristea, I., Niculescu, M., Ionescu, I., and Chiriac, F.L., 2023, Removal efficiency and adsorption kinetics of methyl orange from wastewater by commercial activated carbon, *Sustainability*, 15 (17), 12939.
- [6] Gapusan, R.B., and Balela, M.D.L., 2020, Adsorption of anionic methyl orange dye and lead(II) heavy metal ion by polyaniline-kapok fiber nanocomposite, *Mater. Chem. Phys.*, 243, 122682.
- [7] Jianjun, H., Yuping, D., Jia, Z., Hui, J., Shunhua, L., and Weiping, L., 2011, γ -MnO₂/polyaniline composites: Preparation, characterization, and applications in microwave absorption, *Phys. B*, 406, 1950–1955.
- [8] Shahabuddin, S., Sarih, N.M., Mohamad, S., and Atika Baharin, S.N., 2016, Synthesis and characterization of Co₃O₄ nanocube-doped polyaniline nanocomposites with enhanced methyl orange adsorption from aqueous solution, *RSC Adv.*, 6 (49), 43388–43400.
- [9] Zhao, Y., Chen, H., Li, J., and Chen, C., 2015, Hierarchical MWCNTs/Fe₃O₄/PANI magnetic composite as adsorbent for methyl orange removal, *J. Colloid Interface Sci.*, 450, 189–195.

- [10] Asuha, S., Zhou, X., and Zhao, S., 2010, Adsorption of methyl orange and Cr(VI) on mesoporous TiO₂ prepared by hydrothermal method, *J. Hazard. Mater.*, 181 (1), 204–210.
- [11] Mohammadi, N., Khani, H., Gupta, V.K., Amereh, E., and Agarwal, S., 2011, Adsorption process of methyl orange dye onto mesoporous carbon material—kinetic and thermodynamic studies, *J. Colloid Interface Sci.*, 362 (2), 457–462.
- [12] Zeng, A., and Zeng, A., 2017, Synthesis of a quaternized beta cyclodextrin-montmorillonite composite and its adsorption capacity for Cr(VI), methyl orange, and *p*-nitrophenol, *Water, Air, Soil Pollut.*, 228 (8), 278.
- [13] Llorens, E., Armelin, E., Del Mar Pérez-Madrugal, M., Del Valle, L.J., Alemán, C., and Puiggali, J., 2013, Nanomembranes and nanofibers from biodegradable conducting polymers, *Polymers*, 5 (3), 1115–1157.
- [14] Alesary, H.F., Ismail, H.K., Khudhair, A.F., and Mohammed, M.Q., 2018, Effects of dopant ions on the properties of polyaniline conducting polymer, *Orient. J. Chem.*, 34 (5), 2525.
- [15] Ismail, H.K., Alesary, H.F., Al-Murshedi, A.Y.M., and Kareem, J.H., 2019, Ion and solvent transfer of polyaniline films electrodeposited from deep eutectic solvents via EQCM, *J. Solid State Electrochem.*, 23 (11), 3107–3121.
- [16] Bian, L.J., He, H.L., and Liu, X.X., 2015, Self-doped polyaniline/molybdenum oxide composite nanorods for supercapacitors, *RSC Adv.*, 5 (92), 75374–75379.
- [17] Bakhtiarian, E., Foot, P.J., and Tate, P.C.M., 2016, Conductive poly(epichlorhydrin)-polyaniline dodecylbenzenesulfonate [PECH-PAni.DBSA] rubber blends prepared in solution, *Prog. Rubber Plast. Recycl. Technol.*, 32 (4), 183–200.
- [18] Shahabuddin, S., Muhamad Sarih, N., Mohamad, S., and Joon Ching, J., 2016, SrTiO₃ nanocube-doped polyaniline nanocomposites with enhanced photocatalytic degradation of methylene blue under visible light, *Polymers*, 8 (2), 27.
- [19] Cai, X., Cui, X., Zu, L., Zhang, Y., Gao, X., Lian, H., Liu, Y., and Wang, X., 2017, Ultra high electrical performance of nano nickel oxide and polyaniline composite materials, *Polymers*, 9 (7), 288.
- [20] Wu, T.M., Lin, Y.W., and Liao, C.S., 2005, Preparation and characterization of polyaniline/multi-walled carbon nanotube composites, *Carbon*, 43 (4), 734–740.
- [21] Inzelt, G., 2012, *Conducting Polymers: A New Era in Electrochemistry*, Springer Berlin, Heidelberg.
- [22] Abd Ali, L., Ismail, H.K., Alesary, H.F., and Aboul-Enein, H., 2021, A nanocomposite based on polyaniline, nickel and manganese oxides for dye removal from aqueous solutions, *Int. J. Environ. Sci. Technol.*, 18 (7), 2031–2050.
- [23] Mylarappa, M., Chandruvasan, S., Kantharaju, S., and Rekha, S., 2022, Synthesis and characterization of Rgo doped Nb₂O₅ nano composite for chemical sensor studies, *ECS Trans.*, 107, 269.
- [24] Dessie, Y., Tadesse, S., and Eswaramoorthy, R., 2021, Surface roughness and electrochemical performance properties of biosynthesized α -MnO₂/NiO-based polyaniline ternary composites as efficient catalysts in microbial fuel cells, *J. Nanomater.*, 2021, 7475902.
- [25] Taş, R., Can, M., and Sönmezoğlu, S., 2015, Preparation and characterization of polyaniline microrods synthesized by using dodecylbenzene sulfonic acid and periodic acid, *Turk. J. Chem.*, 39 (3), 589–599.
- [26] Djara, R., Holade, Y., Merzouki, A., Masquelez, N., Cot, D., Rebière, B., Petit, E., Huguet, P., Canaff, C., Morisset, S., Napporn, T.W., Cornu, D., and Tingry, S., 2020, Insights from the physicochemical and electrochemical screening of the potentiality of the chemically synthesized polyaniline, *J. Electrochem. Soc.*, 167 (6), 066503.
- [27] Fuseini, M., El Shazly, A.H., and El-Kady, M.F., 2020, Effects of doping on zeta potential and pH of polyaniline colloidal suspension, *Mater. Sci. Forum*, 1008, 114–120.
- [28] Nawrocki, J., 1997, The silanol group and its role in liquid chromatography, *J. Chromatogr. A*, 779 (1), 29–71.

- [29] Shahabuddin, S., Gaur, R., Mukherjee, N., Chandra, P., and Khanam, R., 2022, Conducting polymers-based nanocomposites: Innovative materials for waste water treatment and energy storage, *Mater. Today: Proc.*, 62, 6950–6955.
- [30] Ansari, R., and Mosayebzadeh, Z., 2011, Application of polyaniline as an efficient and novel adsorbent for azo dyes removal from textile wastewaters, *Chem. Pap.*, 65 (1), 1–8.
- [31] Nasar, A., and Mashkoo, F., 2019, Application of polyaniline-based adsorbents for dye removal from water and wastewater—A review, *Environ. Sci. Pollut. Res.*, 26 (6), 5333–5356.
- [32] Harimu, L., Wahyuni, S., Nasrudin, N., Baari, M.J., and Permana, D., 2022, Fabrication of chitosan/Fe₃O₄ nanocomposite as adsorbent for reduction methylene blue contents, *Indones. J. Chem.*, 22 (3), 878–886.
- [33] Karri, R.R., Tanzifi, M., Tavakkoli Yarak, M., and Sahu, J., 2018, Optimization and modeling of methyl orange adsorption onto polyaniline nano-adsorbent through response surface methodology and differential evolution embedded neural network, *J. Environ. Manage.*, 223, 517–529.
- [34] Al-Ghouti, M.A., and Da'ana, D.A., 2020, Guidelines for the use and interpretation of adsorption isotherm models: A review, *J. Hazard. Mater.*, 393, 122383.
- [35] Ibrahim, R.K., El-Shafie, A., Hin, L.S., Mohd, N.S., Aljumaily, M.M., Ibrahim, S., and AlSaadi, M.A., 2019, A clean approach for functionalized carbon nanotubes by deep eutectic solvents and their performance in the adsorption of methyl orange from aqueous solution, *J. Environ. Manage.*, 235, 521–534.
- [36] Elwakeel, K., El-Bindary, A., Ismail, A., and Morshidy, A., 2017, Magnetic chitosan grafted with polymerized thiourea for remazol brilliant blue R recovery: Effects of uptake conditions *J. Dispersion Sci. Technol.*, 38 (7), 943–952.
- [37] Manzar, M.S., Waheed, A., Qazi, I.W., Blaisi, N.I., and Ullah, N., 2019, Synthesis of a novel epibromohydrin modified crosslinked polyamine resin for highly efficient removal of methyl orange and eriochrome black T, *J. Taiwan Inst. Chem. Eng.*, 97, 424–432.
- [38] Elwakeel, K.Z., El-Bindary, A., El-Sonbati, A., and Hawas, A.R., 2017, Magnetic alginate beads with high basic dye removal potential and excellent regeneration ability, *Can. J. Chem.*, 95 (8), 807–815.
- [39] Sharifpour, E., Alipanahpour Dil, E., Asfaram, A., Ghaedi, M., and Goudarzi, A., 2019, Optimizing adsorptive removal of malachite green and methyl orange dyes from simulated wastewater by Mn-doped CuO-nanoparticles loaded on activated carbon using CCD-RSM: Mechanism, regeneration, isotherm, kinetic, and thermodynamic studies, *Appl. Organomet. Chem.*, 33 (3), e4768.
- [40] Pete, S., Kattil, R.A., and Thomas, L., 2021, Polyaniline-multiwalled carbon nanotubes (PANI-MWCNTs) composite revisited: An efficient and reusable material for methyl orange dye removal, *Diamond Relat. Mater.*, 117, 108455.
- [41] Bekhoukh, A., Moulefera, I., Zeggai, F.Z., Benyoucef, A., and Bachari, K., 2022, Anionic methyl orange removal from aqueous solutions by activated carbon reinforced conducting polyaniline as adsorbent: Synthesis, characterization, adsorption behavior, regeneration and kinetics study, *J. Polym. Environ.*, 30 (3), 886–895.
- [42] Tran, K.N.T., Phan, C.P.K., Ho, V.T., Chau, H.D., and Nguyen, T.N.D., 2023, Adsorption of methyl orange dyes on oriented Co/Fe-MOF bimetallic organic framework in wastewater treatment, *Indones. J. Chem.*, 23 (2), 533–541.
- [43] Mohammadi, R., Massoumi, B., and Galandar, F., 2019, Polyaniline-TiO₂/graphene nanocomposite: An efficient catalyst for the removal of anionic dyes, *Desalin. Water Treat.*, 142, 321–330.

Supplementary Data

This supplementary data is a part of a paper entitled “Discrimination of Biodiesel-Diesel of B7 and B10 by Infrared Spectroscopy with Dendrogram”.

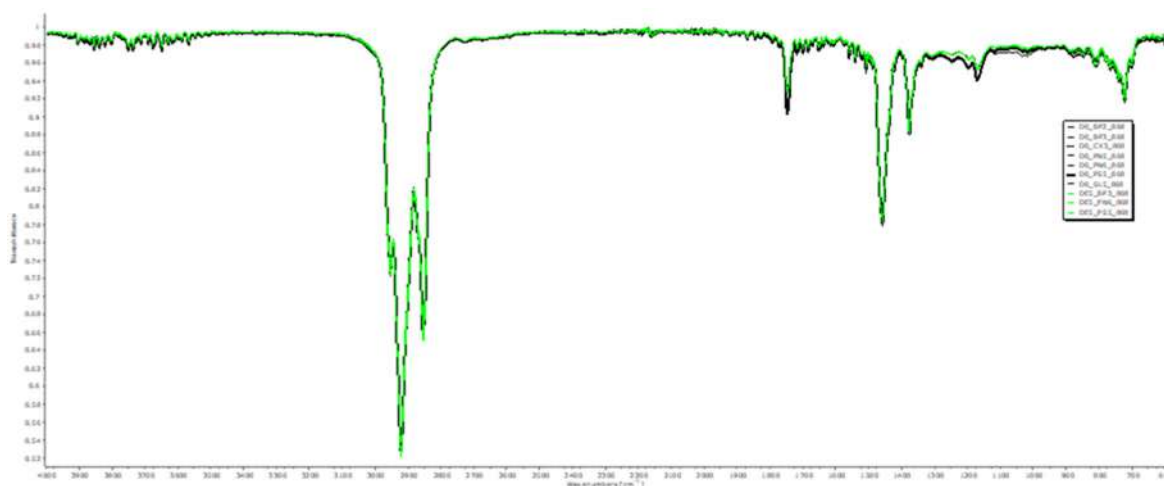


Fig S1. Raw FTIR spectra of B7 and B10 acquired between 600 and 4000 cm^{-1} using a portable BRUKER spectrometer. The sample scan and resolution are 32 and 4 cm^{-1} , respectively. These biodiesel-diesel samples were obtained in Mersing, Malaysia

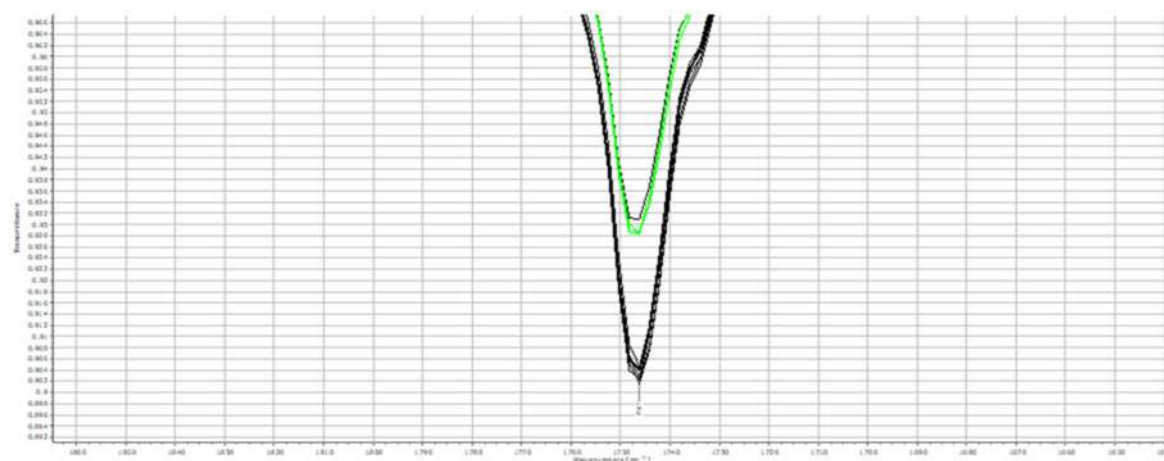


Fig S2. Raw FTIR spectra of B7 and B10 acquired between 1698 and 1777 cm^{-1} using a portable BRUKER spectrometer. The sample scan and resolution are 32 and 4 cm^{-1} , respectively. The peak displayed here show C=O stretching peak at 1747 cm^{-1} . These biodiesel-diesel samples were obtained in Mersing, Malaysia

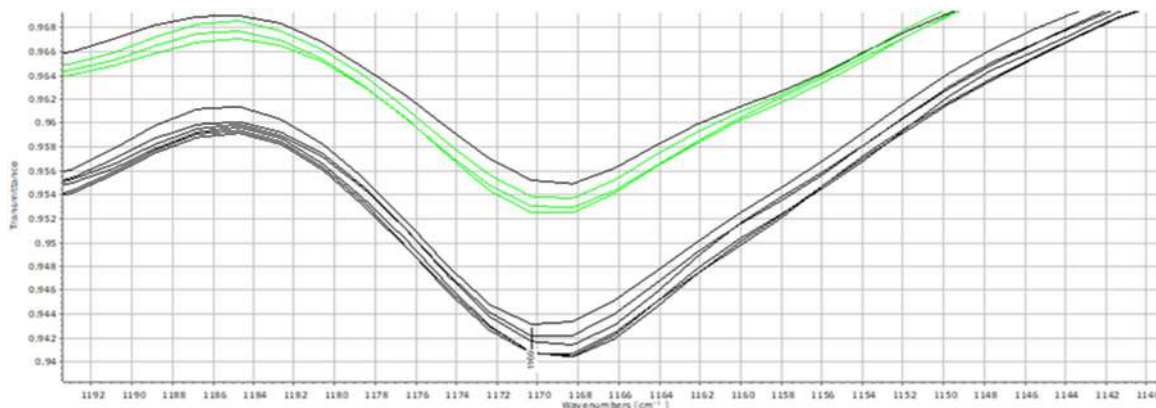


Fig S3. Raw FTIR spectra of B7 and B10 acquired between 1129 and 1186 cm^{-1} using a portable BRUKER spectrometer. The peak displayed here show C-O stretching peak at 1169 cm^{-1} . These biodiesel-diesel samples were obtained in Mersing, Malaysia

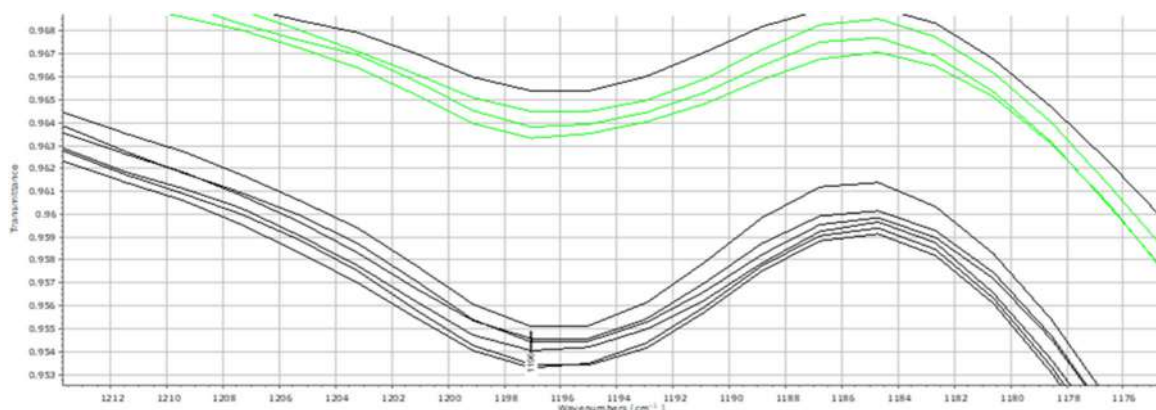


Fig S4. Raw FTIR spectra of B7 and B10 acquired between 1184 and 1223 cm^{-1} using a portable BRUKER spectrometer. The peak displayed here show C-O stretching peak at 1196 cm^{-1} . These biodiesel-diesel samples were obtained in Mersing, Malaysia

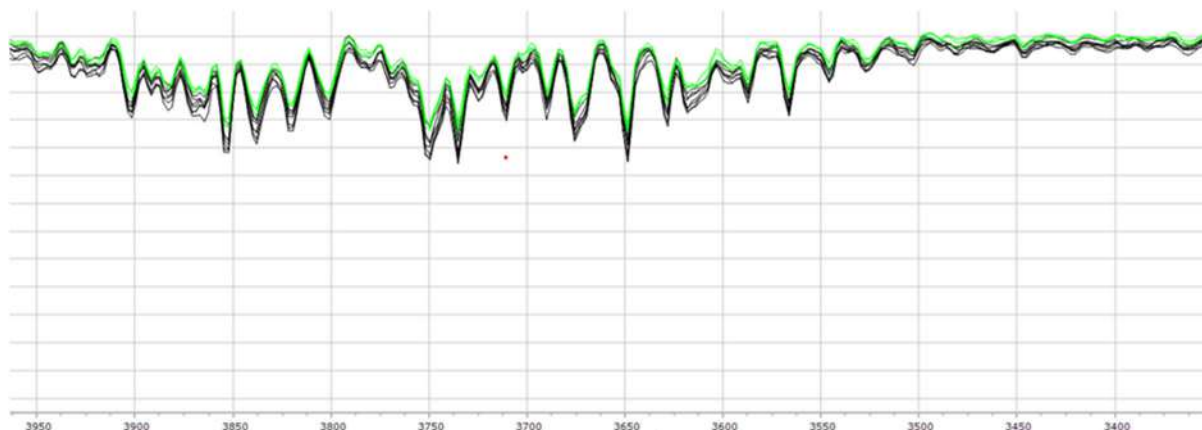


Fig S5. Raw FTIR spectra of B7 and B10 acquired between 3400 and 4000 cm^{-1} using a portable BRUKER spectrometer. The peaks displayed here are very likely showing stretching region of the hydrocarbon. These biodiesel-diesel samples were obtained in Mersing, Malaysia

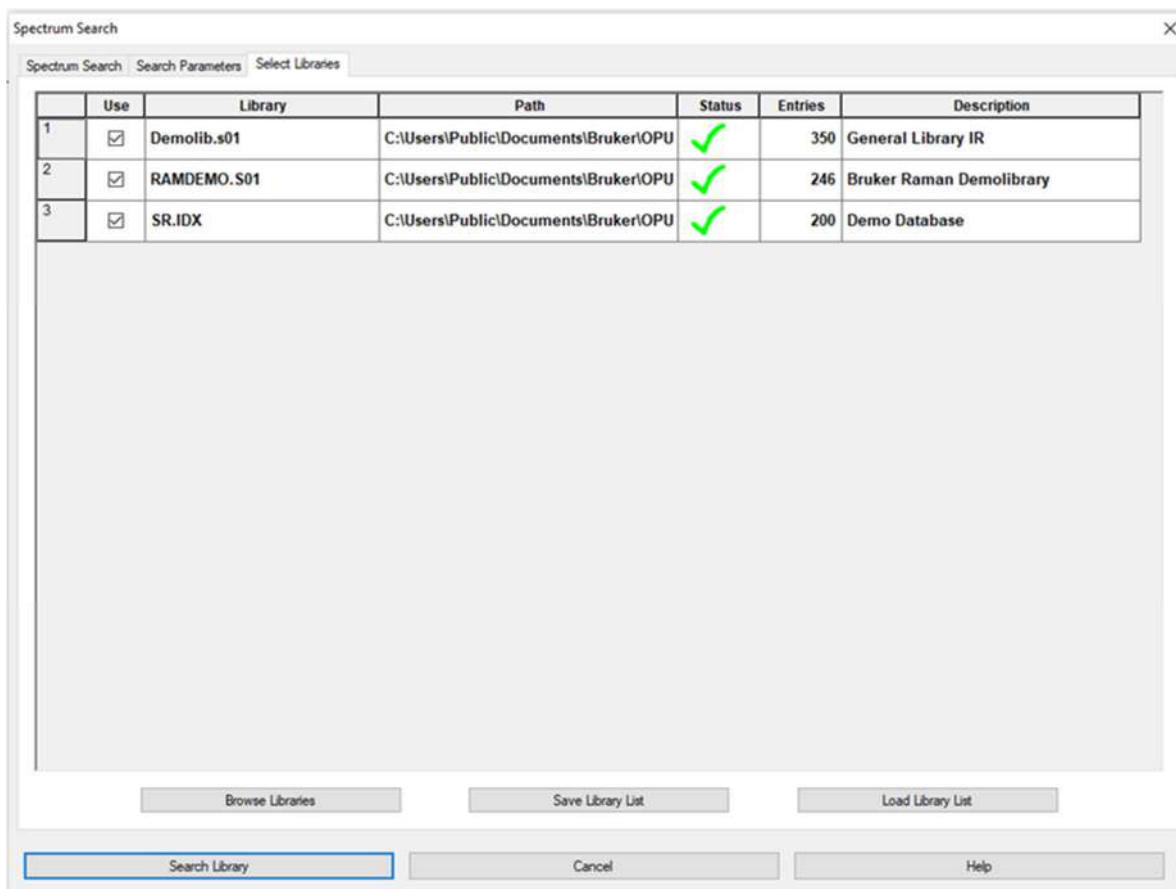


Fig S6. Two different algorithms included in the Opus software was evaluated for analysis of petrol biodiesel samples. Three reference libraries containing respectively 350 (General Library IR), 246 (Bruker Raman Demo library) and 200 (Demo Database) commercialized spectra were used to identify unknown B7 and B10 spectra (n = 10)

Discrimination of Biodiesel-Diesel of B7 and B10 by Infrared Spectroscopy with Dendogram

Mohd Rashidi Abdull Manap^{1*}, Ahmad Fadly Jusoh², Lim Xiang Chuin¹,
Nur Diana Farhana Muhamad Zulkifli¹, Qhurratul Aina Kholili¹, Fatin Abu Hasan¹,
Danish Aiman Akmal Mohd Effendy¹, and Ramizah Azis³

¹Department of Chemistry Faculty of Science, Universiti Putra Malaysia, UPM Serdang, Selangor 43400, Malaysia

²Centre for Global Archaeological Research, Universiti Sains Malaysia, Pulau Pinang 11800, Malaysia

³Jabatan Pengajian Umum IKTBN Sepang, Bandar Baru Salak Tinggi, Selangor 43900, Malaysia

* **Corresponding author:**

email: rashidichemistry@upm.edu.my

Received: February 22, 2023

Accepted: April 16, 2023

DOI: 10.22146/ijc.82499

Abstract: Spectroscopists face an ongoing challenge in identifying fuel spectra due to a wide range of fuel formulations and the increasing abuse of biodiesel-diesel blends. In Malaysia, a new type of biodiesel-diesel blend known as B7 and B10 has been introduced, which requires rapid and reliable discrimination methods. However, current identification methods are costly and time-consuming. To overcome this issue, a spectroscopy study was conducted using a portable Fourier transform infrared (FTIR) spectrometer to identify biodiesel-diesel blends. The study found that direct identification using spectral libraries was reliable in identifying complex samples but unable to differentiate B7 and B10 due to the libraries' focus on hydrocarbons rather than esters. Instead, FTIR spectroscopy provided unique spectral peaks for each blend. Spectral range influences the discrimination, and the truncated region 1697–1777 and 1164–1224 cm^{-1} was shown to be reliable for discriminating the B7 and B10. The study concluded that a combination of algorithms, libraries, and hierarchical cluster analysis (HCA) in FTIR spectroscopy could effectively differentiate the blends. The primary objective was to differentiate B7 and B10 by analyzing liquid samples collected in Malaysia using HCA and IR spectroscopies. FTIR spectroscopy provides molecular-specific vibrational signals and is proven as a rapid identification method.

Keywords: biodiesel; diesel; discrimination; FTIR; Hierarchical Cluster Analysis

■ INTRODUCTION

Petroleum is a naturally occurring, oily, and flammable liquid composed mainly of hydrocarbon materials. On the other hand, vegetable oils consist of glycerol fatty acid esters (triglycerides). Vegetable oils are different from conventional diesel fuels, and vegetable oils are bigger in size than the ones found in petroleum diesel. Meanwhile, biodiesel blends are a renewable and oxygenated fuel that has properties close to petroleum diesel. It is a combination of methyl esters (C15–C17) with any level of petroleum diesel i.e., 1% of pure biodiesel blended with 99% of petrol-diesel [1].

In many countries, including Malaysia, biodiesel-

diesel blends, and petrol are the main energy sources consumed for road and maritime transportation. These fuels consist of hundreds of different hydrocarbon molecules. For example, petrol consists of alkanes (paraffin), alkenes (olefins), and aromatics, while diesel fuel contains paraffin, aromatics, and naphthene. Petroleum products (fuels and oil products) are also the most common environmental contaminants in most industrial countries [2].

The identification and discrimination of fuels and other related fuels is always needed because they are always abused by fuel traffickers in criminal activities such as fuel smuggling and fuel adulteration. For

example, the smuggling of petroleum products across the border regions is an international issue for many countries. Illicit trade of fuel, especially gasoline, along the borders of Brazil is a problem that concerns the authorities responsible for the inspection and surveillance of these areas. The main reason is the significant difference between prices in neighboring countries, including Peru, Paraguay, Bolivia, and Venezuela [3].

Fuel adulteration is a national issue in developing countries, including Brazil, India, Kenya, and Nigeria [4]. Typical adulterated fuel products are high-quality motor oils, kerosene, and diesel. In the case of high-quality motor oil samples, they are adulterated with lower-quality oils such as used oils and standard oils [5]. The higher volume “cocktail” or “adulterated” fuel is then sold as taxed fuel, with the evader keeping the tax revenue. It was reported that the detection of adulterated fuel could be problematic since many potential cocktailing products include compounds that are already present in fuel [6]. Besides the forensic needs, the discrimination of the sample’s source in oil spills in the maritime area also raises a big concern for researchers [7].

Various analytical methods were used for the analysis of petroleum fuel products. For example, gasoline samples were studied using gas chromatography coupled with flame ionization detection (GC-FID) [8]. Next, chromatography-mass spectrometry (GC-MS) was used for the characterization of ninety-one samples of petrol, diesel, and biodiesel [9]. Variety of the obtained compounds in petrol, diesel, and biodiesel were detected with the help of National Institute of Standards and Technology (NIST) mass spectral search program for the NIST/EPA/NIH mass spectral library (version 2.0) [9]. Spectroscopy methods were often used to characterize fuels such as Fourier transform infrared (FTIR), Raman, [10] and ^1H -nuclear-magnetic-resonance (NMR) spectroscopy [11]. Attenuated total reflection (ATR) configuration provides a larger spectral range and better signal-to-noise ratio during the study of diesel samples. Comparisons with commercialized and in-house vibrational spectral libraries were proven for rapid identification of unknown samples [12-14].

Quantitative and qualitative analysis of petroleum

diesel, biodiesel, and a number of hydro-processed esters and fatty acids (HEFA) was achieved using Raman spectroscopy. When analyzing a complex mixture of gasoline samples, NMR spectroscopy is useful because regions of the chemical components’ regions are unique and can be integrated for quantitative analysis [15].

The increased number of recorded crimes related to petroleum fuels has led many researchers to use multiple strategies either by analyzing various adulterants in fuels using the spectroscopy method [16], analysis of explosion residue related to ammonium nitrate fuel oil (ANFO) explosives using Raman spectroscopy [17], analysis of fire debris for the determination of fuel constitution, and ignition source using laser-induced breakdown spectroscopy [18].

ATR-FTIR method is non-destructive and requires no sample preparation. The advantages of FTIR methodology include a rapid method to analyze many samples and rapid identification of samples with the help of the spectral library. Besides being an identification method, it also has evolved as an excellent tool for the detection of many substances with the help of chemometric tools [19]. This study aims to develop and differentiate biodiesel-diesel (B7 and B10) through the analysis of liquid samples collected at various pump stations in Mersing, Malaysia using Hierarchical Cluster Analysis (HCA). First, the local authority in Putrajaya, Malaysia, granted sampling permission to acquire samples from major brands in Mersing. Then, the samples were acquired and characterized using a portable ATR-FTIR spectrometer in the laboratory. Finally, the study used the strong raw FTIR spectra to differentiate biodiesel-diesel (B7 and B10) samples using HCA.

■ EXPERIMENTAL SECTION

Materials

Mersing is a small fishing town in Johor. It is located 136 km north of Johor Bahru, the state capital. Mersing covers a total area of 761 km². According to KPNDHEP Putrajaya, there are ten petrol pump stations operating in this town, including Petronas, Shell, Caltex, BHP, and Petron, in 2021. The specific locations of all pump stations in Mersing are shown in Fig. 1.

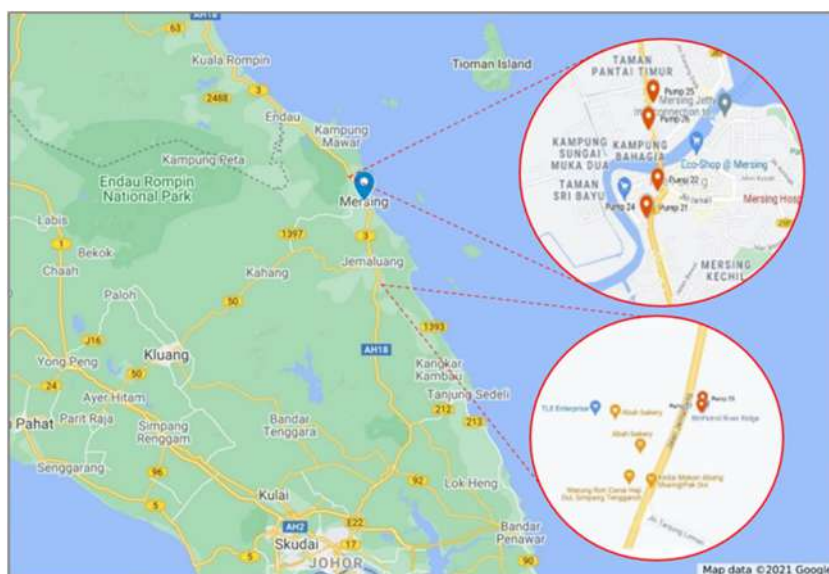


Fig 1. Location of fuel pump stations in Mersing

As many as 10 samples with various fuel brands, as shown in Table 1, were obtained from various company petrol stations that operated in Mersing. This list was produced by the *Kementerian Perdagangan Dalam Negeri dan Hal Ehwal Pengguna* (KPDNHEP). However, only 7 fuel pump stations in Mersing were eligible for sampling.

The lot number was used to record the physical characteristics of the sample. The lot number elements are fuel type, brand, company, and city. The lot number was generated prior to sample collection. All the lot numbers for the samples were printed on a labeling sticker and stuck on the bottle samples. The element of the lot number used in this study is shown in Table 2.

The lot number began with the fuel type, which it contains 6 different labels, P95 (petrol RON95), P97

(petrol RON97), D0 and B10 (biodiesel B10), and DE5 and B7 (biodiesel B7). There are two different labels that indicate the same fuel type, such as D0 and B10, which refer to biodiesel B10 same goes for DE5 and B7, which refer to biodiesel B7. This is due to the improvement made after being informed about the new biodiesel naming in Malaysia.

All the labels with the alphabet 'P' indicated petrol type followed by the Research Octane Number (RON) number, whereas RON 95 and 97 indicate the percentage of unleaded petrol. The alphabet 'D' and 'B' indicate biodiesel type. Biodiesel B7 is a biodiesel with 7% methyl ester blended with diesel. Meanwhile, biodiesel B10 is a biodiesel with 10% methyl ester blended with diesel.

Table 1. Detail of the fuel samples used in this study

Sample number	Fuel type	Fuel brand	Lot number
69	B7	BHPetrol	DE5_BP3_868
70	B7	Petronas	DE5_PS5_868
71	B7	Petron	DE5_PN6_868
72	B10	BHPetrol	D0_BP2_868
73	B10	BHPetrol	D0_BP3_868
74	B10	Petronas	D0_PS5_868
75	B10	Caltex	D0_CX3_868
76	B10	Petron	D0_PN5_868
77	B10	Petron	D0_PN6_868
78	B10	Shell	D0_SL5_868

Table 2. Description of the lot number

Fuel type		Fuel brand		Company		City	
P95	Petrol RON 95	PS	Petronas	1	Each number represents a different company within the city area	868	Mersing
P97	Petrol RON 97	PN	Petron	2			
D0	Biodiesel B10	BP	BHPetrol	3			
B10	Biodiesel B10	CX	Caltex	4			
DE5	Biodiesel B7	SL	Shell	5			
B7	Biodiesel B7			6			

The middle of the lot number indicates the fuel brand, followed by the number that indicates a different branch/company. The end part of the lot number indicates the postcode of '868' (Mersing). Table 2 shows the list of samples with Lot numbers for infrared spectroscopic purposes.

Instrumentation

ATR-FTIR measurements were carried out using an Alpha II (Bruker) spectrometer equipped with a platinum diamond ATR module, a ZnSe beam splitter, and an RT-DLaTGS detector. The transmission spectra were recorded between 550 and 4000 cm^{-1} with a spectra resolution of 4 cm^{-1} and an accumulation of 32 scans.

The acquired FTIR spectra were corrected using the H_2O compensation function of the OPUS software (Bruker, version 7.5) that also drives the spectrometer operation. The instrument status was self-tested prior to data acquisition. The spectra were recorded at room temperature ($\sim 25^\circ\text{C}$). Once the solvent (acetone) was evaporated to dryness, the spectra of the liquid samples were recorded immediately after placing one droplet of sample on the ATR. The pressure applicator was applied to enhance the quality of the spectra. A spectrum of the polymeric material of a hand glove was acquired to verify the performance of the instrument prior to sample analysis. The online instrument monitoring of all relevant system components, including PerformanceGuard and PermaSure was performed to ensure proper instrument operation. The acquired spectra were obtained in .0 (OPUS) file format and analyzed using OPUS software.

Procedure

Library search identification

Molecular identification of petrol diesel samples in

Table 1 and their composition were accomplished through spectral library searches using commercial IR spectral libraries (796 reference spectra). Spectral library searches were performed using a standard and mixture search algorithm in the OPUS software v.7.5 (Bruker Optik GmbH 2014). The quality of the match between the query spectrum and the various library spectra was evaluated based on calculated hit quality index (HQI) values.

Hierarchical Cluster Analysis (HCA)

HCA is used to identify the similarities between the spectra of samples with the use of distances between spectra [20]. A dendrogram showing similarities between the spectra was generated. Spectra were acquired and processed by the OPUS software v8.5 (Bruker Optik GmbH 2020) and Spectragryph software v.1.2.16.1 [21]. For multivariate analysis, the 1697–1777 and 1164 and 1224 cm^{-1} region of the FTIR spectral data, rather than the full spectrum, were subjected to HCA. Dendrograms of each fuel type were generated. Ward linkage algorithm and Euclidean distance were used for cluster analysis, which was provided in the OPUS software v.8.5 (Bruker Optik GmbH 2020).

RESULTS AND DISCUSSION

Spectral Identification Using Spectral Libraries

Three OPUS spectral libraries were used to identify liquid query spectra, which consist of two different types of biodiesel-diesel samples of B7 and B10, by using the "spectrum search" option available in the OPUS 7.5 (Bruker Optik GmbH 2014) software. To evaluate the appropriate comparison criteria of the samples, two different search algorithms: standard and mixture algorithms, were used. Initially, the aim of spectral matching is to identify the composition of the samples.

Table 3. OPUS 7.5 library search results of different samples on the same spectral libraries, in which the best match Hitlist at standard search algorithm and main three components content in mixture search algorithm

Samples/search algorithm	Standard		Mixture	
	Identification hit	HQI	Content	%
DE5_BP3_868*	Parvan 3150, f.n. 3502*refined paraffin wax	662	Vaseline 8401	42.7
	Octane	557	Poly(ethylene), low density	31.0
	Epcar 5875*ethylene/propylene/diene terpolymer	543	Octadecane	26.4
DE5_PN6_868*	Parvan 3150, f.n. 3502*refined paraffin wax	625	Vaseline 8401	78.5
	Epcar 5875*ethylene/propylene/diene terpolymer	544	Poly(ethylene), low density	21.5
	Octane	543		
DE5_PS5_868*	Parvan 3150, f.n. 3502*refined paraffin wax	625	Vaseline 8401	79.3
	Vaseline 8401	583	Poly(ethylene), low density	20.6
	Epcar 5875*ethylene/propylene/diene terpolymer	545		
D0_PS5_868**	Epcar 5875*ethylene/propylene/diene terpolymer	545	Vaseline 8401	44.3
	Rumiten 250 cq*low density polyethylene	541	Poly(ethylene), low density	32.4
	Parvan 3150, f.n. 3502*refined paraffin wax	539	Octadecane	23.3
D0_SL5_868**	Octane	633	Vaseline 8401	43.3
	Parvan 3150, f.n. 3502*refined paraffin wax	620	Poly(ethylene), low density	30.2
	Epcar 5875*ethylene/propylene/diene terpolymer	543	Octadecane	26.5
D0_BP2_868**	Octane	555	Vaseline 8401	83.1
	Epcar 5875*ethylene/propylene/diene terpolymer	543	Poly(ethylene), low density	16.9
	Rumiten 250 cq*low density polyethylene	539		
D0_BP3_868**	Epcar 5875*ethylene/propylene/diene terpolymer	542	Vaseline 8401	83.6
	Rumiten 250 cq*low density polyethylene	540	Cumar r-15 (formerly cumar mh-1 1/2 resin) *coumarone-indene resin	16.4
	Parvan 3150, f.n. 3502*refined paraffin wax	539		
D0_CX3_868**	Epcar 5875*ethylene/propylene/diene terpolymer	543	Vaseline 8401	41.1
	Rumiten 250 cq*low density polyethylene	541	Poly(ethylene), low density	33.7
	Parvan 3150, f.n. 3502*refined paraffin wax	539	Octadecane	25.2
D0_PN5_868**	Parvan 3150, f.n. 3502*refined paraffin wax	544	Vaseline 8401	81.3
	Epcar 5875*ethylene/propylene/diene terpolymer	544	Cumar r-15 (formerly cumar mh-1 1/2 resin) *coumarone-indene resin	18.7
	Rumiten 250 cq*low density polyethylene	542		
D0_PN6_868**	Epcar 5875*ethylene/propylene/diene terpolymer	544	Vaseline 8401	40.9
	Rumiten 250 cq*low density polyethylene	541	Poly(ethylene), low density	34.1
	Parvan 3150, f.n. 3502*refined paraffin wax	540	Octadecane	25.0

* Refers to the B7 type of fuel

** Refers to the B10 type of fuel; the repeated compound in each algorithm is highlighted as Bold

Hence, 10 biodiesel-diesel samples, as shown in Table 1, were analyzed using FTIR spectrometers, and the acquired spectra were evaluated by the algorithm search. During the spectrum search methodology, the spectral

region was consistent between 600 and 4000 cm^{-1} for both search algorithms. The spectrum search results are summarized in Table 3 for 10 unknown biodiesel-diesel samples using two algorithms search.

In the standard search algorithm, the search parameter was set as one main component with min hit value of 100 and a maximum hit value of 30. The standard search algorithm produced a table that contained the HQI values and library spectra with higher similarities to the query spectrum. Each biodiesel-diesel sample was evaluated by HQI values. The HQI can range from 0–1000, in which 0 corresponds to very unlikeness and 1000 corresponds to perfect likeness. As a result, three main identification hits were recorded. All the B7 and B10 samples show the matching spectrum of Epcar 5875*ethylene/propylene/diene terpolymer with HQI value 542–545. Parvan 3150, f.n. 3502*refined paraffin wax, octane, vaseline 8401, and rumiten 250 cq*low density polyethylene were also found in most samples. This result is very likely indicating the presence of hydrocarbon materials in B7 and B10 samples. The low HQI values are probably because of the absence of fuel spectra in the tested library.

In the mixture algorithms, three main components were evaluated to match the query spectrum. Similarly, this algorithm produces a table containing the reference spectra and their percentage composition. It can be defined that the samples are a mixture of compounds with different levels of composition. Vaseline 8401 was found as one of the components in all the studied biodiesel-diesel samples. For example, D0_BP3_868 displayed the highest composition of Vaseline 8401 (83.6%), followed by D0_BP2_868 (83.1%). Vaseline is known as a product made from paraffin wax, which is a by-product of petrol [22]. There is also the presence of poly(ethylene), low-density octadecane cumar r-15 (formerly cumar mh-1 1/2 resin) *coumarone-indene resins in most of the studied samples. Similarly, this result also indicates the presence of hydrocarbon materials in the samples.

To sum up, the spectrum search methodology is less suitable for the direct identification of biodiesel-diesel samples by using both standard search and mixture search algorithms. Despite the presence of different levels of esters in all studied samples, the spectrum search methodology only shows the major component of the hydrocarbon in all biodiesel-diesel samples. Another classification method is needed to identify different levels of esters and

hydrocarbons in biodiesel and diesel, respectively. Prior to this approach, FTIR spectral analysis is needed for the characterization of the samples.

FTIR Spectral Analysis of Biodiesel-Diesel of B7 and B10

In this study, samples were obtained from various pump stations in Mersing, Malaysia, according to the methodology. The presence of local authorities and pump managers ensures the integrity of the sampling procedures. The overlay FTIR spectra of B7 and B10 are given in Fig. 2.

Upon visual inspection, spectra were found similar for both B7 and B10. There are many overlapping peak positions and peak intensities between B7 and B10. However, different FTIR intensities at selected spectral regions were also observed between B7 and B10 after spectral expansion. Distinct regions are shown in Supplementary Information.

The FTIR spectrum represents multiple compositions of the samples. B7 and B10 have slightly different chemical compositions. B7 and B10 are biodiesel-diesel compositions that are 7 and 10% biodiesel mixed with petrodiesel, respectively [23].

Diesel is a complex mixture with hundreds of hydrocarbon components, including alkanes, monocyclic cycloalkane, bicyclic cycloalkanes, tricyclic cycloalkanes, alkylbenzene, hydrindene, tetrahydronaphthalene, indene, naphthalene, acenaphthene, biphenyl, acenaphthylene, and phenanthrene [24]. Although the biodiesel-diesel sample is a complex mixture with hundreds of compositions, vibrational assignment is simple. For this study, the FTIR spectra of B7 and B10 are comparable with palm oil methyl ester in the biodiesel-diesel blend. The FTIR features that are found to be associated with B7 and B10 are 700, 722, 740, 765, 806, 1169, 1196, 1247, 1377, 1459, 1746, 2853, 2922, and 2954 cm^{-1} . Most of them are associated with hydrocarbon signals. However, 1169, 1196, and 1746 cm^{-1} are associated with fatty acid methyl ester.

For diesel samples that contain many hydrocarbons, IR signals at 2900 and 2830 cm^{-1} are associated with symmetric CH_3 stretch and symmetric CH_2 stretch,

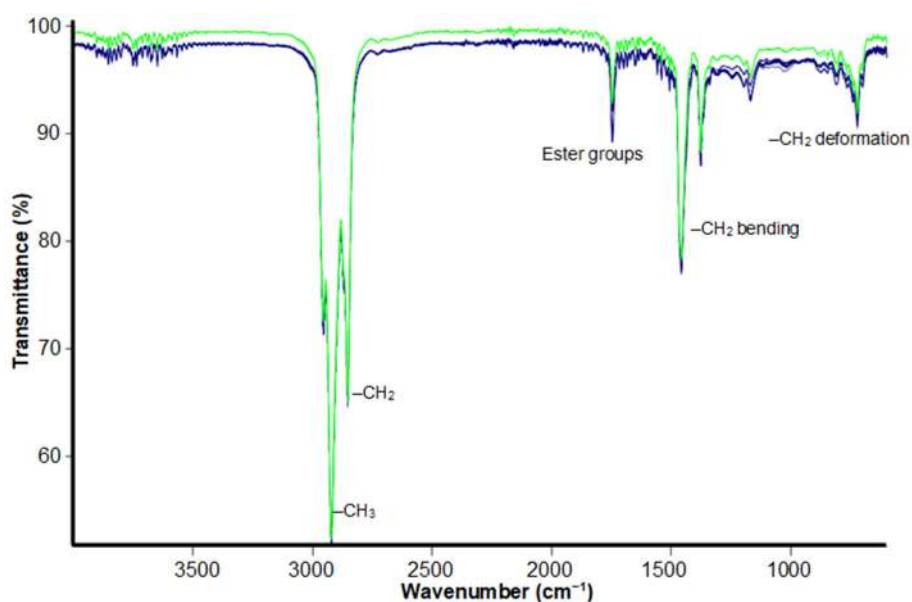


Fig 2. FTIR spectra of B7 (green) and B10 (black) were collected at different pump stations in Mersing whereas the FTIR intensity of B10 was decreased by 0.01

respectively. Two other weak peaks were observed at 1445 and 1400 cm^{-1} caused by the CH_3 and the CH_2 bending vibration, respectively [25]. A signal at 720 cm^{-1} is assigned to the asymmetric angular deformation of CH_2 [26]. Meanwhile, peaks at 1703 and 1728 cm^{-1} correspond to the ester functional group.

Alkanes were determined to be the most common functional group in the FTIR spectra data, with the majority of characteristic wavenumber peaks located between 700 and 1200 cm^{-1} [27]. The main characteristic that distinguishes biodiesel-diesel blend from diesel is its absorption at 1169, 1196, 1247 and 1746 cm^{-1} . Fig. 3 shows the comparison of wavenumber differences with B10. High agreement of wavenumber was found in the mid-infrared spectra region.

In general, no differences in wavenumber and intensity were found among the FTIR spectra for 3 samples of B7 and 7 samples of B10 samples, regardless of brands. However, a spectrum of B10 (D0_SL5_868) interferes with spectra collected from B7 since it contains an overlapping peak position below 1800 cm^{-1} as seen in Fig. 2. Spectral expansion for different regions is shown in Supplementary Information.

Although various spectral regions were interrogated for the small number of samples, discrimination of B7 and

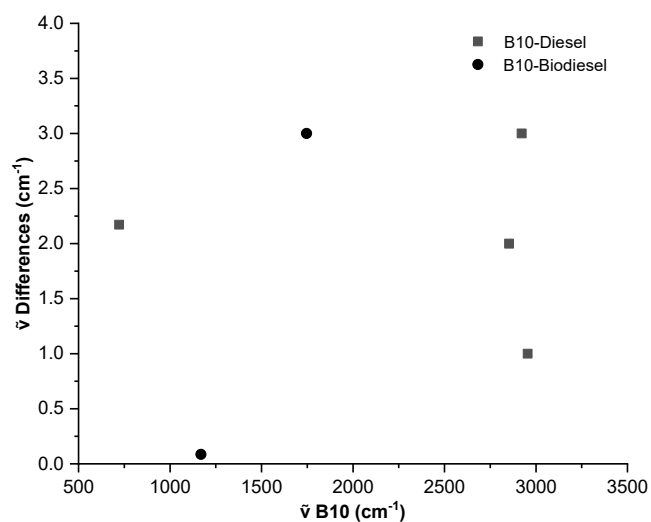


Fig 3. Comparison of the wavenumber differences and B10 wavenumber

B10 using visual inspection would be challenging if the same methodology is used for a large number of samples in the forensic analysis. On top of this, multiple spectral formats prevent rapid data analysis because of incompatibility issues. Thus, the HCA method was performed much easy with the use of the clustering function in OPUS (Bruker) for discrimination of B7 and B10 samples after sample acquisition with Bruker spectrometer.

Cluster Analysis Using HCA

In this study, the results of the HCA on the truncated region between 1697–1777 cm^{-1} using the standard Ward linkage algorithm and Euclidean distance are presented in the form of a dendrogram as shown in Fig. 4.

The dendrogram in Fig. 4 shows the classification of B7 and B10 diesel, where the biodiesel-diesel samples are divided into two major clusters with high heterogeneity levels at 0.25. Cluster B7 groups the samples of D0_SL5_868.0, DE5_BP3_868.0, DE5_PS5_868.0, and DE5_PN6_868.0, while Cluster B10 consists of samples of D0_BP2_868.0, D0_PS5_868.0, D0_PN5_868.0, D0_BP3_868.0, D0_CX3_868.0, and D0_PN6_868.0. Within the particular clusters, it is possible to distinguish additional sub-clusters. Accordingly, in cluster B7, the following sub-clusters may also be distinguished: sub-cluster B7.1 grouping diesel samples DE5_BP3_868.0, DE5_PS5_868.0, and DE5_PN6_868.0. However, two sub-cluster can be identified in B10, which are B10.1 and B10.2 clusters. B10.1 cluster containing grouping diesel samples of D0_BP3_868.0, D0_CX3_868.0, and D0_PN6_868.0 while B10.2 consists of D0_BP2_868.0, D0_PS5_868.0, and D0_PN5_868.0.

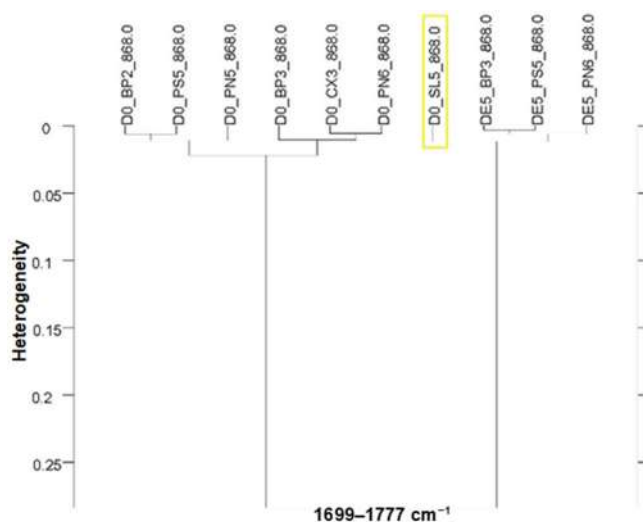


Fig 4. Dendrogram obtained from the HCA of raw spectra of B7 and B10 (10 spectra) partitioned into 2 main groups corresponding to two different types of biodiesel-diesel fuels. The clustering was performed between 1699 and 1777 cm^{-1}

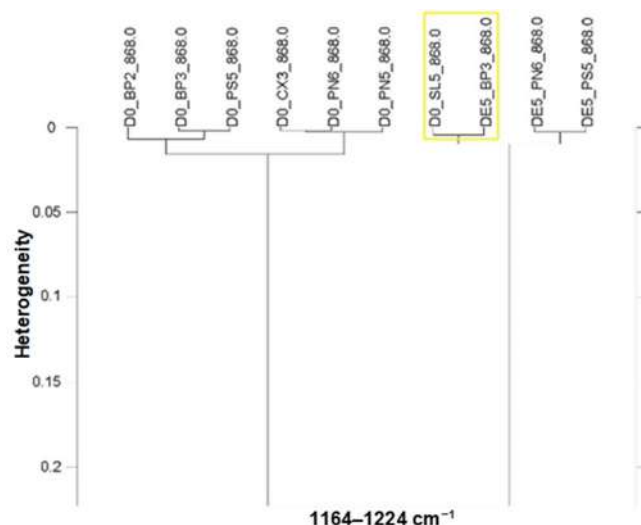


Fig 5. Dendrogram obtained from the HCA of raw spectra of B7 and B10 (10 spectra) partitioned into 2 main groups corresponding to two different types of biodiesel-diesel fuels. The clustering was performed between 1164 and 1224 cm^{-1}

The only sample signed out of their cluster was the D0_SL5_868.0 sample highlighted in yellow color shown in Fig. 4. This sample overlapped with the B7 cluster. In separate clustering between 1164–1224 cm^{-1} (heterogeneity level at 0.2), the samples of D0_SL5_868.0 are clustered together with DE5_BP3_868.0 as shown in Fig. 5.

However, the wrong discrimination of this method still has the potential to find the sample similarity. HCA result shows the region between 1697–1777 cm^{-1} in the mid-infrared spectra containing relevant information than 1164–1224 cm^{-1} to discriminate between B7 and B10 without pre-processing.

CONCLUSION

The current research evaluated the capability of FTIR combined with chemometric analysis. FTIR spectra data were characterized by analyzing the functional groups in different types of samples (B7 and B10). A comparison of spectra between B7 and B10 samples was made to identify overlapping and non-overlapping peaks for clustering. Upon visual inspection, two regions for clustering were successfully selected. With the help of the add-on function of Cluster

Analysis in OPUS, rapid HCA analyses were successful in distinguishing B7 and B10 from Mersing. HCA result shows the region between 1697–1777 cm^{-1} in the mid-infrared spectra containing relevant information than 1164–1224 cm^{-1} to discriminate between B7 and B10 without spectral pre-processing. This discrimination is very likely because of the significant differences in FTIR intensity present.

■ ACKNOWLEDGMENTS

The authors are greatly acknowledging the financial support by the Research Management Centre (RMC) UPM for the *Inisiatif Putra Muda* (GP-IPM) research grant of GP-IPM/2023/9741500, UKM grant GUP-2020-052 and Royal Society of Chemistry (RSC) grant (R22-7843254579). Also, special thanks to *Kementerian Perdagangan Dalam Negeri dan Hal Ehwal Pengguna* (KPDNHEP) for the technical support during the sampling in Mersing, Malaysia.

■ AUTHOR CONTRIBUTIONS

Mohd Rashidi Abdull Manap and Ramizah Azis conducted the design of the experiment and experimental works. Ahmad Fadly Jusoh, and Nur Diana Farhana Muhamad Zulkifli conducted the clustering work and experiment, Lim Xiang Chuin, Qhurratul Aina Kholili, Fatin Abu Hasan, and Danish Aiman Akmal Mohd Effendy conducted the spectral analysis.

■ REFERENCES

- [1] Naber, J.D., and Johnson, J.E., 2014, "Internal Combustion Engine Cycles and Concepts" in *Alternative Fuels and Advanced Vehicle Technologies for Improved Environmental Performance*, Eds. Folkson, R., Woodhead Publishing, Sawston, Cambridge, UK 197–224.
- [2] Gad, S.C., 2014, "Petroleum Hydrocarbons" in *Encyclopedia of Toxicology (Third Edition)*, Eds. Wexler, P., Academic Press, Oxford, UK, 838–840.
- [3] da Silva, N.C., Pimentel, M.F., Honorato, R.S., Talhavini, M., Maldaner, A.O., and Honorato, F.A., 2015, Classification of Brazilian and foreign gasolines adulterated with alcohol using infrared spectroscopy, *Forensic Sci. Int.*, 253, 33–42.
- [4] Chowdhury, M., Gholizadeh, A., and Agah, M., 2021, Rapid detection of fuel adulteration using microfabricated gas chromatography, *Fuel*, 286, 119387.
- [5] Bassbasi, M., Hafid, A., Platikanov, S., Tauler, R., and Oussama, A., 2013, Study of motor oil adulteration by infrared spectroscopy and chemometrics methods, *Fuel*, 104, 798–804.
- [6] Nims, M.K., Melville, A.M., Moran, J.J., Jarman, K.H., and Wright, B.W., 2022, Compound specific stable isotope analysis of aromatics in diesel fuel to identify potential cocktailing, *Forensic Sci. Int.*, 334, 111244.
- [7] Azevedo, R.N.A., Bezerra, K.M.M., Nascimento, R.F., Nelson, R.K., Reddy, C.M., Nascimento, A.P., Oliveira, A.H.B., Martins, L.L., and Cavalcante, R.M., 2022, Is there a similarity between the 2019 and 2022 oil spills that occurred on the coast of Ceará (Northeast Brazil)? An analysis based on forensic environmental geochemistry, *Environ. Pollut.*, 314, 120283.
- [8] Cui, C., Zhang, L., Ma, Y., Billa, T., Hou, Z., Shi, Q., Zhao, S., Xu, C., and Klein, M.T., 2018, Computer-aided gasoline compositional model development based on GC-FID analysis, *Energy Fuels*, 32 (8), 8366–8373.
- [9] Suppajariyawat, P., de Andrade, A.F.B., Elie, M., Baron, M., and Gonzalez-Rodriguez, J., 2019, The use of chemical composition and additives to classify petrol and diesel using gas chromatography-mass spectrometry and chemometric analysis: A UK study, *Open Chem.*, 17 (1), 183–197.
- [10] Xu, Z., Bunker, C.E., and De B. Harrington, P., 2010, Classification of jet fuel properties by near-infrared spectroscopy using fuzzy rule-building expert systems and support vector machines, *Appl. Spectrosc.*, 64 (11), 1251–1258.
- [11] Ure, A.D., O'Brien, J.E., and Dooley, S., 2019, Quantitative NMR spectroscopy for the analysis of fuels: A case study of FACE gasoline F, *Energy Fuels*, 33 (11), 11741–11756.
- [12] Rodriguez, J.D., Westenberger, B.J., Buhse, L.F., and Kauffman, J.F., 2011, Standardization of

- Raman spectra for transfer of spectral libraries across different instruments, *Analyst*, 136 (20), 4232–4240.
- [13] Fremout, W., and Saverwyns, S., 2012, Identification of synthetic organic pigments: the role of a comprehensive digital Raman spectral library, *J. Raman Spectrosc.*, 43 (11), 1536–1544.
- [14] Ghosal, S., and Fang, H., 2015, Raman spectroscopy based identification of flame retardants in consumer products using an acquired reference spectral library, *Talanta*, 132, 635–640.
- [15] Kaiser, C.R., Borges, J.L., dos Santos, A.R., Azevedo, D.A., and D'Avila, L.A., 2010, Quality control of gasoline by ¹H NMR: Aromatics, olefinics, paraffinics, and oxygenated and benzene contents, *Fuel*, 89 (1), 99–104.
- [16] Ferdous, A.H.M.I., Anower, M.S., Musha, A., Habib, M.A., and Shobug, M.A., 2022, A heptagonal PCF-based oil sensor to detect fuel adulteration using terahertz spectrum, *Sens. Bio-Sens. Res.*, 36, 100485.
- [17] Almeida, M.R., Logrado, L.P.L., Zacca, J.J., Correa, D.N., and Poppi, R.J., 2017, Raman hyperspectral imaging in conjunction with independent component analysis as a forensic tool for explosive analysis: The case of an ATM explosion, *Talanta*, 174, 628–632.
- [18] Choi, S., and Yoh, J.J., 2017, Fire debris analysis for forensic fire investigation using laser induced breakdown spectroscopy, *Spectrochim. Acta, Part B*, 134, 75–80.
- [19] Jamwal, R., Amit, A., Kumari, S., Sharma, S., Kelly, S., Cannavan, A., and Singh, D.K., 2021, Recent trends in the use of FTIR spectroscopy integrated with chemometrics for the detection of edible oil adulteration, *Vib. Spectrosc.*, 113, 103222.
- [20] Kepenek, E.S., Severcan, M., Gozen, A.G., and Severcan, F., 2020, Discrimination of heavy metal acclimated environmental strains by chemometric analysis of FTIR spectra, *Ecotoxicol. Environ. Saf.*, 202, 110953.
- [21] Menges, F., 2022, *Spectragryph - Optical Spectroscopy Software*, Version 1.2.16.1, <http://www.ffmpeg2.de/spectragryph/>.
- [22] Bekker, M., Louw, N.R., Jansen Van Rensburg, V.J., and Potgieter, J., 2013, The benefits of Fischer-Tropsch waxes in synthetic petroleum jelly, *Int. J. Cosmet. Sci.*, 35 (1), 99–104.
- [23] Zimmer, A., Cazarolli, J., Teixeira, R.M., Viscardi, S.L.C., Cavalcanti, E.S.H., Gerbase, A.E., Ferrão, M.F., Piatnicki, C.M.S., and Bento, F.M., 2013, Monitoring of efficacy of antimicrobial products during 60 days storage simulation of diesel (B0), biodiesel (B100) and blends (B7 and B10), *Fuel*, 112, 153–162.
- [24] Zhang, X., Zhang, L., Li, J., Zou, X., Jing, X., and Li, W., 2022, Combustion and emission characteristics of diesel with different distillation ranges on the China-VI diesel engine, *Fuel*, 325, 124876.
- [25] Barra, I., Kharbach, M., Qannari, E.M., Hanafi, M., Cherrah, Y., and Bouklouze, A., 2020, Predicting cetane number in diesel fuels using FTIR spectroscopy and PLS regression, *Vib. Spectrosc.*, 111, 103157.
- [26] Bukkarapu, K.R., and Krishnasamy, A., 2022, Predicting engine fuel properties of biodiesel and biodiesel-diesel blends using spectroscopy based approach, *Fuel Process. Technol.*, 230, 107227.
- [27] Chen, C., Liang, R., Xia, S., Hou, D., Abdoulaye, B., Tao, J., Yan, B., Cheng, Z., and Chen, G., 2023, Fast characterization of biodiesel via a combination of ATR-FTIR and machine learning models, *Fuel*, 332, 126177.

Deep Eutectic Solvent (DES) Based on Choline Chloride and Mono-, Di-, Poly-Ethylene Glycol as KI/I₂ Electrolyte Solvents on DSSC Devices

Adhitya Adhitya, Winda Rahmalia*, Intan Syahbanu,
Gusrizal Gusrizal, and Adhitiyawarman Adhitiyawarman

Department of Chemistry, Faculty of Mathematics and Natural Sciences, Tanjungpura University,
Jl. Prof. Dr. Hadari Nawawi, Pontianak 78124, Indonesia

* Corresponding author:

email:

winda.rahmalia@chemistry.untan.ac.id

Received: March 2, 2023

Accepted: August 21, 2023

DOI: 10.22146/ijc.82754

Abstract: Deep eutectic solvent (DES) has high viscosity and electrical conductivity values, so it can be used as an electrolyte solvent in dye-sensitized solar cells (DSSCs). This research was conducted to produce DES based on choline chloride (ChCl) and ethylene glycol (EG), diethylene glycol, and polyethylene glycol-400, which were then used as KI/I₂ couple redox electrolyte solvent to improve the DSSC performance. The synthesis was carried out by mixing each component in several variations of the mole fraction of ChCl (x_{ChCl}) at 80 °C for 15 min, and then was characterized by their pH, freezing point, density, viscosity, and electrical conductivity. A mixture that meets the criteria as a eutectic solvent and has a freezing point of less than -18 °C with the highest electrical conductivity value is DES ChCl:EG with x_{ChCl} 0.3 and x_{ChCl} 0.4. Both DESs were then used as a solvent for KI/I₂, combined with acetonitrile in various compositions. The electrolyte with the highest electrical conductivity value was KI/I₂ dissolved in ChCl:EG with x_{ChCl} 0.3 solvent 6:4 v/v, and then employed in DSSC device. The best performance of DSSC ($I_{\text{sc}} = 0.155 \text{ mA/cm}^2$; $V_{\text{oc}} = 0.465 \text{ V}$; $P_{\text{max}} = 0.719 \text{ W}$; $\eta_{\text{max}} = 0.072\%$) was produced under a light intensity of 0.1 W/cm².

Keywords: deep eutectic solvent; dye-sensitized solar cell; electrolyte; viscosity; electrical conductivity

■ INTRODUCTION

Dye-sensitized solar cell (DSSC) is a third-generation solar cell introduced by Professor Grätzel in 1991. DSSC was chosen as an alternative to convert solar energy into electrical energy because of its low production price, and the ingredients are easier to obtain. In addition, each component of the DSSC can be modified and optimized separately. The electrolyte is one of the main components whose performance must be optimized to increase the efficiency of DSSC. Electrolytes play an essential role in the electron transfer process in DSSC. The function of the electrolyte in DSSC is to replace the loss of electrons in the dye's valence band when the dye absorbs visible light [1]. The electrolyte used in DSSCs is generally a liquid containing an I⁻/I₃⁻. Anion I⁻/I₃⁻ can be obtained from the compound KI/I₂, which is generally dissolved in acetonitrile [2-3].

Acetonitrile is a widely used organic solvent because it has good solvation ability for polar and non-polar compounds. However, as an electrolyte solvent in DSSCs, acetonitrile has very low viscosity and electrical conductivity values. The viscosity of acetonitrile is 0.352 cP with an electrical conductivity of $7 \times 10^{-3} \text{ mS/cm}$ [3]. The low viscosity value can result in leakage or instability, which will affect the electrolyte's quality and reduce the DSSC's efficiency. Therefore, it is necessary to use an alternative solvent with a higher viscosity and electrical conductivity value to replace acetonitrile as an electrolyte solvent to increase DSSC's efficiency. The solvent is known as deep eutectic solvent (DES).

DES is a binary or ternary mixture consisting of a hydrogen bond donor (HBD) and a hydrogen bond acceptor (HBA), which are strongly bound due to interactions with hydrogen bonds. The HBD and HBA

proper molar ratio will produce a eutectic mixture with a freezing point much lower than that of each pure constituent. DES is classified as an ionic liquid (IL), so its electrical conductivity value is relatively large. This is because when an IL is subjected to an electric field, a charge transport event or ion mobility will be associated with an empty space (hole). This ability affects the size of the electrical conductivity value in a liquid [4]. Because of its similarity with ILs, DES has started to be widely applied in electrochemical devices [5-7].

In recent years, choline iodide: glycerol and choline chloride (ChCl): glycerol-based DES have been used as part of the electrolyte composition for DSSC by Jhong et al. [8] and Boldrini et al. [9]. The reported DSSC showed an energy conversion efficiency of 1.70–3.88%. However, the efficiency values were still lower than DSSC using acetonitrile at the same conditions, namely 4.90%. This study aims to synthesize DES, which is then used as a solvent for KI/I₂ in DSSC devices. DES was synthesized by mixing ChCl with several hydrogen bond donor compounds such as ethylene glycol (EG), diethylene glycol (DEG), and polyethylene glycol (PEG). DES produced from a mixture of ChCl and EG has been studied to have a viscosity value of 36 cP and an electrical conductivity value of 7.61 mS/cm [10]. The DES viscosity value is 100× greater than that of acetonitrile. They have a 1000× more excellent electrical conductivity value compared to acetonitrile. Meanwhile, in this study, DEG and PEG were also used as HBD to study the effect of adding alkyl chains to the function of DES as an electrolyte solvent. The volume ratio between DES and acetonitrile, which can produce DSSC with the best efficiency, was also reported.

■ EXPERIMENTAL SECTION

Materials

The materials used in this study include choline chloride (ChCl, ≥ 99%, Sigma Aldrich), EG (C₂H₆OH, ≤ 100%, Supelco), DEG (C₄H₁₀O₃, 99%, Sigma Aldrich), PEG 400 (HOCH₂(CH₂OCH₂)₉CH₂OH, ≤ 100%, Sigma Aldrich), acetonitrile (C₂H₃N, 99.8%, Sigma Aldrich), ethanol absolute (C₂H₅OH, ≥ 99.5%, Supelco), titanium(IV) oxide (TiO₂ anatase nanopowder, < 25 nm

particle size, 99.7% trace metals basis, Sigma Aldrich), potassium iodide (KI, ≤ 100%, Supelco), and iodine (I₂, ≤ 100%, Supelco). Dye (Ruthenizer complex 535-bistba, N719), platisol T/SP (Pt paste), and transparent conductive oxide (TCO) glass with type fluorine-doped tin oxide (FTO) coated TEC-7 conductive glasses were purchased from Solaronix.

Instrumentation

The instruments used in this study included analytical balances, ovens, THERMOLYNE furnaces, IKA C-MAG HS 7 hotplates, standard glassware, spatulas, thermometers, Iwaki Pyrex pycnometer, Oswald Iwaki Pyrex viscometer, Hanna conductivity meter, 500-Watt halogen lamp, solar power meter BTU W/m² tester handheld portable and scientific multimeter 6.5-digit Agilent 34461 A.

Procedure

DES preparation

ChCl solid was weighed with a ChCl mole fraction (x_{ChCl}) of 0, 0.1, 0.2, 0.3, 0.4, 0.5, 0.6, 0.7, 0.8, 0.9, and 1.0, and then they were added into a beaker glass separately. EG was weighed according to the calculation with x_{ChCl} as above and placed into different beakers so that the total mass of the mixture of ChCl and EG was 5 g. The beaker glass containing ChCl and EG was then heated using a hotplate at 80 °C for 15–40 min to obtain dry ChCl solid (white crystals). The EG liquid was then poured into a beaker containing ChCl. The mixture was then stirred using a magnetic stirrer while heated at 80 °C for 15 min until a homogeneous mixture was obtained. The mixture was placed in the bottle at room temperature until further treatment [11]. The preparation of DES with DEG and PEG 400 was done with the same procedure. Homogeneous mixtures were selected for the characterization stage, including measurement of pH, freezing point, density, viscosity, and electrical conductivity.

Electrolyte preparation and characterization

Homogeneous mixtures (ChCl:EG, ChCl:DEG, and ChCl:PEG 400) were mixed with acetonitrile, respectively, with variations in the v/v composition of

the mixture (10:0, 8:2, 6:4, 4:6, 2:8 and 0:10) and the total volume of solvent was 10 mL. KI and I₂ weighed as much as 0.83 and 0.13 g, respectively. They were put into a beaker containing DES and acetonitrile, then wrapped in aluminum foil, and stirred using a magnetic stirrer for 30 min [12]. The electrolyte solution was then transferred into a dark vial. The electrolyte solution was observed for 24 h. The homogeneous electrolyte was further characterized by measuring density, viscosity, and electrical conductivity.

DSSC fabrication and performance analysis

FTO glass preparation. The FTO glass was cut into a square of 2 × 2 cm². The glass was then washed using 70% technical ethanol and sonicated for 30 min. Then, the glass was dried at a temperature of 100 °C for 1 h. The conductive side of the glass was determined [3].

DSSC assembly. An active side (1 × 1 cm²) of FTO glass was made by attaching transparent insulation. The TiO₂ anode and Pt cathode paste were deposited on different FTO glass. Photoanode was prepared by adopting the method of Rahmalia et al. [2]. The anode used was TiO₂ with a 5% TMK (NH₄OH-treated metakaolinite which was previously produced by Rahmalia et al. [2]) mixture. Anatase TiO₂ weighing 2.3751 g and TMK weighing 0.1264 g were measured and then added to 15 mL of absolute ethanol, 800 μL of Triton-X, and 600 μL of acetylacetone. The mixture was stirred for 24 h until a paste was formed. The resulting anode paste was sonicated for 3 h. The anode was calcined at a temperature of 450 °C for 30 min, while the cathode was calcined at 400 °C for 5 min [3].

The anode layer was immersed in a sensitizer solution (1% ruthenium complex prepared by dissolving 0.005 g of ruthenium dye into 5 mL of ethanol) for 24 h [13]. Furthermore, the anode and cathode were assembled like a sandwich and locked using a binder clip. Then, a few drops of electrolyte were through the gap between the two glasses until the electrolyte solution covered and filled all parts of the glass. The cells formed are then sealed with glue [14].

DSSC performance analysis. The light source used in the DSSC performance analysis was a 500 W halogen lamp. The test was carried out with variations in light

intensity of 0.005–0.100 W/cm², which was controlled by dimer and measured using a solar power meter. The values of cell short circuit current (I_{sc}) and open-circuit voltage (V_{oc}) were measured using the scientific multimeter Agilent 34461 A.

■ RESULTS AND DISCUSSION

DES Synthesis and Characterization

The DES in this study is the result of a mixture of quaternary ammonium salt (HBA), namely ChCl and a HBD, namely EG, DEG, and PEG-400. The interaction occurs in the process of forming DES is an intermolecular hydrogen bond formed by the chloride anion group (Cl⁻) in the HBA and the hydroxyl group in the HBD. DES is also described as a mixture of Brønsted or Lewis acids and bases, so that the hydrogen bonds formed in all these systems could cause a significant freezing point depression [15].

The results of DES preparation show that a mixture of ChCl:EG and ChCl:DEG at x_{ChCl} 0.1, 0.2, 0.3, and 0.4 were liquid and transparent, indicating the formation of DES in these compositions. The mixture with x_{ChCl} 0.5–1.0 was crystallized. The acid dissociation, which releases hydrogen atoms, causes choline salts to form so that the mixture cannot change to the liquid phase at room temperature [15]. As for the ChCl:PEG 400 mixture, only the x_{ChCl} 0.1 was liquid and transparent. Therefore, only the mixture with x_{ChCl} 0.1 was indicated as DES.

The prepared DES was observed at room temperature for 24 h to evaluate their homogeneity. Several mixtures of ChCl:EG, ChCl:DEG, and ChCl:PEG 400 (as presented in Table 1) were continued in the characterization stage. They were a mixture that did not change, either phase changes or the formation of crystal deposits.

The pH condition affects solubility because solutes tend to be more soluble in solvents under acidic or neutral conditions than in alkaline conditions [16]. Therefore, pH measurements were carried out to determine whether the DES produced was acidic, neutral, or basic. Measurements showed that all three types of DES were detected at pH 6, so it can be concluded that the DES prepared in this study were weakly acidic.

Table 1. The DES composition was carried forward to the characterization stage

DES type	x_{ChCl}	x_{EG}
DES _{a1}	0.1	0.9
DES _{a2}	0.2	0.8
DES _{a3}	0.3	0.7
DES _{a4}	0.4	0.6
DES _{b1}	0.1	0.9
DES _{b2}	0.2	0.8
DES _{b3}	0.3	0.7
DES _{b4}	0.4	0.6
DES _{c1}	0.1	0.9

Mixing two components at a certain mole fraction formed DES will cause a significant decrease in freezing point so that it will have a lower freezing point than each of its pure constituents [11]. The constituents of DES have different freezing points. The ChCl, EG, DEG, and PEG 400 compounds have a freezing point at 303 °C [15], -12 °C [17], -6.5 °C [18], and -4 °C [19], respectively. There was no phase change in DES_{a1}-DES_{a4} and DES_{b1}-DES_{b4}. They did not freeze when placed in the freezer at a temperature range of -15 to -18 °C for 24 h. This follows the definition of DES because it has a freezing point below the freezing point of the single substance, namely EG, and DEG, and is much lower than the freezing point of ChCl. Meanwhile, DES_{c1} undergoes crystal formation sometime after being put in the freezer. It freezes after being placed for 5 min when a temperature of 0 °C. In this case, the mixture does not reach the eutectic point because it has a freezing point with a higher freezing rate than one of its pure constituents, in this case PEG 400. Therefore, in the next step, only DES_{a1}-DES_{a4} and DES_{b1}-DES_{b4} were used as electrolyte solvents.

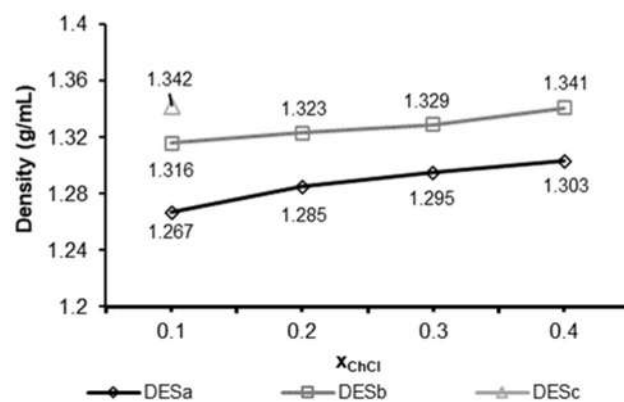
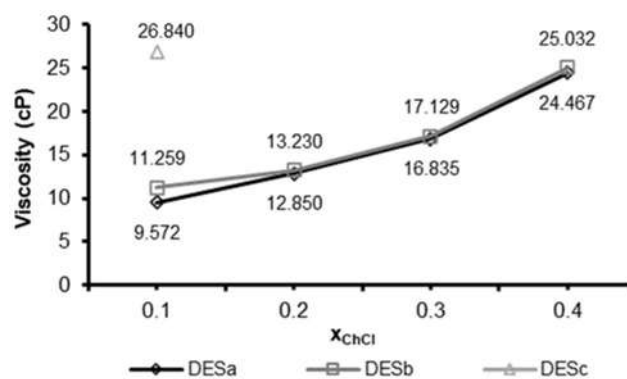
Density and viscosity have a close relationship as factors that affect mass transfer [11]. The type of HBD influences the density of DES. The density of DES will increase with the increase in the number of hydroxyl groups or the length of the HBD chain [4]. The DES constituents' molar ratio also affects the density value [20]. Fig. 1 shows the density measurement results of DES formed in this study.

Based on Fig. 1, it can be observed that the addition of alkyl chain lengths of constituent increased the DES

density value. The longer the alkyl chain, the greater the molecular weight. The increase in molecular weight affects increasing the density value [21]. The EG, DEG, and PEG-400 have a molecular weight of 62.07, 106.12, and 400.00 g/mol, respectively. The DES density value increased along with the increase in the x_{ChCl} in the mixtures. This was due to the contribution of the density of the pure constituents of the mixtures. ChCl, EG, DEG, and PEG-400 have a density of 1.19, 1.11, 1.12, and 1.13 g/mL. Mixing these compounds with ChCl causes an increase in density.

Like density, viscosity is often associated with a hydrogen bond network between HBA and HBD, corresponding to free volume [22]. The viscosity of the eutectic mixture is influenced by the chemical properties of the constituents (HBA and HBD), temperature, and water content [4]. The results of the viscosity measurement of DES in this study are presented in Fig. 2.

Fig. 2 shows that an increase in the x_{ChCl} causes an increase in the viscosity value. The increased viscosity

**Fig 1.** The relationship of x_{ChCl} and DES density**Fig 2.** The relationship of x_{ChCl} and DES viscosity

value due to adding the x_{ChCl} was caused by the high and extensive network of hydrogen bonds between each component resulting in a very viscous mixture [21]. High viscosity can cause an increase in the solvent diffusion coefficient so that the reaction rate will decrease [8]. However, the increase in viscosity also affects slowing the evaporation process to prevent leakage of the electrolyte system after DES was used as an electrolyte solvent in DSSC [23].

Fig. 3 shows the results of the DES electrical conductivity measurements produced in this study. Based on Fig. 3, it can be observed that the addition of the alkyl chain length of the constituent resulted in a decrease in the value of the electrical conductivity of DES. In general, the value of electrical conductivity is influenced by the viscosity of the solution, where the high viscosity of the solution will reduce the movement of free ions [11]. However, there was an increase in the electrical conductivity value when x_{ChCl} increased. This is because the addition of ChCl will result in the formation of more hydrogen bonds so that the intermolecular interactions due to the bond cause the electrical conductivity value to increase. Hydrogen bonding allows intermolecular delocalization, affecting increased electrical conductivity [24]. However, there was a drastic decrease in the electrical conductivity of DES_{a4} . It is probably due to the increase in bond density due to the increasing number of molecule interactions. The molecular interactions can cause an increase in viscosity, resulting in a decrease in electrical conductivity due to the hindered movement of

ions and electrons [25]. Based on the molecular structure, DEG has a longer alkyl chain than EG. However, in DEG, there is a lone pair of electrons in the ether group (R-O-R'). The lone pair of electrons acts as a medium that increases ionic mobility [26]. These factors allow the electrical conductivity of DES_{b4} not to decrease while DES_{a4} has decreased electrical conductivity.

Electrolyte Preparation and Characterization

The DES used as an electrolyte solvent in this work was DES in the form of a homogeneous liquid that has the highest electrical conductivity value, namely DES_{a3} , with a density, viscosity, and electrical conductivity of 1.295 g/mL, 16.835 cP, and 9.940 mS/cm, respectively. In addition, DES_{b4} with a density, viscosity, and electrical conductivity of 1.341 g/mL, 25.032 cP, and 6.660 mS/cm, respectively. Meanwhile, DES_{c1} was not used as an electrolyte solvent because of its small electrical conductivity value of 0.213 mS/cm. There were several volume ratio variations in composition between acetonitrile and DES to dissolve KI and I_2 . For further discussion, electrolytes resulting from dissolution with acetonitrile: DES_{a3} 10:0, 8:2, 6:4, 4:6, 2:8, and 0:10 v/v, are called E_{a1} , E_{a2} , E_{a3} , E_{a4} , E_{a5} , and E_{a6} , respectively. Meanwhile, the electrolyte resulting from dissolution with acetonitrile: DES_{b4} 10:0, 8:2, 6:4, 4:6, 2:8, and 0:10 v/v are referred to as E_{b1} , E_{b2} , E_{b3} , E_{b4} , E_{b5} , and E_{b6} respectively.

Fig. 4 shows that the absence of precipitates at E_{a4} , E_{a5} , E_{a6} , E_{b4} , E_{b5} , and E_{b6} indicated that DES could dissolve

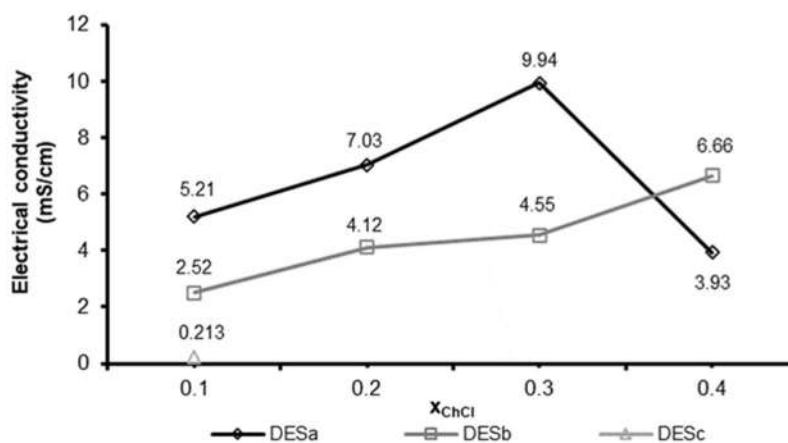


Fig 3. The relationship of x_{ChCl} and DES electrical conductivity



Fig 4. KI/I₂ electrolyte with acetonitrile:DES_{a3} (left) and acetonitrile:DES_{b4} (right) as solvent

the KI/I₂ redox couple better than acetonitrile. Hydrogen bonding in the solvent increases the solvent polarity or polarizability, which can cause higher solubility [27]. A white precipitate exists at E_{a1}, E_{a2}, E_{a3}, E_{b1}, E_{b2}, and E_{b3}. The precipitate is a residual KI compound that cannot be completely dissolved in the solvent. KI compounds have low solubility in organic solvents compared to their solubility in water [28].

Table 2 shows the variations in the volume ratio between acetonitrile and DES affecting the electrolyte's density, viscosity, and electronic conductivity. The relatively high density and viscosity of DES cause an increase in the viscosity of the electrolyte. The electrolyte using 100% acetonitrile as solvent had a density and viscosity of 0.875 g/mL and 0.796 cP, respectively. The presence of DES in the mixture causes the density and viscosity of the electrolyte also to increase.

An interesting thing happened in the observation of electronic conductivity. The electronic conductivity of the electrolyte increased with the addition of DES up to a volume ratio of acetonitrile:DES of 6:4 v/v (E_{a3} and E_{b3}).

The high viscosity of DES is thought to be the cause of the low electrolyte's electrical conductivity value when using more DES in the mixture. Although DES has a much higher electrical conductivity value than acetonitrile, when it is used as a KI/I₂ solvent, the high viscosity of DES can affect the redox system in the electrolyte so that the electrolyte with pure acetonitrile solvent has a higher electrical conductivity value. However, the right combination of these two solvents produces an electrolyte with the highest electrical conductivity value and optimum viscosity so that the mobility of electrons in the redox system is not disturbed and the electrolyte is not easily vaporized reducing the potential for leakage of the electrolyte system in DSSC.

DSSC Fabrication and Performance Analysis

DSSC is a medium used to observe the function and capabilities of KI/I₂-based electrolytes with a combination of DES and acetonitrile as a solvent. DSSC performance analysis was performed on cells using E_{a3}, E_{b3}, and E_{a1} separately. The DSSC performance tested

Table 2. Density, viscosity, and electrical conductivity of electrolytes

Ratio volume Acn:DES	Electrolyte type code	Density (g/mL)	Viscosity (cP)	Electrical conductivity (mS/cm)
10:0	E _{a1}	0.875	0.796	14.140
8:2	E _{a2}	0.923	3.865	22.240
6:4	E _{a3}	0.955	8.639	25.200
4:6	E _{a4}	1.043	12.679	15.350
2:8	E _{a5}	1.192	16.372	12.190
0:10	E _{a6}	1.325	18.466	11.850
10:0	E _{b1}	0.875	0.796	14.140
8:2	E _{b2}	0.996	5.653	15.780
6:4	E _{b3}	1.028	10.712	22.500
4:6	E _{b4}	1.086	16.068	18.900
2:8	E _{b5}	1.205	22.425	8.050
0:10	E _{b6}	1.368	26.682	6.710

includes short-circuit current (I_{sc}), open-circuit voltage (V_{oc}), maximum power (P_{max}), and maximum energy conversion efficiency (η_{max}). The effect of light intensity on the values of I_{sc} , V_{oc} , P_{max} , and η_{max} can be seen in Fig. 5.

The V_{oc} value is generated due to the difference in charge between the anode and cathode. The potential difference that occurred was expressed as a voltage value. Fig. 5 shows that the greater the light intensity was given, the greater the V_{oc} value also increased. Increasing the light intensity higher than 0.06 W/m^2 does not significantly increase the V_{oc} value. Nunno et al. [29] reported the causes and effects of the voltage drop phenomenon. According to their research, the voltage drop is affected by several things, for example, unacceptable termination systems, hot spots, small-sized conductors, and non-uniform conductor materials. These factors will affect the system's increasing local temperature and resistance, causing a decrease in the voltage value [29]. In our research, an increase in light intensity also increases the local temperature of the system so that the V_{oc} value does not increase. It even experiences a slight decrease, an indication of a voltage drop.

Besides affecting the value of V_{oc} , light intensity also impacts the value of I_{sc} . This can happen because I_{sc} is related to the number of photons absorbed, affecting the electron excitation process from the dye used. An increase in light intensity is accompanied by an increase in the value of I_{sc} [30]. The P_{max} continues to increase with increasing light intensity and reaches its highest point at a light intensity of 0.1 W/cm^2 . The highest maximum power is generated from DSSC with E_{a3} which is equal to 0.719 W .

The η_{max} value can be determined after obtaining each cell's V_{oc} and I_{sc} values. In this study, the value of energy conversion efficiency indicates the ability of DSSC to convert solar energy into electrical energy regardless of the fill factor value. DSSC using E_{a3} has a higher energy conversion efficiency value than DSSC using E_{b3} and E_{a1} . These results are directly proportional to the magnitude of the electrical conductivity value that is owned by the E_{a3} solvent. The greater the electrical conductivity value, the higher the movement or mobility of electrons, which is then interpreted as an electric current. Based on the Ohm's Law, voltage (V) is directly proportional to current (I) but inversely proportional to

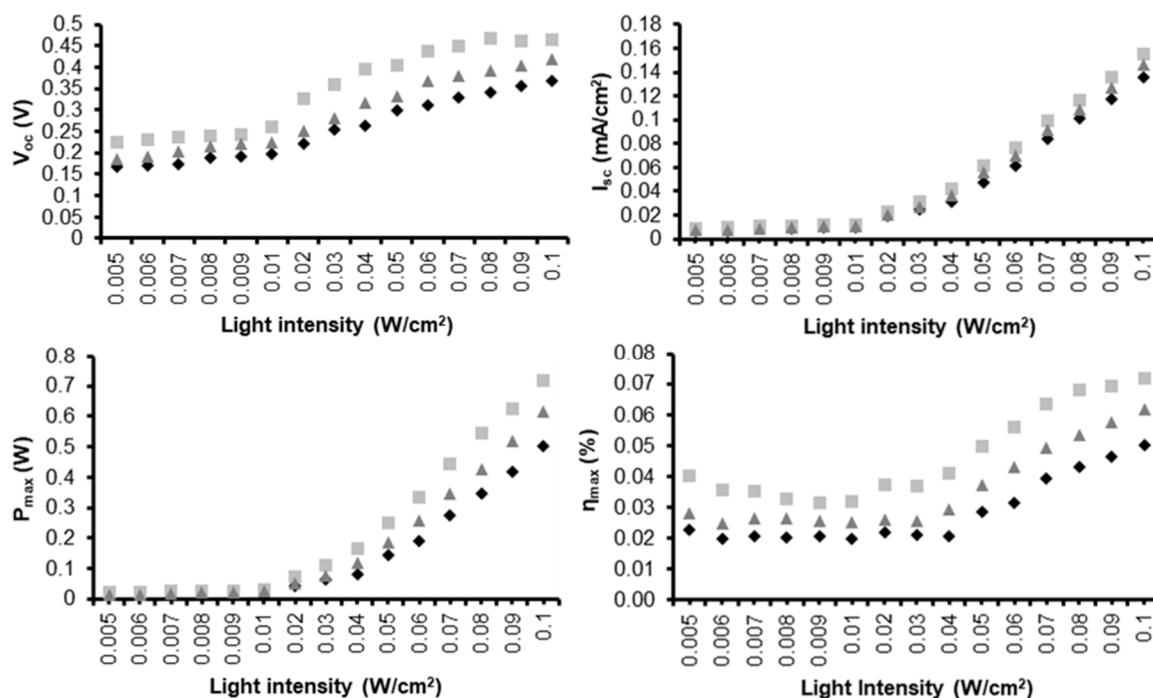


Fig 5. Performance parameters of DSSC with KI/I_2 electrolyte system with combination of acetonitrile:DES solvent (◆ E_{a3} , ■ E_{b3} , ▲ E_{a1})

Table 3. DSSCs performance

Parameter	Electrolyte used in DSSC		
	E _{a1}	E _{a3}	E _{b3}
I _{sc} (mA/cm ²)	0.136	0.155	0.147
V _{oc} (V)	0.369	0.465	0.419
P _{max} (W)	0.502	0.719	0.616
η _{max} (%)	0.050	0.072	0.062

resistance (R) [31-32]. The greater the electrical conductivity value, the resistance or resistance value will decrease, while the current and voltage values will increase.

In addition, based on the density and viscosity parameters in Table 2 shows that E_{a1} has the lowest density and viscosity values, followed by E_{a3} and E_{b3}. The density and viscosity values of the electrolyte that are too small can result in leakage in the electrolyte system at DSSC. However, an increase in relatively high density and viscosity values in the E_{b3} electrolyte causes a decrease in fluid velocity and electrolyte diffusion, which affects charge transport in electrolytes [12]. Therefore, the E_{a3} electrolyte with the best density, viscosity, and conductivity parameters generates the highest energy conversion efficiency.

Table 3 shows that the DSSC using E_{a3} performs better than the DSSC using E_{b3} or E_{a1} because the acetonitrile:DES_{a3} based solvent has a higher electrical conductivity value. In addition, in the DSSC fabrication process, it was also observed that E_{a3} and E_{b3} had a longer shelf life in the cell state that had not been covered with glue when compared to E_{a1}, which experienced faster evaporation. This can happen because E_{a3} and E_{b3} have a higher viscosity value than E_{a1}.

■ CONCLUSION

The potential of deep eutectic solvents as solvents for KI/I₂ redox pairs has been successfully developed to substitute acetonitrile. The suitable volume composition of a mixture of DES and acetonitrile can produce electrolytes with higher viscosity and electrical conductivity than pure acetonitrile. The optimal composition was obtained at the volume ratio of acetonitrile: DES ChCl:EG with x_{ChCl} 0.3 (η = 16.84 cP; κ = 9.94 mS/cm). These characteristics then cause the increased performance of DSSC in converting light

energy into electrical energy. Evaporation and solvent leakage in cells can be prevented, and the electron transport process in the electrolyte system can be improved. To determine the charge transport mechanism, further research will be needed on IPCE measurements and impedance data.

■ AUTHOR CONTRIBUTIONS

Adhitya: conceptualization, methodology, formal analysis, writing-original draft, Winda Rahmalia, Intan Syahbanu, Gusrizal, and Adhityawarman: supervision, resources, project administration, writing-review, editing, and validation. All authors have read and agreed to the published version of the manuscript.

■ REFERENCES

- [1] Iftikhar, I., Sonai, G.G., Hashmi, S.G., Nogueira, A.F., and Lund, P.D., 2019, Progress on electrolytes development in dye-sensitized solar cells, *Materials*, 12 (12), 1998.
- [2] Rahmalia, W., Silalahi, I.H., Usman, T., Fabre, J.F., Mouloungui, Z., and Zissis, G., 2021, Stability, reusability, and equivalent circuit of TiO₂/treated metakaolinite-based dye-sensitized solar cell: Effect of illumination intensity on V_{oc} and I_{sc} values, *Mater. Renewable Sustainable Energy*, 10 (10), 10.
- [3] Rahmalia, W., Septiani, S., Naselia, U.A., Usman, T., Silalahi, I.H., and Mouloungui, Z., 2021, Performance improvements of bixin and metal-bixin complexes sensitized solar cell by 1-methyl-3-propylimidazolium iodide in electrolyte system, *Indones. J. Chem.*, 21 (3), 669–678.
- [4] Poletto Rodrigues, B., Limbach, R., Buzatto de Souza, G., Ebendorff-Heidepriem, H., and Wondraczek, L., 2019, Correlation between ionic mobility and plastic flow events in NaPO₃-NaCl-Na₂SO₄ glasses, *Front. Mater.*, 6, 128.
- [5] Azmi, S., Koudahi, M.F., and Frackowiak, E., 2022, Reline deep eutectic solvent as a green electrolyte for electrochemical energy storage applications, *Energy Environ. Sci.*, 15 (3), 1156–1171.
- [6] Puttaswamy, R., Mondal, C., Mondal, D., and Ghosh, D., 2022, An account on the deep eutectic

- solvents-based electrolytes for rechargeable batteries and supercapacitors, *Sustainable Mater. Technol.*, 33, e00477.
- [7] Dong, P., Zhang, X., Han, K.S., Cha, Y., and Song, M.K., 2022, Deep eutectic solvent-based polymer electrolyte for solid-state lithium metal batteries, *J. Energy Chem.*, 70, 363–372.
- [8] Jhong, H.R., Wong, D.S.H., Wan, C.C., Wang, Y.Y., and Wei, T.C., 2009, A novel deep eutectic solvent-based ionic liquid used as electrolyte for dye-sensitized solar cells, *Electrochem. Commun.*, 11 (1), 209–211.
- [9] Boldrini, C.L., Quivelli, A.F., Manfredi, N., Capriati, V., and Abbotto, A., 2022, Deep eutectic solvents in solar energy technologies, *Molecules*, 27 (3), 709.
- [10] Abbott, A.P., Harris, R.C., and Ryder, K.S., 2007, Application of hole theory to define ionic liquids by their transport properties, *J. Phys. Chem. B*, 111 (18), 4910–4913.
- [11] Wang, D.D., Lu, Z.H., Yang, M.N.O., Guo, H.M., and Yang, Z.H., 2020, A choline chloride-ethylene glycol deep eutectic solvent based on magnetic polydopamine with preconcentration and determination for sulfonylurea herbicides in water samples, *J. Braz. Chem. Soc.*, 31 (7), 1509–1517.
- [12] Gu, P., Yang, D., Zhu, X., Sun, H., Wangyang, P., Li, J., and Tian, H., 2017, Influence of electrolyte proportion on the performance of dye-sensitized solar cell, *AIP Adv.*, 7 (910), 105219.
- [13] Tomar, N., Agrawal, A., Dhaka, V.S., and Surolia, P.K., 2020, Ruthenium complexes based dye sensitized solar cells: Fundamentals and research trends, *Sol. Energy*, 207, 59–67.
- [14] Rahmalia, W., Fabre, J.F., Usman, T., and Mouloungui, Z., 2016, Bixin Adsorption Characteristic on TiO₂, *Proceedings on the IRES 28th International Conference*, 6th February 2016, Jakarta, Indonesia.
- [15] Smith, E.L., Abbott, A.P., and Ryder, K.S., 2014, Deep eutectic solvents (DESSs) and their applications, *Chem. Rev.*, 114 (21), 11060–11082.
- [16] Chang, S.H., Lin, H.T.V., Wu, G.J., and Tsai, G.J., 2015, pH Effects on solubility, zeta potential, and correlation between antibacterial activity and molecular weight of chitosan, *Carbohydr. Polym.*, 134, 74–81.
- [17] Roslan, A., Arbanah, M., Tukiman, N., Ibrahim, N.N., and Juanil, A.R., 2017, The effects of ethylene glycol to ultrapure water on its specific heat capacity and freezing point, *J. Appl. Environ. Biol. Sci.*, 7 (7S), 54–60.
- [18] MEGlobal, 2019, Diethylene Glycol: Product Guide, London, UK.
- [19] Zhang, C., Pang, C., Mao, Y., and Tang, Z., 2022, Effect and mechanism of polyethylene glycol (PEG) used as a phase change composite on cement paste, *Materials*, 15 (8), 2749.
- [20] Abdollahzadeh, M., Khosravi, M., Hajipour Khire Masjidi, B., Samimi Behbahan, A., Bagherzadeh, A., Shahkar, A., and Tat Shahdost, F., 2022, Estimating the density of deep eutectic solvents applying supervised machine learning techniques, *Sci. Rep.*, 12 (1), 4954.
- [21] Nuqui, J.P., Damalerio, R., Meas, S., Yem, S., and Soriano, A., 2021, Generalized Pitzer correlation for density calculations of ionic liquids, *ASEAN J. Chem. Eng.*, 21 (1), 38–51.
- [22] Haghbakhsh, R., Parvaneh, K., Raeissi, S., and Shariati, A., 2018, A general viscosity model for deep eutectic solvents: The free volume theory coupled with association equations of state, *Fluid Phase Equilib.*, 470, 193–202.
- [23] Zhang, Z., Huang, H., Ma, X., Li, G., Wang, Y., Sun, G., Teng, Y., Yan, R., Zhang, N., and Li, A., 2017, Production of diacylglycerols by esterification of oleic acid with glycerol catalyzed by diatomite loaded SO₄²⁻/TiO₂, *J. Ind. Eng. Chem.*, 53, 307–316.
- [24] Isono, T., Kamo, H., Ueda, A., Takahashi, K., Nakao, A., Kumai, R., Nakao, H., Kobayashi, K., Murakami, Y., and Mori, H., 2013, Hydrogen bond-promoted metallic state in a purely organic single-component conductor under pressure, *Nat. Commun.*, 4 (1), 1344.
- [25] Husraini, L., Zahrina, I., and Sunarno, S., 2020, Aplikasi deep eutectic solvents (DESSs) sebagai katalis pada sintesis emulsifier, *JOM*, 7 (1), 1–8.

- [26] Bürger, P., and Riebel, U., 2022, High temperature coronas in air and flue gas from LPG combustion: Current-voltage characteristics, ion mobilities and free electrons, *J. Electrostat.*, 115, 103676.
- [27] Tayyari, S.F., Vakili, M., Nekoei, A.R., Rahemi, H., and Wang, Y.A., 2007, Vibrational assignment and structure of trifluorobenzoylacetone: A density functional theoretical study, *Spectrochim. Acta, Part A*, 66 (3), 626–636.
- [28] Spiteri, L., Baisch, U., and Vella-Zarb, L., 2018, Correlations and statistical analysis of solvent molecule hydrogen bonding – A case study of dimethyl sulfoxide (DMSO), *CrystEngComm*, 20 (9), 1291–1303.
- [29] Nunno, S., Attachie, J.C., and Duah, F.N., 2012, An investigation into the causes and effects of voltage drops on an 11 kV feeder, *Can. J. Electr. Electron. Eng.*, 3 (1), 40–47.
- [30] Long, B., Zhao, D., and Liu, W., 2012, Thermodynamics studies on the solubility of inorganic salt in organic solvent: Application to KI in organic solvents and water-ethanol mixtures, *Ind. Eng. Chem. Res.*, 51 (28), 9456–9467.
- [31] Xu, M., Wang, W., Zhong, Y., Xu, X., Wang, J., Zhou, W., and Shao, Z., 2019, Enhancing the triiodide reduction activity of a perovskite-based electrocatalyst for dye-sensitized solar cells through exsolved silver nanoparticles, *J. Mater. Chem. A*, 7 (29), 17489–17497.
- [32] Tenny, K.M., and Keenaghan, M., 2022, Ohms Law, *National Library of Medicine*, StatPearls Publishing LLC, St. Petersburg, Florida, US.

Facile Production of Biodiesel from Candlenut Oil (*Aleurites moluccana* L.) Using Photocatalytic Method by Nano Sized-ZnO Photocatalytic Agent Synthesized via Polyol Method

Hendro Juwono*, Anizun Zakiyah, Riki Subagyo, and Yuly Kusumawati

Department of Chemistry, Faculty of Science and Data Analytics, Institut Teknologi Sepuluh Nopember, Kampus ITS Keputih, Sukolilo, Surabaya 60111, Indonesia

* Corresponding author:

email: hjachmad@gmail.com

Received: March 8, 2023

Accepted: August 1, 2023

DOI: 10.22146/ijc.82895

Abstract: Biodiesel production from non-edible oil is an alternative way to reduce edible oil dependency and reduce the competition for feed and food. Candlenut oil (*Aleurites moluccana* L.) is one of the non-edible oils which can be used as feedstock for biodiesel production since they have a high oil content. Herein, the biodiesel production from candlenut oil has been conducted using zinc oxide (ZnO) synthesized by the polyol method. Polyol methods facilitated the formation of ZnO nanoparticles with various shapes, including spherical, rod, and hexagonal. Besides, ZnO showed a mesoporous characteristic, facilitating the conversion of fat fatty acid to fatty acid methyl ester (FAME) of 61%. Increasing ZnO dosage led to enhancing the FAME yield. Similarly, the FAME yield was also improved by increasing the reaction time. The results of esterification of candlenut oil and methanol yielded 70.76% FAME with 2% nano-ZnO polyol catalyst at 180 min reaction time at room temperature whilst being stirred constantly at 400 rpm. A good FAME conversion using ZnO at room temperature provides good information to produce biodiesel with a simple method. Apart from that, photocatalytic promoted transesterification at room temperature, which is beneficial for reducing energy consumption.

Keywords: biodiesel; esterification; candlenut oil; ZnO nanoparticle; polyol technique

■ INTRODUCTION

The development of renewable energy has been investigated in order to meet the energy demand. Biodiesel is an alternative fuel among various renewable energy which non-toxic, biodegradable, and environmentally friendly [1-2]. As reviewed by Tabatabaei et al. [3], various method has been developed to yield biodiesel, including direct use and blending, microemulsion, pyrolysis, and transesterification. Direct use and blending showed a high viscosity and free fatty acid due to the incomplete reaction, even though this method offered a low-cost production. Microemulsion methods facilitated biodiesel production with lower viscosity and higher liquidity. However, the obtained biodiesel using the microemulsion method has a heavy deposition of carbon and inadequate combustion. Pyrolysis exhibited satisfactory physical and chemical properties of the yielded biodiesel. Nevertheless,

the production cost of pyrolysis is very high. The transesterification method is a common method for biodiesel production. The transesterification method is carried out at 60–70 °C to convert the oils and fats into biodiesel in the presence of a suitable catalyst [4-5]. Besides, biodiesel production via transesterification methods can be conducted using various types of feedstocks that contain free fatty acids and/or triglycerides [6]. Various edible oil was used for biodiesel production, including canola oil [7-8], rapeseed oil [9], peanut oil [10], sunflower oil [11-12], coconut oil [13], palm oil [14-15], and safflower oil [16]. However, utilizing edible sources for biodiesel production led to ecological imbalances and deforestation. Therefore, non-edible oil can be used as an alternative feedstock for biodiesel production. The usage of non-edible oil decreases the edible oil

dependency and reduces the competition for feed and food [17]. Various non-edible oils have been successfully converted into biodiesel, including jatropha oil [18], karanja oil [19], mahua oil [20], and moringa oil [21]. Among all the potential non-edible oil, candlenut oil is a potentially new feedstock for biodiesel generation. Candlenut (*Aleurites moluccana* L.) is a type of plant that contains a fairly high oil content, approximately 55–65% oil in its seeds. Candlenut oil is flammable making it able to be used as a fuel. Previous research has shown that *A. moluccana* could produce biodiesel with superior properties when combined with an ester content of more than 99% [22]. Generally, biodiesel production via an esterification reaction is carried out using a homogeneous catalyst such as sulfuric acid [23-24], potassium hydroxide [25], and sodium hydroxide [26]. However, the use of homogeneous catalysts still has several disadvantages, such as being less economical since they are only used once and require a lot of solvents to wash the reaction products [27]. Therefore, using heterogeneous catalysts can be an alternative to overcome these problems.

Photocatalytic-assisted transesterification has been developed to generate biodiesel. Photocatalytic-assisted transesterification was carried out at room temperature, which is beneficial to reduce energy consumption since the transesterification process was normally done at various temperatures. Previously, Corro et al. [28] developed photocatalytic-assisted transesterification to yield biodiesel from waste frying oil. They combined chromium (Cr) and silica (SiO₂) as a heterogeneous photocatalyst to produce biodiesel. Interestingly, the addition of Cr on SiO₂ facilitated the photoreaction to yield the biodiesel with a fatty acid methyl ester (FAME) percentage of ~98%. TiO₂ has also been reported for biodiesel production via a photocatalytic process. As reported by Ambrosio et al. [29], FAME percentages were achieved at 95% using TiO₂/H₂O₂ system under Hg lamp vapor irradiation.

Apart from that, zinc oxide (ZnO) was also developed for biodiesel production [4,30]. ZnO has a strong acid site which makes this oxide being able to be applied as a catalyst in reactions that require acidic

properties, such as esterification reactions to produce biodiesel, which composed of FAME [31]. The strong Lewis acid of ZnO was generated by the appearance of Zn²⁺ at the outermost layer of the ZnO surface [32]. In addition, ZnO can easily form nano-sized particle, which plays a crucial role and resolve various bottleneck problems associated with the esterification process in biodiesel production. The nano-sized ZnO also increases the selectivity and catalytic activity [33]. Due to its hexagonal wurtzite nature, nano-sized ZnO also possesses a higher affinity and oxygen vacancy [34-35].

Various methods have been used to obtain nano-sized ZnO, including coprecipitation [36], hydrothermal [37], solvothermal [38], solid-state [39], electrochemical [40], and precursor thermal decomposition [41]. However, the mentioned synthesis methods have disadvantages to the synthesis of nano-sized ZnO. Coprecipitation requires a stabilizer and needs post-treatment to remove the impurities. Hydrothermal and solvothermal require autoclave reactors and are challenging to control the size of ZnO. Solid-state is a simple method to synthesize ZnO. However, this process must be carried out several times in order to yield a nanoparticle of ZnO. The electrochemical method is very suitable for generating ZnO with controlled size and morphology. However, the equipment for the electrochemical process is expensive. Thermal deposition is an excellent method to prepare a high purity of nano-ZnO. Despite its advantages, the equipment is very expensive, and the source material may be limited. In order to overcome the disadvantages, the polyol method has been designed to generate a nano-sized ZnO. The polyol technique is a nanoparticle synthesis method that utilizes different types of diols as reaction media [42]. Polyols also act as stabilizing agents and regulate particle growth. This method has many advantages due to the process being easy, simple, and flexible. Furthermore, the polyol technique offers the ability to form nanoparticles directly, does not require a calcination process, and the growth of nanoparticles can be controlled both in shape and size [43].

As proposed in this work, the production of biodiesel has been done at room temperature using

nano-sized ZnO. ZnO was prepared by polyol methods. The polyol methods facilitated the formation of nano-sized ZnO. In addition, polyol methods also promoted the formation of mesoporous ZnO, which is very advantageous to attach the precursor to obtain biodiesel. The optimization of photocatalyst dosage and reaction time were investigated to provide the optimum condition for biodiesel production using ZnO at room temperature.

■ EXPERIMENTAL SECTION

Materials

The materials used in this study were sodium hydroxide (NaOH, Sigma-Aldrich, 99%), zinc acetate dihydrate ($\text{Zn}(\text{CH}_3\text{COO})_2 \cdot \text{H}_2\text{O}$, Sigma-Aldrich, 99.5%), diethylene glycol (DEG, Sigma-Aldrich, 99%), ethanol (EtOH, Full time, 96%), acetone (Full time, 99%), methanol (Merck, 99%), and demineralized water. The candlenut oil was bought from SIPA, Sidoarjo, Indonesia.

Instrumentation

In this study, several instruments were used to investigate the properties of ZnO. The crystallinity and structural phase of the synthesized ZnO nanocatalyst was verified through X-ray diffraction (XRD, Philips PW1140/90) with Cu-K α radiation (λ) of 0.15406 nm and 0–80° scanning angle range at room temperature. The surface morphologies and the particle sizes were analyzed through the field emission scanning electron microscope (FESEM, Thermo Scientific Quattro S) and transmission electron microscope (TEM Hitachi HT7700). The total surface area and the pore size distributions were measured using the nitrogen (N_2) physisorption (Quantachrome Nova 4200e) at 77 K using the NLDFT analysis method with a degassing temperature of 120 °C for 8 h. The resulted photo-transesterification was analyzed using Gas chromatography-mass spectrometry (GC-MS, Agilent Technologies 7890A GC-5975MS)

Procedure

Synthesis of ZnO nanocatalyst

ZnO nanoparticles were synthesized by polyol technique using a reflux system as shown in Fig. 1(a), the same technique used in the previous study carried out by Hosni et al. [42]. The concentration of Zn^{2+} (z) was

0.5 mol L⁻¹, the ratio of $\text{H}_2\text{O}:\text{Zn}^{2+}$ concentration (h) was 5:1, and the ratio of $\text{NaOH}:\text{Zn}^{2+}$ (b) was 1:1. The synthesis mixture was prepared by dissolving 21.95 g of $\text{Zn}(\text{CH}_3\text{COO})_2 \cdot \text{H}_2\text{O}$, 4 g of NaOH, and 5.4 mL of demineralized water in 194.6 mL of DEG. The mixture was subsequently refluxed for 2 h at 161 °C whilst being stirred at 600 rpm until a white mixture was obtained. The mixture was then centrifuged at 10,000 rpm for 5 min in order to separate the white suspension from the solvent. Next, the white suspension obtained was washed several times with EtOH (Full time, 96%) and acetone (Full time, 99%). Subsequently, the product was dried at 80 °C for 48 h until the white powder was obtained.

Esterification of candlenut oil

The esterification reaction of candlenut oil was carried out with a ratio of oil to methanol of 1:3. Initially, 100 g (108.13 mL) of candlenut oil and 43.25 mL of methanol were prepared in a batch reactor as depicted in Fig. 1(b). Thereafter, the various amounts of ZnO nanocatalyst were added and the running times were started. The reactions were carried out for 60, 120, and 180 min with continuous stirring at 400 rpm. During the reaction, the UV-LED lamp was turned on to drive the photocatalytic reaction. After the reaction times had finished, each phase of the mixture was separated using a centrifuge at 10,000 rpm for 5 min. The mixture was separated into three phases, the upper phase was the excess of the methanol, the middle phase was the main product, and the lower phase was the catalyst. Subsequently, the composition of the main product was further analyzed with GC-MS.

■ RESULTS AND DISCUSSION

Morphologies and Properties of ZnO

The phase structure, crystallinity, and pore properties of the ZnO catalyst were synthesized using the polyol technique, as illustrated in Fig. 1. The XRD results in Fig. 2(a) signified that the synthesized ZnO had similar characteristic peaks with a standard ZnO (JCPDS No. 36-1451), indicating that the synthesized ZnO had a hexagonal (wurtzite) structure. The characteristic peaks of ZnO synthesized by the polyol technique were observed

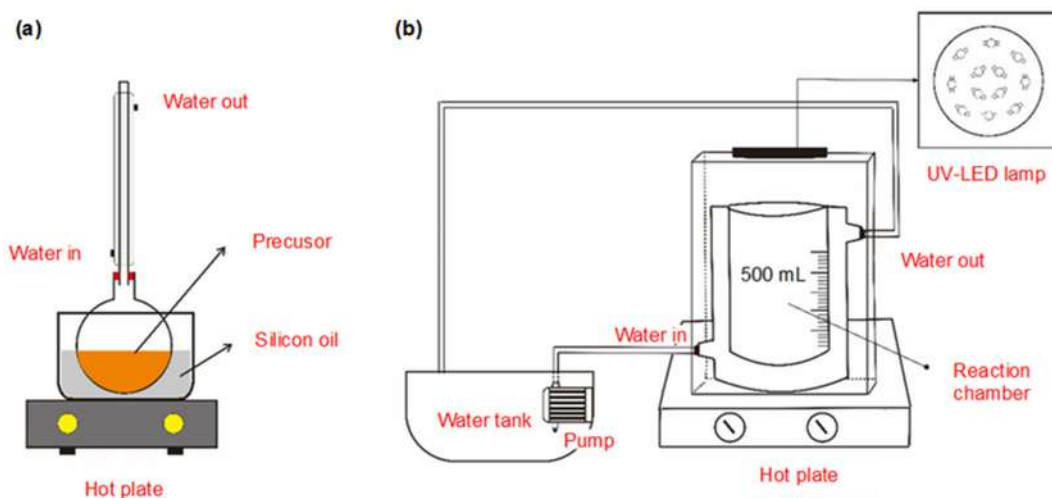


Fig 1. (a) Reflux system for polyol method and (b) batch photocatalytic reactor for biodiesel production

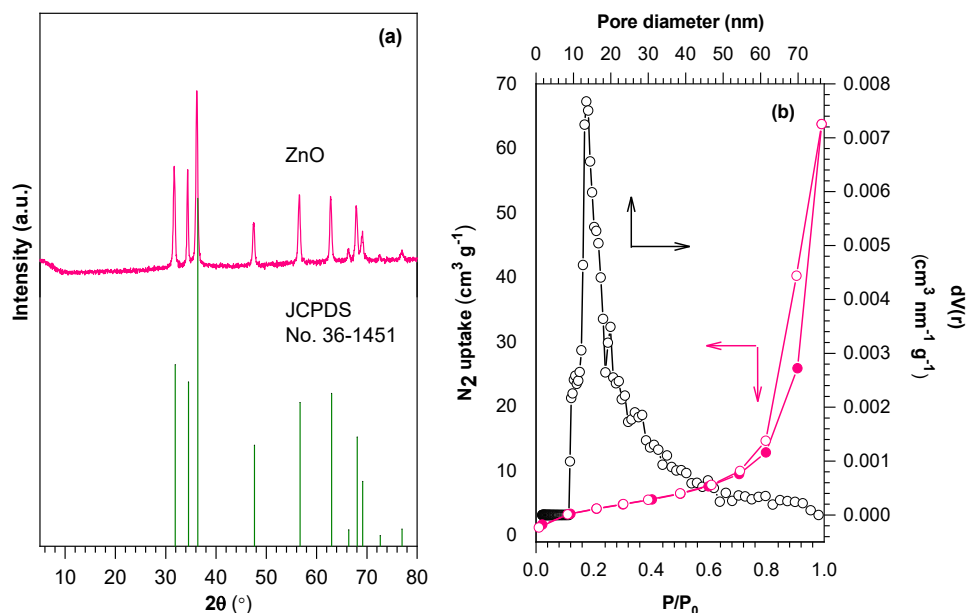


Fig 2. (a) XRD pattern of ZnO, (b) N_2 adsorption-desorption and pore size diameter of ZnO

at $2\theta = 31.67^\circ$, 34.40° , and 36.17° associated with the (100), (002), and (101) plane, which is in line with previous studies [36,44] using coprecipitation methods and gelatine templates, respectively. The sharp peaks with high intensity hinted that the synthesized ZnO had a crystalline structure without any post-synthesis heat treatment. In addition, the absence of impurities was observed, indicating that the polyol method promotes the formation of ZnO with good purity. The intensity of (101) peak is higher compared to other peaks, revealing that ZnO grows to the (101) direction [45]. Additionally, those

peaks are shifted approximately 0.08° compared to the JCPDS standard, indicating the enhancement of interplanar spacing due to the formation of oxygen vacancy [46]. This result is in agreement with the previous study by Bi et al. [47], showing that the formation of oxygen vacancy enhances the interplanar spacing and results in the decrease of (101) diffraction angle.

The porosity of the synthesized ZnO nanocatalyst was investigated using the N_2 adsorption-desorption isotherm. The surface area and pore size distribution were also calculated by implementing the NLDFT

calculation method, and the results are shown in Fig. 2(b). The total surface area of the synthesized ZnO is $15.5 \text{ m}^2 \text{ g}^{-1}$. The prepared ZnO shows a low amount of N_2 adsorption at P/P_0 of 0–0.7 and subsequently enhanced until P/P_0 of 0.99. The obtained isotherm signifies a type IV isotherm according to IUPAC recommendation, revealing that the prepared ZnO is a mesoporous material [44]. The hysteresis loop is also generated in ZnO due to the condensation process during the desorption process [48]. The yielded hysteresis loop in ZnO is associated with H3-type hysteresis, corresponding to interconnected mesopores with non-uniform shape and size [49], which is confirmed by FESEM and TEM analysis. The type of hysteresis demonstrates the mesopores materials with agglomerate or aggregates characteristic of nanoparticles forming slit-shaped pores with non-uniform size and shape [50]. The hysteresis loop at $P/P_0 \sim 0.85\text{--}0.99$ indicates the formation of interparticle voids caused by textural porosity between the particles [51]. Based on the pore size distribution calculation, it is exhibited that the pore sizes of synthesized ZnO are mostly around 12 nm.

FESEM and TEM are shown in Fig. 3. Based on the

FESEM result in Fig. 3(a), the polyol technique used in this study has successfully produced ZnO with nanoparticle sizes. The ZnO nanoparticles agglomerate and generate a big particle size in micrometer. This result is in line with the previous study by Mahamuni et al. [52] that reported the agglomeration of nanoparticle ZnO synthesized by the polyol method. In order to obtain better imaging information in relation to the size and shape of the synthesized ZnO nanoparticles, TEM analysis was carried out, as depicted in Fig. 3(b). In terms of the shapes of the particles, they are relatively hexagonal, rod, and spherical. The particle size of ZnO is confirmed using particle size distribution by estimating 100 individual particles of the projected area in the TEM images, as shown in Fig. 4. The average diameter size of ZnO is found in the range of 10–210 nm. The average diameter of 20–80 nm shows a high frequency of ZnO, indicating that most of the synthesized ZnO size is under 100 nm. Compared to the previous study by Chieng and Loo [53], the obtained ZnO has a similar size (under 100 nm) which confirmed that the polyol method can promote the generation of nano-sized ZnO.

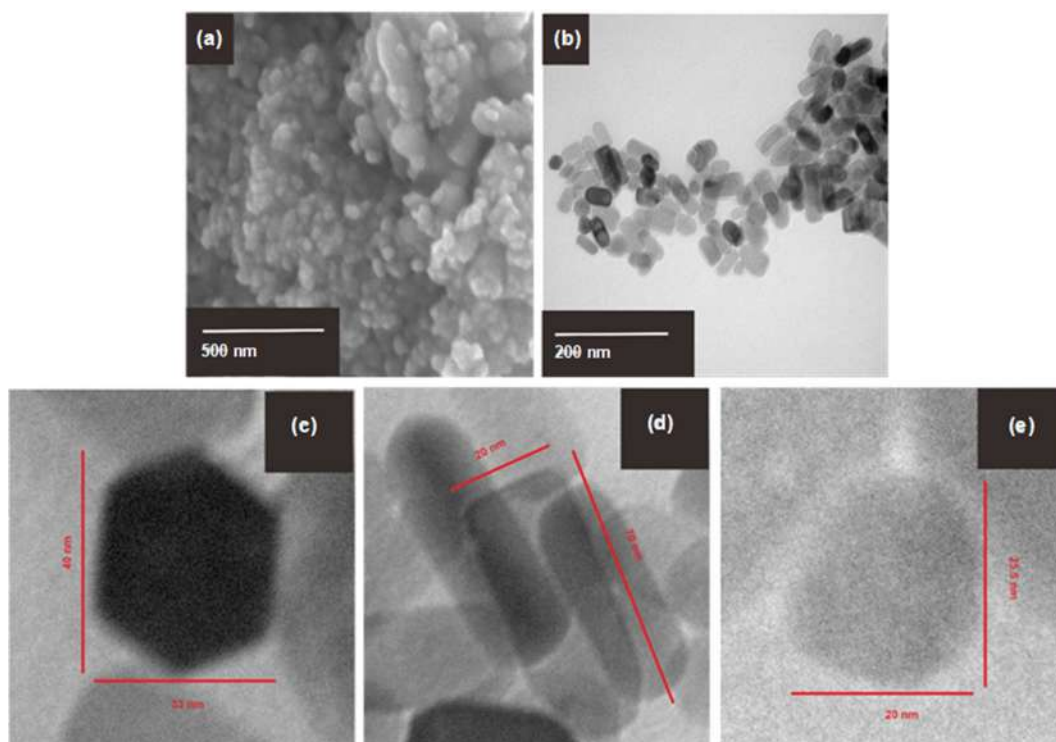


Fig 3. (a) FESEM, (b) TEM images of ZnO, and the (c) hexagonal, (d) rods and (e) sphere morphology of ZnO

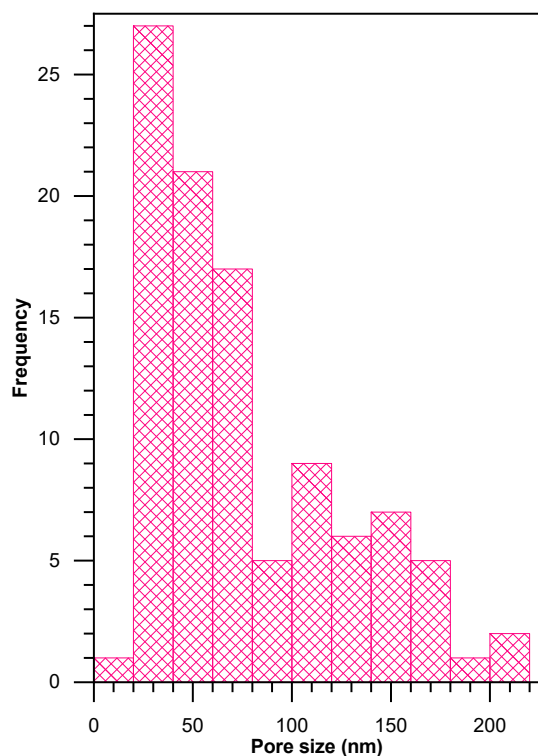


Fig 4. Pore size distribution of ZnO

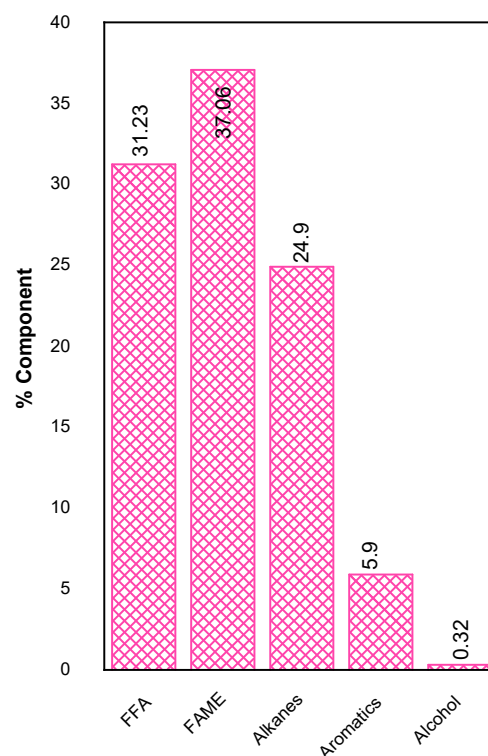


Fig 5. Component of candlenut oil

Photo Esterification of Candlenut Oil

Fig. 5 shows the components of candlenut oil used in this study. The main components were FFA, FAME, and alkanes compounds. Candlenut oil also contains a small number of aromatic compounds and alcohol. The GC-MS results showed that the candlenut oil contained a high amount of FFA of approximately 31.23%. The main FFA compounds in the candlenut oil were linoleic acid (9(Z),12(Z)-octadecadienoic acid) and palmitic acid (*n*-hexadecanoic acid). The candlenut oil itself initially contains approximately 37.06% FAME compounds. In this study, the FFA content of candlenut oil was converted into FAME compounds through an esterification reaction with methanol and ZnO polyol nanocatalyst.

Fig. 6(a) displays the effects of ZnO polyol nanocatalyst amount (%w/w ZnO/candlenut oil) to the FAME percentage results for 180 min esterification time with an oil: methanol ratio of 1:3 at room temperature whilst being stirred at 400 rpm. The results signified that the addition of ZnO polyol nanocatalyst to the reaction was able to increase the FAME yield. The plot also revealed that the amount of FAME percentage increased

with increasing the amount of ZnO polyol nanocatalyst (0.5, 1.5, and 2.0%). Increasing the amount of ZnO led to enhancing the active surface for the photo-transesterification process. Consequently, the amount of generated FAME is increased [54]. An optimum FAME yield can be obtained after adding 2.0% of ZnO polyol nano catalyst to the reaction, with FAME percentage result obtained is approximately 70.76%. This result also demonstrated that the synthesized ZnO nano through the polyol method was successfully performed as a catalyst to convert FFA into FAME in the esterification reaction of candlenut oil. However, the percentage of FAME is slightly reduced compared to the previous study by Zhang et al. [55], reporting that the FAME conversion from waste cooking soybean oil was 100% using graphitic carbon nitride supported molybdenum catalyst. This result is very reasonable since only ZnO is used as a photocatalyst, yielding a fast recombination process compared to modified photocatalysts [56]. As a result, the transesterification process promoted by the photo-redox reaction is low compared to modified photocatalysts.

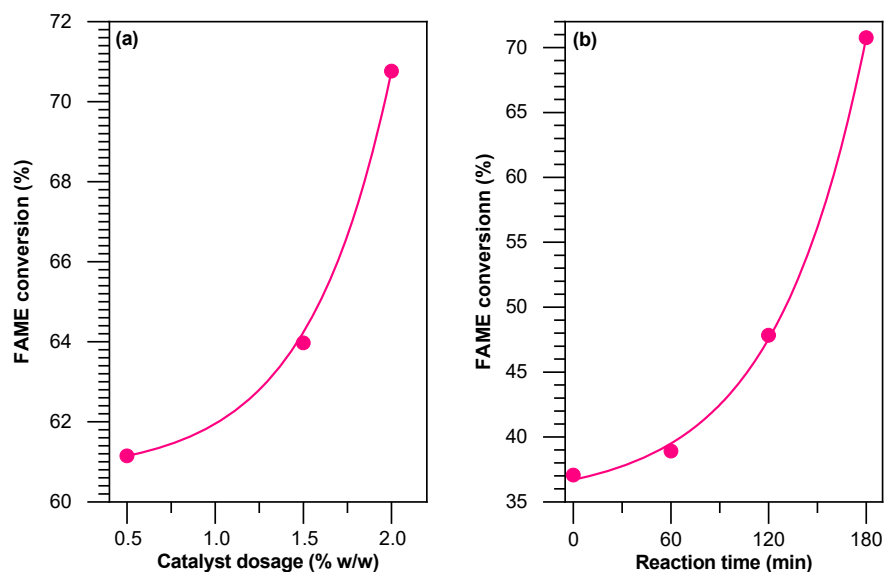


Fig 6. (a) Effect of catalyst dosage (b) Effect of esterification time

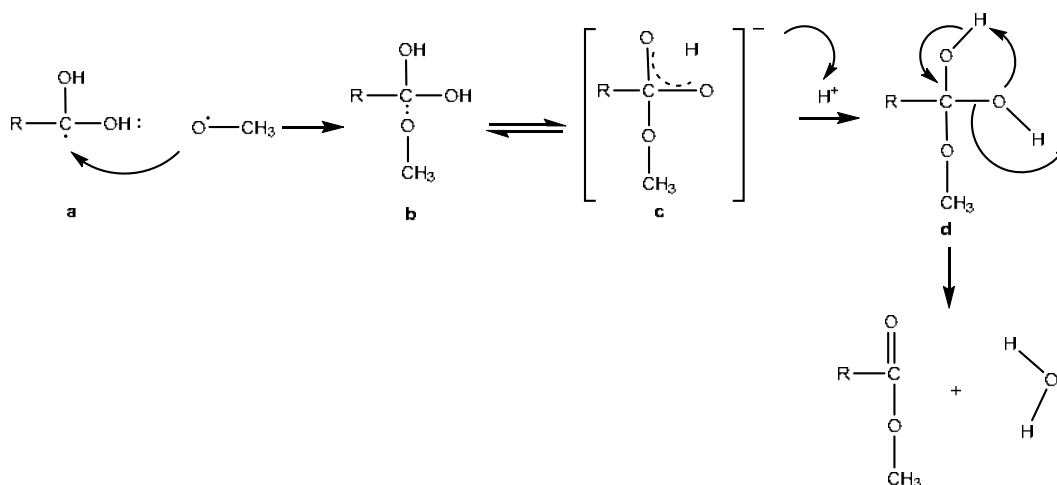


Fig 7. Proposed mechanism of oil and methanol photo-esterification through ZnO catalyst

Fig. 6(b) displays the effects of esterification time (60, 120, and 180 min) with respect to the FAME percentage result in the presence of 2.0% ZnO polyol nanocatalyst with oil: methanol ratio of 1:3 at room temperature whilst being stirred at 400 rpm. The result hinted that the reaction time highly affected the FAME percentage result. A small increase in FAME percentage was obtained after the reagent was being reacted for 60 min. Increasing the reaction time significantly increased the FAME percentage result, which was around 47% and 70% for 120 and 180 min reaction time, respectively. It can be seen that increasing the time temperature enhanced the time of the transesterification

reaction via the photocatalysis process. According to the process, the photocatalytic process promotes the transesterification process to yield biodiesel. During the UV light irradiation, electrons on the valence band (VB) of ZnO were excited to the conduction band of ZnO. At the time, holes were also generated on the VB of ZnO. The electrons would react with the FFA molecule to form a radical compound of FFA (compound a) [28]. Besides, holes would react with methanol to form methanol radicals and protons. Methanol radical would react with FFA methanol to form compound b, followed by attacking H⁺ to yield compound c. Since the oxygen atom has a lone pair electron, it is possible to attack the

hydrogen atom of a hydroxyl group in compound **d**, which has the lowest electronegativity. Thus, the oxygen atom of the hydroxyl group reacted with the hydrogen atom of another hydroxyl group and yielded a water molecule and methyl ester group, as illustrated in Fig. 7.

■ CONCLUSION

The production of biodiesel from candlenut oil using ZnO via photocatalytic-assisted transesterification has been successfully carried out. ZnO was prepared via the polyol method and exhibited a nanoparticle size of 20–200 nm and a surface area of 15.5 m² g⁻¹. The pore size distribution of ZnO was mostly around 10–20 nm. Besides, various morphologies were generated by polyol methods, including spherical, rods, and hexagonal. The GC-MS result reported that the application of the candlenut oil esterification reaction was successfully carried out. The FFA content in candlenut oil has been converted into FAME with the assistance of nano-ZnO polyol as the catalyst. The effect of ZnO percentage and esterification time revealed that the FAME percentage increased either along with the increasing ZnO percentage (0.5, 1.5, and 2.0% w/w) or with the increasing reaction time (0, 60, 120, and 180 min). The yield of FAME percentage was approximately 70.76%, which was obtained in the reaction using 2.0% nano-ZnO polyol under 180 min reaction time at room temperature whilst being stirred constantly at 400 rpm. The photocatalytic process promotes the transesterification process at room temperature, which is beneficial for reducing energy consumption. Apart from that, a moderate FAME percentage is obtained due to the limitation of ZnO in charge carrier transfer and separation as a single photocatalyst.

■ ACKNOWLEDGMENTS

The authors gratefully thank the Deputy for Research and Development, Ministry of Research and Technology of the Republic of Indonesia for funding this research through the Fundamental Research Scheme with contract number 1510/PKS/ITS/2022.

■ REFERENCES

- [1] Maleki, B., and Talesh, S.S.A., 2022, Optimization of ZnO incorporation to $\alpha\text{Fe}_2\text{O}_3$ nanoparticles as an efficient catalyst for biodiesel production in a sonoreactor: Application on the CI engine, *Renewable Energy*, 182, 43–59.
- [2] Abukhadra, M.R., Ibrahim, S.M., Yakout, S.M., El-Zaidy, M.E., and Abdeltawab, A.A., 2019, Synthesis of Na⁺ trapped bentonite/zeolite-P composite as a novel catalyst for effective production of biodiesel from palm oil: Effect of ultrasonic irradiation and mechanism, *Energy Convers. Manage.*, 196, 739–750.
- [3] Tabatabaei, M., Aghbashlo, M., Dehghani, M., Panahi, H.K.S., Mollahosseini, A., Hosseini, M., and Soufiyan, M.M., 2019, Reactor technologies for biodiesel production and processing: A review, *Prog. Energy Combust. Sci.*, 74, 239–303.
- [4] Rao, A.V.R.K., Dudhe, P., and Chelvam, V., 2021, Role of oxygen defects in basicity of Se doped ZnO nanocatalyst for enhanced triglyceride transesterification in biodiesel production, *Catal. Commun.*, 149, 106258.
- [5] Avhad, M.R., and Marchetti, J.M., 2016, Innovation in solid heterogeneous catalysis for the generation of economically viable and ecofriendly biodiesel: A review, *Catal. Rev.: Sci. Eng.*, 58 (2), 157–208.
- [6] Hoekman, S.K., Broch, A., Robbins, C., Cenicerros, E., and Natarajan, M., 2012, Review of biodiesel composition, properties, and specifications, *Renewable Sustainable Energy Rev.*, 16 (1), 143–169.
- [7] Khatibi, M., Khorasheh, F., and Larimi, A., 2021, Biodiesel production via transesterification of canola oil in the presence of Na–K doped CaO derived from calcined eggshell, *Renewable Energy*, 163, 1626–1636.
- [8] Murguía-Ortiz, D., Cordova, I., Manriquez, M.E., Ortiz-Islas, E., Cabrera-Sierra, R., Contreras, J.L., Alcántar-Vázquez, B., Trejo-Rubio, M., Vázquez-Rodríguez, J.T., and Castro, L.V., 2021, Na-CaO/MgO dolomites used as heterogeneous catalysts in canola oil transesterification for biodiesel production, *Mater. Lett.*, 291, 129587.
- [9] Fallah Kelarijani, A., Gholipour Zanjani, N., and Kamran Pirzaman, A., 2020, Ultrasonic assisted transesterification of rapeseed oil to biodiesel using

- nano magnetic catalysts, *Waste Biomass Valorization*, 11 (6), 2613–2621.
- [10] Jung, S., Kim, M., Jeon, Y.J., Tsang, Y.F., Bhatnagar, A., and Kwon, E.E., 2021, Valorization of aflatoxin contaminated peanut into biodiesel through non-catalytic transesterification, *J. Hazard. Mater.*, 416, 125845.
- [11] Salmasi, M.S., Kazemeini, M., and Sadjadi, S., 2020, Transesterification of sunflower oil to biodiesel fuel utilizing a novel K_2CO_3 /Talc catalyst: Process optimization and kinetics investigations, *Ind. Crops Prod.*, 156, 112846.
- [12] Lima, A.C., Hachemane, K., Ribeiro, A.E., Queiroz, A., Gomes, M.C.S., and Brito, P., 2022, Evaluation and kinetic study of alkaline ionic liquid for biodiesel production through transesterification of sunflower oil, *Fuel*, 324, 124586.
- [13] Ahmad, A.A., Zulkurnain, N., Mat Rosid, S.J., Azid, A., Endut, A., Toemen, S., Ismail, S., Wan Abdullah, W.N., Aziz, S.M., Mohammed Yusoff, N., Mat Rosid, S., and Nasir, N.A., 2022, Catalytic transesterification of coconut oil in biodiesel production: A review, *Catal. Surv. Asia*, 26 (3), 129–143.
- [14] Qu, T., Niu, S., Zhang, X., Han, K., and Lu, C., 2021, Preparation of calcium modified Zn-Ce/ Al_2O_3 heterogeneous catalyst for biodiesel production through transesterification of palm oil with methanol optimized by response surface methodology, *Fuel*, 284, 118986.
- [15] Woranuch, W., Ngaosuwan, K., Kiatkittipong, W., Wongsawaeng, D., Appamana, W., Powell, J., Lalthazuala Rokhum, S., and Assabumrungrat, S., 2022, Fine-tuned fabrication parameters of CaO catalyst pellets for transesterification of palm oil to biodiesel, *Fuel*, 323, 124356.
- [16] Nogales-Degaldo, S., Encinar, J.M., and González Cortés, Á., 2021, High oleic safflower oil as a feedstock for stable biodiesel and biolubricant production, *Ind. Crop Prod.*, 170, 113701.
- [17] Mathew, G.M., Raina, D., Narisetty, V., Kumar, V., Saran, S., Pugazhendi, A., Sindhu, R., Pandey, A., and Binod, P., 2021, Recent advances in biodiesel production: Challenges and solutions, *Sci. Total Environ.*, 794, 148751.
- [18] Athar, M., Imdad, S., Zaidi, S., Yusuf, M., Kamyab, H., Jaromír Klemeš, J., and Chelliapan, S., 2022, Biodiesel production by single-step acid-catalysed transesterification of jatropha oil under microwave heating with modelling and optimisation using response surface methodology, *Fuel*, 322, 124205.
- [19] Kumar, R., and Pal, P., 2021, Lipase immobilized graphene oxide biocatalyst assisted enzymatic transesterification of *Pongamia pinnata* (karanja) oil and downstream enrichment of biodiesel by solar-driven direct contact membrane distillation followed by ultrafiltration, *Fuel Process. Technol.*, 211, 106577.
- [20] Gandhi, S.S., and Gogate, P.R., 2021, Process intensification of fatty acid ester production using esterification followed by transesterification of high acid value mahua (*Iluppai ennai*) oil: Comparison of the ultrasonic reactors, *Fuel*, 294, 120560.
- [21] Rashid, U., Anwar, F., Ashraf, M., Saleem, M., and Yusup, S., 2011, Application of response surface methodology for optimizing transesterification of *Moringa oleifera* oil: Biodiesel production, *Energy Convers. Manage.*, 52 (8-9), 3034–3042.
- [22] de O Lima, J.R., Gasparini, F., Camargo, N.D.L., Ghani, Y.A., da Silva, R.B., and de Oliveira, J.E., 2011, Indian-nut (*Aleurites moluccana*) and tucum (*Astrocaryum vulgare*), non agricultural sources for biodiesel production using ethanol composition, characterization and optimization of the reactional production conditions, *World Renewable Energy Congress – Sweden*, 8-13 May 2011, Linköping, Sweden, 109–116.
- [23] Juwono, H., Triyono, T., Sutarno, S., Wahyuni, E.T., Ulfin, I., and Kurniawan, F., 2017, Production of biodiesel from seed oil of nyamplung (*Calophyllum inophyllum*) by Al-MCM-41 and its performance in diesel engine, *Indones. J. Chem.*, 17 (2), 316–321.
- [24] Redjeki, A.S., Sukirno, S., and Slamet, S., 2019, Photocatalytic esterification process for methyl

- ester synthesis from kemiri sunan oil: A novel approach, *AIP Conf. Proc.*, 2085 (1), 020058.
- [25] Rahman, M.A., Aziz, M.A., Al-khulaidim, R.A., Sakib, N., and Islam, M., 2017, Biodiesel production from microalgae *Spirulina maxima* by two step process: Optimization of process variable, *J. Radiat. Res. Appl. Sci.*, 10 (2), 140–147.
- [26] Zhang, Y., and You, H., 2015, Study on biodiesel production from rapeseed oil through the orthogonal method, *Energy Sources, Part A*, 37 (4), 422–427.
- [27] Al-Saadi, A., Mathan, B., and He, Y., 2020, Esterification and transesterification over SrO–ZnO/Al₂O₃ as a novel bifunctional catalyst for biodiesel production, *Renewable Energy*, 158, 388–399.
- [28] Corro, G., Sánchez, N., Pal, U., Cebada, S., and Fierro, J.L.G., 2017, Solar-irradiation driven biodiesel production using Cr/SiO₂ photocatalyst exploiting cooperative interaction between Cr⁶⁺ and Cr³⁺ moieties, *Appl. Catal., B*, 203, 43–52.
- [29] Ambrosio, E., Lucca, D.L., Garcia, M.H.B., de Souza, M.T.F., de S. Freitas, T.K.F., de Souza, R.P., Visentainer, J.V., and Garcia, J.C., 2017, Optimization of photocatalytic degradation of biodiesel using TiO₂/H₂O₂ by experimental design, *Sci. Total Environ.*, 581–582, 1–9.
- [30] Wang, A., Quan, W., Zhang, H., Li, H., and Yang, S., 2021, Heterogeneous ZnO-containing catalysts for efficient biodiesel production, *RSC Adv.*, 11 (33), 20465–20478.
- [31] Bancquart, S., Vanhove, C., Pouilloux, Y., and Barrault, J., 2001, Glycerol transesterification with methyl stearate over solid basic catalysts: I. Relationship between activity and basicity, *Appl. Catal., A*, 218 (1-2), 1–11.
- [32] Kothandapani, J., Ganesan, A., Mani, G.K., Kulandaisamy, A.J., Rayappan, J.B.B., and Selva Ganesan, S., 2016, Zinc oxide surface: A versatile nanoplatform for solvent-free synthesis of diverse isatin derivatives, *Tetrahedron Lett.*, 57 (31), 3472–3475.
- [33] Baskar, G., and Aiswarya, R., 2016, Trends in catalytic production of biodiesel from various feedstocks, *Renewable Sustainable Energy Rev.*, 57, 496–504.
- [34] Yuan, H., Xu, M., and Huang, Q.Z., 2014, Effects of pH of the precursor sol on structural and optical properties of Cu-doped ZnO thin films, *J. Alloys Compd.*, 616, 401–407.
- [35] Dantas, J., Leal, E., Mapossa, A.B., Cornejo, D.R., and Costa, A.C.F.M., 2017, Magnetic nanocatalysts of Ni_{0.5}Zn_{0.5}Fe₂O₄ doped with Cu and performance evaluation in transesterification reaction for biodiesel production, *Fuel*, 191, 463–471.
- [36] Subagyo, R., Kusumawati, Y., and Widayatno, W.B., 2020, Kinetic study of methylene blue photocatalytic decolorization using zinc oxide under UV-LED irradiation, *AIP Conf. Proc.*, 2237, 02001.
- [37] Sun, X.M., Chen, X., Deng, Z.X., and Li, Y.D., 2003, A CTAB-assisted hydrothermal orientation growth of ZnO nanorods, *Mater. Chem. Phys.*, 78 (1), 99–104.
- [38] Guo, L., Ji, Y.L., Xu, H., Simon, P., and Wu, Z., 2002, Regularly shaped, single-crystalline ZnO nanorods with wurtzite structure, *J. Am. Chem. Soc.*, 124 (50), 14864–14865.
- [39] Wang, Z., Zhang, H., Zhang, L., Yuan, J., Yan, S., and Wang, C., 2003, Low-temperature synthesis of ZnO nanoparticles by solid-state pyrolytic, *Nanotechnology*, 14 (1), 11.
- [40] Khaleel, R.S., and Hashim, M.S., 2020, Fabrication of ZnO sensor to measure pressure, humidity and sense vapors at room temperature using the rapid breakdown anodization method, *Kuwait J. Sci.*, 47, 42–49.
- [41] Pillai, S.C., Kelly, J.M., McCormack, D.E., O'Brien, P., and Ramesh, R., 2003, The effect of processing conditions on varistors prepared from nanocrystalline ZnO, *J. Mater. Chem.*, 13 (10), 2586–2590.
- [42] Hosni, M., Kusumawati, Y., Farhat, S., Jouini, N., and Pauporté, T., 2014, Effects of oxide nanoparticle size and shape on electronic structure, charge transport, and recombination in dye-

- sensitized solar cell photoelectrodes, *J. Phys. Chem. C*, 118 (30), 16791–16798.
- [43] Dong, H., Chen, Y.C., and Feldmann, C., 2015, Polyol synthesis of nanoparticles: Status and options regarding metals, oxides, chalcogenides, and non-metal elements, *Green Chem.*, 17 (8), 4107–4132.
- [44] Prasetyoko, D., Sholeha, N.A., Subagyo, R., Ulfa, M., Bahruji, H., Holilah, H., Pradipta, M.F., and Jalil, A.A., 2023, Mesoporous ZnO nanoparticles using gelatin - Pluronic F127 as a double colloidal system for methylene blue photodegradation, *Korean J. Chem. Eng.*, 40 (1), 112–123.
- [45] Das, A., and Nair, R.G., 2020, Effect of aspect ratio on photocatalytic performance of hexagonal ZnO nanorods, *J. Alloys Compd.*, 817, 153277.
- [46] Bi, X., Du, G., Kalam, A., Sun, G., Yu, Y., Su, Q., Xu, B., and Al-Sehemi, A.G., 2021, Tuning oxygen vacancy content in TiO₂ nanoparticles to enhance the photocatalytic performance, *Chem. Eng. Sci.*, 234, 116440.
- [47] Bi, T., Du, Z., Chen, S., He, H., Shen, X., and Fu, Y., 2023, Preparation of flower-like ZnO photocatalyst with oxygen vacancy to enhance the photocatalytic degradation of methyl orange, *Appl. Surf. Sci.*, 614, 156240.
- [48] Subagyo, R., Tehubijuluw, H., Utomo, W.P., Rizqi, H.D., Kusumawati, Y., Bahruji, H., and Prasetyoko, D., 2022, Converting red mud wastes into mesoporous ZSM-5 decorated with TiO₂ as an eco-friendly and efficient adsorbent-photocatalyst for dyes removal, *Arabian J. Chem.*, 15 (5), 103754.
- [49] Liu, Y., She, N., Zhao, J., Peng, T., and Liu, C., 2013, Fabrication of hierarchical porous ZnO and its performance in Ni/ZnO reactive-adsorption desulfurization, *Pet. Sci.*, 10 (4), 589–595.
- [50] Santos, R.M.M., Tronto, J., Briois, V., and Santilli, C.V., 2017, Thermal decomposition and recovery properties of ZnAl-CO₃ layered double hydroxide for anionic dye adsorption: Insight into the aggregative nucleation and growth mechanism of the LDH memory effect, *J. Mater. Chem. A*, 5 (20), 9998–10009.
- [51] A'yuni, Q., Rahmayanti, A., Hartati, H., Purkan, P., Subagyo, R., Rohmah, N., Itsnaini, L.R., and Fitri, M.A., 2023, Synthesis and characterization of silica gel from Lapindo volcanic mud with ethanol as a cosolvent for desiccant applications, *RSC Adv.*, 13 (4), 2692–2699.
- [52] Mahamuni, P.P., Patil, P.M., Dhanavade, M.J., Badiger, M.V., Shadija, P.G., Lokhande, A.C., and Bohara, R.A., 2019, Synthesis and characterization of zinc oxide nanoparticles by using polyol chemistry for their antimicrobial and antibiofilm activity, *Biochem. Biophys. Rep.*, 17, 71–80.
- [53] Chieng, B.W., and Loo, Y.Y., 2012, Synthesis of ZnO nanoparticles by modified polyol method, *Mater. Lett.*, 73, 78–82.
- [54] Qamar, O.A., Jamil, F., Hussain, M., Bae, S., Inayat, A., Shah, N.S., Waris, A., Akhter, P., Kwon, E.E., and Park, Y.K., 2023, Advances in synthesis of TiO₂ nanoparticles and their application to biodiesel production: A review, *Chem. Eng. J.*, 460, 141734.
- [55] Zhang, W., Wang, C., Luo, B., He, P., Li, L., and Wu, G., 2023, Biodiesel production by transesterification of waste cooking oil in the presence of graphitic carbon nitride supported molybdenum catalyst, *Fuel*, 332 (Part 2), 126309.
- [56] Zulfa, L.L., Ediati, R., Hidayat, A.R.P., Subagyo, R., Faaizatunnisa, N., Kusumawati, Y., Hartanto, D., Widiastuti, N., Utomo, W.P., and Santoso, M., 2023, Synergistic effect of modified pore and heterojunction of MOF-derived α -Fe₂O₃/ZnO for superior photocatalytic degradation of methylene blue, *RSC Adv.*, 13 (6), 3818–3834.

Primer Pairs Specificity Test for Frog Meat Identification Using PCR Technique

Norman Yoshi Haryono^{1,2*}, Rizqi Layli Khusufi³, Delia Wahyu Pangesti³, Evi Susanti^{1,4},
Rina Rifqie Mariana⁵, Hartati Eko Wardani⁶, and Norazlinaliza Salim^{7,8}

¹Biotechnology Study Program, Department of Applied Science, Faculty of Mathematics and Natural Sciences, Universitas Negeri Malang, Jl. Semarang No. 5, Malang 65145, Indonesia

²Health and Food Centre, Institute of Research and Community Services, Universitas Negeri Malang, Jl. Semarang No. 5, Malang 65145, Indonesia

³Department of Biology, Faculty of Mathematics and Natural Sciences, Universitas Negeri Malang, Jl. Semarang No. 5, Malang 65145, Indonesia

⁴Department of Chemistry, Faculty of Mathematics and Natural Sciences, Universitas Negeri Malang, Jl. Semarang No. 5, Malang 65145, Indonesia

⁵Department of Culinary Arts, Faculty of Engineering, Universitas Negeri Malang, Jl. Semarang No. 5, Malang 65145, Indonesia

⁶Department of Public Health, Faculty of Sport Sciences, Universitas Negeri Malang, Jl. Semarang No. 5, Malang 65145, Indonesia

⁷Laboratory of Halal Science Research, Halal Products Research Institute, Universiti Putra Malaysia, 43300 UPM Serdang, Selangor, Malaysia

⁸Centre of Foundation Studies for Agricultural Science, Universiti Putra Malaysia, 43300 UPM Serdang, Selangor, Malaysia

* Corresponding author:

email: norman.haryono.fmipa@um.ac.id

Received: April 11, 2023

Accepted: August 16, 2023

DOI: 10.22146/ijc.83626

Abstract: Halal food assurance is becoming more important with the growth of the halal industry globally. Adulteration of halal meat products using non-halal sources such as pork, dog, boar, and even frog meat has become a major problem for moslems. The purpose of this study is to initiate the method for frog meat identification using polymerase chain reaction (PCR) technique. In this study, three primer pairs (Fk1-Rk1, Fk2-Rk2, Fk3-Rk3) were analyzed for their specificity toward frog meat against other common halal meat sources such as beef, chicken, shrimp, squid, and mackerel. The visualization of DNA amplification showed that primer pair Fk1-Rk1 produced primer-dimer, thus cannot be used for this circumstance. Primer pair Fk2-Rk2 showed a better result where DNA amplicon was produced at ~100 bp for frog meat and no amplicons for other meat. Primer pair Fk3-Rk3 showed a different pattern of DNA amplification for all the meat tested, where the amplicon of frog meat was shown at ~100 bp, while the other meat showed multiple amplicons or none. In conclusion, primer pairs Fk2-Rk2 and Fk3-Rk3 showed their potential as primer pairs for frog meat identification using PCR for implementing halal food assurance, although sensitivity analysis needs to be investigated.

Keywords: halal food assurance; adulteration; frog meat; polymerase chain reaction

■ INTRODUCTION

Most people, especially moslems, are now more aware of halal food assurance because moslems are not allowed to consume non-halal food [1-2]. This assurance might be based on the source, the additives, and the

procedures used during the product's preparation. This is in line with the growth of the halal food industry, which contributes 1.6 billion USD worldwide [3-5]. Due to the huge economic growth, halal food and beverages industries are susceptible to adulteration by cheaper and

even non-halal sources. Many sources such as dog, pork, and boar meat are even used as the replacement or addition for beef products for the producer to gain more profit [6]. As a result, the method to identify contaminated non-halal meat in the food product is greatly developed.

One of the meat sources that belong to non-halal food is frog meat. This is based on Fatwa number 4 year 2003, issued by Indonesia Ulema Council (*Majelis Ulama Indonesia*), stating that it is forbidden for moslems to consume frog meat, making it a non-halal food source. On the other hand, Indonesia is one of the biggest frog meat exporters in the world, making it prone to be used as meat substitution for halal food products. Although such a case rarely to none happens, a method for identifying frog meat should be established for precaution. A method that was used to analyze the presence of frog meat in the food products is based on the difference in spectrum profile from frog oil compared to other oils using Fourier transform infrared spectroscopy (FTIR) [7]. Having said that, the investigation did not reveal the comparison between the frog oil spectrum against another oil spectrum.

Another approach in doing determination of meat species is based on the volatile organic compounds (VOCs). A different source of meats produces a different ratio of the VOCs (e.g., hydrocarbons, alcohols, aldehydes, ketones, carboxylic acids, esters, etc.) that can be analyzed using gas chromatography-mass spectrometry (GC-MS) and even sensory device such as electronic nose because the different ratio of VOCs resulting different odor [8-9]. However, the preparation and analysis of oil using FTIR and VOCs using GC-MS are not quite practical. The cooking process and post-mortem treatment of the meat also could contribute to varying those ratios.

The most popular method to make identification of meat sources is based on protein and DNA analysis. Although protein-based analysis has some edges, particularly in the practical sense, such as the availability of various protein kit analyses and relatively affordable, it has a major drawback when compared to DNA-based analysis, especially for products that have been extensively processed [10]. This is because DNA is much more stable

under extreme conditions and not easily denatured [11]. Therefore, DNA-based analysis using polymerase chain reaction (PCR) remains the most popular method to distinguish contamination of non-halal meat in food products.

Identification of the presence of dog meat in beef meatballs was successfully investigated using real-time PCR using the primer pair designed out of cytochrome-*b* nucleotides [12]. Another PCR method, namely two direct-triplex PCR, was used to identify various meat ranging from pork, beef, horse, chicken, turkey, dog, lamb, and buffalo meats, which later developed into direct pentaplex PCR [13-14]. However, the investigation to identify frog meat using the PCR method has yet to be carried out. Therefore, this study aimed to develop the method of frog meat identification using the PCR technique to support the halal food assurance implemented by the government. This study focuses on the selection of primer candidates that can be used for frog meat identification using PCR.

■ EXPERIMENTAL SECTION

Materials

Materials used include various meat such as frog (K), beef (S), chicken (A), shrimp (U), squid (C), mackerel (T), 70% alcohol, sterile distilled water (SDW), DNA isolation reagent DNEasy Blood & Tissue Kit (Qiagen), Dreamtaq Green PCR master Mix 2x (Thermo Fisher Scientific), and three pairs of primers based on cytochrome *b* (cyt-*b*) target gene (primer Fk1-Rk1, Fk2-Rk2, and Fk3-Rk3).

Instrumentation

The instrumentation used were analytical balance (Kern ABJ-2204NM), microcentrifuge (Tomy), NanoDrop Spectrophotometer (Thermo Fisher Scientific), electrophoresis machine (MUPID-eXU), UV transilluminator (Uvitec Firereader V10 Plus), and Mastercycler Nexus PCR Cycler (Eppendorf).

Procedure

Primer design

Primer design was carried out using BioEdit version 7.0.4.1 software. The cyt-*b* genes from eight frog species

and three other *cyt-b* genes from cow, chicken, and goat were aligned to tabulate out the conserved nucleotide region amongst them. The chosen primer pair (later called Fk1 and Rk1) was based on the similarity between eight frog species and the most differences with the other three. All of the genes were obtained from NCBI (<https://www.ncbi.nlm.nih.gov/>) with the accession number as follows: L08376.1 (*Gallus gallus*), D34635.1 (*Bos taurus*), D84201.1 (*Capra hircus*), KU246049.1 (*Rana kukunoris*), MF370348.1 (*Rana amurensis*), KX686108.1 (*Rana catesbeiana*), AF205091.1 (*Rana dybowskii*), AF205087.1 (*Rana nigromaculata*), AF205088.1, (*Rana plancyi*), AF205093.1 (*Rana rugosa*), and NC_042226.1 (*Rana temporaria*). The second and third primer pairs (Fk2, Rk2, Fk3, and Rk3) were microsatellite markers in the common frog (*R. temporaria*) previously used for investigations of population structure and reproductive behavior in *R. temporaria* [15]. The sequence of all primer pairs is shown in Table 1.

DNA isolation and quantification

Frog meat (*R. catesbeiana*) as well as beef, chicken, shrimp, squid, and mackerel meat, were weighed for 100 mg and transferred to a 2 mL microtube. The meat was crushed using micropistol, and the DNA was isolated using DNEasy Blood & Tissue Kit from Qiagen. The amount of isolated DNA and also its purity was quantified using NanoDrop® spectrophotometer (Thermo Fisher Scientific) by measuring the absorbance at 260 and 280 nm. The DNA purity was calculated by dividing the absorbance of 260 nm by the absorbance of 280 nm, which was classified as pure DNA if the result is between 1.8–2.0.

DNA amplification and visualization

DNA amplifications were conducted using the Eppendorf Mastercycler Nexus PCR Cycler with the cocktail PCR in Table 2. The PCR reaction was performed

under the conditions: pre-denaturation at 95 °C for 5 min, denaturation at 95 °C, and annealing for 1 min (annealing temperatures for primer pair number 1, 2, and 3 were 52, 56, and 56 °C, respectively), extension at 72 °C for 1 min, this process was repeated for 40 cycles. For the last cycle, the extension was prolonged for another 10 min.

Qualitative analysis of the DNA band was carried out using the MUPID-eXU electrophoresis machine. Separation of DNA fragments was performed using 1% agarose containing 0.01% (v/v) EtBr at 50 V for 60 min. The DNA band was then visualized using UV transilluminator Uvitec Firereader V10 Plus.

Data analysis

All the selected primers were analyzed using Nucleotide BLAST or BLASTn (<https://blast.ncbi.nlm.nih.gov/Blast.cgi>) to obtain the similarity of the primer sequence with all the databases stored in NCBI. This analysis helps to ensure the specificity of the primers towards the targeted organism. To gather information regarding primer's characteristics such as GC content, melting temperature (T_m) value, and hairpin formation, the online software Sequence Manipulation Suite: PCR Primer Stats (https://www.bioinformatics.org/sms2/pcr_primer_stats.html) was used. These primer characteristics are useful to determine the condition for the amplification process.

Table 1. The Sequence of Frog Primer Pairs

Primer	Sequence (5'→3')
Fk1	GCAGCCCTATCAACCTTCTC
Rk1	TAAGGGAGCGAAGTTTGGAG
Fk2	TCTCTCTTCTTTGTTCCCTGAGC
Rk2	CCTTGAGAGGGGCAAGTAAGGC
Fk3	AGCGCCATGCTTATGCTGAG
Rk3	TTGATATTTGCTTGCGGGGC

Table 2. Cocktail Mixture for PCR Reaction

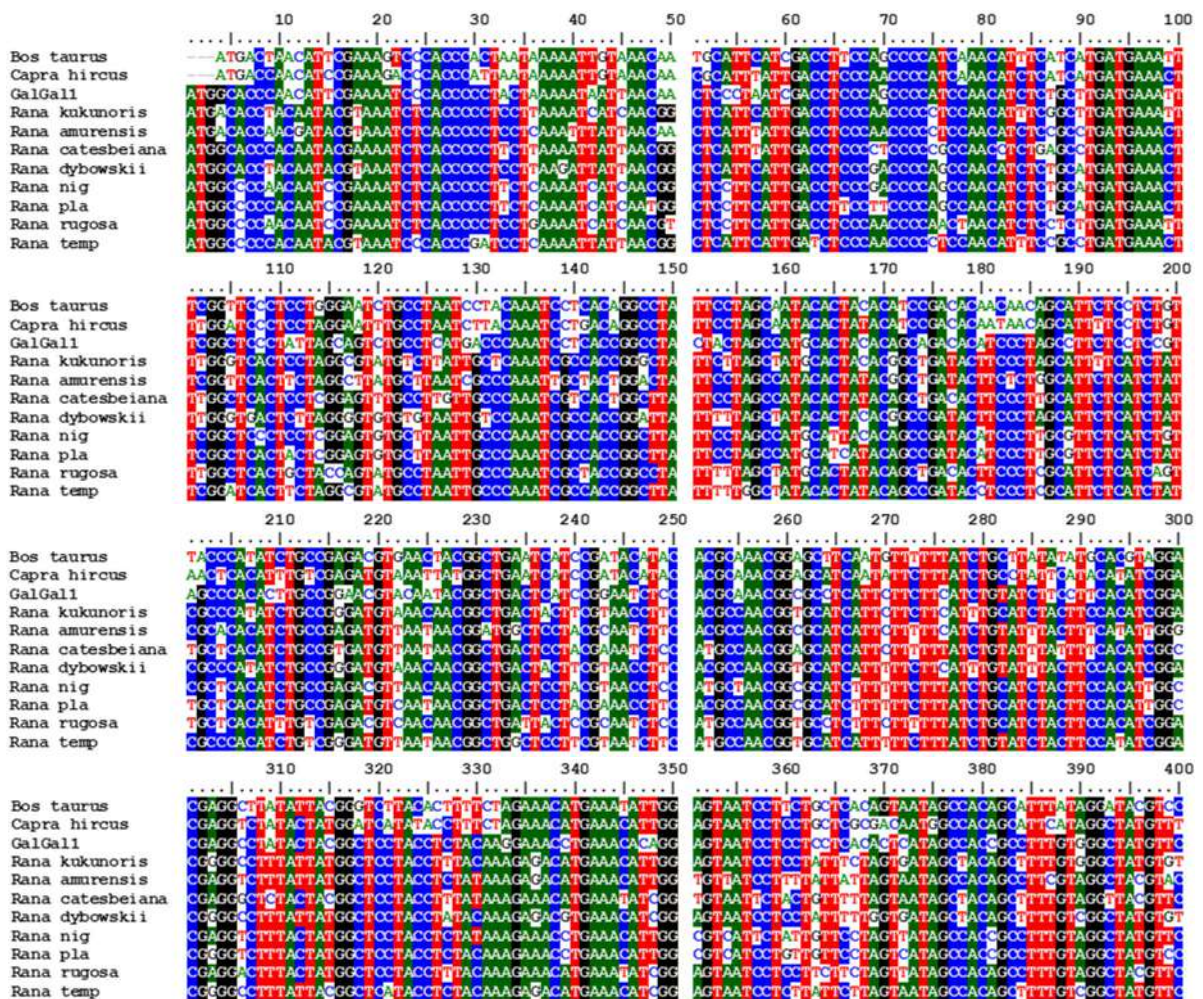
Mixture component	Volume (μL)
Dreamtaq Green Master Mix 2x	12.5
Forward primer (10 μM)	1.00
Reverse primer (10 μM)	1.00
DNA template	According to the amount needed, which is 100 ng
Nuclease Free Water	Until total volume reaches 25 μL

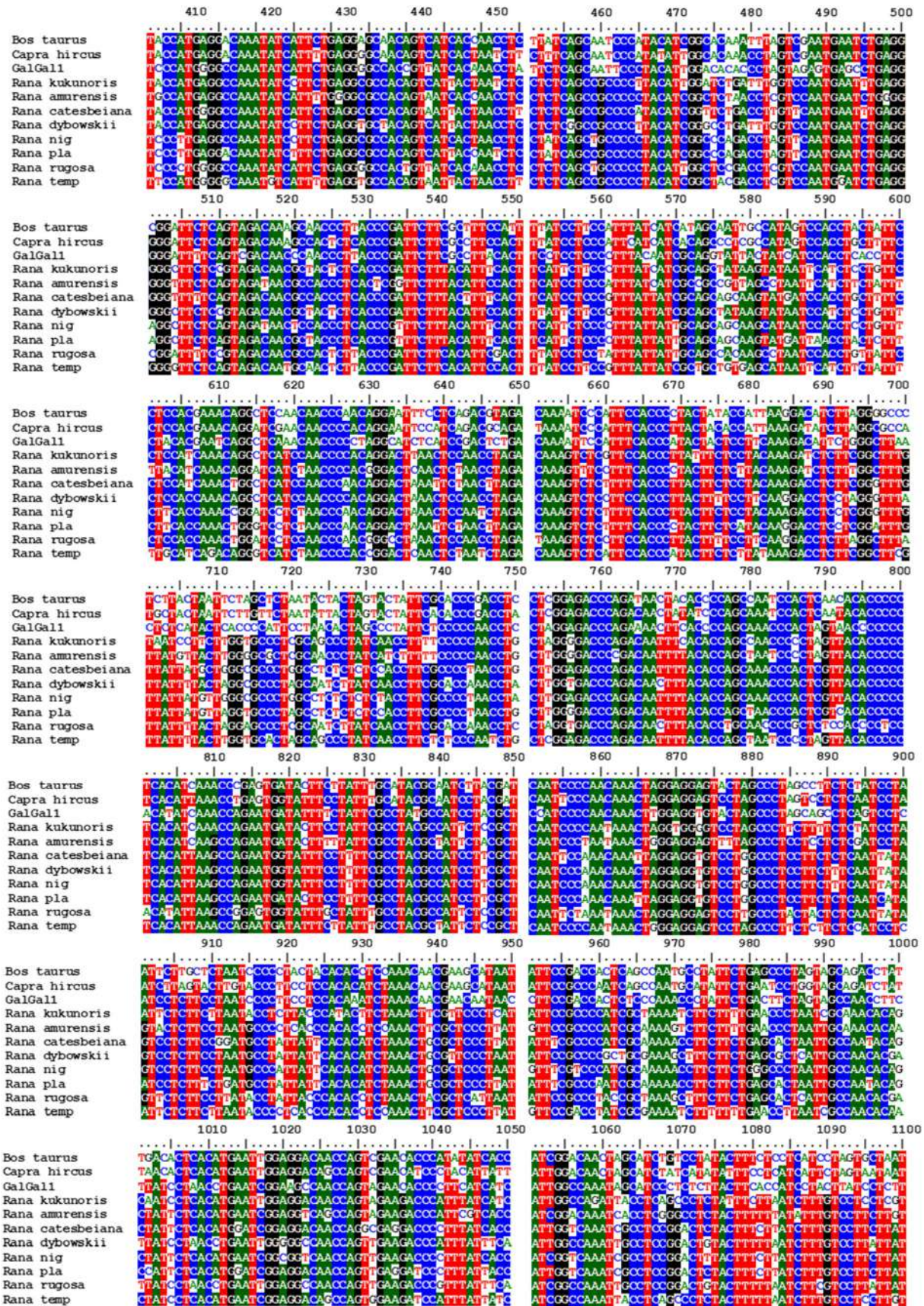
■ RESULTS AND DISCUSSION

The primer design was based on eight organisms' *cyt-b* genes. *Cyt-b* was chosen due to its characteristic of having species-specific mutation sites indicating its usefulness as a marker for species identification [16]. In addition to that, the *cyt-b* gene was reported to have a short DNA fragment that acts as the universal DNA that can be used as a barcode region to differentiate many animal species [17]. Mitochondrial DNA, which encodes the *cyt-b* gene, possesses distinct characteristics being the second genetic information system of eukaryotic cells [18], and has a closed circular double-stranded structure that is able to do self-replication semi-conservatively [19]. All of those characteristics make mitochondrial DNA (*cyt-b* gene) a beneficial resource for understanding the evolution as well as genetic relationship between species [20], therefore suitable for developing specific primers for

the PCR method. Many studies reported that the use of mitochondrial DNA, especially *cyt-b*, has delivered accurate identification for organism identification, such as the detection of pork contamination [21], characterization of tropical fishes [20] and even phylogenetic analysis for some insects [22]. Eleven mitochondrial *cyt-b* genes obtained from NCBI were used for designing primer number 1 (later known as primer Fk1-Rk1), including 3 genes from non-*Rana* species and 8 *Rana* species. The alignment is shown in Fig. 1.

The chosen primer was based on the conserved region between 8 *cyt-b* genes of *Rana* species and also has the most difference of the other 3 *cyt-b* genes from non-*Rana* species. Therefore, the designed primer pair of Fk1 is located in region 721–741 bp, while Rk1 is located in region 930–949 bp. Primer pair numbers 2 and 3 were microsatellite primers constructed from *R. temporaria*





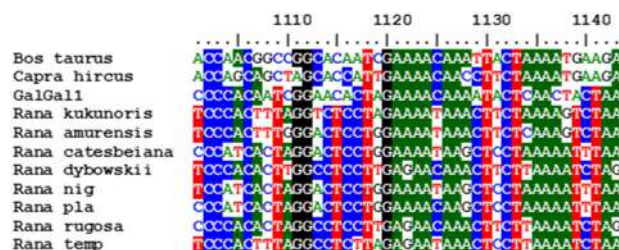


Fig 1. Alignment of *cyt-b* genes from 11 species

Table 3. Summary of primer characteristics

Primer	Sequence (5'-3')	Length (bp)	T _m (°C)	GC (%)	Primer dimer
Fk1	GCAGCCCTATCAACCTTCTC	20	59.3	55.0	No
Rk1	TAAGGGAGCGAAGTTTGGAG	20	57.3	50.0	No
Fk2	TCTCTCTTCTTTGTTCCTGAGC	23	60.6	47.8	No
Rk2	CCTTGAGAGGGGCAAGTAAGGC	22	64.0	59.1	No
Fk3	AGCGCCATGCTTATGCTGAG	20	59.3	55.0	No
Rk3	TTGATATTTGCTTGC GGGGC	20	57.3	50.0	No

that showed characteristics of 10 polymorphic microsatellite loci and a bi-allelic marker [16]. Hence, primer pairs Fk2-Rk2 and Fk3-Rk3 are expected to give different DNA amplification patterns. Meaning instead of a single DNA band amplified by the primer, microsatellite primer can amplify many DNA fragments from many loci. This is because microsatellite belongs to subcategories of tandem repeats (TRs) distributed to make up genomic repetitive regions [23].

The characteristic of the six primers was tabulated in Table 3, and the difference in T_m value for each primer pair was rather significant (especially primer pair Fk2-Rk2). The downfall of having a significant difference between T_m is their annealing temperature (T_a) could be too low for one primer or too high for the other. This could lead to either the occurrence of an unspecific DNA band or no amplification was not carried out. Thus, determining the optimal T_a for each primer pair that has a different T_m value is crucial. On the other hand, the GC content of each primer met the requirement of a good primer for PCR which is 40–60%, because a low GC content could reduce the efficiency of the PCR while high GC content can cause hairpin formation, which can hinder the primers from annealing themselves to the template [24].

The specificity of each primer pair was determined by the DNA amplicon resulting from the amplification

process. Primer pair is said to be specific if only the targeted DNA fragment was produced for the investigated species and no amplification for other species. Amplification using primer pair Fk1-Rk1 did not produce any DNA fragment for all the meat tested (data not shown). This phenomenon indicates that primer pair Fk1-Rk1 does not have any specificity toward all the meat samples that had been tested. Although primer pair Fk1-Rk1 was said not to have the possibility to form primer dimer based on the data from Table 1, some proposed self-dimer structures are actually existing (Table 4). It would suggest that the non-specificity of primer Fk1-Rk1 for not having any amplification is not merely because it is not specifically against the frog DNA template but due to the high possibility of forming a primer dimer.

Amplification using primer Fk2-Rk2 and Fk3-Rk3 is shown in Fig. 2. From the visualization of DNA amplification using both pairs of primers, DNA fragments of frog meat can be seen slightly above the 100 bp region, whereas in other samples (T2, A2, C2, U2, and S2), there was no DNA amplification using Fk2-Rk2 primer pairs and primary dimers occurred using Fk3-Rk3 primer pairs. The primer pair Fk2-Rk2 might be used as a candidate primer for frog meat identification.

In contrast, the primer pair Fk3-Rk3 showed a different pattern of amplification. The targeted sample,

Table 4. Proposed primer dimer structure

Primer	Proposed structure of primer dimer	
Fk1	5'	GCAGCCCTATCAACCTTCTC
	3'	CTCTTCCAACCTATCCCGACG
	5'	GCAGCCCTATCAACCTTCTC
	3'	CTCTTCCAACCTATCCCGACG
Rk1	5'	TAAGGGAGCGAAGTTTGGAG
		:
	3'	GAGGTTTGAAGCGAGGGAAT

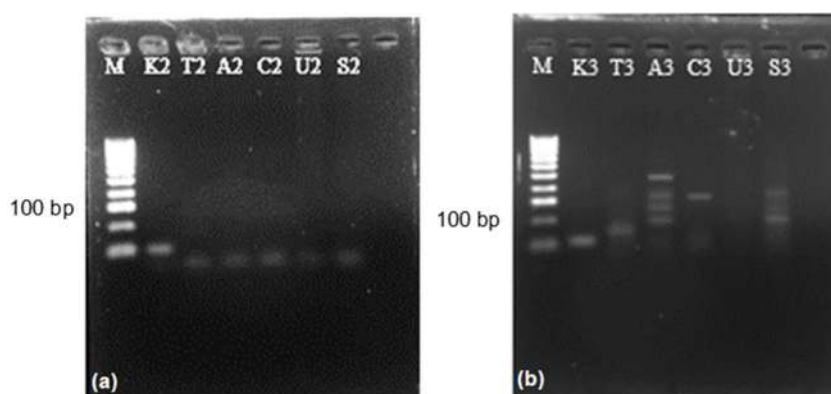


Fig 2. Visualization of DNA amplification using (a) primer Fk2-Rk2 and (b) primer Fk3-Rk3 (M: DNA marker K: frog, T: mackerel, A: chicken, C: squid, U: shrimp, and S: beef)

which is frog meat (K3), also had DNA fragments slightly above the 100 bp region. The amplification from mackerel meat (T3) resulted in DNA fragments at ~150 bp, and amplification from chicken, squid, and beef meat (A3, C3, and S3, respectively) resulted in multiple bands with different patterns from each other. This occurrence was due to the microsatellite primer characteristic that is able to amplify many DNA fragments from the different locus. The last sample, which was shrimp meat (U3), showed no amplification happening. Based on this visualization, primer Fk3-Rk3 could also be a candidate primer for frog meat identification to further improve the development of halal food assurance; that is, the unique pattern of multiple bands could be used to identify species of interest

but would probably suffer from the level of accuracy and reproducibility [25-26]. However, due to the ability to amplify many other meat samples other than frog meat, primer Fk3-Rk3 could not be used for analysis using RT-PCR, as it would generate misleading results [27].

In this study, the identification of various types of meats was successfully carried out using the PCR technique. Since the objective is to develop a method for checking the presence of frog meat as a non-halal food source in food products, therefore only a specificity test is needed, and the primer pair Fk2-Rk2 and Fk3-Rk3 have already shown their potential to do so. Nevertheless, the information derived from this study might complement the technology implemented in the

food supply chain, especially in the halal food industry [28].

■ CONCLUSION

The best primer pair for frog meat identification using the PCR technique in this study was primer pair Fk2-Rk2 and Fk3-Rk3. The primer pairs had distinguished amplification patterns against other common meat for food, while primer pair Fk1-Rk1 did not exhibit the ability to amplify the frog meat DNA. However, it is highly recommended to conduct a further investigation regarding the determination of a limit of detection (sensitivity analysis) and implementation towards food products as well as developing more specific primers, such as multiplex primers for frog meat.

■ ACKNOWLEDGMENTS

This research is fully funded by Research Grant from Universitas Negeri Malang with contract number 19.5.965/UN32.20.1/LT/2022.

■ AUTHOR CONTRIBUTIONS

Norman Yoshi Haryono conceived the original idea. Rizqi Layli Khusufi and Delia Wahyu Pangesti carried out the experiment. Norman Yoshi Haryono with the support from Rina Rifqie Mariana and Hartati Eko Wardani wrote the manuscript. Evi Susanti and Norazlinaliza Salim contributed to the final version of the manuscript.

■ REFERENCES

- [1] Denyingyhot, A., Srinulgray, T., Mahamad, P., Ruangprach, A., Sa-I, S., Saerae, T., Vesaratchavest, M., Dahlan, W., and Keeratipibul, S., 2022, Modern on-site tool for monitoring contamination of halal meat with products from five non-halal animals using multiplex polymerase chain reaction coupled with DNA strip, *Food Control*, 132, 108540.
- [2] Halimi, F.F., Gabarre, S., Rahi, S., Al-Gasawneh, J.A., and Ngah, A.H., 2022, Modelling Muslims' revisit intention of non-halal certified restaurants in Malaysia, *J. Islam. Mark.*, 13 (1), 2437–2461.
- [3] Thomson Reuters, 2014, *State of the global Islamic economy 2014-2015 report*, Thomson Reuters, Dubai.
- [4] Esteki, M., Regueiro, J., and Simal-Gándara, J., 2019, Tackling fraudsters with global strategies to expose fraud in the food chain, *Compr. Rev. Food Sci. Food Saf.*, 18 (2), 425–440.
- [5] Huq, A.K.O., Uddin, I., Ahmed, E., Shiddique, M.A.B., Zaher, M.A., and Nigar, S., 2017, Fats and oil adulteration: Present scenario and rapid detection techniques, *Food Res.*, 6 (1), 5–11.
- [6] Montowska, M., and Pospiech, E., 2011, Authenticity determination of meat and meat products on the protein and DNA basis, *Food Rev. Int.*, 27 (1), 84–100.
- [7] Ali, M.E., Nina Naquiah, A.N., Mustafa, S., and Hamid, S.B.A., 2015, Differentiation of frog fats from vegetable and marine oils by Fourier transform infrared spectroscopy and chemometric analysis, *Croat. J. Food Sci. Technol.*, 7 (1), 1–8.
- [8] Bleicher, J., Ebner, E.E., and Bak, K.H., 2022, Formation and analysis of volatile and odour compounds in meat-A review, *Molecules*, 27 (19), 6703.
- [9] Flores, M., 2017, "Chapter 13 - The Eating Quality of Meat: III-Flavor" in *Lawrie's Meat Science*, 8th Ed., Eds. Toldra', F., Woodhead Publishing, UK, 383–417.
- [10] Montowska, M., Rao, W., Alexander, M.R., Tucker, G.A., and Barrett, D.A., 2014, Tryptic digestion coupled with ambient desorption electrospray ionization and liquid extraction surface analysis mass spectrometry enabling identification of skeletal muscle proteins in mixtures and distinguishing between beef, pork, horse, chicken, and turkey meat, *Anal. Chem.*, 86 (9), 4479–4487.
- [11] Članjak – Kudra, E., Fazlović, N., Alagić, D., Smajlović, M., Čaklovica, K., and Smajlović, A., 2021, An overview of most commonly used methods for detection of fish mislabeling, *Veterinaria*, 70 (2), 169–184.
- [12] Rohman, A., Pebriyanti, N.W., Sisindari, S., Windarsih, A., Ramadhani, D., Larasati, R., and Yulisa, H., 2020, Real-time polymerase chain reaction for identification of dog meat in adulterated beef meatball using specific primer

- targeting on cytochrome-b for halal authentication, *Int. J. Food Prop.*, 23 (1), 2231–2241.
- [13] Thanakiatkrai, P., and Kitpipit, T., 2017, Meat species identification by two direct-triplex real-time PCR assays using low resolution melting, *Food Chem.*, 233, 144–150.
- [14] Thanakiatkrai, P., Dechnakarini, J., Ngasaman, R., and Kitpipit, T., 2019, Direct pentaplex PCR assay: An adjunct panel for meat species identification in Asian food products, *Food Chem.*, 271, 767–772.
- [15] Rowe, G., and Beebe, T.J.C., 2001, polymerase chain reaction primers for microsatellite loci in the common frog *Rana temporaria*, *Mol. Ecol. Notes*, 1 (1-2), 6–7.
- [16] Farag, M.R., El Bohi, K.M., Khalil, S.R., Alagawany, M., Arain, M.A., Sarun, K., Tiwari, R., and Dhama, K., 2020, Forensic applications of mitochondrial cytochrome *b* gene in the identification of domestic and wild animal species, *J. Exp. Biol. Agric. Sci.*, 8 (1), 1–8.
- [17] Yacoub, H.A., Fathi, M.M., and Mahmoud, W.M., 2013, DNA barcode through cytochrome *b* gene information of mtDNA in native chicken strains, *Mitochondrial DNA*, 24 (5), 528–537.
- [18] Ruan, H., Li, M., Li, Z., Huang, J., Chen, W., and Zou, K., 2020, Comparative analysis of complete mitochondrial genomes of three *Gerres* fishes (Perciformes: Gerreidae) and primary exploration of their evolution history, *Int. J. Mol. Sci.*, 21 (5), 1874.
- [19] Paz, F.P., Batista, J.D., and Porto, J.I., 2014, DNA barcodes of Rosy Tetras and allied species (Characiformes: Characidae: *Hyphessobrycon*) from Brazilian Amazon basin, *PLoS One*, 9 (5), 0098603.
- [20] Sun, C.H., Liu, H.Y., Xu, N., Zhang, X.L., Zhang, Q., and Han, B.P., 2021, Mitochondrial genome structures and phylogenetic analyses of two tropical Characidae fishes, *Front. Genet.*, 12, 627402.
- [21] Ni'mah, A., Kartikasari, Y., Pratama, A.D., Kartikasari, L.R., Hertanto, B.S., and Cahyadi, M., 2016, Detection of pork contamination in fresh and cooked beef using genetic marker mitochondrial-DNA cytochrome *b* by duplex-PCR, *J. Indones. Trop. Anim. Agric.*, 41 (1), 7–12.
- [22] Chang, H., Guo, J., Li, M., Gao, Y., Wang, S., Wang, X., and Liu, Y., 2023, Comparative genome and phylogenetic analysis revealed the complex mitochondrial genome and phylogenetic position of *Conopomorpha sinensis* Bradley, *Sci. Rep.*, 13 (1), 4989.
- [23] Gemayel, R., Cho, J., Boeynaems, S., and Verstrepen, K.J., 2012, Beyond junk-variable tandem repeats as facilitators of rapid evolution of regulatory and coding sequences, *Genes*, 3 (3), 461–480.
- [24] Burpo, F.J., 2001, A critical review of PCR primer design algorithms and cross-hybridization case study, *Biochemistry*, 218, 1–11.
- [25] Sasmito, D.E.K., Kurniawan, R., and Muhimmah, L., 2014, Karakteristik primer pada polymerase chain reaction (PCR) untuk sekuensing DNA: Mini review, *Seminar Nasional Informatika Medis*, Faculty of Industrial Technologi, UII, Yogyakarta, December 6, 2014, 93–102.
- [26] Ishii, S., and Sadowsky, M.J., 2009, Application of the rep-PCR DNA fingerprinting technique to study microbial diversity, ecology and evolution, *Environ. Microbiol.*, 11 (4), 733–740.
- [27] Lee, A., and Wong, E., 2009, Optimization and the robustness of BOX AIR PCR for DNA fingerprinting using trout lake *E. coli* isolates, *J. Exp. Microbiol. Immunol.*, 13, 104–113.
- [28] Udvardi, M.K., Czechowski, T., and Scheible, W.R., 2008, Eleven golden rules of quantitative RT-PCR, *Plant Cell*, 20 (7), 1736–1737.

Supplementary Data

This supplementary data is a part of a paper entitled "Synthesis of Zn(II) and Co(II) Complexes with a Schiff Base Derived from Malonic Acid Dihydrazide for Photo-Stabilizers of Polystyrene".

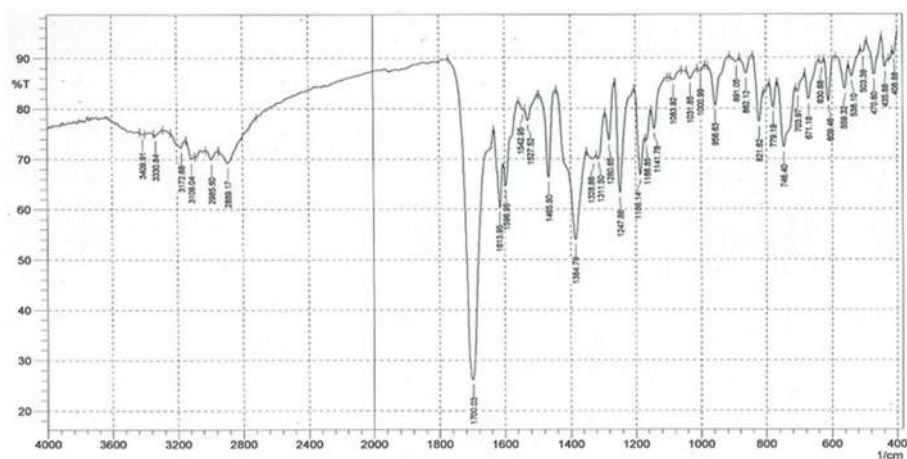


Fig S1. FTIR spectrum of Schiff Base ligand

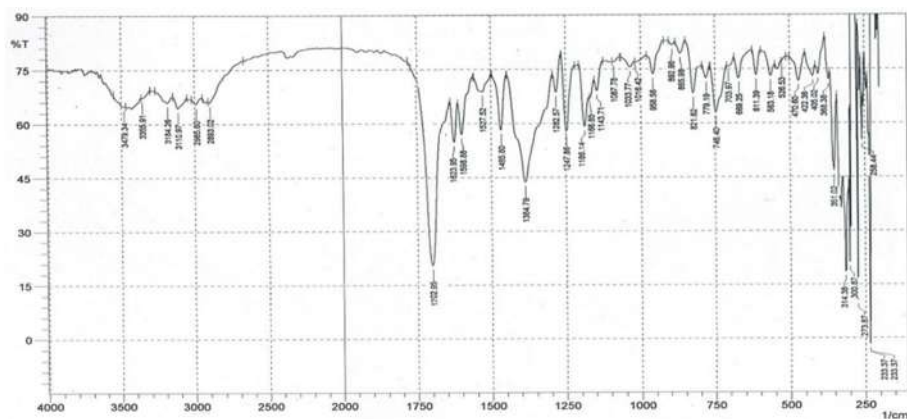


Fig S2. FTIR spectrum of Co(II) complex

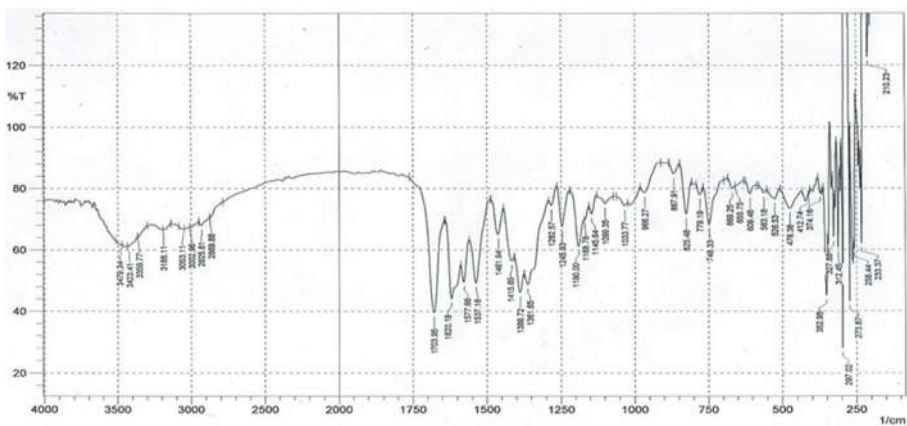


Fig S3. FTIR spectrum of Zn(II) complex

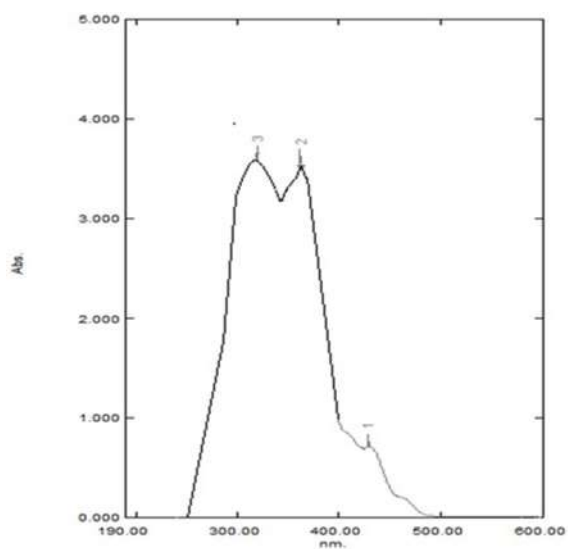


Fig S4. UV-Vis spectra of ligand

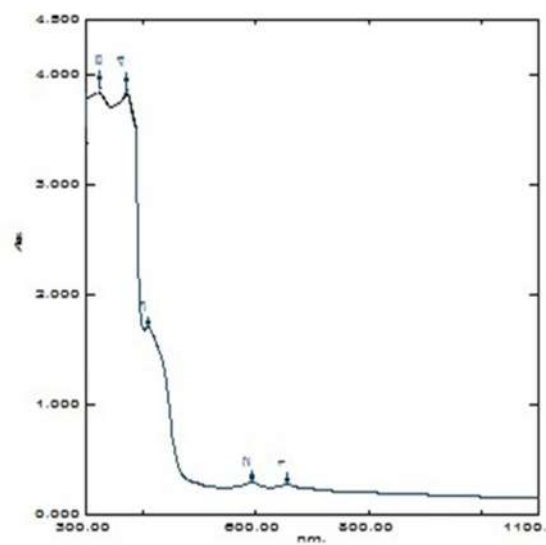


Fig S5. UV-Vis spectra of Co(II) complex

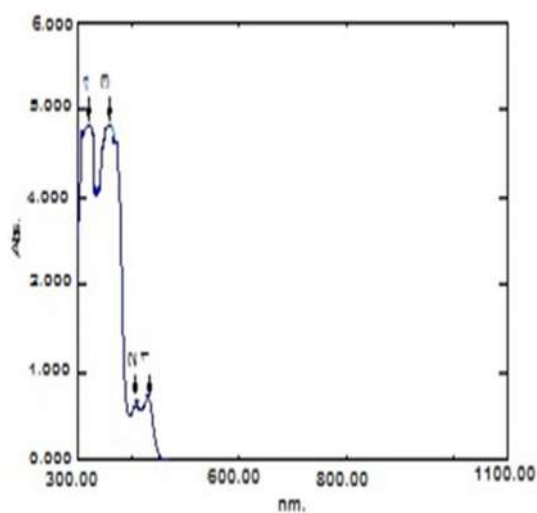


Fig S6. UV-Vis spectra of Zn(II) complex

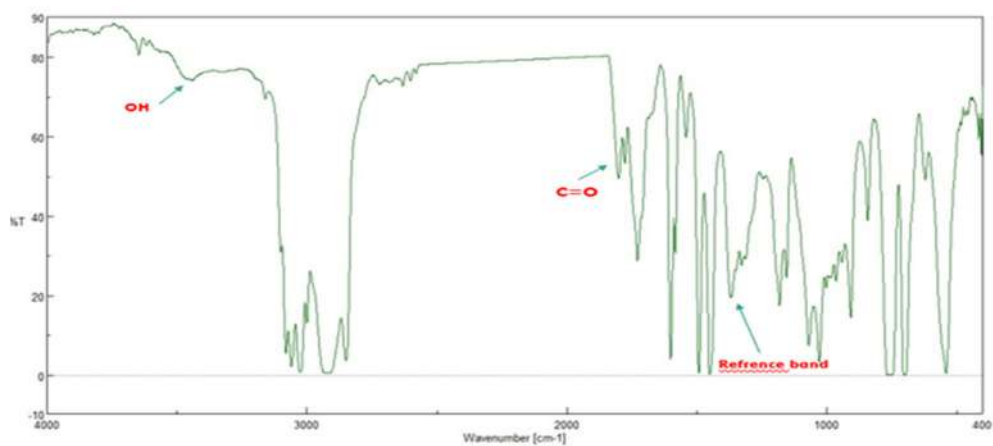


Fig S7. FTIR spectrum of polystyrene before irradiation

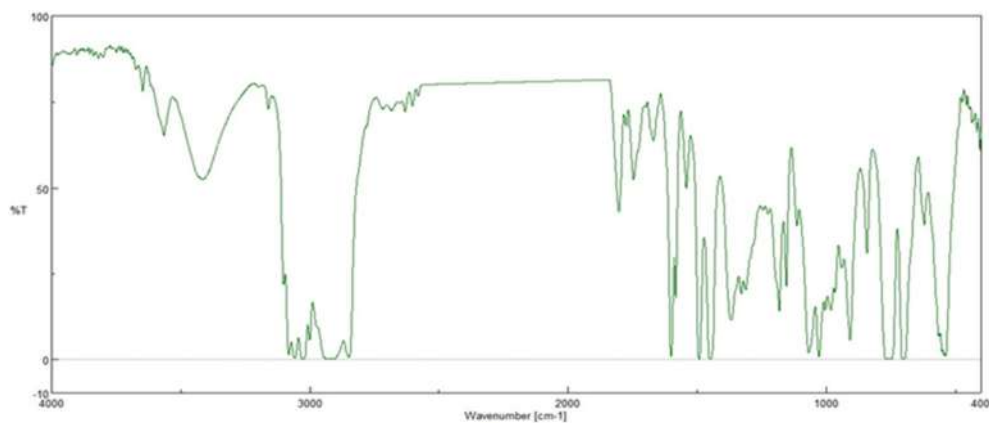


Fig S8. FTIR spectrum of polystyrene after irradiation

Synthesis of Zn(II) and Co(II) Complexes with a Schiff Base Derived from Malonic Acid Dihydrazone for Photo-Stabilizers of Polystyrene

Rehab Ghalib Hammoda and Naser Shaalan*

Department of Chemistry, College of Science for Women, University of Baghdad, Baghdad 10071, Iraq

* Corresponding author:

email:

naserds_chem@cs.w.uobaghdad.edu.iq

Received: April 8, 2023

Accepted: April 26, 2023

DOI: 10.22146/ijc.83730

Abstract: In this study, novel Schiff base complexes with Zn(II) and Co(II) ions were successfully synthesized. The malonic acid dihydrazone was converted into the Schiff base ligand by combining it with 1-hydroxy-2-naphthaldehyde, and the last step required reacting it with the appropriate metal(II) chloride to produce pure target complexes. The generated complexes were thoroughly characterized using FTIR, ¹H-NMR, ¹³C-NMR, GC-mass, and UV-Vis spectroscopies. In order to photo-stabilize polystyrene (PS) and reduce the photodegradation of its polymeric chains, these chemicals have been used in this work. The efficiency of the generated complexes as photo-stabilizers was evaluated using a variety of techniques, including FTIR, weight loss, viscosity average molecular weight, light and atomic force microscopy, scanning electron microscopy (SEM), and energy dispersive X-ray (EDX) mapping. These tests corroborated each other and demonstrated how effectively new compounds stabilize PS photographs. As a result, compared to blank PS, they reduce the photodegradation of PS films containing these complexes after 300 h of exposure to UV radiation with a wavelength of 313 nm. Also, it has demonstrated how effective the cobalt complex is as a photo-stabilizer. The highly conjugated systems in these chemicals are to blame for this.

Keywords: photodegradation; malonyl dihydrazone; photo-stabilization; polystyrene; Schiff base complexes

■ INTRODUCTION

Due to its distinctive qualities, polystyrene (PS) is regarded as one of the most significant plastics. It can withstand many sorts of solvents, acids, and bases and is highly affordable, flexible, durable, light, and transparent. Additionally, it is synthesized in a variety of shapes, including solid and foam. PS is ideal for usage in a variety of applications, including packaging, labeling, and varied technical requirements [1-2]. Plastic polymeric materials are employed in a variety of applications, including organic electronics, polymeric light-emitting diodes (PLED), transistors, sensors, and solar cells, as well as anticorrosive coatings for metals [3].

UV light exposure to polymer chains causes the chemical structure of the polymer to photodegrade by producing free radicals. This causes covalent connections within the polymer structure to break or form new ones [4]. All of these chemical alterations will cause changes in

the PS material's physical, mechanical, optical, and morphological characteristics, such as cracking, staining, paint layer solidification, and altered solubility properties [5]. Because it contains UV light, which has wavelengths within the dissociation energy of many organic polymeric materials, the sun's light is thought to be the primary cause of the photodeterioration of PS materials used outdoors [6].

In the presence of oxygen molecules and sunlight, polystyrene polymer chains undergo an oxidative process. It mostly results in polymer chain breaks or new cross-links being formed inside the polymer structure [7]. Typically, the polymer moieties in PS absorb photons to begin the process of photodegradation. Thus, the energy of the photons that were absorbed was sufficient to dissolve the covalent bonds that held the polymer chains together and create a free radical, which is known as the first stage in the breakdown of the polymer chains [8].

The chemical makeup of the polymer chain can be changed to increase the plastic polymer's photostability.

Even though combining UV absorber chemicals and/or other types of amines as photo stabilizers has demonstrated outstanding plastic protection, this fundamental technique is extremely seldom employed [9]. Organic UV stabilizers have been employed for a very long time to improve the photostability of polymers [10]. However, they are susceptible to degradation and transference inside the polymer chains themselves. Using them in large doses might have negative effects on safety. Numerous studies have utilized a variety of additives, including aromatics [11], Schiff bases [12], and organometallic compounds [13], to stabilize plastic polymer materials against photodegradation. Here, the synthesis, characterization, and effect of the new Schiff base complexes on the features and chemical structure of polystyrene films were described.

■ EXPERIMENTAL SECTION

Materials

The chemicals used in this study were diethyl malonate (Sigma Aldrich, 99%), hydrazine monohydrate (Sigma Aldrich, 99%), 1-hydroxy-2-naphthaldehyde (Sigma Aldrich, 98%), absolute ethanol (BDH, 99%), $\text{CoCl}_2 \cdot 6\text{H}_2\text{O}$ (BDH, 99%), ZnCl_2 (BDH, 98%), and polystyrene (Sigma Aldrich) from Gillingham, UK.

Instrumentation

The carbon, hydrogen and nitrogen contents were determined by Euro Vector EA 3000 A, and FTIR spectra were recorded on a Shimadzu FTIR-8100 spectrometer. ^1H - ^{13}C -NMR spectra of the ligand (L) were measured in d_6 -DMSO solvent using TMS as an internal standard on a Bruker 300 MHz. Using UV-1650 PC Shimadzu spectrophotometer were measured the electronic spectra at 25 °C. Electrical conductivity measurements of the complexes were recorded at 25 ± 2 °C for a 1×10^{-3} M solution of the samples in DMF using a Philips PW-digital conductivity meter. Magnetic susceptibility results were also obtained at 25 °C in the solid state by applying Gouy balance. The molecular weight of the prepared ligand was determined by a GCMS-QP2010 PLUS; DI analysis

Shimadzu, Japan, spectrometer in the laboratory of the University of Samarra. Moreover, all melting point results were recorded on Gallen Kamp melting apparatus at the College of Science for Women, University of Baghdad. PS films were subjected to radiation using an accelerated weather-meter QUV tester that was purchased from Q-Panel Corporation, at 25 °C, and a wavelength of 365 nm ($6.43 \times 10^9 \text{ ein dm}^{-3} \text{ s}^{-1}$). (USA, Homestead, Florida). Atomic force microscopy (AFM) was used to investigate the surface of PS films using Veeco equipment (Plainview, NY, USA). Scanning electron microscopy (SEM) of the PS surface was performed using an Inspect S50 microscope (FEI Corporation, Czechia, Czech Republic) and an accelerating voltage of 15 KV. The Meiji Techno Microscope was used to take minuscule images of the PS surface in Tokyo, Japan. PS films were placed using 0.6 mm thick aluminum plate supports, and a Digital Vernier Caliper 2610A micrometer (Vogel GmbH, Kevelaer, Germany) was used to measure the thickness of the films (approximately 40 μm) (Q-Panel Company, Homestead, FL, USA). Look for signs of accelerated UV weathering. With the aid of an accelerated weather meter QUV tester from Philips, Saarbücken, Germany, PS films were subjected to QUV radiation at 25 °C. The films were exposed for 300 h continuously to UV light with a wavelength of 313 nm and an intensity of $1.052 \times 10^{-8} \text{ ein dm}^{-3} \text{ s}^{-1}$. Using a Digital Vernier Caliper 2610A Micrometer, Polymeric Film Thickness was Measured (Vogel GmbH, Kevelaer, Germany).

Procedure

Preparation of polystyrene films

Polystyrene (1.0 g) was dissolved in 16 mL of tetrahydrofuran (THF), and the mixture was constantly agitated for 1 h at room temperature to produce PS films. The produced metal complexes(II) were added to the PS of THF solution at a weight proportion of 2% (per polymer weight), and the mixture was agitated for an additional hour to ensure that the metal complexes(II) were completely dissolved and the mixture was homogeneous. After that, the excess THF was eliminated from the mixture by putting it on glass plates

of the same size and allowing it to evaporate there for 24 h. Plate thickness is measured using micrometers of this type (2610A), and one approach is to attach cardboard sheets to the target plates and punch holes in them that are 3×2 cm in size.

Irradiation by UV light

It is a technique to assess the impacts of utilizing plastic materials outside following extended exposure to UV or solar radiation (for months or years). The created polymeric films were fastened to a support plate for UV-B 313 light exposure. This stand has a 0.6 mm thickness and is made of aluminum. Constant pressure and temperature were used for testing the films.

PS films' photostability is evaluated using FTIR

An FTIR 8300 Shimadzu spectrophotometer was used to investigate the efficacy of using synthetic compounds as photo-stabilizers to slow down the degradation of PS films. This method was used to monitor the development and growth of polyene and carbonyl groups. Eq. (1) is used to determine the hydroxyl index (I_{OH}) and carbonyl index ($I_{C=O}$) of plain PS, and PS doped with additives.

$$I_s = \frac{A_s}{A_r} \quad (1)$$

Hence for the peak absorption intensity of the functional group, A_s is used, whereas A_r is used for the reference group. I_s , on the other hand, refers to the functional group index [14].

Test of the photostability of PS films using a diet plan

Weighing was done on the polymeric PS films used in this process both before and after UV exposure. This method was carried out for both blank and mixed PS films, and the PS weight reduction was calculated using Eq. (2).

$$\text{Weight loss \%} = \frac{W_0 - W}{W_0} \times 100 \quad (2)$$

Before radiation exposure, the PS film weighed W_0 , and after radiation exposure, the PS film weighed W [15].

Calculating the average molecular weight of the PS polymeric sheets (M_v)

The average molecular weight (M_v) of PS films

before and after irradiation, as well as for blank and mixed PS films, may be calculated by measuring the viscosity of the polymer. The viscosity of PS with and without synthesized complexes was measured at room temperature using an Ostwald U-tube viscometer with THF as the solvent. M_v denotes the average molecular weight of PS. Eq. (5) was used to obtain the average molecular weight of PS [16], whereas Eq. (4) was used to estimate the intrinsic viscosity $[\eta]$.

$$[\eta] = \frac{\left[2(\eta_{sp} - \ln \eta_{rel})\right]^{\frac{1}{2}}}{c} \quad (4)$$

$$[\eta] = 1.63 \times 10^{-2} M_v^{0.766} \quad (5)$$

In addition, Eq. (6) was used to estimate the specific viscosity (η_{sp}), and Eq. (7) to estimate the relative viscosity (η_{rel}).

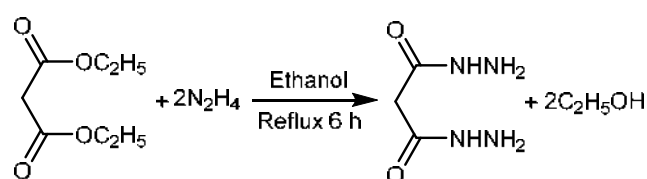
$$\eta_{sp} = \eta_{re} - 1 \quad (6)$$

$$\eta_{re} = \frac{t}{t_0} \quad (7)$$

As a result, the polymer solutions' flow time is given by t , while the solvent's flow time is given by t_0 [17].

Synthesis of malonic acid dihydrazide

Making malonic acid dihydrazide is the first step in the ligand synthesis procedure, as described here. At room temperature, 10 g of diethyl malonate (0.062 mol) was dissolved in 10 mL of ethanol and stirred. Add dropwise of aqueous hydrazine (10 g, 0.124 mol) with continuous stirring followed by 6 h of refluxing the reaction before stopping and allowing it to cool to room temperature. The precipitate was washed with dry ether and methanol after the generated residue was filtered. A white precipitate with an 80% yield (7.1 g) was produced by recrystallizing the product in absolute ethanol at a temperature of 159 °C. This illustrates the manufacture of malonic acid dihydrazide [18] in Scheme 1.



Scheme 1. Preparation of Malonic acid dihydrazide

Synthesis of a Schiff base ligand

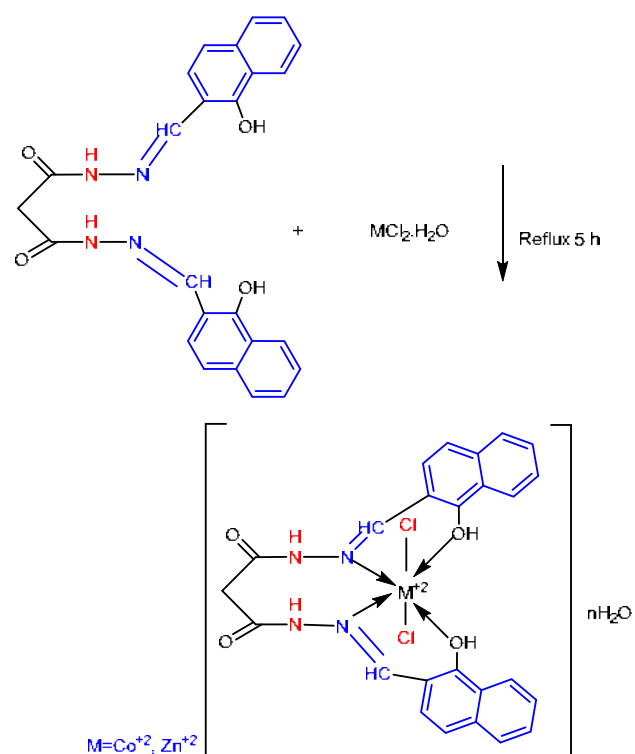
Malonic acid dihydrazide solution (1.0 g, 0.0075 mol), in 10 mL of methanol was produced. Slowly while stirring, 2-hydroxy-1-naphthaldehyde (2.6 g, 0.015 mol) was added. The reaction mixture was then given a final addition of a few drops of glacial acetic acid. The combination was allowed 5 h to react in a reflux environment, at which point a glossy yellow precipitate was generated. This precipitate was recovered by filtering, cleaning, and recrystallizing in hot ethanol. See Scheme 2 for the reaction scheme. The product was dried over anhydrous CaCl_2 in a vacuum to provide 80% (2.88 g) yield, m.p. 230–234 °C.

Synthesis of Schiff base metal complexes

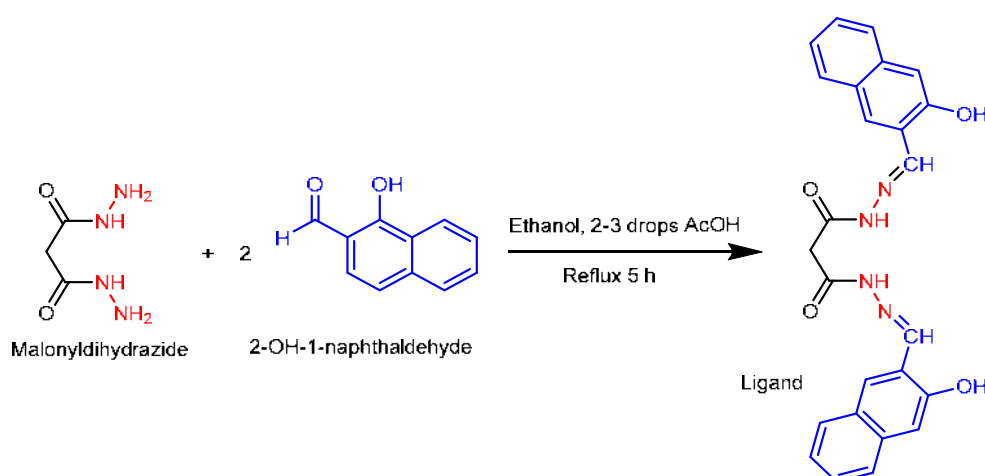
The zinc complex was synthesized by dissolving zinc chloride dehydrate (0.2 g, 0.001 mol) in 10 mL methanol and dissolving the synthesized ligand (0.5 g, 0.001 mol) in 10 mL methanol with continuous stirring for about 10 min and adding a few drops of DMF to complete solubility, followed by adding the solution of the dissolved metal salt onto a solution of the dissolved ligand in the mole ratio 1:1 of metal:ligand. In order to precipitate, the mixture was agitated under reflux for 5 h. The colorful complexes were filtered apart, cleaned with methanol, recrystallized, and allowed to dry for 24 h at room temperature. Cobalt complex ($\text{CoCl}_2 \cdot 6\text{H}_2\text{O}$) was prepared using the same procedure as shown in Scheme 3 with a good percentage yield see Table 1.

RESULTS AND DISCUSSION

Two steps were taken to synthesize the ligand. Diethyl malonate and two moles of aqueous hydrazine monohydrate were initially combined to create malonic acid dihydrazide. By recrystallization from absolute ethanol, the raw product was purified. Two moles of 2-hydroxy-1-naphthaldehyde were added to the pure



Scheme 3. Preparation of Schiff base metal complexes



Scheme 2. Preparation of Schiff base ligand

product to create the target ligand, which was then recrystallized and further purified. Eventually, by reacting it with the appropriate metallic chloride, the obtained ligand was employed to create five new complexes. Table 1 lists the percentage yields and physical characteristics of the produced compounds. As will be discussed in more detail in the following sections, several methods were utilized to characterize the chemical structure of synthesized materials.

Characterization by Element Micro Analysis

Element micro analysis C, H, N, and X was performed, and it was discovered that the actual findings matched the theory, as given in Table 2. Metal salts were utilized in a 1:1 reaction of ligand and metal, and all of the complexes were determined to be non-electrolytes by their molar conductivities.

Characterization of Schiff Base Ligand by $^1\text{H-NMR}$ Spectroscopy

Using $^1\text{H-NMR}$ spectroscopy, the chemical composition of the produced ligand was examined. As a result, as shown in Fig. 1, the $^1\text{H-NMR}$ spectrum exhibits the necessary peaks at the appropriate habitats, integrations, and multiplicity to disclose the chemical structure of the ligand. Due to the structure's two symmetrical imine groups, the proton of the imine group ($\text{N}=\text{CH}$) produces a strong, crisp singlet signal at 8.43 ppm. At chemical shifts of 10.88 and 8.11 ppm,

respectively, the exchange protons of NH and OH groups have displayed singlet peaks. Due to its proximity to the carbonyl group, which is responsible for the de-shielding of protons, it is assumed that the 10.88 ppm in question belongs to the NH group. On the other hand, the protons of aromatic areas exhibit peaks in the aromatic region with sufficient integration, which is between 7.15 and 7.69 ppm. Due to its proximity to two carbonyl groups, the CH_2 group finally displayed a singlet peak in the aliphatic region at 3.07 ppm. Given everything mentioned above, it can be concluded that the ligand has been effectively synthesized with a high degree of purity. Table 3 provides a summary of the synthesized ligand's $^1\text{H-NMR}$ data.

Characterization of Schiff Base Ligand by $^{13}\text{C-NMR}$ Spectroscopy

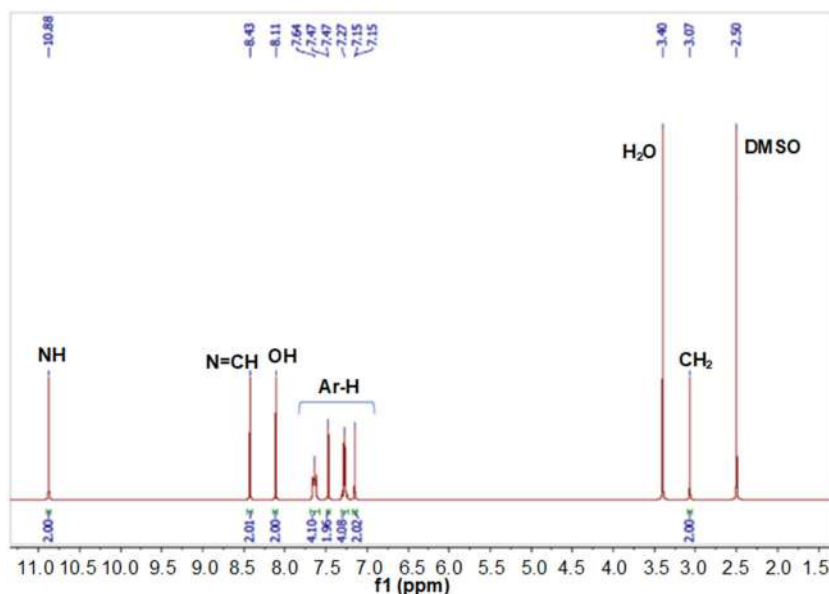
Using $^{13}\text{C-NMR}$ spectroscopy, the chemical composition of the produced ligand was identified. Hence, as shown in Fig. 2, the $^{13}\text{C-NMR}$ spectrum exhibits the necessary peaks at the appropriate habitats to illustrate the chemical structure of the produced ligand. The imine group's carbon atom $\text{N}=\text{CH}$ produces a peak at 148.10 ppm, where Schiff base groups are the spouse. Nevertheless, because oxygen has a greater electronegativity than nitrogen, which results in more de-shielding, carbonyl groups exhibit a peak at 167.11 ppm. Nevertheless, there is still a peak at 157.37 ppm above the aromatic area, which may be due to aromatic

Table 1. The physical properties of the prepared compounds

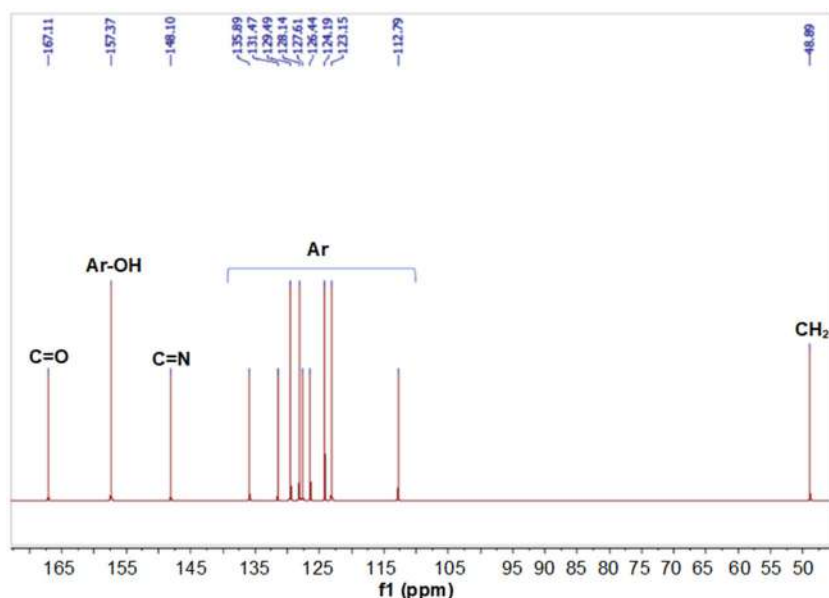
Compound formula	Color	m.p. ($^{\circ}\text{C}$)	M.Wt (g/mol)	Yield%
Ligand	Yellow	230–234	440.36	80
$[\text{CoLCl}_2]\cdot 2\text{H}_2\text{O}$	Brown	245–248	606.32	72
$[\text{ZnLCl}_2]\cdot \text{H}_2\text{O}$	Yellowish	242–246	594.75	83

Table 2. The Element micro analysis C, H, N, and X of the prepared compounds

	Calculated (Analysis)				
	C %	H %	N %	X%	M %
L	68.17	4.58	12.72	---	--
$\text{C}_{25}\text{H}_{20}\text{N}_4\text{O}_4$	(67.53)	(5.62)	((11.94)		
Complex Co	49.52	3.99	9.24	11.69	9.72
$[\text{CoLCl}_2]\cdot 2\text{H}_2\text{O}$	(50.30)	(3.05)	(8.79)	(10.53)	(10.16)
Complex Zn	50.49	3.73	9.72	11.92	10.99
$[\text{ZnLCl}_2]\cdot \text{H}_2\text{O}$	(49.65)	(3.09)	(10.69)	(12.73)	(11.01)

Fig 1. ¹H-NMR spectrum of synthesized ligandTable 3. ¹H-NMR data of synthesized ligand

Compound	¹ H-NMR
Ligand	δ /ppm = 3.07 (2H, CH ₂), 7.15 (s, 2H, Ar-H), 7.20–7.32 (m, 4H, Ar-H), 7.47 (s, 2H, Ar-H), 7.60–7.69 (m, 4H, Ar-H), 8.11 (s, 2H, OH from the phenolic proton), 8.43 (s, 2H, HC=N azomethine), 10.88 (s, 2H, NH)

Fig 2. ¹³C-NMR spectrum of synthesized ligand

carbon atoms positioned near oxygen. As a result, the aromatic area, which is between 112.79 and 135.89 ppm, exhibits nine peaks in the carbon atoms. Lastly, because it is located close to two carbonyl groups, the CH₂ group

displayed a peak at 48.89 ppm in the aliphatic area. Given everything mentioned above, it can be concluded that the ligand has been effectively synthesized with a high degree of purity. Table 4 provides a summary of the

synthesized ligand's ^{13}C -NMR data.

Characterization of Schiff Base Ligand and Its Complexes by FTIR

In order to identify the functional groups and the development of new bands in the produced compounds, FTIR is a useful technique [19]. The complexes formed by the ligand and their FTIR spectroscopy data are shown in Table 5. The tetradentate Schiff base ligand exhibits a sharp band at 3109 and 1596 cm^{-1} , which are ascribed to $\nu(\text{C-H})_{\text{Ar}}$ and $(\text{C}=\text{C})$, respectively. Around 1613 cm^{-1} , the stretching band of the azomethine group was identified as a strong band. As a result of the nitrogen giving electrons to the partly full d-orbitals of the metal ions, the coordination of the metal ions to the nitrogen azomethine causes a shift-up in the frequency of the $\text{C}=\text{N}$ value [20]. The complexes' FTIR spectra display distinctive lines at 1613–1623 cm^{-1} , indicating that the metal ions coordinate with the ligand through the nitrogen atom of the azomethine compound [21]. In the FTIR spectra of the ligands, a significant band at 3409–

3479 cm^{-1} is produced by the stretching vibrations of the phenolic hydroxyl group. The broadness is due to intermolecular hydrogen bonding between the phenolic and azomethine groups. The far-infrared spectra of the complexes showed new stretching modes at 422–476, 526–611, and 312–314 cm^{-1} , which are attributed to M–N, M–O, and M–Cl, respectively [22]. These stretching modes provide evidence for the formation of bonds between the divalent metal ions and the nitrogen azomethine, hydroxyl group, and chloride, respectively. The results mentioned previously are displayed in Fig. S1 to S3.

Characterization of Schiff Bases Ligand and Its Complexes by UV-Vis

Electronic spectra of L and their complexes were recorded in DMF solution at room temperature in the range of 200–1100 nm. The obtained data were presented in Table 6. The UV-Vis spectra of the Schiff base ligand revealed two strong intensity absorption peaks at 309 and 351 nm ascribed to intra-ligand $\pi-\pi^*$ and

Table 4. ^{13}C -NMR data of synthesized ligand

Compound	^{13}C -NMR
Ligand	$\delta/\text{ppm} = 48.89$ (1C, CH_2), 112.79, 123.15, 124.19, 126.44, 127.61, 128.14, 129.49, 131.47, 135.89 (18C, Ar naphthalene), 148.10 (2C, $\text{CH}=\text{N}$ azomethine group), 157.37 (2C, Ar-OH) and 167.11 (2C, $\text{C}=\text{O}$)

Table 5. FTIR spectroscopy measurements of ligand and their complexes

Symbol	O-H phenol	N-H	C-H Ar	C-H Alp	C=O	C=N	C=C	M-O	M-N	M-Cl
Ligand	3409	3330	3109	2889	1700	1613	1596	---	---	---
$[\text{CoLCl}_2] \cdot 2\text{H}_2\text{O}$	3479	3355	3110	2893	1702	1623	1598	611	422	314
Zn	3479	3359	3053	2925	1703	1620	1577	526	476	312

Table 6. UV-Vis spectroscopy measurements of ligand and molar conductivity of metal complexes

Compound	λ_{max} (nm)	Absorption (cm^{-1})	Assignments	μ_{eff} (B.M) Exp (Theory)	Molar Cond. $\text{Ohm}^{-1} \text{cm}^2 \text{mol}^{-1}$	Geometry
Ligand	309	32362.4	$\pi \rightarrow \pi^*$	-		
	351	28490.0	$n \rightarrow \pi^*$			
$[\text{CoLCl}_2] \cdot 2\text{H}_2\text{O}$	412	24271.8	C.T	3.36	18	Octahedral
	582	17182.1	${}^4\text{T}_{1g_F} \rightarrow {}^4\text{T}_{1g_P}$	(3.782)		
	640	15625	${}^4\text{T}_{1g_F} \rightarrow {}^4\text{A}_{2g(F)}$			
$[\text{ZnLCl}_2] \cdot \text{H}_2\text{O}$	410	24390.2	CT	Di	12	Octahedral
	435	22988.5	$\text{M} \rightarrow \text{L}$			

$n-\pi^*$ transitions of azomethine and carbonyl, respectively [23]. Changes in the positions of absorption bands were observed in the spectra of the complexes indicating the coordination of the metal ions through the azomethine and hydroxyl phenol functional groups [24], Fig. S4. The electronic spectrum of the Co(II) complex in DMF gave bands about 412, 582, and 640 nm, respectively assigned to charge transfer and ${}^4T_{1g(F)} \rightarrow {}^4T_{1g(P)}$ and ${}^4T_{1g(F)} \rightarrow {}^4A_{2g(F)}$. The magnetic moment of 3.63 BM and the detected electronic spectrum of the Co(II) complex give the probability of the formation of high-spin octahedral geometry [25], Fig. S5. The electronic spectra of the d^{10} Zn(II) complex exhibited a charge transfer band at 410 and 435 nm [26], Fig. S6. The molar conductivities indicate that all the prepared complexes are non-electrolyte complexes.

Characterization of Schiff Base Ligand by Mass Spectroscopy

The molecular weight of the formed compound is calculated using the mass spectrum, and the fragmentation that belongs to the compound under investigation is identified. The mass spectra of the produced Schiff base ligand were in agreement with the suggested structural formula, $C_{25}H_{20}N_4O_4$. The predicted M^+ value (440.36), as shown in Fig. 3, is matched by the molecular ion peak, which was discovered at m/e 440, validating their formula weight for the ligand. As it was successively fragmented, new unique peaks for the ligand

were visible in the mass spectra.

Examine How Well Synthesis Compounds Work as PS Photo Stabilizers

It is well known that aromatic compounds, in general, have a high capacity to absorb light across a broad range of the ultraviolet spectrum and transform it into harmless heat without changing the chemical composition of the medium's content. This decreases the medium's photolysis capacity, increases its age when used externally, and provides protection from sunlight [27-28].

Using this information as a foundation, several techniques were used to assess the efficacy of synthesis complexes as optical stabilizers for PS films, including measuring the increase in the intensity of active groups formed as a result of irradiation, estimating the percentage of weight loss, and researching the surface formation of polymeric films.

Use the FTIR Method to Examine the PS Photodegradation Rate

By monitoring FTIR spectra in the range of 400–4000 cm^{-1} , the PS polymer film's level of photodegradation was kept track of locating the wide hydroxyl band between 3500 and 3200 cm^{-1} and the carbonyl adsorption band $C=O$ at 1720 cm^{-1} , which are created as a result of irradiating the films. Due to the presence of the unsaturated group in the chemical makeup

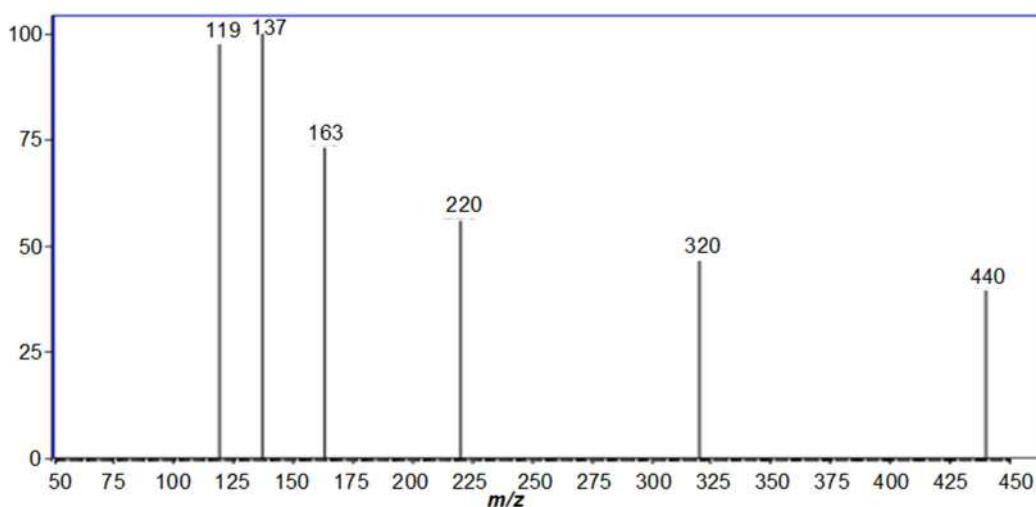


Fig 3. Mass spectrum of L

of the polymer and the difficulty in differentiating between them, the alkene group C=C was not followed up. Every 50 h of exposure time, changes in the carbonyl band C=O and hydroxyl OH intensity were seen, and Eq. (1) was applied as illustrated in Fig. S7 and S8. To track the growth in photolysis.

Accordingly, these beams were used to compare the absorption values of the standard absorption beam 1340 cm^{-1} , which is regarded as standard because it is unaffected by UV light, with the values of the standard absorption beam in order to determine the extent of polymer degradation during irradiation [29-30]. As a result, the absorbance (index) values of the hydroxyl and carbonyl groups were examined to assess the

photodegradation, as illustrated in Fig. 4 and 5. The data and values in Tables 7 and 8 show that, in comparison to PS without additives, doping with synthesis complexes decreased the increasing rate of the I_{OH} and $I_{\text{C=O}}$ indices with increased irradiation duration. The conclusion is that all additives serve as optical stabilizers for PS films, with Co(II) complex serving as the most effective one.

Investigate the Photodegradation Rate of PS Using the Weight Loss Method

The percentage weight loss of the photodegraded PS films following irradiation was used to calculate the photo stabilization effectiveness of the synthesis complexes. This causes weight reduction, which is calculable using

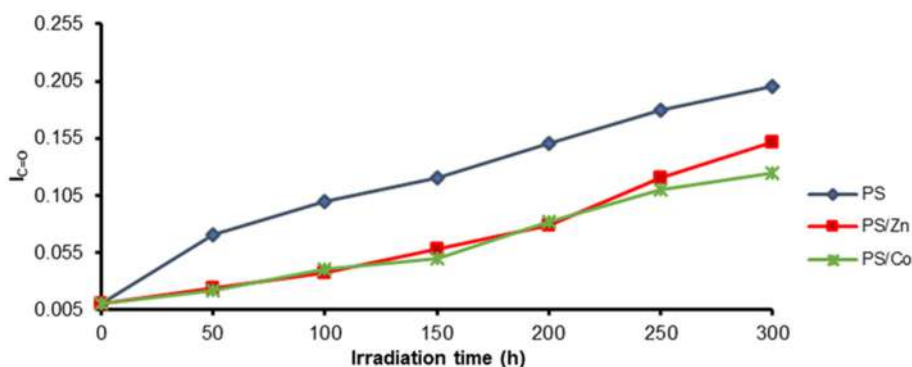


Fig 4. Index of carbonyl group $I_{\text{C=O}}$ for both pure PS and PS doped with stabilizers

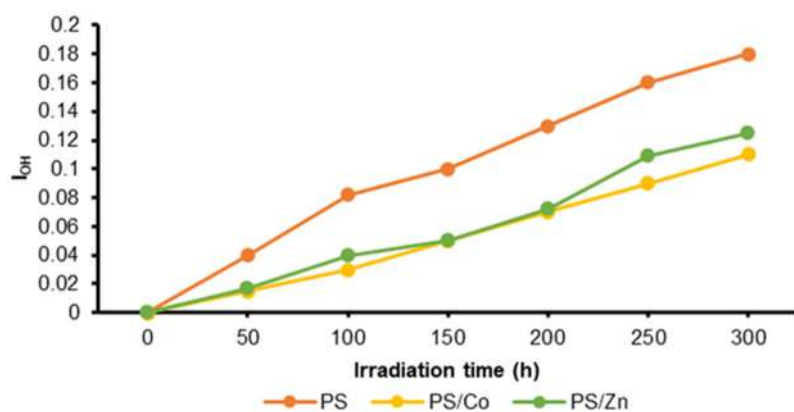


Fig 5. Index of hydroxyl group I_{OH} for both pure PS and PS doped with stabilizers

Table 7. $I_{\text{C=O}}$ data for pure PS and PS doped with stabilizers during the irradiation time

PS films	Irradiation time (h)						
	0	50	100	150	200	250	300
PS	0.010	0.070	0.100	0.120	0.150	0.180	0.200
PS/Zn	0.010	0.024	0.037	0.058	0.079	0.120	0.152
PS/Co	0.010	0.022	0.040	0.050	0.082	0.110	0.125

Table 8. I_{OH} data for both pure PS and doped PS during the irradiation period

PS films	Irradiation time (h)						
	0	50	100	150	200	250	300
PS	0	0.040	0.082	0.100	0.130	0.160	0.180
PS/Co	0	0.0150	0.030	0.050	0.070	0.090	0.110
PS/Zn	0	0.017	0.040	0.050	0.072	0.109	0.125

Eq. (2). Fig. 6 shows that when the irradiation period is increased, polystyrene steadily loses weight [31]. Nevertheless, compared to the undoped PS films, there was less weight loss in the doped PS films. The findings in Table 9 show that the cobalt complex was the most effective.

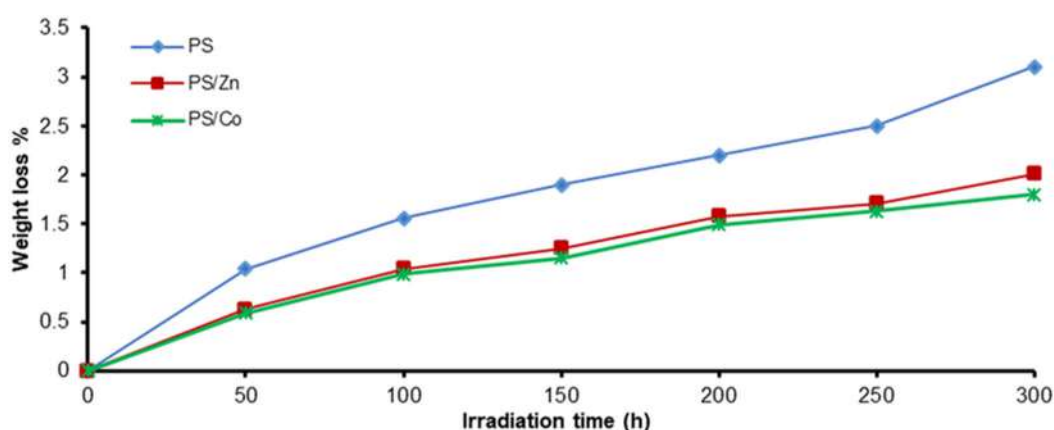
PS Stabilizing Study Using the Variance in the Average Molecular Weight

The primary chains of PS's polymeric structure are reportedly disrupted by photodegradation, which lowers the substance's average molecular weight [32]. The average molecular weight of PS after exposure to radiation is examined in this section, along with its differences from PS without additions. After being exposed to UV light, the PS solution's viscosity was measured, and the average molecular weight (\bar{M}_v) was determined. Using THF as a suitable solvent to dissolve the PS, the viscosity of the irradiation PS was evaluated using a viscometer at various

time intervals. Fig. 6. plots the MV of PS vs the irradiation time. It is clear that the molecular weight decreases with longer irradiation times for both blank and mixed PS. The decrease for bare PS is, however, more severe than it is for PS that contains stabilizers Fig. 7 and Table 10.

Study of the Produced PS Films' Surfaces

The study of how polymer surfaces develop reveals details on the crystalline state, surface regularity, and flaws brought on by photons of light interacting with polymer molecules [33]. Based on this, the mechanism of photolysis and fission of the polymeric chains was identified. The surface morphology and stability of the polymers were also observed following exposure to UV light. Prior to and following irradiation, the surface formation of pure PS and PS doped with aromatic Schiff base complexes was investigated using SEM and AFM. It

**Fig 6.** Weight loss % for both pure PS and PS doped with stabilizers**Table 9.** Weight loss% data for both pure PS and doped PS during the irradiation period

PS films	Irradiation time (h)						
	0	50	100	150	200	250	300
PS	0	1.04	1.56	1.90	2.20	2.50	3.10
PS/Zn	0	0.63	1.04	1.25	1.58	1.71	2.01
PS/Co	0	0.59	0.99	1.15	1.49	1.63	1.80

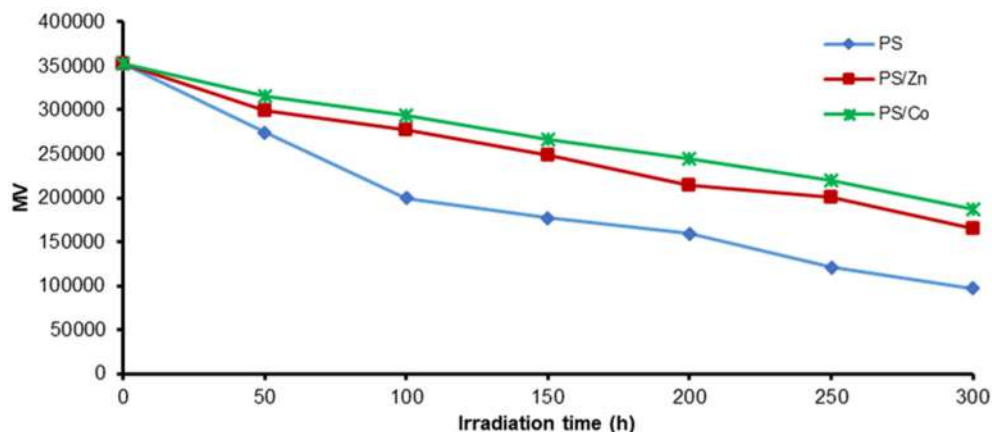


Fig 7. Average molecular weight for both pure PS and PS doped with stabilizers

Table 10. Effect of irradiation on the average molecular weight (\bar{M}_v) of Ps films

PS Films	Irradiation time (h)						
	0	50	100	150	200	250	300
PS	352546	274355	200044	177254	159519	121284	96972
PS/Zn	353254	298685	277219	249244	214574	201154	165750
PS/Co	353244	315385	293219	266244	243874	220254	186650

provides crucial details on how radiation affects the PS surface.

Using Microscopic Images to Examine the Surface of PS Films

Prior research [34] demonstrated that before being exposed to radiation, the polymer's surface had a smooth texture and just a few small fractures. In contrast, the polymer's exposed surface exhibits photodegradation of the polymer chains in the form of many fractures, increased roughness, and a darker hue. This may be caused by the radiation's influence on tiny volatile pieces with a low molecular weight. The microscopic imaging method was utilized to acquire microscopic images of the PS films' surface following irradiation in order to monitor

the deterioration of the films. The microscopic pictures of pure polystyrene before and after irradiation are shown in Fig. 8. Following 300 h of radiation exposure, the pictures demonstrate the formation of large black blotches, as illustrated in Fig. 8(b).

Fig. 10 displays microscopic images of synthetic material-doped polystyrene sheets. Little dark patches are seen on the film surfaces, notably for films doped with Zn complex, as shown in Fig. 9(a). The surfaces of the films are brighter and smoother when they are blended with the Co complex, as shown in Fig. 9(b). This demonstrates the efficiency of synthetic materials and their capacity to impede photodegradation by blocking the damaging effects of light on polystyrene films.

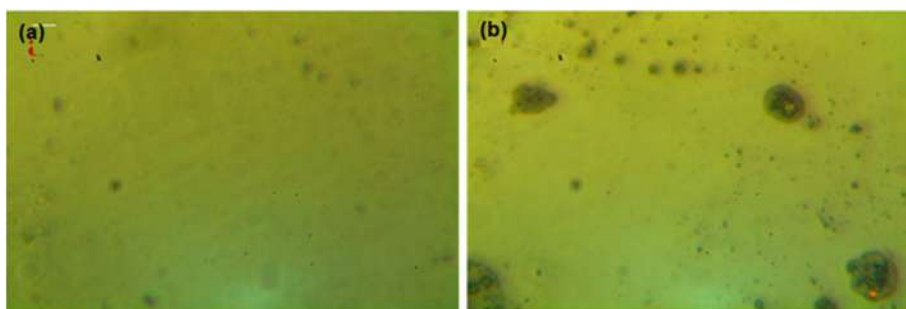


Fig 8. Microscopic images of blank PS film (a) before and (b) after irradiation

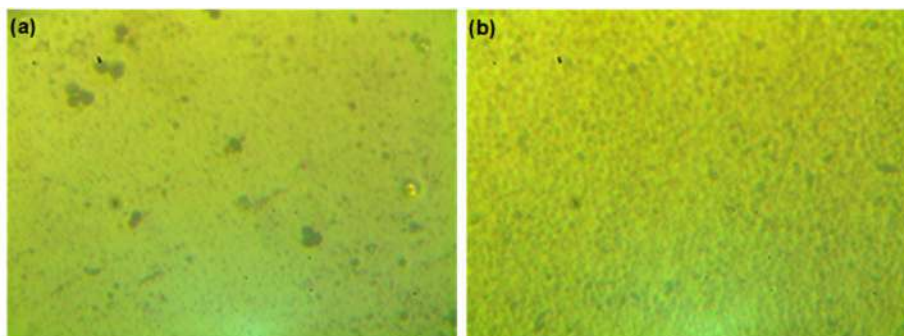


Fig 9. Microscopic images of blend PS films after irradiation (a) Zn(II) and (b) Co(II)

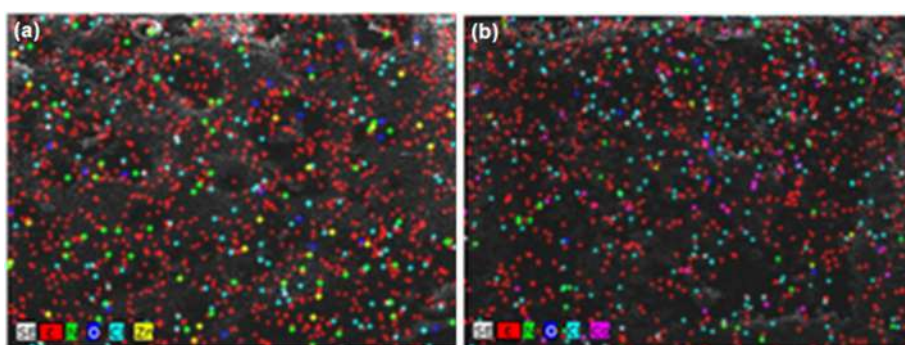


Fig 10. SEM-EDX mapping of blend PS films after irradiation (a) Zn(II) and (b) Co(II)

Energy Dispersive X-ray (EDX) Mapping with Scanning Electron Microscopy (SEM)

Using EDX mapping of doped PS films and SEM, the distribution of generated complexes on the polymeric surface was investigated. This method was utilized to provide specifics on the elemental composition of solid surfaces for PS films combined with synthetic chemicals [35]. It is common practice to use EDX in conjunction with SEM to determine the chemical composition of manufactured films. The SEM images and EDX mapping of doped films by those complexes, as shown in Fig. 10, illustrate the elemental makeup of the produced complexes and their homogenous distribution inside the polymeric chains.

An Atomic Force Microscope (AFM) Is Used to Display the Photostability of Polystyrene Films

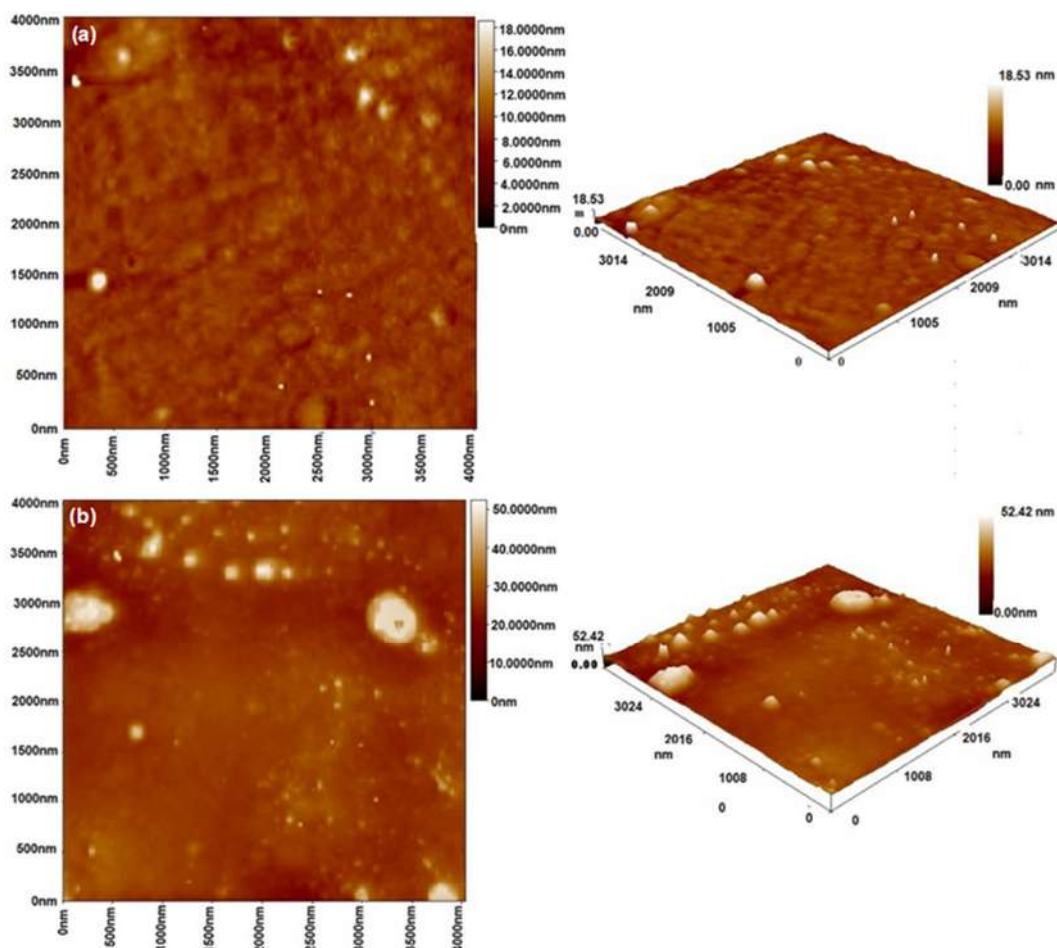
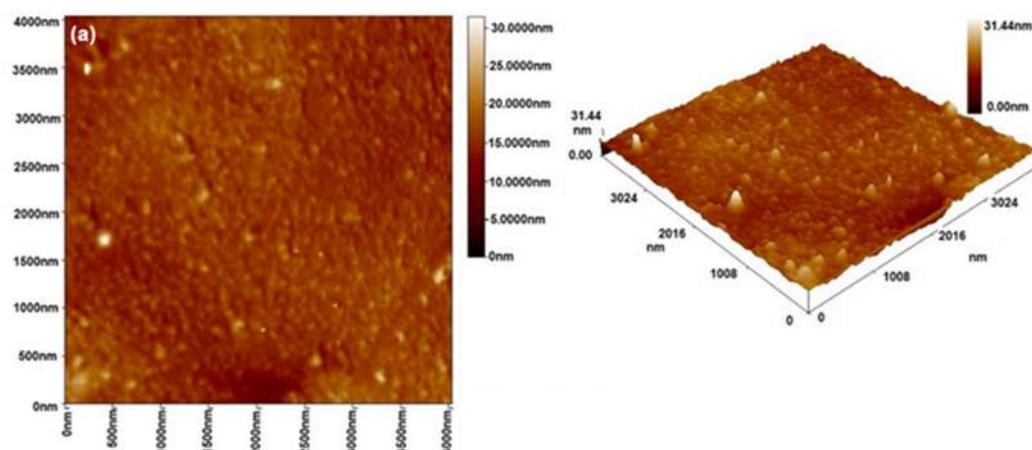
The surface morphologies of PS films were investigated using the AFM method. Due to its ability to scan both two- and three-dimensional topography, it is an effective microscopy instrument for examining surface data at the nanoscale. AFM may be used to assess the PS

surface's features and roughness. The root mean square roughness (S_q), one of the dispersion variables used to assess surface roughness, is derived by first square-rooting each height value in the dataset. Surface skewness is a measurement of the asymmetry of the surface's deviation from the mean plane. Radiation exposure to PS for an extended period of time causes a rough and cracked surface. Topographic AFM pictures of the surface of the PS films in two and three dimensions after 300 h of radiation exposure demonstrate that the root mean square (R_q) and roughness average have significantly risen, going from 0.639 nm (before radiation) to 2.35 nm (after radiation), as shown in Table 11. This is brought on by the photodegradation that radiation exposure causes to PS's chemical structure. Fig. 11 shows AFM images of untreated PS taken both before and after it was exposed to UV light.

In contrast, employing synthetic additives increased the surface roughness of PS following irradiation compared to untreated PS, as seen in Table 11. Hence, PS films with Co(II) doping exhibit the least

Table 11. Roughness data for blank and blended PS films

Films	Roughness average (nm)	Root mean square (Sq) (nm)
Blank PS before irradiation	0.639	0.956
Blank PS after irradiation	2.35	3.89
Zn(II)	2.33	3.29
Co(II)	1.99	2.52

**Fig 11.** AFM images of PS films (a) before and (b) after irradiation at 300 h

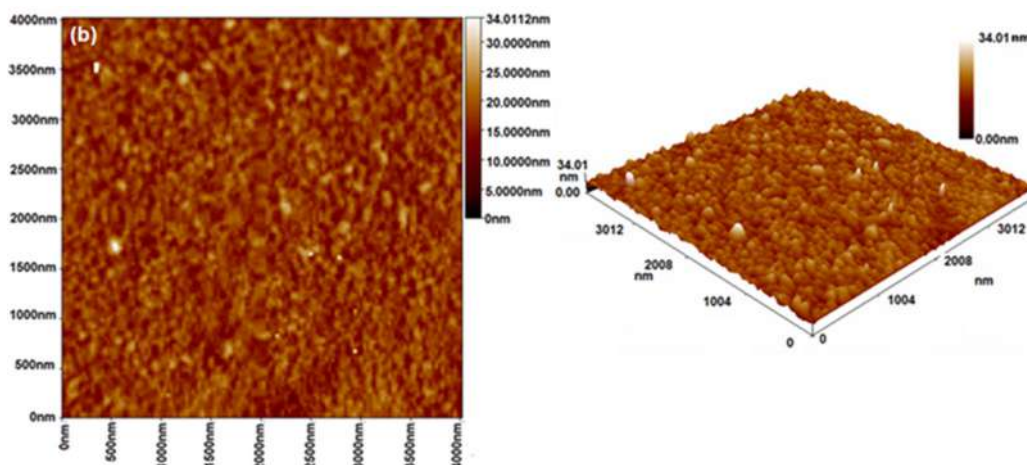


Fig 12. AFM images of blend PS films after irradiation (a) Zn(II) and (b) Co(II)

photodegradation and roughness, with Sq values of 2.52 nm. The addition of stabilizers significantly improved the photostability of PS films. Fig. 12 compares the irradiation-blended PS films with additives with the blank PS film in terms of surface homogeneity, smoothness, and roughness. In an AFM picture, the distance between peaks and valleys is frequently used as a proxy for surface roughness. The AFM technology uses this method to calculate the surface's roughness, which rises with distance. The Sq is believed to be more sensitive than the average roughness for large excursions from the mean line or plane. The PS film with cobalt complex doping had the lowest Sq value and roughness associated with photodegradation. Each of the aforementioned experiments supported this finding, showing that the cobalt complex is the best additive for PS-doped film to stop photodegradation. It is not totally clear what the reason is, therefore, more investigation may be required.

■ CONCLUSION

This work led to the effective synthesis of new Schiff base complexes, including Zn(II) and Co(II) complexes. In order to create pure target complexes, the malonyl dihydrazide had to first be combined with naphthaldehyde, and then it had to be reacted with the metal(II) chloride. The generated complexes were thoroughly characterized using FTIR, $^1\text{H-NMR}$, $^{13}\text{C-NMR}$, mass, and UV-Vis spectroscopies. In this study, a number of chemicals were used to photo-stabilize polystyrene (PS) and reduce the

polymeric chains' photodegradation. The efficiency of the created complexes as photo-stabilizers was evaluated using a variety of techniques, including FTIR, weight loss, viscosity average molecular weight, light and AFM, SEM, and EDX mapping. These tests corroborated each other and demonstrated how effectively the new compounds stabilized PS pictures. They reduce the photodegradation of PS films containing these complexes compared to blank PS after 300 h of UV exposure. It has also shown the potency of the cobalt complex as a photo-stabilizer. These compounds' highly conjugated systems are to fault for this. As plastic waste constitutes a serious danger to the environment, particularly the marine ecosystem, the study's findings have significant implications for reducing PS usage globally.

■ SUPPORTING INFORMATION

Fig. S1 FTIR spectrum of Schiff Base ligand, Fig. S2 FTIR spectrum of Co(II) complex, Fig. S3 FTIR spectrum of Zn(II) Complex, Fig. S4 UV-Vis Spectra of ligand, Fig. S5 UV-Vis Spectra of Co(II) Complex, Fig. S6 UV-Vis Spectra of Zn(II) Complex, Fig. S7 FTIR spectrum of polystyrene before irradiation, Fig. S8 FTIR spectrum of polystyrene after irradiation.

■ ACKNOWLEDGMENTS

Thanks to Department of Chemistry, College of Science for Women, University of Baghdad, Iraq. To provide them with chemicals and research equipment.

■ AUTHOR CONTRIBUTIONS

Naser Shaalan conceived this idea, based on the expressions of Rehab Ghalib Hammuda supervised the project. Rehab Ghalib Hammuda carried out the experiment, wrote the manuscript, and performed the analysis. All authors discussed the results and contributed to the final manuscript.

■ REFERENCES

- [1] Basha, M.H., Sulaiman, S.A., and Uemura, Y., 2020, Co-gasification of palm kernel shell and polystyrene plastic: Effect of different operating conditions, *J. Energy Inst.*, 93 (3), 1045–1052.
- [2] Al-Mashhadani, M.H., Thamer, H., Adil, H., Ahmed, A., Ahmed, D.S., Bufaroosha, M., Jawad, A.H., and Yousif, E., 2021, Environmental and morphological behavior of polystyrene films containing Schiff base moiety, *Mater. Today: Proc.*, 42, 2693–2699.
- [3] Wang, J., Wang, X., Zhao, S., Sun, B., Wang, Z., and Wang, J., 2020, Robust superhydrophobic mesh coated by PANI/TiO₂ nanoclusters for oil/water separation with high flux, self-cleaning, photodegradation and anti-corrosion, *Sep. Purif. Technol.*, 235, 116166.
- [4] Zabaniotou, A., and Kassidi, E., 2003, Life cycle assessment applied to egg packaging made from polystyrene and recycled paper, *J. Cleaner Prod.*, 11 (5), 549–559.
- [5] Wu, Y., Dong, L., Shu, X., Yang, Y., She, W., and Ran, Q., 2022, A review on recent advances in the fabrication and evaluation of superhydrophobic concrete, *Composites, Part B*, 237, 109867.
- [6] Rabie, S.T., Ahmed, A.E., Sabaa, M.W., and Abd El-Ghaffar, M.A., 2013, Maleic diamides as photostabilizers for polystyrene, *J. Ind. Eng. Chem.*, 19 (6), 1869–1878.
- [7] Liu, X., Sun, P., Qu, G., Jing, J., Zhang, T., Shi, H., and Zhao, Y., 2021, Insight into the characteristics and sorption behaviors of aged polystyrene microplastics through three type of accelerated oxidation processes, *J. Hazard. Mater.*, 407, 124836.
- [8] Li, Y., Li, J., Ding, J., Song, Z., Yang, B., Zhang, C., and Guan, B., 2022, Degradation of nano-sized polystyrene plastics by ozonation or chlorination in drinking water disinfection processes, *Chem. Eng. J.*, 427, 131690.
- [9] Khalaf, M., Fadhil, Z., Al-Mashhadani, M.H., Abdallah, M., Bufaroosha, M., Majeed, A., Salih, N., and Yousif, E., 2020, PVC films performance stabilized by dibutyltin(IV) complex for sustainable environment, *J. Phys.: Conf. Ser.*, 1664, 012072.
- [10] Ahmed, A., Al-Mashhadani, M.H., Ahmed, D.S., Ahmed, A.A., Yousif, E., and Yusop, R.M., 2021, Preparation of polymeric films containing Schiff base as UV-absorber with good resistance against UV-photoaging, *Biointerface Res. Appl. Chem.*, 11, 12743–12749.
- [11] Al-Mashhadani, M.H., Salman, E.A., Husain, A.A., Abdallah, M., Bufaroosha, M., and Yousif, E., 2022, Utilizing organic aromatic melamine moiety to modify poly(vinyl chloride) chemical structure and micro CuO that plays an important role to enhance its photophysical features, *Indones. J. Chem.*, 22 (5), 1187–1194.
- [12] Jima'a, R.B., and Shaalan, N., 2023, Synthesis, characterization, and biological activity of new metal ion complexes with Schiff base derived from 2-acetylthiophene and isatin, *Egypt. J. Chem.*, 65 (132), 1409–1419.
- [13] Ahmed, D.S., Mohammed, A., Husain, A.A., El-Hiti, G.A., Kadhom, M., Kariuki, B.M., and Yousif, E., 2022, Fabrication of highly photostable polystyrene films embedded with organometallic complexes, *Polymers*, 14 (5), 1024.
- [14] Fadhil, Z., Zageer, D.S., Faris, A.H., Al-Mashhadani, M.H., Ahmed, A., Hashim, H., and Yousif, E., 2022, Extracted lignin from oil palm empty fruit bunch as natural eco-friendly poly(vinyl chloride) photo-stabilizer, *Mater. Sci. Energy Technol.*, 5, 15–21.
- [15] Jose, T.S., Rajesh, C., Puthukkara, P.A.R., Unnikrishnan, K.S., and Arun, K.J., 2021, Accelerated photodegradation of polystyrene by TiO₂-polyaniline photocatalyst under UV radiation, *Eur. Polym. J.*, 153, 110493.
- [16] Zhang, X., Su, H., Gao, P., Li, B., Feng, L., Liu, Y., Du,

- Z., and Zhang, L., 2022, Effects and mechanisms of aged polystyrene microplastics on the photodegradation of sulfamethoxazole in water under simulated sunlight, *J. Hazard. Mater.*, 433, 128813.
- [17] Mahdi, S.A., Ahmed, A.A., Yousif, E., Al-Mashhadani, M.H., Ahmed, A., Hashim, H., and Jawad, A.H., 2022, New organic PVC photostabilizers derived from synthesised novel coumarine moieties, *Mater. Sci. Energy Technol.*, 5, 278–293.
- [18] Ali, A.A., Karasu, B., Allazov, M.R., and Ilyasli, T.M., 2013, Synthesis and study of $Ce_xPr_xMg_{1-2x}Al_2O_4$ ceramic pigment by combustion method using malonic acid dihydrazide as fuel, *Int. J. Sci. Eng. Res.*, 4 (8), 1686–1690.
- [19] Hussein, K.A., and Shaalan, N., 2022, Synthesis, characterization, and antibacterial activity of lanthanide metal complexes with Schiff base ligand produced from reaction of 4,4-methylene diantipyrine with ethylenediamine, *Indones. J. Chem.*, 22 (5), 1365–1375.
- [20] Shaalan, N., Khalaf, W.M., and Mahdi, S., 2022, Preparation and characterization of new tetradentate N_2O_2 Schiff base with some of metal ions complexes, *Indones. J. Chem.*, 22 (1), 62–71.
- [21] Shaalan, N.D., and Abdulwahhab, S., 2021, Synthesis, characterization and biological activity study of some new metal complexes with Schiff's bases derived from [O-vanillin] with [2-amino-5-(2-hydroxyphenyl)-1,3,4-thiadiazole], *Egypt. J. Chem.*, 64 (8), 4059–4067.
- [22] Tazin, N., Ragole, V.D., and Wankhede, D.S., 2019, Facile one pot synthesis of tetraamide macrocyclic complexes using malonyldihydrazide and *p*-nitrobenzaldehyde at room temperature, *Inorg. Nano-Met. Chem.*, 49 (9), 291–296.
- [23] Jimaa, R.B., and Shaalan, N., 2022, Synthesis, characterization and biological activity new metal ion complexes with Schiff's bases derived from 2-Acetylthiophene and Isatin, *Egypt. J. Chem.*, 65 (13), 1409–1419.
- [24] Hussein, K.A., Mahdi, S., and Shaalan, N., 2023, Synthesis, spectroscopy of new lanthanide complexes with Schiff base derived from (4-antipyrinecarboxaldehyde with ethylene di-amine) and study the bioactivity, *Baghdad Sci. J.*, 20 (2), 469–482.
- [25] Majeed, N.M., Abd. Al-Sahab, S., and Al Shemary, R.K., 2021, Eco-friendly and efficient composition, diagnosis, theoretical, kinetic studies, antibacterial and anticancer activities of mixed some metal complexes of tridentate Schiff base ligand, *Int. J. Pharm. Res.*, 13 (1), 3358–3369.
- [26] Mohan, B., and Shaalan, N., 2023, Highly thermally stable and biologically active compounds prepared to be polymer stabilizers consisting of a Schiff base and its complexes derived from 2-hydroxynaphthaldehyde, *J. Med. Chem. Sci.*, 6 (2), 355–364.
- [27] Alpay, A., Tuna, Ö., and Simsek, E.B., 2020, Deposition of perovskite-type $LaFeO_3$ particles on spherical commercial polystyrene resin: A new platform for enhanced photo-Fenton-catalyzed degradation and simultaneous wastewater purification, *Environ. Technol. Innovation*, 20, 101175.
- [28] Xiao, L., Zhao, Y., Jin, B., Zhang, Q., Chai, Z., and Peng, R., 2020, Synthesis of novel ultraviolet stabilizers based on [60]fullerene and their effects on photo-oxidative degradation of polystyrene, *Fullerenes, Nanotubes Carbon Nanostruct.*, 28 (6), 465–473.
- [29] Fakhri, L.A., Ghanbarzadeh, B., Dehghannya, J., Hosseini, M., and Dadashi, S., 2021, Photo-catalytic and biotic degradation of polystyrene packaging film: Effect of zinc oxide photocatalyst nanoparticles and nanoclay, *Chemosphere*, 283, 130972.
- [30] Luna, C.B.B., Siqueira, D.D., Araújo, E.M., and Fook, M.V.L., 2020, Photodegradation of polystyrene/rubber waste blends compatibilized with SBS copolymer, *J. Elastomers Plast.*, 52 (4), 356–379.

- [31] Yousif, E., Haddad, R., El-Hiti, G.A., and Yusop, R.M., 2017, Spectroscopic and photochemical stability of polystyrene films in the presence of metal complexes, *J. Taibah Univ. Sci.*, 11 (6), 997–1007.
- [32] Mageed, Z.N., Kadhium, S.S., Rodhan, W.F., and Mohammed, H.H., 2022, Study of the photostabilization of polystyrene in the presence and absence of Schiff base derivatives, *Egypt. J. Chem.*, 65 (4), 675–683.
- [33] Slepíčka, P., Neznalová, K., Fajstavr, D., and Švorčík, V., 2020, Nanostructuring of honeycomb-like polystyrene with excimer laser, *Prog. Org. Coat.*, 145, 105670.
- [34] Nguyen, T.N., Rangel, A., and Migonney, V., 2021, Fibronectin adsorption on polystyrene sulfonate-grafted polyester using atomic force microscope, *Biointerphases*, 16 (5), 051003.
- P., 2019, LIPSS structures induced on graphene-polystyrene composite, *Materials*, 12 (21), 3460.

Development of a Rapid and Sensitive Probe for Colorimetric Detection of Ni²⁺ Ion in Water Sample by β -Cyclodextrin Stabilized Silver Nanoparticles

Farrah Nurkhaliza^{1,2}, Ahmad Fathoni², Muhammad Eka Prastya³, Zetryana Puteri Tachrim³, Abdul Aji⁴, and Agustina Sus Andreani^{1*}

¹Research Centre for Chemistry, National Research and Innovation Agency (BRIN), Kawasan Puspiptek, Building 452, Serpong, Banten 15314, Indonesia

²Department of Chemistry, Syarif Hidayatullah State Islamic University, Jl. Ir. H. Djuanda No. 95, Ciputat, Banten 15412, Indonesia

³Research Centre for Pharmaceutical Ingredients and Traditional Medicine, National Research and Innovation Agency (BRIN), Kawasan Puspiptek, Building 466, Serpong, Banten 15314, Indonesia

⁴Department of Chemistry, Institut Teknologi Sumatera, Jl. Terusan Ryacudu, Jati Agung, Lampung 35365, Indonesia

* **Corresponding author:**

email: agus147@brin.go.id

Received: April 10, 2023

Accepted: July 17, 2023

DOI: 10.22146/ijc.83789

Abstract: A rapid and selective colorimetric detection of Ni²⁺ was developed using silver nanoparticles (AgNPs) with β -cyclodextrin (β -CDs) as reducing and stabilizing agents. Characterization was assessed by spectrophotometer UV-vis, Fourier transform infra-red (FTIR), transmission electron microscopy (TEM), and particle size analyzer (PSA). The AgNPs- β -CDs were relatively stable after being stored for 5 months. The addition of Ni²⁺ to the AgNPs- β -CDs shifted the surface plasmon resonance (SPR) band at 409 nm. Synthesized AgNPs- β -CDs had a spherical shape and an average size of 25.07 ± 0.66 nm (analyzed by TEM) and 33.63 ± 0.25 nm, as confirmed by PSA. AgNPs- β -CDs as colorimetric sensors for Ni²⁺ ions had a good linear calibration curve at 409 nm with the R² value of 0.9993. The limit of detection (LoD) was found to be 33.30 ppb, while the limit of quantification (LoQ) was 111.0 ppb. This sensor had been applied to a seawater sample from Ancol Beach, North Jakarta, Indonesia and it exhibited good precision and accuracy. In this work, β -CDs-synthesized AgNPs were able to detect Ni²⁺ ions and were beneficial as an alternative method for Ni²⁺ screening in environmental samples.

Keywords: AgNPs; β -cyclodextrin; colorimetric sensor; Ni²⁺

■ INTRODUCTION

Nickel (Ni) has a wide range of applications in various fields, such as petroleum, coinage, textile, stainless steel manufacture, and printing. Due to being highly used, Ni has become a common contributor to water pollution. Ni²⁺ ion, a toxic environmental pollutant, harms aquatic ecosystems as well as human health. Therefore, Ni²⁺ presence in water is necessary to be detected. The detection of Ni²⁺ is developed through many techniques using several instruments, such as inductively coupled plasma optical emission spectrometry (ICP-OES) [1], atomic absorption spectrometry (AAS) [2], and UV-vis spectroscopy [3]. However, these methods are expensive,

time-consuming, and require trained personnel. Therefore, some alternative techniques have been developed to overcome the increasing demand for user-friendly and rapid metal detection [4]. A detection method based on nanoparticles as a colorimetric sensor offers more advantages than those methods due to their rapid, ease of use, affordability, and effectiveness in analyzing Ni²⁺ as a water pollutant [4-6].

Recently, silver nanoparticles (AgNPs) have been hugely studied for their applications as antibacterial agents [7-8], biosensors [9], catalysts [10-11], and colorimetric sensors [6,12-13]. AgNPs as colorimetric sensors have been an interesting topic to be developed

because they possess a unique characteristic, i.e., surface plasmon resonance (SPR). The SPR band of AgNPs was indicated by the appearance of a peak at 400–500 nm on UV-vis spectra and the yellow color of the solution [8,14]. Owing to this SPR characteristic, AgNPs have been widely used as an alternative method to detect Ni^{2+} based on the colorimetric assay. The change in SPR reflects the change in AgNPs' shape and size. The interaction occurring between AgNPs and Ni^{2+} will cause a change in AgNPs' shape and size as the SPR band and the color solution also change consequently [15].

Many works and studies report on various reducing and stabilizing agents used to prepare AgNPs these past years. Cyclodextrins (CDs) are water soluble and non-toxic cyclic oligosaccharides consisting of 6, 7, or 8 glucopyranose units (named as α -, β -, or γ -, respectively) linked by α -1,4 linkage [16]. β -CDs are commonly utilized in the synthesis of AgNPs due to their low cost compared to other CDs and their ability to have a dual role as both reducing and stabilizing agents simultaneously [17-21]. β -CDs have a toroidal shape with an inner cavity diameter of 0.78 nm [22]. The inner cavity of β -CDs acts as a host to form a stable inclusion complex with a guest molecule [16], while the hydroxyl groups of β -CDs exterior act as a reducing agent [19]. These abilities of β -CDs allow them to reduce and stabilize nanoparticles.

Previously, there have been studies about colorimetric sensors for Ni^{2+} ions from AgNPs that were synthesized by other capping agents. In this work, we synthesized AgNPs using β -CDs as a double role of reducing and stabilizing agents. This could reduce the excessive utilization of chemicals and make the synthesis procedure less time-consuming. The application of β -CDs as a stabilizing agent was investigated on the AgNPs stability over time. AgNPs- β -CDs were expected to be a rapid and sensitive colorimetric sensor for Ni^{2+} in real samples, in line with the SPR change when there was an interaction between AgNPs- β -CDs with Ni^{2+} that resulted in a change of color and particle size.

■ EXPERIMENTAL SECTION

Materials

Silver nitrate (AgNO_3), sodium hydroxide (NaOH),

nitric acid (HNO_3), iron(III) nitrate ($\text{Fe}(\text{NO}_3)_3$), nickel(II) nitrate ($\text{Ni}(\text{NO}_3)_2$), magnesium nitrate ($\text{Mg}(\text{NO}_3)_2$), chromium(III) nitrate ($\text{Cr}(\text{NO}_3)_3$), cobalt(II) nitrate ($\text{Co}(\text{NO}_3)_2$), palladium(II) nitrate ($\text{Pd}(\text{NO}_3)_2$), copper(II) nitrate ($\text{Cu}(\text{NO}_3)_2$), lead(II) nitrate ($\text{Pb}(\text{NO}_3)_2$), cadmium(II) nitrate ($\text{Cd}(\text{NO}_3)_2$), and tin(IV) chloride (SnCl_4) were purchased from Merck. Reducing and stabilizing agents β -CDs were supplied by Sigma Aldrich.

Instrumentation

The UV-vis spectra of samples were recorded by spectrophotometer UV-vis Agilent Cary 60 in the wavelength range of 200–800 nm. FTIR spectra were analyzed by Shimadzu IR Prestige 21 in the 400–4000 cm^{-1} range. Transmission electron microscope (TEM) Tecnai G2 20S-Twin Function was used to determine the morphology of AgNPs. The size of nanoparticles was examined using a particle size analyzer (PSA) Horiba LA-960. The content of Ni^{2+} in seawater samples was measured using atomic absorption spectroscopy (AAS) Agilent 280FS AA.

Procedure

Synthesis of AgNPs- β -CDs

The procedure of AgNPs- β -CDs synthesis was carried out under the optimum conditions as practised in our previous work [23]. AgNO_3 1.5×10^{-4} M was added to β -CDs 5.0×10^{-3} M as reducing and stabilizing agents at pH 12. The pH value of β -CDs was adjusted by adding NaOH 0.1 M. Each solution (5 mL) was mixed in a volume ratio of 1:1 and heated in a water bath at 98 °C for 5 min.

Stability test of AgNPs- β -CDs

The stability test was performed by having the AgNPs- β -CDs stored in the fridge at 4 °C for 5 months. The solution was next measured with a spectrophotometer UV-vis at room temperature, in the wavelength range of 200–800 nm.

Colorimetric response of AgNPs- β -CDs towards metals

Colorimetric response of AgNPs- β -CDs was investigated to several heavy metal ions, such as Fe^{3+} ,

Ni^{2+} , Mg^{2+} , Cr^{3+} , Co^{2+} , Pd^{2+} , Cu^{2+} , Pb^{2+} , Cd^{2+} , and Sn^{2+} . The detection of heavy metals was carried out by mixing AgNPs- β -CDs solution with 100 ppb heavy metal ion solution (1:1 volume ratio), then measured by spectrophotometer UV-vis at room temperature.

Other metal ion interference in the reaction of AgNPs- β -CDs with Ni^{2+}

By adding the inorganic matrix to the mixture of AgNPs- β -CDs and Ni^{2+} (AgNPs- β -CDs- Ni^{2+}), the interference test was determined. The AgNPs- β -CDs- Ni^{2+} solution was prepared by mixing 1 mL of AgNPs- β -CDs and 1 mL of 100 ppb Ni^{2+} . Then the solution was added by 1 mL of 100 ppb inorganic matrix solution (Fe^{3+} , Mg^{2+} , Cr^{3+} , Co^{2+} , Pd^{2+} , Cu^{2+} , Pb^{2+} , Cd^{2+} , and Sn^{2+}) and measured by spectrophotometer UV-vis. The AgNPs- β -CDs- Ni^{2+} solution which did not contain any matrix, was measured to compare the results.

Analytical performance

The calibration curve was plotted by putting the absorbance values at 409 nm versus the concentration of Ni^{2+} . The equation of $\text{LoD} = 3 \times \text{SD}/s$ and $\text{LoQ} = 10 \times \text{SD}/s$ were used to estimate the limit of detection (LoD) and the limit of quantification (LoQ), respectively, where SD is the standard deviation and s is the slope of the calibration curve. Repeatability and reproducibility were performed by analyzing the Ni^{2+} detection of AgNPs- β -CDs three times. The spiking method was done to investigate the

accuracy parameters. The determination of Ni^{2+} standard solution recovery value was determined in sea waters.

Application test to real samples

Seawater samples were collected from Ancol Beach, North Jakarta, Indonesia at three different spots. These samples were filtered with 0.45 μm filter paper and preserved with HNO_3 0.1 M until $\text{pH} < 2$ was reached. The mixture of AgNPs- β -CDs and sample (1:1 volume ratio) was measured by spectrophotometer UV-vis. While AAS measurement was used to analyze the sample as a comparison.

RESULTS AND DISCUSSION

Synthesis and Stability Test of AgNPs- β -CDs

AgNPs- β -CDs were formed through a redox reaction where Ag^+ was reduced to Ag^0 by OH groups of β -CDs. Simultaneously, the OH groups were oxidized to aldehyde and carboxyl groups [24]. The formation of AgNPs- β -CDs was confirmed by the yellow color solution and the SPR band at 412 nm with an absorbance intensity of 0.946 (as shown in Fig. 1). The size of produced AgNPs- β -CDs was relatively small as the SPR peak was sharp and narrow. Ndikau et al. [25] explained that the SPR sharpness depends on the size of nanoparticles. The size of AgNPs would be confirmed by the TEM and PSA analysis.

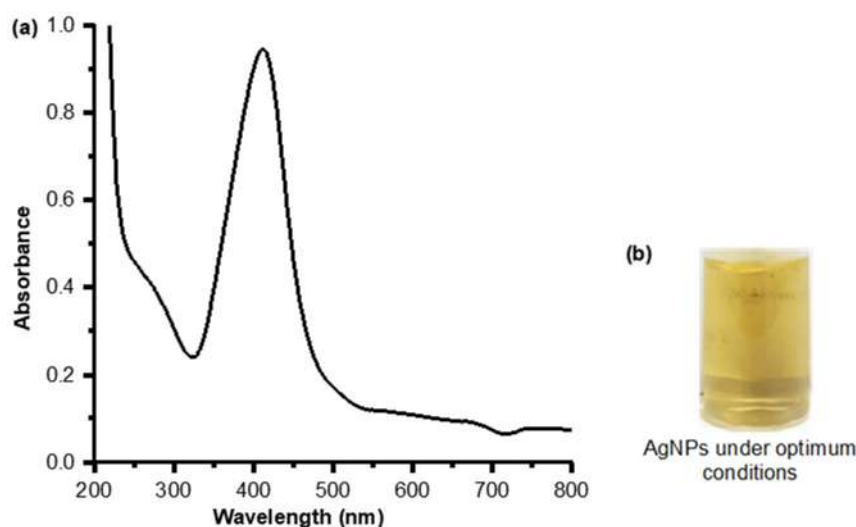


Fig 1. (a) UV spectra of AgNPs- β -CDs under optimum conditions (AgNO_3 1.5×10^{-4} M, β -CDs 5.0×10^{-3} M at pH 12, and 5 min of reaction time), and (b) the solution of AgNPs- β -CDs under optimum conditions

The stability of AgNPs- β -CDs was examined to describe the role of β -CDs as a stabilizing agent and to investigate its ability to stabilize silver nanoparticles over time. β -CDs were used as a stabilizing agent owing to their unique ability to form an inclusion complex with Ag so that the produced AgNPs- β -CDs were protected from heat, light, oxygen, and chemical reactions [26].

The AgNPs- β -CDs were stored in a capped bottle at 4 °C for 5 months. It was observed that there was no color change and no precipitate formed (Fig. 2). These factors showed that AgNPs- β -CDs were relatively stable after 5 months. The wavelength shift and increasing absorbance intensity could also be observed to study the AgNPs- β -CDs stability [27]. Fig. 2 showed the absorbance intensity increased by 0.036 (4.17%) due to the ongoing reduction process of Ag^+ to Ag^0 during the storage time. The wavelength of the SPR band did not go shift, but the peak was broadened after 5 months. It indicated that the AgNPs- β -CDs were slightly aggregated. However, it was considered that the AgNPs- β -CDs solution was still relatively stable after being stored for 5 months.

Colorimetric Response of AgNPs- β -CDs Towards Metals

An amount of 100 ppb solutions of some heavy metal ions such as Fe^{3+} , Ni^{2+} , Mg^{2+} , Cr^{3+} , Co^{2+} , Pd^{2+} , Cu^{2+} ,

Pb^{2+} , Cd^{2+} , and Sn^{2+} were tested to AgNPs- β -CDs to investigate the colorimetric response and then measured by spectrophotometer UV-vis. The UV spectra (Fig. 3(a)) showed that only Ni^{2+} caused a red shift from 409 to 414 nm and a decreasing absorbance of 0.095. The yellow color of the AgNPs- β -CDs solution also changed to greyish after being added by Ni^{2+} . Meanwhile, the other solutions were still the same. This color change happened within 5 s and was visible to the naked eye. As shown in Fig. 3(b), it was evidenced that the AgNPs- β -CDs could selectively detect the presence of Ni^{2+} ion rapidly compared to other ions.

Other Metal Ion Interference in the Reaction of AgNPs- β -CDs with Ni^{2+}

The interference test was assessed by spectrophotometer UV-vis which was carried out to determine the effect of other heavy metal ions on the AgNPs- β -CDs selectivity towards Ni^{2+} . As shown in Fig. 4, the absorbance intensity of AgNPs- β -CDs- Ni^{2+} 100 ppb did not significantly change after the addition of other heavy metal ions (100 ppb). It was evidenced that the AgNPs- β -CDs detection of Ni^{2+} was not affected by the presence of other heavy metal ions, which confirmed the good selectivity of AgNPs- β -CDs towards Ni^{2+} ion.

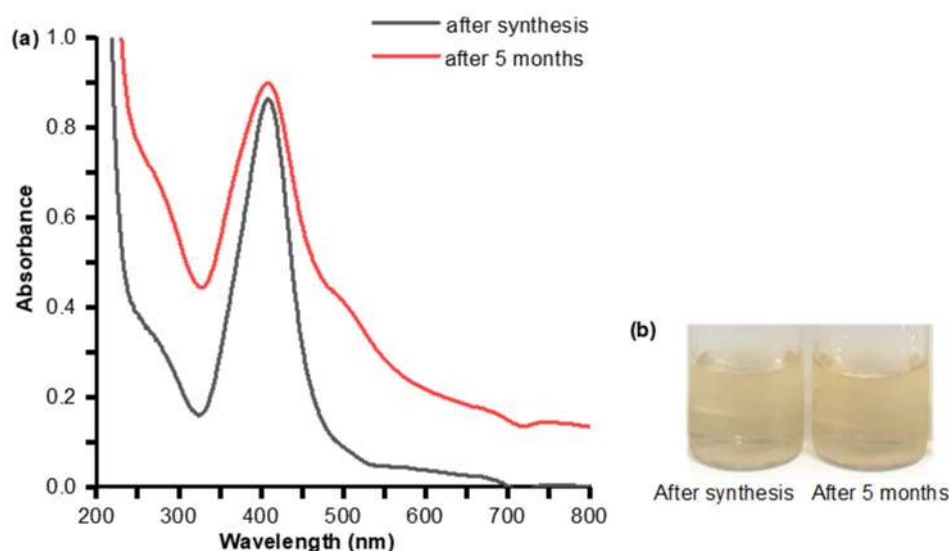


Fig 2. (a) UV spectra of AgNPs- β -CDs stability after 5 months, and (b) the solution of AgNPs- β -CDs after synthesis and after 5 months

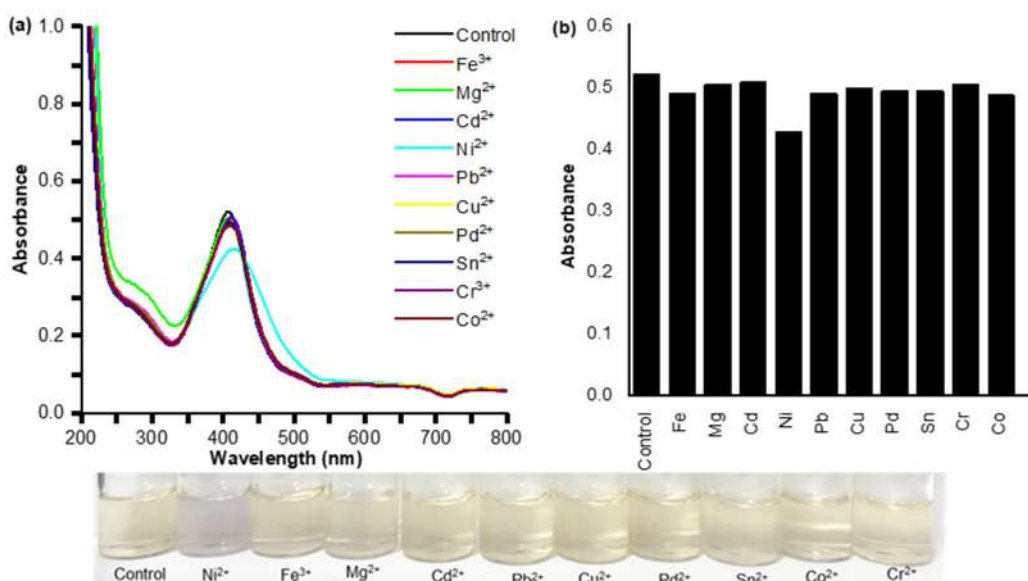


Fig 3. (a) UV spectra of AgNPs-β-CDs detection towards heavy metal solutions at a concentration of 100 ppb, and (b) AgNPs-β-CDs selectivity towards 100 ppb heavy metal solutions

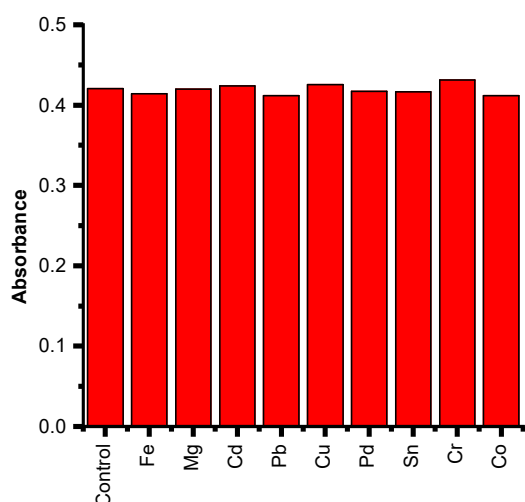


Fig 4. The bars representing the absorbance intensity of AgNPs-β-CDs-Ni²⁺ (409 nm) in the presence of 100 ppb of other heavy metal ions

Characterization

FTIR analysis

The addition of Ni²⁺ to AgNPs-β-CDs (AgNPs-β-CDs-Ni²⁺) showed the interaction between β-CDs and Ni²⁺ ion (Fig. 5 and Table 1). A peak at 3311 cm⁻¹ (AgNPs-β-CDs) was associated with O-H stretching, which was broadened and went shifted to 3348 cm⁻¹ in AgNPs-β-CDs-Ni²⁺ spectra. It explained that Ni²⁺ ion interacted with hydroxyl groups of β-CDs inner cavity [28]. There

was a peak attributed to CH stretching in AgNPs-β-CDs spectra at 2976 and 2918 cm⁻¹. Meanwhile, the ones in AgNPs-β-CDs-Ni²⁺ were shifted to 2922 and 2859 cm⁻¹. A weak peak at 1717 cm⁻¹ (AgNPs-β-CDs) and a strong peak at 1732 cm⁻¹ (AgNPs-β-CDs-Ni²⁺) were assigned to C=O stretching.

He et al. [28] revealed that Ni²⁺ interacted with the C-O bond of β-CDs, which caused a strong peak in AgNPs-β-CDs spectra (1051 cm⁻¹) change to a small peak

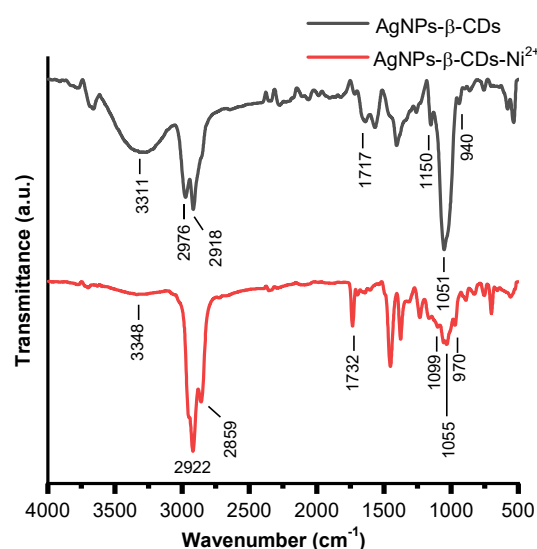
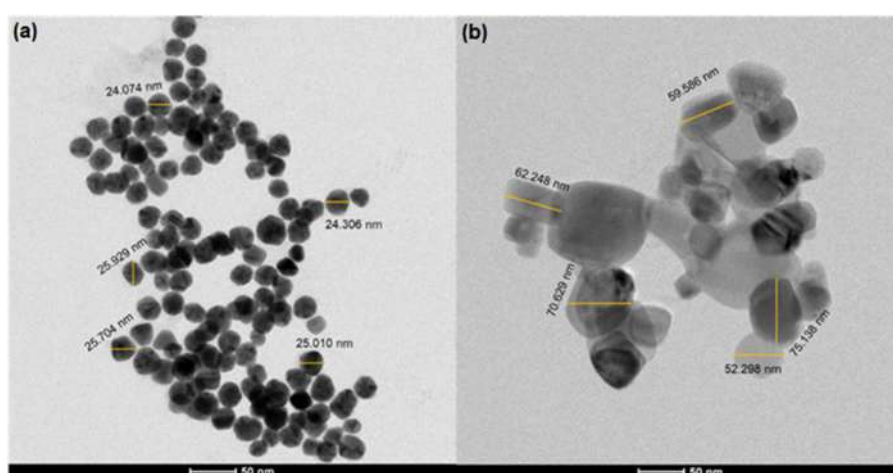


Fig 5. FTIR spectra of AgNPs-β-CDs and AgNPs-β-CDs-Ni²⁺

Table 1. Wavenumbers of AgNPs- β -CDs and AgNPs- β -CDs-Ni²⁺

AgNPs- β -CDs (cm ⁻¹)	AgNPs- β -CDs-Ni ²⁺ (cm ⁻¹)	Functional groups
3311	3348	O-H stretching
2976	2922	C-H stretching
2918	2859	C-H stretching
1717	1732	C=O stretching
1051	1055	C-O stretching
1150	1099	Asymmetrical C-O-C stretching
940	970	Symmetrical C-O-C stretching

**Fig 6.** The morphology and size of (a) AgNPs- β -CDs and (b) AgNPs- β -CDs-Ni²⁺ by TEM analysis

in AgNPs- β -CDs-Ni²⁺ (1055 cm⁻¹). There was an asymmetrical C-O-C stretching at 1150 and 1099 cm⁻¹ in the AgNPs- β -CDs and AgNPs- β -CDs-Ni²⁺ spectra, respectively. The peak corresponding to symmetrical C-O-C stretching appeared at 940 cm⁻¹ (AgNPs- β -CDs) and 970 cm⁻¹ (AgNPs- β -CDs-Ni²⁺).

TEM and PSA analysis

The synthesized AgNPs- β -CDs and AgNPs- β -CDs-Ni²⁺ were characterized by the TEM instrument. Fig. 6 revealed the morphology of AgNPs- β -CDs before and after interacting with Ni²⁺ ions. The average size of AgNPs- β -CDs was 25.07 ± 0.66 nm with a spherical shape (Fig. 6(a)). The addition of Ni²⁺ ion to AgNPs- β -CDs solution caused a size increase (with an average of 63.98 ± 8.09 nm) and particles to aggregate (Fig. 6(b)).

The size of formed AgNPs- β -CDs was confirmed by the PSA analysis. The measurement using PSA revealed that AgNPs- β -CDs had an average size of 33.63 ± 0.25 nm. Meanwhile, the AgNPs- β -CDs-Ni²⁺ was

73.43 ± 1.47 nm. There was an increasing size of particles after the addition of Ni²⁺ owing to the interaction between Ni²⁺ and AgNPs- β -CDs. The interaction led to aggregation because the SPR band got broadened and a red shift occurred [29-30]. The interaction of Ni²⁺ with AgNPs- β -CDs was illustrated in Fig. 7.

Ni²⁺ ion interacted with hydroxyl groups of β -CDs inner cavity through electrostatic interaction [28]. According to Kabbur et al. [31], Ni²⁺ ion had a size of 0.078 nm, and another study by Suárez-Cerda et al. [22] reported that the diameter of β -CDs inner cavity was 0.78 nm. Ni²⁺ ion had a smaller size than the inner cavity diameter of β -CDs, so Ni²⁺ could get into the β -CDs inner cavity and have interaction with the hydroxyl groups in line with FTIR data. It was also observed that the inner cavity of β -CDs had a negative charge due to complete deprotonation at pH 12, thus, the interaction was stronger as the Ni²⁺ ion had positive charges.

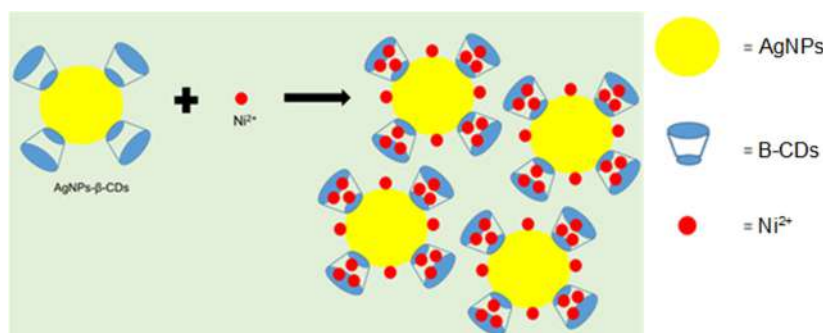


Fig 7. The illustration represents the interaction that happened between AgNPs- β -CDs and Ni^{2+}

Analytical Performance

Linearity

The calibration curve linearity was carried out to evaluate the performance of colorimetric sensor AgNPs- β -CDs in detecting Ni^{2+} ions. Spectrophotometer UV-vis was used to measure the change of absorbance intensity at 409 nm. The difference between the initial absorbance intensity of AgNPs- β -CDs and the decreased absorbance intensity of AgNPs- β -CDs after Ni^{2+} addition was calculated to obtain the change of absorbance intensity (Δ_{Abs}). The Δ_{Abs} versus Ni^{2+} at a concentration of 100–500 ppb was plotted as a calibration plot (Fig. 8). The increasing concentration of Ni^{2+} led to an increased Δ_{Abs} as the SPR band was changed. The linearity equation obtained from the calibration curve was $y = 0.0002x - 0.0106$ with a correlation coefficient (R^2) of 0.9993. It proved that the R^2 obtained was categorized as a good linear regression value as the R^2 was ≥ 0.997 . The concentration level of Ni^{2+} in water samples could be determined by the linearity equation obtained. From the

dynamic linear range of the calibration curve, it also obtained the LoD value of 33.30 ppb and the LoQ of 111.00 ppb.

Table 2 shows the comparison between Ni^{2+} sensors using AgNPs- β -CDs and AgNPs with other stabilizing agents. AgNPs- β -CDs had more advantages than the previous studies [12,32–34], i.e., lower detection limit and the rapid colorimetric response towards Ni^{2+}

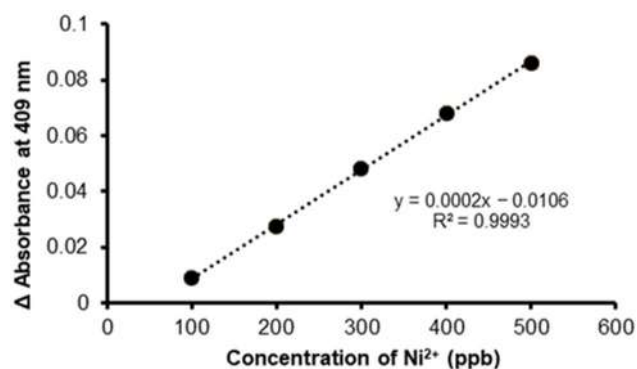


Fig 8. Calibration plot of AgNPs- β -CDs Δ_{Abs} at 409 nm versus the concentration of Ni^{2+}

Table 2. The data comparison of AgNPs- β -CDs and various AgNPs as colorimetric sensors for Ni^{2+}

Stabilizing agents	Samples	Analysis time (min)	LoD (ppb)	References
3-mercapto-1-propanesulfonic acid sodium salt (3MPS)	-	5	500	[12]
Citrate	Tap water	1	44.250	[32]
3,6-di(pyridin-2-yl)-1,4-dihydro-1,2,4,5-tetrazine (H_2pytz)	-	2	554.6	[33]
Adenosine monophosphate and sodium dodecyl sulphonate	Tap water and lake water	5	35.4	[34]
β -cyclodextrin	Sea water	<1	33.30	This research

Table 3. The repeatability and reproducibility of AgNPs- β -CDs at 409 nm

Ni ²⁺ (ppb)	SD	Repeatability		Reproducibility	
		%RSD		%RSD	
		AOAC	Horwitz	AOAC	Horwitz
100	0.000168	0.031294	1.000000	3.288019	1.000000
200	0.000900	0.172146	0.900929	0.442867	0.900929
300	0.000582	0.116802	0.847591	0.450230	0.847591
400	0.000493	0.107833	0.811673	8.311422	0.811673
500	0.000520	0.119042	0.784864	8.460454	0.784864

Table 4. The accuracy of AgNPs- β -CDs for detecting Ni²⁺ in seawater samples

Samples	Spiked (ppb)	Detected (ppb)	Accuracy (%)
Sample I (1.33 ppb)	250	252.31	100.39
Sample II (1.33 ppb)	250	272.91	108.63
Sample III (1.33 ppb)	250	227.14	90.32

less than 1 min. It proved that this research developed a Ni²⁺ colorimetric sensor which provided a better sensitivity and more rapid detection.

Repeatability and reproducibility

The precision method of the Ni²⁺ colorimetric sensor using AgNPs- β -CDs was determined by examining the repeatability and reproducibility. Repeatability was performed where the measurement of absorbance intensity was done in triplicates at 409 nm on the same day, under the optimum conditions. Reproducibility was carried out by measuring the absorbance under the optimum conditions at 409 nm on 3 different days. The %RSD results of both repeatability and reproducibility (Table 3) were lower than the maximum acceptable %RSD according to AOAC (15%) and Horwitz (22.6%) for the Ni²⁺ concentration level of 100 ppb [35]. It was evidenced that AgNPs- β -CDs as Ni²⁺ colorimetric sensors gave acceptable precision results.

Accuracy

The accuracy test was determined by measuring 3 different seawater samples spiked by 250 ppb Ni²⁺ standard solution with a spectrophotometer UV-vis. The results were stated as %Recovery. Table 4 enlisted the recovery value of Ni²⁺ in the seawater samples at the range of 90.32–108.63%. González et al. [35] revealed that the acceptable %Recovery range of 250 ppb Ni²⁺ concentration level was 80–110%. It was implied that the colorimetric sensor of Ni²⁺ using AgNPs- β -CDs could give

Table 5. The results of Ni²⁺ concentration in seawater samples (n = 3)

Samples	AgNPs (ppb)	AAS (ppb)
Sample I	19.95	20
Sample II	19.95	20
Sample III	19.95	20

accurate results as the obtained recovery values were lower than the maximum acceptable percentage.

Application Test to Real Samples

AgNPs- β -CDs as a Ni²⁺ colorimetric sensor were applied to seawater samples collected from Ancol Beach, North Jakarta, Indonesia at three different points. It was performed to assess the Ni²⁺ concentration in the samples. Those samples were filtered by a 0.45 μ m filter paper and preserved by HNO₃ until pH < 2. The measurement with AAS was carried out to compare the Ni²⁺ concentration results.

Table 5 shows the measurement results of Ni²⁺ concentration using AgNPs- β -CDs and AAS. AgNPs- β -CDs as colorimetric sensors provided good results compared to AAS. These data proved that AgNPs- β -CDs could be applied as a colorimetric sensor for Ni²⁺ in seawater samples.

CONCLUSION

This current work inferred that β -CDs as reducing and stabilizing agents could form relatively stable

AgNPs- β -CDs after 5 months. AgNPs- β -CDs as a rapid and selective colorimetric sensor for Ni²⁺ was successfully developed, which was indicated by the yellow color of the solution turning into greyish. This sensor could exhibit good performance as the R² of the linear calibration curve obtained was 0.9993 with an LoD value of 33.30 ppb and an LoQ value of 111.0 ppb. No interference of other ions affected the detection. Furthermore, the precision and accuracy were satisfying for the measurement of Ni²⁺ in seawater. Hence, this sensor could be beneficial for the detection of Ni²⁺ ions in real water samples.

■ ACKNOWLEDGMENTS

This research would like to acknowledge funding from the RIIM Gelombang 3 BRIN (12/II.7/HK/2023) and to acknowledge the facilities, scientific and technical support from Advanced Characterization Laboratories Serpong, National Research and Innovation Agency (BRIN) through *E-Layanan Sains, Badan Riset dan Inovasi Nasional*.

■ AUTHOR CONTRIBUTIONS

Farrah Nurkhaliza: data curation, investigation, formal analysis, writing-original draft; Ahmad Fathoni: investigation, validation, supervision; Muhammad Eka Prastya: validation, methodology, supervision; Zetryana Puteri Tachrim: validation, supervision; Abdul Aji: validation, supervision; Agustina Sus Andreani: conceptualization, formal analysis, funding acquisition, investigation, methodology, supervision, validation, writing-review & editing.

■ REFERENCES

- [1] Tokay, F., and Bağdat, S., 2018, Preconcentration and determination of metal ions using fluorescein-modified silica gel and inductively coupled plasma-optical emission spectrometry, *Anal. Lett.*, 51 (1-2), 119–132.
- [2] Akcin, N., Koyuncu, I., and Akcin, G., 2011, Determination of zinc, nickel and cadmium in natural water samples by flame atomic absorption spectrometry after preconcentration with ion exchange and flotation techniques, *Rev. Anal. Chem.*, 30 (2), 65–71.
- [3] Tu, L.N., Van Tan, L., and Chien, N.X., 2013, Simultaneous spectrophotometric determination of Ni(II) and Zn(II) in waste water by H-point addition standard method using 5-bromosalicylaldehyde thiosemicarbazone, *Eur. Chem. Bull.*, 2 (6), 311–315.
- [4] Rossi, A., Zannotti, M., Cuccioloni, M., Minicucci, M., Petetta, L., Angeletti, M., and Giovannetti, R., 2021, Silver nanoparticle-based sensor for the selective detection of nickel ions, *Nanomaterials*, 11 (7), 1733.
- [5] Azimi, H., Ahmadi, S.H., Manafi, M.R., Husain, S., Mousavi, H., and Najafi, M., 2021, Development a simple and sensitive method for determination low trace of nickel by localized surface plasmon resonance of citrate capped silver nanoparticles, *J. Optoelectron. Nanostruct.*, 6 (2), 23–40.
- [6] Milczarek, G., Rebis, T., and Fabianska, J., 2013, One-step synthesis of lignosulfonate-stabilized silver nanoparticles, *Colloids Surf., B*, 105, 335–341.
- [7] Bindhu, M.R., and Umadevi, M., 2014, Spectroscopy silver and gold nanoparticles for sensor and antibacterial applications, *Spectrochim. Acta, Part A*, 128, 37–45.
- [8] Chouhan, S., and Guleria, S., 2020, Green synthesis of AgNPs using *Cannabis sativa* leaf extract: Characterization, antibacterial, anti-yeast and α -amylase inhibitory activity, *Mater. Sci. Energy Technol.*, 3, 536–544.
- [9] Daoudi, K., Ramachandran, K., Alawadhi, H., Boukherroub, R., Dogheche, E., Khakani, M.A.E., and Gaidi, M., 2021, Ultra-sensitive and fast optical detection of the spike protein of the SARS-CoV-2 using AgNPs/SiNWs nanohybrid based sensors, *Surf. Interfaces*, 27, 101454.
- [10] Bogireddy, N.K.R., Kiran Kumar, H.A., and Mandal, B.K., 2016, Biofabricated silver nanoparticles as green catalyst in the degradation of different textile dyes, *J. Environ. Chem. Eng.*, 4 (1), 56–64.
- [11] Nguyen, T.D., Dang, C.H., and Mai, D.T., 2018, Biosynthesized AgNP capped on novel nanocomposite 2-hydroxypropyl- β -cyclodextrin/

- alginate as a catalyst for degradation of pollutants, *Carbohydr. Polym.* 197, 29–37.
- [12] Mochi, F., Burratti, L., Fratoddi, I., Venditti, I., Battocchio, C., Carlini, L., Iucci, G., Casalbani, M., De Matteis, F., Casciardi, S., Nappini, S., Pis, I., and Proposito, P., 2018, Plasmonic sensor based on interaction between silver nanoparticles and Ni²⁺ or Co²⁺ in water, *Nanomaterials*, 8 (7), 488.
- [13] Oluwafemi, O.S., Anyik, J.L., Zikalala, N.E., and Sakho, E.H.M., 2019, Biosynthesis of silver nanoparticles from water hyacinth plant leaves extract for colourimetric sensing of heavy metals, *Nano-Struct. Nano-Objects*, 20, 100387.
- [14] Pethakamsetty, L., Kothapenta, K., Nammi, H.R., Ruddaraju, L.K., Kollu, P., Yoon, S.G., and Pammi, S.V.N., 2016, Green synthesis, characterization and antimicrobial activity of silver nanoparticles using methanolic root extracts of *Diospyros sylvatica*, *J. Environ. Sci.*, 55, 157–163.
- [15] Andreani, A.S., Kunarti, E.S., Hashimoto, T., Hayashita, T., and Santosa, S.J., 2021, Fast and selective colorimetric detection of Fe³⁺ based on gold nanoparticles capped with *ortho*-hydroxybenzoic acid, *J. Environ. Chem. Eng.*, 9 (5), 105962.
- [16] Veglia, A.V., and Bracamonte, A.G., 2019, β -Cyclodextrin grafted gold nanoparticles with short molecular spacers applied for nanosensors based on plasmonic effects, *Microchem. J.*, 148, 277–284.
- [17] Ilanchelian, M., Retna Raj, C., and Ramaraj, R., 2000, Spectral studies on the cyclodextrin inclusion complexes of toluidine blue O and Meldola's blue in aqueous solution, *J. Inclusion Phenom. Macrocyclic Chem.*, 36 (1), 9–20.
- [18] Premkumar, T., and Geckeler, K.E., 2014, Facile synthesis of silver nanoparticles using unmodified cyclodextrin and their surface-enhanced Raman scattering activity, *New J. Chem.*, 38 (7), 2847–2855.
- [19] Rajamanikandan, R., and Ilanchelian, M., 2018, β -Cyclodextrin functionalised silver nanoparticles as a dual colorimetric probe for ultrasensitive detection of Hg²⁺ and S²⁻ ions in environmental water samples, *Mater. Today Commun.*, 15, 61–69.
- [20] Ma, Q., Song, J., Zhang, S., Wang, M., Guo, Y., and Dong, C., 2016, Colorimetric detection of riboflavin by silver nanoparticles capped with β -cyclodextrin-grafted citrate, *Colloids Surf., B*, 148, 66–72.
- [21] Qiu, X., Gu, J., Yang, T., Ma, C., Li, L., Wu, Y., Zhu, C., Gao, H., Yang, Z., Wang, Z., Li, X., Hu, A., Xu, J., Zhong, L., Shen, J., Huang, A., and Chen, G., 2022, Sensitive determination of norfloxacin in milk based on β -cyclodextrin functionalized silver nanoparticles SERS substrate, *Spectrochim. Acta, Part A*, 276, 121212.
- [22] Suárez-Cerda, J., Nuñez, G. A., Espinoza-Gómez, H., and Flores-López, L. Z., 2014, A comparative study of the effect of α -, β -, and γ -cyclodextrins as stabilizing agents in the synthesis of silver nanoparticles using a green chemistry method, *Mater. Sci. Eng. C*, 43, 21–26.
- [23] Nurkhaliza, F., Fathoni, A., Yati, I., Prastya, M.E., Jenie, S.N.A., and Andreani, A.S., 2023, UV-Vis study on β -cyclodextrin as dual function for synthesis AgNPs and antibacterial application, *Macromol. Symp.*, 409 (1), 2200182.
- [24] Yu, Y., Wang, Q., Yuan, J., Fan, X., and Wang, P., 2016, A novel approach for grafting of β -cyclodextrin onto wool via laccase/TEMPO oxidation, *Carbohydr. Polym.*, 153, 463–470.
- [25] Ndikau, M., Noah, N.M., Andala, D.M., and Masika, E., 2017, Green synthesis and characterization of silver nanoparticles using *Citrullus lanatus* fruit rind extract, *Int. J. Anal. Chem.*, 2017, 8108504.
- [26] Doderò, A., Schlatter, G., Hébraud, A., Vicini, S., and Castellano, M., 2021, Polymer-free cyclodextrin and natural polymer-cyclodextrin electrospun nanofibers: A comprehensive review on current applications and future perspectives, *Carbohydr. Polym.*, 264, 118042.
- [27] Aji, A., Santosa, S.J., and Kunarti, E.S., 2020, Effect of reaction time and stability properties of gold nanoparticles synthesized by *p*-aminobenzoic acid and *p*-aminosalicylic acid, *Indones. J. Chem.*, 20 (2), 413–421.

- [28] He, J., Li, Y., Wang, C., Zhang, K., Lin, D., Kong, L., and Liu, J., 2017, Rapid adsorption of Pb, Cu and Cd from aqueous solutions by β -cyclodextrin polymers, *Appl. Surf. Sci.*, 426, 29–39.
- [29] Ngamchuea, K., Batchelor-McAuley, C., Sokolov, S.V., and Compton, R.G., 2017, Dynamics of silver nanoparticles in aqueous solution in the presence of metal ions, *Anal. Chem.*, 89 (19), 10208–10215.
- [30] Sulistiawaty, L., Sugiarti, S., and Darmawan, N., 2015, Detection of Hg^{2+} metal ions using silver nanoparticles stabilized by gelatin and tween-20, *Indones. J. Chem.*, 15 (1), 1–8.
- [31] Kabbur, S.M., Waghmare, S.D., Ghodake, U.R., and Suryavanshi, S.S., 2018, Synthesis, morphology and electrical properties of Co^{2+} substituted NiCuZn ferrites for MLCI applications, *AIP Conf. Proc.*, 1942 (1), 130002.
- [32] Almaquer, F.E.P., Ricacho, J.S.Y., and Ronquillo, R.L.G., 2019, Simple and rapid colorimetric sensing of Ni(II) ions in tap water based on aggregation of citrate-stabilized silver nanoparticles, *Sustain. Environ. Res.*, 29 (1), 23.
- [33] Samanta, S., Das, S., and Biswas, P., 2014, Synthesis of 3,6-di(pyridin-2-yl)-1,2,4,5-tetrazine (pytz) capped silver nanoparticles using 3,6-di(pyridin-2-yl)-1,4-dihydro-1,2,4,5-tetrazine as reducing agent: Application in naked eye sensing of Cu^{2+} , Ni^{2+} and Ag^+ ions in aqueous solution and paper platform, *Sens. Actuators, B*, 202, 23–30.
- [34] Feng, J., Jin, W., Huang, P., and Wu, F., 2017, Highly selective colorimetric detection of Ni^{2+} using silver nanoparticles cofunctionalized with adenosine monophosphate and sodium dodecyl sulfonate, *J. Nanoparticle Res.*, 19 (9), 306.
- [35] González, A.G., Herrador, M.Á., and Asuero, A.G., 2010, Intra-laboratory assessment of method accuracy (trueness and precision) by using validation standards, *Talanta*, 82 (5), 1995–1998.

Adsorption of Malachite Green Oxalate Dye by $\text{CuCo}_2\text{O}_4/\text{MgO}$ Spinel Oxide Nanocomposite

Tariq Hussein Mgheer¹, Ali Abdulraheem Kadhim^{2*}, Zainab Abdalameer Hussein³, Zaid Kaheel Kadhim⁴, Muneer Abdul Aly Al-Da'amy⁵, Abbas Jassim Atiyah⁶, Salih Hadi Kadhim⁶, and Suma Jaafar Abbas³

¹Department of Chemistry and Biochemistry, College of Medicine, University of Babylon, Hilla 51002, Iraq

²Department of Animal Production, College of Agriculture, University of Kerbala, Karbala 56001, Iraq

³Department of Plant Protection, College of Agriculture, University of Kerbala, Karbala 56001, Iraq

⁴Department of Horticulture and Landscape, College of Agriculture, University of Kerbala, Karbala 56001, Iraq

⁵Department of Chemistry, College of Pure Science for Education, University of Kerbala, Karbala 56001, Iraq

⁶Department of Chemistry, College of Science, University of Babylon, Hilla 51002, Iraq

* **Corresponding author:**

email: ali.abid@uokerbala.edu.iq

Received: April 12, 2023

Accepted: May 15, 2023

DOI: 10.22146/ijc.83850

Abstract: The current study involves a synthesis of a composite of copper oxide and cobalt oxide as a spinel oxide load over magnesium oxide. This synthesis of nanocomposite material was from nitrate salts of the corresponding metals by co-precipitation method, while it was investigated by Fourier transform infrared spectroscopy (FTIR), X-ray diffraction techniques (XRD), field emission scanning electron microscopy (FESEM), atomic force microscopy (AFM), and the activity of these materials was estimated by appreciated adsorption of malachite green oxalate (MGO) dye from its aqueous solution. Adsorption isotherm was investigated using both Freundlich and Langmuir adsorption isotherms. While the results of the spectrophotometric studies showed that the composition of synthesized supported oxides at 450 °C was spinel type with nanoparticle size, and the optimum removal efficiency was around 98% for the adsorption of MGO dye over spinel nanocomposite surface achieved by using a dye concentration of 5 ppm, a mass of adsorbent surface of 5 mg, in terms of the adsorption model's isotherms the obtained results showed that the removal of MGO dye by the surface of this material was more fitted with the Freundlich models' adsorption.

Keywords: malachite green oxalate dye; CuCo_2O_4 spinel oxide; MgO; polluted dyes

■ INTRODUCTION

Spinel structures that exist with transition metal oxides have attracted considerable attention to be used in many applications such as catalysis, photocatalysis, adsorption, and some pharmaceutical and medical applications [1]. Transition metal oxide spinel composites are characterized by abundant resources, low price, and biocompatibility. Due to all these factors, their manufacturers have recently become the research hot spot [2].

The electrocatalytic activities of composites metals oxides such as $\text{Ni}_3\text{O}_4\text{-Co}_3\text{O}_4\text{-Al}_2\text{O}_3$ and $\text{Co}_3\text{O}_4\text{-Fe}_3\text{O}_4/\text{CaO}$ can be enhanced in comparison with their corresponding single metal oxides when the distribution of ions homogeneous in the respective lattice sites [3]. In this context, the captivation arrangement of the unfilled d-orbital electrons and the synergistic effect of both Cu and Co atoms in a unit cell of CuCo_2O_4 [4].

Despite the stability of metal oxides as catalysts, they have defects, including flocculation, toxicity, and

agglomeration [5]. Therefore, its properties were improved by adding other materials that act as carrier surfaces that can improve their physical and chemical properties with improving their catalytic activity [6]. There are also substances called emollients that can increase the efficiency of the catalyst. Important examples of these additives are calcium, zinc, and iron oxides [7].

Magnesium oxide used in this study is also considered a carrier surface on which cobalt and copper oxides are based [8]. The adsorption process is one of its important applications [9]. This probably arises from enhanced catalytic properties, including high BET surface area and moderate band gap [10].

The adsorption process is one of the best processes for removing toxic dyes from polluted environments, including air, water and soil [11]. Arora et al. used *Curcuma caesia*-based activated carbon to remove malachite green dye from an aqueous solution [12]. As well, Sharma et al. [13] used nanocomposite hydrogel for photocatalytic degradation of malachite green oxalate dye.

The present work aims to synthesize $\text{CuCo}_2\text{O}_4/\text{MgO}$ as a composite spinel-supported oxide and characterize a new adsorbent surface. The adsorption ability of the prepared material toward malachite green oxalate dye was investigated. This dye is chosen due to its wide use in the textile industries.

■ EXPERIMENTAL SECTION

Materials

The used chemicals were $\text{Cu}(\text{NO}_3)_2 \cdot 3\text{H}_2\text{O}$, $\text{Mg}(\text{NO}_3)_2 \cdot 6\text{H}_2\text{O}$, $\text{Co}(\text{NO}_3)_2 \cdot 6\text{H}_2\text{O}$, and Na_2CO_3 of high purity 99, 98 and 99 % respectively supplied from B.D.H company. Malachite green oxalate (MGO) dye ($\text{C}_{52}\text{H}_{54}\text{N}_4\text{O}_{12}$) was obtained from BDH Company. Fig. 1 showed the structural formula of the MGO dye [14].

Instrumentation

The experiments use several apparatuses including electronic balance TP-214 (Sartorius, Germany), UV-visible spectrophotometer double beam-6100PC (EMC LAB, Germany), muffle furnace size-two, oven Bs size two (Gallenkamp), ultrasonic set, and heater with magnetic

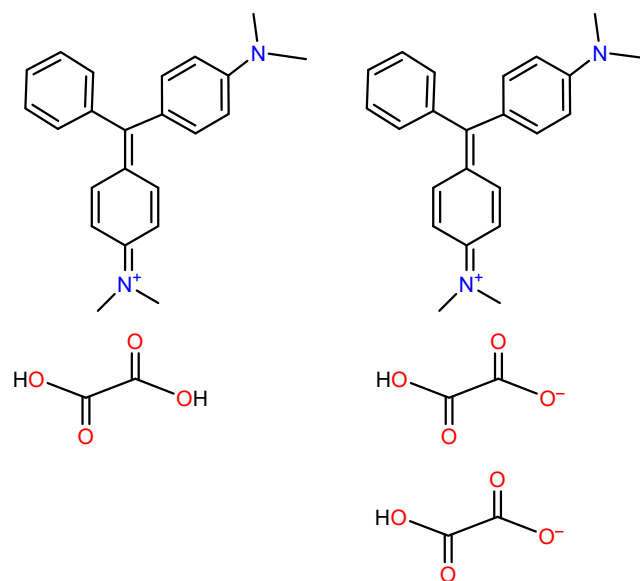


Fig 1. The structural formula of MGO

stir MR Hei-standard (Heldolph, Germany). Instruments used for characterization included X-Ray XRD-6000 and FTIR IRAffinity-1S (Shimadzu, Japan), field-emission scanning electron microscope (FE-SEM) Tescan Mira3 (French), and atomic force microscope (AFM)TT-2 (AFM Workshop, USA).

Procedure

Synthesis of composite spinel oxide

A spinel oxide of copper and cobalt was prepared by calcinating their carbonates through the coprecipitation method [15]. Sodium carbonate was used as a precipitation agent in two ratios of 0.4 (2.431 g) and 0.6 (5.82 g) from their aqueous nitrates, respectively, at a reaction temperature of 60–70 °C. Then, the precipitant was filtered and washed with deionized distilled water until $\text{pH} = 7$. Next, the precipitate was dried at 120 °C for 24 h. After that, it was calcinated at 450 °C for 4 h, following the preparation method described in the previous study [16]. Magnesium oxide was also prepared separately by precipitation method from its aqueous nitrate at the same conditions [17]. Then, the copper and cobalt oxides were loaded on magnesium oxide at a ratio of 0.4 of dual oxide to 0.6 of magnesium oxide and mixed very well in 100 mL of distilled water using ultrasound for 30 min. The homogeneous oxides were filtered and dried, then calcined at 450 °C for 4 h. This is a

modification of the method used by Kadhim [17] for preparing $\text{CuCo}_2\text{O}_4/\text{MgO}$.

Study of conditions of optimization adsorption

A series of volumetric flasks of 25 mL capacity was taken containing a dye solution with a concentration of 8 ppm. A weight of 0.01 mg of the adsorbent was added to each volumetric flask and placed in a water shaker. The percentage of dye removal was measured every 10 min, for 120 min after separating the adsorbent surface from the solution and finding the absorbance of the solution. As for the weight of the adsorbent surface, a series of volumetric flasks of 25 mL capacity of 8 ppm dye solution were also taken, in addition to the different weights in the range of 0.0025–0.015 g of the adsorbent surface and finding the percentage of dye removal at the optimization time [18]. In the same way, the function experiments were carried out with acidity and ionic strength [19];

$$\text{Re}\% = \frac{C_i - C_e}{C_i} \times 100\% \quad (1)$$

$$Q_e = \frac{V(C_i - C_e)}{m} \quad (2)$$

whereas, Re% = the removal efficiency of dye, C_i = the initial concentration of the MGO dye (before adsorption), C_e = equilibrium concentration of the MGO dye (after adsorption), Q_e = the capacity of the adsorbate in mg g^{-1} , m = the weight of $\text{CuCo}_2\text{O}_4/\text{MgO}$ in units of g, and V is the total volume of the adsorbate solution in units L.

Isothermal study for adsorption of MGO dye over $\text{CuCo}_2\text{O}_4/\text{MgO}$ composite

A series of different initial concentrations in the range of 4–12 mg L^{-1} of MGO dye to construct the calibration curve to use for determination of the residual concentration of dye after each of the operations of the removal process. This study was carried out at different temperatures 298, 318, and 338 K and found the adsorption capacity (Q_e) at the optimum conditions of adsorption to study the isothermal adsorption temperature for adsorption of dye according to Giles's classification using the prepared adsorbent surface by plotting between the adsorption capacity Q_e and C_e [20].

RESULTS AND DISCUSSION

Characterization of Synthesized Metal Oxides

Functional groups of the prepared material were investigated using FTIR spectrometry. The obtained results are presented in Fig. 2. From these spectra, it is clear that the vibrations of stretching metal-oxygen bonds appeared in a range of less than 1000 cm^{-1} . The peaks at 436, 550 and 667 cm^{-1} have corresponded to the vibrations of stretching bonds of $\text{Mg}^{2+}-\text{O}^{2-}$, tetrahedral $\text{Co}^{3+}-\text{O}^{2-}$ and octahedral $\text{Cu}^{2+}-\text{O}^{2-}$, respectively. This indicates that the synthesized oxides are a spinel type $\text{CuCo}_2\text{O}_4/\text{MgO}$ [16,21-22]. The peaks around 2400 cm^{-1} are related to the rocking vibrations of the metal oxide bonds [23].

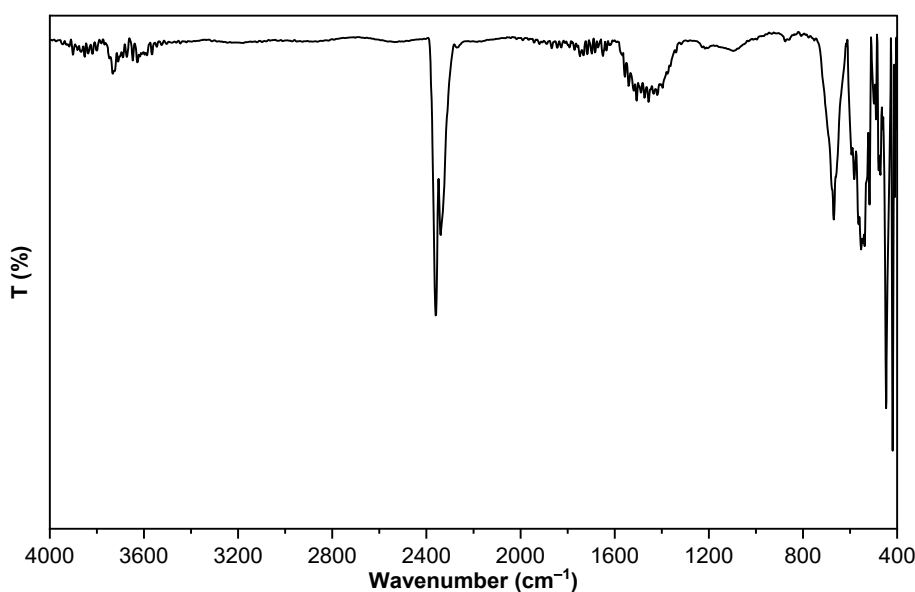


Fig 2. FTIR for Synthesized $\text{CuCo}_2\text{O}_4/\text{MgO}$

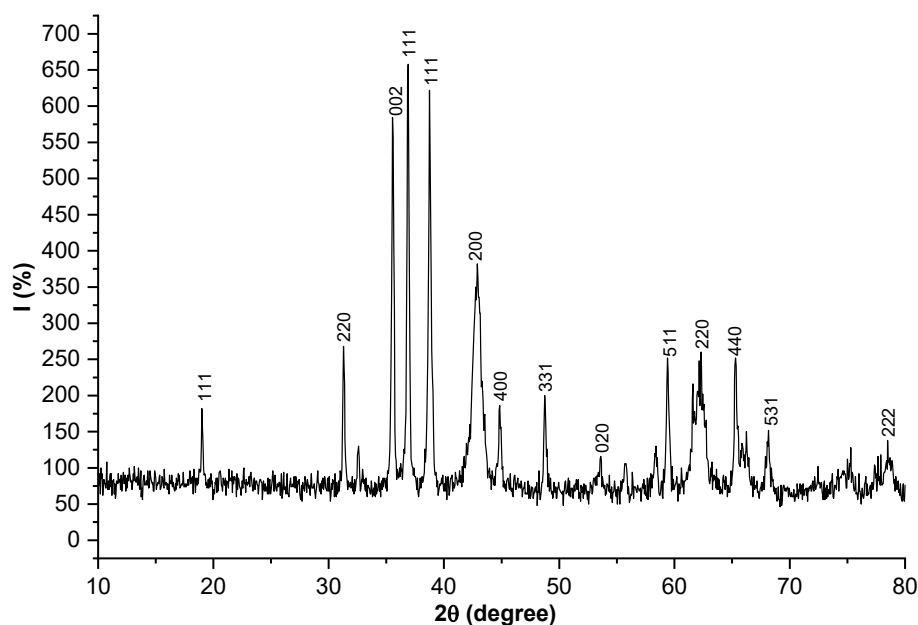


Fig 3. XRD patterns for the synthesized $\text{CuCo}_2\text{O}_4/\text{MgO}$

The crystal structure of the prepared materials was investigated using X-ray diffraction patterns. These patterns are shown in Fig. 3; the main peaks at 2θ 19.03, 31.30, 32.58, 35.57, 36.89, 38.77, 42.93, 44.86, 48.76, 53.43, 55.74, 58.37, 59.41, 62.23, 65.29, 68.11 and 78.52 with Miller coefficients (111), (220), (110), (002), (111), (111), (200), (400), (331), (020), (422), (202), (511), (220), (440), (531), and (222), respectively, identical to the metal oxides of CuCo_2O_4 and MgO according to the standard JCPDS card for these materials [24-25].

The surface morphology of the synthesized material was screened using scanning electron microscopy, and the obtained image is presented in Fig. 4. From the obtained image, it can be seen that the presence of homogeneous flakes with an average particle size of around 33 nm, with the presence of spherical granules particles with an average size of around 27 nm, MgO and CuCo_2O_4 .

AFM was also utilized in the investigation topography of the synthesized materials. The obtained results are presented in Fig. 5. AFM image showed a relative homogeneity of the surface's topography of these oxides and their roughness coefficient.

Optimization Conditions for Removal of MGO Dye by Adsorption over $\text{CuCo}_2\text{O}_4/\text{MgO}$ Spinel Oxide

Fig. 6 shows the calibration curve of MGO dye, which

was done for the determination of the dye concentration after each adsorption process.

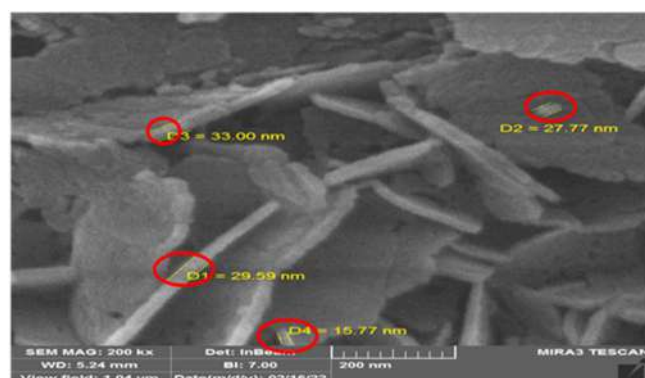


Fig 4. FESEM image for $\text{CuCo}_2\text{O}_4/\text{MgO}$ spinel oxide

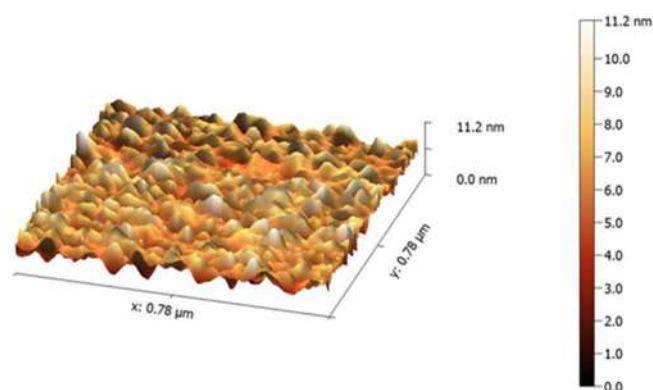


Fig 5. AFM image for synthesized $\text{CuCo}_2\text{O}_4/\text{MgO}$ spinel oxide

Contact time is one of the most important factors influencing the adsorption process, and it is the time required for adsorbent particles to stick to the adsorbent surface. From Fig. 7, we noticed a sudden increase in the removal rate in the first 10 min. Then it was increased to reach a high percentage after 50 min. After that, the removal rate remains almost constant for up to 120 min. As a result of the adhesion of all adsorbent particles to the adsorbed surface during the first 60 min. This observation arises from the gradual filling of active sites at the adsorbent surface with MGO dye molecules with time progress until it becomes fully saturated, which leads to reduce the rate of dye removal over the adsorbent surface [18].

Fig. 8 shows the effect of the adsorbent surface weight on the efficiency of dye removal. From these results, it can be seen that the adsorption capacity was increased with the increase of adsorbent surface weight because this can lead to an increased number of active sites on the adsorbent surface with the increase of the amount of adsorbent surface in the adsorption process [26].

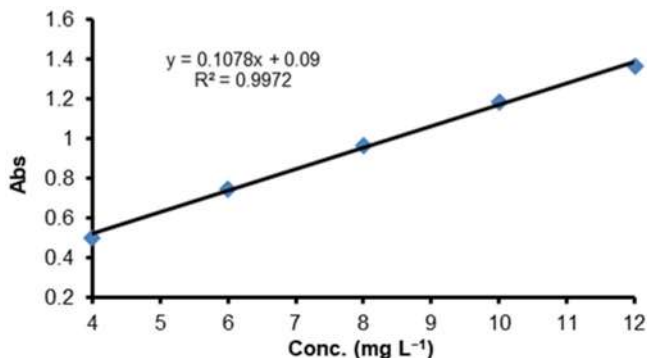


Fig 6. Calibration curve of MGO dye at wavelength 620 nm

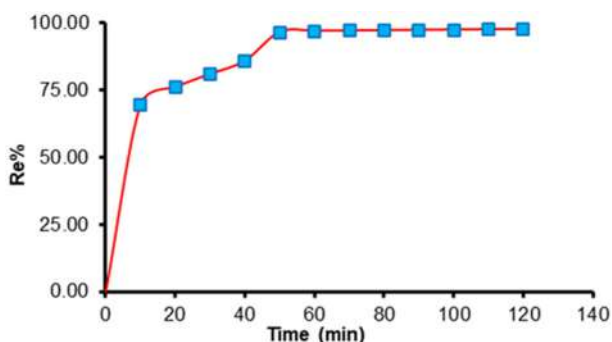


Fig 7. Contact time of MGO dye particles on $\text{CuCo}_2\text{O}_4/\text{MgO}$ adsorbent surface

Fig. 9 shows the adsorption isotherm in which the relationship between the adsorption capacity of Q_e and C_e adsorbents when using different initial concentrations of 4–12 mg L^{-1} was, according to Giles S4 classification, the reason for the high-affinity adsorbents and surface adsorbents at 298–338 K [27].

Figs. 10, 11, and 12 show Freundlich, Langmuir, and Temkin adsorption isotherms; these were calculated according to Eq. (3–5). The values of constants for each of

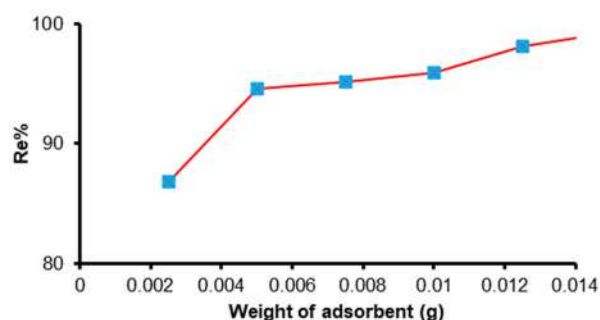


Fig 8. Effect of the weight of $\text{CuCo}_2\text{O}_4/\text{MgO}$ adsorbent surface on adsorption MGO dye

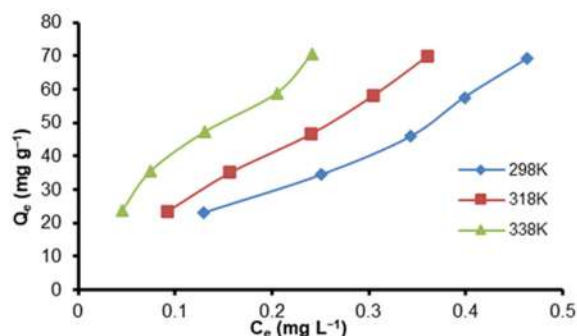


Fig 9. Isothermal of adsorption MGO dye over $\text{CuCo}_2\text{O}_4/\text{MgO}$ adsorbent surface at 298, 318, and 338 K

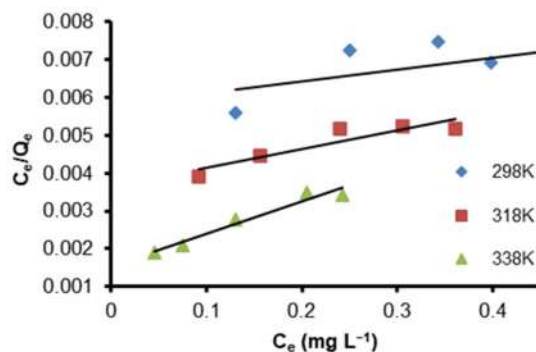


Fig 10. Relationship between C_e/Q_e and C_e for MGO dye over $\text{CuCo}_2\text{O}_4/\text{MgO}$ adsorbent surface at 298, 318, and 338 K

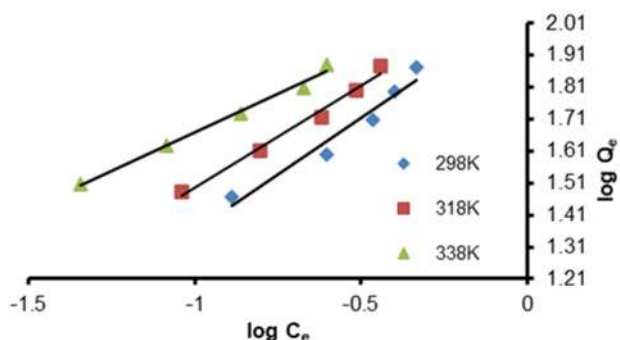


Fig 11. Relationship between $\log Q_e$ and $\log C_e$ for MGO dye over $\text{CuCo}_2\text{O}_4/\text{MgO}$ adsorbent surface at 298, 318, and 338 K

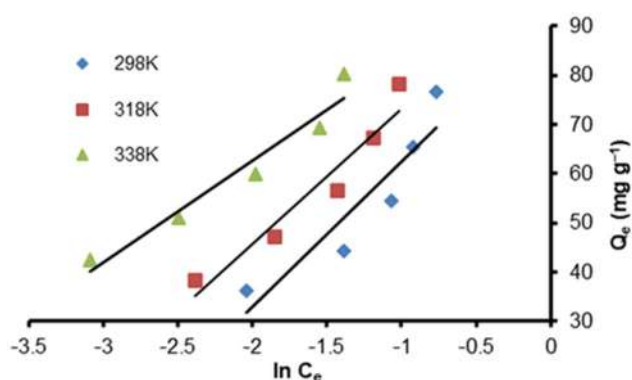


Fig 12. Relationship between Q_e and $\ln C_e$ for MGO dye over $\text{CuCo}_2\text{O}_4/\text{MgO}$ adsorbent surface at 298, 318, and 338 K

the model's adsorption equations and all the results are summarized in Table 1. The adsorption process applies to Freundlich and Temkin equations while the Langmuir equation does not apply to Freundlich because Langmuir originally proposed that the adsorption process occurs on one layer after that, Freundlich and Temkin modified Langmuir's equation for the adsorption process occur in more than one layer [28-29];

$$Q_e = \frac{abC_e}{1 + bC_e} \quad \text{Langmuir} \quad (3)$$

where Q_e is adsorption gravimetric capacity in units (mg g^{-1}), C_e is the concentration of the solute adsorbent at equilibrium in units of mg L^{-1} , (a) best adsorption capacity when the adsorption surface is completely saturated in (mg g^{-1}) units, and b is Langmuir constant [30].

$$Q_e = k_f C_e^{1/n} \quad \text{Freundlich} \quad (4)$$

The k_f and n are the experimental Freundlich constants while n and k_f are a measure of the intensity of adsorption and a measure of the amount of adsorption, respectively [30].

$$Q_e = \frac{RT}{b} \ln A_T C_e \quad \text{Temkin} \quad (5)$$

The A_T is the adsorption equilibrium constant representing the maximum adsorption energy while B is an enabling isotherm constant which is equal to RT/b (R : represents the general gas constant $8.314 \text{ J mol}^{-1} \text{ K}^{-1}$, T represents the absolute temperature K , and b the adsorption heat constant J mol^{-1}) [30].

Study of Thermodynamic Functions (ΔG , ΔH and ΔS)

The effect of temperature on the efficiency of MGO dye removal by adsorption over the prepared materials was studied, and thermodynamic functions (free energy ΔG , enthalpy ΔH , entropy ΔS) for the importance of this conception to the adsorption process and determining the type of reaction spontaneous or not, exothermic or endothermic [33]. The free energy ΔG was calculated using Eq. (10), while ΔH was calculated by sketching the relationship between the equilibrium constant $\ln K_{eq}$, which is shown in Fig. 13 and Table 2. From the negative value of ΔG , it appears that the adsorption process occurs spontaneously and does not need energy. The heat of the reaction is positive, indicating that the adsorption process is an endothermic process, while the

Table 1. Langmuir, Freundlich, and Temkin constants and correlation coefficient for adsorption of MGO dye over $\text{CuCo}_2\text{O}_4/\text{MgO}$

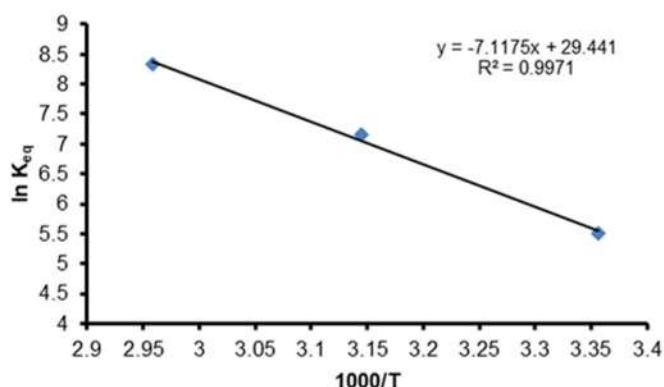
Temperature K	Langmuir isotherm			Freundlich isotherm			Temkin isotherm		
	a	b	R^2	K_f	n	R^2	b_T	K_T	R^2
298	333.33	0.51	0.29	116.76	1.41	0.94	29.51	22.51	0.84
318	204.08	1.32	0.83	136.45	1.55	0.98	27.48	39.04	0.92
338	117.64	5.31	0.95	140.34	2.08	0.99	20.60	154.70	0.94

Table 2. Comparative Langmuir, Freundlich, and Temkin constants and correlation coefficient for adsorption of MGO dye

Adsorbent	Langmuir isotherm			Freundlich isotherm			Temkin isotherm			Ref.
	a	b	R ²	K _f	n	R ²	b _T	K _T	R ²	
SnO ₂ -NP-AC	142.87	2.33	0.9990	76.17	4.98	0.8320	19.91	63.00	0.8750	[31]
TLN	425.63	0.01	0.9528	42.57	3.19	0.9077	23.30	1.17	0.8997	[32]
CuCo ₂ O ₄ /MgO	333.33	0.52	0.2965	116.76	1.41	0.9477	29.52	22.51	0.8499	This work

Table 3. Thermodynamic functions (ΔG , ΔH and ΔS) for the adsorption process

Tem. K	1000/T	K _{eq}	ln K _{eq}	ΔG (kJ mol ⁻¹ K ⁻¹)	ΔH (kJ mol ⁻¹ K ⁻¹)	ΔS (J mol ⁻¹ K ⁻¹)
298	3.35	248.71	5.51	-13.66	59.17	-244.43
318	3.14	1270.02	7.14	-18.89	59.17	-245.50
338	2.95	4177.02	8.33	-23.42	59.17	-244.39

**Fig 13.** Calculation of ΔH for adsorption of MGO dye over the synthesized material by plotting of $\ln K_{eq}$ against $1000/T$

change in entropy showed a change from a positive value but decreasing state with increasing temperature, this may be due to the disturbance of the water molecules around the dye [34-35].

$$\ln K_{eq} = \frac{-RH}{T} + \text{con.} \quad (6)$$

$$K_{eq} = \frac{Q_e m}{C_e V} \quad (7)$$

Substitute of Eq. (2) in Eq. (7):

$$K_{eq} = \frac{C_0 - C_e}{C_e} \quad (8)$$

$$\text{Slope} = -R\Delta H \quad (9)$$

$$\Delta G = -RT \ln K_{eq} \quad (10)$$

$$\Delta S = \frac{\Delta G - \Delta H}{T} \quad (11)$$

From the Isothermal models in Table 2 and thermodynamic values in Table 3, the removal mechanism of MGO dye was physical absorption because ΔG was negative as well. The isothermal models were not identical to the Langmuir model [36-37].

CONCLUSION

The present study involved the synthesis of a new spinel oxide nanocomposite successfully (CuCo₂O₄/MgO). The type of prepared composite was a spinel structure with a nanoparticles range. It showed high efficiency for the removal of MGO dye from its aqueous solutions, which was around 98%. Removal of MGO dye was conducted effectively using small quantities of adsorbent surface weight between 0.0025–0.015 g and dye concentration 5 mg L⁻¹.

ACKNOWLEDGMENTS

The authors would like to thank the Department of Horticulture and Landscape, College of Agriculture, University of Kerbala, Iraq and the College of Science, University of Babylon, for their help and funding to complete this study.

REFERENCES

- [1] Farag, N.M., Deyab, M.A., El-naggar, A.M., Aldhafiri, A.M., Mohamed, M.B., and Heiba, Z.K., 2021, Exploring the functional properties of CuCo₂O₄/CuS nanocomposite as improved

- material for supercapacitor electrode, *J. Mater. Res. Technol.*, 10, 1415–1426.
- [2] Qiao, X., Geng, W., Sun, Y., Zheng, D., Yang, Y., Meng, J., He, J., Bi, K., Cui, M., and Chou, X., 2021, Robust in-plane polarization switching in epitaxial BiFeO₃ films, *J. Alloys Compd.*, 852, 156988.
- [3] Mohamad, E.J., 2015, Comparative Study to Synthesis and Characterization the Catalyst Ni₃O₄-Co₃O₄-Al₂O₃ and Usage in Photooxidation and Adsorption of Removal of Reactive Yellow145 and Bismarck Brown G Dyes, *Thesis*, University of Babylon, Iraq.
- [4] Sun, J., Xu, C., and Chen, H., 2021, A review on the synthesis of CuCo₂O₄-based electrode materials and their applications in supercapacitors, *J. Materiomics*, 7 (1), 98–126.
- [5] Al-samaray, H.S., 2018, Study the Removal of Celestine Blue Dye from Their Aqueous Solutions by Adsorption over the Mixed Oxide NiO-MgO Pure and Doped, *Thesis*, University of Babylon, Iraq.
- [6] Dhara, K., and Debiprosad, R.M., 2019, Review on nanomaterials-enabled electrochemical sensors for ascorbic acid detection, *Anal. Biochem.*, 586, 113415.
- [7] Ismael, H.A., Mohammad, E.J., Atiyah, A.J., Kadhim, S.H., and Kahdum, K.J., 2021, Synthesis and characteristic study of composite zinc oxide and functionalized activated carbon with investigation of its adsorption ability: A kinetic study, *IOP Conf. Ser.: Earth Environ. Sci.*, 722, 012007.
- [8] Ahmadian, A., Bilal, M., Khan, M.A., and Asjad, M.I., 2020, Numerical analysis of thermal conductive hybrid nanofluid flow over the surface of a wavy spinning disk, *Sci. Rep.*, 10 (1), 18776.
- [9] Kadhim, N.J., Mousa, S.A., Muhammed, E.A., and Farhan, A.M., 2020, A comparative study of the adsorption of crystal violet dye from aqueous solution on rice husk and charcoal, *Baghdad Sci. J.*, 17 (1), 295–304.
- [10] Hussein, Z.A., Alazawy, R.A., and Haddawi, S.M., 2020, Adsorption of 2,6-dichlorophenol-indophenol sodium dihydrate salt from aqueous solutions using nano magnesium oxide; A thermodynamic study, *Egypt. J. Chem.*, 63 (10), 4157–4161.
- [11] Al-Abadi, S.I., Al-Da'Amry, M.A., and Kareem, E.T., 2021, Thermodynamic study for removing of crystal violet dye on Iraqi porcelanite rocks powder, *IOP Conf. Ser.: Earth Environ. Sci.*, 790, 012055.
- [12] Arora, C., Kumar, P., Soni, S., Mittal, J., Mittal, A., and Singh, B., 2020, Efficient removal of malachite green dye from aqueous solution using *Curcuma caesia* based activated carbon, *Desalin. Water Treat.*, 195, 341–352.
- [13] Sharma, G., AlOthman, Z.A., Kumar, A., Sharma, S., Ponnusamy, S.K., and Naushad, M., 2017, Fabrication and characterization of a nanocomposite hydrogel for combined photocatalytic degradation of a mixture of malachite green and fast green dye, *Nanotechnol. Environ. Eng.*, 2 (1), 4.
- [14] Ali, L.A.M., Farhood, A.S., and Ali, F.F., 2017, Technique of batch adsorption for the elimination of (malachite green) dye from industrial waste water by exploitation walnut shells as sorbent, *Indones. J. Chem.*, 17 (2), 211–218.
- [15] Janjua, M.R.S.A., 2019, Synthesis of Co₃O₄ nano aggregates by co-precipitation method and its catalytic and fuel additive applications, *Open Chem.*, 17 (1), 865–873.
- [16] Thahy, R.R.A., 2018, Synthesis and Identification of Co₃O₄-Fe₃O₄/M_xO_x/M_xO_{x+1} where (M= Ca, Mg, Al, Ce) Spinel Supported Catalyst and Using It Removal of Bismarck Brown G Dye, *Thesis*, University of Babylon, Iraq.
- [17] Kadhim, S.H., Kadhim, A.A., Al-Da'amy, M.A., and Kadhim, S.H., 2023, Synthesis of CuCo₂O₄-MgO spinel composite as an adsorbent surface for removal of celestine blue B dye, *AIP Conf. Proc.*, 2830 (1), 070034.
- [18] Hicham, A., Hussein, J., and Siba, H., 2022, Kinetic, isotherm and thermodynamic studies on the ciprofloxacin adsorption from aqueous solution using Aleppo bentonite, *Baghdad Sci. J.*, 19 (3), 680–692.
- [19] AL-Khazali, N.A.Y., 2017, Study Removal Remazol Brilliant Blue and Malachite Green Dyes from Aqueous Solutions Using Iraqi Porcelanite Rocks and Modified, *Thesis*, University of Kerbala, Iraq.

- [20] Farhan, A.M., Zaghair, A.M., and Abdullah, H.I., 2022, Adsorption study of Rhodamine-B dye on plant (citrus leaves), *Baghdad Sci. J.*, 19 (4), 838–847.
- [21] Das, A.K., Kim, N.H., Lee, S.H., Sohn, Y., and Lee, J.H., 2018, Facile synthesis of CuCo_2O_4 composite octahedrons for high performance supercapacitor application, *Composites, Part B*, 150, 269–276.
- [22] Devaraja, P.B., Avadhani, D.N., Prashantha, S.C., Nagabhushana, H., Sharma, S.C., Nagabhushana, B.M., and Nagaswarupa, H.P., 2014, Synthesis, structural and luminescence studies of magnesium oxide nanopowder, *Spectrochim. Acta, Part A*, 118, 847–851.
- [23] Sudha, V., Annadurai, K., Kumar, S.M.S., and Thangamuthu, R., 2019, CuCo_2O_4 Nanobricks as electrode for enhanced electrochemical determination of hydroxylamine, *Ionics*, 25 (10), 5023–5034.
- [24] Petrov, K., Krezhov, K., and Konstantinov, P., 1989, Neutron diffraction study of the cationic distribution in $\text{Cu}_x\text{Co}_{3-x}\text{O}_4$ ($0 < x \leq 1.0$) spinels prepared by thermal decomposition of layered hydroxide nitrate precursors, *J. Phys. Chem. Solids*, 50 (6), 577–581.
- [25] Dana, J.D., 2022, *A System of Mineralogy*, Wiley, New Jersey, US.
- [26] Helmy, Q., Notodarmojo, S., Aruan, I.A., and Aprilawati, R., 2017, Removal of color and chemical oxygen demand from textile wastewater using advanced oxydation process (AOPs), *IPTEK J. Proc. Ser.*, 3 (6), 474–481.
- [27] Bonilla-Petriciolet, A., Mendoza-Castillo, D.I., and Reynel-Ávila, H.E., 2017, *Adsorption Processes for Water Treatment and Purification*, Springer, Cham, Switzerland.
- [28] Abdul-aziz Umar, S., and Gaya, U.I., 2019, Optimised photocatalytic degradation of crystal violet over 1wt% MgO-ZnO composite catalyst, *J. Sci. Technol.*, 11 (1), 25–33.
- [29] Obaid, S.A., 2020, Langmuir, Freundlich and Tamkin adsorption isotherms and kinetics for the removal Aartichoke *Tournefortii* straw from agricultural waste, *J Phys Conf Ser*, 1664, 012011.
- [30] Chafat, A.H., Al-Da'amy, M.A., and Kareem, E.T., 2023, Iraqi porcelanite rocks for efficient removal of safranin dye from aqueous solution, *Baghdad Sci. J.*, 20 (2), 434–441.
- [31] Shamsizadeh, A., Ghaedi, M., Ansari, A., Azizian, S., and Purkait, M.K., 2014, Tin oxide nanoparticle loaded on activated carbon as new adsorbent for efficient removal of malachite green-oxalate: Non-linear kinetics and isotherm study, *J. Mol. Liq.*, 195, 212–218.
- [32] Mohamad Zaidi, N.A.H., Lim, L.B.L., and Usman, A., 2019, Enhancing adsorption of malachite green dye using base-modified *Artocarpus odoratissimus* leaves as adsorbents, *Environ. Technol. Innovation*, 13, 211–223.
- [33] Brião, G.V., Jahn, S.L., Foletto, E.L., and Dotto, G.L., 2018, Highly efficient and reusable mesoporous zeolite synthesized from a biopolymer for cationic dyes adsorption, *Colloids Surf., A*, 556, 43–50.
- [34] Hussein, Z.A., Haddawi, S.M., and Kadhim, A.A., 2019, Study of thermodynamic variables to adsorption of aldomete drug (methyldopa) from its water solution on the nano zinc oxide surface, *Int. J. Pharm. Qual. Assur.*, 10 (2), 315–321.
- [35] Fouda, A., Hassan, S.E.D., Abdel-Rahman, M.A., Farag, M.M.S., Shehal-deen, A., Mohamed, A.A., Alsharif, S.M., Saied, E., Moghanim, S.A., and Azab, M.S., 2021, Catalytic degradation of wastewater from the textile and tannery industries by green synthesized hematite ($\alpha\text{-Fe}_2\text{O}_3$) and magnesium oxide (MgO) nanoparticles, *Curr. Res. Biotechnol.*, 3, 29–41.
- [36] Kadhim, S.H., Mgheer, T.H., Ismael, H.I., Kadem, K.J., Abbas, A.S., Atiyah, A.J., and Mohamad, I.J., 2019, Synthesis, characterization and catalytic activity of NiO-CoO-MgO nano-composite catalyst, *Indones. J. Chem.*, 19 (3), 675–683.
- [37] Mustikaningrum, M., Cahyono, R.B., and Yuliansyah, A.T., 2022, Adsorption of methylene blue on nano-crystal cellulose of oil palm trunk: Kinetic and thermodynamic studies, *Indones. J. Chem.*, 22 (4), 953–964.

Propylamine Silica-Titania Hybrid Material Modified with Ni(II) as the Catalyst for Benzyl Alcohol to Benzaldehyde Conversion

Dewi Agustiningsih, Nuryono Nuryono, Sri Juari Santosa, and Eko Sri Kunarti*

Department of Chemistry, Faculty of Mathematics and Natural Sciences, Universitas Gadjah Mada, Sekip Utara, Yogyakarta 55281, Indonesia

* **Corresponding author:**

tel: +62-81578634638

email: eko_kunarti@ugm.ac.id

Received: May 8, 2023

Accepted: June 15, 2023

DOI: 10.22146/ijc.84282

Abstract: $\text{SiO}_2\text{-TiO}_2$ @propylamine-Ni(II) as the catalyst for the benzyl alcohol oxidation has been synthesized by utilizing rice husk ash as the SiO_2 source. This research was started by extracting SiO_2 from rice husk ash and continued by synthesizing the $\text{SiO}_2\text{-TiO}_2$ composite using titanium(IV) tetraisopropoxide (TTIP) as TiO_2 precursor and PEG-40 as template. The composite functionalization and metal modification were carried out by adding (3-aminopropyl)triethoxysilane (APTES) as the source of propylamine linker and impregnating $\text{NiCl}_2\cdot 6\text{H}_2\text{O}$ as the nickel precursor, respectively. The catalysts were synthesized by varying the ratios between each component within the material. The prepared materials were then characterized using ATR-IR, XRD, XRF, PSA, SAA, AAS, SEM-EDX, HR-TEM, and TGA. The catalyst activity was investigated by applying it to the oxidation reaction of benzyl alcohol to benzaldehyde with H_2O_2 as the oxidizing agent under sonication system. The obtained products were then analyzed by using GC-MS to quantify the success of the reaction. All characterizations performed in this research generally indicate the success in the synthesis of $\text{SiO}_2\text{-TiO}_2$ @propylamine-Ni(II) materials. Under the same condition including at room temperature, 1 h reaction time, and sonication system, the optimal oxidation reaction of benzyl alcohol was reached when $\text{SiO}_2\text{-TiO}_2$ @propylamine-Ni(II)5 was used as the catalyst in 98.52% yield.

Keywords: benzaldehyde; benzyl alcohol; catalyst; oxidation reaction; $\text{SiO}_2\text{-TiO}_2$ @propylamine-Ni(II)

■ INTRODUCTION

Alcohol oxidation to many forms of carbonyl-based compounds is one of the vast significances to the development of chemical fabrication [1]. The most notable example is the conversion of benzyl alcohol to benzaldehyde, which provides numerous applications in diverse areas such as coloring agents, medical products, farming, fragrances, foods, drinks, and also chemicals [2]. Most of the aldehyde is produced by a selective oxidation mechanism of alcohol utilizing a homogeneous catalyst. However, this kind of method has some drawbacks, including low reusability, difficult separation, low degree of conversion, and toxic contaminants [3-4]. As a result, it is essential to find an environmentally friendly and effective method to replace the homogeneously catalyzed oxidation reaction. Noble metals such as gold, platinum,

and palladium have long been developed as heterogeneous catalysts in benzyl alcohol to benzaldehyde oxidation reactions. These metals are generally dispersed onto supporting materials and have been observed to have significant catalytic activity [5-6]. Regrettably, the noble metal precludes its widespread potential for application due to its rising cost. Non-noble metals with a lower cost, such as nickel, can be used and have been reported to be advantageous for benzyl alcohol oxidation [7-9].

A catalyst based on nickel metal dispersed on $\text{SiO}_2\text{-TiO}_2$ composite was used in this study. Silica was chosen because it has several advantages, including the ability to form a large framework, abundance in nature and living creatures, great efficiency, selectivity, surface area, thermal stability, also good mechanical properties. Even

so, silica has a limitation as a support material since it forms inadequate compatibility with transition metals, limiting its interaction with these metals. Consequently, the transition metals are distributed poorly on the surface [10]. This major silica limitation can be overcome by combining silica with other metal oxides, one of which is titania. This is driven by the fact that titania can interact well with almost all transition metals, including Au, Cu, Ni, Mn, Pd, Co, and Ru. Titania also has high thermal and chemical stabilities [11]. The optimal interaction between titania and metal will aid the interaction of silica and metal. Hence, combining silica and titania into a composite should result in a support material with high thermal stability, a large surface area, and the ability to interact optimally with the catalyst metal.

Rice husk ash will be used as a silica source in this research. This is owed to the fact that rice husk ash contains silica with a very high purity level of 94–99% [12–13]. There are already so many reported studies about SiO_2 extraction from rice husk ash, including its application as a cement component [14–18], geopolymer [19–23], functional material [24], microelectronic, sensor, nano additives [25], adsorption and filtration membrane [26], photocatalyst [27], bioimaging, as well as drug delivery agent [28]. Despite its extensive utilization and application, there has not been found previous research which addressed the simultaneous modification of silica extracted from rice husk ash with TiO_2 and APTES linker agent as had been conducted in this research.

Even though the SiO_2 - TiO_2 composite has the potential to become an excellent supporting material, there is still a drawback, such as the metal can be easily leached from the composite surface due to the weak physical interaction. This, of course, brings down the activity of the catalyst in the benzyl alcohol oxidation reaction. This problem can be fixed by incorporating organic linker agents such as imines, amines, and oleic acid onto the composite surface to become inorganic-organic hybrid material [29]. The optimal interaction of the metal and the functionalized linker agent on the surface of the supporting material will augment the catalyst stability. In this study, the compound (3-aminopropyl)triethoxysilane was utilized as the source of

propylamine linker agent between the metal ion catalyst and the SiO_2 - TiO_2 composite. Moreover, the sonication method was conducted in the oxidation reaction of benzyl alcohol to benzaldehyde as the application of this research. This method was used owing to its ability to accelerate the reaction and lower the required reaction temperature [30].

■ EXPERIMENTAL SECTION

Materials

The materials used in this research were pro-analysis quality chemicals purchased from Sigma-Aldrich and Merck including HCl 37%, NaOH, Na_2SO_4 99.9%, $\text{C}_9\text{H}_{23}\text{NO}_3\text{Si}$ 99%, $\text{Ti}\{\text{OCH}(\text{CH}_3)_2\}_4$ 97%, PEG-40, $\text{C}_2\text{H}_5\text{OH}$ 99%, $\text{NiCl}_2 \cdot 6\text{H}_2\text{O}$ 99.9%, $\text{C}_6\text{H}_5\text{CH}_2\text{OH}$ 99%, and H_2O_2 30%. Other technical-grade materials were used, including distilled water and rice husk ash obtained from Semarang, Central Java. No further purification was conducted for all used reagents.

Instrumentation

The instrumentations used for the characterization in this study include attenuated total reflectance-infrared spectroscopy (QATR 10, Shimadzu), X-ray diffractometer (XRD-6000, Shimadzu), scanning electron microscope-energy dispersive X-ray (JEC-3000 FC, JEOL), high resolution-transmission electron microscope (Tecnai G^2 20 S-Twin, FEI), thermogravimetric analyzer (STAR^e SW, METTLER), X-ray fluorescence (NEXQC⁺, QUANTEZ), particle size analyzer (SZ-100, HORIBA Scientific), surface area analyzer (Gemini VII Version 5.03, Micromeritics), atomic absorption spectroscopy (iCE 3000 AA01212502, Thermo Scientific), and gas chromatography-mass spectrometer (QP2010S, Shimadzu).

Procedure

Extraction of SiO_2 from rice husk ash

Rice husk ash (RHA) was leached by dissolving it in 1 M HCl at a ratio of 1:10 (w/v). The mixture was stirred at room temperature for 2 h before being washed with distilled water. The RHA was then dried for 8 h at 80 °C before being calcined for 5 h at 550 C. Next, ATR-

IR, XRD, and XRF methods were used to characterize the uncalcined and calcined RHA. To extract the silica, the calcined RHA was then dispersed in 1 M NaOH with a ratio of 1:10 (w/v) and stirred for 2 h at 90 °C. It was next followed by centrifugation at 4000 rpm for 20 min. Afterward, the sodium silicate liquid was then collected as the silica precursor to be used in the next procedure.

Synthesis of SiO₂-TiO₂ composite

To synthesize the SiO₂-TiO₂ composite, 1 mol of sodium silicate was neutralized with 1 M HCl dropwise until a neutral pH was reached. Next, 1 mol of TTIP precursor was dispersed in absolute ethanol at 1:1 (v/v) ratio. The dispersed TTIP in ethanol was then added to the silica gel that had been formed before in the sonication system. The composite was then added dropwise with PEG-40 at a mol ratio of 1:6 (PEG:composite). The mixture of silica, titania, and PEG-40 was sonicated for 1 h to produce a white suspension prior to getting dried at 80 °C for 24 h. The template removal process was completed by dispersing SiO₂-TiO₂@PEG in absolute ethanol with a ratio of 1:10 (w/v) in a sonication system for 1 h at room temperature. The solid was then filtered, washed with cold absolute ethanol, and dried for 8 h at 60 °C. The same procedure was carried out to remove the template twice.

Functionalization of SiO₂-TiO₂ composite

The functionalization procedure was conducted by dispersing SiO₂-TiO₂ composite in absolute ethanol at 1:10 (w/v) ratio. The propylamine with the mass ratio of 1:2 (w/w) to SiO₂-TiO₂ was also then dispersed in ethanol 1:10 (v/v). The propylamine solution was gradually added to the composite mixture before being sonicated for 2 h and stirred for 6 h at room temperature. Just after that, centrifugation was performed to obtain the solid. It was then filtered before being washed with absolute ethanol and distilled water three times for each, afterwards dried at 60 °C for 12 h [31].

Metal impregnation of SiO₂-TiO₂@propylamine hybrid material

As much as 1 g of SiO₂-TiO₂@propylamine hybrid material was dispersed in distilled water with a ratio of 1:100 (w/v) and then added with nickel(II)-chloride

hexahydrate in various moles. The mixture was sonicated for 3 h at room temperature before being filtered and washed three times with distilled water. The obtained greenish-white solid was then dried for 4h at 80 °C, and finally characterized using ATR-IR, XRD, PSA, SAA, AAS, SEM-EDX, HR-TEM, and TGA.

Catalytic activity

In the oxidation reaction of benzyl alcohol, as much as 1 mmol of benzyl alcohol, 50 mg of catalyst material, and 1 mL of H₂O₂ were added into a vial. The reaction was carried out for 1 h at room temperature in a sonication system [2]. When the reaction finished, the solid catalyst was restored through the filtration process. Next, the organic phase was extracted from the filtrate and dried using anhydrous sodium sulfate. Lastly, the final products were then analyzed with GC-MS.

RESULTS AND DISCUSSION

Characterization of SiO₂ from RHA

From Table 1, it is reported that rice husk ash has a high content of silica up to 97.923%. It supports the known fact that rice husk ash is one of the most potential silica natural sources. According to the results of the ATR-IR characterization in Fig. 1, there are peaks in the spectra of the uncalcined RHA that indicate the dominant carbon component. These peaks include 1373 (Csp³-H bending), 1600 (C=C aromatics), 1743 (C=O stretching), 2939 (Csp³-H stretching), and 3424 cm⁻¹ (O-H stretching). Some peaks also indicate the presence of silica in uncalcined RHA, such as 432 (SiO₄ bending mode), 794 (Si-O-Si symmetrical stretching), and 1049 cm⁻¹ (Si-O-Si asymmetrical stretching). After the rice husk ash had been leached and calcined, the carbon

Table 1. Composition of calcined rice husk ash

Component	Content (%mass)
SiO ₂	97.923
Fe ₂ O ₃	0.388
K ₂ O	0.784
CaO	0.647
TiO ₂	0.121
MnO	0.079
Cr ₂ O ₃	0.031

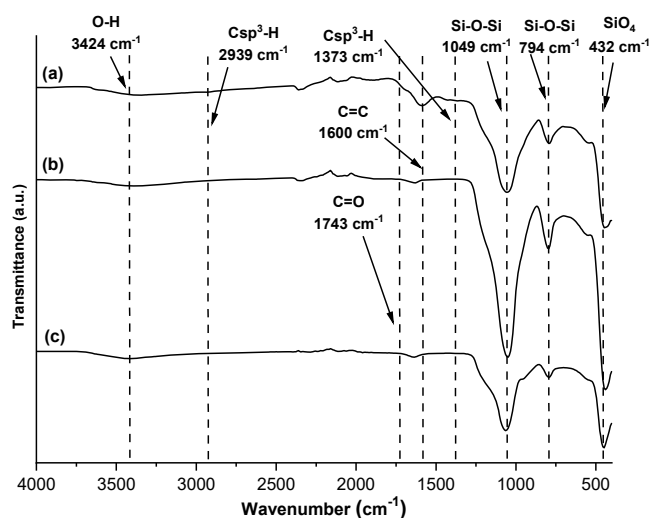


Fig 1. ATR-IR spectra of (a) uncalcined RHA, (b) calcined RHA, and (c) extracted silica

component began to disappear. It is evidenced by the decreasing intensity of the carbon material characteristic peaks and the increasing relative intensity of silica characteristic peaks. Based on these results, it can be concluded that the calcination process to remove the carbon component in rice husk ash was successfully done. The ATR-IR spectra of silica extracted from rice husk ash reveal that it contained high purity. This is clearly indicated by some characteristic peaks belonging to pure silica.

Fig. 2 depicts that calcined and uncalcined RHA exhibit a characteristic pattern of amorphous silica with a broad peak at 2θ around 22° . Moreover, it can be noticed here that the intensity of these peaks increases in leached and calcined rice husk ash spectra. It can be explicated by the fact that metal oxides other than SiO_2 were dissolved after leaching, and the amount of carbon in rice husk ash decreased after calcination. The loss of other metal oxides and carbon increased the relative intensity of the broad peaks from amorphous SiO_2 . The pattern from the extracted silica displays higher intensity and more distinct peaks compared to other spectra in the same region, providing confirmation that it was purely derived from calcined RHA.

Characterization of SiO_2 - TiO_2 before and after Template Removal

The method used in the synthesis of the SiO_2 - TiO_2 composite was sol-gel by adding TTIP precursor to the obtained silica gel. The mixture was then treated with

polyethylene glycol 40 (PEG-40) as the template. PEG is the most used surfactant as a template due to its non-toxic long polymeric chain and good water solubility [32]. It is also known to have good properties such as hydrophilic, water-soluble, biocompatible, non-toxic, and protein-resistant [33]. Subsequently, to produce the SiO_2 - TiO_2 composite, this template must be removed. Instead of calcination, the template removal process in this study was carried out using the sonication method. It was done to prevent exposing the composite to high temperatures, which might result in the formation of crystalline phases for both SiO_2 and TiO_2 . If a crystalline phase is formed, the number of free silanol and titanol groups on the surface tends to decrease because they are used to form crystalline structures. This is disadvantageous since these groups are required for bond formation with propylamine as the interparticle linker agent in the next step.

Fig. 3 shows the ATR-IR spectra of the SiO_2 - TiO_2 composite before and after the template removal. Some characteristic peaks of the composite are detected including at 3400 (O-H stretching of the silanol and titanol groups), 2924 (Csp^3 -H stretching), 1735 (C=O stretching), 1643 (O-H bending from Si-O-H), 1465 (Csp^3 -H bending for $-\text{CH}_2-$), 1350 (Csp^3 -H bending for $-\text{CH}_3$), 1049 (Si-O-Si asymmetrical stretching), 794 (Si-O-Si symmetrical stretching), and 949 cm^{-1} (Si-O-Ti stretching). After the sonication for template removal

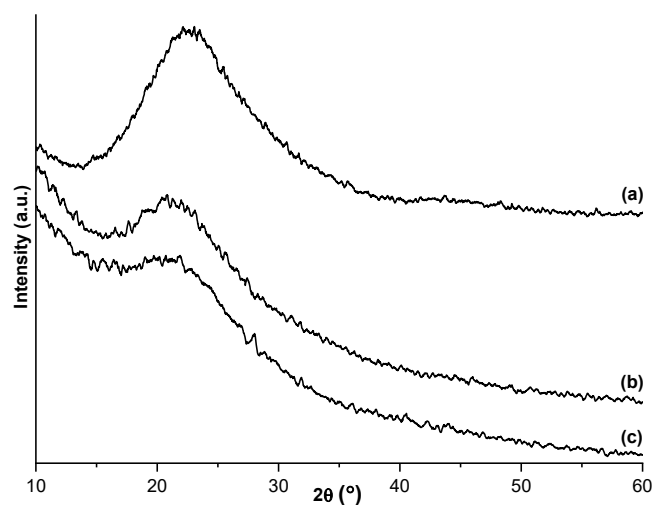


Fig 2. X-ray diffraction pattern of (a) extracted silica, (b) calcined RHA, and (c) uncalcined RHA

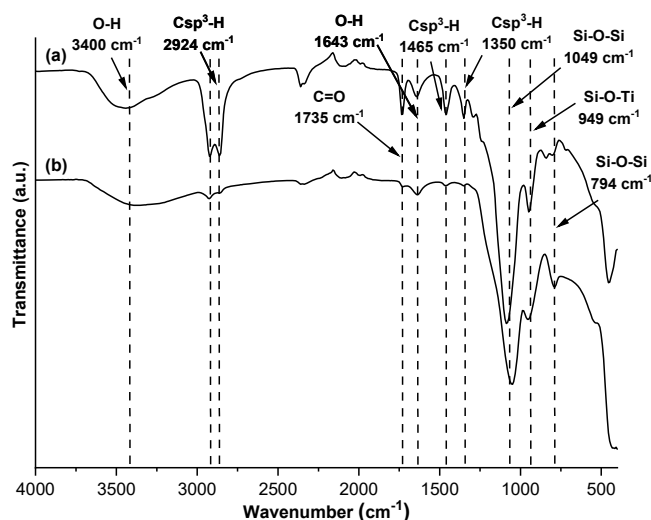


Fig 3. ATR-IR spectra of (a) $\text{SiO}_2\text{-TiO}_2\text{@PEG-40}$ and (b) $\text{SiO}_2\text{-TiO}_2$ after PEG-40 removal

was carried out, the intensity of PEG-40 characteristic peaks comprising 2924 ($\text{Csp}^3\text{-H}$ stretching), 1735 (C=O stretching), 1465 ($\text{Csp}^3\text{-H}$ bending for $-\text{CH}_2-$), and 1350 cm^{-1} ($\text{Csp}^3\text{-H}$ bending for $-\text{CH}_3$) significantly decrease. Based on the difference in mass before and after template removal, the sonication method could remove up to 88.92% of the template at $\text{SiO}_2\text{-TiO}_2$ composite.

According to Fig. 4, the ATR-IR characterization results for the propylamine functionalized composite do not show significant differences from the composite spectra prior to functionalization. However, if we take a closer look, we can see differences in the shape and intensity of the peak at 1550 cm^{-1} . There is no vibration

peak around that wavenumber prior to functionalization. Then after functionalization, a broad peak is observed, indicating the presence of the $-\text{NH}_2$ group deformation vibration in propylamine from APTES [34-35]. After functionalization, the Ti-O-Si vibrational peak appeared to merge with the Si-O-Si peak. The probable answer for this case is that when APTES was added to the composite, the silane groups preferred to bind with silanol groups to form Si-O-Si rather than with titanol groups to form Si-O-Ti . This is most likely since the same size of Si from silane and silanol would optimize the orbital overlap that occurred during the bond formation. Meanwhile, the size difference between Si and Ti shrunk the probability of orbitals overlapping.

The ATR-IR spectra of propylamine-functionalized and Ni(II) -impregnated $\text{SiO}_2\text{-TiO}_2$ in Fig. 5 reveal the characteristic peak of the Ni-N bond at $410\text{-}420\text{ cm}^{-1}$ [36]. This peak suggests that nickel ion was successfully dispersed on the composite surface through the formation of the bond between nickel ion from precursor salt and nitrogen atom belonging to the amine groups from propylamine resulted by APTES.

Based on Fig. 6(b), the diffraction pattern of the composite after template removal exhibits the amorphous properties of silica and titania at $2\theta\ 22^\circ$. This suggests that both silica and titania were obtained as amorphous materials rather than crystalline. It is presumably because the growth of silica and titania crystals did not

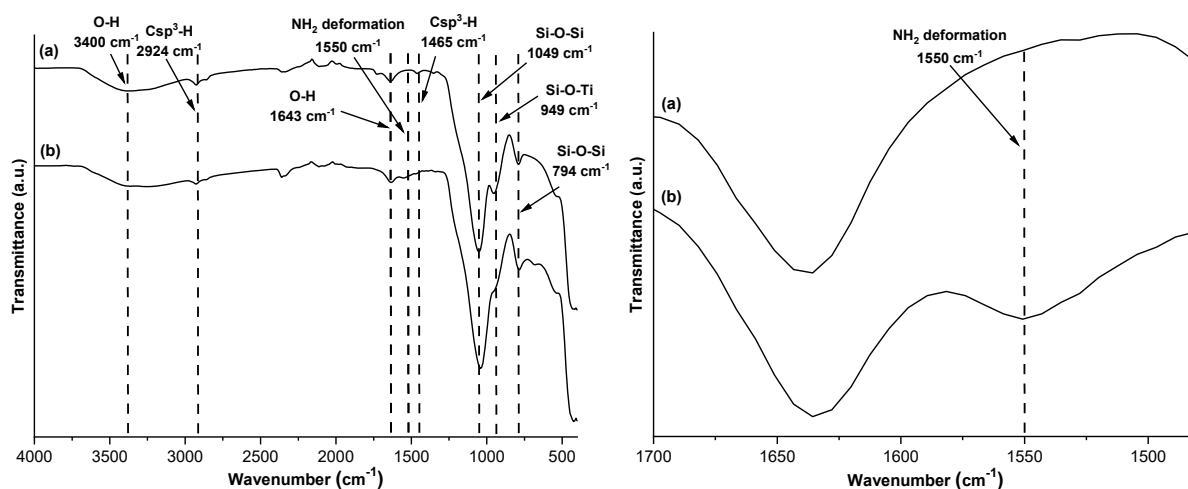


Fig 4. ATR-IR spectra of (a) $\text{SiO}_2\text{-TiO}_2$ and (b) $\text{SiO}_2\text{-TiO}_2\text{@propylamine}$

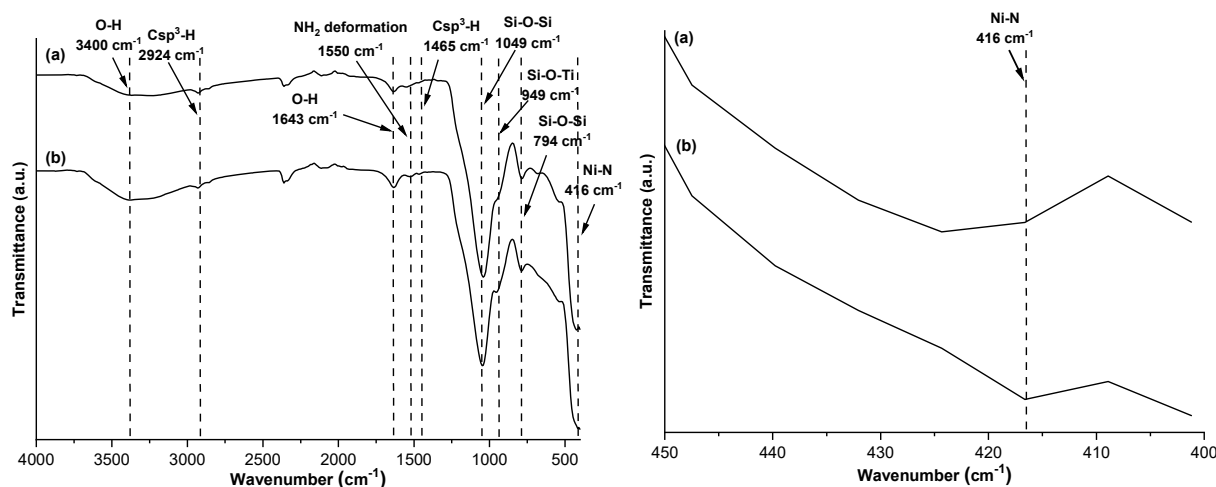


Fig 5. ATR-IR spectra of (a) $\text{SiO}_2\text{-TiO}_2\text{@propylamine}$ and (b) $\text{SiO}_2\text{-TiO}_2\text{@propylamine-Ni(II)}$

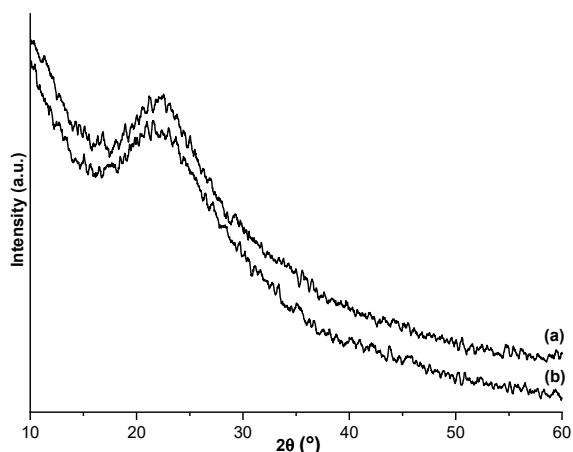


Fig 6. X-ray diffraction pattern of (a) $\text{SiO}_2\text{-TiO}_2\text{@propylamine-Ni(II)}$ and (b) $\text{SiO}_2\text{-TiO}_2$

occur when calcination at high temperatures was not executed during the template removal process. In addition, Fig. 6(a) depicts that the diffraction pattern of $\text{SiO}_2\text{-TiO}_2\text{@propylamine-Ni(II)}$ seems to have an identical amorphous character, and no other additional peaks are observed. It can be explained by two probable reasons, including (i) propylamine from APTES did not contribute to the provision of diffraction patterns, and (ii) the formed nickel in this material was Ni(II). The Ni(II) metal ions did not exhibit a specific diffraction pattern since there was no crystal growth in it [37].

As it is shown in Fig. 7, the average size of $\text{SiO}_2\text{-TiO}_2$ particles beyond the nano dimension (more than 100 nm) is 1365 nm. The formation of sufficiently large particles was driven by the fact that both titania and silica were in

the amorphous phase. The amorphous phase is known to have a greater particle coalescence or agglomeration rate than the crystalline one [38]. Moreover, it can also be noticed here that the presence of APTES and Ni(II) metal ions could decrease the probability of aggregation among the composite particles with an average size of 662 nm. This effect was likely attributed to the capping action exerted by these two modifiers on the surface of the composite.

Based on SAA data, the $\text{SiO}_2\text{-TiO}_2$ composite exhibited a surface area of $234.0573 \text{ m}^2/\text{g}$ and an average pore size of 7.28 nm. Subsequently, upon the addition of APTES and Ni(II), the composite experienced an augmentation in surface area, $243.9891 \text{ m}^2/\text{g}$, alongside a reduction in average pore size, 6.81 nm. The increase in

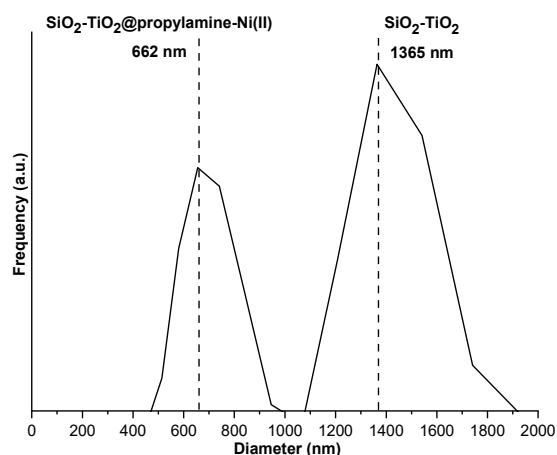


Fig 7. Particle size distribution spectra of the synthesized materials

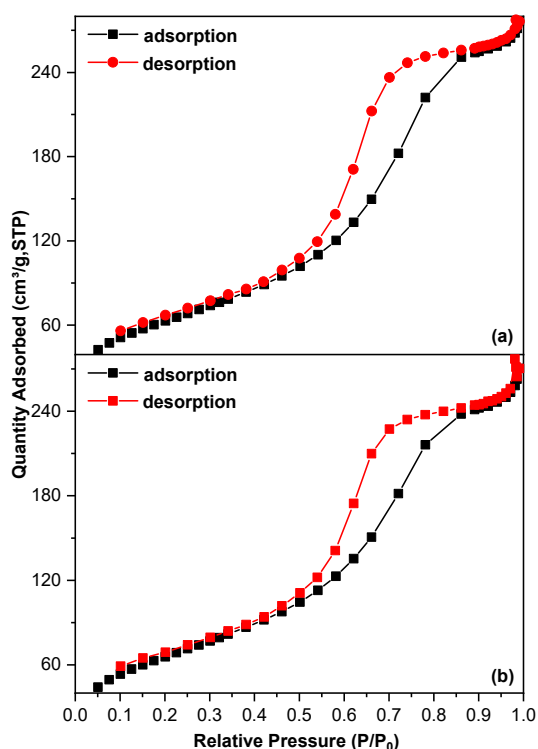


Fig 8. N_2 adsorption-desorption isotherm of (a) SiO_2-TiO_2 and (b) $SiO_2-TiO_2@propylamine-Ni(II)$

surface area could be caused by the presence of metal ions that enhanced the composite roughness and abruptness. Meanwhile, the pore size continued to decrease due to the closure of pores resulting from the presence of APTES and Ni(II) on the surface. In addition, as shown in Fig. 8(a) and (b), the N_2 adsorption-desorption isotherm curves of these two materials illustrate type IV hysteresis as the characteristic type of mesoporous material. The formed

pore sizes are generally greater than 5 nm, indicating that the materials may be used as catalyst in the organic reaction of converting benzyl alcohol to benzaldehyde.

Fig. 9(a) and (b) display the TGA analysis results, indicating two distinct instances of mass loss for the material. The initial mass reduction was attributed to the evaporation of water molecules from the material surface, while the second event arose from the elimination of organic components derived from propylamine. Additionally, it is evident that the composite containing Ni(II) exhibited a lower mass loss compared to the composite without it. In simpler terms, this suggests that the presence of Ni(II) metal ions enhanced the thermal stability of the material. This could be owing to the thermal conductivity properties of nickel as metal, enabling it to restrict the entry of heat into the catalyst material system.

Characterization of $SiO_2-TiO_2@propylamine-Ni(II)$ with Various Amounts of Ni(II)

As can be seen in Fig. 10, each catalyst material with various nickel ion concentrations exhibits a sharp peak in the $1500-1550\text{ cm}^{-1}$ region with the addition of propylamine. Further to that, the peaks between 410 and 420 cm^{-1} are also observed, indicating the Ni-N bond. The Ni-N peak intensity belonging to the catalyst material containing 5 mmol of nickel ion is greater than the others. When the nickel ion concentration in the material reached the upper 5 mmol, the peak intensity decreased. It is because even though the amount of N

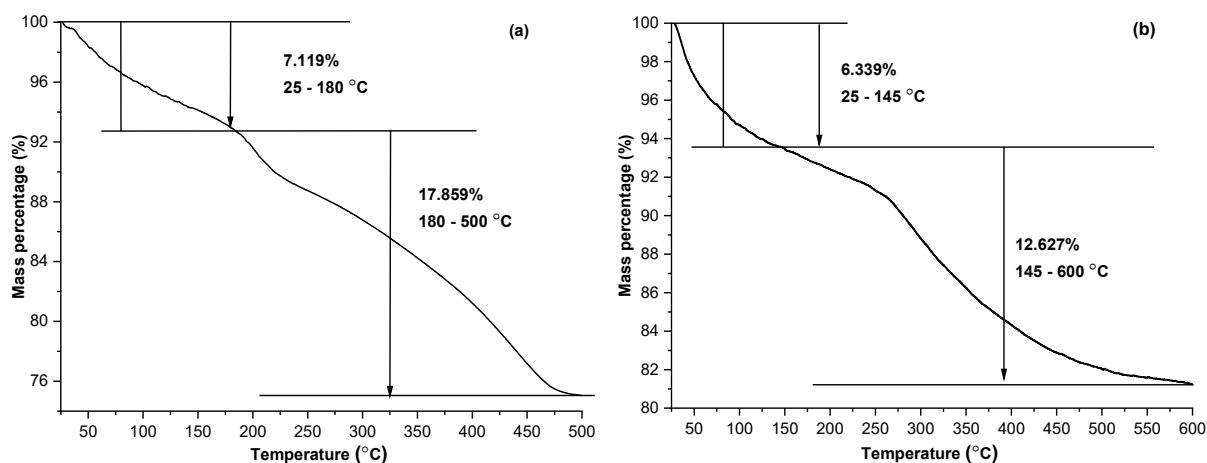


Fig 9. TGA curve of (a) $SiO_2-TiO_2@propylamine$ and (b) $SiO_2-TiO_2@propylamine-Ni(II)$

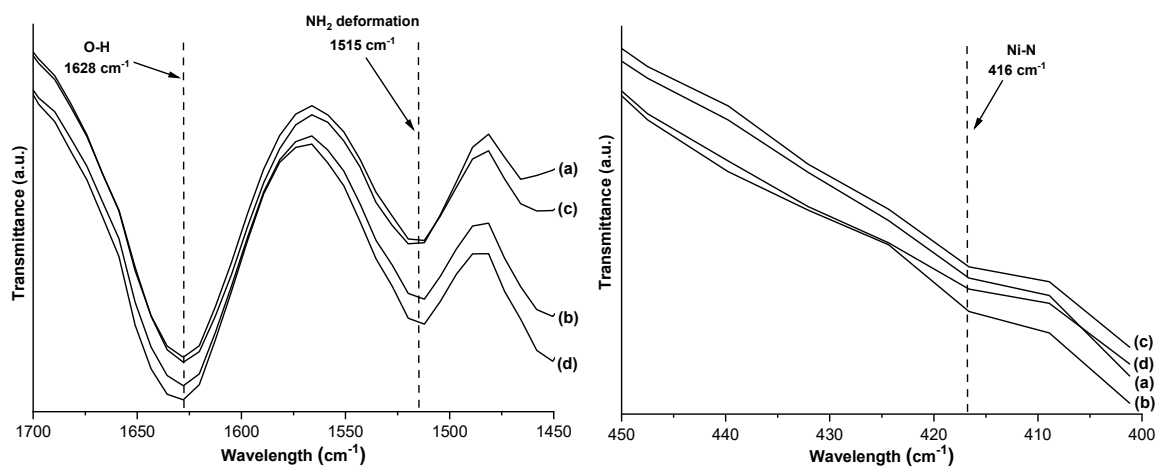


Fig 10. ATR-IR spectra of $\text{SiO}_2\text{-TiO}_2\text{@propylamine-Ni(II)}$ with nickel ion concentrations of (a) 3; (b) 5; (c) 7; and (d) 10 mmol

available from propylamine remained constant, there was more competition between Ni atoms to bind to N. The quantitative analysis results by AAS displayed in Fig. 11 are analogous to the results from this ATR-IR characterization. It is that the optimal amount of successfully attached nickel ion was found in the $\text{SiO}_2\text{-TiO}_2\text{@propylamine-Ni(II)}$ (5 mmol) catalyst.

According to the XRD data depicted in Fig. 12, all materials have amorphous $\text{SiO}_2\text{-TiO}_2$ diffraction patterns. The difference in nickel ion concentrations had no effect on the changes in $\text{SiO}_2\text{-TiO}_2$ diffraction pattern, as the metal ions were only dispersed on the outside of the

framework. Thus, it had no role in the main framework of the $\text{SiO}_2\text{-TiO}_2$ amorphous structure.

As we can see from the SEM data shown in Fig. 13, the morphology of the obtained composites is generally spherical with the grain size of more than 100 nm. In addition, from Table 2, it is known that constituent elements such as Si, Ti, C, O, Ni, and N are detected in each composite based on the EDX data. Fig. 14(a) displays the HR-TEM image of $\text{SiO}_2\text{-TiO}_2\text{@propylamine-Ni(II)}$ particles with 5 mmol nickel ions. It has a quasi-spherical shape with propylamine covering each particle, and the area defined is represented

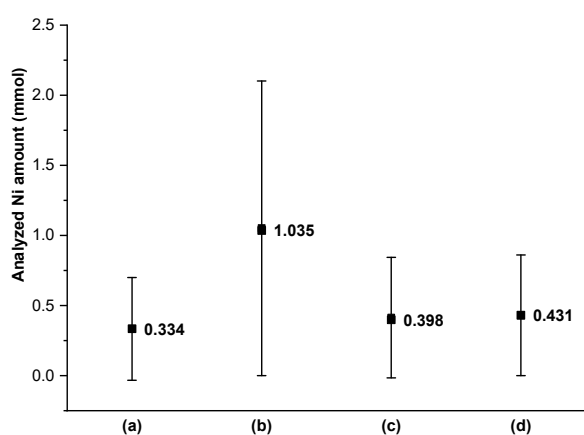


Fig 11. The amount of attached Ni in $\text{SiO}_2\text{-TiO}_2\text{@propylamine-Ni(II)}$ with initial nickel ion concentrations of (a) 3; (b) 5; (c) 7; and (d) 10 mmol by AAS analysis

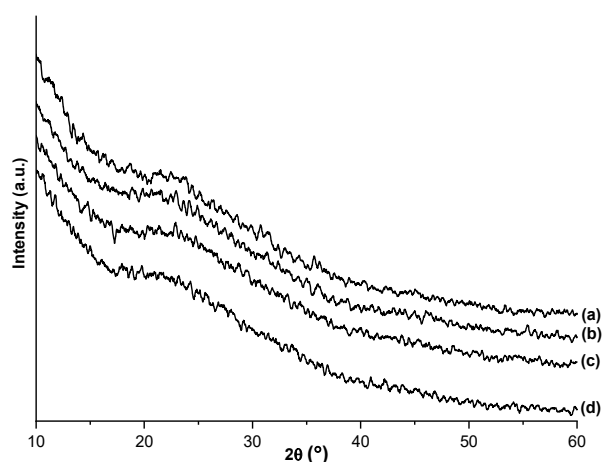


Fig 12. X-ray diffraction pattern of $\text{SiO}_2\text{-TiO}_2\text{@propylamine-Ni(II)}$ with nickel ion concentrations of (a) 3; (b) 5; (c) 7; and (d) 10 mmol

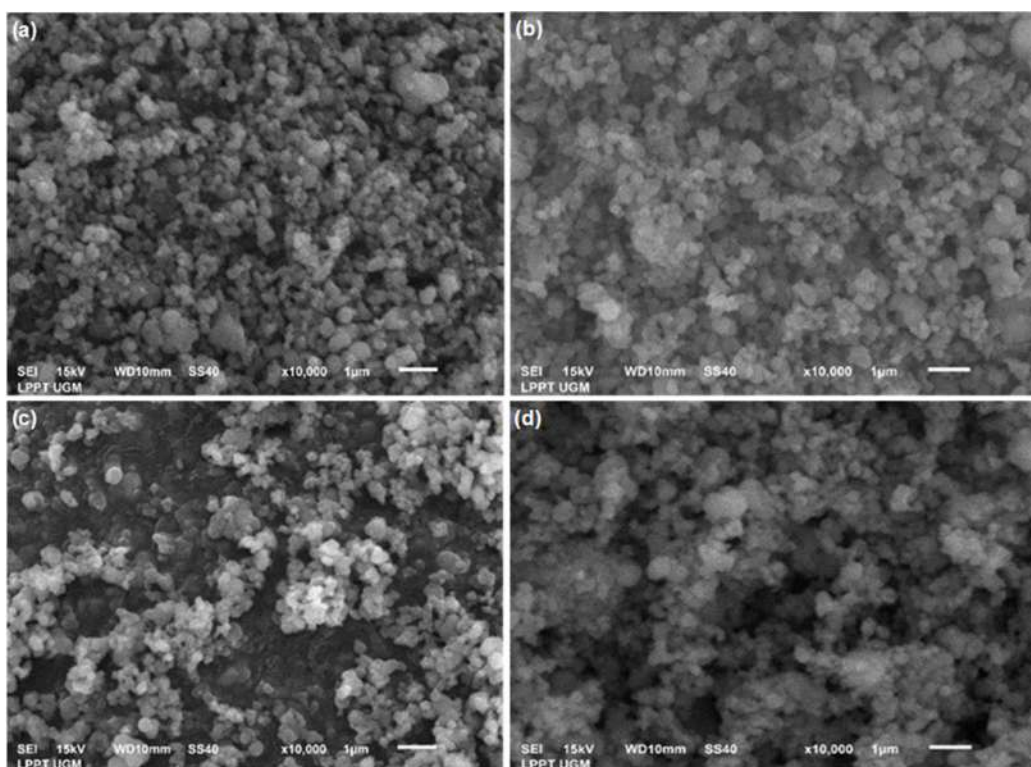


Fig 13. SEM images and EDX spectra of $\text{SiO}_2\text{-TiO}_2\text{@propylamine-Ni(II)}$ with nickel ion concentrations of (a) 3; (b) 5; (c) 7; and (d) 10 mmol

Table 2. Percentage of the detected elements in catalyst materials by EDX

$\text{SiO}_2\text{-TiO}_2\text{@propylamine-Ni(II)}$	Si	Ti	C	O	Ni	N
Ni(II) 3 mmol	30.31	11.90	4.50	40.19	1.27	11.83
Ni(II) 5 mmol	11.36	27.16	9.58	45.13	2.91	3.86
Ni(II) 7 mmol	16.79	24.28	8.01	47.09	2.42	1.41
Ni(II) 10 mmol	18.45	20.49	7.74	45.30	3.67	4.35

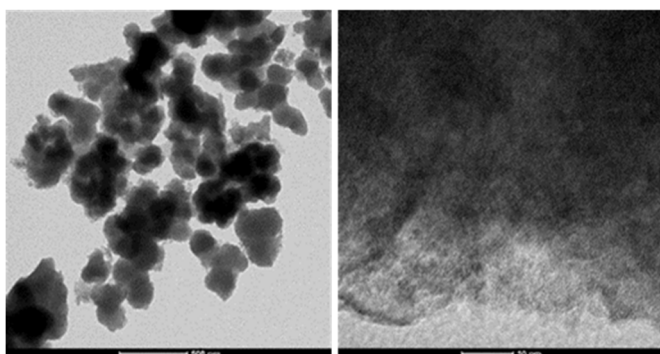


Fig 14. HR-TEM images of $\text{SiO}_2\text{-TiO}_2\text{@propylamine-Ni(II)5}$

by a lighter color. When the magnification was increased in Fig. 14(b), it can be seen that the $\text{SiO}_2\text{-TiO}_2$ as the core is represented by a darker color, propylamine in the outer

lighter color, and Ni(II) in the darker layer out of propylamine.

Catalytic Activity Evaluation

According to Fig. 15 and Table 3, it is known that under the same condition, the most active catalyst was $\text{SiO}_2\text{-TiO}_2\text{@propylamine-Ni(II)5}$, with the yield percentage of 98.52%. It basically confirms that this catalyst had the most nickel ion attached to its surface as the primary catalyst for the oxidation reaction. As a result, the highest activity was achieved, followed by other catalysts with less attached nickel ions. Due to the absence of nickel ion when $\text{SiO}_2\text{-TiO}_2$ was used as the catalyst, a product with a lower yield percentage was generated. The product was still formed despite the lack

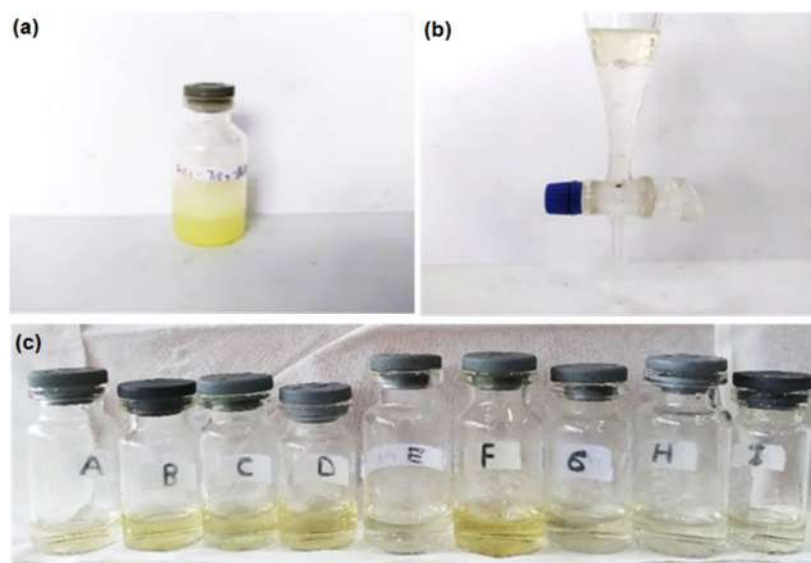


Fig 15. The oxidation reaction of benzyl alcohol to benzaldehyde using $\text{SiO}_2\text{-TiO}_2\text{@propylamine-Ni(II)5}$, including (a) right after reaction, (b) after catalyst separation, and (c) the products obtained from (A) TiO_2 , (B) $\text{SiO}_2\text{-TiO}_2\text{@propylamine}$, (C) $\text{SiO}_2\text{-Ni(II)}$, (D) $\text{TiO}_2\text{-Ni(II)}$, (E) $\text{SiO}_2\text{-TiO}_2\text{@propylamine-Ni(II)3}$, (F) $\text{SiO}_2\text{-TiO}_2\text{@propylamine-Ni(II)5}$, (G) $\text{SiO}_2\text{-TiO}_2\text{@propylamine-Ni(II)7}$, (H) $\text{SiO}_2\text{-TiO}_2\text{@propylamine-Ni(II)10}$, and (I) $\text{SiO}_2\text{-TiO}_2$

Table 3. Oxidation of benzyl alcohol to benzaldehyde

Catalyst	Conversion (%)	Yield (%)	Selectivity (%)
SiO_2	0	0	0
TiO_2	23.44	22.64	96.59
$\text{SiO}_2\text{-TiO}_2\text{@propylamine}$	33.46	33.46	100
$\text{SiO}_2\text{-Ni(II)}$	68.97	67.53	97.91
$\text{TiO}_2\text{-Ni(II)}$	58.73	53.52	91.13
Without catalyst	0	0	0
$\text{SiO}_2\text{-TiO}_2$	55.45	52.56	94.79
$\text{SiO}_2\text{-TiO}_2\text{@propylamine-Ni(II)3}$	87.40	87.40	100
$\text{SiO}_2\text{-TiO}_2\text{@propylamine-Ni(II)5}$	98.62	98.52	99.90
$\text{SiO}_2\text{-TiO}_2\text{@propylamine-Ni(II)7}$	87.40	87.40	100
$\text{SiO}_2\text{-TiO}_2\text{@propylamine-Ni(II)10}$	78.91	77.38	98.06

of nickel ion. This is rooted in the fact that in the presence of visible and UV light, TiO_2 was able to carry out the oxidation reaction by breaking H_2O_2 into OH radicals [39]. The OH radicals would help convert benzyl alcohol to benzaldehyde. This phenomenon was also detected in the result obtained when pure TiO_2 was used as the catalyst. The product was still formed caused by the catalytic process that kept occurring due to the photocatalytic activity of TiO_2 itself. Conversely, there was no product observed when pure SiO_2 was used since this material has no catalytic activity [40].

When the functionalized $\text{SiO}_2\text{-TiO}_2$ was used as the catalyst, the yield whittled down. As the presence of propylamine from APTES partially covered the $\text{SiO}_2\text{-TiO}_2$ surface, causing the interaction between the catalyst and H_2O_2 to be limited. Furthermore, even though the percentage yield of $\text{SiO}_2\text{-Ni(II)}$ and $\text{TiO}_2\text{-Ni(II)}$ catalysts is not relatively high, these materials could still convert benzyl alcohol to benzaldehyde. The oxidation reaction was noticed to occur here due to the role of nickel ion as the main metal catalyst.

According to the results, it is known that $\text{SiO}_2\text{-Ni(II)}$

outperformed $\text{TiO}_2\text{-Ni(II)}$ in terms of yield. Due to the large surface area of silica, nickel ion on the surface was more dispersed and avoided agglomeration, which resulted in higher activity than in titania. Contrary to the previous research revealing that titania interacts well with metal catalysts, in this research, titania was observed to have low activity due to its tendency to agglomerate and lower surface area than silica. Meanwhile, when the reaction was conducted without the use of a catalyst, no product was obtained due to the absence of a catalytic process. Table 4 shows some previous studies related to the oxidation reaction of benzyl alcohol to benzaldehyde. Compared to other catalysts that had been evaluated for

the same reaction, $\text{SiO}_2\text{-TiO}_2\text{@propylamine-Ni(II)}$ produced considerably better performance, shown by its conversion, yield, and selectivity percentages.

This study tried to propose a mechanism for the oxidation reaction of benzyl alcohol to benzaldehyde using the synthesized catalyst as adapted from Javidfar et al. [2]. The role of Ni(II) in facilitating the oxidation reaction can be observed in Fig. 16, as it utilized its empty orbitals to bind both H_2O_2 as the oxidizing agent and benzyl alcohol as the main reactant. Initially, hydrogen peroxide attached to the empty orbitals of Ni(II), followed by the binding of benzyl alcohol. In succession, a water molecule was formed for one hydroxyl

Table 4. The performance of other catalysts in benzyl alcohol to benzaldehyde oxidation reaction

Catalyst	Yield (%)	References
$\text{Ni/Fe}_3\text{O}_4$	99	[7]
$\text{Ni(OH)}_2\text{-modified CdS-MoS}_2$	94.2	[9]
$[\text{Ni(L)}_2(\text{H}_2\text{O})_2]$	45.2	[41]
$\text{TiO}_2/\text{Ti}_3\text{C}_2$	97	[42]
Mesoporous g- C_3N_4	97	[3]
$\text{La(OH)}_3/\text{Fe}_3\text{O}_4\text{@chitosan}$	100	[2]
TiO_2 nanorods	58.1	[43]
$\text{Ru/g-C}_3\text{N}_4$	72	[5]
$\text{SiO}_2\text{-TiO}_2\text{@propylamine-Ni(II)}$	98.52	This study

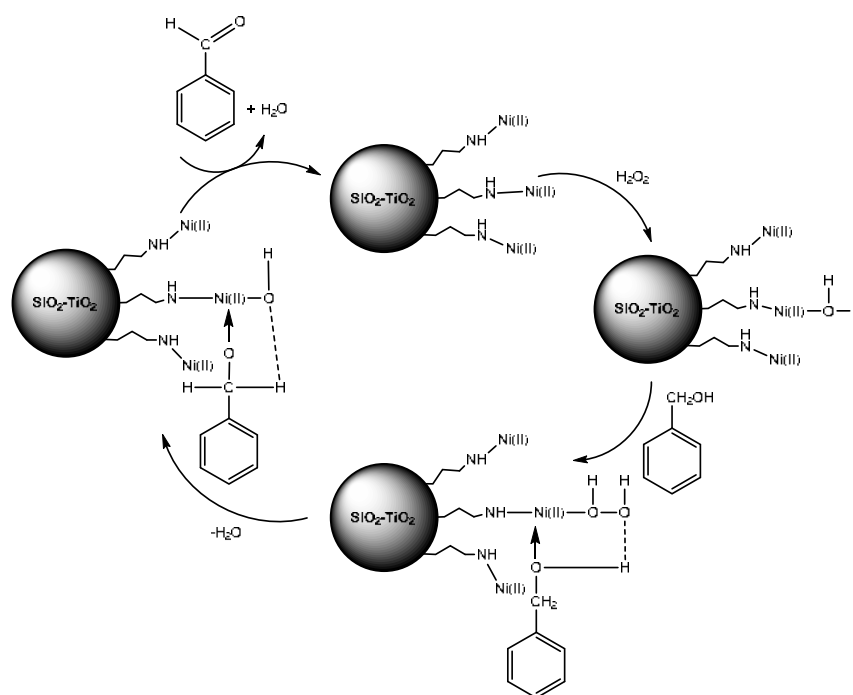


Fig 16. The proposed mechanism of benzyl alcohol to benzaldehyde oxidation reaction using the synthesized catalyst

species from H_2O_2 , accepting one hydrogen atom from benzyl alcohol. The remaining hydrogen atom from benzyl alcohol was then bonded with another hydroxyl group from H_2O_2 , resulting in the production of water molecules and benzaldehyde as the final products. Throughout this series of oxidation reactions, Ni(II) ultimately returned to its original state, like the one when the reaction had not occurred yet. This route can also be adapted to explain why pure TiO_2 was able to accommodate the oxidation reaction. It is because TiO_2 can produce OH radicals as oxidizing agents due to its photoconductivity [44].

■ CONCLUSION

In this study, we successfully synthesized a new heterogeneous catalyst, namely $\text{SiO}_2\text{-TiO}_2\text{@propylamine-Ni(II)}$. The results of all characterizations synergically report the success of the synthesis. This material was used as the catalyst for benzyl alcohol oxidation reaction as one of the important organic reactions in a wide range of applications. The catalyst has been proven to have excellent performance in oxidation reactions by the presence of H_2O_2 as the oxidizing agent in a sonicated system. Every component in the synthesized catalyst played a significant role in enhancing the catalyst activity. The catalyst was also easy to separate from the product after the reaction was complete. This research results in the development of a potentially new heterogeneous catalyst for organic reactions.

■ ACKNOWLEDGMENTS

The authors would like to acknowledge the Ministry of Research, Technology, and Higher Education Indonesia for funding this research under contract number 089/E5/PG.02.00/PT/2022; 1998/UN1/DITLIT/Dit-Lit/PT.01.03/2022. With respect, we also would like to thank the institution for providing Dewi Agustiningih the *Pendidikan Magister Menuju Doktor untuk Sarjana Unggul* (PMDSU) scholarship.

■ REFERENCES

- [1] Kunene, A., Leteba, G., and van Steen, E., 2022, Liquid phase oxidation of benzyl alcohol over Pt and Pt–Ni alloy supported on TiO_2 : Using O_2 or H_2O_2 as oxidant?, *Catal. Lett.*, 152 (6), 1760–1768.
- [2] Javidfar, F., Fadaeian, M., and Ghomi, J.S., 2021, La(OH)_3 nanoparticles immobilized on $\text{Fe}_3\text{O}_4\text{@chitosan}$ composites as novel magnetic nanocatalysts for sonochemical oxidation of benzyl alcohol to benzaldehyde, *RSC Adv.*, 11 (57), 35988–35993.
- [3] Ramesh, A., Da, C.T., Manigandan, R., Bhargav, P.B., and Nguyen-Le, M.T., 2022, Selectivity oxidation of benzyl alcohol using mesoporous $\text{g-C}_3\text{N}_4$ catalysts prepared by hard template method, *Colloid Interface Sci. Commun.*, 48, 100608.
- [4] Vásquez-Céspedes, S., Betori, R.C., Cismesia, M.A., Kirsch, J.K., and Yang, Q., 2021, Heterogeneous catalysis for cross-coupling reactions: An underutilized powerful and sustainable tool in the fine chemical industry?, *Org. Process Res. Dev.*, 25 (4), 740–753.
- [5] Lima, M.J., Tavares, P.B., Silva, A.M.T., Silva, C.G., and Faria, J.L., 2017, Selective photocatalytic oxidation of benzyl alcohol to benzaldehyde by using metal-loaded $\text{g-C}_3\text{N}_4$ photocatalysts, *Catal. Today*, 287, 70–77.
- [6] Wu, P., Cao, Y., Zhao, L., Wang, Y., He, Z., Xing, W., Bai, P., Mintova, S., and Yan, Z., 2019, Formation of PdO on Au–Pd bimetallic catalysts and the effect on benzyl alcohol oxidation, *J. Catal.*, 375, 32–43.
- [7] Wang, Y., Hu, D., Guo, R., Deng, H., Amer, M., Zhao, Z., Xu, H., and Yan, K., 2022, Facile synthesis of $\text{Ni/Fe}_3\text{O}_4$ derived from layered double hydroxides with high performance in the selective hydrogenation of benzaldehyde and furfural, *Mol. Catal.*, 528, 112505.
- [8] Hu, X., Zhang, M., Ren, A., Huang, Y., Yan, X., Feng, R., and Zhao, G., 2022, Mesoporous nickel-cobalt oxide for efficient liquid-phase benzyl alcohol oxidation by air, *Catal. Today*, 405-406, 75–81.
- [9] Cui, C., Zhao, X., Su, X., Gao, W., Zhan, J., Zhang, X., Li, G., Zhang, X. L., Sang, Y., and Liu, H., 2021, Selective oxidation of benzyl alcohol using a Ni(OH)_2 -modified CdS-MoS_2 composite photocatalyst under ambient conditions, *J. Environ.*

- Chem. Eng.*, 9 (6), 106416.
- [10] Ali, M.E., Rahman, M.M., Sarkar, S.M., and Abd Hamid, S.B., 2014, Heterogeneous metal catalysts for oxidation reactions, *J. Nanomater.*, 2014, 192038.
- [11] Bagheri, S., Muhd Julkapli, N., and Bee Abd Hamid, S., 2014, Titanium dioxide as a catalyst support in heterogeneous catalysis, *Sci. World J.*, 2014, 727496.
- [12] Deshmukh, P., Bhatt, J., Peshwe, D., and Pathak, S., 2012, Determination of silica activity index and XRD, SEM and EDS studies of amorphous SiO₂ extracted from rice husk ash, *Trans. Indian Inst. Met.*, 65 (1), 63–70.
- [13] Setyawan, N., Hoerudin, H., and Yuliani, S., 2021, Synthesis of silica from rice husk by sol-gel method, *IOP Conf. Ser.: Earth Environ. Sci.*, 733, 012149.
- [14] Muthukrishnan, S., Gupta, S., and Kua, H.W., 2019, Application of rice husk biochar and thermally treated low silica rice husk ash to improve physical properties of cement mortar, *Theor. Appl. Fract. Mech.*, 104, 102376.
- [15] Ozturk, M., Karaaslan, M., Akgol, O., and Sevim, U.K., 2020, Mechanical and electromagnetic performance of cement based composites containing different replacement levels of ground granulated blast furnace slag, fly ash, silica fume and rice husk ash, *Cem. Concr. Res.*, 136, 106177.
- [16] Santhosh, K.G., Subhani, S.M., and Bahurudeen, A., 2022, Recycling of palm oil fuel ash and rice husk ash in the cleaner production of concrete, *J. Cleaner Prod.*, 354, 131736.
- [17] Avudaiappan, S., Prakatanoju, S., Amran, M., Aepuru, R., Saavedra Flores, E.I., Das, R., Gupta, R., Fediuk, R., and Vatin, N., 2021, Experimental investigation and image processing to predict the properties of concrete with the addition of nano silica and rice husk ash, *Crystals*, 11 (10), 1230.
- [18] Qureshi, L.A., Ali, B., and Ali, A., 2020, Combined effects of supplementary cementitious materials (silica fume, GGBS, fly ash and rice husk ash) and steel fiber on the hardened properties of recycled aggregate concrete, *Constr. Build. Mater.*, 263, 120636.
- [19] Saloni, S., Parveen, P., and Pham, T.M., 2020, Enhanced properties of high-silica rice husk ash-based geopolymer paste by incorporating basalt fibers, *Constr. Build. Mater.*, 245, 118422.
- [20] Hossain, S.S., Roy, P.K., and Bae, C.J., 2021, Utilization of waste rice husk ash for sustainable geopolymer: A review, *Constr. Build. Mater.*, 310, 125218.
- [21] Liang, G., Zhu, H., Li, H., Liu, T., and Guo, H., 2021, Comparative study on the effects of rice husk ash and silica fume on the freezing resistance of metakaolin-based geopolymer, *Constr. Build. Mater.*, 293, 123486.
- [22] Nana, A., Epey, N., Rodrique, K.C., Deutou, J.G.N., Djobo, J.N.Y., Tomé, S., Alomayri, T.S., Ngouné, J., Kamseu, E., and Leonelli, C., 2021, Mechanical strength and microstructure of metakaolin/volcanic ash-based geopolymer composites reinforced with reactive silica from rice husk ash (RHA), *Materialia*, 16, 101083.
- [23] Handayani, L., Aprilia, S., Abdullah, A., Rahmawati, C., Aulia, T.B., Ludvig, P., and Ahmad, J., 2022, Sodium silicate from rice husk ash and their effects as geopolymer cement, *Polymers*, 14 (14), 2920.
- [24] Steven, S., Restiawaty, E., Pasymi, P., and Bindar, Y., 2021, An appropriate acid leaching sequence in rice husk ash extraction to enhance the produced green silica quality for sustainable industrial silica gel purpose, *J. Taiwan Inst. Chem. Eng.*, 122, 51–57.
- [25] Nayak, P.P., and Datta, A.K., 2021, Synthesis of SiO₂-nanoparticles from rice husk ash and its comparison with commercial amorphous silica through material characterization, *Silicon*, 13 (4), 1209–1214.
- [26] Zainal, N.S., Mohamad, Z., Mustapa, M.S., Badarulzaman, N.A., and Zulkifli, A.Z., 2019, The ability of crystalline and amorphous silica from rice husk ash to perform quality hardness for ceramic water filtration membrane, *Int. J. Integr. Eng.*, 11 (5), 229–235.
- [27] Fatimah, I., Said, A., and Hasanah, U.A., 2015, Preparation of TiO₂-SiO₂ using rice husk ash as silica source and the kinetics study as photocatalyst in methyl violet decolorization, *Bull. Chem. React. Eng. Catal.*, 10 (1), 43–49.

- [28] Prabha, S., Durgalakshmi, D., Rajendran, S., and Lichtfouse, E., 2021, Plant-derived silica nanoparticles and composites for biosensors, bioimaging, drug delivery and supercapacitors: A review, *Environ. Chem. Lett.*, 19 (2), 1667–1691.
- [29] Jamwal, B., Kaur, M., Sharma, H., Khajuria, C., Paul, S., and Clark, J.H., 2019, Diamines as interparticle linkers for silica-titania supported PdCu bimetallic nanoparticles in Chan-Lam and Suzuki cross-coupling reactions, *New J. Chem.*, 43 (12), 4919–4928.
- [30] Mardjan, M.I.D., Hariadi, M.F., Putri, I.M., Musyarrofah, N.A., Salimah, M., Priatmoko, P., Purwono, B., and Commeiras, L., 2022, Ultrasonic-assisted-synthesis of isoindolin-1-one derivatives, *RSC Adv.*, 12 (29), 19016–19021.
- [31] Bai, Y., Li, Z., Cheng, B., Zhang, M., and Su, K., 2017, Higher UV-shielding ability and lower photocatalytic activity of TiO₂@SiO₂/APTES and its excellent performance in enhancing the photostability of poly(*p*-phenylene sulfide), *RSC Adv.*, 7 (35), 21758–21767.
- [32] Harraz, F.A., 2008, Polyethylene glycol-assisted hydrothermal growth of magnetite nanowires: Synthesis and magnetic properties, *Phys. E*, 40 (10), 3131–3136.
- [33] Kumar, P., Khanduri, H., Pathak, S., Singh, A., Singh, A., Basheed, G.A., and Pant, R.P., 2020, Temperature selectivity for single phase hydrothermal synthesis of PEG-400 coated magnetite nanoparticles, *Dalton Trans.*, 49 (25), 8672–8683.
- [34] Netzahual-Lopantzi, Á., Sánchez-Ramírez, J.F., Jiménez-Pérez, J.L., Cornejo-Monroy, D., López-Gamboa, G., and Correa-Pacheco, Z.N., 2019, Study of the thermal diffusivity of nanofluids containing SiO₂ decorated with Au nanoparticles by thermal lens spectroscopy, *Appl. Phys. A*, 125 (9), 588.
- [35] Eslami, S., Farhangdoost, B., Shahverdi, H., and Mohammadi, M., 2021, Surface grafting of silica nanoparticles using 3-aminopropyl (triethoxysilane) to improve the CO₂ absorption and enhance the gas consumption during the CO₂ hydrate formation, *Greenhouse Gases: Sci. Technol.*, 11 (5), 939–953.
- [36] Roe, S.P., Hill, J.O., and Magee, R.J., 1991, An infrared and electronic spectroscopic study of a series of nickel(II) amine complexes, *Monatsh. Chem.*, 122 (6), 467–478.
- [37] Ning, X., Lu, Y., Fu, H., Wan, H., Xu, Z., and Zheng, S., 2017, Template-mediated Ni(II) dispersion in mesoporous SiO₂ for preparation of highly dispersed Ni catalysts: Influence of template type, *ACS Appl. Mater. Interfaces*, 9 (22), 19335–19344.
- [38] Tian, Y., Jiao, W., Liu, P., Song, S., Lu, Z., Hirata, A., and Chen, M., 2019, Fast coalescence of metallic glass nanoparticles, *Nat. Commun.*, 10 (1), 5249.
- [39] Haghighi, M., and Gooneh-Farahani, S., 2020, Insights to the oxidative desulfurization process of fossil fuels over organic and inorganic heterogeneous catalysts: Advantages and issues, *Environ. Sci. Pollut. Res.*, 27 (32), 39923–39945.
- [40] Babyszko, A., Wanag, A., Sadłowski, M., Kusiak-Nejman, E., and Morawski, A.W., 2022, Synthesis and characterization of SiO₂/TiO₂ as photocatalyst on methylene blue degradation, *Catalysts*, 12 (11), 1372.
- [41] Wang, L.H., Kong, F.Y., and Tai, X.S., 2022, Synthesis, structural characterization of a new Ni(II) complex and its catalytic activity for oxidation of benzyl alcohol, *Bull. Chem. React. Eng. Catal.*, 17 (2), 375–382.
- [42] Bao, X., Li, H., Wang, Z., Tong, F., Liu, M., Zheng, Z., Wang, P., Cheng, H., Liu, Y., Dai, Y., Fan, Y., Li, Z., and Huang, B., 2021, TiO₂/Ti₃C₂ as an efficient photocatalyst for selective oxidation of benzyl alcohol to benzaldehyde, *Appl. Catal., B*, 286, 119885.
- [43] Qayyum, A., Giannakoudakis, D.A., LaGrow, A.P., Bondarchuk, O., Łomot, D., and Colmenares, J.C., 2022, High-frequency sonication for the synthesis of nanocluster-decorated titania nanorods: Making a better photocatalyst for the selective oxidation of monoaromatic alcohol, *Catal. Commun.*, 163, 106406.
- [44] Hikmah, N., Agustiniingsih, D., Nuryono, N., and Kunarti, E.S., 2022, Preparation of iron-doped SiO₂/TiO₂ using silica from sugarcane bagasse ash for visible light degradation of Congo Red, *Indones. J. Chem.*, 22 (2), 402–412.

Synthesis, Characterization and Staining Ability of Novel Azo Dye Based on Curcumin and Its Au(III) Complex

Wesam Dheyab Kzar¹, Hasan Shamran Mohammed^{1*}, Fatimah Swadi Zghair², and Zahia Zizi³

¹College of Science, Al-Qadissiya University, Al-Diwaniyah 58002, Iraq

²College of Veterinary Medicine, Al-Qadissiya University, Al-Diwaniyah 58001, Iraq

³Laboratory of Advanced Materials and Physicochemistry for Environment and Health, Djillali Liabes University of Sidi Bel Abbes, Sidi Bel Abbès 89, Algeria

* Corresponding author:

email: hasan.sh.mohammed@qu.edu.iq

Received: May 13, 2023

Accepted: June 11, 2023

DOI: 10.22146/ijc.84388

Abstract: Azo dye ligand (HMDA), namely N-(4-((E)-((1E,6E)-1,7-bis(4-hydroxy-3-methoxyphenyl)-3,5-dioxohepta-1,6-dien-4-yl)diazenyl)phenyl)acetamide was prepared by coupling diazonium salt of 4-aminoacetanilide with curcumin in basic conditions. The HMDA ligand and its Au(III) complex were characterized by elemental analysis, mass spectroscopy, ¹H-NMR, FTIR, UV-visible spectra, and molar conductivity. The molar ratio method was applied to ascertain the stoichiometric composition of the Au(III) complex in aqueous solution, which was 1:2 (metal ion to ligand). HMDA ligand binding with Au(III) ion used the enolate form moiety of curcumin under alkaline conditions which was observed by infrared spectra and investigated by elemental analysis and ¹H-NMR. HMDA and its Au(III) complex have been evaluated as stains for intestine, pancreas and kidney tissues of mice and exhibited important contrast. Both compounds showed the most potent staining activity toward blood cells, collagen, muscle fibers and cytoplasm in the selected tissues of mice. This azo dye and its complex of Au(III) succeeded in dyeing mice tissues, compared with the conventional stains.

Keywords: curcumin; azo dye; stain; coordination compound

■ INTRODUCTION

Curcumin is a bright orange-yellow crystalline solid and it is widely used as a coloring and food additive. The light fastness for the dyed fabrics is improved by using azo curcumin dyes and their complexes compared to using only curcumin [1-2]. Azo curcumin derivatives with a variety of colors depending on the type of amine derivative investigated for natural fibers (cotton, silk, and wool) exhibited improving fastness properties of the dyed fabrics to washing and light fastness [1].

Bis-keto tautomeric form of curcumin dominates in acidic and neutral conditions as well as in the solid phase, which could act as a potential donor of hydrogen atoms, while the enolate form of curcumin under alkaline conditions predominates [3-5]. Due to its demonstrated antioxidant qualities, curcumin has recently attracted a lot of attention in the prevention and treatment of diseases.

Turmeric contains curcumin, a hydrophobic, low-molecular-weight polyphenol that is frequently utilized in food [6]. Both forms of curcumin especially in the case of the enolate form (monobasic bidentate ligand) form stable complexes due to effective chelating agents that create stable complexes with the majority of known metal ions [7].

The curcumin probes have also been demonstrated to have better metrological characteristics when used with a nano-system, including low detection limits, repeatability, reproducibility, strong selectivity, and excellent storage stability [8]. Photophysical and inborn fluorescence characteristics are present in curcumin. Binding to metals changes its luminous characteristics. As a result, it is used to improve the efficiency of nano-sensors for detecting important chemicals, ions, metals, and contaminants that are harmful to the environment

as well as, as a natural fluorophore and electrochemical transducer. Additionally, it is employed to chelate metal ions, and the creation of functionalized nanoparticles has made use of this characteristic [9].

Curcumin is considered an excellent scavenger of most reactive oxygen species (ROS). The phenoxyl radicals can be easily formed by abstractable the hydrogen from the phenol-OH group of curcumin to form a stable keto-enol structure by the resonance [2,10].

The staining process is important because it makes things more visible by sharpening the contrast between the organism and its surroundings. It makes it possible to distinguish between a variety of morphological types, such as shape, size, and arrangement, as well as to ascertain an organism's staining characteristics, make a potential diagnosis of a direct illness, and demonstrate a pure culture [11]. The current study is concentrated on the synthesis, structural, and application aspects of the monoazo ligand produced from diazotizing of 4-aminoacetanilide and the active methylene coupling component of curcumin and its Au(III) metal complex and to evaluate the efficacy of azo dye and its Au(III) complex in staining mice tissues (pancreas, intestine, and kidney tissues) comparing with the conventional stains.

■ EXPERIMENTAL SECTION

Materials

4-Aminoacetanilide was purchased from Merck (purity 96%). Sodium hydroxide (NaOH, 98%) was prepared from Thomas baker. Curcumin crystalline was supplied from CDH (purity 96%). Hydrochloric acid (HCl, 38%) was purchased from CGH. Dimethyl sulfoxide (DMSO, 99%) was purchased from LOBA. Hydrogentetrachloroaurate(III) trihydrate was brought from Glentham Life Science (purity 99%).

Instrumentation

The infrared spectra were recorded by Shimadzu FTIR 8400S spectrophotometer in the range of 400–4000 cm^{-1} by using potassium bromide pellet, UV-visible spectrophotometer (UV-1650 PC) was used to record UV-vis spectra using quartz cuvettes 10.0 mm in diameter in the region of 200–1100 nm. Melting points

were recorded by using Sturat digital melting Point/SMP3. NMR spectra were done by Bruker 500 MHz. Mass spectra were done by using Agilent 5375 USA. Elemental analysis (C.H.N) was done by using Elemental analyzer-EA-300.

Procedure

Preparation of the HMDA dye

This dye was prepared by stirring for 2 h in two steps. The first step is to prepare the diazonium salt, which was prepared by dissolving 0.3 g (0.002 mol) of 4-aminoacetanilide in 15 mL ethanol, then adding 3 mL of HCl 12 M and cooling the solution to 0 °C. Sodium nitrite (0.2 g, 0.002 mol) was dissolved in 5 mL of distilled water under cooling to 0 °C, which was added to the acidic solution of 4-aminoacetanilide to produce the diazonium salt. The solution of the diazonium salt was left for 1 h under cooling and stirring then the solution was mixed with the cooling solution of curcumin (0.5 g, 0.002 mol) in 10% NaOH (5%). The mixture solution was left overnight, then it was filtered and washed with distilled water many times then the powder was put in a desiccator to dry. Elemental analysis of the ligand Experimental (%), C: 66.57, H: 5.01, N: 7.91, Theoretical (%), C: 66.78, H: 5.14, N: 7.94.

Au(III) complex preparation

The HMDA ligand (0.24 g, 0.00046 mol) was dissolved in 20 mL of ethanol. Then it was mixed with NaOH (0.02 g, 0.00046 mol). The ligand solution was added slowly to the HAuCl_4 (0.08 g, 0.00023 mol), dissolving in 5 mL distilled water. The reaction mixture was refluxed for 1 h. The reaction solution was left overnight at room temperature, then was filtered, washed with a little cold water, and dried. Elemental analysis of the Au(III) complex, Experimental (%), C: 53.95, H: 4.01, N: 6.51, Theoretical (%), C: 54.02, H: 4.06, N: 6.52.

Histological staining process

Slides containing wax-embedded small intestinal, pancreas, and kidney tissues were dewaxed in 100% xylene for 3 × 10 min each. The tissue was placed twice in 100% ethanol for 10 min. Subsequently, they were placed in 70% ethanol for 2 × 5 min. Slides were then rehydrated twice in distilled water for 5 min each. Slides

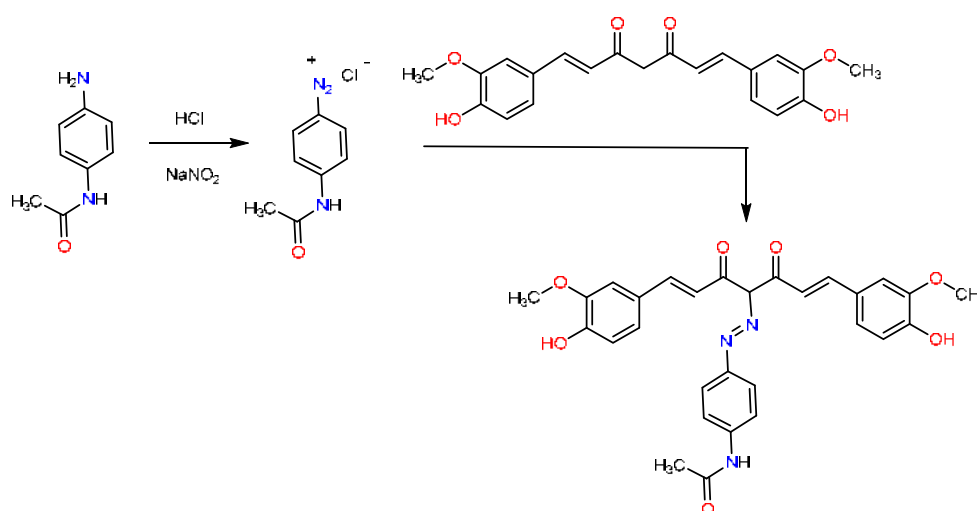
were immersed in bouins solution for 1 h at 59 °C then washed and stained by hametoxyline and washed by distal water, used HMDA ligand and Au(III) complex were used as a counter stain for 20 min at room temperature. Subsequently, slides were rehydrated by grading alcohol. Finally, slides were mounted in DPX. Also, the counter stain by routine H&E process sections was visualized using an epifluorescence microscope, and images were captured with a Canon digital camera (DS126371, Canon Inc, Japan).

RESULTS AND DISCUSSION

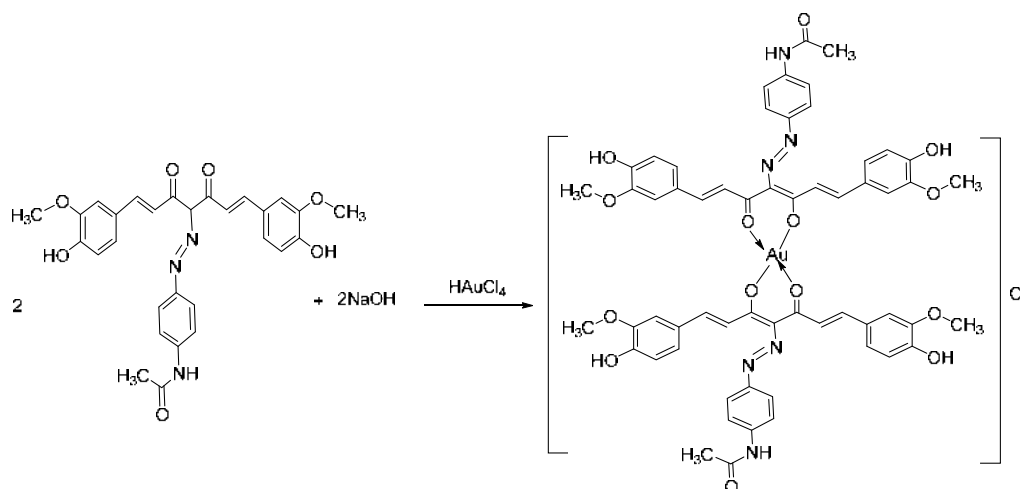
The azo curcumin ligand was prepared by reacting diazonium salt of 4-aminoacetanilide with curcumin, as

shown in Scheme 1. The resulting dye, namely *N*-(4-((*E*)-((1*E*,6*E*)-1,7-bis(4-hydroxy-3-methoxyphenyl)-3,5-dioxohepta-1,6-dien-4-yl)diazenyl)phenyl)acetamide (HMDA) was obtained as a light brown powder with a percentage of 82% and melting point 188 °C. The solid HMDA ligand was insoluble in water but completely soluble in some organic solvents such as dimethylsulfoxide, ethanol, and acetone.

The Au(III) complex was prepared by reacting the HAuCl₄ with two equivalents of HMDA ligand, as shown in Scheme 2. The mass spectrum of HMDA dye (Fig. 1) provided a molecular ion peak at $m/z = 532$, and the molecular ion peak of the Au(III) complex was at $m/z = 1254$, which corresponds to predict the molecular



Scheme 1. Preparation steps of HMDA ligand of azo dye based on curcumin



Scheme 2. Preparation of Au(III) complex for HMDA ligand of azo dye based on curcumin

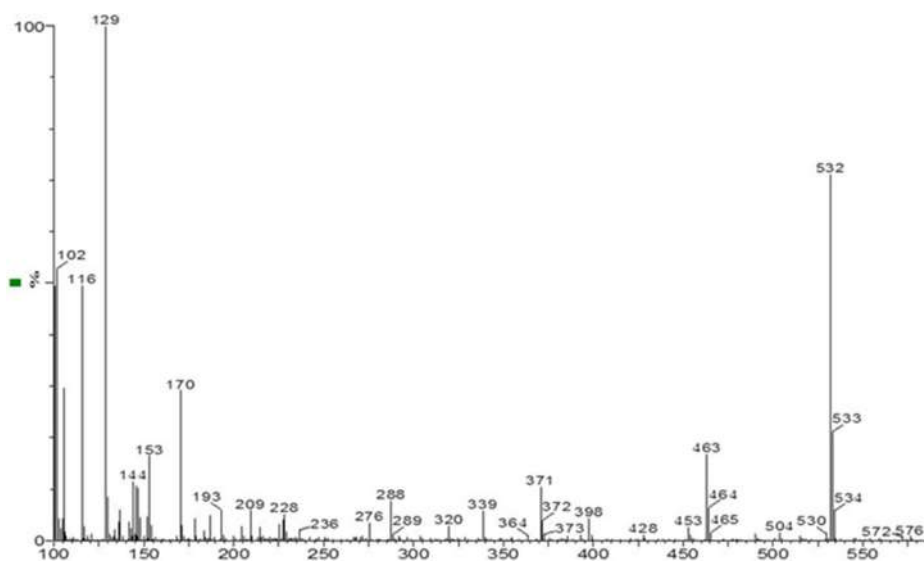


Fig 1. Mass spectrum of HMDA ligand of azo dye based on curcumin

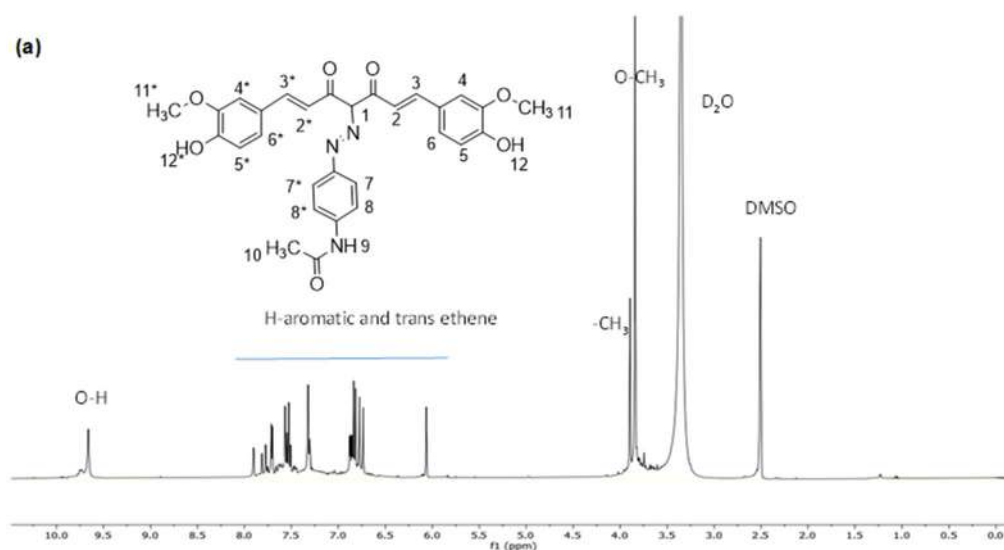
weight of HMDA ligand and the $[\text{Au}(\text{HMDA})_2]\text{Cl}$ formula of Au(III) complex.

The reaction of Au(III) with HMDA ligand in ethanol under reflux led to high yield Au(III) complex, and the results of the elemental analyses of the synthesized Au(III) complex were in good accord with what the proposed formula demanded.

$^1\text{H-NMR}$ spectrum of HMDA ligand as shown in Fig. 2, exhibited many signals related to O–H and N–H at 9.62 and 7.91 ppm, respectively [12]. The signals exhibited at 3.91 and 3.82 ppm due to $\text{O}=\text{CCH}_3$ and $\text{O}-\text{CH}_3$, respectively. The other protons exhibited in the range of 6.55–7.91 ppm. The chemical shifts of the

HMDA ligand are 9.62 (2H, s), 7.91 (1H, d), 7.79 (2H, d), 7.71 (2H, d), 7.55 (2H, d), 7.52 (2H, d), 7.33 (2H, d), 6.87 (2H, d), 6.76 (2H, d), 6.55 (1H, s), 3.91 (6H, s), and 3.82 (6H, s).

$^1\text{H-NMR}$ spectrum of the Au(III) complex was compared to the free ligand of curcumin to gain more information about the nature of the metal complex in the solution. Upon complexation with Au(III), the singlet signal in position 1 in the free ligand vanished in the spectrum of complex. This proton was removed by using an equivalent NaOH base. The aromatic protons and ethene units exhibited in the range of 6.2–7.6 ppm. The signal at 9.85 ppm in the spectrum of the complex is



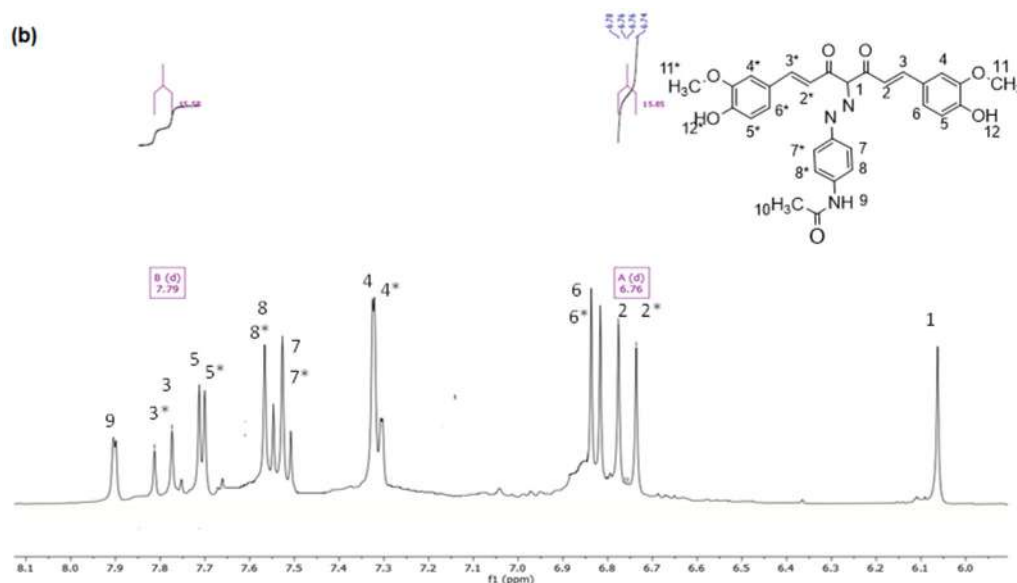


Fig 2. (a) ^1H -NMR spectrum of HMDA ligand of azo dye based on curcumin in $\text{DMSO-}d_6$ solvent and (b) the aromatic region of ^1H -NMR spectrum of HMDA ligand

due to $-\text{OH}$ groups. The signal at 3.4 ppm is due to $-\text{CH}$. The signals exhibited at 3.74 and 3.53 ppm due to $\text{O}=\text{C}-\text{CH}_3$ and $\text{O}-\text{CH}_3$, respectively.

IR Spectra

The important function groups of the HMDA ligand and its Au(III) complex were investigated by infrared spectroscopy. The IR spectra of the HMDA ligand and its Au(III) complex were done by using a KBr disc. Their significant bands are summarized in Table 1, and Fig. 3 and 4 represent their IR spectra.

The IR spectrum of azo ligand (HMDA) revealed the band's absence of the $-\text{NH}_2$ stretching bond of acetanilide and the appearance of $\text{N}=\text{N}$ stretching at 1415 cm^{-1} , indicating the diazotization of 4-aminoacetanilide and formation of the azo dye of curcumin [13]. The spectrum of HMDA ligand shows a medium band at 3360 cm^{-1} due to $\text{N}-\text{H}$ group of acetanilide [14] and a medium band at 3418 cm^{-1} due to $\text{O}-\text{H}$ groups of curcumin. A band had been exhibited at 3060 cm^{-1} in the HMDA ligand spectrum that is due to vibration of $\text{C}-\text{H}$ of phenol ring

and other bands at 2960 and 2837 cm^{-1} are due to the aliphatic stretching of $\text{C}-\text{H}$ in curcumin. These bands of HMDA ligand showed in the same position in the spectrum of Au(III) complex [15-16].

A band at 1669 cm^{-1} in the HMDA spectrum is due to $\text{C}=\text{O}$ group of curcumin, which shifted to low frequency

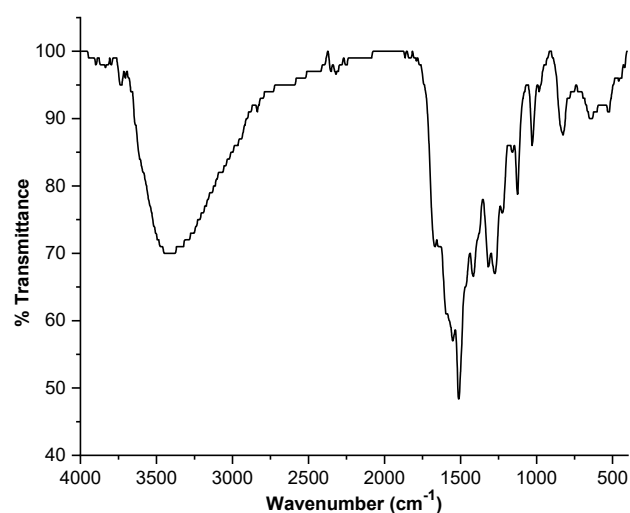


Fig 3. The IR spectrum of HMDA ligand

Table 1. The important vibrations of HMDA ligand and its Au(III) complex

Compound	$-\text{OH}$	$-\text{NH}$	$-\text{CH}$ aromatic	$-\text{CH}$ aliphatic	$\text{C}=\text{O}$	$\text{C}=\text{O}$ curcumin	$\text{C}=\text{C}$	$\text{N}=\text{N}$	$\text{M}-\text{O}$
HMDA ligand	3418	3360	3060	2960, 2837	1672	1669	1510	1415	-
Au(III) complex	3396	3304	3072	2954, 2837	1670	1597	1513	1426	523

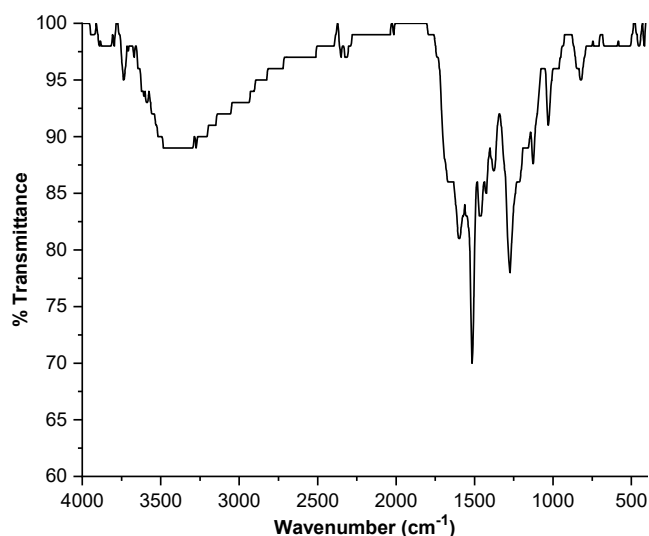


Fig 4. The IR spectrum of Au(III) complex for HMDA ligand

in the spectrum of the gold complex [17]. That indicates that the oxygen of the C=O group is involved in the coordination with metal ions of the Au(III) complex. The IR spectrum of the Au(III) complex appeared to have a new absorption band at 523 cm^{-1} , which is attributed to (M–O) [18]. The IR spectral data indicate that HMDA ligand behaves as a bidentate chelating ligand coordinating through the positions of oxygen of keto-enol groups which were in the resonance process [6].

UV-vis Spectra of HMDA Ligand and Au(III) complex

Electronic transition measurements were conducted in dimethylsulfoxide at room temperature. UV-vis spectra of HMDA ligand and Au(III) complex are listed in Fig. 5. The HMDA ligand showed bands at 260 and 429 nm. These bands are due to $\pi \rightarrow \pi^*$ and $n \rightarrow \pi^*$ transitions, respectively [19-22]. The Au(III) complex

spectrum exhibited bands at 386 and 513 nm due to $^1A_{1g} \rightarrow ^1E_g$ and $^1A_{1g} \rightarrow ^1A_{2g}$ transitions, respectively. These bands represent pretty accurately the square planar shape of the Au(III) ion, and the band at 263 nm is an electronic transition due to the ligand [23].

Staining Process

The tissues of mice stained by yellow color in aqueous solutions under effects of HMDA ligand and Au(III) complex. We added the solution of bouins as a mordant of the staining, and we used the procedure of staining as in reference [24-25]. The effect of portions of HMDA ligand and Au(III) complex on tissue sections as a counter stain for the hematoxylin showing staining ability even after applying them for 20 min at room temperature stain which showed collagen fiber, red blood cells, cytoplasm deep yellow color in HMDA ligand and Au(III) on intestine tissues of the mice, while the stain

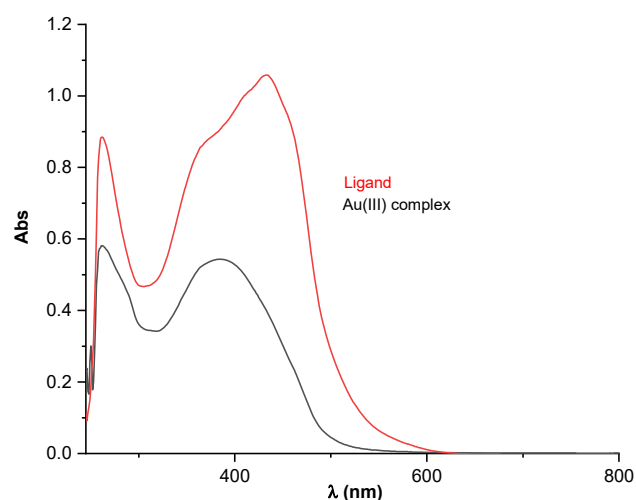


Fig 5. UV-visible spectra of HMDA ligand and Au(III) square complex

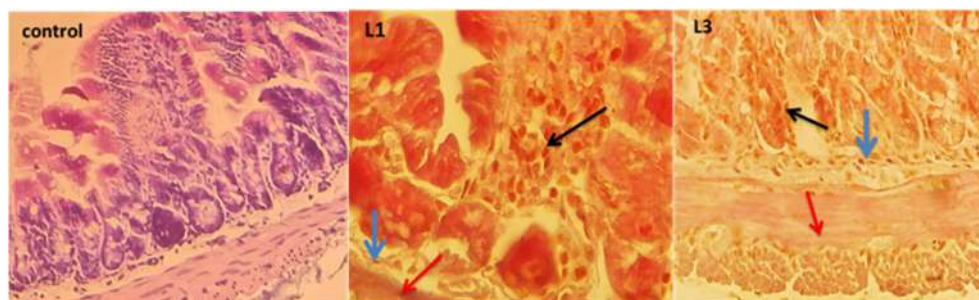


Fig 6. Microscopic images for mice intestine tissue HMDA ligand (L1), Au(III) complex (L3) stain RBC (black arrows), collagen fiber (blue arrows), muscle fiber (red arrows), and control stains of hematoxylin and eosin technique (X100)

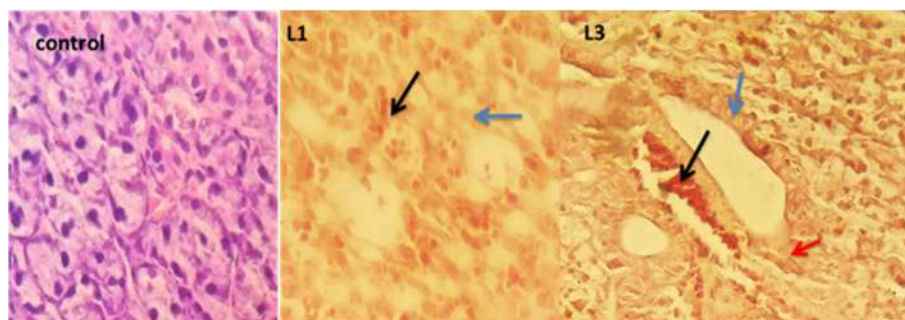


Fig 7. Microscopic images for mice pancreas tissue HMDA ligand (L1), Au(III) complex (L3) stain RBC (black arrows), collagen fiber (blue arrows), and control stains of hematoxylin and eosin technique (X200)

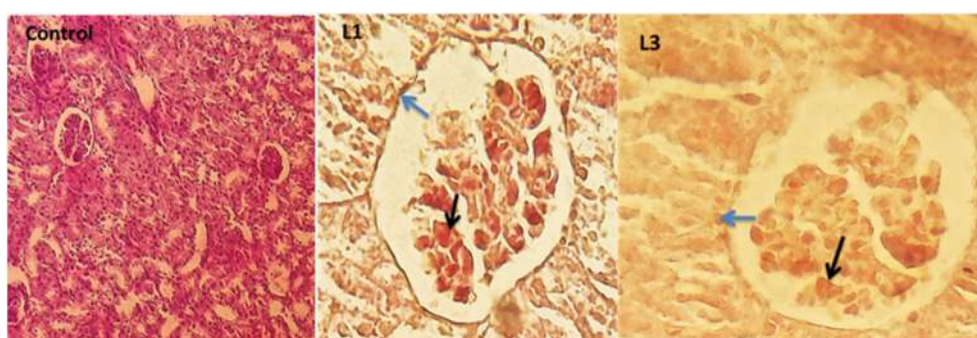


Fig 8. Microscopic images for mice kidney tissue HMDA ligand and Au(III) complex stain RBC (black arrows), collagen fiber (blue arrows), and stains control of hematoxylin and eosin technique (X100, X200)

gave the same level at the HMDA ligand and Au(III) complex in mice pancreas and kidney sections (Fig. 6, 7, and 8). In the case of control, we used stains of hematoxylin-eosin where the nuclei were stained blue, and cytoplasm with collagen fiber and red blood cells were stained pink (Fig. 6, 7, 8, and control).

We noticed that the general staining HMDA ligand and Au(III) complex improved the staining technique for RBC cells and collagen fiber in the intestine tissues of mice accompanied with moderate stain in the case of Au(III) complex (Fig. 6). In Fig. 7 and 8, the general staining by HMDA ligand and Au(III) complex improved the staining technique for RBC cells and collagen fiber in pancreas and kidney tissues of mice.

■ CONCLUSION

In the present work, new azo dye and its Au(III) complex containing curcumin were successfully synthesized and characterized. The HMDA ligand is bidentate and Au(III) complex is a square planar. The mole ratio of reacting the ligand to metal is 2:1. It is noteworthy

to conclude that azo dye and its Au(III) complex could be a safer alternative stain for the natural stains where our dyes have shown similar staining characteristics as compared to hematoxylin and eosin dyes. Dyes have the ability to stain nuclear and cytoplasmic in mice tissues of the pancreas, kidney, and intestine tissues. Azo stain showed superior staining properties in mice tissues such as collagen, muscle fibers and red blood cells, which showed better contrast and therefore found application in collagen and muscular disorders.

■ AUTHOR CONTRIBUTIONS

The authors have the same level of contribution in all parts work. All authors agreed to the final version of this manuscript.

■ REFERENCES

- [1] Rekaby, M.M., Swelam, S.A., Shahin, A.A., and Elhag, F.A., 2018, Evaluation of colouration properties of newly synthesized curcumin derivatives, *Egypt. Pharm. J.*, 17 (3), 155–162.

- [2] Mezgebe, K., and Mulugeta, E., 2022, Synthesis and pharmacological activities of azo dye derivatives incorporating heterocyclic scaffolds: A review, *RSC Adv.*, 12 (40), 25932–25946.
- [3] Prasad, S., DuBourdieu, D., Srivastava, A., Kumar, P., and Lall, R., 2021, Metal–curcumin complexes in therapeutics: An approach to enhance pharmacological effects of curcumin, *Int. J. Mol. Sci.*, 22 (13), 7094–7107.
- [4] Kazakova, O., Lipkovska, N., and Barvinchenko, V., 2022, Keto-enol tautomerism of curcumin in the preparation of nanobiocomposites with fumed silicam, *Spectrochim. Acta, Part A*, 277, 121287.
- [5] Bukhari, S.N.A., Jantan, I., Jasamai, M., Ahmad, W., and Amjad, M.W., 2013, Synthesis and biological evaluation of curcumin analogues, *J. Med. Sci.*, 13 (7), 501–513.
- [6] Priya, R.S., Balachandran, S., Daisy, J., and Mohanan, P.V., 2015, Reactive centers of curcumin and the possible role of metal complexes of curcumin as antioxidants, *Univers. J. Phys. Appl.*, 9 (1), 6–16.
- [7] Priyadarsini, K.I., 2014, The chemistry of curcumin: From extraction to therapeutic agent, *Molecules*, 19 (12), 20091–9112.
- [8] Devasena, T., Balasubramanian, N., Muninathan, N., Baskaran, K., and John, S.T., 2022, Curcumin is an iconic ligand for detecting environmental pollutants, *Bioinorg. Chem. Appl.*, 2022, 9248988.
- [9] Zhang, W., Chen, C., Shi, H., Yang, M., Liu, Y., Ji, P., Chen, H., Tan, R.X., and Li, E., 2016, Curcumin is a biologically active copper chelator with antitumor activity, *Phytomedicine*, 23 (1), 1–8.
- [10] Nakamae, I., Morimoto, T., Shima, H., Shionyu, M., Fujiki, H., Yoneda-Kato, N., Yokoyama, T., Kanaya, S., Kakiuchi, K., Shirai, T., Meiyanto, E., and Kato, J., 2019, Curcumin derivatives verify the essentiality of ROS upregulation in tumor suppression, *Molecules*, 24 (22), 4067.
- [11] Hope-Roberts, M., and Horobin, R.W., 2017, A review of curcumin as a biological stain and as a self-visualizing pharmaceutical agent, *Biotech. Histochem.*, 92 (5), 315–323.
- [12] Sarhan, B.M., and Fyyadh, B.M., 2017, Synthesis and characterization of some metal complexes of [4-methoxy-*N*-(pyrimidine-2-ylcarbamoithiyl) benzamide], *Baghdad Sci. J.*, 14 (4), 765–765.
- [13] Ali, R.R., and Mohammed, H.S., 2021, Biological activity and latent fingerprints detection by azo quinoline dye and its complexes, *Period. Eng. Nat. Sci.*, 9 (3), 317–329.
- [14] Abbas, A.K., and AL-Qaysi, W.W., 2023, Synthesis and characterization of novel nano azo compounds as a new pH sensor, *Arabian J. Sci. Eng.*, 48 (1), 399–415.
- [15] Al-Daffay, R.K.H., and Al-Hamdani, A.A.S., 2022, Synthesis and characterization of some metals complexes with new acidic azo ligand 4-[(2-amino-4-phenylazo)-methyl]-cyclohexane carboxylic acid, *Iraqi J. Sci.*, 63 (8), 3264–3275.
- [16] Falah, N.S., Abdullah, S.A.H., and Jabir, M.S., 2023, Synthesis, characterization, and mass spectral fragmentation of novel azo derivative and its divalent metal ion complexes, *J. Surv. Fish. Sci.*, 10 (3S), 1436–1444.
- [17] Sarhan, B.M., and Neema, B.Z., 2017, Synthesis and spectroscopic studies of some divalent metall ion complexes of 3-(4-hydroxyphenyl)-2-(3-(4-nitrobenzoyl)thioureido)propanoic acid, *Baghdad Sci. J.*, 14 (3), 0588.
- [18] Fyyadh, B.M., Abd, N.A.B., and Sarhan, B.M., 2022, Synthesis and characterization of new Mn(II), Co(II), Cd(II) and Hg(II) complexes with ligand [*N*-(pyrimidin-2-ylcarbamoithiyl)benzamide] and their anti-bacterial study, *IOP Conf. Ser.: Earth Environ. Sci.*, 1029, 012030.
- [19] Witwit, I.N., Motaweq, Z.Y., and Mubark, H.M., 2018, Synthesis, characterization, and biological efficacy on new mixed ligand complexes based from azo dye of 8-hydroxy quinoline as a primary ligand and imidazole as a secondary ligand with some of transition metal ions, *J. Pharm. Sci. Res.*, 10 (12), 3074–3083.
- [20] Mohammed, H.S., Al-Hasan, H.A., Chaieb, Z., Zizi, Z., and Abed, H.N., 2023, Synthesis, characterization,

- DFT calculations and biological evaluation of azo dye ligand containing 1,3-dimethylxanthine and its Co(II), Cu(II) and Zn(II) complexes, *Bull. Chem. Soc. Ethiop.*, 37 (2), 347–356.
- [21] Mohammed, H.S., 2021, Synthesis and characterization of some complexes of azo-chalcone ligand and assessment of their biological activity, *Mater. Plast.*, 58 (3), 23–31.
- [22] Alzamili, S.K., and Shamran, M.H., 2022, Synthesis, characterization and biological activity of azo guanine and its complexes, *Res. J. Chem. Environ.*, 26 (10), 129–141.
- [23] Abbas, A., and Kadhim, R.S., 2016, Preparation, spectral and biological studies of azo ligand derived from proline with Cu(II), Ag(I) and Au(III) metal ion, *IOSR J. Appl. Chem.*, 9 (8), 20–31.
- [24] Lavanya, A., Sowmya, S.V., Rao, R.S., Augustine, D., and Haragannavar, V.C., 2021, Natural stain (*Kumkum*) formulated by the extract of *Curcuma aromatica* and slaked lime in histostaining of oral tissues: An observational study, *J. Oral Maxillofac. Pathol.*, 25 (1), 88–96.
- [25] Al-Redah, S.A.A., Zghair, F.S., and Alhacham, E.I.D., 2021, Pancreas in sheep histochemical and immunohistochemical analysis, *Ann. Rom. Soc. Cell Biol.*, 25 (3), 229–240.

Synthesis and Characterization of Zn(II), Cu(II), and Ni(II)-Levofloxacin Complexes for Carbon Dioxide Storage Media

Hadeel Adil¹, Hamsa Thamer¹, Dina Saadi Ahmed², Raghda Alsayed¹, Muna Bufaroosha^{3*}, Khalid Zainulabdeen¹, Hassan Hashim⁴, Alaa Mohammed⁵, and Emad Yousif^{1**}

¹Department of Chemistry, College of Science, Al-Nahrain University, Baghdad 64021, Iraq

²Department of Chemical Industries, Institute of Technology-Baghdad, Middle Technical University, Baghdad 10074, Iraq

³Department of Chemistry, College of Science, United Arab Emirates University, Al-Ain 1818, United Arab Emirates

⁴Department of Physics, College of Science, Al-Nahrain University, Baghdad 64040, Iraq

⁵Department of Environmental Science, College of Energy and Environmental Science, Alkarkh University of Science, Baghdad 10081, Iraq

* **Corresponding author:**

email: muna.bufaroosha@uaeu.ac.ae*; emad_yousif@hotmail.com**

Received: May 17, 2023

Accepted: July 5, 2023

DOI: 10.22146/ijc.84552

Abstract: Three complexes ($[\text{CuL}_2(\text{H}_2\text{O})_2]$, $[\text{NiL}_2(\text{H}_2\text{O})_2]$, and $[\text{ZnL}_2\text{Cl}_2]$) have been synthesized through the reaction of metal salts and levofloxacin and characterized by spectrophotometers. The morphology of the complexes was investigated using field emission scanning electron microscopy (FESEM). The physicochemical properties of these complexes were evaluated using the Brunauer-Emmett-Teller (BET) and Barrett-Joyner-Halenda (BJH) techniques. Furthermore, the storage capacity of these complexes was verified using the H-sorb 2600 analyzer at a temperature of 323 K and varying pressure conditions. The obtained data substantiates that the synthesized complexes exhibit favorable attributes for CO_2 absorption. The surface area reaches $24.97 \text{ m}^2/\text{g}$ with capacities of $123.073 \text{ m}^3/\text{g}$ and $34.400 \text{ m}^3/\text{g}$ to adsorb CO_2 . The escalating levels of CO_2 in the atmosphere, primarily resulting from the combustion of fossil fuels to meet the surging energy requirements, pose a pressing environmental challenge. Consequently, there has been a surge in research focused on the development of novel materials aimed at facilitating CO_2 storage.

Keywords: levofloxacin; gas storage; global warming; carbon dioxide uptake

■ INTRODUCTION

According to several chemical methods, abundant porous materials have been synthesized [1]. Such of these materials are zeolites, carbons, porous polymers and metal-organic frameworks (MOFs). Many properties, such as pore size and surface area of porous materials, might be affected according to functional groups (e.g., hydroxyl groups), heteroatoms, aromatic rings, polar groups, and polymeric chains which these materials contain, and could increase the interactions with gas molecules [2-3]. Recently, many studies applied porous materials in different fields, including catalysis, environmental protection, biology, energy saving and

conserving [1]. Over the past years, many MOF materials have been prepared, characterized, and applied in different fields. MOF materials could be produced from the formation of coordination bonds between metal and organic molecules [3]. The affinity of the metals to bind with different organic molecules makes the possibility to prepare thousands of these compounds [4].

Over time, several developments were made in the chemistry of MOF materials, which included geometric shapes such as octahedral and tetrahedral. This, in turn, can be affected by the expansion of coordination bonds between a metal and organic molecules [5]. The organic molecules might be carboxylates, phosphate, sulfonate

and *N*-containing heterocyclic [6]. In 1990, the first investigation of the porosity of MOF materials was achieved at high pressure to force the gas molecules to be absorbed on the material's surfaces [7]. The adsorption and desorption measurements of molecules of gas at high and low pressure and temperature prove the permanent porosity of the materials. The first proof was carried out on zinc terephthalate MOF by measuring the nitrogen and carbon dioxide (CO₂) isotherms [8-9].

One of the most common applications of MOF materials is gas storage media [6,10-12]. In the last decades, thousands of studies were performed on the ability of MOFs to absorb and store H₂, CO₂, and CH₄ [13-15]. In particular, CO₂ capture has become the focus of many studies because the industrial revolution and consumption of fossil fuels lead to the increase in the levels of CO₂, which is the major greenhouse as well as leads to "global warming" [16]. In 2015 the National Oceanic and Atmospheric Administration (NOAA) reported that the concentration of CO₂ in the atmosphere reached 403 ppm, which increase of about 25% than in 1958 [17]. In a recent study, several materials have been synthesized which can absorb, store and regenerate greenhouse gases to reduce their level in the atmosphere [18-21].

Several processes have been used to synthesize novel MOFs with high surface areas by using huge and longer organic molecule structures [22]. The studies revealed that the high gravimetric gas uptake by MOFs is proportional to the high surface area and porosity under high pressure [23-25]. As an illustration, M-MOF-74 (M = Mg, Co, Fe, Zn, or Ni) has been synthesized with a large surface area that is measured using the BET method, making it able to capture CO₂ [26]. The acid-base and dipole-quadrupole interactions between the N sites and CO₂ gas molecules would stimulate CO₂ absorption when using the *N*-containing ligands [12]. On the other hand, the electrostatic interactions with the CO₂ quadrupole moment would be enhanced by the presence of water molecules that coordinated with metal. The metal acts as Lewis acid by having partial positive charges on its sites, resulting in a strong interaction between the coordinately unsaturated metal sites and CO₂ molecules [27]. The

structural characteristics of MOF materials that have a large capacity for strong binding sites, which facilitate strong interactions with gas molecules, are distinguished by the hybridization of metal [28].

Zeolite, a CO₂ capture material, has garnered significant attention among researchers. Previous studies have highlighted its notable capacity for adsorbing CO₂ under conditions of 25 °C and low pressure [29-30]. Levofloxacin complexes were considered for gas capture and the inspiration for our research since these compounds' capacities to adsorb gas vary depending on their physical and chemical characteristics. In the pursuit of novel adsorbents for CO₂ capture, our research focus shifted towards heterocyclic compounds, owing to their inherent utility as biologically active substances. Given the potential benefits of these attributes in the realm of CO₂ adsorption, we embarked on synthesizing fresh levofloxacin metal complexes, followed by an extensive investigation into their applicability in the field of CO₂ capture.

■ EXPERIMENTAL SECTION

Materials

The materials used in this study were levofloxacin, metal salts (ZnCl₂, NiCl₂·6H₂O, CuCl₂·6H₂O), and methanol, which were ordered from Sigma-Aldrich (Schnelldorf, Bavaria, Germany).

Instrumentation

The Fourier transform infrared (FTIR) spectra of the metal complexes were carried out on FTIR 8300 Shimadzu spectrophotometer using KBr pellets at 400–4000 cm⁻¹ (Tokyo, Japan). Shimadzu UV-1601 spectrophotometer was utilized to examine the metal complexes' UV-visible absorption spectra in methanol (Tokyo, Japan). Furthermore, a typical portable conductivity meter, the WTW ProfiLine Oxi 3205, (Xylem Inc., Weinheim, Germany), was used to measure the conductivity of the metal complexes in ethanol at a temperature of 25 °C. In addition, a Bruker BM6 magnetic balance (Bruker, Zürich, Switzerland) was employed to test the magnetic susceptibilities of the metal complexes. Finally, in order to analyze the surface

morphology of the metal complexes, ZEISS was applied in conjunction with dispersive X-ray (EDX) and field emission scanning electron microscopy (FESEM) investigations.

Procedure

Metal complexes preparation

A suitable amount of metal salts of ZnCl_2 (1.0 mmol, 0.1363 g), $\text{NiCl}_2 \cdot 6\text{H}_2\text{O}$ (1.0 mmol, 0.2377 g) or $\text{CuCl}_2 \cdot 6\text{H}_2\text{O}$ (1.0 mmol, 0.2425 g) was dissolved in 5 mL of methanol and then added to a solution of levofloxacin (5 mL of MeOH, 2.0 mmol (0.7228 g) of levofloxacin) as illustrated in Schemes 1 and 2. The mixture was heated for 3 h under reflux. After cooling, the solid was filtered, washed with MeOH, and then recrystallized from ethanol to produce the required metal complex. The complexes' measured yield percentages, colors, and melting points are displayed in Table 1.

Porosity and surface area of complexes

The MicroActive for TriStar II Plus Version 2.03 model of Micromeritics analyzers was utilized to investigate the nitrogen adsorption-desorption isotherms for the complexes. The Brunauer-Emmett-Teller (BET) method and the Barrett-Joyner-Halenda (BJH) theory were employed to analyze and estimate the specific pore volumes, diameter, and pore size distribution of the metal complexes.

Gas adsorption analysis

An H-sorb 2600 high-pressure volumetric adsorption analyzer was applied to calculate the volumetric amount of CO_2 gas that the complexes adsorbed.

RESULTS AND DISCUSSION

Characterizing Metal(II) Complexes

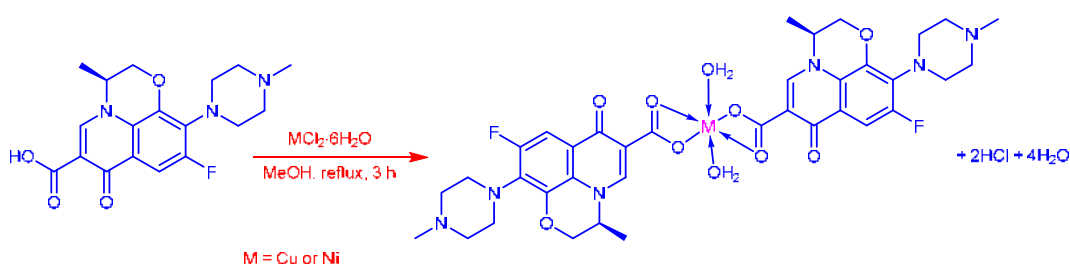
The synthesized complexes are characterized by FTIR and UV-vis spectroscopy. The mean data of FTIR spectra are summarized in Table 2. FTIR spectrum of

Table 1. Physical properties and yield percentages of the complexes

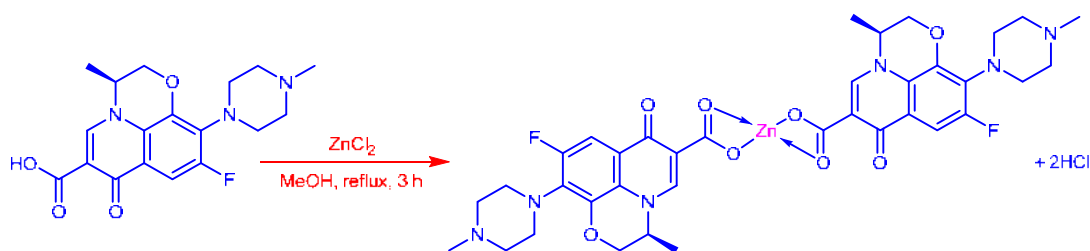
Compounds	Color	M.P. (°C)	Yield%
L	White	213–218 (dec.)	-
$[\text{CuL}_2(\text{H}_2\text{O})_2]$	Blue	280–282	81
$[\text{NiL}_2(\text{H}_2\text{O})_2]$	Green	300 (dec.)	79
$[\text{ZnL}_2\text{Cl}_2]$	White	220 (dec.)	83

Table 2. Ligand and synthetic complex FTIR data values

Compounds	Wavenumber (cm^{-1})		
	C=O _(sym)	C=O _(asym)	$\Delta\nu_{(\text{asym-sym})}$
L	1440	1614	-
$[\text{CuL}_2(\text{H}_2\text{O})_2]$	1445	1612	167
$[\text{NiL}_2(\text{H}_2\text{O})_2]$	1454	1611	157
$[\text{ZnL}_2]$	1468	1613	145



Scheme 1. Synthesis of Cu and Ni complexes



Scheme 2. Synthesis of Zn complexes

ligand, where observed the resonance frequency of symmetry and asymmetry of carbonyl carboxylic acid at 1440 and 1614 cm^{-1} . The synthesized complexes spectra show the difference between asymmetry ($\nu_{(\text{asym})}$) and symmetry ($\nu_{(\text{sym})}$) ranging from 145 to 167 cm^{-1} , which indicates that the ligand was bidentate.

The mean data of UV-vis spectroscopy are tabulated in Table 3. The absorption bands of the ligand spectrum observed at 34,843 and 33,557 cm^{-1} correspond to $\pi \rightarrow \pi^*$ and $n \rightarrow \pi^*$ transitions. The spectrum of the Cu(II) complex shows bands at 29,674 cm^{-1} due to the LMCT (ligand to metal charge transfer), and 27,027 belong to $2E_g \rightarrow 2T_{2g}$ transition. These bands are attributed to distorted octahedral geometry. The electronic spectrum of the Ni(II) complex reveals a band at 29,940 cm^{-1} for the $3A_{2g}(F) \rightarrow 3T_{1g}(P)$ transition, while the $3A_{2g}(F) \rightarrow 3T_{1g}(F)$ transition occurs at 26,882 cm^{-1} for high spin octahedral geometry with magnetic susceptibility 2.9 BM. In the end,

the electronic spectrum of the Zn(II) complex displays bands at 29,674 and 27,248 cm^{-1} due to the charge transfer. The suggested geometry is tetrahedral with the magnetic susceptibility value zero. Based on the molar conductivity (Λ_m) measurements, the results reveal that the complexes were nonelectrolytes [31], and the values ranged from 5 to 22 $\mu\text{S}/\text{cm}$. The UV-vis spectra, magnetic susceptibility (μ_{eff}) and conductivity of the complexes indicate the suggested geometries.

Surface Morphology of Metal(II) Complexes

FESEM was used to examine the complicated surfaces. Fig. 1 presents the FESEM images of the synthesized complexes at 1 μm magnification level. It is evident from the images that the surfaces of the complexes exhibit a uniform structure and feature various porous formations characterized by distinct particle sizes.

Table 3. Electronic transitions, absorption band energies, magnetic moments, geometry, conductivity, and hybridization

Complexes	λ (nm)	Absorption band (cm^{-1})	Transitions	Λ_m ($\mu\text{S}/\text{cm}$)	μ_{eff}	Geometry	Hybridization
L	287	34,843	$\pi \rightarrow \pi^*$	-	-	-	-
	298	33,557	$n \rightarrow \pi^*$				
	285	35,088	$\pi \rightarrow \pi^*$				
CuL ₂ ·2H ₂ O	296	33,784	$n \rightarrow \pi^*$	22	1.8	Distorted Octahedral	sp^3d^2
	337	29,674	LM CT				
	370	27,027	$2E_g \rightarrow 2T_{2g}$				
	283	35,336	$\pi \rightarrow \pi^*$				
NiL ₂ ·2H ₂ O	296	33,784	$n \rightarrow \pi^*$	5	2.9	Octahedral	sp^3d^2 high spin
	334	29,940	$3A_{2g}(F) \rightarrow 3T_{1g}(P)$				
	372	26,882	$3A_{2g}(F) \rightarrow 3T_{1g}(F)$				
	286	34,965	$\pi \rightarrow \pi^*$				
ZnL ₂	296	33,784	$n \rightarrow \pi^*$	13	0	Tetrahedral	sp^3 diamagnetic
	337	29,674	CT				
	367	27,248					

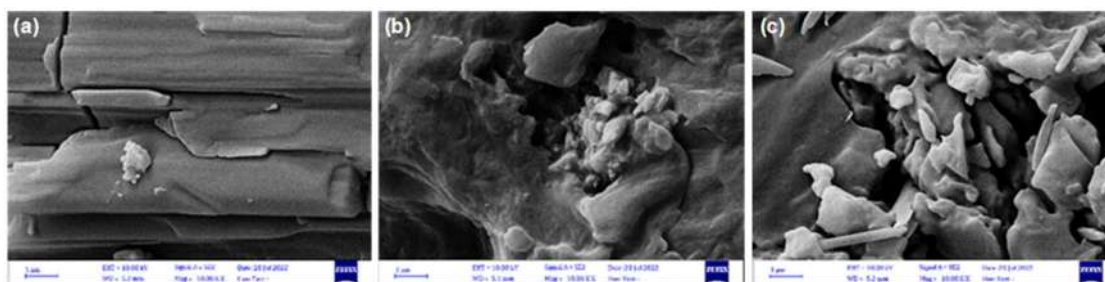


Fig 1. FESEM images of (a) Cu(II), (b) Ni(II), and (c) Zn(II) complexes

EDX analysis was used to determine the elemental composition of complex surfaces. SEM, a common technique in chemical microanalysis, is combined with EDX to determine the chemical structure of produced compounds. The elemental composition of the synthesized complexes was determined based on the EDX mapping, as summarized in Table 4. The EDX data exhibited highly abundant absorption bands corresponding to the carbon atoms, as well as those for N and F from levofloxacin, but in lower proportions.

In order to corroborate the findings of atomic force microscopy (AFM) experiments regarding the porosity of materials exhibiting notable average roughness, characterized by rough surfaces and a prominent porous structure, emphasis was placed on complexes incorporating elevated levels of heteroatoms and aromatic residues. These particular complexes demonstrated enhanced efficacy in reducing surface roughness. Employing this method enables the acquisition of precise

information pertaining to the geometric attributes of particles. Zn complex, specifically, exhibits a marked degree of porosity and possesses a high Rq value. The AFM images of the complexes are presented in Fig. 2.

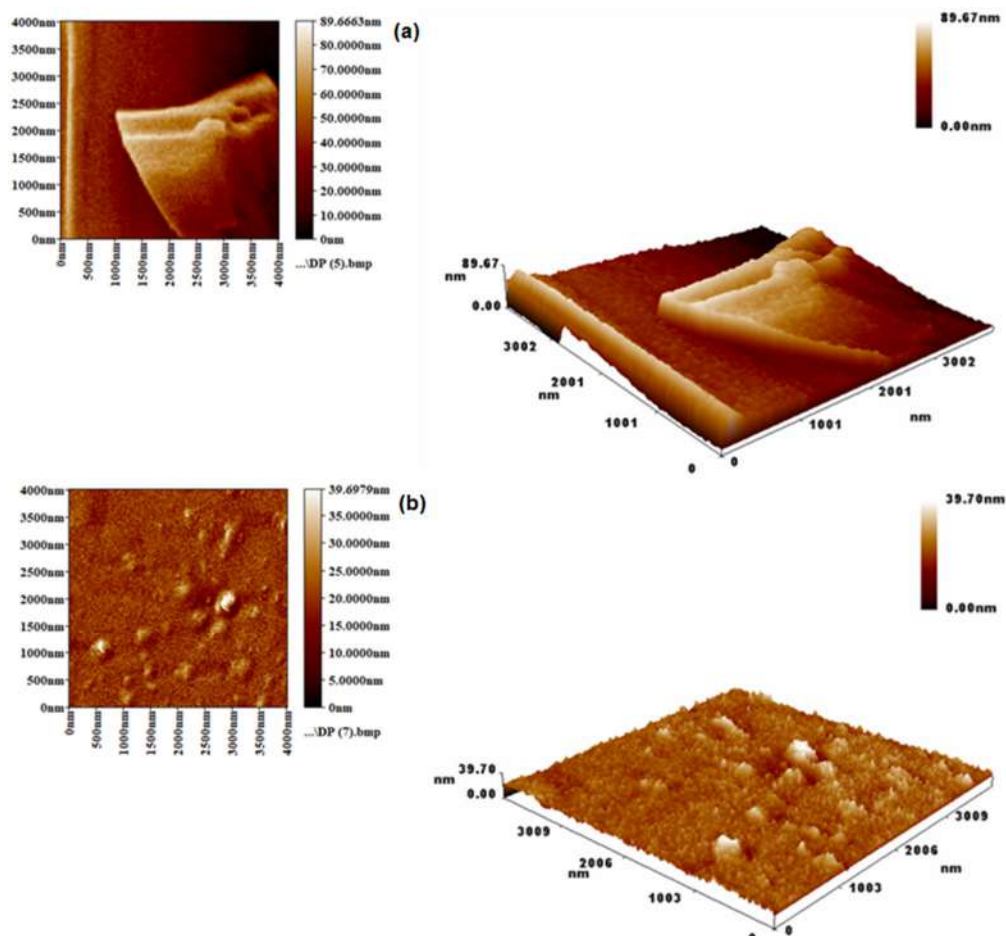
Levofloxacin metal complexes with a high level of heteroatoms and aromaticity resulted in greater improvement in the Rq.

Gas Adsorption Isotherm Measurements

The specific surface area, porosity, and storage capacity were evaluated by N₂ and CO₂ isotherms measurement. The adsorption of N₂ on the solid surface of the produced complexes determines the specific surface

Table 4. EDX data for levofloxacin metal complexes

Complex	%C	%N	%F	%M
CuL ₂ ·2H ₂ O	52.8	10.2	4.6	7.7
NiL ₂ ·2H ₂ O	53.1	10.3	4.6	7.2
ZnL ₂	55.0	10.6	4.8	8.3



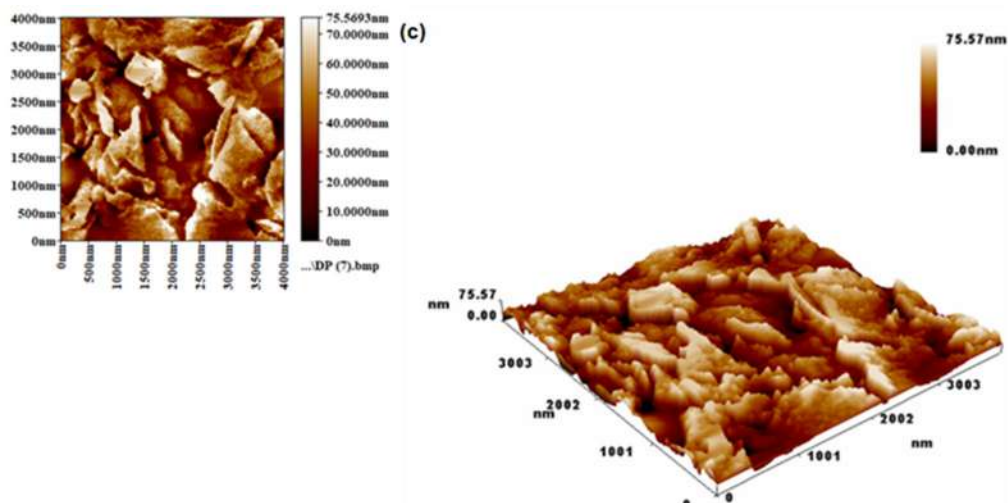


Fig 2. AFM images of (a) Cu(II), (b) Ni(II), and (c) Zn(II) complexes

area and porosity parameters based on BET and BJH techniques [32]. The measurements were carried out at 77 K and 88 kPa. The complexes' N₂ adsorption-desorption isotherms are shown in Fig. 3, where the amount of gas absorbed rises as pressure is increased. According to the IUPAC recommendation, the adsorption-desorption isotherms of the Cu(II) and Zn(II) complexes belong to the type IV isotherm, while the Ni(II) complex has a type V isotherm. Hysteresis

attributed to the materials' mesoporosity can be recognized in types IV and V isotherms [33].

Fig. 4 shows the relationship between pore size distribution and pore size width. The pore diameter ranged between 2.1 and 83.9 nm, corresponding to mesopores [34]. As tabulated in Table 5, the specific surface area of the complexes varies from 0.818 to 24.97 m²/g, while the best amount uptake of N₂ is carried by the Zn(II) complex, which reaches 123.073 m³/g.

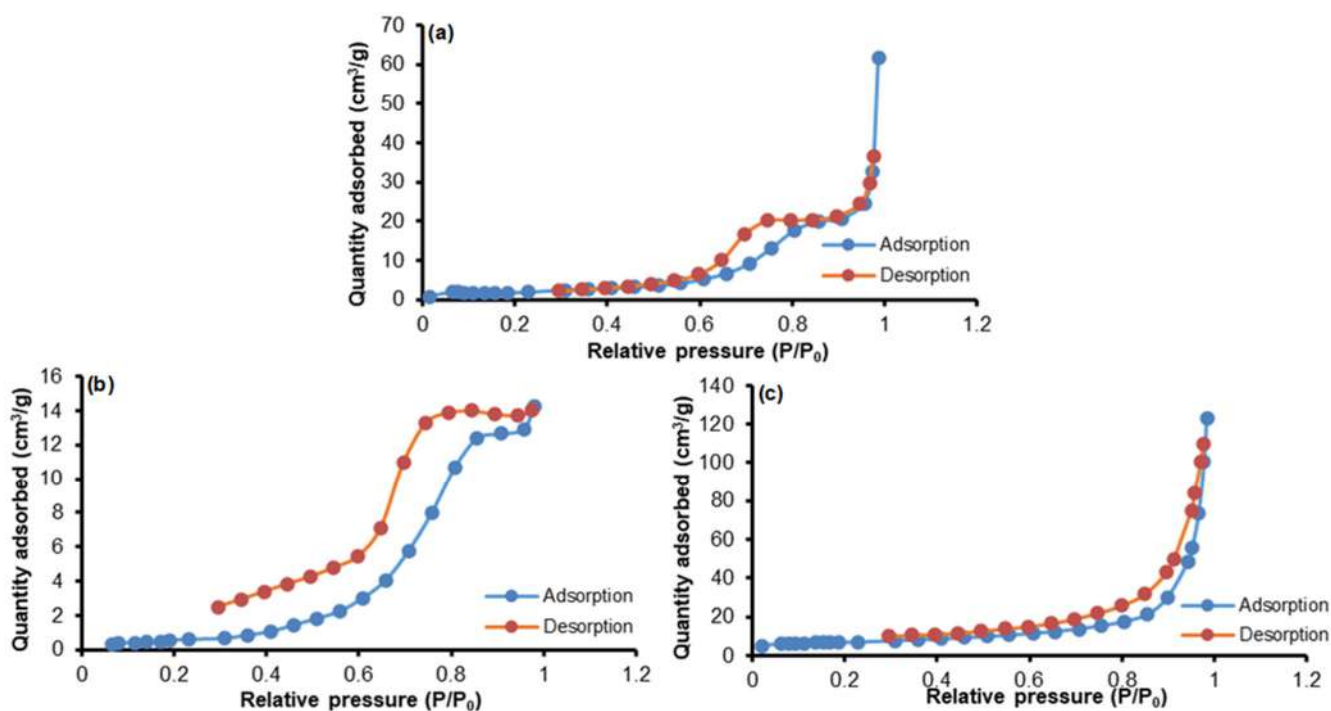


Fig 3. Metal complexes' N₂ adsorption-desorption isotherms on a) Cu(II), b) Ni(II), and c) Zn(II)

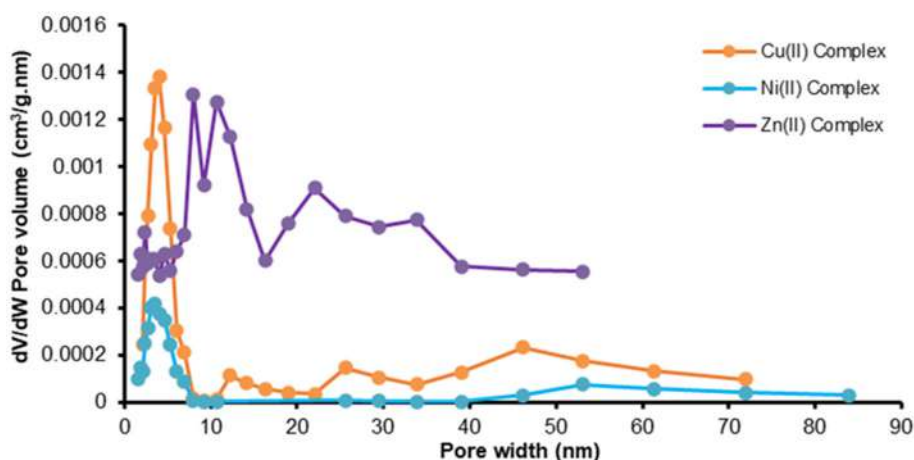


Fig 4. Metal complex's pore size and pore-volume distribution

In another hand, the CO₂ adsorption isotherm for the complexes of the metals has been determined at 323 K and 50 bar, as exhibited in Fig. 5. The Zn(II) complex observed high efficiency in storing CO₂ with a capacity of 34.40 cm³/g, as illustrated in Table 5. The presence of heteroatoms and aromatic rings enhances the interactions with gas molecules [35]. The metals play a very important role in making the complexes more sufficient to capture the gas molecules. In the case of the unsaturated metal sites, a strong interaction with CO₂ molecules could occur, as exhibited by Zn(II) complex [27]. Ultimately, within the context of acid-base chemistry, the metals function as Lewis acids, while CO₂ acts as a Lewis base [36-37]. This interaction is characterized by the inherent acid-base properties of CO₂.

The complexes that were produced performed remarkably well as CO₂ gas adsorbent surfaces. This is because the surface of synthetic materials and CO₂

molecules form robust van der Waals and dipole-dipole interactions.

The capacity for gas absorption of the synthesized complex was evaluated using a high-pressure volumetric adsorption apparatus of type H-sorb 2600. To eliminate any solvent or water traces that may have been trapped inside the pores, the complexes were degassed under

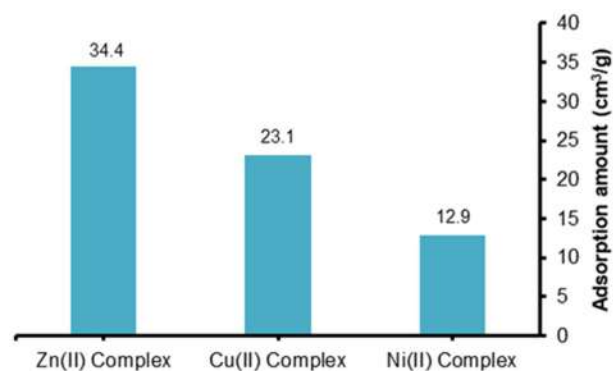


Fig 5. CO₂ adsorption isotherm of metal(II) complexes

Table 5. Porosity properties, specific surface area, and capacity storage of metal complexes and other materials for different studies

Complexes	S _{BET} (m ² /g)	N ₂ adsorption (cm ³ /g)	Average pore diameter (nm)	Total pore volume (cm ³ /g)	CO ₂ adsorption (cm ³ /g)	Ref.
CuL ₂ ·2H ₂ O	12.188	61.77	31.357	0.0116950	23.1	Current project
NiL ₂ ·2H ₂ O	0.818	14.00	66.640	0.0033791	12.9	
ZnL ₂	24.970	123.07	30.493	0.0418390	34.4	
NiL ₂ ·2H ₂ O	22.750	85.45	12.470	0.1080000	34.5	[10]
COF-1	4.682	2.71	34.901	0.0100720	26.3	[38]
Schiff base 1	17.990	5.50	17.020	0.0083000	31.4	[39]
Coumarins	-	-	-	-	31.0	[40]

vacuum and heat using an oven that was run at 50 °C for 1 h. The gas absorption examination was repeated under similar circumstances for the prepared complex to achieve precise data and determine the ideal pressure. The degree of interactions between the adsorbent and adsorbate, such as hydrogen bonds and van der Waals forces, as well as the kind of ligand and the size of the pores, all affect the adsorption of gases. Due to the high quadrupole moment of CO₂, high uptake of CO₂ may also be facilitated by electrostatic forces (van der Waals forces and the polarization force and surface field-molecular dipole interactions). The capacity storage of metal complexes and other materials for different studies is presented in Table 5.

■ CONCLUSION

The relevant complexes were produced via the reaction of levofloxacin with metal salts. Recrystallization was used to purify the products, and FTIR and UV-vis spectroscopy were performed to confirm the chemical composition of the pure chemicals. The peaks required to demonstrate the levofloxacin metal complexes' chemical structure were all adequately validated. Levofloxacin metal complexes with a levofloxacin moiety are produced using a quick and easy procedure. Three complexes were synthesized, characterized and applied as gas storage media. SEM images of the produced materials exhibited a variety of porosity diameters. Additionally, they showed a small collection of particles of various sizes and shapes. The gas adsorption isotherms observed that these complexes are suitable for CO₂ uptake. The Zn(II) complex has a high efficiency to adsorb gas molecules compared to Cu(II) and Ni(II) complexes, due to its high surface area and affinity towards the gas molecules.

■ ACKNOWLEDGMENTS

We thank Al-Nahrain, Middle Technical, United Arab Emirates and AL-Karkh Universities for technical support.

■ AUTHOR CONTRIBUTIONS

Dina S. Ahmed: investigation, original draft preparation, review and editing. Emad Yousif: conceptualization, methodology, software, validation,

formal analysis, resources, data curation, funding, original draft preparation, review and editing. Hadeel Adil, Hamsa Thamer and Raghda Alsayed: methodology, software, validation, formal analysis, data curation, original draft preparation, review and editing. Muna Bufaroosha, Khalid Zainulabdeen and Alaa Mohammed: investigation, original draft preparation, review and editing. Hassan Hashim: software, validation, formal analysis, original draft preparation, review and editing.

■ REFERENCES

- [1] dos Reis, G.S., Guy, M., Mathieu, M., Jebrane, M., Lima, E.C., Thyrel, M., Dotto, G.L., and Larsson, S.H., 2022, A comparative study of chemical treatment by MgCl₂, ZnSO₄, ZnCl₂, and KOH on physicochemical properties and acetaminophen adsorption performance of biobased porous materials from tree bark residues, *Colloids Surf., A*, 642, 128626.
- [2] Wang, W., Zhou, M., and Yuan, D., 2017, Carbon dioxide capture in amorphous porous organic polymers, *J. Mater. Chem. A*, 5 (4), 1334–1347.
- [3] Cai, G., Yan, P., Zhang, L., Zhou, H.C., and Jiang, H.L., 2021, Metal–organic framework-based hierarchically porous materials: Synthesis and applications, *Chem. Rev.*, 121 (20), 12278–12326.
- [4] Li, H., Wang, K., Sun, Y., Lollar, C.T., Li, J., and Zhou, H.C., 2018, Recent advances in gas storage and separation using metal–organic frameworks, *Mater. Today*, 21 (2), 108–121.
- [5] Wen, M., Li, G., Liu, H., Chen, J., An, T., and Yamashita, H., 2019, Metal–organic framework-based nanomaterials for adsorption and photocatalytic degradation of gaseous pollutants: Recent progress and challenges, *Environ. Sci.: Nano*, 6 (4), 1006–1025.
- [6] Li, B., Wen, H.M., Zhou, W., and Chen, B., 2014, Porous metal–organic frameworks for gas storage and separation: What, how, and why?, *J. Phys. Chem. Lett.*, 5 (20), 3468–3479.
- [7] Mason, J.A., Veenstra, M., and Long, J.R., 2014, Evaluating metal–organic frameworks for natural gas storage, *Chem. Sci.*, 5 (1), 32–51.

- [8] Sanz, R., Martínez, F., Orcajo, G., Wojtas, L., and Briones, D., 2013, Synthesis of a honeycomb-like Cu-based metal-organic framework and its carbon dioxide adsorption behaviour, *Dalton Trans.*, 42 (7), 2392–2398.
- [9] Mohammed, A., Ahmed, A.U., Ibraheem, H., Kadhom, M., and Yousif, E., 2022, Physisorption theory of surface area and porosity determination: A short review, *AIP Conf. Proc.*, 2450 (1), 020007.
- [10] Baumann, A.E., Burns, D.A., Liu, B., and Thoi, V.S., 2019, Metal-organic framework functionalization and design strategies for advanced electrochemical energy storage devices, *Commun. Chem.*, 2 (1), 86.
- [11] Ma, S., and Zhou, H.C., 2010, Gas storage in porous metal-organic frameworks for clean energy applications, *Chem. Commun.*, 46 (1), 44–53.
- [12] Lin, Y., Kong, C., Zhang, Q., and Chen, L., 2017, Metal-organic frameworks for carbon dioxide capture and methane storage, *Adv. Energy Mater.*, 7 (4), 1601296.
- [13] Demir, H., Aksu, G.O., Gulbalkan, H.C., and Keskin, S., 2022, MOF membranes for CO₂ capture: Past, present and future, *Carbon Capture Sci. Technol.*, 2, 100026.
- [14] Rosli, A., and Low, S.C., 2020, Molecularly engineered switchable photo-responsive membrane in gas separation for environmental protection, *Environ. Eng. Res.*, 25 (4), 447–461.
- [15] Chaemchuen, S., Kabir, N.A., Zhou, K., and Verpoort, F., 2013, Metal-organic frameworks for upgrading biogas via CO₂ adsorption to biogas green energy, *Chem. Soc. Rev.*, 42 (24), 9304–9332.
- [16] Latake, P.T., Pawar, P., and Ranveer, A.C., 2015, The greenhouse effect and its impacts on environment, *Int. J. Innovative Res. Creat. Technol.*, 1 (3), 333–337.
- [17] Ma, L., Chen, S., Qin, C., Chen, S., Yuan, W., Zhou, X., and Ran, J., 2021, Understanding the effect of H₂S on the capture of CO₂ using K-doped Li₄SiO₄ sorbent, *Fuel*, 283, 119364.
- [18] Yan, Y., Yang, S., Blake, A.J., and Schröder, M., 2014, Studies on metal-organic frameworks of Cu(II) with isophthalate linkers for hydrogen storage, *Acc. Chem. Res.*, 47 (2), 296–307.
- [19] Thomas, D.M., Mechery, J., and Paulose, S.V., 2016, Carbon dioxide capture strategies from flue gas using microalgae: A review, *Environ. Sci. Pollut. Res.*, 23 (17), 16926–16940.
- [20] Aminu, M.D., Nabavi, S.A., Rochelle, C.A., and Manovic, V., 2017, A review of developments in carbon dioxide storage, *Appl. Energy*, 208, 1389–1419.
- [21] Goh, K., Karahan, H.E., Yang, E., and Bae, T.H., 2019, Graphene-based membranes for CO₂/CH₄ separation: Key challenges and perspectives, *Appl. Sci.*, 9 (14), 2784.
- [22] Liu, Y., Wang, S., Meng, X., Ye, Y., Song, X., Liang, Z., and Zhao, Y., 2020, Molecular expansion for constructing porous organic polymers with high surface areas and well-defined nanopores, *Angew. Chem., Int. Ed.*, 59 (44), 19487–19493.
- [23] He, Y., Zhou, W., Yildirim, T., and Chen, B., 2013, A series of metal-organic frameworks with high methane uptake and an empirical equation for predicting methane storage capacity, *Energy Environ. Sci.*, 6 (9), 2735–2744.
- [24] Kong, G.Q., Han, Z.D., He, Y., Ou, S., Zhou, W., Yildirim, T., Krishna, R., Zou, C., Chen, B., and Wu, C.D., 2013, Expanded organic building units for the construction of highly porous metal-organic frameworks, *Chem. - Eur. J.*, 19 (44), 14886–14894.
- [25] Peng, Y., Krungleviciute, V., Eryazici, I., Hupp, J.T., Farha, O.K., and Yildirim, T., 2013, Methane storage in metal-organic frameworks: Current records, surprise findings, and challenges, *J. Am. Chem. Soc.*, 135 (32), 11887–11894.
- [26] Tran, Y.B.N., Nguyen, P.T., Luong, Q.T., and Nguyen, K.D. 2020, Series of M-MOF-184 (M = Mg, Co, Ni, Zn, Cu, Fe) metal-organic frameworks for catalysis cycloaddition of CO₂, *Inorg. Chem.*, 59 (22), 16747–16759.
- [27] Ahmed, D., El-Hiti, G., Yousif, E., Hameed, A., and Abdalla, M., 2017, New eco-friendly phosphorus organic polymers as gas storage media, *Polymers*, 9 (8), 336.
- [28] Liu, B., Yao, S., Shi, C., Li, G., Huo, Q., and Liu, Y., 2016, Significant enhancement of gas uptake

- capacity and selectivity via the judicious increase of open metal sites and Lewis basic sites within two polyhedron-based metal-organic frameworks, *Chem. Commun.*, 52 (15), 3223–3226.
- [29] Wardani, A.R., and Widiastuti, N., 2016, Synthesis of zeolite-X supported on glasswool for CO₂ capture material: Variation of immersion time and NaOH concentration at glasswool activation, *Indones. J. Chem.*, 16 (1), 1–7.
- [30] Ediati, R., Mukminin, A., and Widiastuti, N., 2017, Impregnation nickel on mesoporous ZSM-5 templated carbons as a candidate material for hydrogen storage, *Indones. J. Chem.*, 17 (1), 30–36.
- [31] Ahmed, D.S., Mohammed, A., Husain, A.A., El-Hiti, G.A., Kadhom, M., Kariuki, B.M., and Yousif, E., 2022, Fabrication of highly photostable polystyrene films embedded with organometallic complexes, *Polymers*, 14 (5), 1024.
- [32] Bardestani, R., Patience, G.S., and Kaliaguine, S., 2019, Experimental methods in chemical engineering: Specific surface area and pore size distribution measurements—BET, BJH, and DFT, *Can. J. Chem. Eng.*, 97 (11), 2781–2791.
- [33] Thommes, M., Kaneko, K., Neimark, A.V., Olivier, J.P., Rodriguez-Reinoso, F., Rouquerol, J., and Sing, K.S.W., 2015, Physisorption of gases, with special reference to the evaluation of surface area and pore size distribution (IUPAC Technical Report), *Pure Appl. Chem.*, 87 (9-10), 1051–1069.
- [34] Sreethawong, T., Suzuki, Y., and Yoshikawa, S., 2005, Synthesis, characterization, and photocatalytic activity for hydrogen evolution of nanocrystalline mesoporous titania prepared by surfactant-assisted templating sol-gel process, *J. Solid State Chem.*, 178 (1), 329–338.
- [35] Trickett, C.A., Helal, A., Al-Maythaly, B.A., Yamani, Z.H., Cordova, K.E., and Yaghi, O.M., 2017, The chemistry of metal-organic frameworks for CO₂ capture, regeneration and conversion, *Nat. Rev. Mater.*, 2 (8), 17045.
- [36] Ahmed, A.J., Alias, M., Ahmed, D.S., Abdallah, M., Bufaroosha, M., Jawad, A.H., and Yousif, E., 2023, Investigating CO₂ storage properties of Pd(II) and Co(II) chelates of a Schiff's base ligand, *J. Umm Al-Qura Univ. Appl. Sci.*, 9 (1), 96–104.
- [37] Kazemi, S., and Safarifard, V., 2018, Carbon dioxide capture on metal-organic frameworks with amide-decorated pores, *Nanochem. Res.*, 3 (1), 62–78.
- [38] Saleh, T., Yousif, E., Al-Tikrity, E., Ahmed, D., Bufaroosha, M., Al-Mashhadani, M., and Yaseen, A., 2022, Design, synthesis, structure, and gas (CO₂, CH₄, and H₂) storage properties of porous imine-linkage organic compounds, *Mater. Sci. Energy Technol.*, 5, 344–352.
- [39] Yaseen, A.A., Yousif, E., Al-Tikrity, T.B., Kadhom, M., Yusop, M.R., and Ahmed, D.S., 2022, Environmental performance of alternative Schiff bases synthesis routes: A proposal for CO₂ storages, *Pollution*, 8 (1), 239–248.
- [40] Mahdi, S.A., Ahmed, A.A., Yousif, E., Ahmed, D., Al-Mashhadani, M.H., and Bufaroosha, M., 2022, Comarine derivatives designed as carbon dioxide and hydrogen storage, *Mater. Sci. Energy Technol.*, 5, 197–207.

Supplementary Data

This supplementary data is a part of a paper entitled “Volatile Organic Compounds and Antioxidant, Cytotoxic Activities of Extracts from the Leaves of *Grewia bulot*”.

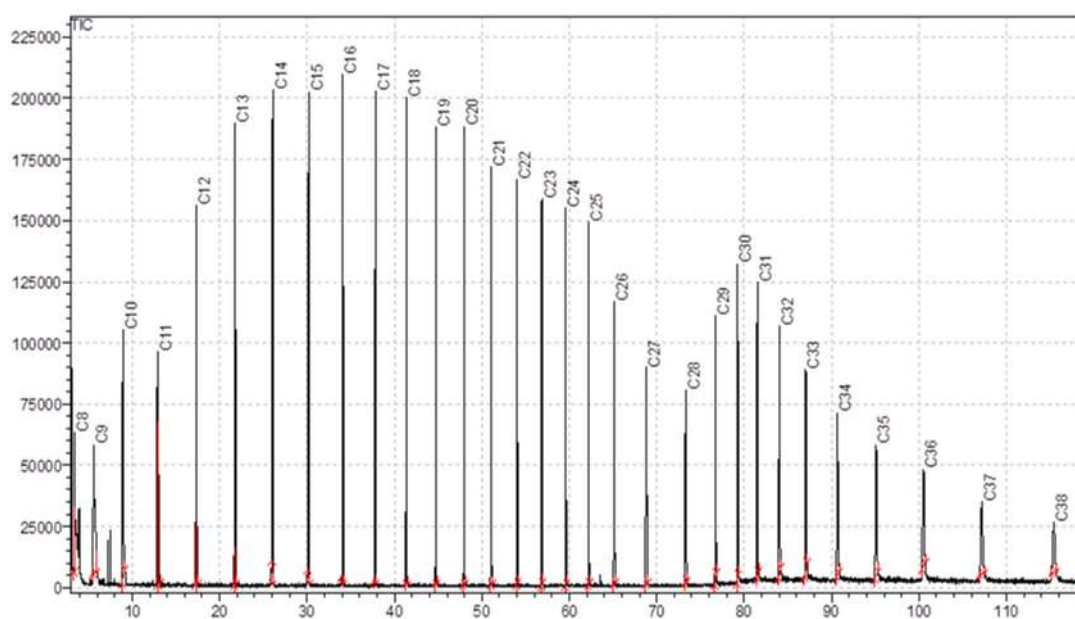


Fig S1. GC-MS data of *n*-alkanes

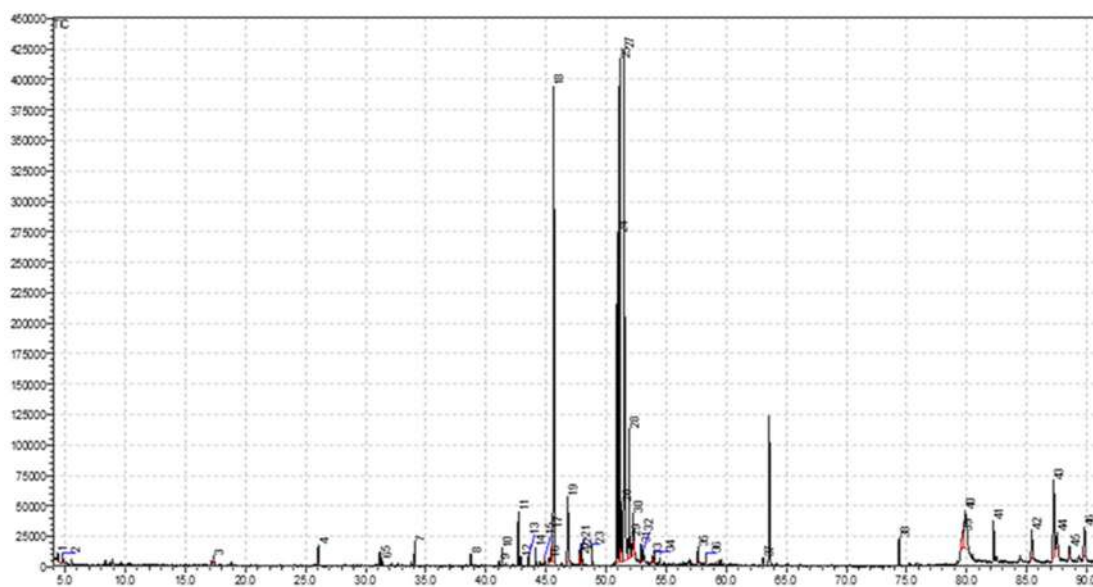


Fig S2. GC-MS data of *n*-hexane fraction

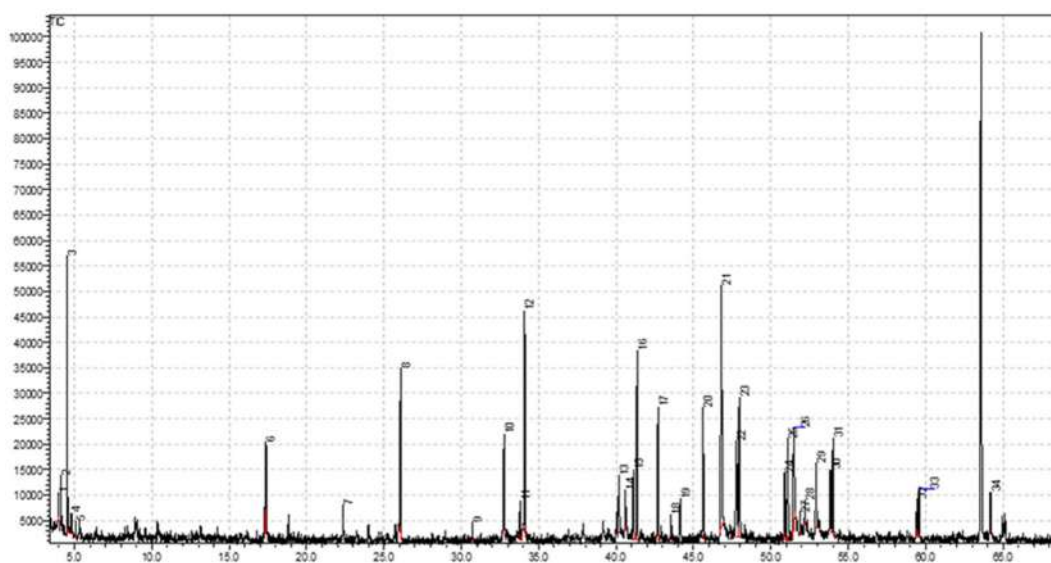


Fig S3. GC-MS data of dichloromethane fraction

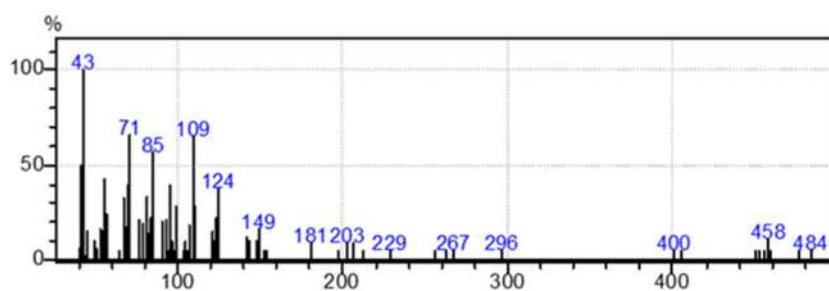


Fig S4. EI-MS of compound 13

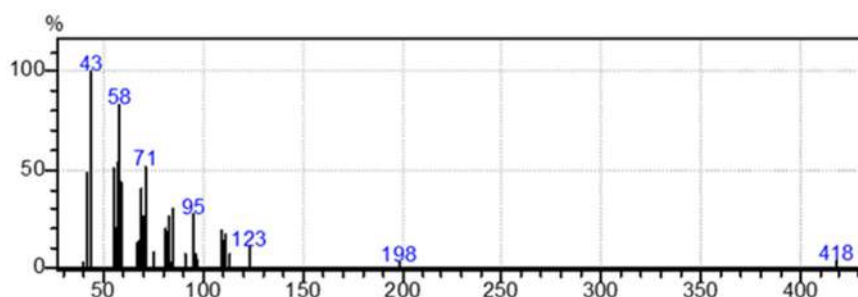


Fig S5. EI-MS of compound 17

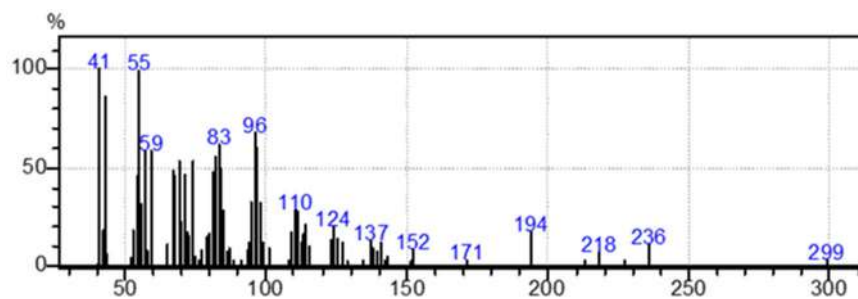


Fig S6. EI-MS of compound 18

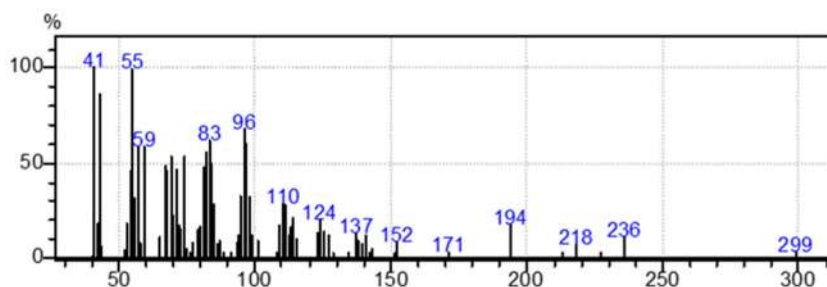


Fig S7. EI-MS of compound 21

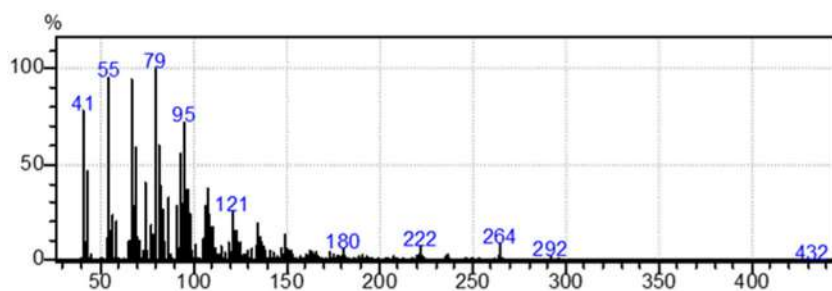


Fig S8. EI-MS of compound 29

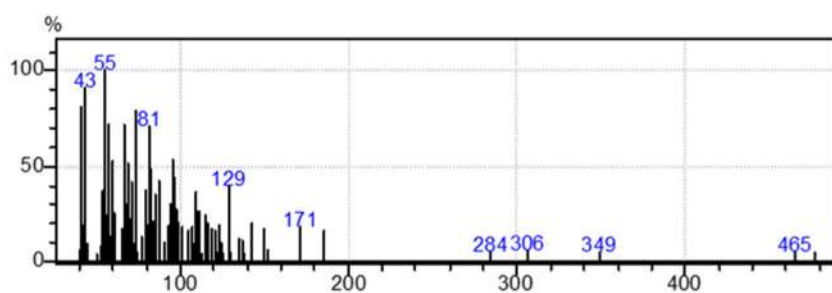


Fig S9. EI-MS of compound 35

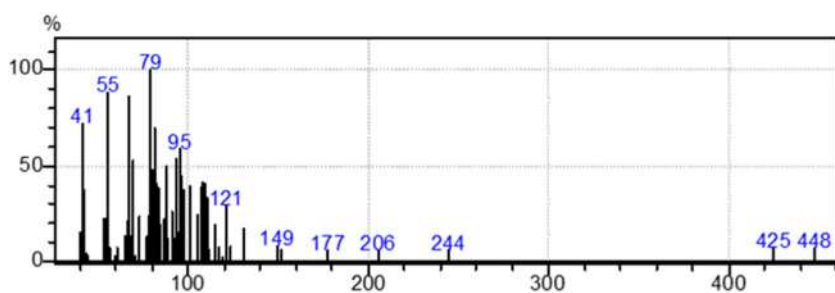


Fig S10. EI-MS of compound 36

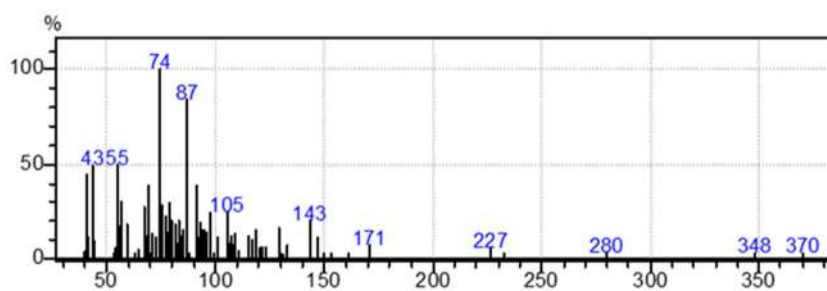


Fig S11. EI-MS of compound 39

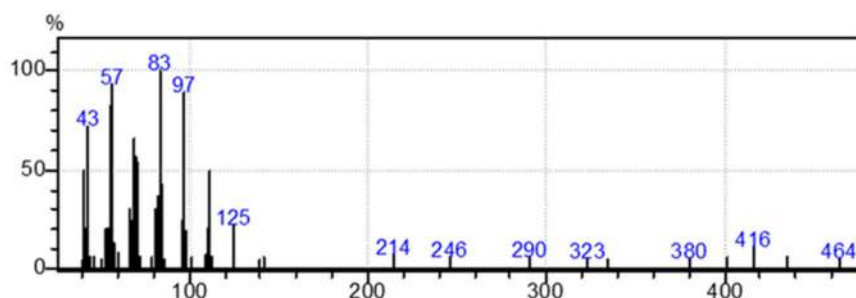


Fig S12. EI-MS of compound 40

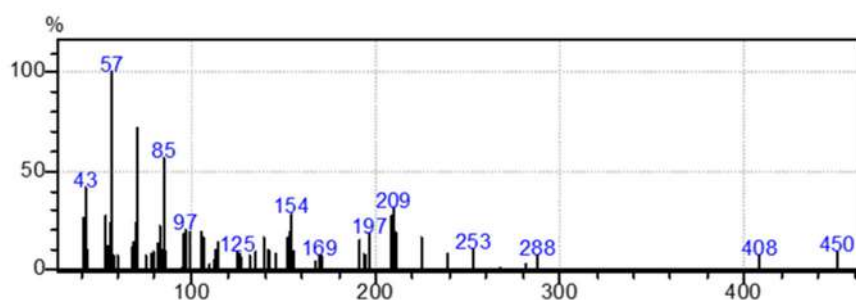


Fig S13. EI-MS of compound 45

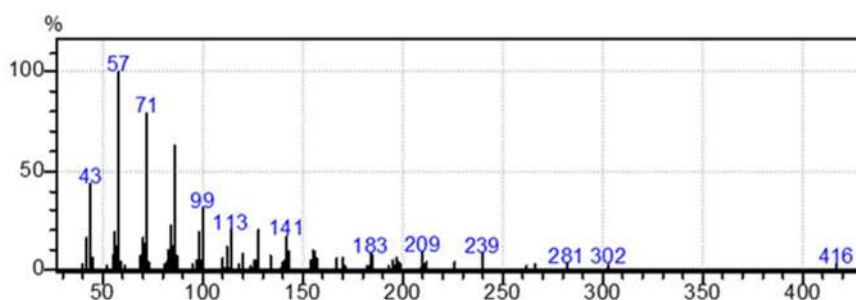


Fig S14. EI-MS of compound 46

Table S1. Volatile compositions (%) of the *n*-hexane and dichloromethane fractions of *Grewia bulot* leaves

No.	RT	Compound ^a	<i>n</i> -hexane fraction	Dichloromethane fraction	Identification ^{b,c}
1	3.95	Isovaleric acid	-	0.9	MS, RI, O
2	4.78	2- <i>tert</i> -Butoxyethanol	0.2	5.3	MS, RI, O
3	17.37	Dodecane	0.5	3.4	MS, RI, O
4	22.37	2-Methoxy-4-vinylphenol	-	1.1	MS, RI, O
5	26.06	Tetradecane	0.7	4.9	MS, RI, O
6	31.18	Methyl laurate	0.4	-	MS, RI, O
7	31.35	Dihydroactinidiolide	0.2	-	MS, RI, O
8	32.75	Lauric acid	-	4.0	MS, RI, O
9	33.78	1-Hexadecene	-	1.3	MS, RI, O
10	34.08	Hexadecane	0.8	7.4	MS, RI, O
11	38.75	Methyl tetradecanoate	0.4	-	MS, RI, O
12	40.17	Loliolide	-	2.7	MS, RI, O
13	40.58	Unidentified	-	2.1	MS, RI, O
14	41.11	1-Octadecene	0.1	2.2	MS, RI, O

No.	RT	Compound ^a	<i>n</i> -hexane fraction	Dichloromethane fraction	Identification ^{b,c}
15	41.35	Octadecane	0.5	6.0	MS, RI, O
16	42.71	Phytol	1.4	4.4	MS, RI, O
17	42.92	Unidentified	0.3	-	MS, RI, O
18	43.54	Unidentified	0.3	0.8	MS, RI, O
19	44.14	3,7,11,15-Tetramethyl-2-hexadecen-1-ol	0.5	1.6	MS, RI, O
20	44.91	Methyl oleate	0.2	0.2	MS, RI, O
21	45.49	Unidentified	1.1	-	MS, RI, O
22	45.65	Methyl palmitate	14.4	3.9	MS, RI, O
23	46.83	Palmitic acid	2.9	9.8	MS, RI, O
24	47.77	1-Eicosene	0.6	4.7	MS, RI, O
25	47.82	Ethyl palmitate	0.6	-	MS, RI, O
26	47.97	Eicosane	0.5	4.9	MS, RI, O
27	48.83	Methyl margarate	0.6	-	MS, RI, O
28	50.93	Methyl linoleate	9.7	2.5	MS, RI, O
29	51.13	Unidentified	16.0	3.6	MS, RI, O
30	51.28	Methyl elaidate	1.6	-	MS, RI, O
31	51.51	Neophytadiene	18.2	5.3	MS, RI, O
32	51.91	Methyl stearate	3.4	0.7	MS, RI, O
33	52.05	Linoleic acid	0.6	-	MS, RI, O
34	52.24	Oleic acid	1.9	0.8	MS, RI, O
35	52.92	Unidentified	0.5	2.8	MS, RI, O
36	53.11	Unidentified	0.4	-	MS, RI, O
37	53.84	1-Docosene	0.3	2.3	MS, RI, O
38	54.02	Docosane	0.3	3.0	MS, RI, O
39	57.67	Unidentified	0.8	-	MS, RI, O
40	59.43	Unidentified	-	1.4	MS, RI, O
41	59.58	Tetracosane	-	1.6	MS, RI, O
42	63.07	Methyl octacosanoate	0.3	-	MS, RI, O
43	64.18	Heptadecyl heptadecanoate	-	2.1	MS, RI, O
44	74.38	Squalene	1.2	-	MS, RI, O
45	79.68	Unidentified	1.4	-	MS, RI, O
46	79.88	Unidentified	2.9	-	MS, RI, O
47	82.24	α -Tocopherol	1.4	-	MS, RI, O
48	85.41	β -Sitostenone	1.8	-	MS, RI, O
49	87.24	β -Sitosterol	4.5	-	MS, RI, O
50	87.51	Lupeol	1.9	-	MS, RI, O
51	88.57	Unidentified	0.7	-	MS, RI, O
52	89.80	Lupeol acetate	2.3	-	MS, RI, O
		Total	99.3	97.7	
		Unidentified	24.4	10.6	
		Hemiterpenoids/Acids	0.0	0.9	
		Alkanes	3.2	31.2	
		Alkenes	1.0	10.6	
		Alcohols	0.7	6.9	
		Aromatic compounds	1.4	1.1	

No.	RT	Compound ^a	<i>n</i> -hexane fraction	Dichloromethane fraction	Identification ^{b,c}
		Diterpenes	18.2	5.3	
		Triterpenes	1.2	0.0	
		Monoterpenoids	0.2	2.7	
		Diterpenoids	1.4	4.4	
		Triterpenoids	4.2	0.0	
		Steroids	6.3	0.0	
		Fatty acids	5.4	14.6	
		Fatty acid esters	31.6	9.4	

^aCompound listed according to the elution order of column Equity-5; ^bRetention Index (RI) calculated using a homologous series of *n*-alkanes (C₈-C₃₈) in a capillary column (Equity-5); ^cIdentification based on the comparison of mass spectra (MS), retention index (RI) with NIST11, WILEY7, Adams (2017) data libraries, along with <http://www.thegoodscentscompany.com/search2.html> (accessed on 1 March 2023) (O). Area (%): is the percentage of the area occupied by the compound within the chromatogram; - Not identified

Table S2. SC₅₀ values of DPPH scavenging of different extract/fractions of *Grewia bulot* leaves

Concentration (µg/mL)	% DPPH scavenging					
	GBD		GBM		GBH	
	Average	SD	Average	SD	Average	SD
500	95.07	0.91	98.65	1.07	93.64	1.14
100	84.83	1.07	89.90	0.30	41.27	1.44
20	40.59	0.46	75.86	0.68	15.62	1.25
4	19.25	0.54	25.72	0.65	10.51	0.82
SC ₅₀ ^a	25.51 ± 0.58		9.39 ± 0.90		153.78 ± 7.60	
Concentration (µg/mL)	GBE		GBW		L-Ascorbic acid ^b	
	Average	SD	Average	SD	Average	SD
	500	94.52	1.52	96.19	1.32	
100	90.73	0.24	90.35	0.59	92.51	0.23
20	59.47	0.23	33.59	1.23	89.13	1.36
4	21.67	1.48	9.45	1.18	29.20	1.03
0.8					6.61	0.43
SC ₅₀	15.42 ± 0.74		31.55 ± 0.79		7.27 ± 0.12	

^aSC₅₀ (concentration that scavenges 50% of DPPH radical); ^bPositive control; GBM: methanol extract; GBH: *n*-hexane, GBD: dichloromethane, GBE: ethyl acetate, and GBW: water fraction, respectively; SD: Standard Deviation

Table S3. Cytotoxic activities of the extract/fractions against four human cancer cell lines

Concentration (µg/mL)	GBH							
	MCF-7		Hep-G2		SK-LU-1		KB	
	% Inhibition	SD	% Inhibition	SD	% Inhibition	SD	% Inhibition	SD
100	50.70	1.97	50.96	1.31	54.05	2.82	58.54	1.44
50	35.92	1.16	27.55	1.21	23.72	2.27	20.29	1.91
25	25.82	1.22	16.82	0.82	14.60	0.98	11.71	0.99
12.5	17.23	1.04	7.99	0.64	7.59	0.65	9.07	0.63
6.25	9.60	0.87	3.58	0.36	4.26	0.15	4.85	0.36
IC ₅₀	97.94 ± 6.79		98.27 ± 2.77		93.79 ± 3.52		90.77 ± 1.13	
	GBD							

Concentration ($\mu\text{g/mL}$)	MCF-7		Hep-G2		SK-LU-1		KB	
	% Inhibition	SD	% Inhibition	SD	% Inhibition	SD	% Inhibition	SD
100	52.71	1.22	43.76	3.40	51.28	2.74	38.87	2.48
50	36.17	1.19	13.05	1.45	29.42	1.06	18.60	1.44
25	26.89	1.68	7.06	0.76	16.96	0.69	8.88	0.57
12.5	15.66	0.93	4.07	0.34	11.17	0.76	4.27	0.29
6.25	8.27	0.67	1.96	0.16	5.32	0.53	2.11	0.22
IC ₅₀	90.60 \pm 3.49		>100		97.09 \pm 5.40		>100	

Concentration ($\mu\text{g/mL}$)	MCF-7		Hep-G2		SK-LU-1		KB	
	% Inhibition	SD	% Inhibition	SD	% Inhibition	SD	% Inhibition	SD
100	34.91	2.66	24.80	0.93	32.44	2.34	15.30	0.78
50	29.55	1.89	8.43	1.30	16.61	1.80	10.12	0.91
25	20.08	1.06	5.13	0.13	11.37	0.69	6.72	0.81
12.5	12.82	0.97	3.56	0.44	7.89	0.79	3.45	0.34
6.25	7.39	0.38	0.50	0.06	3.35	0.40	1.38	0.20
IC ₅₀	>100		>100		>100		>100	

Concentration ($\mu\text{g/mL}$)	MCF-7		Hep-G2		SK-LU-1		KB	
	% Inhibition	SD	% Inhibition	SD	% Inhibition	SD	% Inhibition	SD
100	44.76	1.93	39.39	1.74	45.10	1.14	23.69	1.73
50	13.26	1.18	12.79	1.22	30.83	1.57	11.23	0.96
25	8.33	0.87	6.72	0.82	18.02	1.05	7.32	0.64
12.5	4.17	0.64	4.31	0.35	9.50	0.68	3.16	0.34
6.25	2.40	0.28	1.52	0.15	4.51	0.38	-2.18	0.22
IC ₅₀	>100		>100		>100		>100	

Concentration ($\mu\text{g/mL}$)	MCF-7		Hep-G2		SK-LU-1		KB	
	% Inhibition	SD	% Inhibition	SD	% Inhibition	SD	% Inhibition	SD
100	14.77	1.26	30.27	2.71	35.37	1.41	26.93	2.57
50	9.15	0.83	15.75	1.01	13.69	0.86	17.24	0.76
25	5.18	0.67	8.32	0.58	8.70	0.32	10.18	0.54
12.5	3.16	0.28	5.21	0.37	4.71	0.30	6.34	0.63
6.25	1.83	0.19	2.28	0.26	2.75	0.29	2.75	0.29
IC ₅₀	>100		>100		>100		>100	

Concentration ($\mu\text{g/mL}$)	MCF-7		Hep-G2		SK-LU-1		KB	
	% Inhibition	SD	% Inhibition	SD	% Inhibition	SD	% Inhibition	SD
10	84.56	1.81	90.71	1.69	95.27	2.14	98.49	2.75
2	72.33	1.28	75.12	1.54	76.18	1.10	80.33	1.06
0.4	48.63	1.12	49.02	0.56	49.16	1.08	51.74	1.22
0.08	21.41	0.92	22.02	0.84	22.42	0.98	22.79	1.39
IC ₅₀	0.42 \pm 0.02		0.39 \pm 0.03		0.45 \pm 0.02		0.39 \pm 0.01	

^aPositive control; GBM: methanol extract; GBH: *n*-hexane, GBD: dichloromethane, GBE: ethyl acetate, and GBW: water fraction, respectively; SD: Standard Deviation

Volatile Organic Compounds and Antioxidant, Cytotoxic Activities of Extracts from the Leaves of *Grewia bulot*

Ty Viet Pham¹, Duc Viet Ho², Anh Tuan Le³, Y Duy Ngo¹, Nhan Thanh Thi Dang¹, Thang Quoc Le¹, and Bao Chi Nguyen^{4*}

¹Faculty of Chemistry, University of Education, Hue University, 34 Le Loi, Hue City 530000, Vietnam

²Faculty of Pharmacy, University of Medicine and Pharmacy, Hue University, 06 Ngo Quyen, Hue City 530000, Vietnam

³Mien Trung Institute for Scientific Research, Vietnam National Museum of Nature, VAST, 321 Huynh Thuc Khang Street, Thua Thien Hue 530000, Vietnam

⁴Department of Science, Technology and International Relations, Hue University, 04 Le Loi, Hue City 530000, Vietnam

* **Corresponding author:**

email: ncbao@hueuni.edu.vn

Received: May 20, 2023

Accepted: July 17, 2023

DOI: 10.22146/ijc.84619

Abstract: This research aims to determine the volatile compounds present in *Grewia bulot* leaf extracts and evaluate their cytotoxic and antioxidant activities. The volatile constituents of the n-hexane and dichloromethane extracts were identified by using gas chromatography–mass spectrometry. The main compounds identified in the former were neophytadiene (18.2%), methyl palmitate (14.4%), methyl linoleate (9.7%), β -sitosterol (4.5%), and methyl stearate (3.4%), while those in the latter were palmitic acid (9.8%), hexadecane (7.4%), octadecane (6.0%), neophytadiene (5.3%), and 2-tert-butoxyethanol (5.3%). The cytotoxicities of the extracts were examined against four human cancer cell lines (SK-LU-1, Hep-G2, MCF-7, and KB), while their antioxidant activities were assessed using the DPPH radical scavenging assay. The n-hexane and dichloromethane extracts displayed weak activity against these cancer cell lines, with IC₅₀ values ranging from 90.60 ± 3.49 to 98.27 ± 2.77 µg/mL. All extracts showed antioxidant activities, and the methanol extract exhibited the strongest at an SC₅₀ value of 9.39 ± 0.90 µg/mL. This is the first report on the volatile constituents and bioactivities of *G. bulot* leaf extracts, suggesting their potential application as antioxidants.

Keywords: *Grewia bulot*; cytotoxic; antioxidant; GC-MS; volatile compound

■ INTRODUCTION

Pharmacotherapy is largely relied on natural products and structural analogs, particularly in the treatment of cancer and infectious diseases [1]. In addition, the use of medicinal plants for disease prevention and treatment has increased worldwide during the past few decades [2]. *Grewia* is a genus of evergreen shrubs/small trees of the family Malvaceae, including more than 400 species distributed mainly in the tropical and subtropical regions of Africa, Asia, and Australia. *Grewia* species is a source of food, fodder, and firewood and is notably used in traditional medicine to cure several ailments, including rheumatism, diabetes, diarrhea, and heart and blood disorders; protect the liver;

cure inflammation; treat fever; and relieve pain [3-4]. A literature survey indicated that the secondary metabolites from the genus *Grewia* show diverse biological effects, such as antioxidant [5-8], antimalarial [8-9], antibacterial [10-12], antidiabetic [13], anticholinesterase [7], anticancer [8,14-16], antiplasmodial, antileishmanial, and antitrypanosomal activities [17]. Previous studies have examined the anticancer and antioxidant abilities of extracts from some plant species. Notably, the chemical constituents isolated from *Mitrephora winitii* twigs and leaves have shown significant activity against the KB and MCF-7 cancer cell lines [18]. Further, using the microwave–ultrasound-assisted method, *Moringa oleifera* leaf

extracts, which were rich in flavonoids, displayed the highest activity in a DPPH scavenging test ($IC_{50} = 72.31 \mu\text{g/mL}$) [19]. In addition, the *n*-butanol, ethyl acetate, and dichloromethane leaf extracts of *Petroselinum sativum* have demonstrated powerful free radical scavenging activity [20].

Of the 24 species of the genus *Grewia* L. distributed in Vietnam, only *G. bilamellata* has been studied [9,21-22]. Given the potential of drug discovery from plants, this work aims to examine the cytotoxic activities against four human cancer cell lines – including SK-LU-1 (human lung adenocarcinoma), Hep-G2 (human hepatocarcinoma), MCF-7 (human breast carcinoma), and KB (human oral carcinoma) – and the antioxidant activities of five leaf extracts from *G. bulot* Gagn., a species of flowering plant native to Vietnam [3,22-23].

■ EXPERIMENTAL SECTION

Materials

Specimen collection

In January 2022, *G. bulot* leaves were harvested in Quang Tri Province, Vietnam (geographical coordinates: 16°29'30.0"N 107°01'18.4"E). Dr. Nguyen Sinh Khang (Institute of Ecology and Biological Resources, VAST, Vietnam) verified the plant's authenticity. A voucher specimen (Hue.22-01) has been deposited at the Faculty of Chemistry, University of Education, Hue University, Vietnam.

Chemicals and reagents manufactures

L-glutamine, fetal bovine serum (FBS), sodium bicarbonate, 2,2-diphenyl-1-picrylhydrazyl (DPPH), trypsin, ethylene diamine tetraacetic acid (EDTA), trichloroacetic acid, L-ascorbic acid, aspirate, dimethyl sulfoxide (DMSO), and a homologous series of *n*-alkanes (C_7 – C_{40}) were obtained from Sigma-Aldrich (USA). The solvents, *n*-hexane, dichloromethane, ethyl acetate, and methanol, were also obtained from Sigma-Aldrich. Human cancer cell lines (SK-LU-1, Hep-G2, KB, and MCF-7) were generously supplied by Prof. J.M. Pezzuto (Long-Island University, USA) and Prof. J. Maier (University of Milan, Italy). Cell culture flasks and 96-well plates were obtained from Corning Inc. (USA).

Instrumentation

The volatile compositions were investigated by Gas Chromatography–Mass Spectrometry (GC-MS) method which was conducted on the Shimadzu GC-MS QP2010 Plus system. The absorbance of the cells in the cytotoxicity test was measured by the ELISA Plate Reader (USA).

Procedure

Solvent extraction process

G. bulot dried leaves (4.2 kg) were firstly powdered and then extracted with methanol (5 times, 5.0 L each) at room temperature. The resulting extract was concentrated under low pressure to afford 175.42 g of a black solid extract, with a yield of 4.2% (w/w). This extract was distributed in water and then alternately partitioned with *n*-hexane, dichloromethane (CH_2Cl_2), and ethyl acetate (EtOAc) (5.0 L, 3 times each) to obtain the *n*-hexane (GBH, 29.94 g), the CH_2Cl_2 (GBD, 21.33 g), the EtOAc (GBE, 38.22 g), and the retained water (GBW, 85.93 g) layers after removing the solvents under low pressure. GC-MS was used to analyze the *n*-hexane and dichloromethane extracts.

Determination of the volatile constituents

The volatile constituents were investigated by GC-MS method conducted on a Shimadzu GC-MS-QP2010 Plus system (Japan) equipped with an Equity-5 capillary column (30 m length, 0.25 mm diameter, 0.25 μm film thickness) and a mass spectrometer (MSD QP2010 Plus). The *n*-hexane and dichloromethane extracts (1 mg, each) were diluted in a 1:100 ratio with dichloromethane, and 1 μL of the diluted solution was used for determination. The following analytical conditions were employed: a carrier helium flow rate of 1.5 mL/min, an injector and an interface temperature of 280 °C, column temperature program starting from 60 °C (2 min hold), ramping at 3 °C/min to 240 °C (10 min hold) and subsequently increasing to 280 °C at 5 °C/min (40 min hold). The samples were injected by the split-less injection mode. For mass spectrometry, acquisitions were performed in the scan mode with a mass range of $m/z = 40$ –500 at a sampling rate of 1.0 scan/s,

using an ionization voltage of 70 eV. The retention indices (RI) of the compounds were investigated by co-injecting a homologous series of *n*-alkanes (C₇–C₄₀) under the same conditions. The compounds were determined by comparing their mass spectra with those in Wiley 7 and NIST 11 libraries from the GC-MS system, as well as relevant literature data. Data quantification of the constituents was determined by the relative peak area [24].

Cell culture

Hep-G2, LU-1, MCF-7, and KB cell lines were chosen to use in the cytotoxicity tests. Stock cultures were grown in T-75 flasks containing 10 mL of Dulbecco's Modified Eagle Medium (DMEM) with 10% Fetal Bovine Serum (FBS), 1.5 g L⁻¹ sodium bicarbonate and 2 mM L-glutamine. Media were changed every 48 h. After that, the cells were dissociated with 0.05% trypsin-EDTA, and then subcultured at 3–5 day intervals in a ratio of 1:3, and incubated at 37 °C in a humidified atmosphere of 5% CO₂.

Cytotoxicity assays

The *in vitro* cytotoxicity assay has been confirmed by the US National Cancer Institute (NCI) as a principal test for the biological evaluation and screening of substances capable of inhibiting growth or killing cancer cells under *in vitro* conditions. This test was performed based on Skehan et al. method [25]. The cells were stained with Sulforhodamine B (SRB), and the optical density (OD) value was used to investigate the total cellular protein content. The amount of SRB attached to the protein molecule is directly related to the OD value. Thus, the more cells, as well as the more protein, correspond to higher OD values. The test was conducted following these specific conditions: Trypsinization to separate and count cells in a counting chamber to customize the suitable density. Continue to provide 190 µL of cells are performed in a 96-well plate. The test sample is dissolved in 100% DMSO to obtain an initial concentration of 20 mM. Dilute the sample on a 96-well plate with cell culture medium (without FBS) into 4 concentration ranges from high to low. Diluted reagents at different concentrations (10 µL) were introduced into the prepared 96-well plate above. Wells without reagent but with

cancer cells (190 µL) + DMSO 1% (10 µL) will be used as zero-day control. After 1 h, zero-day control wells of cells will be fixed with trichloroacetic acid (TCA) 20%. Cells were incubated for 72 h and then proceeded to fix with TCA for 1 h, stained with the SRB at 37 °C for 30 min. After that, the cells were washed 3 times with acetic acid, and then dried at room temperature. Dissolving 10 mM unbuffered tris base into the SRB, gently shaking for 10 min, and reading the OD results at 540 nm on an ELISA Plate Reader (Bio-Rad, California, USA). The inhibition rate (IR) of the cells was calculated by the following formula: $IR\% = \{100\% - [(OD_t - OD_0)/(OD_c - OD_0)] \times 100\}$. The test was repeated 3 times to ensure accuracy. Ellipticine solutions at the concentrations of 10, 2, 0.4, and 0.08 µg/mL were used as reference control. A solution of 1% DMSO was used as a negative sample with a final concentration of 0.05%. The concentration that inhibits 50% of growth (IC₅₀) was investigated by using TableCurve 2Dv4 software. The extract will be considered active if the value of IC₅₀ is not more than 20 µg/mL, while the pure compound will be evaluated to have good activity if the IC₅₀ value is less than 5 µM, as stated by the US NCI [26].

DPPH radical scavenging activity

The DPPH radical scavenging tests were carried out based on the method of Abramovič et al. [27] with some modifications. The sample is diluted with a stock solution in methanol, and then followed by diluting a range of solutions with different concentrations with double distilled water. L-ascorbic acid (Sigma) was used as a reference control. Ascorbic acid aqueous solutions at different concentrations were diluted with double distilled water. A DPPH (Sigma) 0.25 M solution was prepared by dissolving DPPH in methanol (100%). Firstly, 100 µL methanol solution of the research sample at different concentrations was placed in a 96-well plate, and then the as-prepared DPPH solutions were added to the wells with a ratio of 1:1. The control well (blank well) included water (100 µL) and DPPH (100 µL). After that, they were incubated for 30 min at room temperature. After completing the reactions, the absorbance of the solutions (OD) was measured at 517 nm. The ability to

neutralize the free radicals created from the DPPH of the test sample was determined by Eq. (1–3):

$$\% \text{ Scavenging activities} = \frac{\text{OD}_c - \text{OD}_s}{\text{OD}_c} \times 100 \quad (1)$$

$$\text{where: } \text{OD}_c = \text{OD}_{\text{well without reagent}} - \text{OD}_{\text{blank well}} \quad (2)$$

$$\text{OD}_s = \text{OD}_{\text{reagent well}} - \text{OD}_{\text{blank well}} \quad (3)$$

SC₅₀ value (Scavenging Concentration at 50% – concentration that neutralizes 50% of DPPH free radicals) was investigated by using TableCurve 2Dv4 software.

■ RESULTS AND DISCUSSION

By the GC-MS analysis, 33 volatile compounds were identified in the *n*-hexane leaf extract, which accounted for 74.9% (Table 1, Fig. 1). With 31.6%, fatty acid esters were the major chemical class of the identified compounds, followed by diterpenes (18.2%), steroids (6.3%), fatty acids (5.4%), triterpenoids (4.2%), alkanes (3.2%), aromatic compounds (1.4%), diterpenoids (1.4%), triterpenes (1.2%), alkenes (1.0%), alcohols (0.7%), and monoterpenoids (0.2%). As can be seen from Table 1,

neophytadiene reached the highest amount of 18.2%, followed by methyl palmitate (14.4%), methyl linoleate (9.7%), β-sitosterol (4.5%) and methyl stearate (3.4%). Other components were determined including palmitic acid (2.9%), lupeol acetate (2.3%), lupeol (1.9%), oleic acid (1.9%), β-sitostenone (1.8%), methyl elaidate (1.6%), α-tocopherol (1.4%), and squalene (1.2%). Especially worth noting that our research was discovered from *G. bulot* leaf with five unknown compounds present in the *n*-hexane extract with 21.9%. Indeed, some unknown compounds were recorded with an amount greater than 1.0% at retention time of 51.13 (16.0%), 79.88 (2.9%), 79.68 (1.4%), and 45.49 (1.1%).

For the dichloromethane extract, a total of 26 volatile components were determined, which represented 87.1% (Table 1, Fig. 2). Alkanes (31.2%), fatty acids (14.6%), and alkenes (10.6%) were the main chemical classes. Dichloromethane extract was also characterized by the presence of fatty acid esters (9.4%), alcohols (6.9%), diterpenes (5.3%), diterpenoids (4.4%),

Table 1. Volatile compositions (%) of the *n*-hexane and dichloromethane extracts of *Grewia bulot* leaves

No.	RT	Compound ^a	<i>n</i> -hexane	Dichloromethane	Identification ^{b,c}
			extract	extract	
1	3.95	Isovaleric acid	-	0.9	MS, RI, O
2	4.78	2-tert-Butoxyethanol	0.2	5.3	MS, RI, O
3	17.4	Dodecane	0.5	3.4	MS, RI, O
4	22.4	2-Methoxy-4-vinylphenol	-	1.1	MS, RI, O
5	26.1	Tetradecane	0.7	4.9	MS, RI, O
6	31.2	Methyl laurate	0.4	-	MS, RI, O
7	31.4	Dihydroactinidiolide	0.2	-	MS, RI, O
8	32.8	Lauric acid	-	4.0	MS, RI, O
9	33.8	1-Hexadecene	-	1.3	MS, RI, O
10	34.1	Hexadecane	0.8	7.4	MS, RI, O
11	38.8	Methyl tetradecanoate	0.4	-	MS, RI, O
12	40.2	Loliolide	-	2.7	MS, RI, O
13	40.6	Unidentified	-	2.1	MS, RI, O
14	41.1	1-Octadecene	0.1	2.2	MS, RI, O
15	41.4	Octadecane	0.5	6.0	MS, RI, O
16	42.7	Phytol	1.4	4.4	MS, RI, O
17	44.1	3,7,11,15-Tetramethyl-2-hexadecen-1-ol	0.5	1.6	MS, RI, O
18	44.9	Methyl oleate	0.2	0.2	MS, RI, O
19	45.5	Unidentified	1.1	-	MS, RI, O
20	45.7	Methyl palmitate	14.4	3.9	MS, RI, O
21	46.8	Palmitic acid	2.9	9.8	MS, RI, O

No.	RT	Compound ^a	<i>n</i> -hexane	Dichloromethane	Identification ^{b,c}
			extract	extract	
22	47.8	1-Eicosene	0.6	4.7	MS, RI, O
23	47.8	Ethyl palmitate	0.6	-	MS, RI, O
24	48.0	Eicosane	0.5	4.9	MS, RI, O
25	48.8	Methyl margarate	0.6	-	MS, RI, O
26	50.9	Methyl linoleate	9.7	2.5	MS, RI, O
27	51.1	Unidentified	16.0	3.6	MS, RI, O
28	51.3	Methyl elaidate	1.6	-	MS, RI, O
29	51.5	Neophytadiene	18.2	5.3	MS, RI, O
30	51.9	Methyl stearate	3.4	0.7	MS, RI, O
31	52.1	Linoleic acid	0.6	-	MS, RI, O
32	52.2	Oleic acid	1.9	0.8	MS, RI, O
33	52.9	Unidentified	0.5	2.8	MS, RI, O
34	53.8	1-Docosene	0.3	2.3	MS, RI, O
35	54.0	Docosane	0.3	3.0	MS, RI, O
36	59.4	Unidentified	-	1.4	MS, RI, O
37	59.6	Tetracosane	-	1.6	MS, RI, O
38	63.1	Methyl octacosanoate	0.3	-	MS, RI, O
39	64.2	Heptadecyl heptadecanoate	-	2.1	MS, RI, O
40	74.4	Squalene	1.2	-	MS, RI, O
41	79.7	Unidentified	1.4	-	MS, RI, O
42	79.9	Unidentified	2.9	-	MS, RI, O
43	82.2	α -Tocopherol	1.4	-	MS, RI, O
44	85.4	β -Sitostenone	1.8	-	MS, RI, O
45	87.2	β -Sitosterol	4.5	-	MS, RI, O
46	87.5	Lupeol	1.9	-	MS, RI, O
47	89.8	Lupeol acetate	2.3	-	MS, RI, O
Total			96.8	96.9	
Unidentified			21.9	9.8	
Hemiterpenoids/Acids			0	0.9	
Alkanes			3.2	31.2	
Alkenes			1.0	10.6	
Alcohols			0.7	6.9	
Aromatic compounds			1.4	1.1	
Diterpenes			18.2	5.3	
Triterpenes			1.2	0	
Monoterpenoids			0.2	2.7	
Diterpenoids			1.4	4.4	
Triterpenoids			4.2	0	
Steroids			6.3	0	
Fatty acids			5.4	14.6	
Fatty acid esters			31.6	9.4	

^aCompound listed according to the elution order of column Equity-5; ^b Retention Index (RI) calculated using a homologous series of *n*-alkanes (C₇-C₄₀) in a capillary column (Equity-5) (see supplementary data); ^c Identification based on the matching of mass spectra (MS), retention index (RI) of the compounds with NIST11, WILEY7, Adams (2017) data libraries, along with the data in the website <http://www.thegoodscentcompany.com/search2.html> (accessed on 1 March 2023) (O). Area (%): is the percentage of the area occupied by the compound within the chromatogram; - Not identified

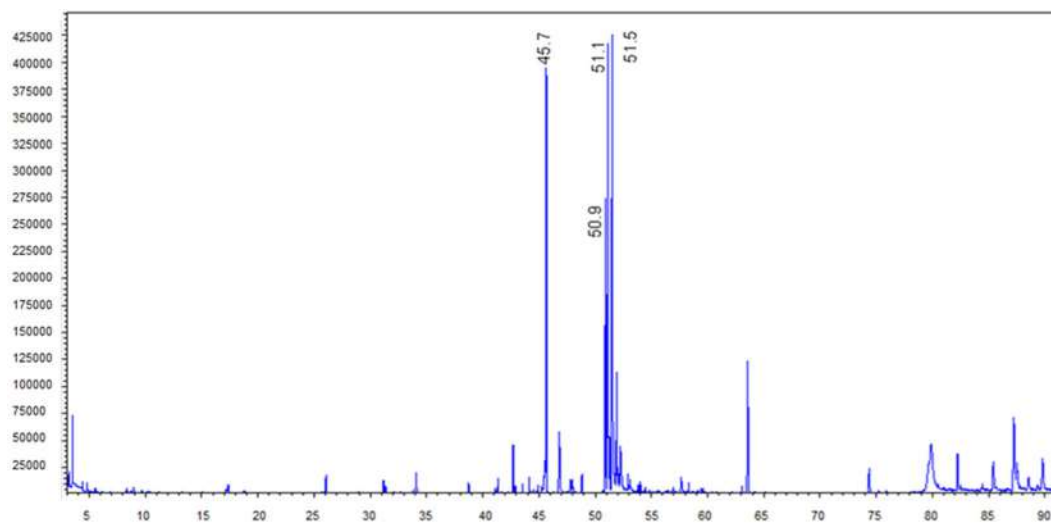


Fig 1. GC-MS data of *n*-hexane extract of *Grewia bulot* leaf

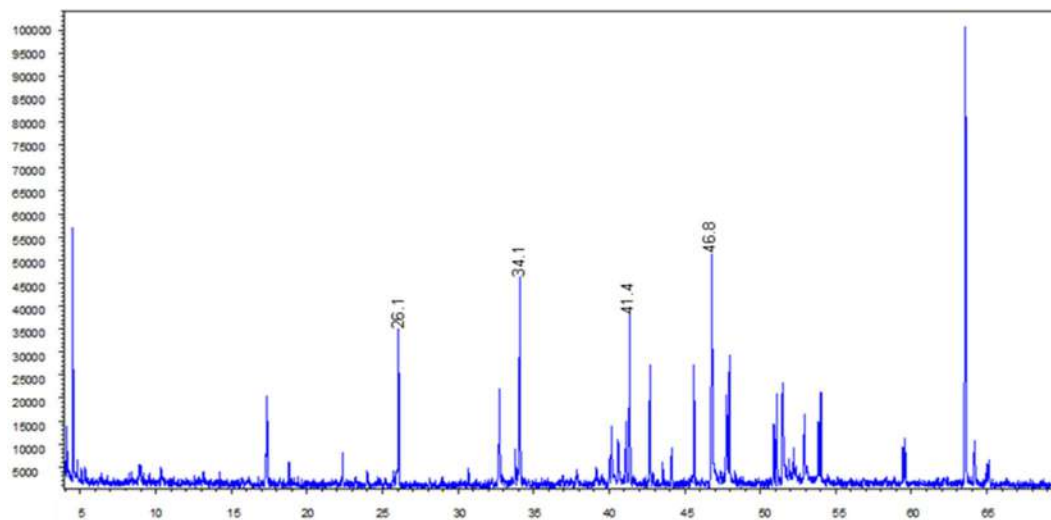


Fig 2. GC-MS data of dichloromethane extract of *Grewia bulot* leaf

monoterpenoids (2.7%), aromatic compounds (1.7%), and hemiterpenoids/acids (0.9%). In addition, the presence of unknown compounds in leaf volatile accounted for 9.8%, including compounds at retention time 51.13 (3.6%), 52.92 (2.8%), 40.58 (2.1%), and 59.43 (1.4%). A significant amount of alkanes, fatty acids, alkenes, fatty acid esters, and alcohols were found in dichloromethane extract, accounting for 31.2, 14.6, 10.6, 9.4, and 6.9%, respectively. The principal palmitic acid (9.8%), hexadecane (7.4%), octadecane (6.0%), 2-*tert*-butoxyethanol (5.3%), tetradecane (4.9%), eicosane (4.9%), and 1-eicosene (4.7%) were determined with higher content than those of the *n*-hexane extract. Additionally, several compounds

(> 1.0%) were also found in the dichloromethane extract, consisting of phytol (4.4%), lauric acid (4.0%), methyl palmitate (3.9%), dodecane (3.4%), docosane (3.0%), loliolide (2.7%), methyl linoleate (2.5%), 1-docosene (2.3%), 1-octadecene (2.2%), heptadecyl heptadecanoate (2.1%), 3,7,11,15-tetramethyl-2-hexadecen-1-ol (1.6%), tetracosane (1.6%), and 1-hexadecene (1.3%).

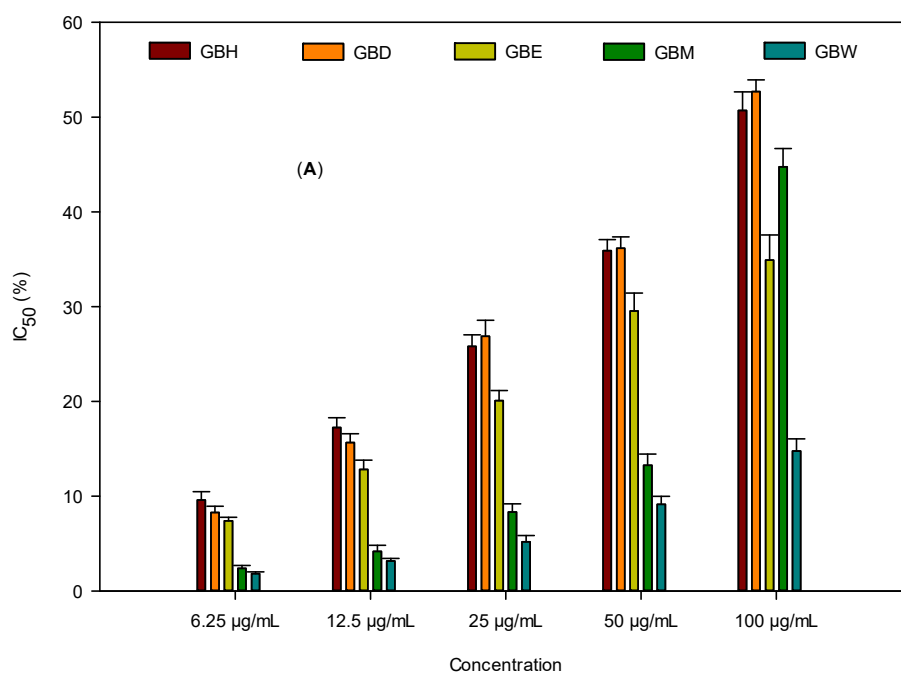
Literature survey showed that the main volatile compounds in the *n*-hexane extract from stem bark of *G. lasiocarpa* were investigated included hexadecane (10.2%), heptadecane (9.7%), tetratetracontane (7.5%), heneicosane (6.5%), hexatriacontane (5.9%), sitosterol

(5.6%), and lupeol (4.9%). Lupeol (13.7%), γ -sitosterol (7.3%), and 9Z-octadecenamide (6.3%) were determined in the stem bark's chloroform extract, while lupeol acetate (12.9%), 1,6-bis[(2S)-2-ethylhexyl]hexanedioate (9.9%), 4-((1E)-3-hydroxy-1-propenyl)-2-methoxyphenol (8.2%), δ -4,6-cholestadienol (5.7%), palmitic acid (5.2%), and β -sitosterol (5.2%) were identified in the methanol extract of this species [8]. Regarding the chemical constituents of *G. tenax*, sixty-three volatile compounds were identified from the fruit, in which the major compounds were acetic acid (61.0%); methylhydrazine (4.8%), 2,3-butanediol (4.1%), palmitic acid (3.5%), and 1,3-butanediol (2.4%) [28]. Generally, the volatile compositions are similar among *Grewia* species, but their content is much different to a great extent.

The cytotoxicity of *n*-hexane (GBH), dichloromethane (GBD), ethyl acetate (GBE), methanol (GBM), and water (GBW) was studied (see supplementary data). *G. bulot* extracts against the growth of the MCF-7, Hep-G2, SK-LU-1, and KB cell lines were tested using a sulforhodamine B assay (Fig. 3) [25]. The GBH and GBD samples show cytotoxic activity against some cell lines, with IC_{50} values ranging from 90.60 to 98.27 $\mu\text{g/mL}$, while the remaining samples do not exhibit

such activity at the tested concentrations. According to previous reports, the essential oil extracted from the fresh leaves of *G. lasiocarpa* showed cytotoxic activity at 1 mg/mL ($IC_{50} = 555.70 \mu\text{g/mL}$) against HeLa cells, while that from the stem bark exhibited no significant activity ($IC_{50} > 1000 \mu\text{g/mL}$) [29]. Furthermore, aqueous leaf and fruit extracts from *G. asiatica* showed significant anticancer activity against liver and breast cancer, with IC_{50} values of 59.03 and 58.65 $\mu\text{g/mL}$ (leaf extract) and 50.37 and 61.23 $\mu\text{g/mL}$ (fruit extract), respectively, while the methanol leaf extract exhibited activity against four human cancer cell lines – HL-60, K-562, MCF-7, and HeLa – with IC_{50} values of 53.70; 54.90; 199.5 and 177.8 $\mu\text{g/mL}$, respectively [30]. In another study, the cytotoxic activity of the CHCl_3 fraction of *G. bilamellata* (combined leaves, twigs, and stems) against the KB cell line involved an $ED_{50} > 20 \mu\text{M}$ [9]. In addition, the methanol extract of *G. hirsuta* leaves had a cytotoxic effect on the Hep-G2 cell line, with an IC_{50} value of 15.6 $\mu\text{g/mL}$, and showed a cell viability of 50.4% [15].

Furthermore, the antioxidant activities of the five crude extracts were tested by measuring their DPPH scavenging capacity, as shown in Fig. 4. All extracts exhibit antioxidant activity, with SC_{50} values ranging from



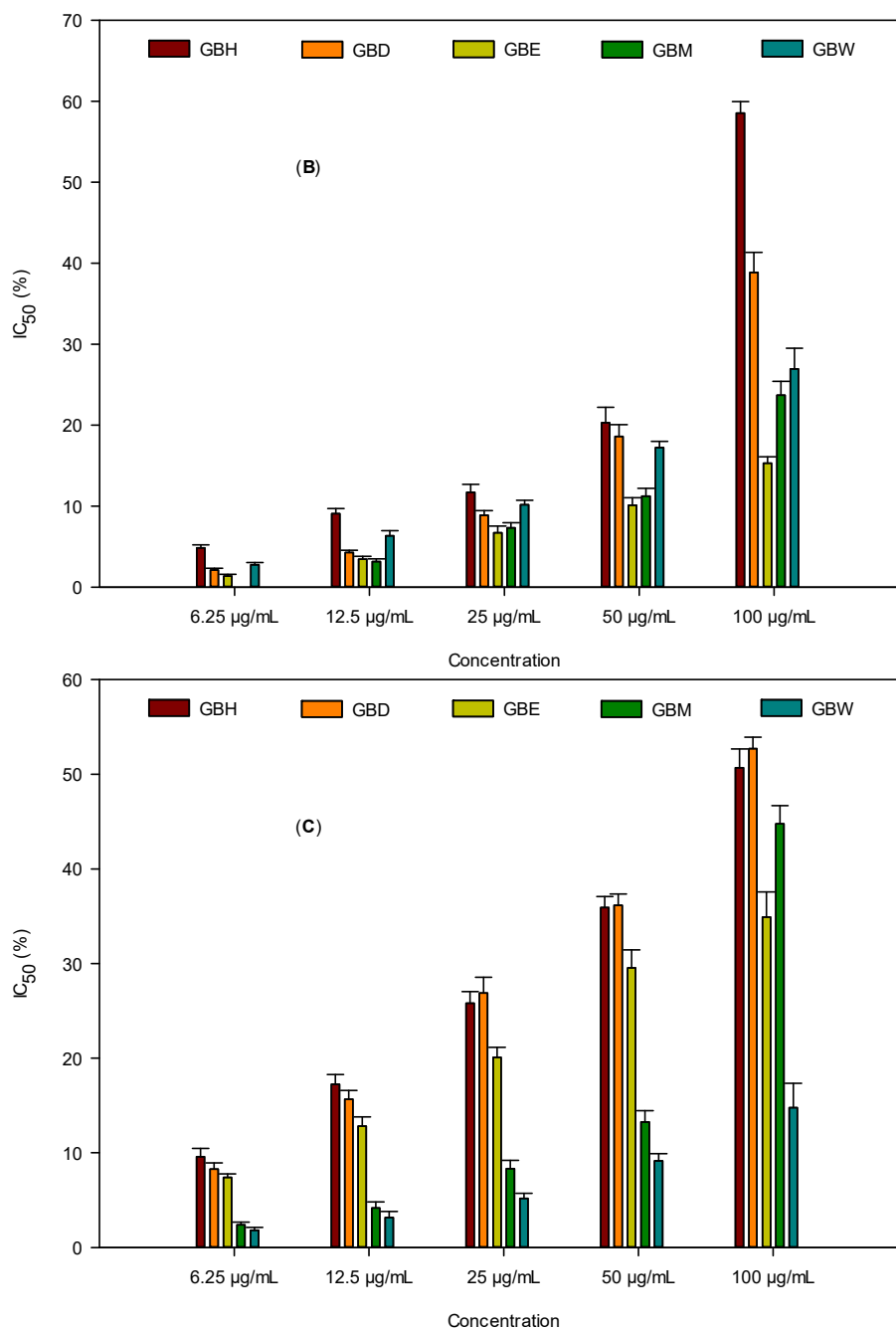


Fig 3. Effects of GBH, GBD, GBE, GBM, and GBW extracts from the *Grewia bulot* leaf on the viability of Hep-G2 (A), KB (B), MCF-7 (C), and SK-LU-1 (D), respectively. Data were expressed as a percentage of control

9.39 to 153.78 µg/mL, and the scavenging efficacy of the extracts follows the order GBM > GBE > GBD > GBW > GBH. The methanol extract (GBM) shows the strongest activity, with an SC₅₀ value of 9.39 ± 0.90 µg/mL, comparable to that of the positive control, ascorbic acid (SC₅₀ = 7.27 ± 0.12 µg/mL); its effectiveness as an

antioxidant is attributed to its higher concentration of total phenolic compounds. As is commonly known, the antioxidant activity of an extract is directly correlated with the amount of phenolic compounds present; therefore, extracts with higher phenolic content exhibit greater antioxidant activity. This makes this plant a good

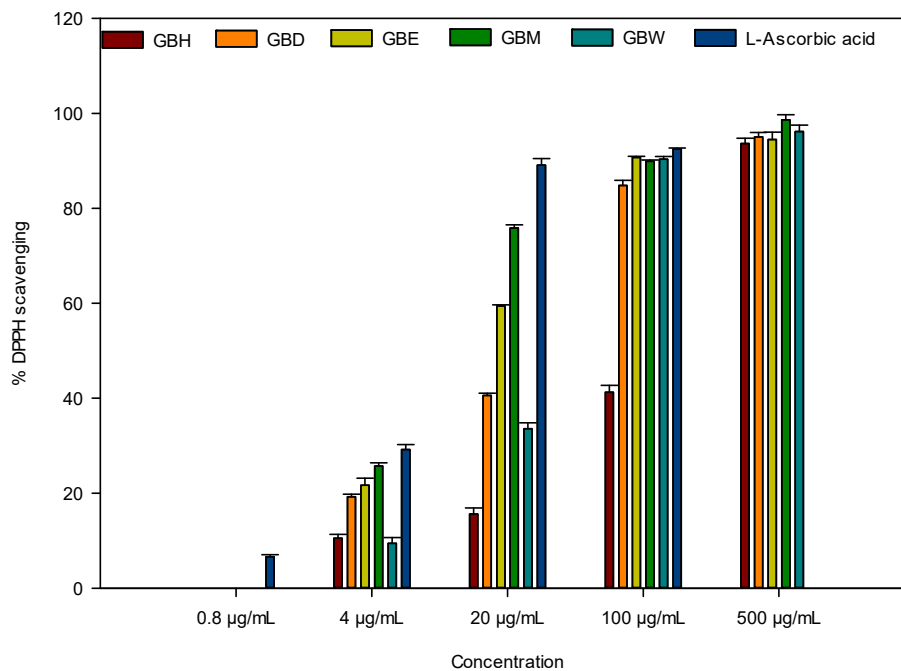


Fig 4. % DPPH scavenging efficiency of *Grewia bulot* leaf extracts

antioxidant [31] and indicates the presence of free-radical-scavenging active metabolites, such as 2-methoxy-4-vinylphenol [32], loliolide [33], phytol [34], neophytadiene [35], squalene [36], and α -tocopherol [37]. Previously, the methanol extract of *G. villosa* showed the weakest DPPH scavenging effect at 0.2, 0.4, 0.6, 0.8, and 1.0 mg/mL, comparable to that of standard vitamin E [38], while the methanol and acetone extracts of *G. optiva* leaves did not possess antioxidant activity [39]. In another study, the antioxidant activities of the syrup, jam, and seed of *G. tenax* were evaluated, with the seed extract containing the highest antioxidant content [40]. Further, the antioxidant potential was highest in *G. tenax* ($85.49 \pm 2.68 \mu\text{g/mL}$) and lowest in *G. tiliifolia* ($76.11 \pm 1.77 \mu\text{g/mL}$) and *G. asiatica* ($82.5 \pm 5.66 \mu\text{g/mL}$) [41]. As determined via DPPH assays, the methanol extract of *G. sapida* showed antioxidant activity, with an IC_{50} value of $257.666 \pm 2.516 \mu\text{g/mL}$ [42]. In another study, the crude chloroform and methanol stem bark extracts of *G. lasiocarpa* showed the highest inhibition with IC_{50} of 92.94 and 75.19 $\mu\text{g/mL}$ for the FRAP and DPPH assays, respectively, in terms of antioxidant activity [29]. Further, an evaluation of the methanol extract of *G. asiatica* investigated the significant antioxidant activity of

its fruits [43], and the petroleum ether fraction of *G. abutilifolia* leaf had the highest activity ($\text{IC}_{50} = 3.82 \pm 0.055 \mu\text{g/mL}$) in a DPPH scavenging assay [44]. Comparing the DPPH radical scavenging activity of *G. bulot* with that of other *Grewia* species reported in the literature implies that in most cases, *G. bulot* exhibits stronger activity; therefore, it can be used as a potential source of ethnic medicinal plants to develop new forms of antioxidant therapy.

CONCLUSION

The current study provides a comprehensive analysis of the chemical compositions of Vietnamese *Grewia bulot* leaf extracts and investigates their antioxidant and anticancer activities. The main chemical classes identified in the *n*-hexane extract were fatty acid esters (31.6%), diterpenes (18.2%), and steroids (6.3%). In contrast, the dichloromethane extract contained alkanes (31.2%), fatty acids (14.6%), alkenes (10.6%), fatty acid esters (9.4%), and alcohols (6.9%). Further, the major compounds found in the *n*-hexane extract were neophytadiene (18.2%), methyl palmitate (14.4%), methyl linoleate (9.7%), and β -sitosterol (4.5%). On the other hand, the dichloromethane extract was

characterized by palmitic acid (9.8%), hexadecane (7.4%), octadecane (6.0%), 2-*tert*-butoxyethanol (5.3%), and neophytadiene (5.3%). Both extracts exhibited weak activity against four human cancer cell lines (MCF-7, Hep-G2, SK-LU-1, and KB), with IC₅₀ values ranging from 90.60 ± 3.49 to 98.27 ± 2.77 µg/mL. Additionally, all five crude extracts displayed significant antioxidant potential, with the methanol extract showing the highest activity (SC₅₀ = 9.39 ± 0.90 µg/mL). These findings suggest the potential application of *Grewia bulot* leaf extracts as a source of antioxidants.

■ ACKNOWLEDGMENTS

This study was financially supported by the Ministry of Education and Training (Vietnam) with code B2022-DHH-13 and the partial support of Hue University under the Core Research Program, Grant No. NCM.DHH.2023.02.

■ AUTHOR CONTRIBUTIONS

Ty Viet Pham conducted the experiment, Anh Tuan Le, Y Duy Ngo, Nhan Thi Thanh Dang, and Thang Quoc Le analyzed the data, Bao Chi Nguyen, and Duc Viet Ho wrote and revised the manuscript. All authors agreed to the final version of this manuscript.

■ REFERENCES

- [1] Atanasov, A.G., Zotchev, S.B., Dirsch, V.M., Orhan, I.E., Banach, M., Rollinger, J.M., Barreca, D., Weckwerth, W., Bauer, R., Bayer, E.A., Majeed, M., Bishayee, A., Bochkov, V., Bonn, G.K., Braid, N., Bucar, F., Cifuentes, A., D'Onofrio, G., Bodkin, M., Diederich, M., Dinkova-Kostova, A.T., Efferth, T., El Bairi, K., Arkells, N., Fan, T.P., Fiebich, B.L., Freissmuth, M., Georgiev, M.I., Gibbons, S., Godfrey, K.M., Gruber, C.W., Heer, J., Huber, L.A., Ibanez, E., Kijjoo, A., Kiss, A.K., Lu, A., Macias, F.A., Miller, M.J.S., Mocan, A., Müller, R., Nicoletti, F., Perry, G., Pittalà, V., Rastrelli, L., Ristow, M., Russo, G.L., Silva, A.S., Schuster, D., Sheridan, H., Skalicka-Woźniak, K., Skaltsounis, L., Sobarzo-Sánchez, E., Brecht, D.S., Stuppner, H., Sureda, A., Tzvetkov, N.T., Vacca, R.A., Aggarwal, B.B., Battino, M., Giampieri, F., Wink, M., Wolfender, J.L., Xiao, J., Yeung, A.W.K., Lizard, G., Popp, M.A., Heinrich, M., Berindan-Neogoe, I., Stadler, M., Daglia, M., Verpoorte, R., and Supuran, C.T., 2021, Natural products in drug discovery: Advances and opportunities, *Nat. Rev. Drug Discovery*, 20 (3), 200–216.
- [2] Thomford, N.E., Senthelane, D.A., Rowe, A., Munro, D., Seele, P., Maroyi, A., and Dzobo, K., 2018, Natural products for drug discovery in the 21st century: Innovations for novel drug discovery, *Int. J. Mol. Sci.*, 19 (6), 1578.
- [3] Dev, R., Kannan, V., Kumar, M.S., Dayal, D., and Patel, R., 2019, "Grewia Species: Diversity, Distribution, Traditional Knowledge and Utilization" in *Wild Fruits: Composition, Nutritional Value and Products*, Eds. Mariod, A.A., Springer International Publishing, Cham, Switzerland, 395–426.
- [4] Sonawane, P.P., and Patil, R.P., 2019, The comparative study of phytoconstituents of genus *Grewia* from Western Maharashtra, *J. Gujarat Res. Soc.*, 21 (14), 1874–1879.
- [5] Shukla, R., Sharma, D.C., Pathak, N., and Bajpai, P., 2016, Estimation of phytochemicals and *in vitro* antioxidant activity of different solvent extracts of *Grewia asiatica* fruit, *Res. Rev.: J. Bot. Sci.*, 5 (3), 43–49.
- [6] Zahoor, M., Bari, W.U., Zeb, A., and Khan I., 2020, Toxicological, anticholinesterase, antilipidemic, antidiabetic and antioxidant potentials of *Grewia optiva* Drummond ex Burret extracts, *J. Basic. Clin. Physiol. Pharmacol.*, 31 (2), 1–16.
- [7] Ul Bari, W., Zahoor, M., Zeb, A., Sahibzada, M.U.K., Ullah, R., Shahat, A.A., Mahmood, H.M., and Khan, I., 2019, Isolation, pharmacological evaluation and molecular docking studies of bioactive compounds from *Grewia optiva*, *Drug Des., Dev. Ther.*, 13, 3029–3036.
- [8] Akwu, N.A., Naidoo, Y., Singh, M., Nundkumar, N., and Lin, J., 2019, Phytochemical screening, *in vitro* evaluation of the antimicrobial, antioxidant and cytotoxicity potentials of *Grewia lasiocarpa* E. Mey. ex Harv., *S. Afr. J. Bot.*, 123, 180–192.
- [9] Ma, C., Zhang, H.J., Tan, G.T., Hung, N.V., Cuong, N.M., Soejarto, D.D., and Fong, H.H.S., 2006,

- Antimalarial compounds from *Grewia bilamellata*, *J. Nat. Prod.*, 69 (3), 346–350.
- [10] Do Jogo, S.F.S., 2019, Antibacterial activity of the chemical constituents of the African medicinal plant *Grewia hexamita* against resistant bacteria, *Dissertation*, Faculdade de Farmácia, Universidade de Lisboa.
- [11] Nasrin, M., Dash, P.R., and Ali, M.S., 2015, *In vitro* antibacterial and *in vivo* cytotoxic activities of *Grewia paniculate*, *Avicenna J. Phytomed.*, 5 (2), 98–104.
- [12] Nyalo, P.O., Omwenga, G.I., and Ngugi, M.P., 2023, Antibacterial properties and GC-MS analysis of ethyl acetate extracts of *Xerophyta spekei* (Baker) and *Grewia tembensis* (Fresen), *Heliyon*, 9 (3), e14461.
- [13] Natarajan, A., Sugumar, S., Bitragunta, S., and Balasubramanyan N., 2015, Molecular docking studies of (4Z, 12Z)-cyclopentadeca-4,12-dienone from *Grewia hirsuta* with some targets related to type 2 diabetes, *BMC Complementary Altern. Med.*, 15 (1), 73.
- [14] Rajavel, T., Mohankumar, R., Archunan, G., Ruckmani, K., and Devi, K.P., 2017, Beta sitosterol and daucosterol (phytosterols identified in *Grewia tiliaefolia*) perturbs cell cycle and induces apoptotic cell death in A549 cells, *Sci. Rep.*, 7 (1), 3418.
- [15] Ema, A., Kumar, M.S., Rebecca, L.J., Sindhu, S., Anbarasi, P., Sagadevan, E., and Arumugam, P., 2013, Evaluation of antiproliferative effect of *Grewia hirsuta* on HepG2 cell lines, *J. Acad. Ind. Res.*, 2, 1–5.
- [16] Abirami, N., and Natarajan, B., 2014, Isolation and characterization of (4Z, 12Z)-cyclopentadeca-4,12-dienone from Indian medicinal plant *Grewia hirsuta* and its hyperglycemic effect on 3T3 and L6 cell lines, *Int. J. Pharmacogn. Phytochem. Res.*, 6(2), 393–398.
- [17] Al-Musayeb, N.M., Mothana, R.A., Matheussen, A., Cos, P., and Maes L., 2012, *In vitro* antiplasmodial, antileishmanial and antitrypanosomal activities of selected medicinal plants used in the traditional Arabian Peninsular region, *BMC Complementary Altern. Med.*, 12 (1), 49.
- [18] Sukdee, S., Meepowpan, P., Nantasaen, N., Jungsuttiwong, S., Hadsadee, S., and Pompimon, W., 2021, Anticancer activities of chemical constituents from leaves and twigs of *Mitrephora winitii*, *Indones. J. Chem.*, 21 (3), 699–707.
- [19] Prasetyaningrum, A., Jos, B., Ratnawati, R., Rokhati, N., Riyanto, T., and Prinanda, G.R., 2022, Sequential microwave-ultrasound assisted extraction of flavonoid from *Moringa oleifera*: Product characteristic, antioxidant and antibacterial activity, *Indones. J. Chem.*, 22 (2), 303–316.
- [20] Benmekhbi, L., Mosbah, S., Laamraoui, H., Hamlaoui, I., Bencheriet, S., and Ibrahim, D., 2022, Evaluation of phytochemical properties and biological activities of leaf extracts and oil of *Petroselinum sativum* collected from Algeria, *Indones. J. Chem.*, 22 (6), 1566–1573.
- [21] Bich, D.H., 2007, *Herbal Plants and Animals Used as Medicaments in Vietnam*, Vol I, Publishing House for Science and Technology, Hanoi, Vietnam, 472–473.
- [22] Ho, P.H., 1999, *An Illustrated the Flora of Vietnam*, Vol. I. Young Publisher, Ho Chi Minh, Vietnam, 480–486.
- [23] Do, H.T.T., Grant, J.C., Trinh, B.N., Zimmer, H.C., and Nichols, J.D., 2017, Diversity depends on scale in the forests of the central highlands of Vietnam, *J. Asia-Pac. Biodivers.*, 10 (4), 472–488.
- [24] Pham, T.V., Ngo, H.P.T., Thi Thanh Dang, N., Khoa Nguyen, H., Thi Nhu Hoang, H., and Pham, T., 2022, Volatile constituents and anti-osteoporotic activity of the *n*-hexane extract from *Homalomena gigantea* rhizome, *Nat. Prod. Commun.*, 17 (9), 1934578X221125433.
- [25] Skehan, P., Storeng, R., Scudiero, D., Monks, A., McMahon, J., Vistica, D., Warren, J.T., Bokesch, H., Kenney, S., and Boyd, M.R., 1990, New colorimetric cytotoxic assay for anticancer-drug screening, *J. Natl. Cancer Inst.*, 82 (13), 1107–1112.
- [26] Hughes, J.P., Rees, S., Kalindjian, S.B., and Philpott, K.L., 2011, Principles of early drug discovery, *Br. J. Pharmacol.*, 162 (6), 1239–1249.
- [27] Abramović, H., Grobin, B., Poklar Ulrih, N., and Cigić, B., 2018, Relevance and standardization of *in vitro* antioxidant assays: ABTS, DPPH, and Folin-Ciocalteu, *J. Chem.*, 2018, 4608405.

- [28] Aboagarib, E.A.A., Yang, R., Hua, X., and Siddeeg, A., 2014, Chemical compositions, nutritional properties and volatile compounds of guddaim (*Grewia tenax* Forssk.) fiori. fruits, *J. Food Nutr. Res.*, 2 (4), 187–192.
- [29] Akwu, N.A., Naidoo, Y., Channangihalli, S.T., Singh, M., Nundkumar, N., and Lin, J., 2021, The essential oils of *Grewia lasiocarpa* E. Mey. Ex Harv.: Chemical composition, *in vitro* biological activity and cytotoxic effect on Hela cells, *An. Acad. Bras. Cienc.*, 93 (2), e20190343.
- [30] Zia-Ul-Haq, M., Stanković, M.S., Rizwan, K., and Feo, V.D., 2013, *Grewia asiatica* L., a food plant with multiple uses, *Molecules*, 18 (3), 2663–2682.
- [31] Elements, T., Yabalak, E., and Gizir, A.M., 2017, Evaluation of total polyphenol content, antioxidant activity and chemical composition of methanolic extract from *Allium kharputense* Freyn Et. Sint. and determination of mineral and trace elements, *J. Turk. Chem. Soc., Sect. A*, 4 (3), 691–708.
- [32] Nadeem, A., Ahmed, B., Shahzad, H., Craker, L.E., and Muntean, T., 2021, *Verbascum thapsus* (mullein) versatile polarity extracts: GC-MS analysis, phytochemical profiling, anti-bacterial potential and anti-oxidant activity, *Pharmacogn. J.*, 13 (6), 1488–1497.
- [33] Han, E.J., Fernando, I.P.S., Kim, H.S., Lee, D.S., Kim, A., Je, J.G., Seo, M.J., Jee, Y.H., Jeon, Y.J., Kim, S.Y., and Ahn, G., 2021, (-)-Loliolide isolated from *Sargassum horneri* suppressed oxidative stress and inflammation by activating Nrf2/HO-1 signaling in IFN- γ /TNF- α -stimulated HaCaT keratinocytes, *Antioxidants*, 10 (6), 856.
- [34] Santos, C.C.M.P., Salvadori, M.S., Mota, V.G., Costa, L.M., de Almeida, A.A.C., de Oliveira, G.A.L., Costa, J.P., de Sousa, D.P., de Freitas, R.M., and de Almeida, R.N., 2013, Antinociceptive and antioxidant activities of phytol *in vivo* and *in vitro* models, *Neurosci. J.*, 2013, 949452.
- [35] Grabarczyk, M., Wińska, K., Mączka, W., Potaniec, B., and Anioł, M., 2015, Loliolide - the most ubiquitous lactone, *Acta Univ. Lodz., Folia Biol. Oecol.*, 11, 1–8.
- [36] Mendes, A., Azevedo-Silva, J., and Fernandes, J.C., 2022, From sharks to yeasts: Squalene in the development of vaccine adjuvants, *Pharmaceuticals*, 15 (3), 265.
- [37] Zhang, L., Liu, Z., Sun, Y., Wang, X., and Li, L., 2020, Effect of α -tocopherol antioxidant on rheological and physicochemical properties of chitosan/zein edible films, *LWT*, 118, 198799.
- [38] Hegazy, A.K., Mohamed, A.A., Ali, S.I., Alghamdi, N.M., Abdel-Rahman, A.M., and Al-Sobeai, S., 2019, Chemical ingredients and antioxidant activities of underutilized wild fruits, *Heliyon*, 5 (6), e01874.
- [39] Arora, S., 2011, Antibacterial, antifungal, antioxidant and phytochemical study on the leaves extract of *Grewia optiva*, *J. Pharm. Res.*, 4 (9), 3130–3132.
- [40] Suliman, Z.E.A., Zidan, N.S., and Foudah, S.H.I., 2018, Chemical compositions, antioxidant, and nutritional properties of the food products of Guddaim (*Grewia tenax*), *Int. J. Pharm. Res. Allied Sci.*, 7 (3), 172–182.
- [41] Sharma, C., Malgaonkar, M., Sangvikar, S.G., Murthy, S.N., and Pawar, S.D., 2016, *In vitro* evaluation of antimicrobial and antioxidant profile of *Grewia* L. root extracts, *J. Appl. Life Sci. Int.*, 7 (1), 1–9.
- [42] Islary, A., Sarmah, J., and Basumatary, S., 2016, Proximate composition, mineral content, phytochemical analysis and *in vitro* antioxidant activities of a wild edible fruit (*Grewia sapida* Roxb. ex DC.) found in Assam of North-East India, *J. Invest. Biochem.*, 5, 21–31.
- [43] Srivastava, J., Kumar, S., and Vankar, P.S., 2012, Correlation of antioxidant activity and phytochemical profile in native plants, *Nutr. Food Sci.*, 42 (2), 71–79.
- [44] Salam, R., and Rafe, R., 2018, *In vitro* antioxidant study and determination of flavonoids, flavonols, total phenolic and proanthocyanidins content of *Grewia abutilifolia* leaf extracts, *Phytothérapie*, 18 (3-4), 140–147.

Enhancing the CO₂ Adsorption Performance of UiO-66 by Imidazolium-Based Room-Temperature Ionic Liquids (RTILs) Incorporation

Laela Mukaromah, Andi Haryanto, Yessi Permana, and Aep Patah*

Division of Inorganic and Physical Chemistry, Faculty of Mathematics and Natural Sciences, Institut Teknologi Bandung, Jl. Ganesha No. 10, Bandung 40132, Indonesia

* Corresponding author:

email: aep@itb.ac.id

Received: May 23, 2023

Accepted: July 17, 2023

DOI: 10.22146/ijc.84669

Abstract: Functionalization of metal-organic frameworks resulting in efficient CO₂ adsorption materials became substantial in preventing the worsening environment upon the emission of CO₂. In this study, several room-temperature ionic liquids (RTILs) with an imidazolium-based cation of 1-butyl-3-methylimidazolium [bmim]⁺ and anions of bis(trifluoromethylsulfonyl)imide [TFSI]⁻, trifluoromethanesulfonate [OTf]⁻, hexafluorophosphate [PF₆]⁻, and tetrafluoroborate [BF₄]⁻ were incorporated into UiO-66 by wet impregnation method under air. The RTILs/UiO-66 composites were characterized by PXRD, FTIR, TGA, nitrogen physisorption, and CO₂ adsorption. Based on the type of anions of imidazolium-based RTILs, the CO₂ uptake of RTILs/UiO-66 composites followed the trend: [OTf]⁻ > [TFSI]⁻ > [PF₆]⁻ > [BF₄]⁻ at low temperature (273 K) and pressure (100 kPa). The CO₂ uptake of pristine UiO-66 increased approximately 1.5 times upon incorporating [bmim][OTf]. The type of anions of imidazolium-based RTILs influences the CO₂ adsorption performance of RTILs/UiO-66 composites in which anions containing fluoroalkyl group ([OTf]⁻, [TFSI]⁻) exhibited a higher CO₂ uptake compared to inorganic fluorinated anions ([BF₄]⁻, [PF₆]⁻). Hence, the incorporation of hydrophobic imidazolium-based RTILs showed a potential to enhance the performance of UiO-66 for CO₂ adsorption application.

Keywords: CO₂ adsorption; imidazolium-based RTILs; incorporation; UiO-66

■ INTRODUCTION

High greenhouse gas (GHG) emissions directly induce global warming and climate change. They are serious environmental issues that have been attracting worldwide attention [1]. Carbon dioxide (CO₂), the major component in GHG emissions, is mostly generated from combustion sources [2]. The amount of CO₂ released to the atmosphere significantly increases following the rapid development in industrial and energy infrastructures with a high demand for fossil fuels [3]. To prevent the worsening impact, the utilization of natural gas producing less CO₂ emission over fossil fuels and coal has been initiated [4]. Natural gas offers several advantages, such as being more abundant, environmentally friendly, and relatively inexpensive [5]. However, raw natural gas also contains impurities like CO₂, which must be removed before further use due to its corrosive property [6].

Natural gas purification from CO₂ has been extensively conducted using a robust technology known as amine scrubbing [7]. This technology generally uses a primary alkanolamine solution of 20–30 wt.% monoethanolamine, besides diethanolamine, triethanolamine, or *N*-methyldiethanolamine, as secondary, tertiary, and ternary alkanolamines, respectively [8]. Although this technology is highly efficient for CO₂ separation, alkanolamine solutions also have several drawbacks, *i.e.*, amine degradation toward heating, high energy demand for amine regeneration, and corrosive toward equipment, leading to environmental issues and significant expense for industrial scale [9]. Therefore, a thermally stable material needs to be developed as an alternative approach for CO₂ separation on a large scale.

An emerging generation of crystalline materials with

exceptional porosity is defined as metal-organic frameworks (MOFs), also known as porous coordination polymers [10]. The structure of MOFs is built from metal ions in the form of secondary building units as nodes and organic linkers as spokes, connected with coordination bonds [11]. MOFs are recognized for their tunability and feasibility in structure, which make them ideal for gas adsorption and separation [12]. Nevertheless, designing MOFs with excellent CO₂ selectivity similar to alkanolamine solutions remains challenging [13]. Several post-synthetic modifications on MOFs are carried out to enhance the CO₂ selectivity. Despite its high CO₂ capture, the functionalization of MOFs using alkylamines deals with pore accessibility control upon the formation of amine aggregates [14]. The incorporation of MOFs into polymer membranes concerns with non-uniform particle distribution within the matrix, which can cause severe agglomeration [15].

A novel functionalization of MOFs with room-temperature ionic liquids (RTILs) has been increasingly investigated, particularly using imidazolium-based cation. RTILs are liquid-phase salts at room temperature or lower, commonly arranged from asymmetric organic cations with symmetric organic or inorganic anions [16]. Owing several outstanding properties, *i.e.*, high thermal stability, null volatility, negligible flammability, and good solubility toward CO₂ make them promising to be incorporated into MOFs for CO₂ adsorption or separation [17]. Zeeshan et al. [13] investigated the performance of [hemim][DCA]/ZIF-8 composite in a core-shell type for CO₂ separation. They concluded that the composite exhibits CO₂ adsorption and CO₂/CH₄ selectivity up to 5.7 and 45 times higher, respectively, compared to the unmodified ZIF-8 at low pressure. Kinik et al. [18] examined the incorporation of ZIF-8 with [bmim][PF₆] for CO₂ separation. They found that the double CO₂ selectivity over CH₄ and N₂ is generated from ZIF-8 and [bmim][PF₆] direct interaction. Oliveira et al. [19] performed the molecular simulations of [bmim][PF₆] and [bmim][TFSI] incorporated with MIL-100(Fe) for CO₂ adsorption. They showed that the presence of RTILs increases CO₂ adsorption and selectivity (CO₂/CH₄ and CO₂/N₂) at low pressure.

Herein, we study the incorporation of imidazolium-based RTILs into Zr-based MOFs of UiO-66 for CO₂ adsorption. Featuring Zr₆O₄(OH)₄ nodes in 12 coordination of linkers [20], UiO-66 shows excellent thermal stability alongside octahedral and tetrahedral cages that make it suitable for gas adsorption or separation [21]. While imidazolium-based RTILs are widely utilized for CO₂ adsorption or separation owing to their good CO₂ solubility [22]. Furthermore, the influence of the following anions: tetrafluoroborate [BF₄]⁻, hexafluorophosphate [PF₆]⁻, trifluoromethanesulfonate [OTf]⁻, and bis(trifluoromethylsulfonyl)imide [TFSI]⁻, with a cation of 1-butyl-3-methylimidazolium [bmim]⁺ in the imidazolium-based RTILs/UiO-66 composites is investigated toward the CO₂ adsorption performance at low temperature and pressure.

■ EXPERIMENTAL SECTION

Materials

All materials were commercially available and employed without further purification: 1-butyl-3-methylimidazolium tetrafluoroborate ([bmim][BF₄], ≥98% purity Merck, Germany), 1-butyl-3-methylimidazolium hexafluorophosphate ([bmim][PF₆], 97% purity Merck, Germany), 1-butyl-3-methylimidazolium trifluoromethanesulfonate ([bmim][OTf], 97% purity Merck, Germany), 1-butyl-3-methylimidazolium bis(trifluoromethylsulfonyl)imide ([bmim][TFSI], ≥98% purity Merck, Germany), zirconium(IV) chloride (ZrCl₄, ≥98% purity Merck, Germany), 1,4-benzenedicarboxylic acid (H₂BDC, ≥98% purity Merck, Germany), *N,N*-dimethylformamide (DMF, ≥99.8% purity Merck, Germany), chloroform (≥99% purity Merck, Germany), and acetone (≥99.8% purity Merck, Germany).

Instrumentation

Phase identification of samples was collected by powder X-ray diffractometer (PXRD, Rigaku MiniFlex 600) in the range of 2θ from 5 to 50° using a source of radiation of Cu-Kα and wavelength of 1.540593 Å. The functional group coordination of samples was obtained by Fourier-transformed infrared spectrometer (FTIR,

Bruker Alpha series) with a splitter of ZnSe beam in the wavenumber range from 500 to 4000 cm^{-1} using KBr to disperse the samples. The thermal stability of samples was performed on a thermogravimetric analysis instrument (TGA, Hitachi STA7300) by heating the samples on an aluminium pan in the range of temperature from 30 to 500 $^{\circ}\text{C}$ with 20 $^{\circ}\text{C cm}^{-1}$ heating rate under nitrogen. Sample pore analysis was carried out using a nitrogen physisorption measurements instrument at 77 K (Quantachrome NOVA 2200e). CO_2 adsorption performance of samples was conducted using CO_2 adsorption measurements instrument at 273 K (MicrotracBel BELSORP-max). Before nitrogen physisorption and CO_2 adsorption measurements, UiO-66 and RTILs/UiO-66 composites samples were degassed at 160 and 105 $^{\circ}\text{C}$ for 6 h under a vacuum, respectively.

Procedure

Synthesis of UiO-66

UiO-66 was synthesized using a conventional heating method, slightly modified from the previous reports [20,23]. As much as 0.233 g of ZrCl_4 (1.0 mmol) was mixed with 10 mL of DMF in a nitrogen-charged glove box and then sonicated for 10 min at room temperature. An amount of 0.166 g of 1,4-benzenedicarboxylic acid (H_2BDC , 1.0 mmol) and 0.1 mL of acetic acid 10% (v/v) were added to the mixture, and then sonicated again for 20 min. The mixture was put into the oven and heated at 120 $^{\circ}\text{C}$ for 1 d. The reaction solvent was decanted from the solid product after cooling down. The washing process was conducted by soaking the solid product in 5 mL of chloroform, decanted, and repeated three times. After that, the solid product was filtered at room temperature and then degassed at 160 $^{\circ}\text{C}$ for 6 h under a vacuum.

Synthesis of RTILs/UiO-66 composites

Imidazolium-based RTILs/UiO-66 composites with 30% loading of RTILs were synthesized using the wet impregnation method, slightly modified from the previous report [24]. The first composite was prepared by room temperature stirring of 15 mL of acetone and 0.15 g of [bmim][BF_4] for 1 h under air. The mixture was added with 0.35 g of activated UiO-66, and then continuously stirred for 6 h. The solid product was filtered at room temperature,

and then degassed at 105 $^{\circ}\text{C}$ for 6 h under a vacuum. Other imidazolium-based RTILs/UiO-66 composites with [bmim][PF_6], [bmim][OTf], and [bmim][TFSI] were also synthesized according to this procedure.

RESULTS AND DISCUSSION

The incorporation of imidazolium-based RTILs series, *i.e.*, [bmim][BF_4], [bmim][PF_6], [bmim][OTf], and [bmim][TFSI] denoted as Im-B, Im-P, Im-O, and Im-T, respectively, into zirconium-based MOFs of UiO-66 was carried out by wet impregnation method at room temperature under air. The four RTILs/UiO-66 composites hereafter were denoted as Im-B/UiO-66, Im-P/UiO-66, Im-O/UiO-66, and Im-T/UiO-66. Solvated RTILs/UiO-66 composites show consistency with the characteristic diffraction peaks of pristine UiO-66 at 2θ of 7.43 and 8.55 $^{\circ}$ corresponding to reflection planes of (111) and (200), respectively, in agreement with the previous studies [25-26], as presented in the PXRD patterns (Fig. 1). Furthermore, there is no decrease in the relative intensity of UiO-66 in comparison to Im-B/UiO-66, Im-P/UiO-66, Im-O/UiO-66, and Im-T/UiO-66 composites explain that the incorporation of imidazolium-based RTILs into UiO-66 does not alter its pristine structure, following previous reports on [bmim][BF_4]/CuBTC and [bmim][PF_6]/ZIF-8 composites [18,24]. PXRD patterns of all RTILs/UiO-66 composites also remain consistent after degassing (Fig. 2).

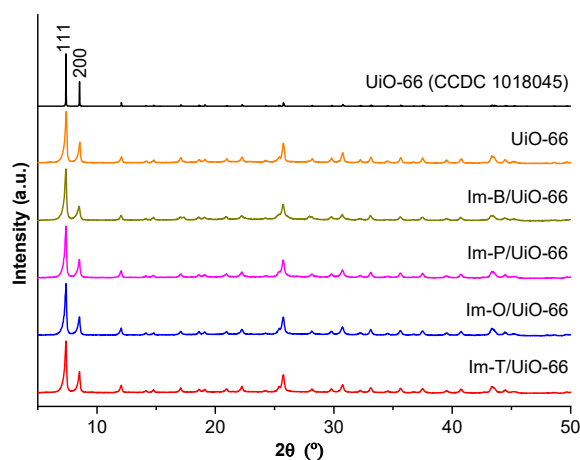


Fig 1. PXRD patterns of UiO-66 (orange), Im-B/UiO-66 (dark yellow), Im-P/UiO-66 (magenta), Im-O/UiO-66 (blue), and Im-T/UiO-66 (red)

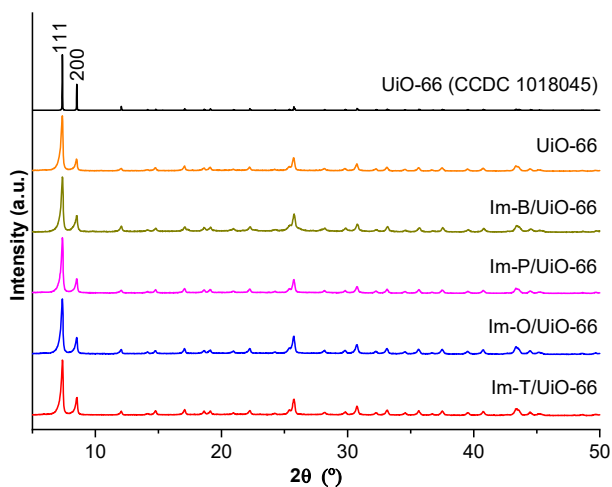


Fig 2. PXRD patterns of activated UiO-66 (orange), Im-B/UiO-66 (dark yellow), Im-P/UiO-66 (magenta), Im-O/UiO-66 (blue), and Im-T/UiO-66 (red)

Fig. 3 displays the FTIR spectra of pristine UiO-66 and H₂BDC ligand. The peaks at 1682 and 1424 cm⁻¹ correspond to asymmetric and symmetric stretching bands of the carboxyl group of H₂BDC. The formation of Zr₆O₄(OH)₄(CO₂)₁₂ clusters of UiO-66 is confirmed by the weakening of carboxyl groups vibrations of H₂BDC, from 1682 and 1424 cm⁻¹ in the free ligand to 1580 and 1400 cm⁻¹ in the UiO-66, in agreement with the previous study [25]. However, the significant changes in the peak positions of UiO-66 upon the incorporation with imidazolium-based RTILs were hardly observed from the FTIR spectra from 500 to 1800 cm⁻¹ range of wavenumber (Fig. 4). There is no shifting from the μ₃-O bridging bond peak of UiO-66 at 667 cm⁻¹ explaining the direct interactions between imidazolium-based RTILs and metal nodes of UiO-66 in the Im-B/UiO-66, Im-P/UiO-66, Im-O/UiO-66, and Im-T/UiO-6 composites were not strong, similar to reported [bmim][MeSO₄]/UiO-66 composite [25]. Furthermore, the stretching vibrations of the carboxyl group and bending vibration of -CH of UiO-66 also remain the same after incorporation, confirming the lack of interactions with RTILs. In this case, water as impurities in RTILs and unremoved synthesis solvents inside the pore of MOFs likely contribute to the weak interactions between the two components [13,16].

Thermogravimetric analysis (TGA) curves of Im-B/UiO-66, Im-P/UiO-66, Im-O/UiO-66, and Im-T/UiO-66

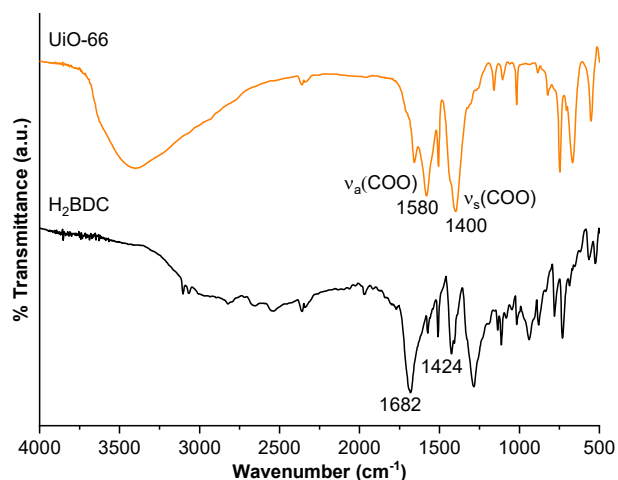


Fig 3. FTIR spectra of UiO-66 (orange) and H₂BDC ligand (black)

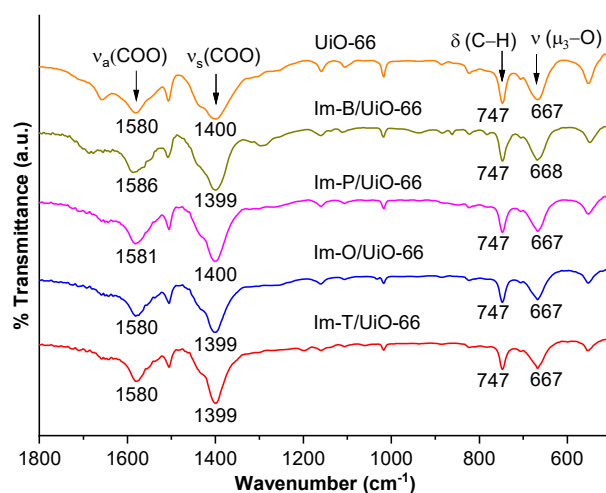


Fig 4. FTIR spectra of UiO-66 (orange), Im-B/UiO-66 (dark yellow), Im-P/UiO-66 (magenta), Im-O/UiO-66 (blue), and Im-T/UiO-66 (red)

composites demonstrate a more extensive weight loss than pristine UiO-66 upon heating to 500 °C under nitrogen (Fig. 5). Im-O/UiO-66 and Im-T/UiO-66 composites generate an identical decomposition temperature, followed by the Im-P/UiO-66 composite, which is similar, but the Im-B/UiO-66 composite exhibits a different trend. This result may also be influenced by the hydrophilicity property of the imidazolium-based RTILs, in which [bmim][OTf], [bmim][TFSI], and [bmim][PF₆] are hydrophobic, while [bmim][BF₄] is hydrophilic [27]. The first weight loss of about 13.6, 23, 24.5, and 24.3% are observed below 100 °C, corresponding

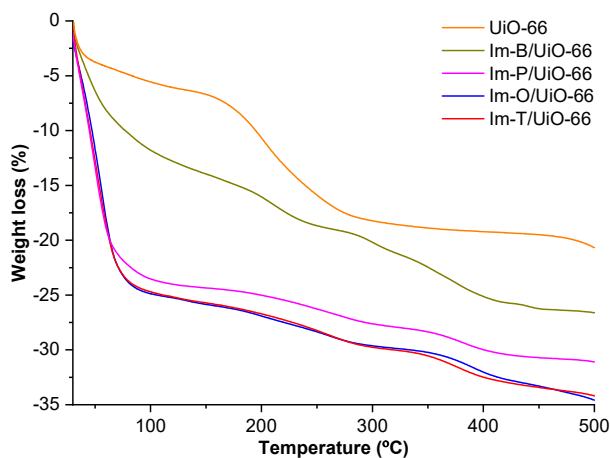


Fig 5. TGA curves of UiO-66 (orange), Im-B/UiO-66 (dark yellow), Im-P/UiO-66 (magenta), Im-O/UiO-66 (blue), and Im-T/UiO-66 (red)

on the removal of acetone molecules (RTILs impregnation solvent) for Im-B/UiO-66, Im-P/UiO-66, Im-O/UiO-66, and Im-T/UiO-66 composites, respectively. At the same temperature, the Im-B/UiO-66 composite shows less acetone removal, indicating the composite is more polar than other RTILs/UiO-66 composites. The second weight loss from 100 to 300 °C is ascribed to the removal of moisture and DMF molecules (UiO-66 synthesis solvent). Meanwhile, the Im-B/UiO-66 composite shows two weight loss steps up to 300 °C. The weight loss from 300 to 400 °C corresponds to the decomposition of [bmim][BF₄], [bmim][PF₆], [bmim][OTf], and [bmim][TFSI] from the RTILs/UiO-66 composites. Furthermore, the frameworks of UiO-66 start to collapse above 450 °C for pristine MOFs, above 400 °C for the Im-B/UiO-66 composite, and for other composites above 350 °C, referring to the partial loss of BDC linkers. Accordingly, incorporating several imidazolium-based RTILs into UiO-66 alleviates the pristine thermal stability, illustrating the interaction of both components in the composites, consistent with previous studies [24,28].

Table 1. Pore analysis of UiO-66 and RTILs/UiO-66 composites

Sample	BET surface area (m ² g ⁻¹)	Total pore volume (cm ³ g ⁻¹)
UiO-66	883	0.543
Im-B/UiO-66	722	0.442
Im-P/UiO-66	1100	0.645
Im-O/UiO-66	1043	0.665
Im-T/UiO-66	1104	0.677

Nitrogen physisorption measurements at 77 K reveal type I adsorption isotherm, indicating that pristine UiO-66 and all RTILs/UiO-66 composites are microporous materials (Fig. 6). The difference in hydrophilicity property of imidazolium-based RTILs likely influences the nitrogen uptake of the RTILs/UiO-66 composites. Im-B/UiO-66, Im-P/UiO-66, Im-O/UiO-66, and Im-T/UiO-66 composites exhibit nitrogen uptake of 285.62, 412.44, 429.69, and 437.50 cm³ g⁻¹, respectively, while for pristine UiO-66 is 350.87 cm³ g⁻¹. The Im-B/UiO-66 composite with hydrophilic RTILs shows a decrement in pore analysis values compared to pristine UiO-66, while Im-P/UiO-66, Im-O/UiO-66, and Im-T/UiO-66 composites with hydrophobic RTILs possess larger values (Table 1). This result trend is the opposite of several previous studies, in which incorporating RTILs reduces pore analysis values of pristine MOFs even though both components have similar hydrophilicity [19,24]. The incomplete removal of trapped DMF molecules from the frameworks of UiO-66 during degassing process may limit the accessibility of

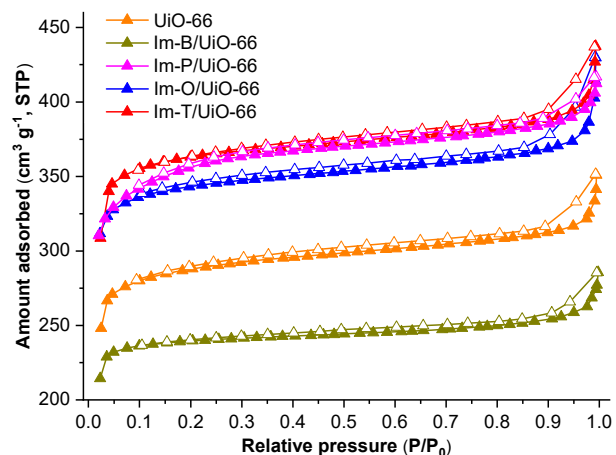


Fig 6. N₂ physisorption isotherms of UiO-66 (orange), Im-B/UiO-66 (dark yellow), Im-P/UiO-66 (magenta), Im-O/UiO-66 (blue), and Im-T/UiO-66 (red)

nitrogen due to pore blockage, which generates MOFs with a low Brunauer-Emmett-Teller (BET) surface area [29]. Conversely, the enhanced BET surface area observed in the Im-P/UiO-66, Im-O/UiO-66, and Im-T/UiO-66 composites can be assigned to the additional role of acetone as the exchange solvent for DMF from the structure of UiO-66, aside as the impregnation solvent for RTILs. Therefore, instead of prolonging the degassing process of MOFs using the thermal activation method, employing acetone for the washing process of MOFs can be an alternative way to optimize the pore analysis values and minimize the structural damage of MOFs [30].

CO₂ adsorption performances of pristine UiO-66, Im-B/UiO-66, Im-P/UiO-66, Im-O/UiO-66, and Im-T/UiO-66 composites measured at 273 K exhibit a similar result trend as observed in TGA measurements, with only Im-B/UiO-66 composite displaying an opposite behavior compared to other composites. Incorporating imidazolium-based RTILs enhances CO₂ uptake of UiO-66 in the RTILs/UiO-66 composites as presented in the CO₂ adsorption isotherms (Fig. 7). The CO₂ uptake amounts of Im-B/UiO-66, Im-P/UiO-66, Im-O/UiO-66, and Im-T/UiO-66 composites are 28.016, 67.647, 75.965, and 72.300 cm³ g⁻¹, respectively, while pristine UiO-66 is 51.382 cm³ g⁻¹. Although some previous simulation and experimental studies reported the improvement in CO₂ uptake of MOFs upon the incorporation of RTILs at low pressure, such as in RTILs/ZIF-8 [13,18], RTILs/MIL-100(Fe) [19], and RTILs/CuBTC composites [31], the reduced CO₂ uptake was declared in RTILs/UiO-66 and RTILs/NU-1000 composites [32]. The shrinkage in BET surface area of UiO-66 upon the incorporation of [bmim][BF₄] from 883 to 722 m² g⁻¹ yields a less number of adsorption sites in the Im-B/UiO-66 composite leading to a low CO₂ uptake, similar to a previous report on [bmim][BF₄]/CuBTC composite [24]. In addition, a low CO₂ uptake in Im-B/UiO-66 composite is presumably influenced by the difference in polarity from [BF₄]⁻ anion compared to other anions, making it less preferable for a polar gas like CO₂ [28], following TGA measurement results.

Nevertheless, the pore analysis values of the four imidazolium-based RTILs/UiO-66 composites are not the

main factor determining their CO₂ uptake when the CO₂ adsorption performances are measured at low pressure. For instance, the Im-T/UiO-66 composite possesses the largest BET surface area, yet the highest CO₂ uptake is found in the Im-O/UiO-66 composite. Aside from the BET surface area, the solubility of CO₂ in RTILs also holds a prominent role in CO₂ uptake. Aki et al. [33] found that the type of anion in imidazolium-based RTILs strongly influences the CO₂ solubility, in which anions containing fluoroalkyl group ([TFSI]⁻, [OTf]⁻) generated a higher CO₂ uptake compared to inorganic fluorinated anions ([PF₆]⁻, [BF₄]⁻). Muldoon et al. [34] revealed that the solubility of CO₂ was improved following the increase of fluoroalkyl chains in either cation or anion of RTILs. Even though [TFSI]⁻ anion contains more fluoroalkyl group than [OTf]⁻ anion, the Im-T/UiO-66 composite exhibits a lower CO₂ uptake compared to the Im-O/UiO-66 composite, which is likely

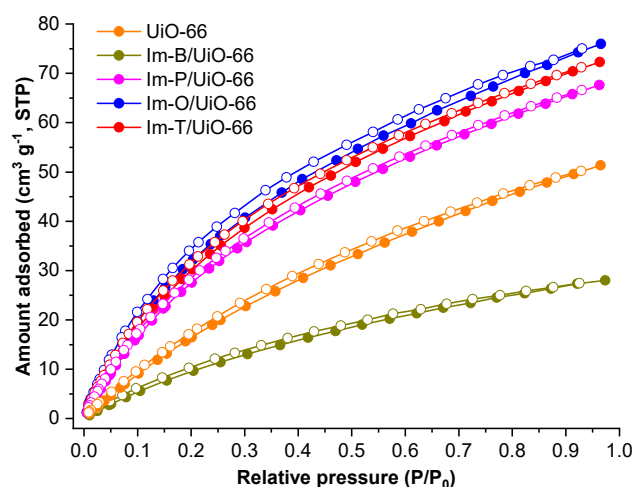


Fig 7. CO₂ adsorption isotherms of UiO-66 (orange), Im-B/UiO-66 (dark yellow), Im-P/UiO-66 (magenta), Im-O/UiO-66 (blue), and Im-T/UiO-66 (red)

Table 2. Cation and anion radii of imidazolium-based RTILs obtained from reference [35]

Ion	Ionic radius (Å)
[bmim] ⁺	4.57
[BF ₄] ⁻	3.37
[PF ₆] ⁻	3.58
[OTf] ⁻	3.89
[TFSI] ⁻	4.44

attributed to the larger ionic radius of [TFSI]⁻ than [OTf]⁻, as presented in Table 2. Therefore, aside from the increased fluorination number of the anion, the size of anion may also influence the solubility of CO₂ resulting in the CO₂ uptake order of Im-O/UiO-66 > Im-T/UiO-66 > Im-P/UiO-66 > Im-B/UiO-66.

■ CONCLUSION

Imidazolium-based RTILs/UiO-66 composites with 30% loading of RTILs, *i.e.*, [bmim][BF₄]/UiO-66, [bmim][PF₆]/UiO-66, [bmim][OTf]/UiO-66, and [bmim][TFSI]/UiO-66 were successfully synthesized by wet impregnation method under air. The enhanced CO₂ uptake measured at low pressure (100 kPa) was observed upon the incorporation of [bmim][PF₆], [bmim][OTf], and [bmim][TFSI] into UiO-66, while [bmim][BF₄] showed the reduced CO₂ uptake compared to pristine UiO-66. The BET surface area of [bmim][BF₄]/UiO-66, [bmim][PF₆]/UiO-66, [bmim][OTf]/UiO-66, and [bmim][TFSI]/UiO-66 composites was 722, 1100, 1043, and 1104 m² g⁻¹, respectively. However, the CO₂ uptake amounts of [bmim][BF₄]/UiO-66, [bmim][PF₆]/UiO-66, [bmim][OTf]/UiO-66, and [bmim][TFSI]/UiO-66 composites were 28.016, 67.647, 75.965, and 72.300 cm³ g⁻¹, respectively. These results explained that besides the BET surface area, the properties of the anion of RTILs, such as fluorination number, polarity, and ionic radii, might also influence the CO₂ adsorption performance of imidazolium-based RTILs/UiO-66 composites at low pressure, following the order: [bmim][OTf]/UiO-66 > [bmim][TFSI]/UiO-66 > [bmim][PF₆]/UiO-66 > [bmim][BF₄]/UiO-66. Furthermore, the CO₂ adsorption performances at different temperatures and reusability of these imidazolium-based RTILs/UiO-66 composites must be investigated for future application.

■ ACKNOWLEDGMENTS

This study was funded by Institut Teknologi Bandung (ITB) through the Research Program 2020 (2I/I1.C01/PL/2020). The authors thank Prof. Satoshi Horike and Dr. Masakazu Higuchi for the CO₂ adsorption measurements at the Institute for Integrated Cell-Material Sciences (iCeMS), Kyoto University Institute for Advanced Study (KUIAS), Japan.

■ AUTHOR CONTRIBUTIONS

Conceptualization: Laela Mukaromah and Andi Haryanto, methodology: Laela Mukaromah and Andi Haryanto, data acquisition: Laela Mukaromah and Andi Haryanto, data analysis: Laela Mukaromah, Andi Haryanto, and Aep Patah, funding acquisition: Aep Patah and Yessi Permana, resources: Aep Patah and Yessi Permana, writing-original draft: Laela Mukaromah, writing-review and editing: Laela Mukaromah, Andi Haryanto, and Aep Patah. All authors have agreed to the final version of this manuscript.

■ REFERENCES

- [1] Sylvia, N., Fitriani, F., Dewi, R., Mulyawan, R., Muslim, A., Husin, H., Yunardi, Y., and Reza, M., 2021, Characterization of bottom ash waste adsorbent from palm oil plant boiler burning process to adsorb carbon dioxide in a fixed bed column, *Indones. J. Chem.*, 21 (6), 1454–1462.
- [2] Wardani, A.R.K., and Widiastuti, N., 2016, Synthesis of zeolite-X supported on glasswool for CO₂ capture material: Variation of immersion time and NaOH concentration at glasswool activation, *Indones. J. Chem.*, 16 (1), 1–7.
- [3] Li, B., Wen, H.M., Yu, Y., Cui, Y., Zhou, W., Chen, B., and Qian, G., 2018, Nanospace within metal-organic frameworks for gas storage and separation, *Mater. Today Nano*, 2, 21–49.
- [4] Chen, Y., Wu, H., Liu, Z., Sun, X., Xia, Q., and Li, Z., 2018, Liquid-assisted mechanochemical synthesis of copper based MOF-505 for the separation of CO₂ over CH₄ or N₂, *Ind. Eng. Chem. Res.*, 57 (2), 703–709.
- [5] Belmabkhout, Y., Bhatt, P.M., Adil, K., Pillai, R.S., Cadiau, A., Shkurenko, A., Maurin, G., Gongping, L., Koros, W.J., and Eddaoudi, M., 2018, Natural gas upgrading using a fluorinated MOF with tuned H₂S and CO₂ adsorption selectivity, *Nat. Energy*, 3 (12), 1059–1066.
- [6] Sun, T., Ren, X., Hu, J., and Wang, S., 2014, Expanding pore size of Al-BDC metal-organic frameworks as a way to achieve high adsorption

- selectivity for CO₂/CH₄ separation, *J. Phys. Chem. C*, 118 (29), 15630–15639.
- [7] Gao, W., Zheng, W., Sun, W., and Zhao, L., 2022, Understanding the effective capture of H₂S/CO₂ from natural gas using ionic liquid@MOF composites, *J. Phys. Chem. C*, 126 (46), 19872–19882.
- [8] Sumida, K., Rogow, D.L., Mason, J.A., McDonald, T.M., Bloch, E.D., Herm, Z.R., Bae, T.H., and Long, J.R., 2012, Carbon dioxide capture in metal-organic frameworks, *Chem. Rev.*, 112 (2), 724–781.
- [9] Yoon, H.C., Rallapalli, P.B.S., Beum, H.T., Han, S.S., and Kim, J.N., 2018, Hybrid postsynthetic functionalization of tetraethylenepentamine onto MIL-101(Cr) for separation of CO₂ from CH₄, *Energy Fuels*, 32 (2), 1365–1373.
- [10] Kitao, T., Zhang, Y., Kitagawa, S., Wang, B., and Uemura, T., 2017, Hybridization of MOFs and polymers, *Chem. Soc. Rev.*, 46 (11), 3108–3133.
- [11] Furukawa, S., Reboul, J., Diring, S., Sumida, K., and Kitagawa, S., 2014, Structuring of metal-organic frameworks at the mesoscopic/macroscale, *Chem. Soc. Rev.*, 43 (16), 5700–5734.
- [12] Li, H., Wang, K., Sun, Y., Lollar, C.T., Li, J., and Zhou, H.C., 2018, Recent advances in gas storage and separation using metal-organic frameworks, *Mater. Today*, 21 (2), 108–121.
- [13] Zeeshan, M., Nozari, V., Yagci, M.B., Isik, T., Unal, U., Ortalan, V., Keskin, S., and Uzun, A., 2018, Core-shell type ionic liquid/metal organic framework composite: An exceptionally high CO₂/CH₄ selectivity, *J. Am. Chem. Soc.*, 140 (32), 10113–10116.
- [14] Flaig, R.W., Osborn Popp, T.M., Fracaroli, A.M., Kapustin, E.A., Kalmutzki, M.J., Altamimi, R.M., Fathieh, F., Reimer, J.A., and Yaghi, O.M., 2017, The chemistry of CO₂ capture in an amine-functionalized metal-organic framework under dry and humid conditions, *J. Am. Chem. Soc.*, 139 (35), 12125–12128.
- [15] Marti, A.M., Venna, S.R., Roth, E.A., Culp, J.T., and Hopkinson, D.P., 2018, Simple fabrication method for mixed matrix membranes with in situ MOF growth for gas separation, *ACS Appl. Mater. Interfaces*, 10 (29), 24784–24790.
- [16] Zhang, S., Zhang, J., Zhang, Y., and Deng, Y., 2017, Nanoconfined ionic liquids, *Chem. Rev.*, 117 (10), 6755–6833.
- [17] Zeng, S., Zhang, X., Bai, L., Zhang, X., Wang, H., Wang, J., Bao, D., Li, M., Liu, X., and Zhang, S., 2017, Ionic-liquid-based CO₂ capture systems: Structure, interaction and process, *Chem. Rev.*, 117 (14), 9625–9673.
- [18] Kinik, F.P., Altintas, C., Balci, V., Koyuturk, B., Uzun, A., and Keskin, S., 2016, [BMIM][PF₆] Incorporation doubles CO₂ selectivity of ZIF-8: Elucidation of interactions and their consequences on performance, *ACS Appl. Mater. Interfaces*, 8 (45), 30992–31005.
- [19] Oliveira, L.T., Gonçalves, R.V., Gonçalves, D.V., de Azevedo, D.C.S., and de Lucena, S.M.P., 2019, Superior performance of mesoporous MOF MIL-100 (Fe) impregnated with ionic liquids for CO₂ adsorption, *J. Chem. Eng. Data*, 64 (5), 2221–2228.
- [20] Cavka, J.H., Jakobsen, S., Olsbye, U., Guillou, N., Lamberti, C., Bordiga, S., and Lillerud, K.P., 2008, A new zirconium inorganic building brick forming metal organic frameworks with exceptional stability, *J. Am. Chem. Soc.*, 130 (42), 13850–13851.
- [21] Pirzadeh, K., Esfandiari, K., Ghoreyshi, A.A., and Rahimnejad, M., 2020, CO₂ and N₂ adsorption and separation using aminated UiO-66 and Cu₃(BTC)₂: A comparative study, *Korean J. Chem. Eng.*, 37 (3), 513–524.
- [22] Sun, Y., Huang, H., Vardhan, H., Aguila, B., Zhong, C., Perman, J.A., Al-Enizi, A.M., Nafady, A., and Ma, S., 2018, Facile approach to graft ionic liquid into MOF for improving the efficiency of CO₂ chemical fixation, *ACS Appl. Mater. Interfaces*, 10 (32), 27124–27130.
- [23] Øien, S., Wragg, D., Reinsch, H., Svelle, S., Bordiga, S., Lamberti, C., and Lillerud, K.P., 2014, Detailed structure analysis of atomic positions and defects in zirconium metal-organic frameworks, *Cryst. Growth Des.*, 14 (11), 5370–5372.
- [24] Sezginel, K.B., Keskin, S., and Uzun, A., 2016, Tuning the gas separation performance of CuBTC

- by ionic liquid incorporation, *Langmuir*, 32 (4), 1139–1147.
- [25] Durak, Ö., Kulak, H., Kavak, S., Polat, H.M., Keskin, S., and Uzun, A., 2020, Towards complete elucidation of structural factors controlling thermal stability of IL/MOF composites: Effects of ligand functionalization on MOFs, *J. Phys.: Condens. Matter*, 32 (48), 484001.
- [26] Kavak, S., Kulak, H., Polat, H.M., Keskin, S., and Uzun, A., 2020, Fast and selective adsorption of methylene blue from water using [BMIM][PF₆]-incorporated UiO-66 and NH₂-UiO-66, *Cryst. Growth Des.*, 20 (6), 3590–3595.
- [27] Huddleston, J.G., Visser, A.E., Reichert, W.M., Willauer, H.D., Broker, G.A., and Rogers, R.D., 2001, Characterization and comparison of hydrophilic and hydrophobic room temperature ionic liquids incorporating the imidazolium cation, *Green Chem.*, 3 (4), 156–164.
- [28] Ferreira, T.J., Ribeiro, R.P.P.L., Mota, J.P.B., Rebelo, L.P.N., Esperança, J.M.S.S., and Esteves, I.A.A.C., 2019, Ionic liquid-impregnated metal-organic frameworks for CO₂/CH₄ separation, *ACS Appl. Nano Mater.*, 2 (12), 7933–7950.
- [29] Arrozi, U.S.F., Wijaya, H.W., Patah, A., and Permana, Y., 2015, Efficient acetalization of benzaldehydes using UiO-66 and UiO-67: Substrates accessibility or Lewis acidity of zirconium, *Appl. Catal., A*, 506, 77–84.
- [30] Kim, H.K., Yun, W.S., Kim, M.B., Kim, J.Y., Bae, Y.S., Lee, J.D., and Jeong, N.C., 2015, A chemical route to activation of open metal sites in the copper-based metal-organic framework materials HKUST-1 and Cu-MOF-2, *J. Am. Chem. Soc.*, 137 (31), 10009–10015.
- [31] Vicent-Luna, J.M., Gutiérrez-Sevillano, J.J., Anta, J.A., and Calero, S., 2013, Effect of room-temperature ionic liquids on CO₂ separation by a Cu-BTC metal-organic framework, *J. Phys. Chem. C*, 117 (40), 20762–20768.
- [32] Xia, X., Hu, G., Li, W., and Li, S., 2019, Understanding reduced CO₂ uptake of ionic liquid/metal-organic framework (IL/MOF) composites, *ACS Appl. Nano Mater.*, 2 (9), 6022–6029.
- [33] Aki, S.N.V.K., Mellein, B.R., Saurer, E.M., and Brennecke, J.F., 2004, High-pressure phase behavior of carbon dioxide with imidazolium-based ionic liquids, *J. Phys. Chem. B*, 108 (52), 20355–20365.
- [34] Muldoon, M.J., Aki, S.N.V.K., Anderson, J.L., Dixon, J.K., and Brennecke, J.F., 2007, Improving carbon dioxide solubility in ionic liquids, *J. Phys. Chem. B*, 111 (30), 9001–9009.
- [35] Kazemiabnavi, S., Zhang, Z., Thornton, K., and Banerjee, S., 2016, Electrochemical stability window of imidazolium-based ionic liquids as electrolytes for lithium batteries, *J. Phys. Chem. B*, 120 (25), 5691–5702.

Supplementary Data

This supplementary data is a part of a paper entitled "Determination of Heavy Metal Concentrations in Household Dusts in Irbid and Mafrqa Cities, Jordan".

Table S1. Statistical parameters of heavy metals concentrations (mg/kg dry weight) in the house dust samples collected from Irbid and Mafrqa cities in the all sampling sites during the summer season

Sample number	Latitude (°N)	Longitude (°E)	Pb	Cd	Zn	Cu	Fe	Cr
S1	32.574722	35.860181	58.0	4.00	436	107	4553	38.0
S2	32.581111	35.868611	71.0	4.00	483	126	6714	38.0
S3	32.575059	35.869444	125	5.00	352	46.0	12653	47.0
S4	32.573699	35.867696	121	11.0	403	106	5179	32.0
S5	32.571111	35.871389	88.0	12.0	624	339	7597	56.0
S6	32.568836	35.862295	45.0	13.0	497	115	11570	58.0
S7	32.577611	35.870403	85.0	6.00	294	67.0	6090	38.0
S8	32.571553	35.871961	150	14.0	406	90.0	9170	44.0
S9	32.573916	35.873322	73.0	14.0	386	105	5721	41.0
S10	32.569497	35.873491	92.0	4.00	146	29.0	7013	31.0
S11	32.569249	35.872572	86.0	11.0	686	42.0	7643	33.0
S12	32.571633	35.871317	110	11.0	298	89.0	6304	35.0
S13	32.572258	35.867919	75.0	11.0	379	70.0	8294	31.0
S14	32.580446	35.869213	92.0	11.0	334	83.0	8683	35.0
S15	32.579514	35.868511	82.0	5.00	147	40.0	31062	110
S16	32.552965	35.873681	63.0	7.00	439	114	5968	39.0
S17	32.559511	35.878446	79.0	7.00	471	92.0	10037	71.0
S18	32.557287	35.872729	96.0	10.0	533	143	11270	54.0
S19	32.556345	35.876582	66.0	11.0	365	112	7297	47.0
S20	32.555442	35.864659	57.0	15.0	346	84.0	6774	35.0
S21	32.553504	35.880375	56.0	15.0	412	150	3907	23.0
S22	32.550137	35.878065	57.0	14.0	447	137	5185	38.0
S23	32.557719	35.879299	76.0	15.0	337	58.0	5346	23.0
S24	32.558713	35.861175	74.0	5.00	378	79.0	4417	24.0
S25	32.561078	35.861912	72.0	5.00	465	91.0	4171	27.0
S26	32.562808	35.880387	44.0	9.00	379	112	6275	32.0
S27	32.560391	35.875832	72.0	15.0	243	34.0	8829	32.0
S28	32.550343	35.874026	66.0	15.0	376	59.0	8574	38.0
S29	32.551565	35.857388	65.0	16.0	220	39.0	8859	37.0
S30	32.552785	35.859018	65.0	9.00	397	74.0	9129	42.0
S31	32.534522	35.895116	44.0	9.00	379	112	6275	32.0
S32	32.534872	35.893478	40.0	12.0	382	91.0	4564	33.0
S33	32.530166	35.902633	41.0	15.0	159	40.0	1626	18.0
S34	32.541122	35.893572	45.0	14.0	344	124	3315	23.0
S35	32.534218	35.898213	36.0	13.0	238	52.0	2858	22.0
S36	32.535929	35.895832	48.0	14.0	414	57.0	6866	38.0

Sample number	Latitude (°N)	Longitude (°E)	Pb	Cd	Zn	Cu	Fe	Cr
S37	32.540952	35.887877	44.0	14.0	392	66.0	9091	24.0
S38	32.540994	35.888351	62.0	6.00	388	80.0	6001	29.0
S39	32.543681	35.884583	55.0	11.0	387	83.0	5115	32.0
S40	32.539738	35.898522	81.0	13.0	363	90.0	3717	24.0
S41	32.543463	35.891536	60.0	4.00	340	70.0	9642	390
S42	32.536347	35.903113	44.0	14.0	449	162	6882	38.0
S43	32.531357	35.906495	55.0	17.0	335	53.0	10142	46.0
S44	32.536454	35.887964	32.0	12.0	493	76.0	5834	38.0
S45	32.472345	36.052888	70.0	16.0	305	87.0	4977	24.0
S46	32.516984	35.941786	103	17.0	582	127	11177	41.0
S47	32.526423	35.915228	120	12.0	341	73.0	8171	34.0
S48	32.433726	36.097648	54.0	16.0	338	56.0	6060	29.0
S49	32.389108	36.199549	53.0	12.0	300	48.0	10181	40.0
S50	32.416413	36.169941	52.0	12.0	228	45.0	5395	27.0
S51	32.473953	36.056218	74.0	7.00	123	31.0	23649	80.0
S52	32.420467	36.143563	46.0	6.00	269	60.0	5112	24.0
S53	32.467307	36.059183	52.0	5.00	146	31.0	19008	72.0
S54	32.513784	35.989306	99.0	6.00	158	32.0	17766	86.0
S55	32.387311	36.202722	75.0	12.0	251	164	10232	40.0
S56	32.409183	36.164821	49.0	9.00	267	74.0	3958	22.0
S57	32.370501	36.209249	58.0	11.0	500	59.0	8753	34.0
S58	32.386251	36.215979	54.0	14.0	230	29.0	6849	36.0
S59	32.340279	36.209114	49.0	8.00	318	131	6087	38.0
S60	32.335466	36.201761	37.0	10.0	290	38.0	3022	22.0
S61	32.338781	36.210434	120	14.0	308	62.0	6477	34.0
S62	32.341725	36.207361	60.0	12.0	401	134	5589	29.0
S63	32.343582	36.208301	52.0	11.0	391	79.0	3825	18.0
S64	32.339066	36.206194	35.0	4.00	460	123	4644	27.0
S65	32.339573	36.205621	73.0	12.0	392	66.0	3380	22.0
S66	32.344681	36.206812	62.0	11.0	538	68.0	8976	52.0
S67	32.335064	36.208331	40.0	7.00	470	135	7203	32.0
S68	32.337331	36.201253	37.0	13.0	500	111	4958	41.0
S69	32.338586	36.204705	52.0	4.00	383	66.0	6251	11.0
S70	32.337967	36.207832	76.0	11.0	393	71.0	5401	29.0
S71	32.341815	36.209456	78.0	7.00	465	150	13194	47.0
S72	32.333439	36.205776	49.0	12.0	308	58.0	3693	23.0
S73	32.343119	36.208328	72.0	7.00	305	52.0	7018	34.0
S74	32.346371	36.214957	55.0	6.00	338	6.00	11486	45.0
S75	32.349472	36.207892	78.0	8.00	394	60.0	6808	36.0
S76	32.349241	36.214203	60.0	10.0	288	89.0	4223	18.0
S77	32.350647	36.207949	44.0	9.00	320	53.0	3876	24.0
S78	32.347015	36.212107	71.0	11.0	412	69.0	4558	32.0
S79	32.357254	36.209631	69.0	14.0	324	58.0	8345	42.0
S80	32.349022	36.203043	48.0	13.0	362	85.0	5358	25.0

Sample number	Latitude (°N)	Longitude (°E)	Pb	Cd	Zn	Cu	Fe	Cr
S81	32.345164	36.208945	69.0	13.0	317	55.0	7258	38.0
S82	32.358018	36.206916	58.0	16.0	322	46.0	10270	46.0
S83	32.350711	36.206179	70.0	15.0	635	73.0	4653	23.0
S84	32.345784	36.212291	71.0	14.0	302	43.0	7383	39.0
S85	32.352986	36.201241	80.0	15.0	359	79.0	9915	62.0
S86	32.346112	36.201142	60.0	11.0	383	75.0	8586	49.0
S87	32.363729	36.206542	68.0	16.0	283	63.0	12022	46.0
S88	32.358015	36.203092	55.0	5.00	425	82.0	5619	34.0
Average			66.8	10.8	366	81.6	7586	37.2
SD			22.4	3.75	108	43.9	4304	15.4
Median			64.0	11.0	371	73.5	6744	35.0
C.V. (%)			33.0	35.0	29.0	54.0	57.0	41.0
Min.			32.0	4.00	123	6.00	1626	11.0
Max.			150	17.0	686	339	31062	110

Table S2. Statistical parameters of heavy metals concentrations (mg/Kg dry weight) in the house dust samples collected from Irbid and Mafraq cities in the all sampling sites during the winter season

Sample number	Corresponding summer sampling site	Type of heating system	Pb	Cd	Zn	Cu	Fe	Cr	Co	Ni	Mn
W1	S1	Gas	67.0	3.00	189	85.4	659	14.0	17.4	48.2	67.1
W2	S4	Gas	105	11.0	482	218	4315	20.0	20.0	33.6	91.5
W3	S16	Kerosene	74.0	3.00	175	317	8076	53.0	22.0	40.7	74.3
W4	S20	Gas	70.0	2.00	162	104	2571	17.0	13.6	92.1	64.5
W5	S21	Kerosene	181	3.20	441	64.0	2088	28.0	13.8	33.6	80.1
W6	S32	Gas	50.0	2.00	328	53.0	2547	23.0	14.0	24.6	97.5
W7	S36	Kerosene	100	3.30	243	319	5346	19.0	18.7	56.6	110
W8	S39	Gas	54.0	2.22	264	203	2433	20.0	15.4	31.5	117
W9	S48	Gas	53.7	3.00	218	85.0	5726	26.0	20.4	40.4	177
W10	S49	Wood	406	16.0	452	71.0	13211	52.0	25.8	45.6	115
W11	S50	Gas	55.5	1.80	334	61.0	6440	26.0	18.5	32.9	162
W12	S51	Central heating	65.5	2.00	168	59.0	3581	22.4	17.2	35.5	111
W13	S55	Gas	96.0	3.00	499	43.0	5812	27.0	17.2	50.5	171
W14	S56	Gas	48.0	15.0	150	31.0	260	7.00	15.5	39.3	95.5
W15	S59	Kerosene	94.0	11.0	555	75.0	6031	13.0	18.8	55.0	121
W16	S62	Gas	105	2.00	318	232	4118	27.0	16.5	75.4	81.8
W17	S63	Gas	79.0	2.5	256	57.0	3157	17.8	20.9	32.4	80.0
W18	S65	Wood	95.0	3.00	160	82.0	8565	23.0	25.3	42.1	291
W19	S67	Central heating	49.0	1.00	147	107	2066	16.0	14.1	41.0	50.7
W20	S69	Wood	73.0	2.00	200	67.0	6012	26.0	21.6	42.0	310
W21	S72	Wood	107	2.20	138	38.0	346.0	27.0	22.9	26.3	227
W22	S75	Gas	117	12.0	662	86.0	7922	23.0	24.6	29.8	153
W23	S77	Kerosene	83.0	2.40	157	68.0	5258	17.3	21.8	37.2	127
W24	S79	Gas	74.0	3.20	319	82.0	2998	82.0	15.7	24.6	101
W25	S82	Central heating	58.0	2.10	188	40.1	6489	27.0	17.6	31.9	214

Sample number	Corresponding summer sampling site	Type of heating system	Pb	Cd	Zn	Cu	Fe	Cr	Co	Ni	Mn
W26	S84	Wood	87.0	9.00	743	274	14459	32.0	19.6	38.4	125
W27	S85	Wood	119	3.00	252	64.0	13248	28.0	21.3	50.6	295
W28	S86	Wood	87.0	12.0	424	441	676.0	10.0	22.6	27.0	119
W29	S87	Wood	81.0	14.0	284	64.0	10704	46.0	17.5	40.9	169
W30	S88	Central heating	50.0	0.02	236	814	6454	42.0	10.8	66.3	160
Average			92.8	5.10	305	144	5385	27.1	18.7	42.2	139
SD			65.5	4.75	160	163	3812	15.1	3.7	15.1	69.2
Median			80.0	3.00	254	78.5	5302	24.5	18.6	39.85	118.2
C.V. (%)			71.0	94.0	53.0	113	71.0	56.0	20.0	36.0	50.0
Min.			48.0	0.02	138	31.0	260	7.00	10.8	24.6	50.7
Max.			406	16.0	743	814	14459	82.0	28.8	92.1	310

Table S3. Enrichment factor (EFs) of Pb, Cd, Zn, Cu, Fe, and Cr in the analyzed house dust samples collected from the all sampling sites during the summer season

Sample number	Fe	Pb	Cd	Zn	Cu	Cr
S1	1.0	22	342	48	33	8.4
S2	1.0	19	232	36	26	6.0
S3	1.0	17	154	14	5.0	4.0
S4	1.0	41	826	39	29	6.2
S5	1.0	20	614	41	63	7.4
S6	1.0	7.0	437	22	14	5.0
S7	1.0	24	383	24	15	6.2
S8	1.0	29	594	22	14	5.0
S9	1.0	22	952	34	26	7.1
S10	1.0	23	222	10	6.0	4.4
S11	1.0	20	560	45	8.0	4.3
S12	1.0	31	679	24	20	6.0
S13	1.0	16	516	23	12	4.0
S14	1.0	19	493	19	13	4.0
S15	1.0	5.0	62.6	2.0	2.0	4.0
S16	1.0	19	456	37	27	7.0
S17	1.0	14	271	24	13	7.1
S18	1.0	15	345	24	18	5.0
S19	1.0	16	586	25	22	6.4
S20	1.0	15	861	26	17	5.2
S21	1.0	25	1493	53	54	6.0
S22	1.0	19	1050	43	37	7.3
S23	1.0	25	1091	32	15	4.3
S24	1.0	29	440	43	25	5.4
S25	1.0	30	466	56	31	7.0
S26	1.0	12	558	30	25	5.1
S27	1.0	14	661	14	5.0	4.0
S28	1.0	14	680	22	10	4.4
S29	1.0	13	702	12	6.0	4.2

Sample number	Fe	Pb	Cd	Zn	Cu	Cr
S30	1.0	13	383	22	11	5.0
S31	1.0	12	558	30	25	5.1
S32	1.0	15	1023	42	28	7.2
S33	1.0	44	3588	49	34	11
S34	1.0	24	1642	52	52	7.0
S35	1.0	22	1769	42	24	8.0
S36	1.0	12	793	30	12	6.0
S37	1.0	9.0	599	22	10	3.0
S38	1.0	18	389	32	19	5.0
S39	1.0	19	836	38	23	6.3
S40	1.0	38	1360	49	34	6.5
S41	1.0	11	161	18	10	4.0
S42	1.0	11	791	33	33	6.0
S43	1.0	10	652	17	7.0	5.0
S44	1.0	10	800	42	18	7.0
S45	1.0	25	1250	31	25	5.0
S46	1.0	16	592	26	16	4.0
S47	1.0	26	571	21	13	4.2
S48	1.0	16	1027	28	13	5.0
S49	1.0	9.0	458	15	7.0	4.0
S50	1.0	17	865	21	12	5.0
S51	1.0	6.0	115	3.0	2.0	3.4
S52	1.0	16	456	26	16	5.0
S53	1.0	8.0	102	4.0	2.0	4.0
S54	1.0	10	131	4.0	3.0	5.0
S55	1.0	13	456	12	22	4.0
S56	1.0	22	884	34	26	6.0
S57	1.0	12	489	29	9.0	4.0
S58	1.0	14	795	17	6.0	5.3
S59	1.0	14	511	26	30	6.2
S60	1.0	21	1287	48	18	7.3
S61	1.0	32	841	24	13	5.3
S62	1.0	19	835	36	34	5.2
S63	1.0	24	1118	51	29	5.0
S64	1.0	13	335	50	37	6.0
S65	1.0	38	1381	58	27	7.0
S66	1.0	12	477	30	11	6.0
S67	1.0	10	378	33	26	4.4
S68	1.0	13	1020	50	31	8.3
S69	1.0	15	249	31	15	2.0
S70	1.0	25	792	36	18	5.4
S71	1.0	10	206	18	16	4.0
S72	1.0	23	1264	42	22	6.2
S73	1.0	18	388	22	10	5.0
S74	1.0	8.0	203	15	0.7	4.0

Sample number	Fe	Pb	Cd	Zn	Cu	Cr
S75	1.0	20	457	29	12	5.3
S76	1.0	25	921	34	30	4.3
S77	1.0	20	903	41	19	6.2
S78	1.0	27	939	45	21	7.0
S79	1.0	15	652	19	10	5.0
S80	1.0	16	944	34	22	5.0
S81	1.0	17	697	22	11	5.2
S82	1.0	10	606	16	6.0	4.5
S83	1.0	26	1254	68	22	4.9
S84	1.0	17	737	21	8.0	5.3
S85	1.0	14	588	18	11	6.3
S86	1.0	12	498	22	12	6.0
S87	1.0	10	518	12	7.0	4.0
S88	1.0	17	346	38	20	6.1
Average	1.0	18	700	30	19	5.3
SD	0.0	7.9	476	14	12	1.4
Range	(1.0–1.0)	(5.0–44)	(63–3588)	(2.0–68)	(0.7–63)	(2.0–11)

Determination of Heavy Metal Concentrations in Household Dusts in Irbid and Mafraq Cities, Jordan

Asmaa Al-Serhan¹, "Ayat Allah" Al-Massaedh^{1*}, and Idrees Faleh Al-Momani²

¹Department of Chemistry, Faculty of Science, Al al-Bayt University, Mafraq 25113, Jordan

²Department of Chemistry, Faculty of Science, Yarmouk University, Irbid 21163, Jordan

* **Corresponding author:**

email: almassaedh@aabu.edu.jo

Received: May 31, 2023

Accepted: August 13, 2023

DOI: 10.22146/ijc.85062

Abstract: The objective of this study was to measure the concentrations of selected heavy metals (Pb, Cd, Zn, Cu, Fe, Cr, Co, Ni, and Mn) in house dust collected during the summer and winter seasons from Mafraq and Irbid cities, Jordan. The average concentrations (\pm SD) of the metals were found to be 66.8 (\pm 22.4), 10.8 (\pm 3.75), 366 (\pm 108), 81.6 (\pm 43.9), 7586 (\pm 4304), and 37.2 (\pm 15.4) mg/kg, for Pb, Cd, Zn, Cu, Fe, and Cr, respectively, in the summer season. The average concentrations (\pm SD) of the metals were found to be 92.8 (\pm 65.5), 5.10 (\pm 4.75), 305 (\pm 160), 144 (\pm 163), 5385 (\pm 3812), 27.1 (\pm 15.1), 18.7 (\pm 3.70), 42.2 (\pm 15.1), and 139 (\pm 69.2) mg/kg, for Pb, Cd, Zn, Cu, Fe, Cr, Co, Ni, and Mn, respectively, in the winter season. The influence of different heating systems on the concentration of heavy metal was examined by comparing the results obtained in both summer and winter seasons. The concentrations of the metals in this study were compared with those reported by other researchers around the world. This study shows that the significant accumulation of heavy metals in house dust should be considered a serious risk to the health of residents in Mafraq and Irbid cities.

Keywords: house dust; pollution; Irbid; Mafraq; Jordan

■ INTRODUCTION

Air is the most important and essential part of environmental elements because it receives contaminants coming from different natural and anthropogenic sources. Good indoor air quality is very important for survival and for a healthy life, but it is negatively affected by outdoor and indoor air pollution [1-6]. Air is defined as polluted when it contains toxic chemicals or compounds that result in undesirable changes in its physical, chemical, or biological properties [7]. Air pollution can be indoor or outdoor and can cause adverse effects on human health including respiratory diseases, high blood pressure, neurological disorders, cardiovascular disease, asthma, kidney pathology, allergies, and lung cancer [3-4,8-14]. Additionally, air pollution has become a major environmental problem with a significant impact on climate change [1,15-16].

During the last years, the quality of indoor air has attracted much attention as a serious worldwide health

and environmental issue [9,12-13,16-19]. This is because people, especially children, infants, and older adults, spend most of their time indoor (e.g., in homes, offices, or classrooms), and much of this time, which was estimated at about 80–90% of the daily life, is generally spent in contact with contaminated surfaces like floors, desks, windows, or furniture [1-2,11,13,18,20-21]. Children and infants are the most sensitive groups that are more susceptible to air pollution compared to adults due to their hand-to-mouth behavior, small body size, developing lungs and neurological system, and active digestion system [1,3,21-22].

Dust is described as a very small size fine solid particulate matter that is settled on the surface of objects and on the ground [2,7,11]. The rate of deposition of dust particles is directly related to their sizes, so smaller size particles have lower deposition rates than larger particles, and hence they can stay suspended in the air for a long time [23]. In urbanized and industrialized areas, house dust is a heterogeneous and complex mixture of organic

and inorganic particles of various origins, shapes, sizes, and toxicity [3,17,23]. House dust may originate either from natural sources like bedrocks erosion or from anthropogenic sources like infiltration of outdoor emissions from vehicles, soil, refineries, building materials, wildfires, fossil fuel burning, and industries into the indoor environment [2,3,9,13,24-26]. In addition, house dust may originate from different indoor activities like smoking, incense burning, cooking, cleaning, fibers, hairs, furniture material, aerosols, and paint pigments [4,6,9,13,16,24-25]. Furthermore, it is reported that the type of heating system has a significant role in indoor air pollution [24].

A wide variety of inorganic and organic toxic pollutants like polycyclic aromatic hydrocarbons, heavy metals, or pesticides can be transferred with the air from the street into the indoor environment and attach to house dust particles [11,27-28]. Among these pollutants, heavy metals are chemical compounds that normally occur in nature, but different anthropogenic sources can also introduce them in significant amounts in different environmental elements (water, soil, and air) [28-29]. According to the International Agency for Research on Cancer (IARC), heavy metals are classified as toxic and carcinogenic substances, and different health organizations such as World Health Organization (WHO), Food and Agriculture Organization (FAO), or the United States Environmental Protection Agency (US-EPA) have established the maximum permissible limits for these metals as reported by the recent literatures [18,30-31]. Heavy metals like iron (Fe), copper (Cu), zinc (Zn), manganese (Mn), or magnesium (Mg) are essential micronutrients for human life but are toxic at elevated levels [31-34]. On the other side, toxic heavy metals like cobalt (Co), cadmium (Cd), lead (Pb), Nickel (Ni), or arsenic (As) are the most hazardous environmental pollutants when permissible concentration limits are exceeded [28-29,34-36]. In urban environments, heavy metals originate from different anthropogenic sources such as vehicle emissions, disposal of municipal and industrial wastes, fossil fuel combustion, wear of brake lining materials, and use of large quantities of fertilizers and metal-based pesticides [28,31,35,37]. Heavy metals are generally toxic, even at very low concentrations, due

to their non-biodegradable nature, persistence in the environment, thermostable, carcinogenic nature, and long biological half-lives [28,31,33,38-39]. Toxic heavy metals can cause many health problems when consumed excessively. For example, accumulation of Pb in the human body can cause significant health problems such as damage to the kidneys, headache, respiratory disorders, chronic cardiovascular impairments, increased blood pressure, neurological impairments, muscle weakness, and mental disorders [33,40]. The toxic symptoms caused by Cd include lung cancer, kidney dysfunction, bone diseases, reproductive deficiencies, and cancer [30,41]. High levels of Ni in the body lead to skin sensitivity, asthma, diarrhea, heart attack, lung fibrosis, chronic cough, kidney and cardiovascular infections, and low blood pressure [40,42].

In recent years, contamination of house dust by heavy metals has been studied extensively, and several metals such as Pb, Co, Ni, Cd, Zn, Cr, and others have been estimated [2,13,18,22,43]. The sources of heavy metals in house dust are varied and depend on several factors, such as the geographic location of the house, indoor activities, and outdoor pollution sources [22]. Several studies have indicated that heavy traffic, industrial emissions, contaminated soil, and building renovation materials are the major sources of heavy metals in house dust [11,13,22]. House dusts act as a medium for heavy metals deposition in the urban environment [44]. Thus, they are a major pathway of human exposure to toxic heavy metals [2,9,44]. This implies that heavy metals in house dust will accumulate to higher levels in the human body via inhalation of tiny size dust particles, via ingestion of contaminated food and drinks due to hand-to-mouth contact, or via skin absorption [2,11,13,18]. In this context, it is reported that house dust contaminated with high concentrations of Pb are a major source of Pb exposure for urban children [45]. Moreover, several environmental studies have reported the impact of indoor pollutants on the academic achievement and mental stability of children [3,4,22].

Jordan has been facing air pollution issues during the last few years due to rapid and uncontrolled industrialization and urbanization, especially due to

extensive refugee migration from neighboring countries to different cities in Jordan. As a result, different environmental elements (air, water, and soil) have been heavily affected, especially in urbanized areas. For example, Al-Madanat et al. [25] determined the concentrations of eight heavy metals (Mn, Ti, Cu, Pb, Cr, V, Ni, and As) in indoor and outdoor dust samples collected from residential and commercial areas in Al-Karak city, Jordan. The authors reported that the concentrations of Cu, Cr, Ni in residential areas and Ti, Cu and Pb in commercial areas were higher in indoor dust compared with outdoor dust. They reported that Ni, Cr and Cu were found at a higher concentration in the indoor dust samples than the outdoor dust samples due to many household products such as leaded paint, furniture, and appliances of the residential area. The authors concluded that traffic emissions are the major sources of heavy metal pollution in Al-Karak city [25]. In 2015, Al-Momani [24] studied the influence of different heating systems (kerosene, natural gas, wood/olive residue, and central heating) on the concentrations of heavy metals (Al, As, Ca, Cd, Co, Cr, Cu, Fe, K, Mg, Mn, Na, Ni, P, Pb, Sr, V, Ti and Zn) in house dust samples collected from Ajlune city, Jordan. The author concluded that the levels of the studied metals in the analyzed dust samples followed the order of wood/olive residue samples > kerosene samples > natural gas samples > central heating samples > reference samples [24].

Although a large number of environmental studies have been performed to investigate heavy metal pollution in house dust, street dust, roadside surface soils, air, food, and agriculture soils in Jordan [24-25,29-31,35-36,43,46-48], there is a lack of information, on the best knowledge of the author, regarding the concentrations of heavy metals in house dust in Irbid and Mafraq cities, Jordan. Therefore, this is the first study reporting heavy metal concentrations of house dust collected during the summer and winter seasons from Irbid and Mafraq cities in Jordan. These cities were selected for this study because they have been facing serious air pollution due to rapid industrial and population growth, which may also highly contribute to indoor air pollution in these cities. The main objectives of this study are (i) to estimate the concentrations of selected heavy metals (Pb, Cd, Zn, Cu, Fe, Cr, Co, Ni, and Mn) in house

dust samples collected from different locations during the summer and winter seasons including industrial zone (Irbid), commercial zone (Irbid), residential zone (Irbid), Irbid-Mafraq highway, commercial zone (Mafraq), and residential zone (Mafraq), Jordan, (ii) to investigate the influence of different heating systems (kerosene, gas, central heating, or wood) on the concentrations of heavy metals in house dust samples, and (iii) to compare the results obtained in this study with similar studies performed in Jordan and in neighboring countries and other countries in the world.

■ EXPERIMENTAL SECTION

Materials

All chemicals and reagents used in this study were of analytical grade. A multi-element standard solution of 1000 mg/L of each tested metal (Pb, Cd, Zn, Cu, Fe, Cr, Co, Ni, and Mn) was obtained from Merck KGaA, Darmstadt, Germany. Nitric acid (HNO₃, 70% v/v, extra pure-trace analysis grade) was obtained from Carlo Erba Reagent, France. Hydrogen peroxide (H₂O₂, 35% w/w, extra pure) and hydrofluoric acid (HF, 40%) were obtained from Union LAR. Supplies. Ultrapure deionized water was used to prepare standard and sample solutions.

Instrumentation

The instrumentations used in this study were flame atomic absorption spectrometry (Varian Spectra AA-55B, Australia) equipped with a deuterium background correction was used for measuring the concentrations of Pb, Cd, Cu, Zn, Fe, Cr, Co, Ni, and Mn in the collected dust samples. Measurements were made using the specific hollow cathode lamp for each metal. The proper wavelength and the slit width were adjusted. Analysis using FAAS was carried out at the most sensitive wavelength of the examined metals.

Procedure

Study area

The study area is located on the northern side of Amman, the capital of Jordan. Mafraq city (142401 population, 26551 km² total area) is around 60 km north of Amman at the crossroads of Iraq to the east and Syria to the north. Mafraq has a hot and semi-arid climate in

which most of the rainfall is in the winter season. The prevailing wind direction in Mafraq city is from west to east. During the last few years, Mafraq has witnessed significant commercial, industrial, and residential activities due to rapid industrialization and due to extensive migration of refugees from neighboring countries. New agricultural, plastic, concrete, food, fertilizers, and detergent factories represent the recent industrial development in this city. In addition, Mafraq city is surrounded by desert from all sides; thus, it is always subjected to dust storms throughout the year. During the last few years, dust storms have been added to Mafraq as an anthropogenic source of air pollution. Irbid city (951452 populations, 1572 km² total area) is around 80 km north of the capital of Jordan, Amman. Irbid is the second largest population, and it has the highest population density in Jordan. The Irbid city is a major ground transportation hub between Amman, Syria, to the north and Mafraq to the east. The climatic conditions in Irbid are characterized by long, hot, dry summers and short, cool, rainy winters. New plastic, cement, food, textile, steel, and detergent factories represent the recent

industrial development in this city.

In the present study, dust samples from different houses were collected during the summer and winter seasons from six sampling sites, as shown in Fig. 1. The first sampling site is the industrial zone (Irbid). It is a highly crowded area located near the main industrial area in Irbid city. This sampling site is characterized by having a high traffic volume, garage repairs, wear of brake lining, shopping centers, and gas stations. The second sampling site is the commercial zone (Irbid). It is a highly crowded urban area close to the city center of Irbid city and witnessing a large commercial movement. This sampling site has a large number of shopping centers and high traffic intensity. The third sampling site is the residential zone (Irbid) which represents the Hawara area. It is one of the oldest and most densely populated areas in the Irbid city. The fourth sampling site represents the area along the Irbid-Mafraq highway. This sampling site is characterized by a high traffic volume of 24 h a day. The fifth sampling site is the commercial zone (Mafraq), which is a highly crowded area that represents the center of Mafraq city. This

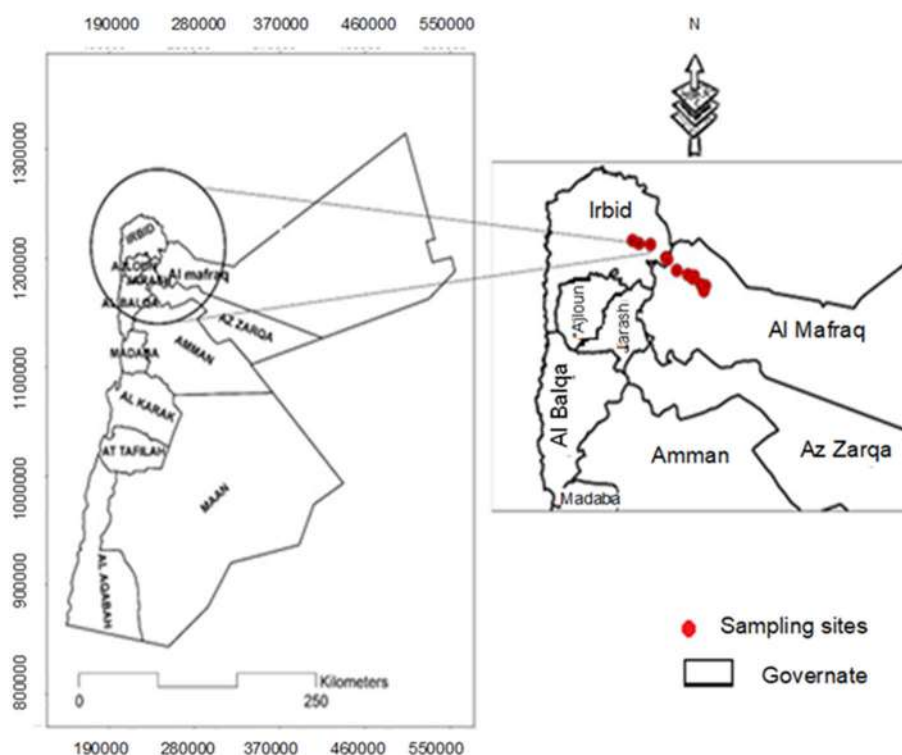


Fig 1. Irbid and Mafraq map shows the study area and sampling sites

sampling site has two main bus stations and a large number of shopping centers and gas stations. The sixth sampling site is the residential zone (Mafraq), which is composed of officers and the Al Hussein neighborhood. These sampling sites are the oldest areas in the city, with severe overcrowding and high population density.

Sample collection and pretreatment

In this study, a total of 88 dust samples were collected from six sampling sites during the summer season (June–August 2019) including the industrial zone (Irbid), commercial zone (Irbid), residential zone (Irbid), Irbid-Mafraq highway, commercial zone (Mafraq), and residential zone (Mafraq), Jordan. In addition, 30 dust samples were recollected from the same houses using different heating systems during the winter season. In order to make a comparison of the results based on the type of heating system, all dust samples were collected in the middle of the winter season (January 2020). This approach will reduce the influences of different anthropogenic sources (e.g., indoor human activities and traffic emissions) on the concentration of the studied metals in the collected dust samples.

In this study, dust samples were collected from all parts of the house (bedrooms, kitchen, living room, etc.) using vacuum cleaners. In order to increase the accuracy of the analysis method and reduce the risk of contamination, all required precautions were taken during sample collection and preparation as follows: (i) new vacuum cleaner bags were used for samples collection, and the vacuum cleaners were permanently cleaned before collecting the next dust sample; (ii) dust samples were collected from the inner bag of the vacuum cleaner, emptied into labeled polyethylene bags, and prepared in a clean laboratory; (iii) a trace element grade nitric acid HNO₃ (70% extra-pure HNO₃) was used for digestion and solution preparation; and (iv) all glassware apparatuses were effectively cleaned and previously soaked in 20% (v/v) HNO₃ for 24 h, then rinsed with deionized water and dried prior to use.

Sample preparation

All collected dust samples were sieved through a 2-mm plastic mesh to remove large impurities such as hair, plastic parts, cigarettes, or glasses. The sieved samples

were dried at 85 °C for about 24 h to a constant weight. The dried dust samples were then homogenized with a mortar and pestle, stored in clean, and sealed polyethylene bags for subsequent analysis. A microwave digestion system (Anton Paar, Multiwave Eco.) was used to extract metal ions from the collected dust samples. A mass of 0.5 g of each sieved dust sample was accurately weighed and transferred into a labeled microwave Teflon vessel. To each vessel, 8 mL of HNO₃ (70% extra-pure HNO₃), 2 mL HF, and 2 mL H₂O₂ were then added. The mixture was allowed to stand in the vessel for 10 min prior to sealing. The microwave was operated at a power of 850 W, and the vessels were heated to 200 °C over 10 min and then held at 200 °C for 10 min. At the end of the digestion procedure, the solutions were filtered and quantitatively transferred into 50 mL volumetric flasks and brought to volume with deionized water. Each extract solution was analyzed by using FAAS.

Calibration

Working standard solutions of each studied metal were freshly prepared by diluting an appropriate aliquot of standard stock solution of 1000 mg/L using 1% (v/v) HNO₃. The method of linear least squares was used for the calculation of correlation coefficient (R^2), slope with standard error ($m \pm S_b$), and intercept with standard error ($a \pm S_a$). From the linear calibration curve, the limit of detection (LOD, mg/kg) and limit of quantitation (LOQ, mg/kg) were calculated using Eq. (1) and (2) [31,35]:

$$\text{LOD} = \frac{3.3 \times S_a}{m} \quad (1)$$

$$\text{LOQ} = \frac{10 \times S_a}{m} \quad (2)$$

where m is the slope of the calibration curve, and S_a is the standard error of the y -intercept of a regression line.

Quality control and assurance

In an analysis of real samples, analysis of blank is the most important way to detect and correct any contamination problem [24]. In this study, the results obtained for the dust samples were blank-corrected to obtain the exact concentration of each metal in the collected dust samples. With the aim to assess the accuracy and reproducibility of the instrumental

method used for the analysis of the studied metals in the dust samples, a quality assurance program was employed, and standard reference materials for these metals were analyzed. In this context, three standard reference materials, SRM-1646a (Estuarine Sediment), SRM-1633b (Trace elements in coal fly ash), and SRM-2702 (Inorganics in marine sediment), were prepared in the same manner as for the original dust samples and analyzed along with dust samples. The results obtained in this study indicated that the measured values for the examined metals are in good agreement with their certified values provided by the National Institute of Standards and Technology (NIST) (Table 1). These results confirm the good accuracy, validity, and robustness of the FAAS analysis method used for the determination of heavy metal concentration in the investigated dust samples.

■ RESULTS AND DISCUSSION

Limit of Detection and Limit of Quantitation

The LOD and LOQ values obtained for each metal were summarized in Table 1. The calibration curves of the studied metals were linear with correlation coefficients $R^2 > 0.97$ (Table 1). The LOD values of the studied metals ranged between 0.0085 mg/kg for Cu and 0.2277 mg/kg for Fe, while LOQ ranged between 0.0284 and 0.7589 mg/kg for both metals, respectively (Table 1). The low LOD and LOQ demonstrate the sensitivity of the FAAS method used for the metal analysis in the dust samples.

Metal Concentrations in House Dust Samples

A total of 88 house dust samples were collected during the summer season, and 30 dust samples were re-collected from the same houses using different heating systems during the winter season. These samples were evaluated for determination of the concentrations of six heavy metals (Pb, Cd, Zn, Cu, Fe, and Cr) in the summer season, and nine heavy metals (Pb, Cd, Zn, Cu, Fe, Cr, Co, Ni, and Mn) in the winter season using FAAS. The average concentrations (mean \pm SD) of the studied metals are summarized in Tables 2 and 3 (for detailed data about the concentration of the investigated metals in all sampling sites, see Tables S1 and S2). With the aim to show the influence of the heating system on the concentration of heavy metal in dust samples, the summer-to-winter ratio (average concentration of metal in the summer season/average concentration of metal in the winter season) was calculated for each metal and listed in Table 3. The average concentrations (\pm SD) of the studied metals found in the analyzed dust samples in the summer season were found to be 66.8 (\pm 22.4), 10.8 (\pm 3.75), 366 (\pm 108), 81.6 (\pm 43.9), 7586 (\pm 4304), and 37.2 (\pm 15.4) mg/kg for Pb, Cd, Zn, Cu, Fe, and Cr, respectively (Table S1). The average concentrations (\pm SD) of the investigated metals found in the analyzed dust samples in the winter season were found to be 92.8 (\pm 65.5), 5.10 (\pm 4.75), 305 (\pm 160), 144 (\pm 163), 5385 (\pm 3812), 27.1 (\pm 15.1), 18.7 (\pm 3.7), 42.2 (\pm 15.1), and 139 (\pm 69.2) mg/kg, for Pb, Cd, Zn, Cu, Fe, Cr, Co, Ni, and Mn, respectively (Table S2). The average concentrations

Table 1. Limit of detection (LOD), limit of quantitation (LOQ), correlation coefficient (R^2), and percent recovery (based on the three standard reference materials) of each metal

Heavy metal	LOD (mg/kg)	LOQ (mg/kg)	R^2	SRM-1646a	SRM-1633b	SRM-2702
				Recovery (%)	Recovery (%)	Recovery (%)
Cu	0.0085	0.0284	0.9994	93	97	96
Cd	0.0121	0.0303	0.9989	99	95	93
Zn	0.0195	0.0653	0.9894	98	94	94
Pb	0.1050	0.3504	0.9991	97	93	92
Fe	0.2277	0.7589	0.9911	97	95	93
Cr	0.0310	0.1030	0.9993	98	95	95
Co	0.0188	0.0627	0.9987	96	93	95
Ni	0.0289	0.0963	0.9996	95	93	97
Mn	0.0089	0.0299	0.9997	93	96	98

Table 2. Statistical heavy metal concentration (mg/kg) in different areas of Irbid and Mafraq cities, Jordan, during the summer season

Location	Pb	Cd	Zn	Cu	Fe	Cr
Industrial zone-Irbid (N = 15)						
Average	90.2	9.10	391	96.9	9216	44.5
(±SD)	(±27.0)	(±3.88)	(±148)	(±73.4)	(±6439)	(±20.0)
C.V (%)	30	43	40	76	70	45
Range	45–150	4–14	146–686	29–339	4553–31062	31–110
Commercial zone-Irbid (N = 15)						
Average	67.2	11.2	387	91.9	7069	37.5
(±SD)	(±12.1)	(±4.00)	(±82.4)	(±36.1)	(±2286)	(±12.8)
C.V (%)	18	36	21	39	32	34
Range	44–96	5–16	220–533	34–150	3907–11270	23–71
Residential zone-Irbid (N = 14)						
Average	49.1	12	362	82.6	5852	31.1
(±SD)	(±12.7)	(±3.50)	(±82.5)	(±32.6)	(±2565)	(±8.12)
C.V (%)	26	29	23	39	44	26
Range	32–81	4–17	159–493	40–162	1626–10142	18–46
Irbid-Mafraq Highway (N = 14)						
Average	70.6	11.1	288	65.4	10092	42.1
(±SD)	(±23.0)	(±3.97)	(±127)	(±39.0)	(±5989)	(±21.3)
C.V (%)	33	36	44	59	60	51
Range	46–120	5–17	123–582	29–164	3958–23649	22–86
Commercial zone-Mafraq (N = 15)						
Average	59.5	9.50	395	89.6	5981	30.6
(±SD)	(±22.3)	(±3.16)	(±78.7)	(±36.7)	(±2572)	(±11.0)
C.V (%)	37	33	20	41	43	36
Range	35–120	4–14	290–538	38–150	3022–13194	11–52
Residential zone-Mafraq (N = 15)						
Average	63.7	11.7	364	62.4	7357	37.3
(±SD)	(±10.5)	(±3.50)	(±86.7)	(±21.0)	(±2682)	(±11.7)
C.V (%)	16	30	24	34	36	31
Range	44–80	5–16	283–635	6–89	3876–12022	18–62

of the studied metals in the analyzed house dust samples followed the order of Fe > Zn > Cu > Pb > Cr > Cd in the summer season, while these values in the winter season followed the order of Fe > Zn > Cu > Mn > Pb > Ni > Cr > Co > Cd (Tables 2 and 3). As a general trend, it is observed that the standard deviations are high for most of the studied metals. The high standard deviation values are expected because of the large variability in the sampling sites and variations in the chemical nature of the sampling site. Currently, there are no standard values for the maximum permissible limits of heavy metals in dust. Therefore, the

FAO/WHO, Dutch, Nigeria, and other guidelines for soil were used as references to estimate the contamination levels of the studied heavy metals in dust [49-53].

Lead (Pb)

According to the results presented in Tables 2 and 3, the average concentrations of Pb in the analyzed dust samples ranged from 49.1 to 90.2 mg/kg with a mean of 66.8 mg/kg in the summer season and from 68.0 to 121 mg/kg with a mean of 92.8 mg/kg in the winter season (for details refer to Tables S1 and S2). The maximum Pb concentration permitted in the soil is

Table 3. Mean (\pm SD) of heavy metals (mg/kg) and S/W ratio in house dust samples collected from all sampling sites during the winter season

Heavy metal	Mean (\pm SD)					
	S/W					
	Industrial zone (Irbid)	Commercial zone (Irbid)	Residential zone (Irbid)	Irbid-Mafraq highway	Commercial zone (Mafraq)	Residential zone (Mafraq)
Pb	86 (\pm 27) 1.1	108 (\pm 63) 0.62	68 (\pm 28) 0.72	121 (\pm 141) 0.58	86 (\pm 21) 0.69	84 (\pm 23) 0.76
Cd	7.0 (\pm 5.7) 1.3	2.7 (\pm 0.6) 4.1	2.5 (\pm 0.7) 4.8	6.8 (\pm 6.8) 1.6	3.4 (\pm 3.4) 2.8	4.4 (\pm 5.3) 1.8
Zn	336 (\pm 207) 1.2	259 (\pm 157) 1.5	278 (\pm 44.3) 1.3	304 (\pm 149) 0.95	253 (\pm 148) 1.6	363 (\pm 208) 1.0
Cu	152 (\pm 93.8) 0.64	162 (\pm 136) 0.57	192 (\pm 133) 0.43	58.0 (\pm 19.3) 1.12	94.0 (\pm 64.5) 0.95	215 (\pm 261) 0.29
Fe	2487 (\pm 2585) 3.7	4245 (\pm 3327) 1.7	3442 (\pm 1650) 1.7	5838 (\pm 4265) 1.73	4328 (\pm 2771) 1.4	7579 (\pm 4553) 0.97
Cr	17 (\pm 4.2) 2.6	33 (\pm 18) 1.2	21 (\pm 2.1) 1.5	27 (\pm 15) 1.6	21 (\pm 5.8) 1.4	34 (\pm 21) 1.1
Co	19 (\pm 1.8)	16.5 (\pm 4.8)	16 (\pm 2.4)	19 (\pm 3.7)	20 (\pm 3.8)	19 (\pm 4.2)
Ni	41 (\pm 10)	55 (\pm 32)	38 (\pm 17)	41 (\pm 6.5)	45 (\pm 16)	39 (\pm 13)
Mn	79 (\pm 17)	73 (\pm 7.9)	108 (\pm 10)	139 (\pm 35)	166 (\pm 108)	163 (\pm 60)

S/W = Average concentration of metal in the summer season/average concentration of metal in the winter season

100 mg/kg according to FAO/WHO [49] and 85 mg/kg according to Dutch and Nigeria standards [50,52]. These findings indicate that the average concentrations of Pb in the analyzed dust samples were found to be within the permissible limits according to these guidelines. The highest Pb concentration was found in the industrial zone (Irbid) with a mean of 90.2 mg/kg followed by the Irbid-Mafraq highway during the summer season (Table 2). This is expected because of the proximity of the studied houses to the industrial zone and due to the high traffic density at the Irbid-Mafraq highway. The average concentrations of Pb in the analyzed dust samples followed the order of industrial zone (Irbid) > Irbid-Mafraq highway > commercial zone (Irbid) > residential zone (Mafraq) > commercial zone (Mafraq) > residential zone (Irbid) in the summer season (Table 2, Fig. 2). The elevated levels of Pb found in the analyzed dust samples could be due to the indoor sources like leaded paint, spills from batteries, cable cover, pigments, or furnishing, and due to infiltration of contaminated dust particles from the outdoor sources like combustion of leaded fuel, burning gas for heating, tires and brake abrasions, plating, gasoline

additives, or engine wear [2,12,25-26,33,54-55]. The summer-to-winter ratio of Pb was found to be less than 1.0 in most sampling sites (Table 3). This means that the average concentration of Pb was higher in the winter season than in the summer season. These results indicate that there is a significant influence of different heating systems on the concentrations of Pb found in the analyzed dust samples. In addition, it is observed that there is an increase in the concentration of Pb in the dust samples collected from the houses using wood for heating compared to the houses using other heating systems. These results were in agreement with the conclusion reported by Al-Momani et al. [24]. The author reported in his study that the type of heating system (e.g., wood/olive residue, kerosene, natural gas, and central heating) has a significant impact on the concentrations of the studied metals found in the house dust samples collected from Ajlune city, Jordan [24]. Compared to other studies, the average concentration of Pb in this study was higher than those found in Malaysia [56], Kingdom of Saudi Arabia [57], Turkey [26], China [38], and Jordan, Al-Karak city [25], but lower than those

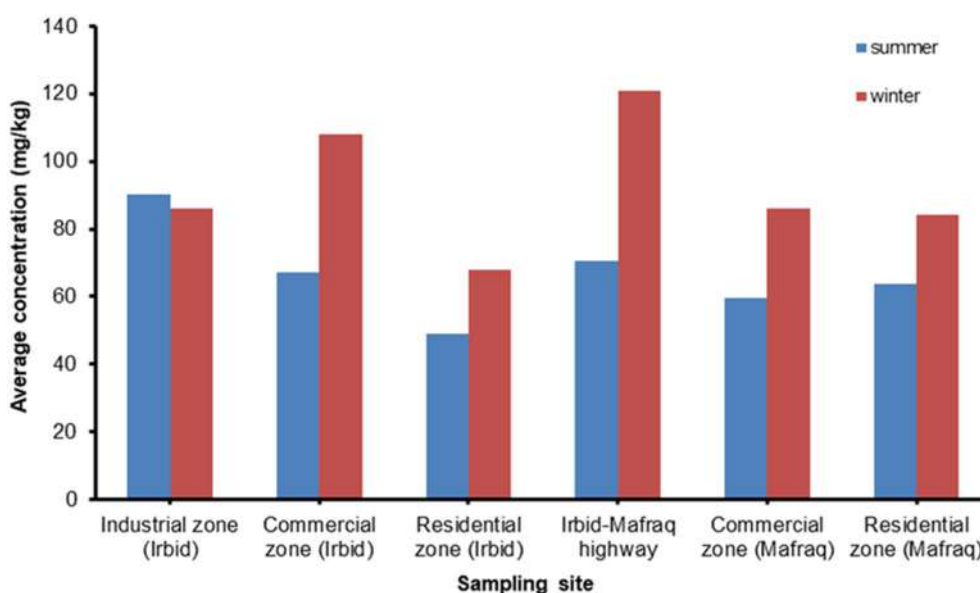


Fig 2. Average concentrations of Pb in the analyzed dust samples collected from the studied areas during the summer and winter seasons

found in Egypt [55], Australia [54], Canada [58], and Jordan, Amman city [43] as described in Table 4.

Cadmium (Cd)

Based on the results listed in Tables 2 and 3, the average concentrations of Cd in the analyzed dust samples ranged from 9.1 to 12 mg/kg with a mean of 10.8 mg/kg in the summer season and from 2.5 to 7.00 mg/kg with a mean of 5.10 mg/kg in the winter season (for details refer to Tables S1 and S2). The maximum Cd levels permitted in soil are 3.0 mg/kg according to WHO/FAO and EU [49,52] and 0.8 mg/kg according to Dutch and Nigeria standards [50-52]. These findings confirm that the

average concentrations of Cd in the analyzed dust samples were found to be above the permissible limits set by these standards. The highest concentration of Cd was found in the residential zone (Irbid) with a mean of 12 mg/kg during the summer season (Table 2). The average concentrations of Cd in the analyzed dust samples followed the order of residential zone (Irbid) > residential zone (Mafraq) > commercial zone (Irbid) > Irbid-Mafraq highway > commercial zone (Mafraq) > industrial zone (Irbid) in the summer season (Table 2, Fig. 3). The elevated levels of Cd found in the analyzed dust samples could be due to the indoor sources such as

Table 4. Average concentrations of selected heavy metals (mg/kg) in house dust samples collected from Irbid and Mafraq cities, Jordan in the summer and winter seasons compared with other studies in different countries

Country	Pb	Cd	Zn	Cu	Fe	Cr	Co	Ni	Mn	Reference
Jordan, Amman city	206	4.50	3104	160	-	77.0	23.0	47.0	304	[43]
Jordan, Al-Karak city	52.3	-	-	74.0	-	62.1	-	40.0	251	[25]
Malaysia	31.2	-	149	30.2	4225	16.9	-	9.00	-	[56]
Kingdom of Saudi Arabia	23.0	-	141	52.8	17962	-	7.20	-	260	[57]
Australia	389	4.40	657	147	5850	83.6	-	27.2	76.1	[54]
Canada	406	6.50	717	206	14135	86.7	8.90	62.9	269	[58]
Egypt, Alexandria (March 2016)	260	0.77	771	141	-	29.2	3.20	25.1	237	[55]
Turkey, Ankara	27.5	0.35	263	65.7	-	23.8	2.25	32.3	65.9	[26]
China	40.7	2.29	166	16.9	-	19.8	-	-	-	[38]
Jordan (summer)	66.8	10.8	366	81.6	7586	37.2	-	-	-	This study
Jordan (winter)	92.8	5.10	305	144	5385	27.1	18.7	42.2	139	This study

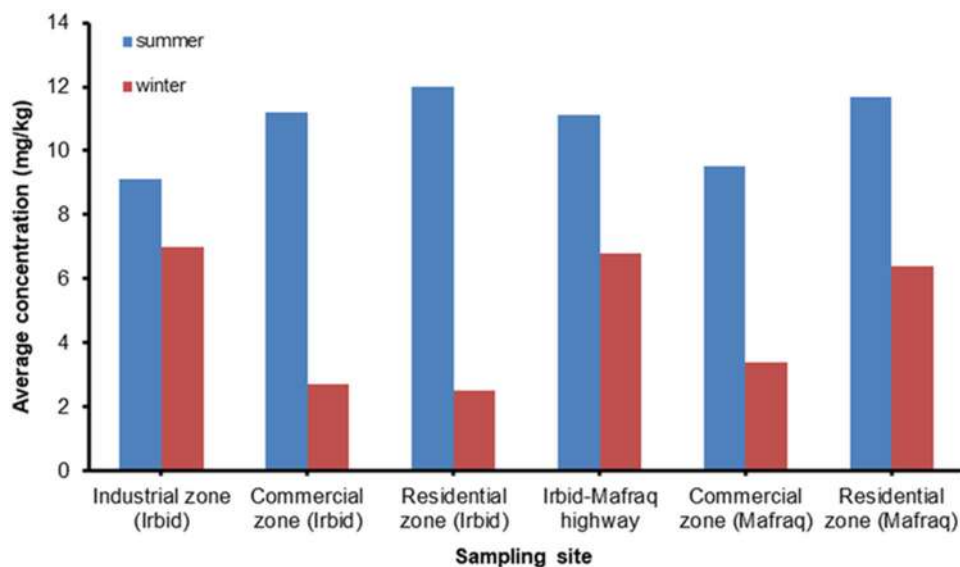


Fig 3. Average concentrations of Cd in the analyzed dust samples collected from the studied areas during the summer and winter seasons

smoking, spills from batteries, or building painting, and due to the infiltration of contaminated dust particles from the outdoor sources like combustion of leaded gasoline, Ni-Cd batteries, corrosion of brake linings, or old car tires [2,8-9,38,41,59]. The summer-to-winter ratio of Cd was found to be greater than 1.0 in all sampling sites (Table 3). This means that the average concentration of Cd was higher in the summer season than in the winter season, which confirms that there is no strong influence of different heating systems on the concentrations of Cd detected in the analyzed dust samples. Compared to other studies, the average concentration of Cd determined in this study was much higher than those reported by other researchers, as shown in Table 4.

Zinc (Zn)

The results in Tables 2 and 3 show that the average concentrations of Zn in the analyzed house dust samples ranged from 288 to 395 mg/kg with a mean of 366 mg/kg in the summer season and from 253 to 363 mg/kg with a mean of 305 mg/kg in the winter season (for details refer to Tables S1 and S2). The maximum permissible Zn limit in soil recommended by WHO/FAO is 300 mg/kg [49], while Dutch and Nigeria standards set this level at 140 mg/kg [50,52]. This implies that the average concentrations of Zn in the analyzed dust samples were found to be above the permissible limits set by these

health organizations. The highest concentration of Zn was found in the commercial zone (Mafraq) with a mean of 395 mg/kg followed by the industrial zone (Irbid) during the summer season. This is because of the proximity of the studied houses to the pollution sources at these sampling sites (Table 2). The average concentrations of Zn in the analyzed dust samples followed the order of commercial zone (Mafraq) > Industrial zone (Irbid) > commercial zone (Irbid) > residential zone (Mafraq) > residential zone (Irbid) > Irbid-Mafraq highway in the summer season (Table 2, Fig. 4). The elevated levels of Zn in the analyzed dust samples might be due to the indoor human activities such as alloys, building materials, rubber, paints, or wood preservatives, and due to the infiltration of contaminated dust particles from the outdoor sources like wear and tear of automobile tires, traffic emission, brake linings, corrosion of galvanized vehicular parts, or waste combustion [7,51,60-61]. With the exception of the dust samples collected from the Irbid-Mafraq highway, the results showed that the summer-to-winter ratio of Zn was found to be greater than 1.0 in all sampling sites (Table 3). These findings reveal that there is no strong influence of different heating systems on the concentrations of Zn found in the analyzed dust samples. The average concentration of Zn obtained in

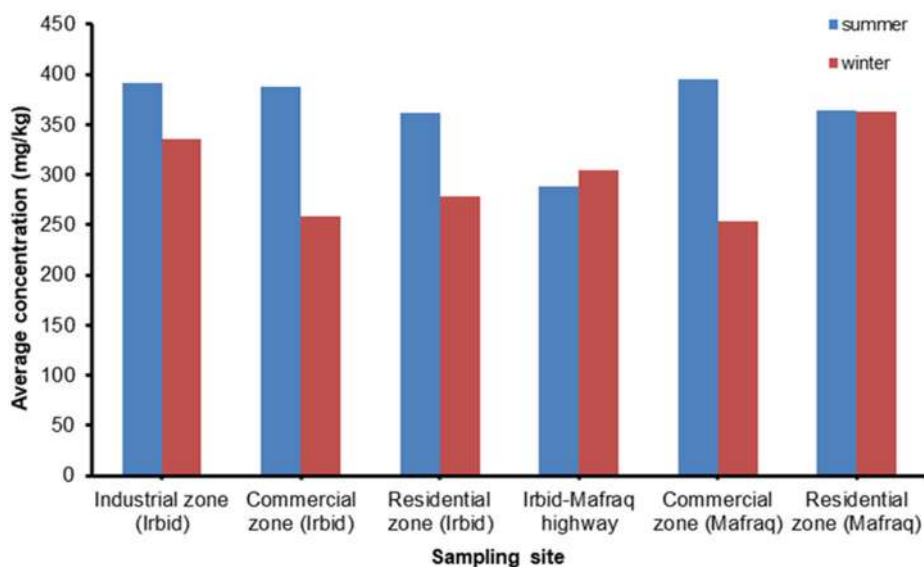


Fig 4. Average concentrations of Zn in the analyzed dust samples collected from the studied areas during the summer and winter seasons

this study was higher than those found in the Kingdom of Saudi Arabia [57], China [38], Turkey [26], and Malaysia [56], but lower than those found in Australia [54], Egypt [55], Canada [58], and Jordan, Amman city [43] as shown in Table 4.

Copper (Cu)

According to the results presented in Tables 2 and 3, the average concentrations of Cu found in the analyzed house dust samples ranged from 62.4 to 96.9 mg/kg with a mean of 81.6 mg/kg in the summer season and from 58.0 to 215 mg/kg with a mean of 144 mg/kg in the winter season (for details refer to Tables S1 and S2). The maximum Cu concentration permitted in the soil is 100 mg/kg according to WHO/FAO [49] and 36 mg/kg according to Dutch and Nigeria standards [50,52]. These findings reveal that the average concentrations of Cu detected in the dust samples in the summer season were found to be within the permissible limits set by WHO/FAO, but higher than those set by Dutch and Nigeria standards. Additionally, the average concentrations of Cu found in the dust samples during the winter season exceeded the permissible limits set by these health organizations. The highest concentration of Cu was found in the industrial zone (Irbid), where Pb and Cr were also at the maximum during the summer season (Table 2). This is expected because Cu is mostly derived

from the car components, tire abrasion, lubricants corrosion of cars, and engine wear [25,35,59,61]. In addition, it is reported that power wires made from copper are considered major sources of Cu in residential areas [25,35]. The average concentrations of Cu in the analyzed house dust samples followed the order of Industrial zone (Irbid) > commercial zone (Irbid) > commercial zone (Mafraq) > residential zone (Irbid) > Irbid-Mafraq highway > residential zone (Mafraq) in the summer season (Table 2, Fig. 5). The elevated levels of Cu found in the analyzed dust samples could be due to the indoor sources like interior paint, metal objects, or building materials, and due to the infiltration of dust particles from the outdoor sources like tire wear, car lubricant wear, brush, or brake dust [12,56,61]. With the exception of the dust samples collected from the Irbid-Mafraq highway, the summer-to-winter ratio of Cu was found to be less than 1.0 in all sampling sites (Table 3). These results confirm that there is a significant influence of different heating systems on the concentrations of Cu found in the analyzed dust samples. In addition, it is observed that there is an increase in the concentration of Cu in the dust samples collected from the houses using wood for heating compared to the houses using other different heating systems. Compared to other studies, the average concentration of Cu obtained in this study

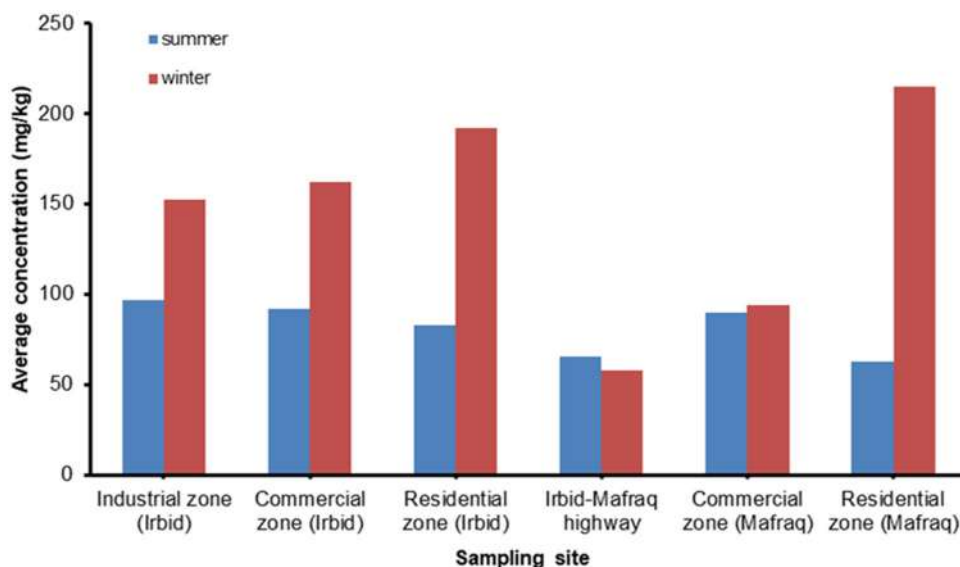


Fig 5. Average concentrations of Cu in the analyzed dust samples collected from the studied areas during the summer and winter seasons

was higher than those found in the Kingdom of Saudi Arabia [57], China [38], Turkey [26], Malaysia [56], and Jordan, Karak city [25], but lower than those found in Egypt [55], Australia [54], Canada [58], and Jordan, Amman city [43] as described in Table 4.

Chrome (Cr)

For the concentrations of Cr in the analyzed house dust samples, the results in Tables 2 and 3 show that the average concentrations of Cr ranged from 30.6 to 44.5 mg/kg with a mean of 37.2 mg/kg in the summer season and from 17.0 to 34.0 mg/kg with a mean of 27.1 mg/kg in the winter season (for details refer to Tables S1 and S2). The maximum concentration of Cr permitted in the soil is 100 mg/kg according to WHO/FAO, Dutch, and Nigeria standards [49-50,52]. These results indicate that the average concentrations of Cr found in the analyzed dust samples were found to be within the permissible limits set by these health organizations. The highest Cr concentration was found at the industrial zone (Irbid) with a mean of 44.5 mg/kg followed by the Irbid-Mafraq highway during the summer season (Table 2, Fig. 6). As reported in the literature, the elevated levels of Cr in house dust samples might be attributed to chrome steel manufacturing, tire abrasion, engine wear, using metal-based pesticides, combustion of fossil fuels, or coal burning [2,12,35]. The average concentrations of Cr

found in the analyzed dust samples followed the order of Industrial zone (Irbid) > Irbid-Mafraq highway > commercial zone (Irbid) > residential zone (Mafraq) > residential zone (Irbid) > commercial zone (Mafraq) in the summer season (Table 2, Fig. 6). The elevated levels of Cr found in the analyzed dust samples could be due to the indoor activities such as interior paint, metallic objects, building materials, corrosion of appliances, or using of chrome-plated household products, and due to the infiltration of dust particles from the outdoor sources like vehicle emissions, vehicle lubricant wear, engine wear, or brake dust [2,13]. The results show that the summer-to-winter ratio of Cr was found to be greater than 1.0 in all sampling sites, indicating that there is no strong influence of different heating systems on the concentrations of Cr found in the analyzed house dust samples (Table 3). Compared to other studies, the average concentration of Cr in this study was higher than those found in Malaysia [56], China [38], Turkey [26], and Egypt [55] but lower than those found in Canada [58], Australia [54], Jordan, Amman city [43], and Jordan, Al-Karak city [25] as shown in Table 4.

Iron (Fe)

The results in Tables 2 and 3 show that the average concentrations of Fe determined in the analyzed dust samples ranged from 5852 to 10092 mg/kg with a mean

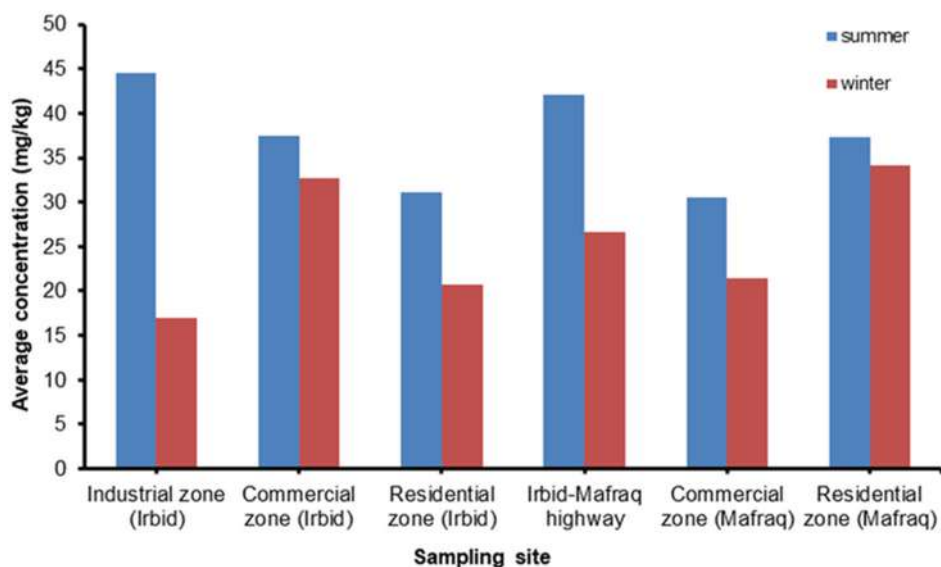


Fig 6. Average concentrations of Cr in the analyzed dust samples collected from the studied areas during the summer and winter seasons

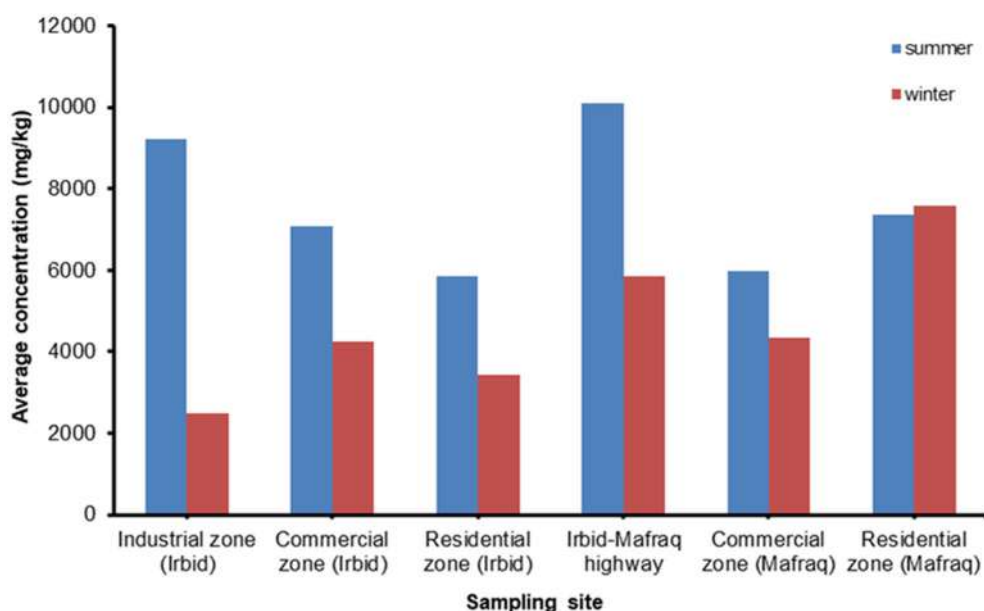


Fig 7. Average concentrations of Fe in the analyzed dust samples collected from the studied areas during the summer and winter seasons

of 7586 mg/kg in the summer season and from 2487 to 7579 mg/kg with a mean of 5385 mg/kg in the winter season (for details refer to Tables S1 and S2). The highest Fe concentration was found at the Irbid-Mafraq highway with a mean of 10092 mg/kg during the summer season, which might be attributed to the presence of the steel factory in Irbid city. The average concentrations of Fe in the analyzed dust samples followed the order of Irbid-

Mafraq highway > industrial zone (Irbid) > residential zone (Mafraq) > commercial zone (Irbid) > commercial zone (Mafraq) > residential zone (Irbid) in the summer season (Table 2, Fig. 7). In this study, there are several anthropogenic sources that increase the concentration of Fe in the analyzed dust samples such as the presence of the steel factory (Howara city, Irbid), brake linings, and vehicle wear [57]. The summer-to-winter ratio of Fe

was found to be greater than 1.0 in most sampling sites, which confirms that there is no significant influence of different heating systems on the concentrations of Fe found in the analyzed dust samples. The average concentration of Fe determined in this study was higher than those found in Malaysia [56] and Australia [54] but lower than those found in the Kingdom of Saudi Arabia [57] and Canada [58], as shown in Table 4.

Cobalt (Co)

According to the results presented in Table 3, the average concentrations of Co found in the analyzed house dust samples ranged from 16.0 to 20.0 mg/kg with a mean of 18.7 mg/kg in the winter season (for details refer to Table S2). According to the Dutch and Nigeria standards, the maximum Co levels permitted in soil are 9.0 and 20 mg/kg, respectively [50,52]. These results indicate that the average concentrations of Co in the dust samples were found to be within the permissible limit set by Nigeria standards but exceeded the permissible limit set by Dutch standards. The elevated levels of Co found in the analyzed dust samples might be due to indoor sources such as building materials, cigarette ash, combustion devices, or paints, and due to the infiltration of contaminated dust particles from outdoor sources like combustion of leaded fuel, wearing out of car tires, burning coal, oil leakage, or vehicle emissions [12,26,57]. As shown in Table 3, there was no significant difference between the average concentrations of Co detected in the different sampling sites. However, the highest concentration of Co was found in the commercial zone (Mafraq), where Mn is also at its maximum during the winter season (Table 3). This is expected because Co is mainly derived from the combustion of leaded gasoline, oil leakage, wearing out of car tires, and corrosion of batteries [35]. Compared to other studies, the average concentration of Co in this study was higher than those found in Canada [58], Turkey [26], Egypt [55], and the Kingdom of Saudi Arabia [57] but lower than those found in Jordan, Amman city [43] as described in Table 4.

Nickel (Ni)

According to the results presented in Table 3, the average concentrations of Ni found in the analyzed house dust samples ranged from 38 to 55 mg/kg with a mean of

42.2 mg/kg in the winter season (for details refer to Table S2). The maximum Ni concentrations permitted in soil are 50 mg/kg according to WHO/FAO [49] and 35 mg/kg according to Dutch and Nigeria standards [50,52]. These results reveal that the average concentrations of Ni in the dust samples were found to be within the permissible limits set by WHO/FAO standards but exceeded the permissible limits set by Dutch and Nigeria standards. It is reported that the presence of Ni in house dust samples could be due to lubricant corrosion of cars, use of Ni-plated household products, nickel plating, vehicle alloys containing nickel, erosion of metallic surfaces, tire abrasion, engine wear, heavy oil combustion, and brake dust [2,35,56]. The average concentrations of Ni in the analyzed house dust samples followed the order of commercial zone (Irbid) > commercial zone (Mafraq) > industrial zone (Irbid) > Irbid-Mafraq highway > residential zone (Mafraq) > residential zone (Irbid) in the winter season (Table 3). Compared to other studies, the average concentration of Ni found in this study was higher than those found in Turkey [26], Egypt [55], Australia [54], Malaysia [56], and Jordan, Al-Karak city [25], but lower than those found in Canada [58], and Jordan, Amman city [43] as described in Table 4.

Manganese (Mn)

For the concentrations of Mn in the analyzed house dust samples, the results in Table 3 show that the average concentrations of Mn found in the analyzed house dust samples ranged from 73.0 to 166 mg/kg with a mean of 139 mg/kg in the winter season (for details refer to Table S2). The maximum Mn concentration permitted in the soil is 2000 mg/kg according to WHO/FAO standards [49]. These findings indicate that the average concentrations of Mn in the analyzed dust samples were found to be within the permissible limits set by WHO/FAO. The presence of Mn in the analyzed dust samples might be due to Ni-Mn batteries, household cleaning agents, and infiltration of vehicle emissions [51]. The average concentrations of Mn in the analyzed house dust samples followed the order of commercial zone (Mafraq) > residential zone (Mafraq) > Irbid-Mafraq highway > residential zone (Irbid) > industrial

zone (Irbid) > commercial zone (Irbid) in the winter season (Table 3). Compared to other studies, the average concentration of Mn found in this study was higher than those found in Australia [54] and Turkey [26], but lower than those found in Canada [58], the Kingdom of Saudi Arabia [57], Jordan, Al-Karak city [25], Egypt [55], and Jordan, Amman city [43] as described in Table 4.

Enrichment Factor

In order to determine whether the origin of heavy metal pollution in the analyzed house dust samples is due to anthropogenic or natural sources, the enrichment factor (EF) for selected heavy metals (Pb, Cd, Zn, Cu, and Cr) was calculated and listed in Table 5 (for details refer to Table S3). The EF for a given metal is usually used to assess the degree of anthropogenic pollution in environmental media based on the normalization of the concentration of the investigated metal in a house dust sample against background or crustal metals such as Al or Fe [35]. In this study, the EF for metal in the analyzed dust samples is calculated using the Eq. (3) [35,47]:

$$EF = \frac{[M]_{\text{dust}}/[Fe]_{\text{dust}}}{[M]_{\text{crust}}/[Fe]_{\text{crust}}} \quad (3)$$

where $[M]_{\text{dust}}$ is the concentration of metal in the house dust sample, $[Fe]_{\text{dust}}$ is the concentration of Fe (as reference metal) in the house dust sample, $[M]_{\text{crust}}$ is the concentration of metal in the earth crust, and $[Fe]_{\text{crust}}$ is the concentration of Fe in the earth crust. Aprile and Bouvy [62] classified contamination levels into five categories based on the EF values: (i) no enrichment (EF = 1 to < 2); (ii) minor enrichment (EF = 2 to < 5); (iii) moderate enrichment (EF = 5 to < 10); (iv) high enrichment (EF = 10 to < 50); and (v) extremely high enrichment (EF > 50). Alsbou and Al-Khashman [47]

reported that EF values less than 10 indicate low enrichment, EF values from 10 to 100 indicate medium enrichment, and EF values greater than 100 indicate high enrichment.

In this study, the average EF values for the investigated metals were calculated in the dust samples collected during the summer season and listed in Table 5. According to these results, the high enrichments of the studied metals were obtained in the dust samples collected from the residential zone (Irbid) and commercial zone (Mafraq). These findings can be attributed to the presence of steel factories in the Irbid city, traffic emissions, brake linings, and vehicle wear. The average EF values of the studied metals followed the order of Cd > Zn > Cu > Pb > Cr (Table 5). The results show that Cd has an extremely high enrichment factor (ranging from 471 to 1069) in all sampling sites (Table 5). These results indicate that the origin of this metal in the analyzed dust samples is due to anthropogenic sources like smoking, building paint, fossil fuel combustion, vehicle emissions, and old car tires [35]. In addition, the the results listed in Table 5 show that Pb, Zn, and Cu have medium enrichment ($10 \leq EF \leq 100$). These results confirm that the presence of these metals in the analyzed dust samples is due to different anthropogenic sources (mainly related to vehicle emissions and industrial activities). For Cr, the average EF values were found to be lower than 10 in all sampling sites, which implies that the origin of this metal in the analyzed dust samples is due to natural sources.

Influence of Different Heating Systems

With the aim to investigate the influence of different heating systems on the concentration of the

Table 5. Average values (\pm SD) of enrichment factor for selected heavy meals in dust samples collected during the summer season from different studied areas in Irbid and Mafraq cities, Jordan

Heavy metal	Industrial zone (Irbid)	Commercial zone (Irbid)	Residential zone (Irbid)	Irbid-Mafraq highway	Commercial zone (Mafraq)	Residential zone (Mafraq)
Pb	21 (\pm 9)	18 (\pm 6)	18 (\pm 11)	15 (\pm 6)	19 (\pm 8)	17 (\pm 6)
Cd	471 (\pm 248)	670 (\pm 332)	1069 (\pm 854)	585 (\pm 347)	739 (\pm 405)	684 (\pm 272)
Zn	27 (\pm 13)	31 (\pm 13)	35 (\pm 11)	19 (\pm 10)	37 (\pm 12)	29 (\pm 15)
Cu	19 (\pm 15)	21 (\pm 13)	24 (\pm 13)	12 (\pm 8)	23 (\pm 9)	14 (\pm 8)
Cr	5 (\pm 2)	5 (\pm 1)	6 (\pm 2)	4 (\pm 1)	5 (\pm 2)	5 (\pm 1)

studied metals in the collected house dust, a total of 30 samples were collected during the winter season from houses using different heating systems including (i) kerosene (indoor combustion of kerosene), (ii) gas (indoor combustion of natural gas), (iii) central heating (outdoor diesel boilers), and (iv) wood (indoor combustion of wood).

The average concentrations of the studied metals in the analyzed dust samples are listed in Table 6. As a general trend, dust samples collected from houses using indoor combustion of wood for heating contain the highest concentrations of Pb, Cd, Zn, Fe, Cr, Co, and Mn as compared to other heating systems. Wood ash is the residue remaining after the complete burning of wood. It is mostly composed of several essential metals (e.g., Ca, K, P, Mg, Mn, Na, Fe, or Al) that are needed for adequate plant growth. On the other side, wood ash contains some toxic heavy metals (e.g., Pb, Cd, Co, As, or Cr) that pose health and environmental problems. Wood ash is considered as the major constituent of dust in houses using wood for heating. The presence of elevated levels of the studied metals in dust samples collected from houses using wood for heating can be explained based on the fact that plants absorb heavy metals from soil, irrigation water, and the atmosphere during their growth cycle. Results in Table 6 show that the average concentrations of Fe in the analyzed dust samples were the highest among all investigated metals. For example, the average concentration of Fe in the wood samples is 8403 followed by 5360, 4648, and 3766 mg/kg for kerosene, central

heating, and gas, respectively (Table 6). Furthermore, results presented in Table 6 show that dust samples collected from houses using central heating contain the highest concentrations of Cu and Ni as compared to all other heating systems.

The overall results for the analyzed dust samples collected from different houses using different heating systems indicated that the average concentrations of the studied metals in the house dust samples followed the order of wood samples > kerosene samples > gas samples > central heating samples (Table 6). These results were in good agreement with those reported by Al-Momani et al. [24]. The author reported that dust samples collected from houses (Ajlune city, Jordan) using wood and/or olive residue for heating contain the highest concentrations of Al, As, Ca, Cd, Co, Cr, Cu, Fe, K, Mg, Mn, Na, Ni, P, Pb, Sr, V, Ti and Zn followed by kerosene, natural gas, and central heating [24].

Statistical Analysis of Results

In the present study, analysis of variance (ANOVA) was employed to decide whether there is a significant difference in metal concentrations between dust samples collected from the different studied areas investigated in this study (industrial zone (Irbid), commercial zone (Irbid), residential zone (Irbid), Irbid-Mafraq highway, commercial zone (Mafraq), and residential zone (Mafraq)). From the statistical analysis of the results obtained in the summer season, the P values for Zn, Cu, Cd, and Cr concentrations were found

Table 6. Average concentrations (\pm SD) of heavy metals (mg/kg) in house dust samples collected from houses using different heating systems

Heavy metal	Gas N = 13	Kerosene N = 5	Wood N = 8	Central heating N = 4
Pb	75 (\pm 24)	106 (\pm 43)	132 (\pm 111)	56 (\pm 7.7)
Cd	4.8 (\pm 4.6)	4.6 (\pm 3.6)	7.7 (\pm 5.8)	1.3 (\pm 1.0)
Zn	322 (\pm 148)	314 (\pm 176)	332 (\pm 202)	185 (\pm 38)
Cu	103 (\pm 69)	169 (\pm 136)	138 (\pm 143)	255 (\pm 373)
Fe	3766 (\pm 2244)	5360 (\pm 2153)	8403 (\pm 5592)	4648 (\pm 2195)
Cr	25 (\pm 18)	26 (\pm 16)	31 (\pm 13)	27 (\pm 11)
Co	18 (\pm 3.0)	19 (\pm 3.3)	22 (\pm 3.0)	15 (\pm 3.0)
Ni	43 (\pm 20)	45 (\pm 11)	39 (\pm 9.0)	44 (\pm 16)
Mn	112 (\pm 40)	102 (\pm 24)	206 (\pm 85)	134 (\pm 70)

to be 0.08, 0.16, 0.18, and 0.08, respectively. These findings indicate that there was no significant difference in metal concentration between the analyzed dust samples collected from the different studied areas ($p > 0.05$). On the other side, the p values for Pb and Fe were 6.62×10^{-6} and 0.04, indicating that there was a significant difference in the concentrations of these metals between the analyzed dust samples collected from the different studied areas ($p < 0.05$). One possible explanation for the variation of the concentrations of Pb and Fe between the analyzed dust samples might be due to anthropogenic sources such as traffic emissions, industrial emissions, and smoking. In addition, ANOVA was also employed for the results obtained during the winter season. According to these results, the p values obtained for Pb, Cd, Zn, Cu, Fe, Cr, Ni, Mn, and Co concentrations were found to be 0.88, 0.53, 0.84, 0.53, 0.34, 0.47, 0.67, 0.23, and 0.64, respectively. These findings confirm that there was no significant difference in metal concentration in dust samples collected from the different studied areas investigated in this study ($p > 0.05$).

■ CONCLUSION

This study showed a significant concentration of metals in dust samples collected from Irbid and Mafraq cities. For the dust samples collected during the summer season, it is found that the highest concentration of Cd is present at the residential zone (Irbid), Fe at the Irbid-Mafraq highway, and Zn at the commercial zone (Mafraq). The average concentrations of the studied metals in dust samples collected from houses using different heating systems followed the order of wood samples > kerosene samples > gas samples > central heating samples. The enrichment factor results showed that Pb, Zn, Cu, and Cd were found to be highly enriched in the analyzed dust samples, indicating heavy metal pollution from anthropogenic sources such as smoking, building paint, and traffic emissions. Vehicle emissions appear to be the major outdoor source of heavy metal pollution in the analyzed house dust samples in Irbid and Mafraq cities. Therefore, the use of fuel without lead and vehicles with catalytic converters are highly recommended and should be encouraged to reduce vehicle emissions yielded toxic

heavy metals in house dust. The results of this study suggest that the levels of the studied heavy metals (Pb, Cd, Zn, Cu, Fe, Cr, Co, Ni, and Mn) in the analyzed house dust should be monitored regularly.

■ ACKNOWLEDGMENTS

The authors thank Al al-Bayt University (Mafraq, Jordan) and Yarmouk University (Irbid, Jordan) for providing the required facilities to perform this work and carry out the FAAS analysis on the dust samples.

■ AUTHOR CONTRIBUTIONS

Asmaa Al-Serhan collected and prepared dust samples for analysis. Idrees Faleh Al-Momani performed the FAAS studies. "Ayat Allah" Al-Massaedh and Asmaa Al-Serhan wrote the draft of the manuscript. All authors analyzed and interpreted the results obtained during this study. All authors read and approved the final manuscript.

■ REFERENCES

- [1] Kalimeri, K.K., Saraga, D.E., Lazaridis, V.D., Legkas, N.A., Missia, D.A., Tolis, E.I., and Bartzis, J.G., 2016, Indoor air quality investigation of the school environment and estimated health risks: Two-season measurements in primary schools in Kozani, Greece, *Atmos. Pollut. Res.*, 7 (6), 1128–1142.
- [2] Sabzevari, E., and Sobhanardakani, S., 2018, Analysis of selected heavy metals in indoor dust collected from city of Khorramabad, Iran: A case study, *Jundishapur J. Health Sci.*, 10 (3), e67382.
- [3] Naimabadi, A., Gholami, A., and Ramezani, A.M., 2021, Determination of heavy metals and health risk assessment in indoor dust from different functional areas in Neyshabur, Iran, *Indoor Built Environ.*, 30 (10), 1781–1795.
- [4] Peng, Z., Deng, W., and Tenorio, R., 2017, Investigation of indoor air quality and the identification of influential factors at primary schools in the North of China, *Sustainability*, 9 (7), 1180.
- [5] Rehman, K., Fatima, F., Waheed, I., and Akash, M.S.H., 2018, Prevalence of exposure of heavy

- metals and their impact on health consequences, *J. Cell. Biochem.*, 119 (1), 157–184.
- [6] Yadav, I.C., Devi, N.L., Singh, V.K., Li, J., and Zhang, G., 2019, Spatial distribution, source analysis, and health risk assessment of heavy metals contamination in house dust and surface soil from four major cities of Nepal, *Chemosphere*, 218, 1100–1113.
- [7] Bamidele, O., Boisa, N., and Obunwo, C.C., 2020, Determination and risk assessment of heavy metals concentrations collected from indoor houses at Lagos State of Nigeria, *Int. J. Adv. Sci. Res. Eng.*, 6 (3), 77–94.
- [8] Alghamdi, A.G., El-Saeid, M.H., Alzahrani, A.J., and Ibrahim, H.M., 2022, Heavy metal pollution and associated health risk assessment of urban dust in Riyadh, Saudi Arabia, *PLoS One*, 17 (1), e0261957.
- [9] Kim, K.H., Kabir, E., and Kabir, S., 2015, A review on the human health impact of airborne particulate matter, *Environ. Int.*, 74, 136–143.
- [10] Jain, S., Sharma, S.K., Vijayan, N., and Mandal, T.K., 2021, Investigating the seasonal variability in source contribution to PM_{2.5} and PM₁₀ using different receptor models during 2013-2016 in Delhi, India, *Environ. Sci. Pollut. Res.*, 28 (4), 4660–4675.
- [11] Tan, S.Y., Praveena, S.M., Abidin, E.Z., and Cheema, M.S., 2016, A review of heavy metals in indoor dust and its human health-risk implications, *Rev. Environ. Health*, 31 (4), 447–456.
- [12] Lin, Y., Fang, F., Wang, F., and Xu, M., 2015, Pollution distribution and health risk assessment of heavy metals in indoor dust in Anhui rural, China, *Environ. Monit. Assess.*, 187 (9), 565.
- [13] Shi, T., and Wang, Y., 2021, Heavy metals in indoor dust: Spatial distribution, influencing factors, and potential health risks, *Sci. Total Environ.*, 755, 142367.
- [14] Cao, S., Chen, X., Zhang, L., Xing, X., Wen, D., Wang, B., Qin, N., Wei, F., and Duan, X., 2020, Quantificational exposure, sources, and health risks posed by heavy metals in indoor and outdoor household dust in a typical smelting area in China, *Indoor Air*, 30 (5), 872–884.
- [15] Theodosi, C., Tsagkaraki, M., Zarmas, P., Grivas, G., Liakakou, E., Paraskevopoulou, D., Lianou, M., Gerasopoulos, E., and Mihalopoulos, N., 2018, Multi-year chemical composition of the fine-aerosol fraction in Athens, Greece, with emphasis on the contribution of residential heating in wintertime, *Atmos. Chem. Phys.*, 18 (19), 14371–14391.
- [16] Rajagopalan, P., and Goodman, N., 2021, Improving the indoor air quality of residential buildings during bushfire smoke events, *Climate*, 9 (2), 32.
- [17] Patel, S., Sankhyani, S., Boedicker, E.K., DeCarlo, P.F., Farmer, D.K., Goldstein, A.H., Katz, E.F., Nazaroff, W.W., Tian, Y., Vanhanen, J., and Vance, M.E., 2020, Indoor particulate matter during HOMEChem: Concentrations, size distributions, and exposures, *Environ. Sci. Technol.*, 54 (12), 7107–7116.
- [18] Tashakor, M., Behrooz, R.D., Asvad, S.R., and Kaskaoutis, D.G., 2022, Tracing of heavy metals embedded in indoor dust particles from the industrial city of Asaluyeh, south of Iran, *Int. J. Environ. Res. Public Health*, 19 (13), 7905.
- [19] Safiur Rahman, M., Khan, M.D.H., Jolly, Y.N., Kabir, J., Akter, S., and Salam, A., 2019, Assessing risk to human health for heavy metal contamination through street dust in the Southeast Asian Megacity: Dhaka, Bangladesh, *Sci. Total Environ.*, 660, 1610–1622.
- [20] Amato, F., Rivas, I., Viana, M., Moreno, T., Bouso, L., Reche, C., Álvarez-Pedrerol, M., Alastuey, A., Sunyer, J., and Querol, X., 2014, Sources of indoor and outdoor PM_{2.5} concentrations in primary schools, *Sci. Total Environ.*, 490, 757–765.
- [21] Jin, Y., O'Connor, D., Ok, Y.S., Tsang, D.C.W., Liu, A., and Hou, D., 2019, Assessment of sources of heavy metals in soil and dust at children's playgrounds in Beijing using GIS and multivariate statistical analysis, *Environ. Int.*, 124, 320–328.
- [22] Latif, M.T., Yong, S.M., Saad, A., Mohamad, N., Baharudin, N.H., Bin Mokhtar, M., and Mohd Tahir, N., 2014, Composition of heavy metals in indoor dust and their possible exposure: A case

- study of preschool children in Malaysia, *Air Qual., Atmos. Health*, 7 (2), 181–193.
- [23] Pedersen, E.K., Bjørseth, O., Syversen, T., and Mathiesen, M., 2001, Physical changes of indoor dust caused by hot surface contact, *Atmos. Environ.*, 35 (24), 4149–4157.
- [24] Al-Momani, I.F., Attiyat, A.S., and Al-Momani, R.M., 2015, Influence of different heating systems on the bioavailable fractions of some elements in house dust, *Jordan J. Chem.*, 10 (3), 194–204.
- [25] Al-Madanat, O., Jiries, A., Batarseh, M., and Al-Nasir, F., 2017, Indoor and outdoor pollution with heavy metals in Al-Karak city, Jordan, *J. Int. Environ. Appl. Sci.*, 12 (2), 131–139.
- [26] Gul, H.K., Gullu, G., Babaei, P., Nikravan, A., Kurt-Karakus, P.B., and Salihoglu, G., 2023, Assessment of house dust trace elements and human exposure in Ankara, Turkey, *Environ. Sci. Pollut. Res.*, 30 (3), 7718–7735.
- [27] Fadel, M., Ledoux, F., Afif, C., and Courcot, D., 2022, Human health risk assessment for PAHs, phthalates, elements, PCDD/Fs, and DL-PCBs in PM_{2.5} and for NMVOCs in two East-Mediterranean urban sites under industrial influence, *Atmos. Pollut. Res.*, 13 (1), 101261.
- [28] Massányi, P., Massányi, M., Madeddu, R., Stawarz, R., and Lukáč, N., 2020, Effects of cadmium, lead, and mercury on the structure and function of reproductive organs, *Toxics*, 8 (4), 94.
- [29] Dabaibeh, R.N., 2021, Spatial distribution of heavy metals in Al-Zarqa, Jordan, *Indones. J. Chem.*, 21 (2), 478–493.
- [30] Massadeh, A.M., Al-Massaedh, A.A.T., and Kharibeh, S., 2018, Determination of selected elements in canned food sold in Jordan markets, *Environ. Sci. Pollut. Res.*, 25 (4), 3501–3509.
- [31] Al-Massaedh, A.A., Gharaibeh, A., Radaydeh, S., and Al-Momani, I., 2018, Assessment of toxic and essential heavy metals in imported dried fruits sold in the local markets of Jordan, *Eur. J. Chem.*, 9 (4), 394–399.
- [32] Belay, K., and Abisa, Z., 2015, Developing a method for trace metal analysis in spices using spectroscopic techniques: A review, *Int. J. Chem. Nat. Sci.*, 3 (1), 195–199.
- [33] Ali, I., Burakov, A., Melezhik, A.V., Babkin, A.V., Burakova, I.V., Neskoromnaya, E.A., Galunin, E., and Tkachev, A.G., 2019, The uptake of Pb(II) metal ion in water using polyhydroquinone/graphene nanocomposite material: Kinetics, thermodynamics and mechanism studies, *Adv. Mater. Technol.*, 4 (16), 3–12.
- [34] Ali, I., Gupta, V.K., and Aboul-Enein, H.Y., 2005, Metal ion speciation and capillary electrophoresis: Application in the new millennium, *Electrophoresis*, 26, 3988–4002.
- [35] Al-Massaedh, A.A., and Al-Momani, I., 2020, Assessment of heavy metal contamination in roadside soils along Irbid-Amman Highway, Jordan by ICP-OES, *Jordan J. Chem.*, 15 (1), 1–12.
- [36] Massadeh, A.M., and Al-Massaedh, A.A.T., 2018, Determination of heavy metals in canned fruits and vegetables sold in Jordan market, *Environ. Sci. Pollut. Res.*, 25 (2), 1914–1920.
- [37] Alzahrani, H.R., Kumakli, H., Ampiah, E., Mehari, T., Thornton, A.J., Babyak, C.M., and Fakayode, S.O., 2017, Determination of macro, essential trace elements, toxic heavy metal concentrations, crude oil extracts and ash composition from Saudi Arabian fruits and vegetables having medicinal values, *Arabian J. Chem.*, 10 (7), 906–913.
- [38] Liu, B., Huang, F., Yu, Y., Li, X., He, Y., Gao, L., and Hu, X., 2021, Heavy metals in indoor dust across China: Occurrence, sources and health risk assessment, *Arch. Environ. Contam. Toxicol.*, 81 (1), 67–76.
- [39] Isangedighi, I.A., and David, G.S., 2019, Heavy metals contamination in fish: Effects on human health, *J. Aquat. Sci. Mar. Biol.*, 2 (4), 7–12.
- [40] Ohiagu, F.O., Chikezie, P.C., Ahaneku, C.C., and Chikezie, C.M., 2022, Human exposure to heavy metals: Toxicity mechanisms and health implications, *Mater. Sci. Eng.*, 6 (2), 78–87.
- [41] Zhao, X., Li, Z., Tao, Y., Wang, D., Huang, J., Qiao, F., Lei, L., and Xing, Q., 2020, Distribution characteristics, source appointment, and health risk

- assessment of Cd exposure via household dust in six cities of China, *Build. Environ.*, 172, 106728.
- [42] Zhao, X., Li, Z., Wang, D., Tao, Y., Qiao, F., Lei, L., Huang, J., and Ting, Z., 2021, Characteristics, source apportionment and health risk assessment of heavy metals exposure via household dust from six cities in China, *Sci. Total Environ.*, 762, 143126.
- [43] Al-Momani, I.F., 2007, Trace elements in street and household dusts in Amman, Jordan, *Soil Sediment Contam.: Int. J.*, 16 (5), 485–496.
- [44] Abdul Wahab, N.A., Muhammad Darus, F., Isa, N., Sumari, S.M., and Muhammad Hanafi, N.F., 2012, Heavy metal concentration of settled surface dust in residential building, *Malays. J. Anal. Sci.*, 16 (1), 18–23.
- [45] Lanphear, B.P., 2015, The impact of toxins on the developing brain, *Annu. Rev. Public Health*, 36, 211–230.
- [46] Al-Momani, I.F., and Shatnawi, W.M., 2017, Chemical characterization and source determination of trace elements in PM_{2.5} and PM₁₀ from an Urban Area, Northern Jordan, *Int. J. Environ. Monit. Anal.*, 5 (4), 103–108.
- [47] Alsbou, E.M.E., and Al-Khashman, O.A., 2018, Heavy metal concentrations in roadside soil and street dust from Petra region, Jordan, *Environ. Monit. Assess.*, 190 (1), 48.
- [48] Alomary, A., El Jamal, E., Al-Momani, I., Attiyat, A., and Obeidat, S., 2013, Pb in medicinal plants from Jordan, *Environ. Chem. Lett.*, 11 (1), 55–63.
- [49] FAO/WHO (Food and Agriculture Organization/World Health Organization), 2001, *Food Additives and Contaminants*, Joint Codex Alimentarius Commission, FAO/WHO Food Standards Program, ALINORM 10/12A, 1–289.
- [50] VROM (Volkshuisvesting, Ruimtelijke Ordening en Milieubeheer), 2000, *Circular on Target Values and Intervention Values for Soil Remediation*, Dutch Ministry of Housing, Spatial Planning and Environment, Netherlands.
- [51] Iwegbue, C.M.A., Obi, G., Emoyan, O.O., Odali, E.W., Egobueze, F.E., Tesi, G.O., Nwajei, G.E., and Martincigh, B.S., 2018, Characterization of metals in indoor dusts from electronic workshops, cybercafés and offices in southern Nigeria: Implications for on-site human exposure, *Ecotoxicol. Environ. Saf.*, 159, 342–353.
- [52] DPR (Department of Petroleum Resources), 2002, *Environmental Guidelines and Standards for the Petroleum Industry in Nigeria (Revised Edition)*, Department of Petroleum Resources, Ministry of Petroleum and Mineral Resources, Abuja, Nigeria.
- [53] Selvi, A., Rajasekar, A., Theerthagiri, J., Ananthaselvam, A., Sathishkumar, K., Madhavan, J., and Rahman, P.K., 2019, Integrated remediation processes toward heavy metal removal/recovery from various environments-A review, *Front. Environ. Sci.*, 7, 66.
- [54] Chattopadhyay, G., Lin, K.C.P., and Feitz, A.J., 2003, Household dust metal levels in the Sydney metropolitan area, *Environ. Res.*, 93 (3), 301–307.
- [55] Jadoon, W.A., Abdel-Dayem, S.M.M.A., Saqib, Z., Takeda, K., Sakugawa, H., Hussain, M., Shah, G.M., Rehman, W., and Syed, J.H., 2021, Heavy metals in urban dusts from Alexandria and Kafr El-Sheikh, Egypt: Implications for human health, *Environ. Sci. Pollut. Res.*, 28 (2), 2007–2018.
- [56] Darus, F.M., Nasir, R.A., Sumari, S.M., Ismail, Z.S., and Omar, N.A., 2012, Heavy metals composition of indoor dust in nursery schools building, *Procedia - Soc. Behav. Sci.*, 38, 169–175.
- [57] Harb, M.K., Ebqa'ai, M., Al-rashidi, A., Alaziqi, B.H., Al Rashdi, M.S., and Ibrahim, B., 2015, Investigation of selected heavy metals in street and house dust from Al-Qunfudah, Kingdom of Saudi Arabia, *Environ. Earth Sci.*, 74 (2), 1755–1763.
- [58] Rasmussen, P.E., Subramanian, K.S., and Jessiman, B.J., 2001, A multi-element profile of house dust in relation to exterior dust and soils in the city of Ottawa, Canada, *Sci. Total Environ.*, 267 (1-3), 125–140.
- [59] Wang, G., Zeng, C., Zhang, F., Zhang, Y., Scott, C.A., and Yan, X., 2017, Traffic-related trace elements in soils along six highway segments on the Tibetan Plateau: Influence factors and spatial variation, *Sci. Total Environ.*, 581-582, 811–821.

- [60] Li, Y., Fang, F., Lin, Y., Wang, Y., Kuang, Y., and Wu, M., 2020, Heavy metal contamination and health risks of indoor dust around Xinqiao Mining Area, Tongling, China, *Hum. Ecol. Risk Assess.: Int. J.*, 26 (1), 46–56.
- [61] Dingle, J.H., Kohl, L., Khan, N., Meng, M., Shi, Y.A., Pedroza-Brambila, M., Chow, C.W., and Chan, A.W.H., 2021, Sources and composition of metals in indoor house dust in a mid-size Canadian city, *Environ. Pollut.*, 289, 117867.
- [62] Aprile, F.M., and Bouvy, M., 2008, Distribution and enrichment of the heavy metals in sediments at the Tapacurá river basin, Northeastern Brazil, *Braz. J. Aquat. Sci. Technol.*, 12 (1), 1–8.

Synthesis of Cellulose Acetate from Screw Pine (*Pandanus tectorius*) Leaves for Enhancing Water Permeability and Fouling Resistance of PVDF Membrane

Elyna Wahyu Trisnawati, Venty Suryanti*, Edi Pramono, Indri Sri Cahyani, and Diah Safriyani

Department of Chemistry, Faculty of Mathematics and Natural Sciences, Universitas Sebelas Maret,
Jl. Ir. Sutami 36A, Surakarta 57126, Indonesia

* **Corresponding author:**

email: venty@mipa.uns.ac.id

Received: June 15, 2023

Accepted: September 11, 2023

DOI: 10.22146/ijc.85726

Abstract: Cellulose derivatives from natural resources continuously develop to find the best hydrophobic polymer-based membrane technology performance. This study was conducted to improve the hydrophilicity, performance, and anti-fouling of polyvinylidene fluoride (PVDF) membrane with cellulose acetate (CA) filler synthesized from screw pine (*Pandanus tectorius*) leaf cellulose. CA was synthesized by the Fischer esterification mechanism and the PVDF membrane was fabricated using the phase inversion method with 0.3% CA concentration. FTIR analysis of CA shows an absorption at 1700 cm^{-1} suggesting that the hydroxyl group of cellulose had been successfully substituted with an ester group (C=O), and CA has a high degree of substitution (DS) value of 3.50. Adding CA improved the hydrophilicity and anti-fouling properties of up to 86.45% of PVDF membranes. Furthermore, CA increased the value of water permeability 2–3 times than pristine PVDF membrane. The presence of CA enhanced the porosity of the PVDF membrane, which promoted the membrane's effectiveness for MB filtering. As a result, CA from screw pine leaf cellulose has promising features as a filler for PVDF membranes and potential dye filtration.

Keywords: anti-fouling; cellulose; cellulose acetate; polyvinylidene fluoride; water permeability

■ INTRODUCTION

Polyvinylidene Fluoride (PVDF), commonly known as poly(1,1-difluoroethylene), has a repeating unit of $(\text{CH}_2-\text{CF}_2)$ [1]. PVDF is a polymer that is frequently utilized as a matrix membrane due to its excellent properties, such as thermal stability, membrane-forming ability, and high mechanical strength [2]. Nonetheless, the hydrophobic nature of PVDF membrane causes fouling, decreasing the membrane performance and shortening the membrane lifetime [3-4]. It is crucial to increase hydrophilicity to reduce PVDF membrane fouling.

Among the numerous materials utilized to promote PVDF membrane hydrophilicity, natural polymer has received attention due to its low cost and ease of availability [5]. Cellulose is one of the most common natural polymers in the world, accounting for 700,000 billion tons of total biomass production per year [6]. Natural cellulose-based fibers have several advantages over synthetic fibers, including low cost, low density, good strength, good

stiffness, environmentally friendly, biodegradable, renewable, and health-safe [7-8]. The cellulose skeleton's hydroxyl groups can be chemically modified to form ester groups that are insoluble in water [8-10].

Cellulose acetate (CA) is a cellulose ester derivative that has been widely applied in membranes. CA is a desirable polymer due to its low cost, biocompatibility, biodegradability, and acceptable physical qualities in industry [11-12]. CA is utilized in food packaging, coatings, sealants, and membrane separation [13]. Wood and cotton are the most important material resources for industrial synthesizing CA, although they have a high lignin content which requires more chemicals to remove cellulose [14]. Screw pine (*Pandanus tectorius*) is a non-wood plant of Pandanaceae family that grows naturally on river banks and swamps in the tropics that are rarely utilized. Isolation of cellulose from non-wood materials can reduce the usage of chemicals [8,15]. The functional groups of screw pine fibers are similar to those of flax,

kenaf, and linen natural fibers [16]. Screw pine leaves have a chemical composition of 37.3% cellulose, 34.4% hemicellulose, 15.7% pentose, 24% lignin, and 2.5% others [17]. As a result, Screw pine leaves can potentially be a source of CA synthesis.

Previous research used commercial CA [18-20] for matrix membranes and generated CA [14,21-23]. CA commercial has been used to improve water flux and fouling resistance in polyethersulfone (PES) [24], polysulfone (PSf) [25], and PVDF membranes [12,26-27]. So far, synthetic CA has not been used as a matrix membrane filler. No previous research has employed CA synthesized from screw pine as a PVDF membrane filler. This study used screw pine (*P. tectorius*) leaves as the starting material to synthesize cellulose acetate. It was used as a filler for PVDF membranes to improve water permeability and anti-fouling qualities. Water permeability, rejection, and anti-fouling from the flux recovery ratio (FRR) test were used to evaluate the performance of the manufactured PVDF/CA membrane.

■ EXPERIMENTAL SECTION

Materials

The materials used in this study were screw pine leaves collected from Yogyakarta coastal area, aquadest, NaOH, HCl, NaOCl, acetic acid anhydride, acetic acid glacial, H₂SO₄, DMAc, and PEG 400. Chemicals were purchased from e-Merck, Germany. PVDF (Solef PVDF 1010 Mw 352 kDa) was obtained from Solvay.

Instrumentation

The instrumentations used in this study were Fourier transform infrared (FTIR) Shimadzu FTIR Prestige 21 Model 8201 PC, scanning electron microscope (SEM) JEOL JSM-6510LA, thermogravimetric analyzer (TGA), and differential scanning calorimetry (DSC) STA Linseis PT 1600.

Procedure

Isolation of cellulose from screw pine leaves

Cellulose from screw pine leaves was isolated [17]. Screw pine leaves were collected from Yogyakarta coastal area. Screw pine leaves are stripped of their thorns and cut into 12 × 3 cm pieces. The leaf pieces were then sun-dried.

Dried screw pine leaves were cut into smaller pieces of around 1 × 1 cm and immersed in water for 3 × 24 h, with the water changed regularly. The screw pine leaves were then sun-dried again and grounded. Screw pine leave powder (100 g) was mixed in 10% NaOH for 2 h at 100 °C, with a screw pine leave to NaOH ratio of 1:20. The mixture was then neutralized to pH 7 and dried for 3 h at 60 °C. The dry powder was mixed with 4% NaOCl pH 4.5 at 100 °C for 2 h with a 1:20 alkalization product to NaOCl ratio. To obtain cellulose from screw pine leaves, the mixture was neutralized to pH 7 and dried at 60 °C for 3 h.

Synthesis of CA

CA was synthesized following [28] with modifications. Screw pine leaf cellulose (1 g) was added with glacial acetic acid (2.4 mL) and agitated for 60 min at 38 °C. The mixture was then stirred for 45 min at 38 °C with glacial acetic acid (4 mL) and sulfuric acid (0.5 mL). The mixture was then chilled to 18 °C. The acetylation procedure was then carried out. Acetic anhydride (10 mL) and sulfuric acid (0.5 mL) were added to the mixture and agitated for 90 min at 35 °C. The acetylation process was stopped by adding distilled water (1 mL) and glacial acetic acid (2 mL) and stirring at room temperature for 1 h. The mixture was neutralized with distilled water. The product was dried at 60 °C for 3 h to obtain cellulose acetate.

PVDF/CA membrane fabrication

Membrane PVDF/CA was fabricated by phase inversion [17]. First, DMAc (9.32 g) and PEG 400 (0.48 g) were stirred 5 min. The mixture was then added with cellulose acetate (0.036 g) and stirred for 10 min. Finally, PVDF (2.16 g) was added to the mixture and agitated at 60 °C for 24 h to prepare the dope solution for the PVDF/CA membrane. Otherwise, the PVDF dope solution was made using the same method, but without the CA filler. The dope solution was then cast in a glass plate and placed in a coagulation bath containing distilled water to produce the membranes.

Characterization of cellulose acetate

The FTIR spectral analysis was used to calculate the degree of substitution (DS) of cellulose acetate.

According to Eq. (1), the absorbance of C=O cellulose acetate was compared to the absorbance of C-O cellulose.

$$DS = \frac{Abs_{C=O}}{Abs_{C-O}} \quad (1)$$

The functional groups of the cellulose and cellulose esters were determined by FTIR spectrophotometer. The dried samples were combined in a 1:100 ratio with potassium bromide (KBr) powder, compressed into a thin transparent pellet, and the transmission was measured at 4000–400 cm^{-1} .

The surface morphologies of cellulose and cellulose acetate were analyzed by SEM. Coated samples with a thin layer of gold were mounted and imaged at 500–5000× magnifications with 10 kV accelerating voltage at a pressure of 70 Pa. The thermal stability of cellulose and cellulose acetate was studied by TGA. The samples were heated up to 600 °C at a heating rate of 10 °C/min under an air atmosphere.

PVDF and PVDF/CA membranes characterization and performance evaluation

The performance of PVDF and PVDF/CA membranes was evaluated [17]. PVDF and PVDF/CA membranes were evaluated by water contact angle, porosity (ϵ), pure water flux (PWF), water flux, rejection, and flux recovery ratio (FRR). Membrane porosity was determined using the gravimetric technique and Eq. (2),

$$\epsilon(\%) = \left(\frac{W_{wet} - W_{dried}}{A \times I_{wet} \times \rho} \right) \quad (2)$$

where W_{wet} is the weight of the membrane (g), I_{wet} is the thickness of the membrane (cm) in wet condition, W_{dried} is the weight of the dry membrane (g) after oven at 60 °C for 24 h, ρ is water density ($g\ cm^{-3}$), and A is the membrane area (m^2).

The membrane performance was evaluated using a dead-end system with continuous measurements beginning with PWF, water flux, rejection, and FRR. The membrane (diameter 5 cm) was placed in a stirred cell and then filled with distilled water to measure PWF (J_1) (Eq. (3)). To assess water flux and rejection (%R) (Eq. (4)), the distilled water was replaced with a 100-ppm methylene blue (MB) solution. Before performing the FRR test (Eq. (5)), the MB solution was partially replaced with distilled water and swirled without pressure to

eliminate any leftover MB on the surface membrane before being completely replaced with new distilled water. All measurements were taken using a two-bar system compaction for 15 min.

$$J_1 = \frac{v}{A \times t} \quad (3)$$

$$\%R = \left(1 - \frac{C_p}{C_r} \right) \times 100 \quad (4)$$

$$FRR = \frac{J_2}{J_1} \times 100\% \quad (5)$$

J_1 denotes PWF (L/m^2h), v permeates volume (L), A membrane surface area (m^2), t time (h), C_p permeate concentration, and C_r concentration J_2 is water flux (L/m^2h), and retentate was determined using a UV-vis spectrophotometer at 664 nm. The thermal stability of PVDF and PVDF/CA membranes was evaluated by TGA. The membranes were heated up to 900 °C at a heating rate of 10 °C/min under an air atmosphere.

RESULTS AND DISCUSSION

Isolation of Cellulose and Synthesis of CA from Screw Pine Leaves

Initially, cellulose was isolated by soaking screw pine leaf powder in water to remove pentose sugar, tannins, and pigments. White powders of cellulose were obtained at 40.24% yield. The fiber does not appear in SEM images of screw pine leaf powder (Fig. 1(a) and 1(b)) because it was bonded by lignin and hemicellulose [7]. An alkalization method was used to remove lignin and hemicellulose. The bleaching process was performed to degrade the remaining lignin to increase cellulose purity [29-30]. SEM images of cellulose and the magnification (Fig. 1(c) and 1(d)) revealed the individual fiber after alkalization and bleaching. Cellulose was successfully isolated from screw pine leaves, as confirmed by SEM. The isolated cellulose was converted into CA. Cellulose morphology changed after the acetylation process. SEM images of CA and the magnification (Fig. 1(e) and 1(f)) showed that CA formed aggregates with produce hole, where no fibers were found in synthesized CA. Morphological changes from cellulose to CA occur due to acetylation substitution towards the -OH group, in which initially

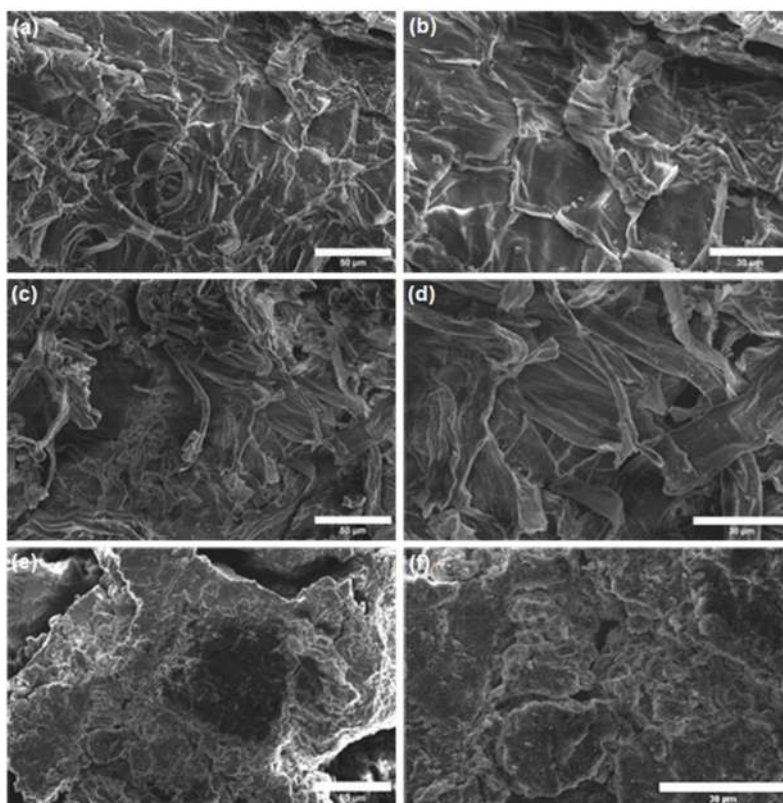


Fig 1. SEM image and the magnification of (a, b) screw pine leaf powder, (c, d) cellulose, and (e, f) CA

intramolecular hydrogen bonds of the $-OH$ functional group were formed [31].

Analysis of the functional group of screw pine leaf powder, cellulose, and cellulose acetate was investigated using FTIR (Fig. 2). The absence of peaks at 1504 and 1235 cm^{-1} for $C=C$ stretching lignin in cellulose spectra [8] indicated that lignin was eliminated, and cellulose was successfully isolated. In the FTIR spectra of CA, bands appeared at 1754 , 1374 , and 1235 cm^{-1} , corresponding to functional groups of $C=O$ stretching for carbonyl ester, $C-H$ in $O-(C=O)-CH_3$, and $C-O$ stretching for acetyl. The decrease in absorption intensity for $-OH$ stretching at 3384 cm^{-1} shows that the $-OH$ group of cellulose was substituted with acetyl groups from acetic anhydride [28,32-33]. The success of CA synthesis was validated by FTIR data, which matched the CA obtained in prior studies [28,32,34]. Furthermore, the DS value supports the successful CA synthesis. The DS of CA was 3.50, confirming the formation of cellulose triacetate.

The Fischer mechanism reaction was used to synthesize CA (Fig. 3). The initial esterification reaction

was carried out by substituting cellulose hydroxyl groups with acetyl groups. CA synthesis begins by enhancing the reactivity of cellulose's acetyl group with glacial acetic acid. The acetylation process requires a large cellulose surface, and the rate of the acetylation reaction is determined by the accessibility of the surface

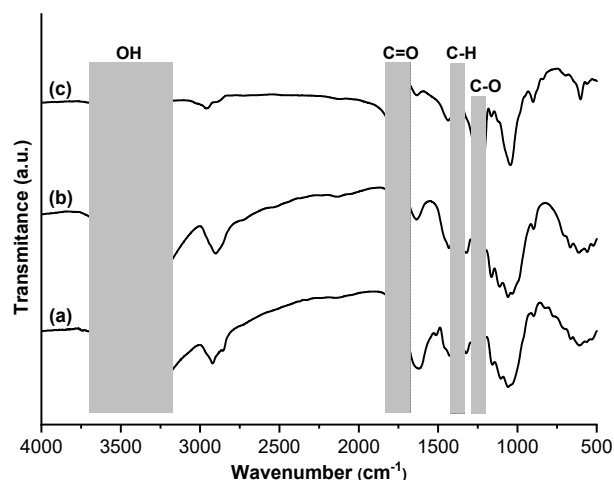


Fig 2. FT-IR spectra of (a) screw pine leaf, (b) cellulose, and (c) CA

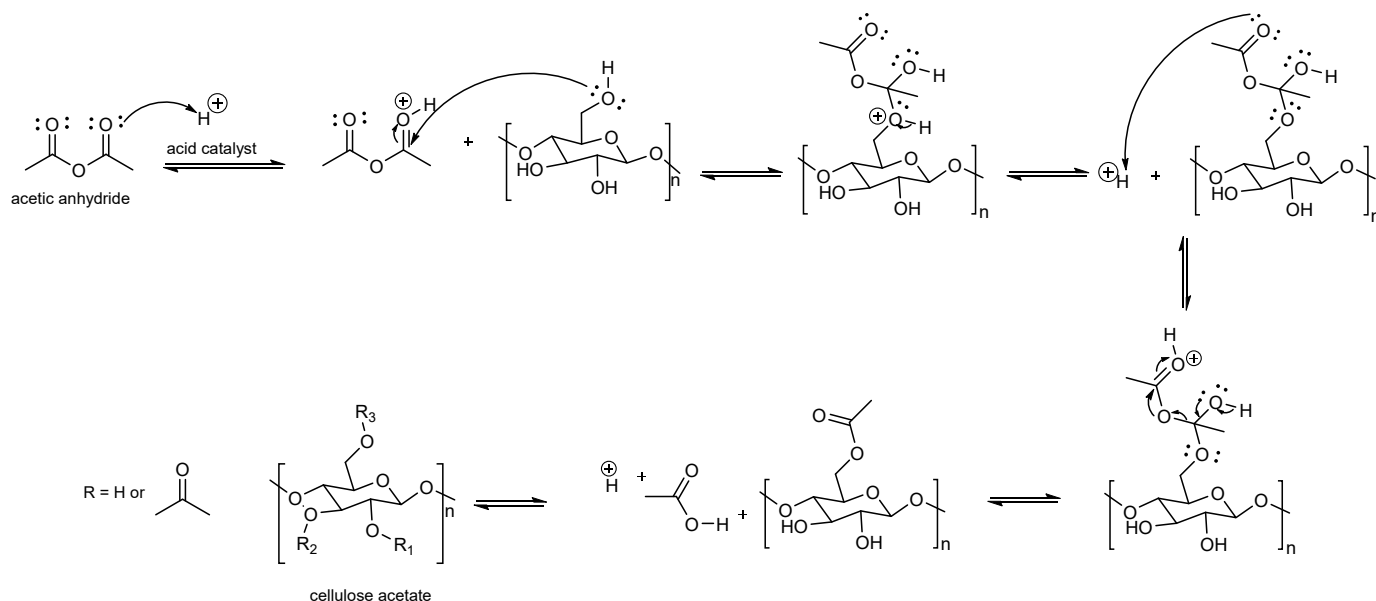


Fig 3. Fischer esterification mechanism reaction

opening ability of the cellulose fiber. The greater the surface area of the cellulose fiber, the easier the subsequent acetylation reactions [35]. Acetylation was accomplished by using acetic anhydride, and sulfuric acid was used as a catalyst. When the -OH group of cellulose is exchanged with the acetyl group of acetic anhydride, the desired CA and acetic acid are produced as a result. Because acetylation is an exothermic reaction, the reaction was carried out at a low temperature to maintain the cellulose is being degraded. The acetylation reaction is terminated through a hydrolysis process with the addition of acetic acid. This method eliminates unreacted acetic anhydride and releases the acetyl group [34]. CA was obtained as a white powder in 89% yield.

The cellulose and CA thermograms revealed three stages of degradation (Fig. 4). The first degradation occurred below 100 °C, exhibiting water evaporation. Because of the acetylation process of cellulose, mass reduction of cellulose was greater than CA in the first degradation (Table 1). Water absorption of cellulose acetate is reduced when hydroxyl groups are replaced with acetate groups. In the second stage, the cellulose and CA polymer chains degraded, with CA having more excellent thermal stability than cellulose [14]. CA polymer chain degradation is identical to CA produced by Chuayplod and Aht-Ong [36], which degraded at 298–375 °C. The

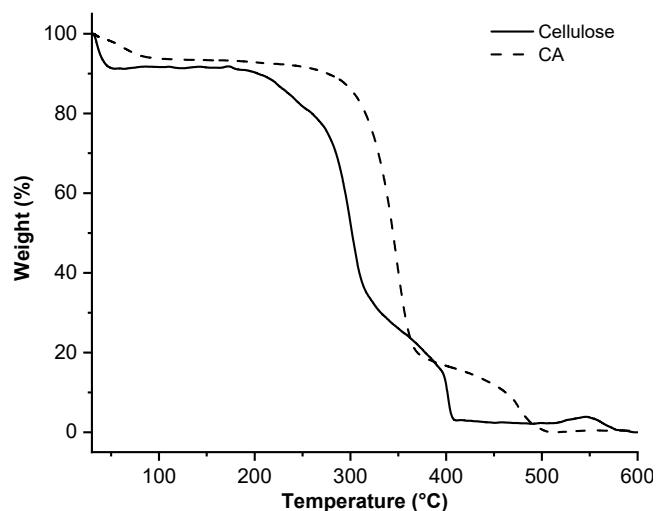


Fig 4. Thermogram of (a) cellulose and (b) CA

Table 1. Thermal stability of cellulose and CA

Samples	Temperature (°C)	Mass reduction (%)
Cellulose	31–54	8.76
	205–407	86.52
	407–600	3.28
CA	31–90	5.99
	270–370	70.59
	390–600	17.16

third stage is cellulose and CA backbone degradation [14]. This finding demonstrated that the acetylation process improved cellulose's thermal stability.

Characterization and Performance Evaluation of PVDF and PVDF/CA Membranes

PVDF and PVDF/CA membranes were characterized by TGA and DTG analysis. Thermograms of PVDF and PVDF/CA membranes (Fig. 5(a)) showed similar thermal stability. Degradation at temperatures under 100 °C appeared in the PVDF membrane due to water evaporation [4,17]. Whereas evaporation of water in the PVDF/CA membrane did not appear. Degradation of PVDF polymer matrix in PVDF and PVDF/CA membrane occurred at a relatively similar temperature at 420 and 490 °C. Therefore, the addition of CA in the PVDF matrix membrane did not drastically affect the thermal stability of the PVDF membrane. DSC thermogram of PVDF and PVDF/CA membrane (Fig. 5(b)) showed the endotherm peak. The addition of CA caused a shift in melting temperature (T_m) from 169 to 171 °C. It showed that the PVDF membrane has two crystalline phases, α and β phases [37]. The addition of CA

did not decrease the characteristic melting point of the PVDF membrane.

Water contact angle, porosity, PWF, water flux, rejection, and FRR were used to evaluate the performance of PVDF and PVDF/CA membranes, as shown in Table 2. The addition of cellulose acetate decreased the water contact angle of the PVDF membrane. The acetylation process decreases the number of cellulose hydroxyl groups [38]. Whereas cellulose hydroxyl groups unsubstituted with acetate groups can ensure the hydrophilic properties of CA. The porosity of the PVDF membrane increases up to 85.47% with CA addition. The difference in hydrophilicity between PVDF and CA causes a repulsive force that increases the porosity of the PVDF membrane [4].

PWF and water flux increased twice in the PVDF/CA membrane. Increasing the porosity of PVDF/CA improves membrane water permeability because water can easily travel through the membrane.

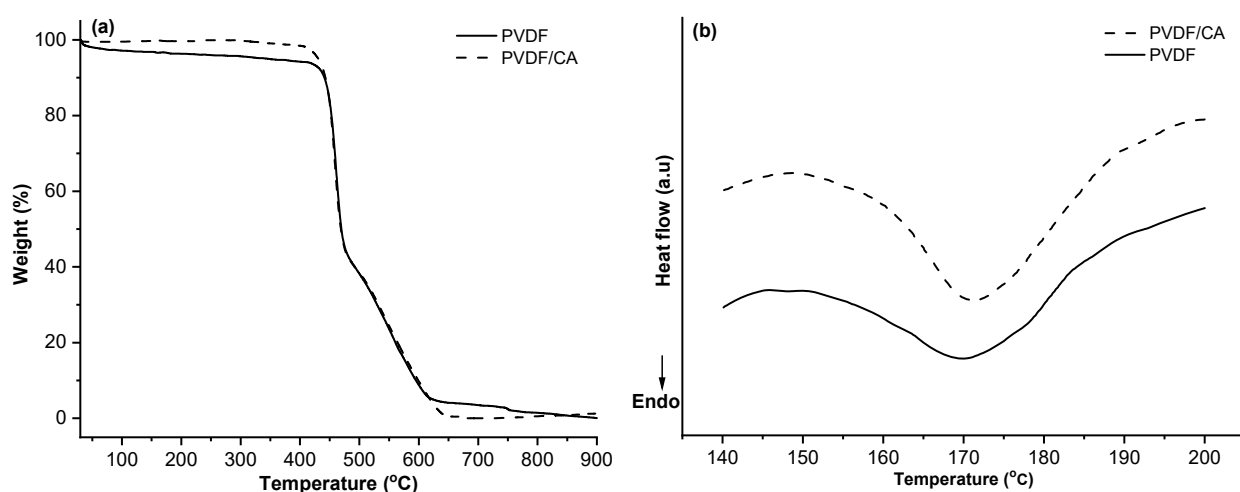


Fig 5. (a) TGA and (b) DSC of PVDF and PVDF/cellulose membranes

Table 2. Performance evaluation of PVDF and PVDF/CA membranes and the comparison with PVDF/CA membrane other studies

Membrane	Feed molecule	Water contact angle (°)	Porosity (%)	PWF (L/m ² h)	Water flux (L/m ² h)	Rejection (%)	FRR (%)	Ref.
PVDF	MB	89.70 ± 2.12	70.70 ± 0.48	17.08 ± 2.02	11.22 ± 0.18	82.89 ± 2.11	80.26 ± 0.68	This work
PVDF/CA	MB	88.13 ± 1.01	85.47 ± 0.88	45.42 ± 3.07	42.15 ± 3.08	77.73 ± 3.57	86.45 ± 3.62	This work
PVDF/CA	PEG	~93.00	-	136.20	-	3.00	94.20	[12]
PVDF/CA	PEG	~61.00	~82.00	522.00	~300.00	~68.00	~76.00	[26]
PVDF/CA	MB	56.43	~84.00	140.00	83.17	90.24	95.77	[27]

The higher the porosity of the PVDF/CA membrane, the lower MB rejection because the MB molecule can pass through the membrane. Lower membrane rejection is achieved by increasing water permeability [17,39]. PVDF membrane anti-fouling properties improved with the addition of CA, which has an excellent anti-fouling performance and minimizes interaction between MB and surface membrane [40]. The washing treatment performed before the FRR test improved the anti-fouling value of the PVDF/CA membrane. PVDF/CA membrane performed well and was comparable to earlier studies that employed commercial CA as a filler for PVDF membrane. Table 2 shows a comparison of membrane performance with previous studies. Our PVDF/CA membrane performances are comparable to other commercial PVDF membranes with the addition of CA. In this work, including CA synthesized from screw pine cellulose resulted in higher porosity, water permeability, and FRR values than the PVDF membrane. As a result, the PVDF/CA membrane developed in this work has the potential to be used in dye wastewater filtration.

■ CONCLUSION

Cellulose was successfully isolated from screw pine (*Pandanus tectorius*) leaves by alkalization and bleaching treatment which was confirmed by FTIR, SEM, and TGA analysis. Cellulose acetate (CA) was produced with high yields of 89% utilizing Fischer esterification processes and acetic anhydride reagents. The cellulose acetates were more thermally stable than cellulose and had a high DS of 3.50. The presence of CA did not affect the thermal stability of the PVDF membrane. The addition of CA improves PVDF membrane performance by increasing water permeability by twice and anti-fouling qualities up to 86.45%. PVDF/CA membrane also has good filtration ability against methylene blue (MB) up to 77.73%. Thus, these membranes have the potential for dye wastewater treatment. This synthesized CA has good properties as a filler to PVDF membrane for filtration MB.

■ ACKNOWLEDGMENTS

The project presented in this article is supported by Universitas Sebelas Maret through a grant with contract

number 260/UN27.22/HK.07.00/2021 and 254/27.22/PT.01.03/2022.

■ AUTHOR CONTRIBUTIONS

Elyna Wahyu Trisnawati conducted research, analyzed data and wrote an original draft; Indri Sri Cahyani and Diah Safriyani performed the experiments and data collection; Edi Pramono developed methodology and verification data; Venty Suryanti conducted formulation and verification data as well as wrote a manuscript (review and editing). All authors agreed to the final version of this manuscript.

■ REFERENCES

- [1] Saxena, P., and Shukla, P., 2021, A comprehensive review on fundamental properties and applications of poly(vinylidene fluoride) (PVDF), *Adv. Compos. Hybrid Mater.*, 4 (1), 8–26.
- [2] Ayyaru, S., and Ahn, Y.H., 2017, Application of sulfonic acid group functionalized graphene oxide to improve hydrophilicity, permeability, and antifouling of PVDF nanocomposite ultrafiltration membranes, *J. Membr. Sci.*, 525, 210–219.
- [3] Deng, W., and Li, Y., 2021, Novel superhydrophilic antifouling PVDF-BiOCl nanocomposite membranes fabricated via a modified blending-phase inversion method, *Sep. Purif. Technol.*, 254, 117656.
- [4] Pramono, E., Zakaria, M.A., Fridiasari, K.F., Ndruru, S.T.C.L., Bagaskara, M., Mustofa, R.E., Sejati, G.P.W., Purnawan, C., and Saputra, O.A., 2022, Cellulose derived from oil palm empty fruit bunches as filler on polyvinylidene fluoride based membrane for water containing humic acid treatment, *Groundwater Sustainable Dev.*, 17, 100744.
- [5] Anita Lett, J., Sagadevan, S., Fatimah, I., Hoque, M.E., Lokanathan, Y., Léonard, E., Alshahateet, S.F., Schirhagl, R., and Oh, W.C., 2021, Recent advances in natural polymer-based hydroxyapatite scaffolds: Properties and applications, *Eur. Polym. J.*, 148, 110360.
- [6] de Melo Brites, M., Cerón, A.A., Costa, S.M., Oliveira, R.C., Ferraz, H.G., Catalani, L.H., and

- Costa, S.A., 2020, Bromelain immobilization in cellulose triacetate nanofiber membranes from sugarcane bagasse by electrospinning technique, *Enzyme Microb. Technol.*, 132, 109384.
- [7] Afolabi, L.O., Megat-Yusoff, P.S.M., Ariff, Z.M., and Hamizol, M.S., 2019, Fabrication of *Pandanus tectorius* (screw-pine) natural fiber using vacuum resin infusion for polymer composite application, *J. Mater. Res. Technol.*, 8 (3), 3102–3113.
- [8] Suryanti, V., Kusumaningsih, T., Safriyani, D., and Cahyani, I. S., 2023, Synthesis and characterization of cellulose ethers from screw pine (*Pandanus tectorius*) leaves cellulose as food additives, *Int. J. Technol.*, 14 (3), 291–319.
- [9] Zhou, Y., Zhang, X., Cheng, Y., Zhang, J., Mi, Q., Yin, C., Wu, J., and Zhang, J., 2022, Super-rapid and highly-efficient esterification of cellulose to achieve an accurate chromatographic analysis of its molecular weight, *Carbohydr. Polym.*, 286, 119301.
- [10] Sun, B., Zhang, M., Shen, J., He, Z., Fatehi, P., and Ni, Y., 2019, Applications of cellulose-based materials in sustained drug delivery systems, *Curr. Med. Chem.*, 26 (14), 2485–2501.
- [11] Vatanpour, V., Pasaoglu, M.E., Barzegar, H., Teber, O.O., Kaya, R., Bastug, M., Khataee, A., and Koyuncu, I., 2022, Cellulose acetate in fabrication of polymeric membranes: A review, *Chemosphere*, 295, 133914.
- [12] Mu, C., Su, Y., Sun, M., Chen, W., and Jiang, Z., 2010, Remarkable improvement of the performance of poly(vinylidene fluoride) microfiltration membranes by the additive of cellulose acetate, *J. Membr. Sci.*, 350 (1-2), 293–300.
- [13] Nilsson, R., Olsson, M., Westman, G., Matic, A., and Larsson, A., 2022, Screening of hydrogen bonds in modified cellulose acetates with alkyl chain substitutions, *Carbohydr. Polym.*, 285, 119188.
- [14] Candido, R.G., Godoy, G.G., and Gonçalves, A.R., 2017, Characterization and application of cellulose acetate synthesized from sugarcane bagasse, *Carbohydr. Polym.*, 167, 280–289.
- [15] Gallaher, T., Callmander, M.W., Buerki, S., and Keeley, S.C., 2015, A long distance dispersal hypothesis for the Pandanaceae and the origins of the *Pandanus tectorius* complex, *Mol. Phylogenet. Evol.*, 83, 20–32.
- [16] Mat Piah, M.R.M., Baharum, A., and Abdullah, I., 2016, Mechanical properties of bio-composite natural rubber/high density polyethylene/mengkuang fiber (NRHDE/MK), *Polym. Polym. Compos.*, 24 (9), 767–774.
- [17] Trisnawati, E.W., Cahyani, I.S., Safriyani, D., Pramono, E., and Suryanti, V., 2023, Cellulose, cellulose benzoate and cellulose citrate from screw pine (*Pandanus tectorius*) leaves as PVDF filler for improved permeability and anti-fouling properties, *Period. Polytech., Chem. Eng.*, 67 (3), 504–515.
- [18] Silva, M.A., Belmonte-Reche, E., and de Amorim, M.T.P., 2021, Morphology and water flux of produced cellulose acetate membranes reinforced by the design of experiments (DOE), *Carbohydr. Polym.*, 254, 117407.
- [19] Guo, H., Peng, Y., Liu, Y., Wang, Z., Hu, J., Liu, J., Ding, Q., and Gu, J., 2020, Development and investigation of novel antifouling cellulose acetate ultrafiltration membrane based on dopamine modification, *Int. J. Biol. Macromol.*, 160, 652–659.
- [20] Han, B., Zhang, D., Shao, Z., Kong, L., and Lv, S., 2013, Preparation and characterization of cellulose acetate/carboxymethyl cellulose acetate blend ultrafiltration membranes, *Desalination*, 311, 80–89.
- [21] Radiman, C.L., Widyaningsih, S., and Sugesty, S., 2008, New applications of kenaf (*Hibiscus cannabinus* L.) as microfiltration membranes, *J. Membr. Sci.*, 315 (1-2), 141–146.
- [22] Filho, G.R., da Cruz, S.F., Pasquini, D., Cerqueira, D.A., Prado, V.S., and de Assunção, R.M.N., 2000, Water flux through cellulose triacetate films produced from heterogeneous acetylation of sugar cane bagasse, *J. Membr. Sci.*, 177 (1), 225–231.
- [23] Meireles, C.S., Filho, G.R., Fernandes Ferreira, M., Cerqueira, D.A., Assunção, R.M.N., Ribeiro, E.A.M., Poletto, P., and Zeni, M., 2010, Characterization of asymmetric membranes of cellulose acetate from biomass: Newspaper and mango seed, *Carbohydr. Polym.*, 80 (3), 954–961.

- [24] Mansourizadeh, A., and Javadi Azad, A., 2014, Preparation of blend polyethersulfone/cellulose acetate/polyethylene glycol asymmetric membranes for oil–water separation, *J. Polym. Res.*, 21 (3), 375.
- [25] Moradihamedani, P., and Abdullah, A.H., 2019, Ammonia removal from aquaculture wastewater by high flux and high rejection polysulfone/cellulose acetate blend membrane, *Polym. Bull.*, 76 (5), 2481–2497.
- [26] Hossein Razzaghi, M., Safekordi, A., Tavakolmoghadam, M., Rekabdar, F., and Hemmati, M., 2014, Morphological and separation performance study of PVDF/CA blend membranes, *J. Membr. Sci.*, 470, 547–557.
- [27] Reza, M., Promono, E., and Radiman, C.L., 2022, Improving separation performance of PVDF ultrafiltration membranes by blending with cellulose acetate, *Iran. J. Chem. Chem. Eng.*, 42 (3), 1017–1029.
- [28] Candido, R.G., and Gonçalves, A.R., 2016, Synthesis of cellulose acetate and carboxymethylcellulose from sugarcane straw, *Carbohydr. Polym.*, 152, 679–686.
- [29] Adawiyah, R., Suryanti, V., and Pranoto, P., 2022, Preparation and characterization of microcrystalline cellulose from Lembang (*Typha angustifolia* L.), *J. Phys.: Conf. Ser.*, 2190, 012007.
- [30] Pranoto, P., Suryanti, V., and Adawiyah, R., 2023, Andisol and microcrystalline cellulose from *Typha angustifolia* for auramine O adsorption, *Int. J. Adv. Appl. Sci.*, 12 (1), 27–36.
- [31] Goswami, M., and Das, A.M., 2019, Synthesis and characterization of a biodegradable cellulose acetate-montmorillonite composite for effective adsorption of Eosin Y, *Carbohydr. Polym.*, 206, 863–872.
- [32] Andrade Alves, J.A., Lisboa dos Santos, M.D., Morais, C.C., Ramirez Ascheri, J.L., Signini, R., dos Santos, D.M., Cavalcante Bastos, S.M., and Ramirez Ascheri, D.P., 2019, Sorghum straw: Pulping and bleaching process optimization and synthesis of cellulose acetate, *Int. J. Biol. Macromol.*, 135, 877–886.
- [33] Araújo, D., Castro, M.C.R., Figueiredo, A., Vilarinho, M., and Machado, A., 2020, Green synthesis of cellulose acetate from corncob: Physicochemical properties and assessment of environmental impacts, *J. Cleaner Prod.*, 260, 120865.
- [34] Suhartini, M., Ernawati, E.E., Roshanova, A., Haryono, H., and Mellawati, J., 2020, Cellulose acetate of rice husk blend membranes: Preparation, morphology and application, *Indones. J. Chem.*, 20 (5), 1061–1069.
- [35] Mauliana, M., Kurniasih, E., and Syafruddin, S., 2019, Synthesis of acetate cellulose from the palm oil empty floor through the reaction of activation, *JSTR*, 17 (1), 1–5.
- [36] Chuayplod, P., and Aht-Ong, D., 2018, Mechanochemical-assisted heterogeneous surface modification of parawood microcrystalline cellulose and its effect on the properties of polypropylene composites, *World J. Eng.*, 15 (6), 719–730.
- [37] Martins, P., Lopes, A.C., and Lanceros-Mendez, S., 2014, Electroactive phases of poly(vinylidene fluoride): Determination, processing and applications, *Prog. Polym. Sci.*, 39 (4), 683–706.
- [38] Rahimi Kord Sofla, M., Batchelor, W., Kosinkova, J., Pepper, R., Brown, R., and Rainey, T., 2019, Cellulose nanofibres from bagasse using a high-speed blender and acetylation as a pretreatment, *Cellulose*, 26 (8), 4799–4814.
- [39] Teow, Y.H., Amirudin, S.N., and Ho, K.C., 2020, Sustainable approach to the synthesis of cellulose membrane from oil palm empty fruit bunch for dye wastewater treatment, *J. Water Process Eng.*, 34, 101182.
- [40] Sharma, M., Das, P.P., Sood, T., Chakraborty, A., and Purkait, M.K., 2022, Reduced graphene oxide incorporated polyvinylidene fluoride/cellulose acetate proton exchange membrane for energy extraction using microbial fuel cells, *J. Electroanal. Chem.*, 907, 115890.

Synthesis of Cellulose Acetate from Screw Pine (*Pandanus tectorius*) Leaves for Enhancing Water Permeability and Fouling Resistance of PVDF Membrane

Elyna Wahyu Trisnawati, Venty Suryanti*, Edi Pramono, Indri Sri Cahyani, and Diah Safriyani

Department of Chemistry, Faculty of Mathematics and Natural Sciences, Universitas Sebelas Maret,
Jl. Ir. Sutami 36A, Surakarta 57126, Indonesia

* **Corresponding author:**

email: venty@mipa.uns.ac.id

Received: June 15, 2023

Accepted: September 11, 2023

DOI: 10.22146/ijc.85726

Abstract: Cellulose derivatives from natural resources continuously develop to find the best hydrophobic polymer-based membrane technology performance. This study was conducted to improve the hydrophilicity, performance, and anti-fouling of polyvinylidene fluoride (PVDF) membrane with cellulose acetate (CA) filler synthesized from screw pine (*Pandanus tectorius*) leaf cellulose. CA was synthesized by the Fischer esterification mechanism and the PVDF membrane was fabricated using the phase inversion method with 0.3% CA concentration. FTIR analysis of CA shows an absorption at 1700 cm^{-1} suggesting that the hydroxyl group of cellulose had been successfully substituted with an ester group (C=O), and CA has a high degree of substitution (DS) value of 3.50. Adding CA improved the hydrophilicity and anti-fouling properties of up to 86.45% of PVDF membranes. Furthermore, CA increased the value of water permeability 2–3 times than pristine PVDF membrane. The presence of CA enhanced the porosity of the PVDF membrane, which promoted the membrane's effectiveness for MB filtering. As a result, CA from screw pine leaf cellulose has promising features as a filler for PVDF membranes and potential dye filtration.

Keywords: anti-fouling; cellulose; cellulose acetate; polyvinylidene fluoride; water permeability

■ INTRODUCTION

Polyvinylidene Fluoride (PVDF), commonly known as poly(1,1-difluoroethylene), has a repeating unit of $(\text{CH}_2-\text{CF}_2)$ [1]. PVDF is a polymer that is frequently utilized as a matrix membrane due to its excellent properties, such as thermal stability, membrane-forming ability, and high mechanical strength [2]. Nonetheless, the hydrophobic nature of PVDF membrane causes fouling, decreasing the membrane performance and shortening the membrane lifetime [3-4]. It is crucial to increase hydrophilicity to reduce PVDF membrane fouling.

Among the numerous materials utilized to promote PVDF membrane hydrophilicity, natural polymer has received attention due to its low cost and ease of availability [5]. Cellulose is one of the most common natural polymers in the world, accounting for 700,000 billion tons of total biomass production per year [6]. Natural cellulose-based fibers have several advantages over synthetic fibers, including low cost, low density, good strength, good

stiffness, environmentally friendly, biodegradable, renewable, and health-safe [7-8]. The cellulose skeleton's hydroxyl groups can be chemically modified to form ester groups that are insoluble in water [8-10].

Cellulose acetate (CA) is a cellulose ester derivative that has been widely applied in membranes. CA is a desirable polymer due to its low cost, biocompatibility, biodegradability, and acceptable physical qualities in industry [11-12]. CA is utilized in food packaging, coatings, sealants, and membrane separation [13]. Wood and cotton are the most important material resources for industrial synthesizing CA, although they have a high lignin content which requires more chemicals to remove cellulose [14]. Screw pine (*Pandanus tectorius*) is a non-wood plant of Pandanaceae family that grows naturally on river banks and swamps in the tropics that are rarely utilized. Isolation of cellulose from non-wood materials can reduce the usage of chemicals [8,15]. The functional groups of screw pine fibers are similar to those of flax,

kenaf, and linen natural fibers [16]. Screw pine leaves have a chemical composition of 37.3% cellulose, 34.4% hemicellulose, 15.7% pentose, 24% lignin, and 2.5% others [17]. As a result, Screw pine leaves can potentially be a source of CA synthesis.

Previous research used commercial CA [18-20] for matrix membranes and generated CA [14,21-23]. CA commercial has been used to improve water flux and fouling resistance in polyethersulfone (PES) [24], polysulfone (PSf) [25], and PVDF membranes [12,26-27]. So far, synthetic CA has not been used as a matrix membrane filler. No previous research has employed CA synthesized from screw pine as a PVDF membrane filler. This study used screw pine (*P. tectorius*) leaves as the starting material to synthesize cellulose acetate. It was used as a filler for PVDF membranes to improve water permeability and anti-fouling qualities. Water permeability, rejection, and anti-fouling from the flux recovery ratio (FRR) test were used to evaluate the performance of the manufactured PVDF/CA membrane.

■ EXPERIMENTAL SECTION

Materials

The materials used in this study were screw pine leaves collected from Yogyakarta coastal area, aquadest, NaOH, HCl, NaOCl, acetic acid anhydride, acetic acid glacial, H₂SO₄, DMAc, and PEG 400. Chemicals were purchased from e-Merck, Germany. PVDF (Solef PVDF 1010 Mw 352 kDa) was obtained from Solvay.

Instrumentation

The instrumentations used in this study were Fourier transform infrared (FTIR) Shimadzu FTIR Prestige 21 Model 8201 PC, scanning electron microscope (SEM) JEOL JSM-6510LA, thermogravimetric analyzer (TGA), and differential scanning calorimetry (DSC) STA Linseis PT 1600.

Procedure

Isolation of cellulose from screw pine leaves

Cellulose from screw pine leaves was isolated [17]. Screw pine leaves were collected from Yogyakarta coastal area. Screw pine leaves are stripped of their thorns and cut into 12 × 3 cm pieces. The leaf pieces were then sun-dried.

Dried screw pine leaves were cut into smaller pieces of around 1 × 1 cm and immersed in water for 3 × 24 h, with the water changed regularly. The screw pine leaves were then sun-dried again and grounded. Screw pine leave powder (100 g) was mixed in 10% NaOH for 2 h at 100 °C, with a screw pine leave to NaOH ratio of 1:20. The mixture was then neutralized to pH 7 and dried for 3 h at 60 °C. The dry powder was mixed with 4% NaOCl pH 4.5 at 100 °C for 2 h with a 1:20 alkalization product to NaOCl ratio. To obtain cellulose from screw pine leaves, the mixture was neutralized to pH 7 and dried at 60 °C for 3 h.

Synthesis of CA

CA was synthesized following [28] with modifications. Screw pine leaf cellulose (1 g) was added with glacial acetic acid (2.4 mL) and agitated for 60 min at 38 °C. The mixture was then stirred for 45 min at 38 °C with glacial acetic acid (4 mL) and sulfuric acid (0.5 mL). The mixture was then chilled to 18 °C. The acetylation procedure was then carried out. Acetic anhydride (10 mL) and sulfuric acid (0.5 mL) were added to the mixture and agitated for 90 min at 35 °C. The acetylation process was stopped by adding distilled water (1 mL) and glacial acetic acid (2 mL) and stirring at room temperature for 1 h. The mixture was neutralized with distilled water. The product was dried at 60 °C for 3 h to obtain cellulose acetate.

PVDF/CA membrane fabrication

Membrane PVDF/CA was fabricated by phase inversion [17]. First, DMAc (9.32 g) and PEG 400 (0.48 g) were stirred 5 min. The mixture was then added with cellulose acetate (0.036 g) and stirred for 10 min. Finally, PVDF (2.16 g) was added to the mixture and agitated at 60 °C for 24 h to prepare the dope solution for the PVDF/CA membrane. Otherwise, the PVDF dope solution was made using the same method, but without the CA filler. The dope solution was then cast in a glass plate and placed in a coagulation bath containing distilled water to produce the membranes.

Characterization of cellulose acetate

The FTIR spectral analysis was used to calculate the degree of substitution (DS) of cellulose acetate.

According to Eq. (1), the absorbance of C=O cellulose acetate was compared to the absorbance of C-O cellulose.

$$DS = \frac{Abs_{C=O}}{Abs_{C-O}} \quad (1)$$

The functional groups of the cellulose and cellulose esters were determined by FTIR spectrophotometer. The dried samples were combined in a 1:100 ratio with potassium bromide (KBr) powder, compressed into a thin transparent pellet, and the transmission was measured at 4000–400 cm^{-1} .

The surface morphologies of cellulose and cellulose acetate were analyzed by SEM. Coated samples with a thin layer of gold were mounted and imaged at 500–5000× magnifications with 10 kV accelerating voltage at a pressure of 70 Pa. The thermal stability of cellulose and cellulose acetate was studied by TGA. The samples were heated up to 600 °C at a heating rate of 10 °C/min under an air atmosphere.

PVDF and PVDF/CA membranes characterization and performance evaluation

The performance of PVDF and PVDF/CA membranes was evaluated [17]. PVDF and PVDF/CA membranes were evaluated by water contact angle, porosity (ϵ), pure water flux (PWF), water flux, rejection, and flux recovery ratio (FRR). Membrane porosity was determined using the gravimetric technique and Eq. (2),

$$\epsilon(\%) = \left(\frac{W_{wet} - W_{dried}}{A \times I_{wet} \times \rho} \right) \quad (2)$$

where W_{wet} is the weight of the membrane (g), I_{wet} is the thickness of the membrane (cm) in wet condition, W_{dried} is the weight of the dry membrane (g) after oven at 60 °C for 24 h, ρ is water density ($g\ cm^{-3}$), and A is the membrane area (m^2).

The membrane performance was evaluated using a dead-end system with continuous measurements beginning with PWF, water flux, rejection, and FRR. The membrane (diameter 5 cm) was placed in a stirred cell and then filled with distilled water to measure PWF (J_1) (Eq. (3)). To assess water flux and rejection (%R) (Eq. (4)), the distilled water was replaced with a 100-ppm methylene blue (MB) solution. Before performing the FRR test (Eq. (5)), the MB solution was partially replaced with distilled water and swirled without pressure to

eliminate any leftover MB on the surface membrane before being completely replaced with new distilled water. All measurements were taken using a two-bar system compaction for 15 min.

$$J_1 = \frac{v}{A \times t} \quad (3)$$

$$\%R = \left(1 - \frac{C_p}{C_r} \right) \times 100 \quad (4)$$

$$FRR = \frac{J_2}{J_1} \times 100\% \quad (5)$$

J_1 denotes PWF (L/m^2h), v permeates volume (L), A membrane surface area (m^2), t time (h), C_p permeate concentration, and C_r concentration J_2 is water flux (L/m^2h), and retentate was determined using a UV-vis spectrophotometer at 664 nm. The thermal stability of PVDF and PVDF/CA membranes was evaluated by TGA. The membranes were heated up to 900 °C at a heating rate of 10 °C/min under an air atmosphere.

RESULTS AND DISCUSSION

Isolation of Cellulose and Synthesis of CA from Screw Pine Leaves

Initially, cellulose was isolated by soaking screw pine leaf powder in water to remove pentose sugar, tannins, and pigments. White powders of cellulose were obtained at 40.24% yield. The fiber does not appear in SEM images of screw pine leaf powder (Fig. 1(a) and 1(b)) because it was bonded by lignin and hemicellulose [7]. An alkalization method was used to remove lignin and hemicellulose. The bleaching process was performed to degrade the remaining lignin to increase cellulose purity [29-30]. SEM images of cellulose and the magnification (Fig. 1(c) and 1(d)) revealed the individual fiber after alkalization and bleaching. Cellulose was successfully isolated from screw pine leaves, as confirmed by SEM. The isolated cellulose was converted into CA. Cellulose morphology changed after the acetylation process. SEM images of CA and the magnification (Fig. 1(e) and 1(f)) showed that CA formed aggregates with produce hole, where no fibers were found in synthesized CA. Morphological changes from cellulose to CA occur due to acetylation substitution towards the -OH group, in which initially

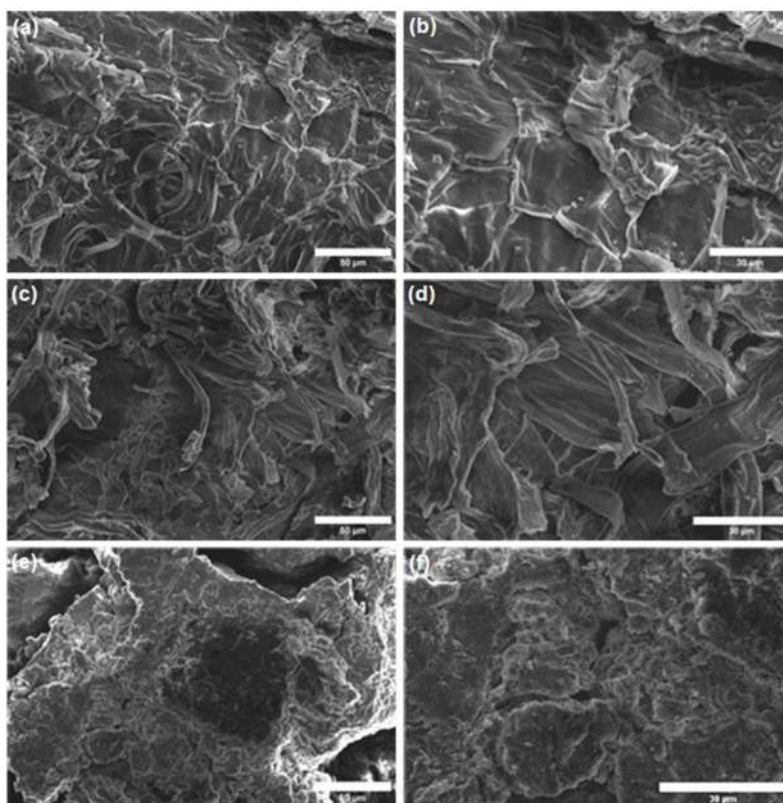


Fig 1. SEM image and the magnification of (a, b) screw pine leaf powder, (c, d) cellulose, and (e, f) CA

intramolecular hydrogen bonds of the $-OH$ functional group were formed [31].

Analysis of the functional group of screw pine leaf powder, cellulose, and cellulose acetate was investigated using FTIR (Fig. 2). The absence of peaks at 1504 and 1235 cm^{-1} for $C=C$ stretching lignin in cellulose spectra [8] indicated that lignin was eliminated, and cellulose was successfully isolated. In the FTIR spectra of CA, bands appeared at 1754 , 1374 , and 1235 cm^{-1} , corresponding to functional groups of $C=O$ stretching for carbonyl ester, $C-H$ in $O-(C=O)-CH_3$, and $C-O$ stretching for acetyl. The decrease in absorption intensity for $-OH$ stretching at 3384 cm^{-1} shows that the $-OH$ group of cellulose was substituted with acetyl groups from acetic anhydride [28,32-33]. The success of CA synthesis was validated by FTIR data, which matched the CA obtained in prior studies [28,32,34]. Furthermore, the DS value supports the successful CA synthesis. The DS of CA was 3.50, confirming the formation of cellulose triacetate.

The Fischer mechanism reaction was used to synthesize CA (Fig. 3). The initial esterification reaction

was carried out by substituting cellulose hydroxyl groups with acetyl groups. CA synthesis begins by enhancing the reactivity of cellulose's acetyl group with glacial acetic acid. The acetylation process requires a large cellulose surface, and the rate of the acetylation reaction is determined by the accessibility of the surface

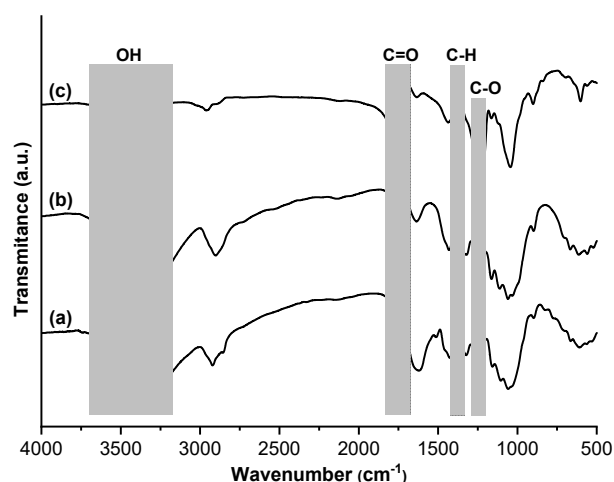


Fig 2. FT-IR spectra of (a) screw pine leaf, (b) cellulose, and (c) CA

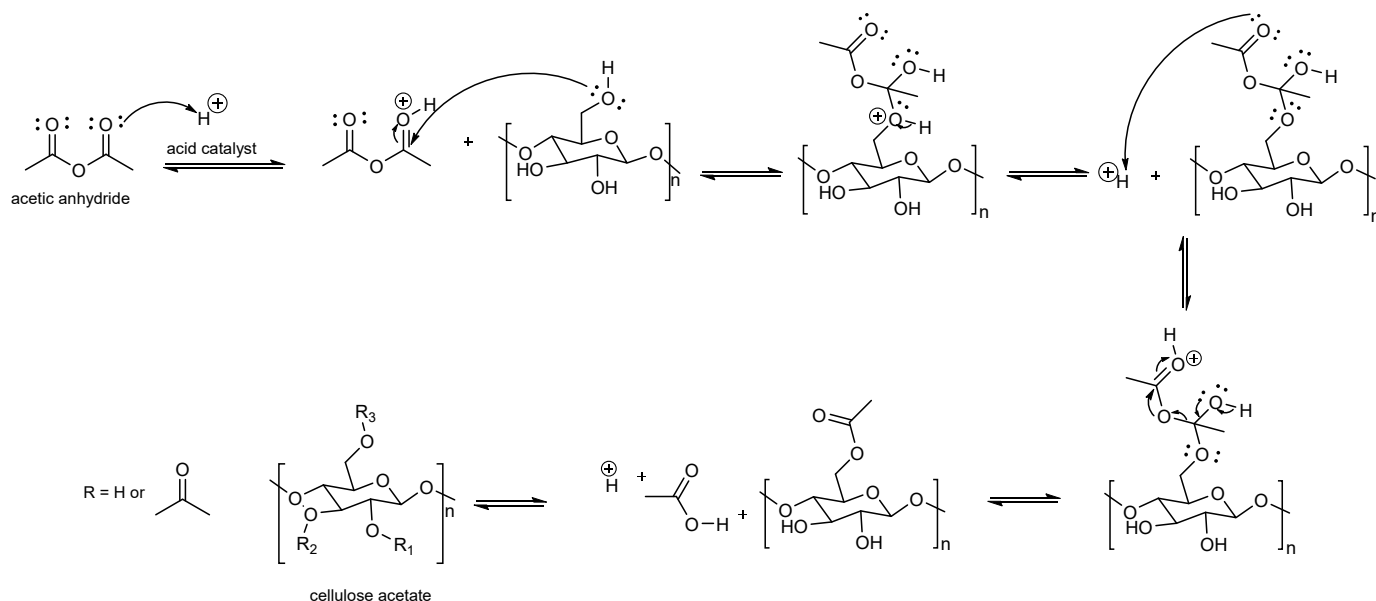


Fig 3. Fischer esterification mechanism reaction

opening ability of the cellulose fiber. The greater the surface area of the cellulose fiber, the easier the subsequent acetylation reactions [35]. Acetylation was accomplished by using acetic anhydride, and sulfuric acid was used as a catalyst. When the -OH group of cellulose is exchanged with the acetyl group of acetic anhydride, the desired CA and acetic acid are produced as a result. Because acetylation is an exothermic reaction, the reaction was carried out at a low temperature to maintain the cellulose is being degraded. The acetylation reaction is terminated through a hydrolysis process with the addition of acetic acid. This method eliminates unreacted acetic anhydride and releases the acetyl group [34]. CA was obtained as a white powder in 89% yield.

The cellulose and CA thermograms revealed three stages of degradation (Fig. 4). The first degradation occurred below 100 °C, exhibiting water evaporation. Because of the acetylation process of cellulose, mass reduction of cellulose was greater than CA in the first degradation (Table 1). Water absorption of cellulose acetate is reduced when hydroxyl groups are replaced with acetate groups. In the second stage, the cellulose and CA polymer chains degraded, with CA having more excellent thermal stability than cellulose [14]. CA polymer chain degradation is identical to CA produced by Chuayplod and Aht-Ong [36], which degraded at 298–375 °C. The

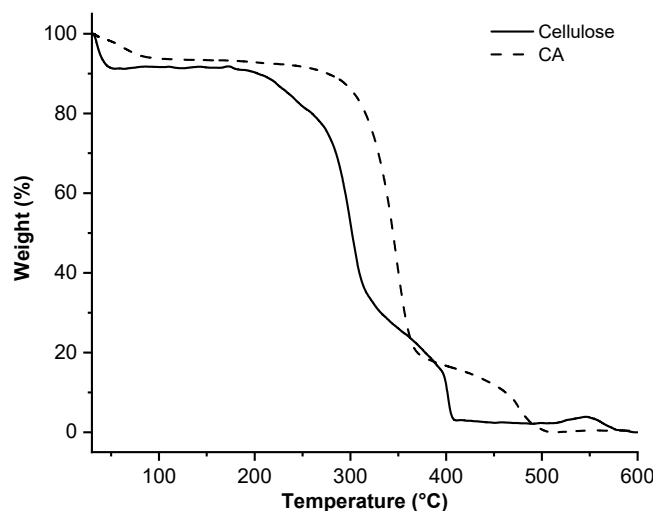


Fig 4. Thermogram of (a) cellulose and (b) CA

Table 1. Thermal stability of cellulose and CA

Samples	Temperature (°C)	Mass reduction (%)
Cellulose	31–54	8.76
	205–407	86.52
	407–600	3.28
CA	31–90	5.99
	270–370	70.59
	390–600	17.16

third stage is cellulose and CA backbone degradation [14]. This finding demonstrated that the acetylation process improved cellulose's thermal stability.

Characterization and Performance Evaluation of PVDF and PVDF/CA Membranes

PVDF and PVDF/CA membranes were characterized by TGA and DTG analysis. Thermograms of PVDF and PVDF/CA membranes (Fig. 5(a)) showed similar thermal stability. Degradation at temperatures under 100 °C appeared in the PVDF membrane due to water evaporation [4,17]. Whereas evaporation of water in the PVDF/CA membrane did not appear. Degradation of PVDF polymer matrix in PVDF and PVDF/CA membrane occurred at a relatively similar temperature at 420 and 490 °C. Therefore, the addition of CA in the PVDF matrix membrane did not drastically affect the thermal stability of the PVDF membrane. DSC thermogram of PVDF and PVDF/CA membrane (Fig. 5(b)) showed the endotherm peak. The addition of CA caused a shift in melting temperature (T_m) from 169 to 171 °C. It showed that the PVDF membrane has two crystalline phases, α and β phases [37]. The addition of CA

did not decrease the characteristic melting point of the PVDF membrane.

Water contact angle, porosity, PWF, water flux, rejection, and FRR were used to evaluate the performance of PVDF and PVDF/CA membranes, as shown in Table 2. The addition of cellulose acetate decreased the water contact angle of the PVDF membrane. The acetylation process decreases the number of cellulose hydroxyl groups [38]. Whereas cellulose hydroxyl groups unsubstituted with acetate groups can ensure the hydrophilic properties of CA. The porosity of the PVDF membrane increases up to 85.47% with CA addition. The difference in hydrophilicity between PVDF and CA causes a repulsive force that increases the porosity of the PVDF membrane [4].

PWF and water flux increased twice in the PVDF/CA membrane. Increasing the porosity of PVDF/CA improves membrane water permeability because water can easily travel through the membrane.

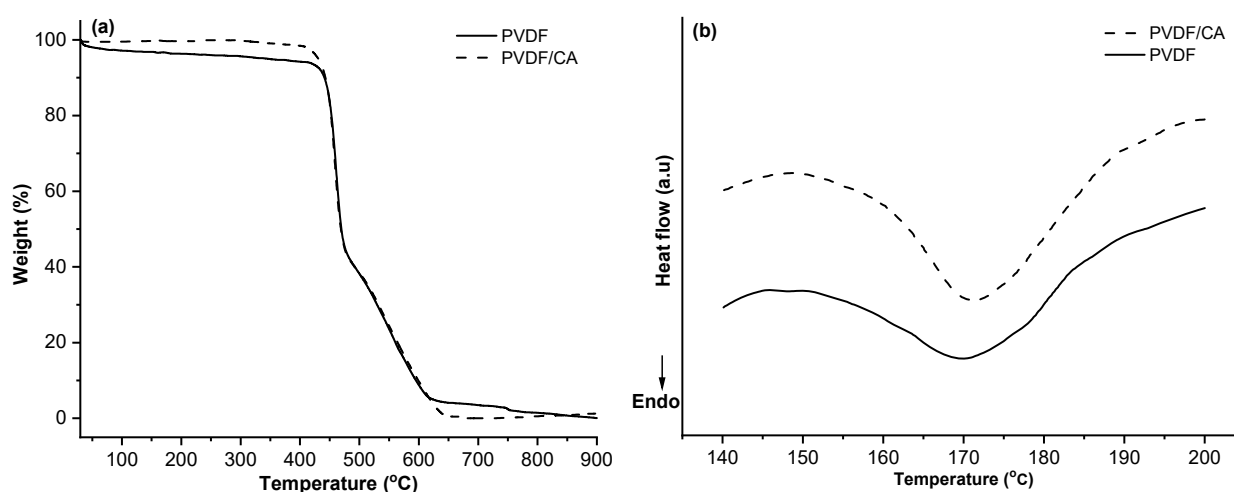


Fig 5. (a) TGA and (b) DSC of PVDF and PVDF/cellulose membranes

Table 2. Performance evaluation of PVDF and PVDF/CA membranes and the comparison with PVDF/CA membrane other studies

Membrane	Feed molecule	Water contact angle (°)	Porosity (%)	PWF (L/m ² h)	Water flux (L/m ² h)	Rejection (%)	FRR (%)	Ref.
PVDF	MB	89.70 ± 2.12	70.70 ± 0.48	17.08 ± 2.02	11.22 ± 0.18	82.89 ± 2.11	80.26 ± 0.68	This work
PVDF/CA	MB	88.13 ± 1.01	85.47 ± 0.88	45.42 ± 3.07	42.15 ± 3.08	77.73 ± 3.57	86.45 ± 3.62	This work
PVDF/CA	PEG	~93.00	-	136.20	-	3.00	94.20	[12]
PVDF/CA	PEG	~61.00	~82.00	522.00	~300.00	~68.00	~76.00	[26]
PVDF/CA	MB	56.43	~84.00	140.00	83.17	90.24	95.77	[27]

The higher the porosity of the PVDF/CA membrane, the lower MB rejection because the MB molecule can pass through the membrane. Lower membrane rejection is achieved by increasing water permeability [17,39]. PVDF membrane anti-fouling properties improved with the addition of CA, which has an excellent anti-fouling performance and minimizes interaction between MB and surface membrane [40]. The washing treatment performed before the FRR test improved the anti-fouling value of the PVDF/CA membrane. PVDF/CA membrane performed well and was comparable to earlier studies that employed commercial CA as a filler for PVDF membrane. Table 2 shows a comparison of membrane performance with previous studies. Our PVDF/CA membrane performances are comparable to other commercial PVDF membranes with the addition of CA. In this work, including CA synthesized from screw pine cellulose resulted in higher porosity, water permeability, and FRR values than the PVDF membrane. As a result, the PVDF/CA membrane developed in this work has the potential to be used in dye wastewater filtration.

■ CONCLUSION

Cellulose was successfully isolated from screw pine (*Pandanus tectorius*) leaves by alkalization and bleaching treatment which was confirmed by FTIR, SEM, and TGA analysis. Cellulose acetate (CA) was produced with high yields of 89% utilizing Fischer esterification processes and acetic anhydride reagents. The cellulose acetates were more thermally stable than cellulose and had a high DS of 3.50. The presence of CA did not affect the thermal stability of the PVDF membrane. The addition of CA improves PVDF membrane performance by increasing water permeability by twice and anti-fouling qualities up to 86.45%. PVDF/CA membrane also has good filtration ability against methylene blue (MB) up to 77.73%. Thus, these membranes have the potential for dye wastewater treatment. This synthesized CA has good properties as a filler to PVDF membrane for filtration MB.

■ ACKNOWLEDGMENTS

The project presented in this article is supported by Universitas Sebelas Maret through a grant with contract

number 260/UN27.22/HK.07.00/2021 and 254/27.22/PT.01.03/2022.

■ AUTHOR CONTRIBUTIONS

Elyna Wahyu Trisnawati conducted research, analyzed data and wrote an original draft; Indri Sri Cahyani and Diah Safriyani performed the experiments and data collection; Edi Pramono developed methodology and verification data; Venty Suryanti conducted formulation and verification data as well as wrote a manuscript (review and editing). All authors agreed to the final version of this manuscript.

■ REFERENCES

- [1] Saxena, P., and Shukla, P., 2021, A comprehensive review on fundamental properties and applications of poly(vinylidene fluoride) (PVDF), *Adv. Compos. Hybrid Mater.*, 4 (1), 8–26.
- [2] Ayyaru, S., and Ahn, Y.H., 2017, Application of sulfonic acid group functionalized graphene oxide to improve hydrophilicity, permeability, and antifouling of PVDF nanocomposite ultrafiltration membranes, *J. Membr. Sci.*, 525, 210–219.
- [3] Deng, W., and Li, Y., 2021, Novel superhydrophilic antifouling PVDF-BiOCl nanocomposite membranes fabricated via a modified blending-phase inversion method, *Sep. Purif. Technol.*, 254, 117656.
- [4] Pramono, E., Zakaria, M.A., Fridiasari, K.F., Ndruru, S.T.C.L., Bagaskara, M., Mustofa, R.E., Sejati, G.P.W., Purnawan, C., and Saputra, O.A., 2022, Cellulose derived from oil palm empty fruit bunches as filler on polyvinylidene fluoride based membrane for water containing humic acid treatment, *Groundwater Sustainable Dev.*, 17, 100744.
- [5] Anita Lett, J., Sagadevan, S., Fatimah, I., Hoque, M.E., Lokanathan, Y., Léonard, E., Alshahateet, S.F., Schirhagl, R., and Oh, W.C., 2021, Recent advances in natural polymer-based hydroxyapatite scaffolds: Properties and applications, *Eur. Polym. J.*, 148, 110360.
- [6] de Melo Brites, M., Cerón, A.A., Costa, S.M., Oliveira, R.C., Ferraz, H.G., Catalani, L.H., and

- Costa, S.A., 2020, Bromelain immobilization in cellulose triacetate nanofiber membranes from sugarcane bagasse by electrospinning technique, *Enzyme Microb. Technol.*, 132, 109384.
- [7] Afolabi, L.O., Megat-Yusoff, P.S.M., Ariff, Z.M., and Hamizol, M.S., 2019, Fabrication of *Pandanus tectorius* (screw-pine) natural fiber using vacuum resin infusion for polymer composite application, *J. Mater. Res. Technol.*, 8 (3), 3102–3113.
- [8] Suryanti, V., Kusumaningsih, T., Safriyani, D., and Cahyani, I. S., 2023, Synthesis and characterization of cellulose ethers from screw pine (*Pandanus tectorius*) leaves cellulose as food additives, *Int. J. Technol.*, 14 (3), 291–319.
- [9] Zhou, Y., Zhang, X., Cheng, Y., Zhang, J., Mi, Q., Yin, C., Wu, J., and Zhang, J., 2022, Super-rapid and highly-efficient esterification of cellulose to achieve an accurate chromatographic analysis of its molecular weight, *Carbohydr. Polym.*, 286, 119301.
- [10] Sun, B., Zhang, M., Shen, J., He, Z., Fatehi, P., and Ni, Y., 2019, Applications of cellulose-based materials in sustained drug delivery systems, *Curr. Med. Chem.*, 26 (14), 2485–2501.
- [11] Vatanpour, V., Pasaoglu, M.E., Barzegar, H., Teber, O.O., Kaya, R., Bastug, M., Khataee, A., and Koyuncu, I., 2022, Cellulose acetate in fabrication of polymeric membranes: A review, *Chemosphere*, 295, 133914.
- [12] Mu, C., Su, Y., Sun, M., Chen, W., and Jiang, Z., 2010, Remarkable improvement of the performance of poly(vinylidene fluoride) microfiltration membranes by the additive of cellulose acetate, *J. Membr. Sci.*, 350 (1-2), 293–300.
- [13] Nilsson, R., Olsson, M., Westman, G., Matic, A., and Larsson, A., 2022, Screening of hydrogen bonds in modified cellulose acetates with alkyl chain substitutions, *Carbohydr. Polym.*, 285, 119188.
- [14] Candido, R.G., Godoy, G.G., and Gonçalves, A.R., 2017, Characterization and application of cellulose acetate synthesized from sugarcane bagasse, *Carbohydr. Polym.*, 167, 280–289.
- [15] Gallaher, T., Callmander, M.W., Buerki, S., and Keeley, S.C., 2015, A long distance dispersal hypothesis for the Pandanaceae and the origins of the *Pandanus tectorius* complex, *Mol. Phylogenet. Evol.*, 83, 20–32.
- [16] Mat Piah, M.R.M., Baharum, A., and Abdullah, I., 2016, Mechanical properties of bio-composite natural rubber/high density polyethylene/mengkuang fiber (NRHDE/MK), *Polym. Polym. Compos.*, 24 (9), 767–774.
- [17] Trisnawati, E.W., Cahyani, I.S., Safriyani, D., Pramono, E., and Suryanti, V., 2023, Cellulose, cellulose benzoate and cellulose citrate from screw pine (*Pandanus tectorius*) leaves as PVDF filler for improved permeability and anti-fouling properties, *Period. Polytech., Chem. Eng.*, 67 (3), 504–515.
- [18] Silva, M.A., Belmonte-Reche, E., and de Amorim, M.T.P., 2021, Morphology and water flux of produced cellulose acetate membranes reinforced by the design of experiments (DOE), *Carbohydr. Polym.*, 254, 117407.
- [19] Guo, H., Peng, Y., Liu, Y., Wang, Z., Hu, J., Liu, J., Ding, Q., and Gu, J., 2020, Development and investigation of novel antifouling cellulose acetate ultrafiltration membrane based on dopamine modification, *Int. J. Biol. Macromol.*, 160, 652–659.
- [20] Han, B., Zhang, D., Shao, Z., Kong, L., and Lv, S., 2013, Preparation and characterization of cellulose acetate/carboxymethyl cellulose acetate blend ultrafiltration membranes, *Desalination*, 311, 80–89.
- [21] Radiman, C.L., Widyaningsih, S., and Sugesty, S., 2008, New applications of kenaf (*Hibiscus cannabinus* L.) as microfiltration membranes, *J. Membr. Sci.*, 315 (1-2), 141–146.
- [22] Filho, G.R., da Cruz, S.F., Pasquini, D., Cerqueira, D.A., Prado, V.S., and de Assunção, R.M.N., 2000, Water flux through cellulose triacetate films produced from heterogeneous acetylation of sugar cane bagasse, *J. Membr. Sci.*, 177 (1), 225–231.
- [23] Meireles, C.S., Filho, G.R., Fernandes Ferreira, M., Cerqueira, D.A., Assunção, R.M.N., Ribeiro, E.A.M., Poletto, P., and Zeni, M., 2010, Characterization of asymmetric membranes of cellulose acetate from biomass: Newspaper and mango seed, *Carbohydr. Polym.*, 80 (3), 954–961.

- [24] Mansourizadeh, A., and Javadi Azad, A., 2014, Preparation of blend polyethersulfone/cellulose acetate/polyethylene glycol asymmetric membranes for oil–water separation, *J. Polym. Res.*, 21 (3), 375.
- [25] Moradihamedani, P., and Abdullah, A.H., 2019, Ammonia removal from aquaculture wastewater by high flux and high rejection polysulfone/cellulose acetate blend membrane, *Polym. Bull.*, 76 (5), 2481–2497.
- [26] Hossein Razzaghi, M., Safekordi, A., Tavakolmoghadam, M., Rekabdar, F., and Hemmati, M., 2014, Morphological and separation performance study of PVDF/CA blend membranes, *J. Membr. Sci.*, 470, 547–557.
- [27] Reza, M., Promono, E., and Radiman, C.L., 2022, Improving separation performance of PVDF ultrafiltration membranes by blending with cellulose acetate, *Iran. J. Chem. Chem. Eng.*, 42 (3), 1017–1029.
- [28] Candido, R.G., and Gonçalves, A.R., 2016, Synthesis of cellulose acetate and carboxymethylcellulose from sugarcane straw, *Carbohydr. Polym.*, 152, 679–686.
- [29] Adawiyah, R., Suryanti, V., and Pranoto, P., 2022, Preparation and characterization of microcrystalline cellulose from Lembang (*Typha angustifolia* L.), *J. Phys.: Conf. Ser.*, 2190, 012007.
- [30] Pranoto, P., Suryanti, V., and Adawiyah, R., 2023, Andisol and microcrystalline cellulose from *Typha angustifolia* for auramine O adsorption, *Int. J. Adv. Appl. Sci.*, 12 (1), 27–36.
- [31] Goswami, M., and Das, A.M., 2019, Synthesis and characterization of a biodegradable cellulose acetate-montmorillonite composite for effective adsorption of Eosin Y, *Carbohydr. Polym.*, 206, 863–872.
- [32] Andrade Alves, J.A., Lisboa dos Santos, M.D., Morais, C.C., Ramirez Ascheri, J.L., Signini, R., dos Santos, D.M., Cavalcante Bastos, S.M., and Ramirez Ascheri, D.P., 2019, Sorghum straw: Pulping and bleaching process optimization and synthesis of cellulose acetate, *Int. J. Biol. Macromol.*, 135, 877–886.
- [33] Araújo, D., Castro, M.C.R., Figueiredo, A., Vilarinho, M., and Machado, A., 2020, Green synthesis of cellulose acetate from corncob: Physicochemical properties and assessment of environmental impacts, *J. Cleaner Prod.*, 260, 120865.
- [34] Suhartini, M., Ernawati, E.E., Roshanova, A., Haryono, H., and Mellawati, J., 2020, Cellulose acetate of rice husk blend membranes: Preparation, morphology and application, *Indones. J. Chem.*, 20 (5), 1061–1069.
- [35] Mauliana, M., Kurniasih, E., and Syafruddin, S., 2019, Synthesis of acetate cellulose from the palm oil empty floor through the reaction of activation, *JSTR*, 17 (1), 1–5.
- [36] Chuayplod, P., and Aht-Ong, D., 2018, Mechanochemical-assisted heterogeneous surface modification of parawood microcrystalline cellulose and its effect on the properties of polypropylene composites, *World J. Eng.*, 15 (6), 719–730.
- [37] Martins, P., Lopes, A.C., and Lanceros-Mendez, S., 2014, Electroactive phases of poly(vinylidene fluoride): Determination, processing and applications, *Prog. Polym. Sci.*, 39 (4), 683–706.
- [38] Rahimi Kord Sofla, M., Batchelor, W., Kosinkova, J., Pepper, R., Brown, R., and Rainey, T., 2019, Cellulose nanofibres from bagasse using a high-speed blender and acetylation as a pretreatment, *Cellulose*, 26 (8), 4799–4814.
- [39] Teow, Y.H., Amirudin, S.N., and Ho, K.C., 2020, Sustainable approach to the synthesis of cellulose membrane from oil palm empty fruit bunch for dye wastewater treatment, *J. Water Process Eng.*, 34, 101182.
- [40] Sharma, M., Das, P.P., Sood, T., Chakraborty, A., and Purkait, M.K., 2022, Reduced graphene oxide incorporated polyvinylidene fluoride/cellulose acetate proton exchange membrane for energy extraction using microbial fuel cells, *J. Electroanal. Chem.*, 907, 115890.

Drying of Merbau (*Intsia bijuga*) Sawdust Extract: Effect of Temperature on the Quality of Natural Dye Product

Aswati Mindaryani^{1,2*}, Vincent Sutresno Hadi Sujoto¹, Sandrina Christine Michelin Silalahi¹, Himawan Tri Bayu Murti Petrus^{1,2}, and Edia Rahayuningsih^{1,2}

¹Sustainable Mineral Processing Research Group, Department of Chemical Engineering, Faculty of Engineering, Universitas Gadjah Mada, Jl. Grafika No. 2, Yogyakarta 55281, Indonesia

²Indonesia Natural Dye Institute (INDI), Integrated Research and Testing Laboratory (LPPT), Universitas Gadjah Mada, Sekip Utara, Yogyakarta 55281, Indonesia

* **Corresponding author:**

email: amindaryani@ugm.ac.id

Received: August 2, 2023

Accepted: August 31, 2023

DOI: 10.22146/ijc.87624

Abstract: The textile sector leaves 80% of effluent untreated. Carcinogenic, mutagenic, and poisonous synthetic colors in textile waste streams harm the ecosystem. Biodegradable natural dyes are safer than synthetic dyes. Merbau sawdust is abundant in Papua but underutilized. Merbau wood (*Intsia bijuga*) has considerable tannin and dye potential. Tannin diffuses to the surface, coloring it brown in humid air or water. Merbau extract can be dried to make powdered natural dye. This study examines Merbau sawdust extract drying and natural dye quality at different temperatures. The drying process was carried out in a convective oven at 60, 75, and 90 °C. The data showed that the solid product of natural dye was already dried at 60–90 °C within 100 min. The content of tannin in the dried natural dye powder was analyzed by titration method. The tannin content in the solid product was 0.5–0.9 g tannin/g solid. The drying rate during the constant drying rate period is around 0.00137 to 0.00256 g/cm² min. The effect of drying temperature (60 to 90 °C) on the tannin degradation is insignificant, based on the titration method and FTIR analysis.

Keywords: drying; natural dye; *Intsia bijuga*; mass and heat transfer; tannin

■ INTRODUCTION

The textile industry is one of the largest water-consuming industries and the most significant contributor to pollution in water bodies. Synthetic dyes are more widely used in the textile industry because they produce consistent colors for each batch production and do not easily fade when applied to the fabrics [1]. However, the chemicals contained in synthetic dyes can be harmful to the environment [2]. In the textile industry, untreated dye-containing wastewater potentially contributes up to 80% of all emissions [1-2]. In most of the waste generated from the textile industry, there are very high levels of biochemical oxygen demand (BOD) and chemical oxygen demand (COD). In addition, synthetic dyes can inhibit plant growth and photosynthesis and increase bioaccumulation, toxicity,

mutagenic, and carcinogenic properties [3]. An alternative dye that is safe for the environment, non-toxic, and easily degraded in nature is needed.

Dye is a pigmented compound that colors a material or object [4-5]. Dyes are divided into two types, namely natural and synthetic dyes. Natural dyes are extracted from plants, animals, or microorganisms available in nature [5-6]. Meanwhile, synthetic dyes are made from artificial materials resulting from derivatives of hydrocarbon compounds such as benzene and naphthalene. The advantage of natural dyes is that they do not contain harmful chemicals and are biodegradable or decomposed naturally by the environment, so they do not harm the ecosystem. Natural dyes fade faster than synthetic dyes, so fixative compounds such as salt or vinegar are needed [7]. In addition, there is no specific

natural dye production method to produce the same color composition each time it is made.

In contrast, the production method of synthetic dye can be adjusted to the desired color composition. However, the drawback is that synthetic dyes can produce carcinogenic, toxic, and mutagenic wastes, harming the living things around them. Therefore, it is necessary to empower natural dyes more [8].

Natural dyes are often obtained from plants with color pigments in their roots, stems, leaves, fruit, and skin [8-11]. There are two various ways to isolate the natural dyes, which are: (a) extraction of natural dyes with water or organic solvent at high or low temperatures for a specific time [12], and (b) extraction of natural dyes by hydrolyzing the material with acids or bases, according to its polarity.

Natural dyes can be used in various industries, such as food, textile, cosmetics, and pharmaceuticals [12-14]. Some examples of natural dyes that are often used in the textile industry are indigo (*Indigofera* sp.), soga bark (*Ceriops candolleana* Arn.), tegeran wood (*Cudraina javenensis*), and kesumba (*Bixa orellana*). To prevent the color on the textile from fading quickly, adding a dye fixator or mordant in the fabric dyeing process is necessary. Mordant can be selected from non-toxic materials to prevent environmental pollution [15]. Some of the most commonly used fixators are alum, borax, lime water, vinegar, and palm sugar.

Various studies have been conducted on numerous plants to produce natural dyes [8,10]. Many plants in Indonesia can be utilized as natural sources of dyes, such as *Indigofera*, turmeric, tegeran wood. Fatubun et al. [14] used eight different types of plants to create a diverse range of colors, including red, blue, yellow, and brown. Their innovative approach involves harnessing the natural pigments present in these plants to produce vibrant and varied hues. This method showcases the rich biodiversity of plant-based colorants and highlights the potential for sustainable and eco-friendly alternatives in various industries.

Moreover, Fauziyah and Hakim [15] utilized ten different types of plants to create a spectrum of colors, ranging from deep crimson to bright green and even

shades like olive and lime. Their research highlights the extensive palette that natural sources can offer, showcasing variations from deep scarlet to vibrant emerald, demonstrating the diverse applications of plant-based coloration in various fields. In addition, The availability of multiple plants in Indonesia can be a potential for Indonesia to compete in the international market. One of the plants are widely available in Indonesia that can produce a natural brown color is the wood of the Merbau (*Intsia bijuga*).

Merbau trees commonly can grow to a height of more than 30 m. The wood of this tree is often used as a building material and as a wooden floor for ships. The Merbau tree, known as ironwood by the people of Papua, can produce multifunctional Merbau wood. This wood does not rot quickly if not in contact with soil and is stronger than teak [16]. Merbau wood has high economic value and has been used locally and exported. The Merbau tree is a type of tree commonly found both in Papua and Java [17]. Many timber mills and plywood industries in Papua utilize Merbau wood as raw material and produce sawdust as waste.

The speciality of Merbau timber is its very high tannin content. Tannins are a type of polyphenol that is found in many plant species, including trees, and serve to protect the plant from herbivores and other environmental stressors. Merbau wood, which comes from the *Intsia* spp. tree, contains a group of tannins known as proanthocyanidins [18]. These tannins are also commonly referred to as condensed tannins or polyflavonoid tannins. Merbau tree wood contains tannin pigment, which is brown. The pigments in these plants can be used as natural dyes with high economic value. Therefore, the tannins in Merbau sawdust can be extracted as a natural dye.

Tannins are polyphenols consisting of several hydroxyl groups which can be extracted from plants [19]. The extraction process is generally carried out using the Soxhlet or extractor. After the natural dyes are extracted from Merbau wood, the extracts can be dried to form natural dye powder using a dryer. The tannins in natural dyes will be easily damaged if exposed to high temperatures. Drying the extract to produce powder

requires a relatively high temperature and quite a long time so it will affect the quality of the natural dyes produced. From this research, parameters of drying rate and drying conditions can relatively maintain the quality of the natural dye product. An analysis of the degradation of tannins during drying and the tannin content in natural dye powders is carried out to determine the temperature effect on the natural dye product quality.

■ EXPERIMENTAL SECTION

Materials

The materials used in this study are Merbau sawdust extract obtained from Gama Indigo, Yogyakarta, and Merbau sawdust obtained from CV Karui, Jayapura, Papua. Distilled water, KMnO_4 (99% purity Merck, Germany), indigo carmine (C.I.73015 Merck, Germany), and H_2SO_4 (95–97% purity Merck, Germany).

Instrumentation

The experimental rig used in this research consists of an oven equipped with thermometers to measure wet bulb and dry bulb temperatures. This oven has a temperature controller that can be adjusted according to the experimental requirements. Additionally, an exhaust system regulates air circulation within the oven, maintaining a stable experimental environment and ensuring consistent results. The oven unit is the Memmert UN 30 Universal model and it is equipped with a 32-L capacity and allows for temperature adjustments of up to 300°C. The oven is a key component in the research, allowing for precise control and monitoring of

temperature conditions, thus enabling the collection of accurate and reliable data for further analysis in the study. FTIR unit is Shimadzu FTIR IR-Spirit Serial No A224158. The experimental rig is shown in Fig. 1.

Procedure

Drying

Washed and dried petri dishes were weighed on a digital analytical balance, and their mass was recorded. Each petri dish was filled with 10 mL Merbau extract using a volume pipette, weighed, and its initial mass sample was recorded.

The oven was turned on, and the dry bulb temperature was set to 60 °C. When the dry bulb temperature was stable, the four petri dishes containing the extracts were put into the oven and positioned, as shown in Fig. 1. The four samples were weighed at the time interval of 5 min until the sample mass was constant.

The petri dishes containing dried samples were removed from the oven and then cooled in a desiccator for 10 min. Petri dishes were weighed, and the results were recorded. The petri dishes were covered with aluminum foil and left at room temperature for 24 h. The petri dishes were dried again at 110 °C for 1 h and weighted as a dry weight. The above steps were repeated for temperatures of 75 and 90 °C. The experimental data was a mass of samples at various times for 60, 75, and 90 °C drying temperatures.

Tannin content analysis

The analyses of tannin content in plant extracts were

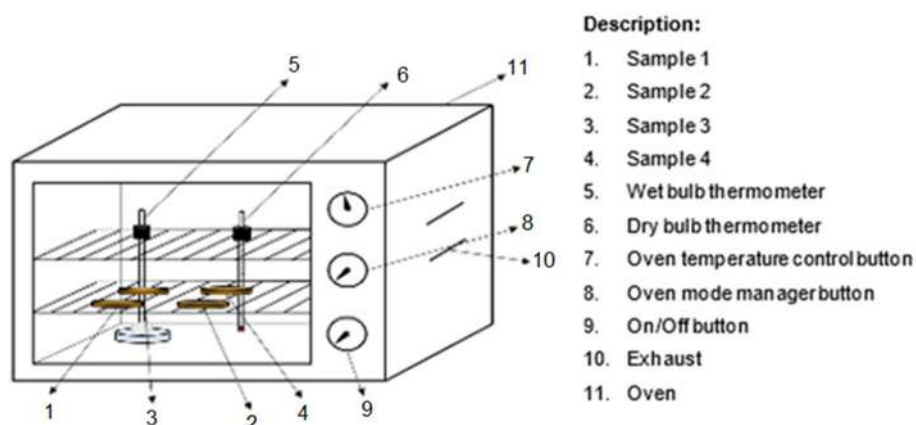


Fig 1. Experimental apparatus for drying

performed according to the International Pharmacopoeia and AOAC method in Kumari and Jain [20]. The preparation of 0.1 M KMnO_4 solution was mixing 0.79 g of KMnO_4 with 100 mL of distilled water in a beaker glass. The solution was heated for 15 min and left overnight at room temperature. The solution was filtered and added by distilled water up to 250 mL. Indigo carmine indicator solution was prepared by mixing 3 g of indigo carmine with 100 mL of distilled water and dissolving with 25 mL of concentrated H_2SO_4 . The solution was heated for 15 min and left overnight at room temperature. The solution was then diluted until 500 mL with distilled water.

Tannin analysis was performed by titration. A blank solution (without extract sample) was prepared by adding 20 mL of the indigo carmine solution with 180 mL distilled water. The blank solution was titrated with KMnO_4 until the color changed from blue to yellow. Titration was carried out three times. A total of 10 mL of liquid Merbau sample was put into a 200 mL volumetric flask. As much as 20 mL of indigo carmine solution was put into a volumetric flask, and then distilled water was added until it reached 200 mL. The liquid sample solution with indigo carmine was titrated with KMnO_4 until the color changed from blue to reddish brown. Titration was carried out three times. A petri dish containing dried samples was added with sufficient distilled water to form a solution. The entire sample solution on the petri dish was put into a 200 mL volumetric flask. Then, 20 mL of indigo carmine solution and 180 mL of distilled water were added and shaken until homogeneous. A 50 mL sample solution with indigo carmine was titrated with 0.1 M KMnO_4 solution. The titration was carried out until the color changed from blue to reddish brown. The titration was repeated three times for each sample.

Tannin degradation

An empty petri dish was prepared, and the initial mass was recorded. Merbau extract as much as 10 mL was put into a petri dish. The mass of the petri dish containing Merbau sample was weighed. The petri dish containing the sample was put into the oven at a specific temperature to heat and dry for 20 min. After that, the petri dish containing the sample was removed, cooled, and then weighed. This step was repeated for heating and drying at

40, 60, 80, 100, and 120 min at the same position in the oven. The sample phase at each drying time was recorded.

The first sample (drying time 20 min) from the previous step was dissolved with sufficient distilled water in a petri dish. The tannin content in the solution was then analyzed using the described method. The experiment was conducted for heating and drying temperatures of 60, 75, and 90 °C.

FTIR analysis

A sample of dried tannin was also analyzed with its related functional groups (especially -OH and C-O) using a FTIR unit, that is Shimadzu FTIR IR-Spirit Serial No A224158. This type of FTIR unit does not need special sample preparation, in which a solid sample can be examined directly without further preparation. The dried tannin samples from several drying temperatures (60–100 °C) were examined.

Data analysis

The water content in the sample was calculated using Eq. (1a) for wet basis and Eq. (1b) for dry basis [21];

$$x = \frac{W_{st} - W_{sc}}{W_{s0} - W_0} \quad (1a)$$

$$x = \frac{W_{st} - W_{sc}}{W_{sc} - W_0} \quad (1b)$$

where x represents the water content in the sample (g H_2O /g wet sample), W_{st} represents the mass of the sample and container at time t min (g), W_{sc} represents the mass of the dry sample and container at the end of the drying process (g), W_{s0} is the mass of the initial sample and container (g), and W_0 is the mass of the empty container (g). The tannin content in the sample can be calculated using Eq. (2) [22];

$$\begin{aligned} \text{Tannin content} &= \left(\frac{\text{g of tannin}}{\text{mL of sample}} \right) \\ &= \frac{(V_1 - V_2) \times 0.004157 \times \text{FP}}{V} \end{aligned} \quad (2)$$

where FP denotes the dilution factor (200 mL/50 mL), V_1 denotes the volume of KMnO_4 used for sample titration (mL), V_2 denotes the volume of KMnO_4 used for blank titration (mL), and V denotes the volume of

Merbau sample dried on a petri dish (10 mL). One mL of 0.1 M KMnO_4 is equivalent to 0.004157 g of tannin.

Meanwhile, the drying rate N can be calculated using Eq. (3) [23].

$$N = -\frac{1}{A} \cdot \frac{dW_s}{dt} \quad (3)$$

In this case, W_s (g) represents the mass of the sample at any time ($= W_{st} - W_0$), A is the effective drying surface area (cm^2), and t is the drying time (min). During the constant drying rate, the curve W_s against drying time t is essentially a linear line, with its slope equal to drying rate N . The mass transfer coefficient (K_Y) in the constant drying rate period can be calculated by Eq. (4) and (5) [24];

$$N = K_Y (Y_s' - Y') \quad (4)$$

$$K_Y = \frac{N}{(Y_s' - Y')} \quad (5)$$

where N denotes the drying rate at a constant drying period ($\text{g H}_2\text{O}/\text{cm}^2 \text{ min}$), K_Y denotes the gas phase mass transfer coefficient ($\text{g}/\text{cm}^2 \text{ min } \Delta Y$), Y_s' is the saturated humidity of air at wet bulb temperature ($\text{g H}_2\text{O}/\text{g}$ of dry air), and Y' is the humidity of the drying air ($\text{g H}_2\text{O}/\text{g}$ of dry air). The Y_s' and Y' values can be calculated using Eq. (6-9) [24];

$$Y_s' = 0.622 \frac{P_{as}}{(P_t - P_{as})} \quad (6)$$

$$Y = \frac{\lambda_w Y_s' - 0.24(T_d - T_w)}{\lambda_w + 0.45(T_d - T_w)} \quad (7)$$

$$C_s = 0.24 + 0.45Y \quad (8)$$

$$Y' = Y_s' - \frac{C_s}{\lambda_w} (T_d - T_w) \quad (9)$$

where P_{as} denotes the saturated vapor pressure of water at wet bulb temperature (mmHg), P_t is the total system pressure (760 mmHg), C_s denotes humid heat, (Btu/lb °F), 0.24 and 0.45 are values of the specific heat of the air and water vapor (Btu/lb °F), respectively, λ_w denotes latent heat of vapor (Btu/lb), T_d denotes dry bulb temperature (°F), and T_w is the wet bulb temperature (°F). Eq. (10) and (11) estimate the heat transfer coefficient during constant drying rate (N) [24];

$$N = \frac{Q}{A \cdot \lambda_w} = \frac{hA(T_d - T_w)}{\lambda_w} \quad (10)$$

$$h = \frac{N \times \lambda_w}{(T_d - T_w)} \quad (11)$$

where N represents the constant drying rate ($\text{g H}_2\text{O}/\text{m}^2 \text{ s}$), h is the convection heat transfer coefficient ($\text{W}/\text{m}^2 \text{ }^\circ\text{C}$), and Q denotes heat transfer rate (J/s).

The tannin degradation or content reduction rate is estimated by first-order reaction, as commonly used in degradation reactions (Eq. (12));

$$\frac{dM_{ta}}{dt} = -k_d M_{ta} \quad (12)$$

M_{ta} is the tannin content, and k_d is the degradation rate constant. Integration of Eq. (12) from $t = 0$ (initial condition with tannin content $= M_{ta0}$) results in Eq. (13) [25].

$$\ln\left(\frac{M_{ta}}{M_{ta0}}\right) = -k_d t \quad (13)$$

The degradation rate constant k_d can be expressed as the Arrhenius equation in this case.

RESULTS AND DISCUSSION

The variation of the drying process was the oven temperatures of 60, 75, and 90 °C. Fig. 2 shows the water content on a wet basis, and Fig. 3 shows the water content on a dry basis as a function of drying time. Fig. 2 presents a drastic decrease in water content in the initial period. Fig. 3 demonstrates that the dry basis water content linearly decreases with the time in the initial period of the drying process, known as a constant-rate period.

The drying process goes through three stages: the initial period, the constant-rate period, and the falling-rate period. The initial drying period occurs at several minutes. The constant drying rate follows after the initial drying period, where the sample mass decreases linearly with the drying time. The value of drying rate constant can be estimated from Fig. 2, which is based on Eq. (3). The value of the constant drying rate is used to calculate the mass transfer coefficient and the heat transfer coefficient.

From Fig. 4, it can be seen that the longer the drying time, the more the sample mass will decrease. The sample mass became constant after drying for 100 min at 60 °C, 60 min at 75 °C, and 40 min at 90 °C. Table 1 presents the value of the constant drying rate of 4 samples at 60, 75, and 90 °C. It shows that the sample

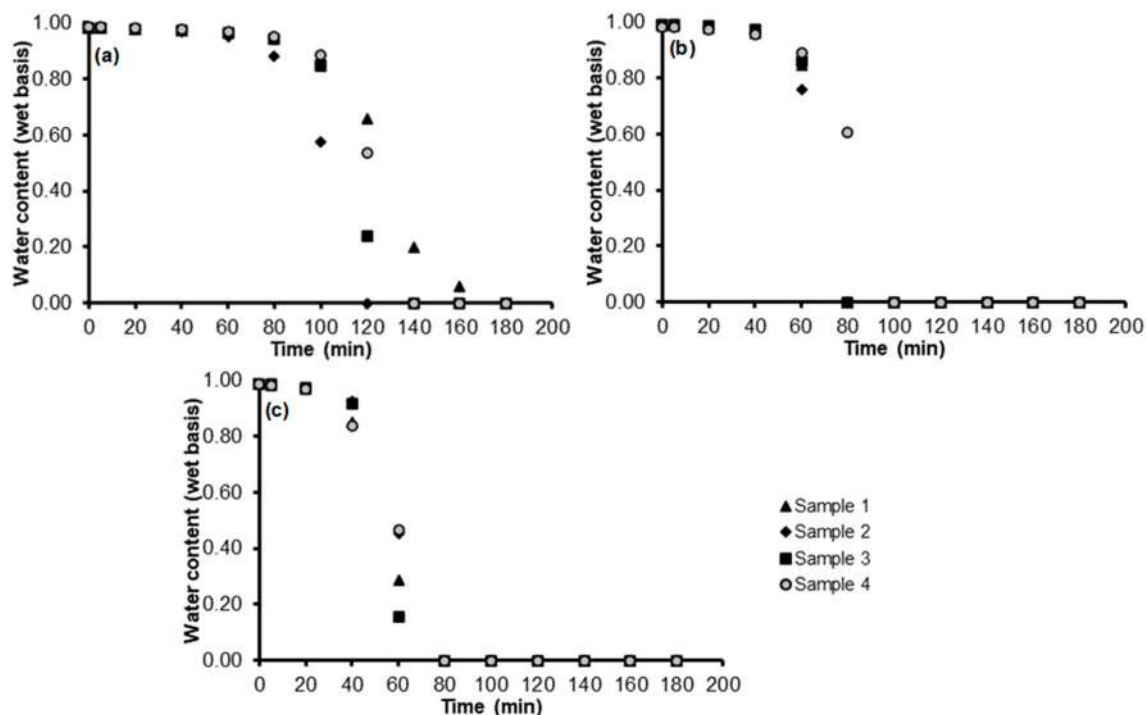


Fig 2. Water content (wet basis) at various times, temperature:(a) 60 °C, (b) 75 °C, and (c) 90 °C

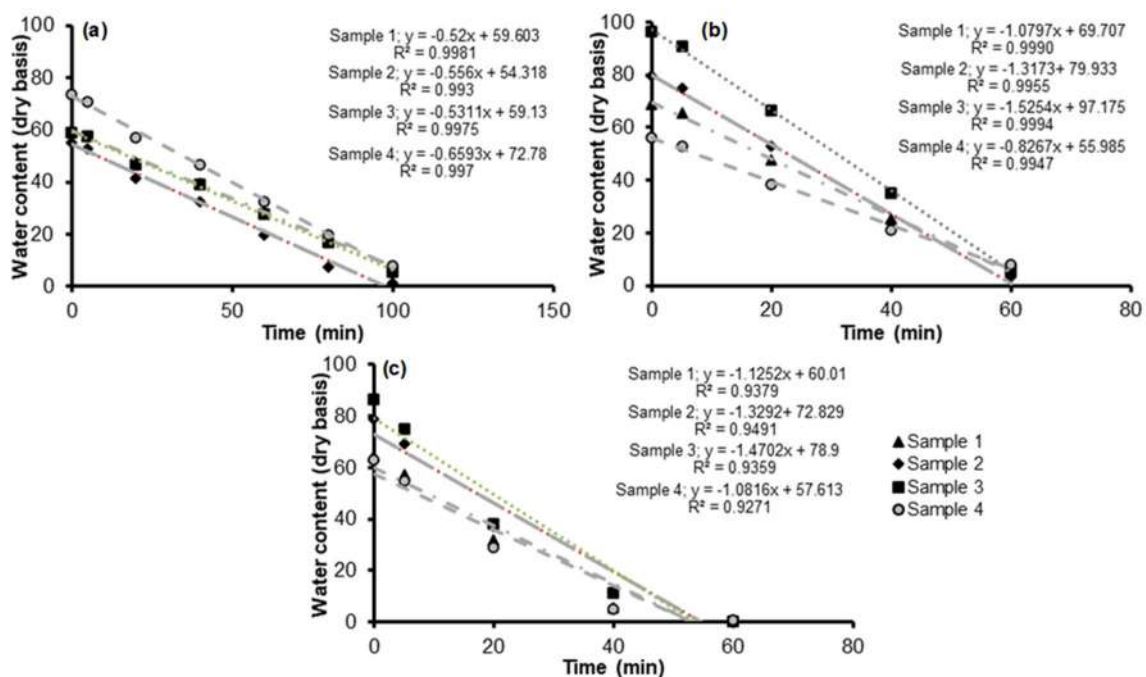


Fig 3. Water content (dry basis) as a time function, temperature: (a) 60 °C, (b) 75 °C, and (c) 90 °C

Table 1. Values of constant drying rate at 60 to 90 °C

Temperature (°C)	Sample 1	Sample 2	Sample 3	Sample 4	N avg (g/cm ² min)
60	0.00131	0.00149	0.00134	0.00135	0.00137
75	0.00238	0.00249	0.00240	0.00221	0.00237
90	0.00265	0.00251	0.00254	0.00255	0.00256

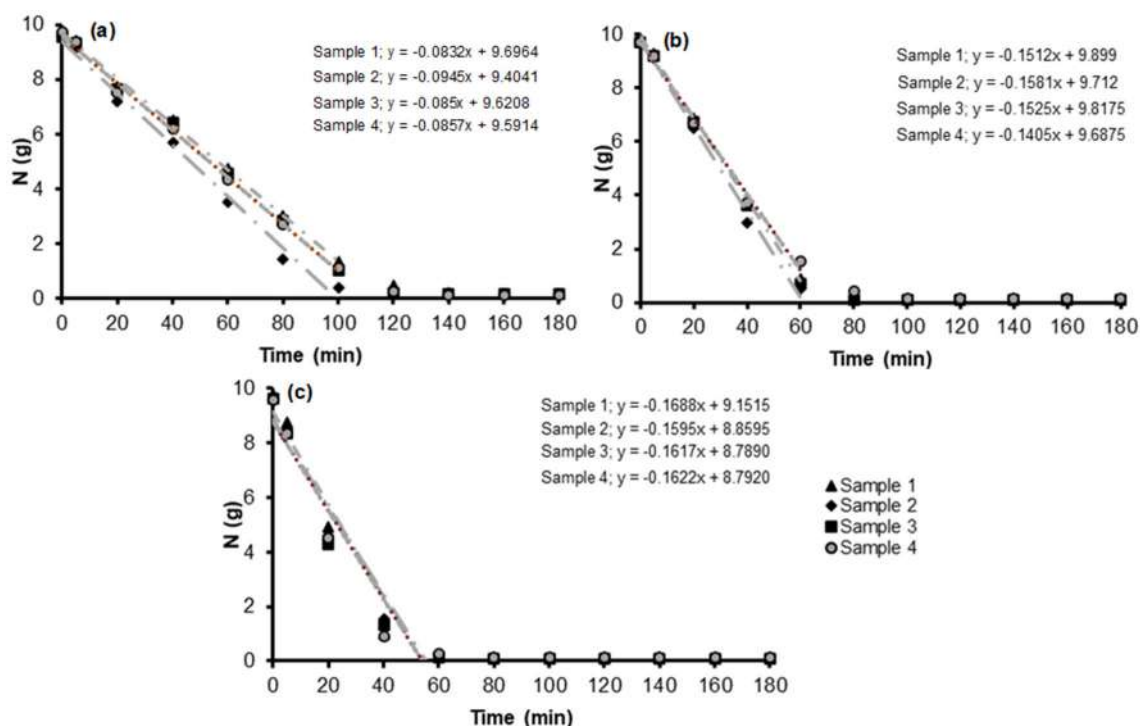


Fig 4. The sample mass as a time function at temperatures of (a) 60 °C, (b) 75 °C, and (c) 90 °C

position within the dryer tray does not affect the drying rate, so the value of the constant drying rate is taken as the average of 4 samples.

Based on Eq. (4-9), the average mass transfer coefficient at a constant drying rate and the average heat transfer coefficient can be calculated. Table 2 summarizes the values of mass transfer and heat transfer coefficients.

Ndukwu et al. [26] studied the drying of cocoyam slices using a drying oven, similar to this research. They found that the mass and heat transfer coefficients were around 1.01×10^{-6} – 3.45×10^{-6} m/s and 1.18–3.58 W/m²K, respectively. The heat transfer coefficient from this research is higher than that of Ndukwu et al [26]. For comparison, the K_Y unit in this research is converted into a m/s unit, which results in 1.43×10^{-5} – 2.42×10^{-5} m/s. Table 3 compares heat and mass transfer coefficients between this research's and other research results. This

phenomenon shows that the mass and heat transfer coefficients in this research are more or less within the range of other research results.

The tannin content in the four samples was analyzed by the volumetric method. Table 4 presents the values of tannin content for all drying temperatures.

Table 3. Comparison of mass and heat transfer coefficients

	K_Y (m/s)	\bar{h} (W/m ² °C)
This research	1.43×10^{-5} – 2.42×10^{-5}	11.06–14.64
Ndukwu et al. [26]	1.01×10^{-6} – 3.45×10^{-6}	1.18–3.58
Kumar et al. [27]	-	33.35–58.0
Chen et al. [28]	-	19.96

Table 2. Mass transfer coefficient and heat transfer coefficient at various temperatures

Drying temperature (°C)	\bar{K}_Y (g H ₂ O/cm ² min)	\bar{h} (W/m ² °C)
60	0.0859	14.64
75	0.1067	11.06
90	0.1452	12.29

Table 4. The tannin content in the dried sample (after the drying process)

Temperature (°C)	Sample 1	Sample 2	Sample 3	Sample 4	Average (g/g)
60	0.556	0.523	0.561	0.684	0.581
75	0.653	0.762	0.906	0.533	0.714
90	0.593	0.816	0.786	0.593	0.697

Based on the value of tannin content at each drying temperature, as shown in Table 4, the highest average tannin content was obtained at a drying temperature of 75 °C. However, the value of tannin content much varied, which was around 0.5 to 0.9 g tannin/g. Hence, the effect of drying temperature cannot be observed from merely tannin content at various temperatures. The effect of heating on the tannin quality or content over time was then investigated by heating and drying samples for 20 to 120 min at temperatures of 60, 75, and 90 °C. Fig. 5 presents tannin content (in 10 mL initial Merbau extract) at various times.

The tannin content in sample data can be used to evaluate the rate of tannin degradation based on Eq. (14). Three lines in Fig. 5 show the estimated correlation between tannin content and drying time at temperatures of 60, 75, and 90 °C. The degradation rate constant is given in Table 5, which is quite small. This phenomenon indicates that the tannin degradation rate is very low.

This rate constant k_d is expressed in the Arrhenius equation, Eq. (14):

$$k_d = 1.0061 \exp(-15.11/RT) \text{ min}^{-1} \quad (14)$$

It shows that activation energy = 15.11 J/mol is small;

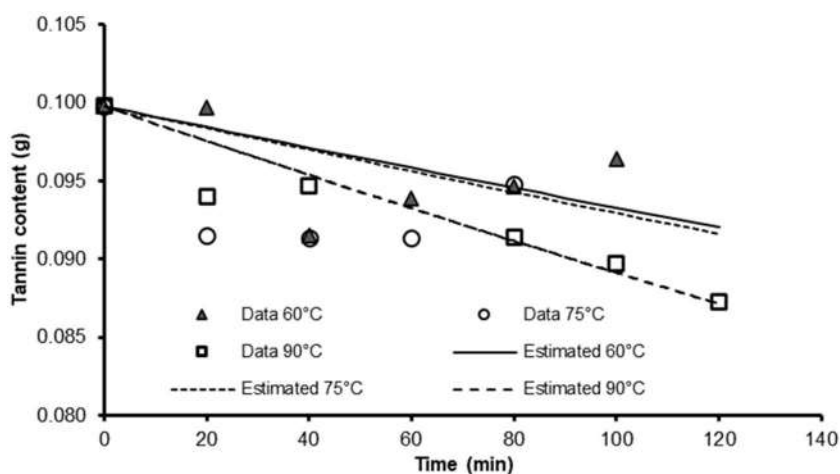
therefore, the temperature effect on tannin degradation is insignificant.

The effect of temperature on the quality of tannin content was then investigated through the concentration or content of functional groups within the tannin sample drying at various temperatures. In this case, the corresponding functional groups in tannin are hydroxyl (O–H) and carbonyl (C=O and C–O) functional groups. Examination of these functional groups was carried out using FTIR.

Fig. 6 depicts the tannic acid spectrum, which exhibits high absorption between 3500 and 2900 cm^{-1} , with a broad band centered at 3262 cm^{-1} . The hydroxyl groups (O–H) H-bonded broadly and powerfully, and the C–H are responsible for this band (aromatic medium). A strong peak caused by the alkane medium (C–H) is seen at 2718 cm^{-1} . The sharp and robust peak between 2920 and 2807 cm^{-1} corresponds to the symmetric and

Table 5. The tannin degradation rate constant

Temperature (°C)	Constant k_d (min^{-1})
60	0.000673
75	0.000712
90	0.001130

**Fig 5.** The tannin content in 10 mL sample at various times and temperatures

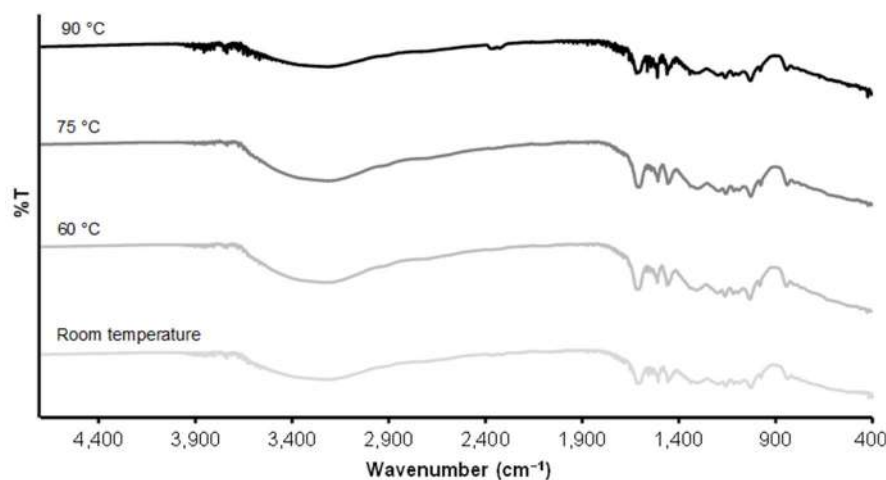


Fig 6. FTIR analysis results of samples at various drying temperatures

antisymmetric C–H stretching vibrations of the CH₂ and CH₃ groups, respectively. Due to the signal properties of carbonyl groups C=O stretching (1610 cm⁻¹) and C–O, tannic acid contains certain aromatic esters (1160 cm⁻¹).

Further experiments were conducted to investigate the thermal degradation of tannin. Some tannin solution was dried at several temperatures, i.e., from 60 to 100 °C, until solid tannin was produced. The drying process was around 3 h. FTIR then examined this solid tannin product. Based on the FTIR results of absorbance values for functional groups, the concentration of O–H at 3200 cm⁻¹, C–O at 1160 cm⁻¹, and aromatic C–H at 1450 cm⁻¹ were estimated by their absorbance values. In this case, the amount of aromatic C–H was assumed to be

constant along the drying process, irrespective of the drying temperature.

On the other hand, hydroxyls in tannin probably occurred to react to give the C–O functional group, as follows slowly, Eq. (15).

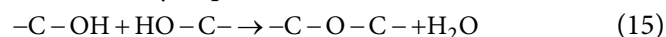


Fig. 7 depicts the O–H and C–O absorbance ratio, compared to aromatic C–H absorbance, based on FTIR results at 60 to 100 °C. Fig. 6 indicates that during the drying process, there was a slight decrease in the O–H group when the drying temperature rose, and according to the reaction in Eq. (15), the C–O group also slowly but steadily increased. However, a small reduction of O–H and an increase in the C–O group have little effect on

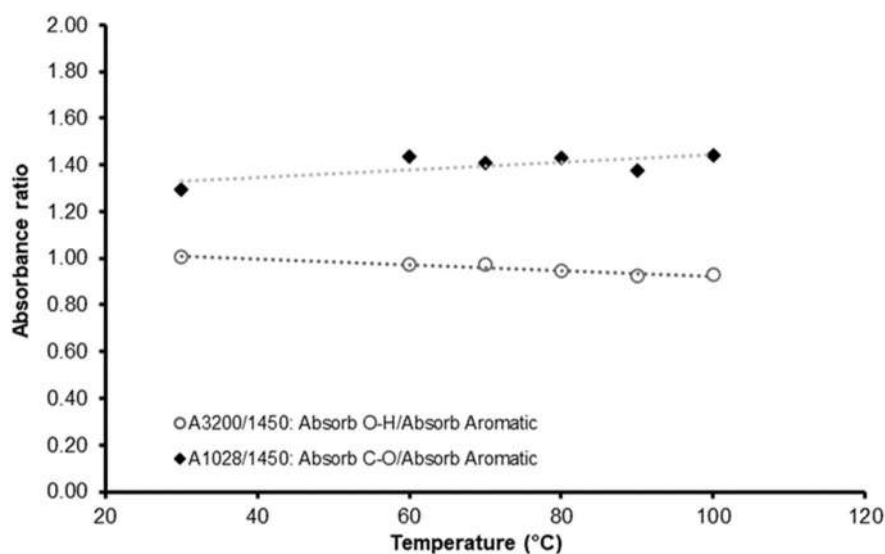


Fig 7. Absorbance changes of tannin hydroxyl and C–O functional groups at various drying temperatures

tannin quality. As shown in Table 4, the value of tannin content has significant variation, irrespective of drying temperature. It can be concluded that drying temperature in the range of 60 to 90 °C has little effect on the quality of natural dye products.

■ CONCLUSION

In this study, several conclusions can be drawn. During the constant drying period, the drying rate is around 0.00137 to 0.00256 g/cm² min, in which the tannin solid product is already dry within 100 min at 60–90 °C. The tannin content in the dried product is around 0.5 to 0.9 g tannin/g solid. The drying temperature has little effect on the quality of tannin products. Observation of the absorbance intensity of hydroxyl and carbonyl functional groups using FTIR indicates that higher drying temperature tends to reduce the amount of hydroxyl group slightly and to increase the number of carbonyl groups. At drying temperatures of 60 to 90 °C, the average mass transfer coefficient, K_Y , is 0.0859–0.1452 g H₂O/cm² min and the average heat transfer coefficient, h , is 11.06–14.64 W/m² °C. Both titration method and FTIR analysis show that the effect of drying temperature (60 to 90 °C) on tannin degradation is insignificant.

■ ACKNOWLEDGMENTS

The authors are grateful for the support of the Chemical Engineering Department, Universitas Gadjah Mada, for the laboratory facilities provided in this research. This research is supported by the Research Funding Scheme of *Penelitian Pengembangan Unggulan Perguruan Tinggi* 2020-2022, under contract number 1699/UN1/DITLIT/Dit-Lit/PT.01.03/2022 from the Directorate General of Higher Education (DIKTI).

■ AUTHOR CONTRIBUTIONS

Aswati Mindaryani, Sandrina Christine Michelin Silalahi, and Vincent Sutresno Hadi Sujoto conducted the experiment, Aswati Mindaryani, Vincent Sutresno Hadi Sujoto, Himawan Tri Bayu Murti Petrus wrote and revised the manuscript, Edia Rahayuningsih revised the manuscript. All authors agreed to the final version of this manuscript.

■ REFERENCES

- [1] Wang, L., Li, Y., and He, W., 2017, The energy footprint of China's textile industry: Perspectives from decoupling and decomposition analysis, *Energies*, 10 (10), 1461.
- [2] Bhatia, S.C., 2017, *Pollution Control in Textile Industry*, 1st Ed., Eds. Devraj, S., WPI Publishing, New York, US.
- [3] Lellis, B., Fávaro-Polonio, C.Z., Pamphile, J.A., and Polonio, J.C., 2019, Effects of textile dyes on health and the environment and bioremediation potential of living organisms, *Biotechnol. Res. Innovation*, 3 (2), 275–290.
- [4] Daberao, A.M., Kolte, P.P., and Turukmane, R.N., 2016, Cotton dyeing with natural dye, *Int. J. Res. Sci. Innovation*, 3 (8), 157–161.
- [5] Rahayuningsih, E., Fatimah, W.S., Pamungkas, M.S., and Marfitania, T., 2022, Effect of physicochemical process variables on natural indigo dye production from *Strobilanthes cusia* leaves by response surface methodology, *Indones. J. Chem.*, 22 (2), 342–351.
- [6] Reningtyas, R., Rahayuningsih, E., Kusumastuti, Y., and Kartini, I., 2022, Photofading of natural indigo dye in cotton coated with zinc oxide nanoparticles synthesized by precipitation method, *Int. J. Technol.*, 13 (3), 553–564.
- [7] Křížová, H., 2015, “Natural Dyes: Their Past, Present, Future, and Sustainability” in *Recent Developments in Fibrous Material Science*, Eds. Křemenáková, D., and Militký, J., OPS, Kanina, Czechia, 59–71.
- [8] Mindaryani, A., Rahayuningsih, E., Adriyanti, D.T., Parthasiwi, L.D., Widhiasih, M.S., and Larasati, F., 2020, Production of tannin-based natural dye from mangrove (*Rhizophora mangle*) tree bark waste from wood chips industry: A feasibility study, *IOP Conf. Ser.: Mater. Sci. Eng.*, 778 (1), 012001.
- [9] Tresnawati, N., Saleh, I., Sudarmin, S., and Wardani, S., 2020, The utilization of local plants as natural dye Ciwaringin batik, Cirebon, Indonesia, *EurAsian J. BioSci.*, 14, 7357–7364.

- [10] Evitasari, R.T., Rahayuningsih, E., and Mindaryani, A., 2019, Dyeing of cotton fabric with natural dye from *Peristrophe bivalvis* extract, *AIP Conf. Proc.*, 2085, 020055.
- [11] Neimsuwan, T., Hengniran, P., Siramon, P., and Punsuvon, V., 2017, Tannin extraction of rhizophora bark from residual charcoal production, *J. Trop. For. Res.*, 1 (1), 36–50.
- [12] Iqbal, S., and Ansari, T.N., 2021, “Extraction and Application of Natural Dyes” in *Sustainable Practices in the Textile Industry*, Eds. Rather, L.J., Shabbir, M., and Haji, A., Scrivener Publishing LLC, Beverly, Massachusetts, US, 1–40.
- [13] Kurniasari, I.D., and Maharani, D.K., 2015, Pembuatan komposit kitosan alumina sebagai agen fiksasi zat warna rodamin B pada kain katun, *UNESA J. Chem.*, 4 (1), 75–80.
- [14] Fatubun, A., Susanti, C.M.E., Sinaga, N.I., Wanma, J.F., and Lea, M.M., 2023, Natural dyes used by the byak tribe and its prospects as raw materials for the natural dyes industry, *IOP Conf. Ser.: Earth Environ. Sci.*, 1192 (1), 012023.
- [15] Fauziyah, N., and Hakim, L., 2015, Plants as natural dyes for jonegoroan batik processing in Jono cultural tourism village, Bojonegoro, East Java, *JITODE*, 3 (2), 41–44.
- [16] Lemmens, R.H.M.J., Soerianegara, I., and Wong, W.C., 1996, Plant resources of South-East Asia. No. 5(2). Timber trees: Minor commercial timbers, *Taxon*, 45 (3), 581.
- [17] Pamoengkas, P., Siregar, I.Z., and Dwisutono, A.N., 2018, Stand structure and species composition of Merbau in logged-over forest in Papua, Indonesia, *Biodiversitas*, 19 (1), 163–171.
- [18] Malik, J., Santoso, A., Mulyana, Y., and Ozarska, B., 2016, Characterization of Merbau extractives as a potential wood-impregnating material, *BioResources*, 11 (3), 7737–7753.
- [19] Pizzi, A., 2008, “Tannins: Major Sources, Properties and Applications” in *Monomers, Polymers and Composites from Renewable Resources*, Eds. Belgacem, M.N., and Gandini, A., Elsevier, Amsterdam, 179–199.
- [20] Kumari, M., and Jain, S., 2015, Screening of potential sources of tannin and its therapeutic application, *Int. J. Nutr. Food Sci.*, 4 (2-1), 26-29.
- [21] Ekechukwu, O.V., 1999, Review of solar-energy drying systems I: An overview of drying principles and theory, *Energy Convers. Manage.*, 40 (6), 593–613.
- [22] Putri, N.P., Niawanti, H., Rifaldiannur, M., and Desy, K., 2019, Modeling of tannin mass transfer on the *Averrhoa bilimbi* leaf extraction, *Ekoloji*, 28 (108), 2755–2760.
- [23] Afolabi, T.J., Tunde-Akintunde, T.Y., and Adeyanju, J.A., 2015, Mathematical modeling of drying kinetics of untreated and pretreated cocoyam slices, *J. Food Sci. Technol.*, 52 (5), 2731–2740.
- [24] Geankoplis, C.J., 1993, *Transport Processes and Unit Operations*, 3rd Ed. Prentice-Hall, Hoboken, New Jersey, US.
- [25] Nama Medoua, G., and Mbofung, C.M.F., 2007, Kinetics studies of some physico-chemical substances during roasting and preparation of beverage made by *Cassia occidentalis* seeds, *LWT-Food Sci. Technol.*, 40 (4), 730–736.
- [26] Ndukwu, M.C., Dirioha, C., Abam, F.I., and Ihediwa, V.E., 2017, Heat and mass transfer parameters in the drying of cocoyam slice, *Case Stud. Therm. Eng.*, 9, 62–71.
- [27] Kumar, A., Kandasamy, P., Chakraborty, I., and Hangshing, L., 2022, Analysis of energy consumption, heat and mass transfer, drying kinetics and effective moisture diffusivity during foam-mat drying of mango in a convective hot-air dryer, *Biosyst. Eng.*, 219, 85–102.
- [28] Chen, B.L., Jang, J.H., Amani, M., and Yan, W.M., 2023, Numerical and experimental study on the heat and mass transfer of kiwifruit during vacuum freeze-drying process, *Alexandria Eng. J.*, 73, 427–442.

Short Communication:**Application of *Nannochloris* sp. for Landfill Leachate Biotreatment and Lipids Production****Ildefonso Baldiris-Navarro^{1*}, Jorge Sanchez², Martha Torres Virviescas³, Alvaro Realpe-Jimenez¹, and Juan Fajardo-Cuadro⁴**¹Chemical Engineering Program, Universidad de Cartagena, Cartagena 130015, Colombia²Environmental Public Establishment of Cartagena, Cartagena 130015, Colombia³Marine Science Program, Universidad del Sinú, GIDEAM Group, Cartagena 130015, Colombia⁴Mechanical Engineering Program, Universidad Tecnológica de Bolívar, EOLITO Group, Cartagena 130015, Colombia*** Corresponding author:**email: ibaldirisn@unicartagena.edu.co

Received: February 21, 2023

Accepted: May 15, 2023

DOI: 10.22146/ijc.82483

Abstract: The sparse treatment of highly toxic leachates produced in landfills due to the excessive generation of urban solid waste is a common problem worldwide. For this reason, this research aims to show the convenience of the use of algal biotechnology in leachate bioremediation processes. *Nannochloris* sp. species was used in this research. It was isolated and cultured for bioassays. The leachate was diluted to 5 and 10% in the microalgae cultures during a period of 8 d in which the growth of the species. Then removal of nutrients (phosphate and nitrate) and the production of lipids by the microalgae were measured. *Nannochloris* sp. removed more than 70% of the phosphates and 60% of the nitrates from samples. This result shows the benefits of using these microalgae to treat landfill leachate at low cost and also with the potential to obtain bio-lipids that may be useful for biodiesel production.

Keywords: bioremoval; bio-lipids; landfill leachate; microalgae; *Nannochloris* sp.

■ INTRODUCTION

Excessive population growth, industrialization, and global consumerism have led to different threatening conditions for humanity such as global warming, plagues, and food shortages. Additionally, overpopulation has caused the uncontrolled generation of solid wastes, which are deposited in holes called landfills, which through the years, decompose and become highly toxic by-products named leachate, which has toxic organic and inorganic components [1-2]. These leachates have high levels of biochemical oxygen demand (BOD₅), chemical oxygen demand (COD), solids, nutrients, and heavy metals [3]. For the elimination of these substances, expensive processes such as membrane technologies, ion exchange, adsorption with activated carbon, flocculation coagulation, or advanced oxidation processes are required [4-5].

In Cartagena, the leachates are maintained in collection ponds where the pH is kept close to neutral and evaporated due to the action of high local temperatures. Nevertheless, the ponds may suffer spills due to leaks in the membranes they have. These leachate leaks might cause eutrophication of water sources if they get in contact, which may produce the appearance of algae bloom, a drop in oxygen levels, increase toxicity and turbidity, and may also reach the human food chain, which could be a threat for public health [6-7].

On the other hand, the bioremediation of wastewater using microalgae has recently gained interest due to its advantages, such as the removal of nutrients from contaminated water, low investment, and low environmental damage since it does not require or generate harmful chemicals in the process. Additionally, microalgae consume carbon dioxide (CO₂) that they use

as a carbon source and produce more oxygen than trees via photosynthesis [8-9].

The diversity of the biomass obtained from microalgae cultures, combined with new large-scale cultivation technologies, has allowed the biomass obtained from these organisms to be used for commercial purposes in different fields, for example, as a source of protein, fatty acids for biofuels, pigments, biomolecules for pharmaceutical use and personal care products [10-11]. Previous studies have confirmed that microalgae may be cultivated in wastewater not only from piggeries, wine factories, palm oil mills and municipal but also in leachate from landfills. Microalgae may remove large amounts of dissolved pollutants from these effluents and also generate biomass rich in bioproducts of high-added value [12-15]. Additionally, polyunsaturated fatty acids obtained from microalgae may be used as feedstock in the production of biofuels, which are vital due to the imminent depletion of fossil fuels [16]. Biodiesel is a promising alternative because of its renewable nature. Unlike traditional land crops, microalgae may be rapidly grown in small spaces at any time of the year, which favors a greater production of biomass and lipids [17-18].

Due to the increase in the contamination of water resources and the urgent necessity to find a sustainable and renewable source of polyunsaturated fatty acids to generate biofuels, microalgal biotechnology appears as a viable and attractive alternative to achieve both goals. Therefore, this study aimed to determine the efficiency of nutrient removal (phosphate and nitrate) from landfill leachate using the microalga *Nannochloris* sp. Additionally, we determine the amount of lipids recovered in the bioremediation process to analyze their potential use in biofuel production.

■ EXPERIMENTAL SECTION

Materials

Microalgae and culture medium

Nannochloris sp. was isolated and cultured for bioassays with leachate in the Universidad del Sinu and Sena Cinaflup aquaculture biotechnology laboratories in Cartagena, Colombia. The culture medium used was the modified Conway medium, which contains the following

substances: $\text{FeCl}_3 \cdot 6\text{H}_2\text{O}$ (26 g), $\text{MnCl}_2 \cdot 4\text{H}_2\text{O}$ (0.72 g), H_3BO_3 (67.2 g), EDTA (90 g), $\text{Na}_2\text{HPO}_4 \cdot 12\text{H}_2\text{O}$ (40 g), NaNO_3 (200 g), Na_2SiO_3 (40 g), H_2O (2 L), trace metals (2 mL), and vitamin solution (100 mL). The trace metal solution contained ZnCl_2 (2.1 g), $\text{CoCl}_2 \cdot 6\text{H}_2\text{O}$ (2 g), $(\text{NH}_4)_6\text{Mo}_7\text{O}_{24} \cdot 4\text{H}_2\text{O}$ (0.9 g), $\text{CuSO}_4 \cdot 5\text{H}_2\text{O}$ (2 g), and distilled water (100 mL), while the vitamin solution was composed of decamyl (210 mg) and distilled water (100 mL) [19].

Landfill leachate

For pollutant removal bioassays, the leachate was obtained from Los Cocos landfill, located in Cartagena city, Colombia. For its characterization, tests standardized by the American Public Health Association (APHA) were applied to determine the content of various contaminants before starting the assays. The measured parameters of the landfill leachate are provided in Table 1 [20].

Instrumentation

All concentration measures were done using GENESYS™ 50 UV-vis spectrophotometer of single cell holder, Model: Genesys 50, made by Thermo Fisher Scientific Inc. Ultrasound extraction procedures were conducted in an ultrasonic bath, model HH-S4, Zenith Lab (Jiangsu) Co., Ltd No. 12 Hongshan Road, China. Solvent extraction procedures were made using Pyrex Soxhlet extraction apparatus, model CLS3740S, Merck KGaA, Darmstadt, Alemania.

Procedure

Bioremediation experiments

To carry out the bioassays, the leachate was diluted without any pretreatment to 5% and 10% (v/w) in 1000 mL Erlenmeyer flasks using the microalgae cultures in the growth phase as solvent. The final volume of each bioassay was 400 mL. The optical density at 680 nm was measured daily to assess culture growth, phosphate content was measured by the ascorbic acid method, and nitrate content by the cadmium reduction method. All procedures were done by spectrophotometry.

The percentage of contaminant removal was calculated using the Eq. (1):

$$\% \text{Removal} = \frac{C_0 - C_f}{C_0} \times 100 \quad (1)$$

where C_f is the final concentration of the contaminant and C_0 is the initial concentration. The percentage of inhibition was calculated for the cultures using the Eq. (2):

$$\% \text{Inhibition} = \frac{DO_C - DO_m}{DO_C} \times 100 \quad (2)$$

where DO_C is the optical density of the control and DO_m is the optical density of the sample.

Lipids extraction

Lipids were extracted from dry samples of *Nannochloris* sp. microalgae biomass following the method provided by Bligh & Dyer [21] and Hu et al. [22] with modifications. Initially, 0.5 g of lyophilized biomass was stirred in 30 mL of chloroform: methanol solution (2:1 v/v) for 60 min, and then ultrasound was applied to the mixture for another 60 min. Then, the phases were separated by centrifugation at 2000 rpm and the solvent mixture was evaporated using a rotary evaporator. The percentage of lipids was found by gravimetry using the Eq. (3):

$$\text{Percentage of lipid} = \frac{P_L}{P_M} \times 100\% \quad (3)$$

where P_L is dry weight of total lipids and P_M is dry weight of microalgae biomass.

RESULTS AND DISCUSSION

Characterization of Landfill Leachate

The landfill leachate had a dark color, an unpleasant odor, a high COD content and also showed high levels of nutrients, especially ammoniacal nitrogen (Table 1). According to the literature, the N:P ratio must be in the range of 5–40 for optimal growth of the microalgae; in this case, it was 49.79, which according to other authors, may be a usable value, so no phosphorous supplement was added to the culture. The pH is an essential parameter for microalgae growth that must be between 7 and 9. According to the literature review, this range was reached for bioassays with the effect of dilution at 5 and 10%. The phenol content in leachate was less than 0.10 mg/L, so it does not affect the growth of the microalgae since it does not reach values greater than 70 mg/L that inhibit the growth of the microorganisms [23]. The values found for the leachate characterization are in Table 1.

Table 1. Leachate properties

Parameter	Mean value (mg/L)
DQO	1272.00
Ammonium N - NH_4^+	1277.00
Nitrates N - NO_3^-	12.45
Nitrites N - NO_2^-	5.10
Phosphates P - PO_4^{3-}	26.00
N:P	49.79
pH	8.90
Phenol	< 0.10

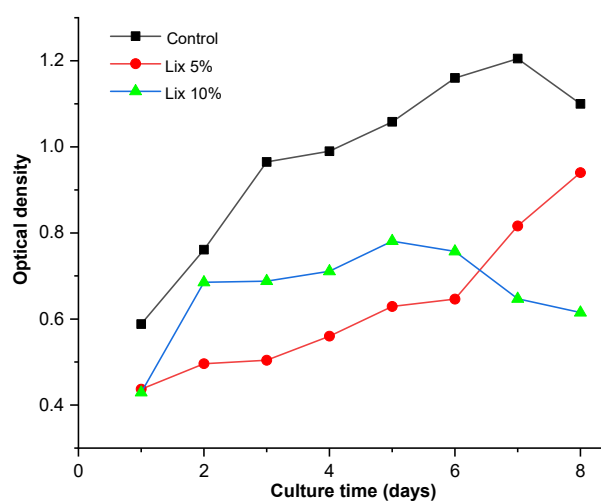


Fig 1. Growth of microalgae in leachate

Culture Growth

All the experiments showed a clear inhibition in the growth of the microalgae induced by the interaction with leachate. The solution at 5% leachate presented better growth at the end of the bioassays, which indicates that the microalgae initially adapted to the adverse conditions during the first 6 d. Then it could reproduce satisfactorily in that concentration the following days. In contrast, the microalgae in the 10% leachate solution showed a good start, growing in the first 5 d, but then the growth rate declined (Fig. 1).

Regardless of the percentage of dilution of the leachate, a clear inhibition was noted in the growth of the microalgae. The 5% bioassays were inhibited by 21.99% in their growth, while the 10% bioassays suffered a 35.20% growth inhibition according to Eq. (2).

These results may be associated with high turbidity or excessive color of the contaminant since this decreases the penetration of light into the culture and may limit

photosynthesis and biomass production. High ammonium content (> 1000 mg/L) may also affect the growth of the microalgae, so at a higher concentration of leachate (10%) the growth of the microalgae was lower in the bioassays affected probably by this fact. Several authors recommend that in order to obtain better cell growth rates, a complementary addition of phosphorus (in the form of K_2HPO_4) should be made to lower the N:P ratio and thus achieve higher cell density in cultures [24]. Other factors that could affect growth are the presence of bacteria since no pretreatment was carried out on the leachate and the presence of other contaminants like toxic heavy metals as reported by Khanzada and Övez [25].

Phosphate Removal

For phosphates bioremediation, it was found that removal in the 5% solution was equal to 75.3% and a removal of 78.6% was achieved for the 10% solution. In Fig. 2, it may be seen that the behavior in the removal of phosphates was similar for the two dilutions of leachate that were tested.

The removal for the 5% solution occurred during the first 4 d and then reached a constant value during the rest of the bioassays. For the 10% sample, it was observed that the maximum removal occurred during the first 3 d of the bioassays to stabilize for the other days of the experiments (Fig. 2).

Phosphorus is an essential nutrient in the energy metabolism of microalgae. It can be found in nucleic acids, proteins, lipids, and intermediate products of carbohydrate metabolism. Furthermore, culture medium with low phosphorus concentrations results in low cell densities in microalgae cultures. During the metabolic process, phosphate (PO_4^{3-}) is assimilated in the form of $H_2PO_4^-$ and HPO_4^{2-} and incorporated into cells through a phosphorylation mechanism, where much of the PO_4^{3-} is used to obtain adenosine triphosphate (ATP) starting from adenosine diphosphate (ADP), thus the microalgae obtain its cellular energy source [26-27]. Similar results for phosphorus removal were found by Hu et al. [22], where the authors diluted leachate to 5, 10, and 15% and observed removal of 80% of the phosphate content when samples were bio-treated with a consortium of microalgae

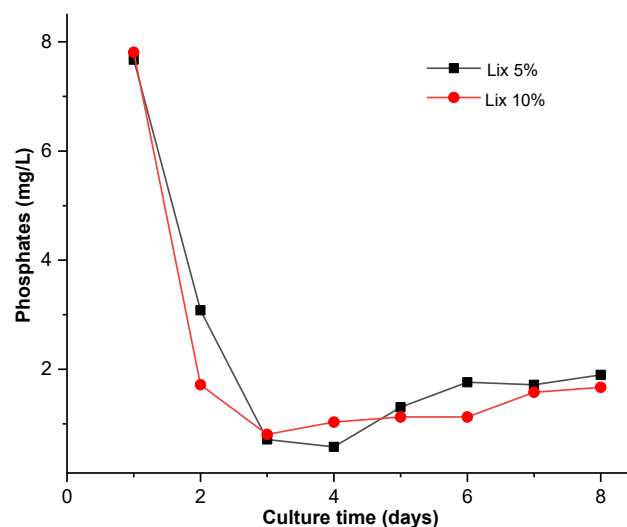


Fig 2. Phosphate removal from leachate

Chlorella vulgaris and *Scenedesmus dimorphus*. Similarly, de Souza et al. [28] found phosphate removals between 67.8 and 92.0% using the microalga *Scenedesmus* sp. to bioremediate pre-treated leachate. On the other hand, in cases where there is little available phosphorus, like in this study, the microalgae probably first accumulate the available phosphorus internally for later use in the assimilation of ammoniacal nitrogen [24-25]. Fig. 2 shows that in both leachate dilutions, a high removal of available phosphate was achieved, and the microalgae first accumulated for posterior consumption.

Nitrate Removal

The nitrate removal percentage for the 5% leachate solution was 62.2%, while for the 10% leachate solution was 42.9%. It may be seen in Fig. 3 that the concentration of nitrates in the 5% solution began the bioassays with lower removal levels than the 10% solution, but on the sixth day, it showed a considerable removal of nitrates, which is consistent with the increase in cell growth of the microalgae in the 5% solution on this day (Fig. 3).

Nitrogen is an essential nutrient required for the growth of microalgae and it is also the basic component of nucleic acids, amino acids, and all proteins, which are essential for the functioning of these microorganisms. Microalgae, to growth assimilate nitrogen that they remove from the environment. The nitrates (NO_3^-) obtained from the environment must be reduced to

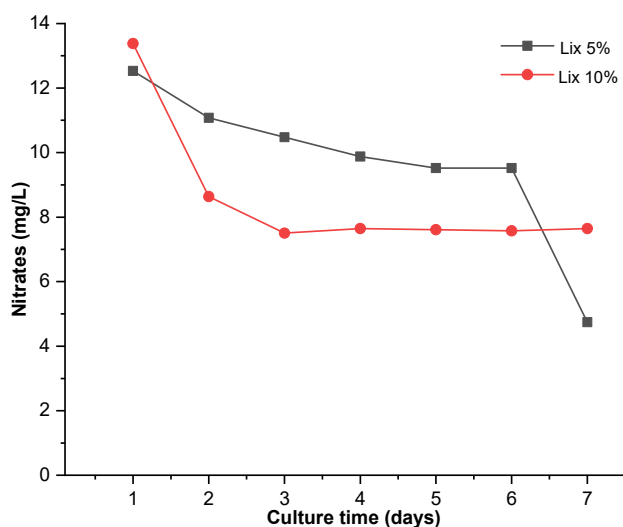


Fig 3. Nitrate removal from leachate

nitrites (NO_2^-) and finally reduced to ammonium ion (NH_4^+). This implies an energy expenditure, and then they incorporate it directly into the amino acids by condensation with glutamate [29]. In this study, the microalgae initially had to adapt to the high levels of contaminants in the leachate, which is reflected in the growth levels, and it was the 5% bioassays that achieved the greatest removal of nitrates and, therefore, the greatest cell density at the end of the bioassays (Fig. 3). Similar levels of nitrate removal were obtained by Chang et al. [1] that removing 61% of nitrates using *C. vulgaris* in photobioreactors and de Souza et al. [28] that obtained nitrate removal rates between 24 and 67% in leachates treated with *Scenedesmus* sp. microalga.

Lipids Production

The composition of the biomass obtained is critical data to evaluate the potential of the microalgae to produce biodiesel. Due to the fact that the bioassays with 5% dilution achieved the highest cell growth, only this one was analyzed to determine the percentage of lipids in the biomass. In this order of ideas, the biomass obtained from the *Nannochloris* sp. microalgae reached 23% lipids when exposed to 5% diluted leachate.

Hernández-García et al. [30] reported a lipid content similar to this study was reported, reaching 20.0% of lipids while culturing *Desmodesmus* sp. and *Scenedesmus obliquus* in landfill leachate. Also, Paiva et al. [12] reported 16.6% of lipids with *Chlorella* sp. and *Scenedesmus* sp., Zhao et

al. [31] reported values of 14.5 and 20.8% of lipid composition for *Chlamydomonas* sp. grown on landfill leachate. Hu et al. [22] obtained 26.0–29.0% lipids culturing *C. vulgaris* and *S. dimorphus* in landfill leachate. Viegas et al. [4] cultured *C. vulgaris* and obtained 23.8% of lipids and obtained 22.6% of lipids with *Scenedesmus* sp.. The lipid yields of the above authors were approximately the same as those found in this work. This means that if *Nannochloris* sp. culture conditions are optimized, the lipid composition could also be improved.

CONCLUSION

In this study, the bioremediation of leachate from a local landfill in Cartagena, Colombia was evaluated using the *Nannochloris* sp. microalgae. When compared to the control bioassay, the microalgae's growth showed an inhibition of between 20 and 30%. This could be attributed to the cultures' extremely high N:P ratio, high ammonium content, and black hue due to the leachate addition. The percentage of nutrient removal was high in both cases, which makes microalgae a feasible alternative to bioremediate this type of toxic waste. The production of lipids from *Nannochloris* sp. achieved a good level even in non-optimized conditions. This study demonstrated the successful cultivation of isolated native *Nannochloris* sp. using local landfill leachate for simultaneously remarkable nutrient removal and significant lipid production by this strain.

ACKNOWLEDGMENTS

The authors acknowledge the financial support for this work by Sena Sennova, project code 8300–sgps–2021, Universidad del Sinu-Cartagena and Universidad de Cartagena.

AUTHOR CONTRIBUTIONS

The conception and design of this study include contributions from all authors. Experimental procedures, microalgae growth and bioremediation were performed by Ildefonso Baldiris-Navarro, Jorge Sanchez, and Martha Torres Virviescas. Data analysis, writing, review and editing carried out by Ildefonso Baldiris-Navarro, Alvaro Realpe-Jimenez, and Juan Fajardo-Cuadro.

■ REFERENCES

- [1] Chang, H., Quan, X., Zhong, N., Zhang, Z., Lu, C., Li, G., Cheng, Z., and Yang, L., 2018, High-efficiency nutrients reclamation from landfill leachate by microalgae *Chlorella vulgaris* in membrane photobioreactor for bio-lipid production, *Bioresour. Technol.*, 266 (5), 374–381.
- [2] Chang, H., Feng, H., Wang, R., Zhang, X., Wang, J., Li, C., Zhang, Y., Li, L., and Ho, S., 2023, Enhanced energy recovery from landfill leachate by linking light and dark bio-reactions: Underlying synergistic effects of dual microalgal interaction, *Water Res.*, 231, 119578.
- [3] Putra, R.S., and Hastika, F.Y., 2018, Removal of heavy metals from leachate using electro-assisted phytoremediation (EAPR) and up-take by water hyacinth (*Eichornia crassipes*), *Indones. J. Chem.*, 18 (2), 306–312.
- [4] Viegas, C., Nobre, C., Mota, A., Vilarinho, C., Gouveia, L., and Gonçalves, M., 2021, A circular approach for landfill leachate treatment: Chemical precipitation with biomass ash followed by bioremediation through microalgae, *J. Environ. Chem. Eng.*, 9 (3), 150–163.
- [5] Tang, C., Gao, X., Hu, D., Dai, D., Qv, M., Liu, D., and Zhu, L., 2023, Nutrient removal and lipid production by the co-cultivation of *Chlorella vulgaris* and *Scenedesmus dimorphus* in landfill leachate diluted with recycled harvesting water, *Bioresour. Technol.*, 369, 128496.
- [6] Nair, A.T., Senthilnathan, J., and Nagendra, S.M.S., 2019, Application of the phycoremediation process for tertiary treatment of landfill leachate and carbon dioxide mitigation, *J. Water Process Eng.*, 28, 322–330.
- [7] Tagliaferro, G.V., Filho, H.J.I., Chandel, A.K., da Silva, S.S., Silva, M.B., and dos Santos, J.C., 2019, Continuous cultivation of *Chlorella minutissima* 26a in landfill leachate-based medium using concentric tube airlift photobioreactor, *Algal Res.*, 41, 101549.
- [8] Liu, X., Chen, G., Tao, Y., and Wang, J., 2020, Application of effluent from WWTP in cultivation of four microalgae for nutrients removal and lipid production under the supply of CO₂, *Renewable Energy*, 149, 708–715.
- [9] Lakshmikandan, M., Murugesan, A.G., Wang, S., Abomohra, A.E.F., Jovita, P.A., and Kiruthiga, S., 2020, Sustainable biomass production under CO₂ conditions and effective wet microalgae lipid extraction for biodiesel production, *J. Cleaner Prod.*, 247, 119398.
- [10] Quan, X., Hu, R., Chang, H., Tang, X., Huang, X., Cheng, C., Zhong, N., and Yang, L., 2020, Enhancing microalgae growth and landfill leachate treatment through ozonization, *J. Cleaner Prod.*, 248, 119182.
- [11] Vyas, S., Patel, A., Nabil Risse, E., Krikigianni, E., Rova, U., Christakopoulos, P., and Matsakas, L., 2022, Biosynthesis of microalgal lipids, proteins, lutein, and carbohydrates using fish farming wastewater and forest biomass under photoautotrophic and heterotrophic cultivation, *Bioresour. Technol.*, 359, 127494.
- [12] Paiva, A.L.P., Gonçalves da Fonseca Silva, D., and Couto, E., 2021, Recycling of landfill leachate nutrients from microalgae and potential applications for biomass valorization, *J. Environ. Chem. Eng.*, 9 (5), 105952.
- [13] Scarponi, P., Izzo, F.C., Bravi, M., and Cavinato, C., 2021, *C vulgaris* growth batch tests using winery waste digestate as promising raw material for biodiesel and stearin production, *Waste Manage.*, 136, 266–272.
- [14] Hazman, N.A.S., Mohd Yasin, N.H., Takriff, M.S., Abu Hasan, H., Kamarudin, K.F., and Mohd Hakimi, N.I.N., 2018, Integrated palm oil mill effluent treatment and CO₂ sequestration by microalgae, *Sains Malays.*, 47 (7), 1455–1464.
- [15] Purba, L.D.A., Othman, F.S., Yuzir, A., Mohamad, S.E., Iwamoto, K., Abdullah, N., Shimizu, K., and Hermana, J., 2022, Enhanced cultivation and lipid production of isolated microalgae strains using municipal wastewater, *Environ. Technol. Innovation*, 27, 102444.
- [16] Edmundson, S.J., and Wilkie, A.C., 2013, Landfill leachate—a water and nutrient resource for algae-

- based biofuels, *Environ. Technol.*, 34 (13-14), 1849–1857.
- [17] Malakar, B., Das, D., and Mohanty, K., 2023, Utilization of *Chlorella* biomass grown in waste peels-based substrate for simultaneous production of biofuel and value-added products under microalgal biorefinery approach, *Waste Biomass Valorization*, 2023, s12649-023-02058-y.
- [18] Eldiehy, K.S.H., Daimary, N., Borah, D., Mandal, M., and Deka, D., 2023, Biodiesel production from *Chlorella homosphaera* by two-step catalytic conversion using waste radish leaves as a source for heterogeneous catalyst, *Appl. Biochem. Biotechnol.*, 195 (7), 4347–4367.
- [19] Baldiris-Navarro, I., and Aponte, J.S., 2020, Growth optimization of *Chlorella vulgaris* in mixotrophic culture enriched with nutrients using experimental design, *IOP Conf. Ser.: Mater. Sci. Eng.*, 844 (1), 012025.
- [20] Baird, R., and Bridgewater, L., 2017, *Standard Methods for the Examination of Water and Wastewater*, 23rd Ed., American Public Health Association, Washington, DC, US.
- [21] Bligh, E.G., and Dyer, W.J., 1959, A rapid method of total lipid extraction and purification, *Can. J. Biochem. Physiol.*, 37 (8), 911–917.
- [22] Hu, D., Zhang, J., Chu, R., Yin, Z., Hu, J., Nugroho, Y.K., Li, Z., and Zhu, L., 2021, Microalgae *Chlorella vulgaris* and *Scenedesmus dimorphus* co-cultivation with landfill leachate for pollutant removal and lipid production, *Bioresour. Technol.*, 342, 126003.
- [23] Tighiri, H.O., and Erkurt, E.A., 2019, Biotreatment of landfill leachate by microalgae-bacteria consortium in sequencing batch mode and product utilization, *Bioresour. Technol.*, 286, 121396.
- [24] Paskuliakova, A., Tonry, S., and Touzet, N., 2016, Phycoremediation of landfill leachate with chlorophytes: Phosphate a limiting factor on ammonia nitrogen removal, *Water Res.*, 99, 180–187.
- [25] Khanzada, Z.T., and Övez, S., 2017, Microalgae as a sustainable biological system for improving leachate quality, *Energy*, 140, 757–765.
- [26] Beltrán-Rocha, J.C., Guajardo-Barbosa, C., Barceló-Quintal, I., and López-Chuken, U.J., 2017, Biotratamiento de efluentes secundarios municipales utilizando microalgas: Efecto del pH, nutrientes (C, N y P) y enriquecimiento con CO₂, *Rev. Biol. Mar. Oceanogr.*, 52 (3), 417–427.
- [27] Cai, T., Park, S.Y., and Li, Y., 2013, Nutrient recovery from wastewater streams by microalgae: Status and prospects, *Renew. Sust. Energ. Rev.*, 19, 360–369.
- [28] de Souza, L., Lima, A.S., Matos, Â.P., Wheeler, R.M., Bork, J.A., Vieira Cubas, A.L., and Moecke, E.H.S., 2021, Biopolishing sanitary landfill leachate via cultivation of lipid-rich *Scenedesmus* microalgae, *J. Cleaner Prod.*, 303, 127094.
- [29] Umamaheswari, J., and Shanthakumar, S., 2016, Efficacy of microalgae for industrial wastewater treatment: A review on operating conditions, treatment efficiency and biomass productivity, *Rev. Environ. Sci. Bio/Technol.*, 15 (2), 265–284.
- [30] Hernández-García, A., Velásquez-Orta, S.B., Novelo, E., Yáñez-Noguez, I., Monje-Ramírez, I., and Orta Ledesma, M.T., 2019, Wastewater-leachate treatment by microalgae: Biomass, carbohydrate and lipid production, *Ecotoxicol. Environ. Saf.*, 174, 435–444.
- [31] Zhao, X., Zhou, Y., Huang, S., Qiu, D., Schideman, L., Chai, X., and Zhao, Y., 2014, Characterization of microalgae-bacteria consortium cultured in landfill leachate for carbon fixation and lipid production, *Bioresour. Technol.*, 156, 322–328.

Short Communication:**Synthesis, Antibacterial and Antioxidant Evaluation of 2-Substituted-4-arylidene-5(4H)-oxazolone Derivatives**Lina Saadi^{1*} and Shaimaa Adnan²¹Department of Pharmaceutical Chemistry, College of Pharmacy, University of Al-Qadisiyah, Diwaniyah 58001, Iraq²Department of Chemistry, College of Education, University of Al-Qadisiyah, Diwaniyah 58001, Iraq*** Corresponding author:**

email: lena.saadi@qu.edu.iq

Received: March 13, 2023

Accepted: August 4, 2023

DOI: 10.22146/ijc.83052

Abstract: In this research, the synthesis of new substituted oxazolone derivatives is described via Erlenmeyer synthesis of N-acyl amino acid. Firstly, the azo derivative **1** was prepared by coupling the diazonium salt of 3-amino-4-methoxybenzoic acid with 4,5-dichloroimidazole in sodium hydroxide solution. Benzoyl chloride derivative **2**, the key intermediate of the synthesis, was synthesized by the acylation of azo-carboxylic acid derivative **1** with thionyl chloride. The resulting acyl chloride derivative reacted with glycine in a basic catalyst to form a hippuric acid derivative **3**. After that, oxazolone derivatives **4a-4f** were prepared via the reaction of the hippuric acid derivative with various aromatic aldehydes. All new compound structures were confirmed by spectral techniques, i.e., FTIR, ¹H-NMR, ¹³C-NMR spectroscopy, and elemental analysis. The antimicrobial activity (Staphylococcus aureus and Escherichia coli) of all new compounds was screened in vitro. The results against S. aureus and E. coli showed that most of the tested compounds have an activity ranging from moderate to low. The antioxidant activity of derivative **4a** was also evaluated and showed good antioxidant activity.

Keywords: antibacterial; antioxidants; Erlenmeyer reaction; glycine; oxazolone

■ INTRODUCTION

The Erlenmeyer azlactones, also known as 4-arylidene-2-substituted-5(4H)-oxazolones, were first introduced in 1983 by Friedrich Gustav Carl Emil Erlenmeyer [1]. This family of compounds is distinguished by its five-membered heterocyclic (γ -lactone) ring that contains nitrogen, oxygen atoms, and an exocyclic C=C [2]. Due to their broad range of biological and pharmacological qualities, they have attracted much more attention [3]. They serve as intermediates and suitable building blocks for the production of a variety of physiologic active compounds like amino acids and heterocyclic compounds [4-6]. In addition, these compounds are particularly effective as antioxidants [7], antitumors [8], antimicrobials [9], and antihypertensives [10] agents. The Erlenmeyer method is the most used method for creating oxazolones [11], which includes a condensation reaction of hippuric acid or its derivatives

with aryl aldehydes in dehydrating agent as acetic anhydride and basic catalyst as anhydrous sodium acetate [12]. Among the numerous heterocyclic compounds containing nitrogen atoms, the imidazole ring, a typical component of natural products, has particular structural features and a variety of biological activities [13]. The unique structure of the imidazole ring was utilized to design, formulate, and develop imidazole-based therapeutic agents in medical fields, including anticonvulsant, antimicrobial, anticancer, anti-HIV, anti-hypertensive, antidepressant, anti-inflammatory, antileishmanial, pain-relieving, and anti-inflammatory [14-16]. Moreover, azo compounds have been used as hypotensive, anticancer, antifungal, antibacterial, anti-inflammatory, and antiviral therapeutic agents [17-20].

Due to various pharmaceutical activities to oxazolone, imidazole, and azo functions and since differing substituents is a common method in medicinal

chemistry for drug design and as a continuation of previous studies, this study aimed to synthesize and study antibacterial and *in vitro* antioxidant activity of the new oxazolone derivatives.

■ EXPERIMENTAL SECTION

Materials

In this study, the chemicals utilized included *p*-anisic acid and 4,5-dichloroimidazole were purchased from Fluorochem. Thionyl chloride and *p*-nitrobenzaldehyde were purchased from CDH while 3,4-methoxybenzaldehyde, *p*-tolualdehyde, 2,2-diphenyl-1-picrylhydrazyl (DPPH), ascorbic acid, DMSO, methanol and ethanol 99% were purchased from Sigma Aldrich. The vanillin, 4-bromobenzaldehyde, 4-hydroxybenzaldehyde (TCL), acetic anhydride 99% (Scharlau), glycine, hydrochloric acid, sodium nitrite, Mueller–Hinton agar (Himedia), sodium hydroxide (B.D.H), and anhydrous sodium acetate (Fluka) were also used in this work.

Instrumentation

The digital melting point device from Stuart, UK was used to measure the melting points. The reactions were monitored on Merck silica gel plates TLC 60 F254 and the products were visualized by iodine vapor. On a Bruker 400 MHz device, ¹H and ¹³C-NMR spectra were obtained, tetramethylsilane was employed as an internal standard and DMSO-*d*₆ as a solvent, values in parts per million are supplied for all NMR chemical shifts in University of Basrah, College of Education of Pure Sciences, Chemistry Department, Iraq. On the EuroFA elemental analyzer apparatus, elemental analysis (C.H.N) were counted. Infrared spectra were recorded and represented in wavenumber on (Shimadzu FTIR-8400S) spectrophotometer.

Procedure

Synthesis of azo derivative 3-((4,5-dichloro-1,3-diazole-2-yl)diazenyl)-4-anisic acid (1)

The synthesis was carried out in two steps, the first step includes diazonium salt formation by dissolving *p*-anisic acid (0.16 g, 1 mmol) in an acidic solution consisting of distilled water (20 mL) and concentrated

HCl (4 mL) with cooling to 0 °C. The solution was treated with sodium nitrite (0.069 g, 1 mmol) in distilled water (5 mL) at the same temperature and continued stirring the above mixture for half an hour. A clear solution of diazonium salt was obtained, which was used directly in the second step by adding it slowly to 4,5-dichloroimidazole (0.13 g, 1 mmol) in absolute ethyl alcohol (15 mL) and (10 mL) of 10% NaOH with stirring for 2 h below 5 °C. The mixture was adjusted at pH 6 [21], and the orange precipitate was formed, then isolated by filtering, washed many times with distilled water, dried, and recrystallization from absolute ethanol. An orange powder with a yield 90%, and a melting point 231–233 °C, as shown in Scheme 1.

FTIR using KBr, ν (cm⁻¹): 3173 (NH imidazole), 3400–2500 (OH carboxylic acid), 3070 (C–H aromatic), 2993 (C–H aliphatic), 1604 (C=N imidazole), 1681 (C=O), 1575–1504 (C=C aromatic), 1450 (N=N), 864 (C–Cl). ¹H-NMR (400 MHz, DMSO-*d*₆), δ (ppm): 12.84 (1H, br, OH), 11.74 (1H, s, NH), 7.40–8.14 (3H, m, aromatic), 4.06 (3H, s, OCH₃). ¹³C-NMR spectrum (DMSO-*d*₆, 100 MHz, δ_c , ppm): 56.8 (C-17), 114.0 (C-15), 117.9 (C-13), 123.5 (C-12), 128.5 (C-2), 131.0 (C-131), 134.8 (C-14), 141.0 (C-11), 150.9 (C-5), 160.3 (C-10), 167.0 (C-18). C₁₁H₈Cl₂N₄O₃, Found, %: C 41.73; H 2.74; N 17.75. Calculated, %: C 41.93; H 2.56; N 17.78.

Synthesis of 3-((4,5-dichloro-1,3-diazole-2-yl)diazenyl)-4-methoxybenzoyl chloride (2)

To a carboxylic acid derivative **1** (0.3 g, 1 mmol), thionyl chloride (13.7 mol, 6 mL) was added slowly by a dropping funnel with stirring at room temperature, then refluxed at 70 °C for 7 h. After the completion of the reaction (followed up by TLC), the excess thionyl chloride was removed by reduced pressure and the product was used immediately in the next step [22]. A red powder with a yield of 91%, and a melting point of 195–197 °C, as shown in Scheme 1.

FTIR using KBr, ν (cm⁻¹): 3172 (N–H), 3085 (C–H aromatic), 2846 (C–H aliphatic), 1751 (C=O acyl), 1604 (C=N imidazole), 1535–1512 (C=C aromatic), 1442 (N=N aromatic) and 825 (C–Cl). ¹H-NMR (400 MHz, DMSO-*d*₆), δ (ppm): 11.83 (s, 1H, NH), 7.25–8.09 (m, 3H, aromatic), 3.91 (s, 3H, OCH₃). ¹³C-NMR (100 MHz,

DMSO-*d*₆, δ , ppm): 171.1 (C-17), 155.8 (C-10), 148.8 (C-5), 142.2 (C-11), 131.8 (C-14), 131.5 (C-3), 129.8 (C-12), 128.7 (C-13), 122.7 (C-2), 114.2 (C-15) and 57.0 (C-20). Found, %: C 39.20; H 2.22; N 16.13. C₁₁H₇Cl₃N₄O₂. Calculated, %: C 39.60; H 2.12; N 16.97.

Synthesis of (3-((4,5-dichloro-1,3-diazole-2-yl)diazenyl)-4-methoxybenzoyl) glycine (3)

Aryl benzoyl chloride 2 (0.333 g, 1 mmol) in a minimum amount of acetone was added slowly over a 30 min period with portions to a mixture of glycine (0.075 g, 1 mmol) and sodium hydroxide (10 mL, 10%). The reaction mixture continued stirring vigorously for one day at room temperature, and the reaction progress was monitored through TLC (benzene: methanol 4:1, v/v). Crushed ice was added to the mixture and then acidified with HCl (concentrated) to pH 2–3. The formed precipitate was filtered and washed several times with cold distilled water, dried, and recrystallized from methanol [23]. The reddish-orange powder with a yield of 64% and the melting point of the compound (decompose at 196 °C), as shown in Scheme 1.

FTIR using KBr, ν (cm⁻¹): 2543–3548 (O–H acid), 3371 (N–H amide), 3178 (N–H), 3070 (C–H aromatic), 2985, 2846 (C–H aliphatic), 1712 (C=O acid), 1697 (C=O amide), 1604 (C=N imidazole), 1535–1504 (C=C aromatic), 1450 (N=N) and 825 (C–Cl). ¹H-NMR (400 MHz, DMSO-*d*₆), δ (ppm): 12.95 (br s, 1H, OH acid), 11.96 (s, 1H, NH imidazole), 7.40–8.19 (m, 3H, aromatic), 7.84 (s, 1H, NH amide), 4.05 (s, 2H, CH₂), 3.83 (s, 3H, OCH₃). ¹³C-NMR (100 MHz, DMSO-*d*₆), δ , ppm): 172.2 (C-22), 167.7 (C-16), 151.4 (C-10), 148.8 (C-5), 142.2 (C-11), 131.7 (C-14), 128.1 (C-13), 125.3 (C-3), 124.0 (C-12), 123.7 (C-2), 114.1 (C-15), 56.9 (C-21) and 46.3 (C-18). Found, %: C 41.61; H 2.83; N 18.16. C₁₃H₁₁Cl₂N₅O₄. Calculated, %: C 41.95; H 2.97; N 18.86.

Synthesis of 2-substituted-4-arylidene-5(4H)-oxazolones derivatives (4a-4f)

A mixture of *N*-acyl amino acid compound 3 (0.37 g, 1 mmol), various aromatic aldehydes (1 mmol), anhydrous sodium acetate (1 mmol), and acetic anhydride (20 mL, 10.5 mol) was shaken for 30 min at room temperature. Then, the mixture was refluxed at

80 °C. Absolute ethanol (5 mL) was added slowly with stirring after the completion of the reaction (TLC monitored), the pot of reaction was left standing overnight, and the solid product was filtered, washed with distilled water, dried, and recrystallized using ethanol [24], as shown in Scheme 1.

2-(3-((4,5-Dichloro-1,3-diazole-2-yl)diazenyl)-4-methoxyphenyl)-4-(4-hydroxybenzylidene)oxazol-5(4H)-one (4a).

4-Hydroxybenzaldehyde (0.12 g, 1 mmol), Dark brown powder with a yield (65%), and a melting point of 229–231 °C, R_f = 0.65 (benzene: methanol 4:1, v/v). FTIR using KBr, ν (cm⁻¹): 3394 (O–H), 3163 (N–H), 3132 (C–H aromatic), 3008 (C–H olefin), 2908, 2839 (C–H aliphatic), 1733 (C=O oxazolone), 1675 (C=N oxazolone), 1650 (C=N imidazole), 1604 (C=C alkene), 1558–1512 (C=C aromatic), 1458 (N=N aromatic), 1218 (C–O) and 840 (C–Cl). ¹H-NMR (400 MHz, DMSO-*d*₆), δ (ppm): 11.32 (br s, 1H, NH), 8.80 (s, 1H, C–H olefin), 6.93–8.24 (m, 7H, aromatic), 7.82 (br s, 1H, OH), 3.99 (s, 3H, OCH₃). ¹³C-NMR (100 MHz, DMSO-*d*₆), δ , ppm): 168.9 (C-19), 166.1 (C-18), 160.1 (C-25), 155.4 (C-10), 148.8 (C-5), 144.2 (C-11), 137.5 (C-16), 134.7 (C-23,27), 132.3 (C-21), 130.1 (C-14), 128.5 (C-22), 126.7 (C-12), 126.4 (C-3), 124.1 (C-2), 121.7 (C-13), 116.3 (C-26,24), 111.7 (C-15), and 56.4 (C-30). Found, %: C 52.70; H 2.69; N 15.45. C₂₀H₁₃Cl₂N₅O₄. Calculated, %: C 52.42; H 2.86; N 15.28.

4-(4-Bromobenzylidene)-2-(3-((4,5-dichloro-1,3-diazole-2-yl)diazenyl)-4-methoxyphenyl)oxazol-5(4H)-one (4b).

4-Bromobenzaldehyde (0.18 g, 1 mmol), Light brown powder with a yield 69%, and the melting point 210–212 °C, R_f = 0.3 (hexane: ethyl acetate 5:1, v/v). FTIR using KBr, ν (cm⁻¹): 3163 (N–H), 3101 (C–H aromatic), 3085 (C–H olefin), 2931, 2854 (C–H aliphatic), 1778 (C=O oxazolone), 1680 (C=N oxazolone), 1650 (C=N imidazole), 1612 (C=C alkene), 1558–1519 (C=C aromatic), 1458 (N=N aromatic), 1226 (C–O) and 887 (C–Cl). ¹H-NMR (400 MHz, DMSO-*d*₆), δ (ppm): 11.82 (br s, 1H, NH), 8.92 (s, 1H, C–H olefin), 7.03–8.27 (m, 7H, aromatic), 3.89 (s, 3H, OCH₃). ¹³C-NMR (100 MHz, DMSO-*d*₆), δ , ppm): 167.3 (C-19), 161.9 (C-18), 155.4 (C-10), 149.1 (C-5), 138.3 (C-11), 135.4 (C-16), 134.4 (C-24,26), 132.7 (C-22), 132.1 (C-23,27),

128.3 (C-12), 128.0 (C-3), 123.9 (C-25), 121.6 (C-2), 121.5 (C-13), 112.6 (C-15), and 57.2 (C-30). Found, %: C 46.21; H 2.55; N 13.63. $C_{20}H_{12}BrCl_2N_5O_3$. Calculated, %: C 46.09; H 2.32; N 13.43.

2-(3-((4,5-Dichloro-1,3-diazole-2-yl)diazenyl)-4-methoxyphenyl)-4-(3,4-

dimethoxybenzylidene)oxazol-5(4H)-one (4c). 3,4-Dimethoxybenzaldehyde (0.16 g, 1 mmol), Caramel color powder with a yield 63%, and the melting point 137–139 °C, $R_f = 0.6$ (chloroform: methanol 4:1, v/v). FTIR using KBr, ν (cm^{-1}): 3178 (N–H), 3132 (C–H aromatic), 3078 (C–H olefin), 2962, 2839 (C–H aliphatic), 1727 (C=O oxazolone), 1668 (C=N oxazolone), 1634 (C=N imidazole), 1610 (C=C olefin), 1589–1512 (C=C aromatic), 1458 (N=N aromatic), 1272 (C–O) and 810 (C–Cl). 1H -NMR (400 MHz, DMSO- d_6), δ (ppm): 11.83 (br s, 1H, NH), 8.42 (s, 1H, C–H olefin), 7.02–8.28 (m, 6H, aromatic), 4.00 (s, 3H, OCH₃), 3.88 (s, 3H, OCH₃), 3.70 (s, 3H, OCH₃). ^{13}C -NMR (100 MHz, DMSO- d_6), δ (ppm): 166.0 (C-19), 160.9 (C-18), 154.6 (C-10), 150.4 (C-25), 149.7 (C-26), 148.1 (C-5), 144.9 (C-11), 131.8 (C-16), 130.7 (C-24), 130 (C-14), 129.9 (C-22), 128.9 (C-23), 127.7 (C-3), 126.6 (C-12), 122.6 (C-2), 121.5 (C-13), 114.2 (C-27), 112.6 (C-24), 111.7 (C-15), 56.2 (C-29), 56.3 (C-32), and 56.9 (C-34). Found, %: C 52.86; H 3.09; N 13.52. $C_{22}H_{17}Cl_2N_5O_5$. Calculated, %: C 52.60; H 3.41; N 13.94.

2-(3-((4,5-Dichloro-1,3-diazole-2-yl)diazenyl)-4-methoxyphenyl)-4-(4-hydroxy-3-methoxybenzylidene)oxazol-5(4H)-one (4d).

Vanillin (0.15 g, 1 mmol), Umber color powder, Yield (71%), m.p = 151–153 °C, $R_f = 0.5$ (chloroform: methanol 4:1, v/v). FTIR using KBr, ν (cm^{-1}): 3271 (O–H), 3163 (N–H), 3132 (C–H aromatic), 3016 (C–H olefin), 2947, 2839 (C–H aliphatic), 1715 (C=O oxazolone), 1662 (C=N oxazolone), 1645 (C=N imidazole), 1635 (C=C olefin), 1589–1512 (C=C aromatic), 1458 (N=N aromatic), 1218 (C–O) and 825 (C–Cl). 1H -NMR (400 MHz, DMSO- d_6), δ (ppm): 11.83 (br s, 1H, NH), 9.27 (br s, 1H, OH), 8.25 (s, 1H, C–H olefin), 7.01–8.13 (m, 6H, aromatic), 3.98 (s, 3H, OCH₃), 3.82 (s, 3H, OCH₃). ^{13}C -NMR (100 MHz, DMSO- d_6), δ (ppm): 166.9 (C-19), 160.2 (C-18), 155.1 (C-10), 153.6 (C-25), 149.5 (C-5), 148.6 (C-26), 144.5 (C-11), 136.1 (C-16), 135.9 (C-21), 131.8 (C-14), 129.9 (C-23),

129.09 (C-3), 126.5 (C-22), 123.9 (C-12), 123.2 (C-2), 119.8 (C-13), 114.2 (C-24), 113.0 (C-27), 111.1 (C-15), 56.0 (C-30), and 55.9 (C-33). Found, %: C 51.75; H 3.22; N 14.19. $C_{21}H_{15}Cl_2N_5O_5$. Calculated, %: C 51.65; H 3.09; N 14.34.

2-(3-((4,5-Dichloro-1,3-diazole-2-yl)diazenyl)-4-methoxyphenyl)-4-(4-methylbenzylidene)oxazol-5(4H)-one (4e).

4-Methylbenzaldehyde (0.12 g, 1 mmol), Brown powder with a yield 70%, and the melting point 215–217 °C, $R_f = 0.35$ (chloroform: methanol 4:1, v/v). FTIR using KBr, ν (cm^{-1}): 3209 (N–H), 3147 (C–H aromatic), 3093 (C–H olefin), 2923, 2854 (C–H aliphatic), 1740 (C=O oxazolone), 1685 (C=N oxazolone), 1660 (C=N imidazole), 1623 (C=C olefin), 1604–1512 (C=C aromatic), 1442 (N=N aromatic), 1265 (C–O) and 825 (C–Cl). 1H -NMR (400 MHz, DMSO- d_6), δ (ppm): 11.83 (br s, 1H, NH), 8.63 (s, 1H, C–H olefin), 7.01–8.57 (m, 7H, aromatic), 3.99 (s, 3H, OCH₃), 2.37 (s, 3H, CH₃). ^{13}C -NMR (100 MHz, DMSO- d_6), δ (ppm): 166.7 (C-19), 159.3 (C-18), 155.0 (C-10), 145.6 (C-5), 144.6 (C-11), 138.1 (C-25), 136.9 (C-16), 136.0 (C-22), 135.1 (C-21), 133.2 (C-14), 131.8 (C-23,27), 129.8 (C-26,24), 129.6 (C-12), 126.3 (C-3), 123.3 (C-2), 121.3 (C-13), 114.2 (C-15), 56.0 (C-30), and 21.6 (C-28). Found, %: C 55.61; H 3.08; N 15.67. $C_{21}H_{15}Cl_2N_5O_3$. Calculated, %: C 55.29; H 3.31; N 15.35.

2-(3-((4,5-Dichloro-1,3-diazole-2-yl)diazenyl)-4-methoxyphenyl)-4-(4-nitrobenzylidene)oxazol-5(4H)-one (4f).

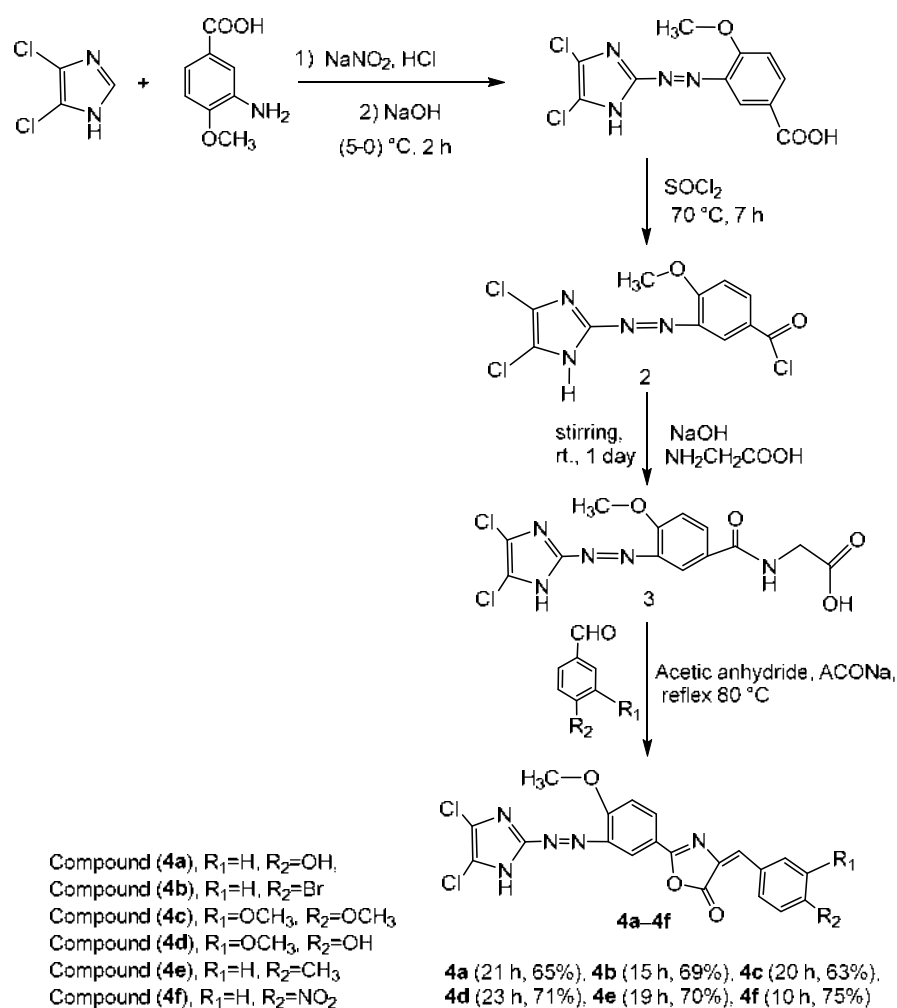
4-Nitrobenzaldehyde (0.15 g, 1 mmol), Reddish brown powder with a yield 75%, and the melting point 240–242 °C, $R_f = 0.55$ (benzene: methanol 4:1, v/v). FTIR using KBr, ν (cm^{-1}): 3209 (N–H), 3109 (C–H aromatic), 3085 (C–H olefin), 2908, 2846 (C–H aliphatic), 1789 (C=O oxazolone), 1698 (C=N oxazolone), 1655 (C=N imidazole), 1633 (C=C olefin), 1527–1546 (C=C aromatic), 1458 (N=N aromatic), 1265 (C–O), 848 (C–Cl) and 1564, 1378 (NO₂). 1H -NMR (400 MHz, DMSO- d_6), δ (ppm): 11.84 (br s, 1H, NH), 8.88 (s, 1H, C–H olefin), 7.20–8.42 (m, 7H, aromatic), 3.89 (s, 3H, OCH₃). ^{13}C -NMR (100 MHz, DMSO- d_6), δ (ppm): 167.4 (C-19), 160.9 (C-18), 155.8 (C-10), 148.2 (C-5), 147.6 (C-25), 144.9 (C-11), 136.8 (C-22), 131.8 (C-16), 131.4 (C-23,27), 131.1 (C-21), 130.8 (C-14),

124.7 (C-3), 124.5 (C-12), 124.2 (C-24,26), 123.4 (C-2), 122.3 (C-13), 114.2 (C-15), and 56.4 (C-29). Found, %: C 49.58; H 2.56; N 17.40. $C_{20}H_{12}Cl_2N_6O_5$. Calculated, %: C 49.30; H 2.48; N 17.25.

RESULTS AND DISCUSSION

The study design includes the synthesis of new oxazolone derivatives bearing imidazole moiety. The synthesis of different derivatives **1–3** and target compounds **4a–4f** is outlined in Scheme 1. At first, we prepared azo derivative **1** with a high yield of 90% through the general method that includes two steps, diazotization of primary amine and then coupling with aromatic compound. The produced azo derivative **1** was used to synthesize acid chloride derivative **2** under anhydrous conditions in a high yield of 91% with thionyl chloride.

Then, compound **2** was used immediately in the Schotten Baumann reaction by reacting with glycine in 10% NaOH to afford hippuric acid derivative **3** through the nucleophilic displacement mechanism. Compound **3** was utilized to synthesize oxazolone derivatives **4a–4f** by Erlenmeyer condensation reaction with acetic anhydride in the presence of anhydrous sodium acetate and different aldehydes (4-hydroxybenzaldehyde, 4-bromobenzaldehyde, 3,4-dimethoxybenzaldehyde, vanillin, *p*-tolualdehyde, and 4-nitrobenzaldehyde). One of the observations that attracted our attention during the synthesis of oxazolone derivatives is that the reaction time is directly affected by the type of benzaldehyde used. It was observed that the substituted benzaldehyde with NO_2 and Br groups required 10 and 15 h to complete the reaction, respectively. Meanwhile, benzaldehydes



Scheme 1. Synthesis of oxazolone derivatives (**4a–4f**)

substituted with electron-donating groups such as OH and OCH₃, needed more time, 21 and 23 h, respectively. It is clear that the substituents in the aromatic ring play an essential role in determining the reaction time and rate. All synthesized compounds were characterized by spectral techniques like ¹H, ¹³C-NMR, and FTIR in addition to C.H.N analyses.

The FTIR spectrum results showed that compound **1** has a medium band at 1450 cm⁻¹ due to the azo group. The stretching vibration of the carbonyl of acid showed a strong band at 1661 cm⁻¹. The ¹H-NMR spectrum of compound **1** shows a broad peak at 12.84 ppm due to acid proton and also a single peak at 11.74 ppm attributed to (NH imidazole) while ¹³C-NMR spectra show signals at 167.0 for the carbon of carbonyl acid.

The FTIR analysis of compound **2** shows a shifting of the carbonyl band of acid to higher frequencies at 1751 cm⁻¹, indicating the formation of acid chloride in addition to the disappearance of a broad band of acid hydroxyl. The ¹H-NMR spectra of compound **2** show the disappearance of hydroxyl protons of acid while ¹³C-NMR gives an important signal at 171.1 ppm belonging to the carbon of carbonyl group.

The FTIR analysis of compound **3** shows characterized new bands. The broad band at 2543–3548 cm⁻¹ belongs to OH acid (Glycine). Also, sharp bands attributed to carbonyl groups at 1697 and 1712 cm⁻¹. In addition to a new stretching vibration of NH amide bond appearance at 3371 cm⁻¹.

The ¹H-NMR of compound **3** shows many peaks, at 12.95 ppm belonging to (OH acid). Another new single peak belongs to the NH amide proton at 7.89 ppm in addition to methylene (CH₂) protons at 4.05 ppm. On the other hand, ¹³C-NMR gives new signals at 172 ppm belonging to the carbonyl of acid. A characteristic signal at 167.7 ppm was attributed to the carbonyl of amide. The methylene group also gave a new signal at 46.3 ppm.

Compounds **4a–4f** that synthesized by the reaction between compound **3** and various aromatic aldehydes. These compounds show many new bands at different regions in FTIR spectra; the new bands in the range 3008–3093 cm⁻¹ belong to the olefin C–H bond in oxazolone

derivatives. Other new bands in the range 1662–1698 cm⁻¹ were attributed to (C=N Oxazolone), the stretching vibration at 1715–1789 cm⁻¹ belong to (C=O oxazolone), new C=C olefin bands also appear in the range 1604–1635 cm⁻¹ while absorption bands of C–O of oxazolone ring appear in the fingerprint region in the range 1218–1265 cm⁻¹.

¹H-NMR of compounds **4a–4f** shows the appearance of new peaks in the range 8.90–8.25 ppm belonging to =C–H olefin proton. On the other hand, ¹³C-NMR spectra of compounds **4a–4f** were given special packages; the bands at the range 159–166 ppm were attributed to the carbon of C=N oxazolone (C-18), the bands in the range 160–168 ppm were attributed to the carbon of C=O oxazolone (C-19). Elemental analysis was also performed for the prepared compounds, and it was found that the theoretical or calculated value is close to the practical value, and thus this supports the validity of the synthesized chemical compositions.

The compounds were screened for their growth inhibition activity *in vitro* against two types of bacterial strains, Gram-positive and -negative, and derivative **4a** was also tested for its antioxidant activity.

Antibacterial Effectiveness

The well plate method was utilized to evaluate the newly synthesized derivatives *in vitro* against Gram-positive (*Staphylococcus aureus*) and Gram-negative (*Escherichia coli*) microorganisms [25–26] where was taken 100 µg/mL concentration from each compound in dimethyl sulfoxide (DMSO) as a solvent, after incubation for 24 h, the inhibitory zone diameter has been calculated. Most of the evaluated compounds that underwent antibacterial testing exhibited moderate activity against the growth of the tested microbial strains.

The findings indicated that, among synthetic compounds, **4a** showed no activity against *S. aureus* (inhibition zone less than 5 mm), while **3**, **4b**, **4c**, **4d**, **4e**, and **4f** showed low activity against *S. aureus* bacteria. On the other hand, *E. coli* response to the produced chemicals was better, ranging between moderate and low activities, whereas compounds **3**, **4a**, **4d**, and **4f** showed

Table 1. Antimicrobial activity zone of synthesized compounds

Compounds	Inhibition zone diameter (mm)	
	<i>E. coli</i>	<i>S. aureus</i>
2	10	5
3	11	7
4a	12	3
4b	10	5
4c	9	10
4d	12	7
4e	6	8
4f	13	6
S1(Amoxicillin drug)	15	14
S2(Ciprofloxacin drug)	40	25
DMSO	-	-

moderate activities, which have a higher inhibition zone than the rest of the synthesized compounds. The inhibition zone diameters were classified as very strong (≥ 20 mm), strong (15–20 mm), moderate (10–15 mm), weak or low (< 10 mm) [27-28].

The results of the structure-activity relationship of the synthesized compounds oxazolone **4a–4f** have shown that the derivatives **4a**, **4d**, and **4f** that contain strong electron donating groups such as OH and OCH₃ in para and meta positions and strong electron withdrawal groups as NO₂ in the para position, respectively, showed higher inhibitory activity than the rest of the other derivatives. The presence of halogen group (**4b**) and methyl group (**4e**) in the *p*-position of the phenyl ring does not have a significant influence on the activity. It should be noted that the effect of hydroxy, methoxy, and nitro groups is higher on *E. coli* than *S. aureus*. Table 1 indicates antibacterial efficiency as compared to the reference drugs.

Antioxidant Activity

The antioxidant activity of the prepared oxazolone derivative containing the hydroxyl group was evaluated using the rapid method (DPPH radical scavenging) in

which the DPPH radical is characterized by its strong absorption and at a wavelength of 517 nm [29-31], which changes color in the presence of an oxidizing substance from violet to yellow. Methanol-DMSO mixture was used as the sample solvent.

One of the target compounds, which is the oxazolone derivative **4a**, was chosen to test its ability to scavenge free radicals, as we expected that the oxazolone derivative **4a** could give higher antioxidant activity than the other synthesized compounds because it possesses a hydroxyl group at the phenyl ring that can donate a hydrogen atom to the free radical DPPH and converts it to a stable molecule. The experimental results of compound **4a** supported our previous expectations, as they demonstrated that compound **4a** has a significant free radical scavenging rate of 77% and is close to vitamin C. The antioxidant capacity of a synthetic derivative **4a** was examined utilizing several concentrations from 200 to 12.5 $\mu\text{g/mL}$. The percentage inhibition of DPPH scavenging activity showed that 200 $\mu\text{g/mL}$, the highest dose of the tested compound **4a** had the highest antioxidant activity (77.16%) with IC₅₀ of 23.40 $\mu\text{g/mL}$ compared to ascorbic acid (80.36%) with IC₅₀ of 21.04 $\mu\text{g/mL}$, which was used as a standard. Data are depicted as mean \pm SD. Table 2 illustrates the results of antioxidant efficiency.

CONCLUSION

In summary, this study has synthesized new imidazole-based oxazolone derivatives from the condensation of hippuric acid derivative with aromatic aldehydes with different substituents and evaluated their antibacterial and antioxidant activities. The results above indicate that the *p*-nitro substituted group on the benzene ring of oxazolone derivative highly affects the antibacterial activity against *E. coli*, the same effect shown in a hydroxy group at the same position and a methoxy group at the meta position. Furthermore, the oxazolone

Table 2. Antioxidant activity of synthesized compound **4a**

Compound	Inhibition of DPPH (%)					IC ₅₀ , $\mu\text{g/mL}$
	200 $\mu\text{g/mL}$	100 $\mu\text{g/mL}$	50 $\mu\text{g/mL}$	25 $\mu\text{g/mL}$	12.5 $\mu\text{g/mL}$	
4a	77.16 \pm 2.41	71.37 \pm 6.21	65.93 \pm 2.41	51.47 \pm 3.07	43.48 \pm 3.57	23.40
Ascorbic acid (standard)	80.36 \pm 2.87	69.48 \pm 3.71	54.48 \pm 2.41	40.43 \pm 7.08	17.63 \pm 7.20	21.04

derivative **4a** that evaluated its antioxidant activity exhibited good and close action to the activity of the standard drug used for the purpose of comparison in this study in the DPPH test. However, more research focusing on the mechanisms of action of oxazolones on bacterial response is needed.

■ REFERENCES

- [1] Kushwaha, N., and Kushwaha, S., 2021, Synthetic approaches and biological significance of oxazolone moieties: A review, *Biointerface Res. Appl. Chem.*, 12 (5), 6460–6486.
- [2] Rodrigues, C.A.B., Martinho, J.M.G., and Afonso, C.A.M., 2015, Synthesis of a biologically active oxazol-5-(4*H*)-one via an Erlenmeyer–Plöchl reaction, *J. Chem. Educ.*, 92 (9), 1543–1546.
- [3] Hammouda, M.B., Boudriga, S., Hamden, K., Askri, M., Knorr, M., Strohmman, C., Brieger, L., Krupp, A., Anouar, E.H., Snoussi, M., Aouadi, K., and Kadri, A., 2022, New spiropyrrolothiazole derivatives bearing an oxazolone moiety as potential antidiabetic agent: Design, synthesis, crystal structure, Hirshfeld surface analysis, ADME and molecular docking studies, *J. Mol. Struct.*, 1254, 132398.
- [4] Almalki, A.J., Ibrahim, T.S., Taher, E.S., Mohamed, M.F.A., Youns, M., Hegazy, W.A., and Al-Mahmoudy, A.M.M., 2022, Synthesis, antimicrobial, anti-virulence and anticancer evaluation of new 5(4*H*)-oxazolone-based sulfonamides, *Molecules*, 27 (3), 671.
- [5] Algehary, A.M., and Alhalafi, M.H., 2022., Design, synthesis and evaluate of imidazole, triazine and metastable oxazolone derivatives as chemosensor for detecting metals, *J. Saudi Chem. Soc.*, 26 (6), 101537.
- [6] Zhou, B., and Chen, W., 2013, The zwitterionic imidazolium salt: First used for synthesis of 4-arylidene-2-phenyl-5(4*H*)-oxazolones under solvent-free conditions, *J. Chem.*, 2013, 280585.
- [7] Parveen, M., Ali, A., Ahmed, S., Malla, A.M., Alam, M., Pereira Silva, P.S., Silva, M.R., and Lee, D.U., 2013, Synthesis, bioassay, crystal structure and ab initio studies of Erlenmeyer azlactones, *Spectrochim. Acta, Part A*, 104, 538–545.
- [8] Alghamdi, S.S., Suliman, R.S., Alshehri, R.A., Almahmoud, R.S., and Alhujirey, R.I., 2022, N-heterocycle derivatives: An update on the biological activity in correlation with computational predictions, *J. Appl. Pharm. Sci.*, 12 (5), 59–77.
- [9] Ahmed, N.G., and Hamad, A.N., 2023, Synthesis and preliminary pharmacological profile of some new 3,5-dihydro-4*H*-imidazol-4-one and α,β -dehydroamino acid derivatives, *Zanco J. Pure Appl. Sci.*, 35 (1), 223–240.
- [10] Jadhav, S.A., Sarkate, A.P., Farooqui, M., and Shinde, D.B., 2017, Greener approach: Ionic liquid $[\text{Et}_3\text{NH}][\text{HSO}_4]$ -catalyzed multicomponent synthesis of 4-arylidene-2-phenyl-5(4*H*) oxazolones under solvent-free condition, *Synth. Commun.*, 47 (18), 1676–1683.
- [11] Mobinikhaledi, A., Moghanian, H., and Pakdel, S., 2015, Microwave-assisted efficient synthesis of azlactone derivatives using 2-aminopyridine-functionalized sphere SiO_2 nanoparticles as a reusable heterogeneous catalyst, *Chin. Chem. Lett.*, 26 (5), 557–563.
- [12] Fadda, A.A., Mohammed, R.M., Tawfik, E.H., and Hammouda, M.A., 2021, Synthesis and anticancer activity of new 2-aryl-4-(4-methoxybenzylidene)-5-oxazolone scaffolds, *Biointerface Res. Appl. Chem.*, 11 (1), 8096–8109.
- [13] Gaba, M., and Mohan, C., 2016, Development of drugs based on imidazole and benzimidazole bioactive heterocycles: Recent advances and future directions, *Med. Chem. Res.*, 25 (2), 173–210.
- [14] Saudi, M., Zmurko, J., Kaptein, S., Rozenski, J., Neyts, J., and Van Aerschot, A., 2014, Synthesis and evaluation of imidazole-4,5- and pyrazine-2,3-dicarboxamides targeting dengue and yellow fever virus, *Eur. J. Med. Chem.*, 87, 529–539.
- [15] Aleksandrova, E.V., Kravchenko, A.N., and Kochergin, P.M., 2011, Properties of haloimidazoles (review), *Chem. Heterocycl. Comp.*, 47 (3), 261–289.
- [16] Peng, X.M., LV Damu, G., and Zhou, C.H., 2013, Current developments of coumarin compounds in

- medicinal chemistry, *Curr. Pharm. Des.*, 19 (21), 3884–3930.
- [17] Shridhar, A.H., Keshavayya, J., Peethambar, S.K., and Joy Hoskeri, H., 2016, Synthesis and biological activities of bis alkyl 1,3,4-oxadiazole incorporated azo dye derivatives, *Arabian J. Chem.*, 9 (Suppl. 2), S1643–S1648.
- [18] Gaber, M., El-Sayed, Y.S., El-Baradie, K.Y., and Fahmy, R.M., 2013, Complex formation, thermal behavior and stability competition between Cu(II) ion and Cu⁰ nanoparticles with some new azo dyes. Antioxidant and *in vitro* cytotoxic activity, *Spectrochim. Acta, Part A*, 107, 359–370.
- [19] Rizk, H.F., Ibrahim, S.A., and El-Borai, M.A., 2017, Synthesis, dyeing performance on polyester fiber and antimicrobial studies of some novel pyrazolotriazine and pyrazolyl pyrazolone azo dyes, *Arabian J. Chem.*, 10 (Suppl. 2), S3303–S3309.
- [20] Dhaef, H.K., Al-Asadi, R.H., Shenta, A.A., and Mohammed, M.K., 2021, Novel bis maleimide derivatives containing azo group: Synthesis, corrosion inhibition, and theoretical study, *Indones. J. Chem.*, 21 (5), 1212–1220.
- [21] Yahya, W.I., Mgheed, T.H., and Kadhum, A.J., 2022, Preparation, characterization of some metal complexes of new mixed ligands derived from 5-methyl imidazole and study the biological activity of palladium(II) complex as anticancer, *NeuroQuantology*, 20 (1), 71–83.
- [22] El Newahie, A.M.S., Nissan, Y.M., Ismail, N.S., Abou El Ella, D.A., Khojah, S.M., and Abouzid, K.A.M., 2019, Design and synthesis of new quinoxaline derivatives as anticancer agents and apoptotic inducers, *Molecules*, 24 (6), 1175.
- [23] Abdul-Amir, R.M., Al-Hassan, N.M.A., and Ghadban, H., 2021, Synthesis of some new heterocyclic compounds derived from *p*-chlorobenzoylchloride and investigation of biological effectiveness, *J. Phys.: Conf. Ser.*, 1853 (1), 012009.
- [24] Dube, P.N., Mokale, S.N., Shaikh, S.I., Patil, Y., Yadav, B., Deshmukh, P., and Sabde, S., 2015, Synthesis and molecular docking analysis of imidazol-5-one derivatives as anti-HIV NNRTIs, *Pharm. Chem. J.*, 49 (2), 125–131.
- [25] Mollea, C., Bosco, F., and Fissore, D., 2022, Agar plate methods for assessing the antibacterial activity of thyme and oregano essential oils against *S. epidermidis* and *E. coli*, *Antibiotics*, 11 (12), 1809.
- [26] Ali, A.T., Mosa, M.N., Alshaheen, Z.G., and Muhammad-Ali, M.A., 2020, Synthesis, characterization and antibacterial evaluation of oxoazetidone - benzene sulfonamide derivatives as a hybrid antimicrobial agent, *Syst. Rev. Pharm.*, 11 (2), 487–494.
- [27] Al-Joufi, F.A., Salem-Bekhit, M.M., Taha, E.I., Ibrahim, M.A., Muharram, M.M., Alshehri, S., Ghoneim, M.M., and Shakeel, F., 2022, Enhancing ocular bioavailability of ciprofloxacin using colloidal lipid-based carrier for the management of post-surgical infection, *Molecules*, 27 (3), 733.
- [28] Kim, G., Gan, R.Y., Zhang, D., Farha, A.K., Habimana, O., Mavumengwana, V., Li, H.B., Wang, X.H., and Corke, H., 2020, Large-scale screening of 239 traditional Chinese medicinal plant extracts for their antibacterial activities against multidrug-resistant *Staphylococcus aureus* and cytotoxic activities, *Pathogens*, 9 (3), 185–203.
- [29] Dvornikova, I.A., Buravlev, E.V., Fedorova, I.V., Shevchenko, O.G., Chukicheva, I.Y., and Kutchin, A.V., 2019, Synthesis and antioxidant properties of benzimidazole derivatives with isobornylphenol fragments, *Russ. Chem. Bull.*, 68 (5), 1000–1005.
- [30] Tiéba, T.N., Baptiste, K.N.J., Daouda, B., Claude, K.A.L., Guillaume, K.C., Bernard, Y.O., and Nahossé, Z., 2021, Antioxidant activity evaluation in a series of heterocyclic compounds derived from 1,8-diaminonaphthalene, *J. Biophys. Chem.*, 12 (1), 1–9.
- [31] Kizilkaya, H., Dag, B., Aral, T., Genc, N., and Erenler, R., 2020, Synthesis, characterization, and antioxidant activity of heterocyclic Schiff bases, *J. Chin. Chem. Soc.*, 67 (9), 1696–1701.

Short Communication:**Determination of Cadmium Levels in Agricultural Soils of Some Regions in Syria**

Ranim Ibrahim, Sophie Barguil, and Sondos Hesenow*

Department of Pharmacology and Toxicology, Faculty of Pharmacy, Damascus University, Syria

*** Corresponding author:**

email: sondos.pharma@gmail.com

Received: May 19, 2023

Accepted: August 24, 2023

DOI: 10.22146/ijc.84607

Abstract: Soil pollution with heavy metals has become a serious global threat, largely due to anthropogenic activities, and cadmium (Cd) is one of the most toxic known heavy metals. This study aimed to assess cadmium levels in several agricultural soils in several Syrian regions. Soil samples were taken from six agricultural lands, prepared, and processed to determine the total content of cadmium using a graphite furnace atomic absorption spectrometry. The results showed that the values of cadmium concentration ranged between 0.60 and 1.48 ppm in the studied soil samples, exceeding the permissible limit in some areas. Cadmium values were higher in farmland soils near industrial facilities than those far from them. This study indicates the spread of Cd contamination throughout the study area, significantly near the industrial activities; thus, it may impact local agricultural production safety and human health.

Keywords: cadmium; contamination; agricultural soil; atomic absorption spectrometry

■ INTRODUCTION

Soil pollution with heavy metals has become a serious global threat to the ecosystem and food security [1]. This may occur mainly due to anthropogenic activities resulting from rapid development in agriculture and industry, urbanization, and increment growth of the population [1-2]. These anthropogenic activities, such as mining and processing of metal ores, burning of fossil fuels, using fertilizers, including sewage sludge and pesticides, transport, and many other industrial processes, have caused an accumulation of heavy metals in soil and in plants [1-3]. This makes its impact on the safety of agricultural products a significant concern [4].

Heavy metals are toxic and non-degradable, and their presence in soil persists long after being released into the environment [5-7]. They can result in potential health risks to human beings and ecosystems through direct ingestion or contact with contaminated soil, the food chain (soil-plant-human or soil-plant-animal-human), drinking of contaminated groundwater, reduction in food quality, and reduction in land usability for agricultural production [5-6]. In addition, Heavy metal contamination in soil has a combined worldwide

economic impact estimated to be more than US\$10 billion per year [1].

Cadmium (Cd) is one of the heavy metals known widely and the most toxic [4,8]. Cadmium is used in Ni/Cd batteries, anticorrosive coatings for metals, pigments, polyvinyl chloride (PVC) stabilizers, and alloys and electronic compounds. Cd is also an impurity in several products, including phosphate fertilizers, detergents, and refined petroleum products [4-9]. The application of agricultural inputs containing Cd, such as fertilizers, pesticides, and biosolids (sewage sludge), the disposal of industrial wastes, or the deposition of atmospheric contaminants increases the total concentration of Cd in soils [5-9].

Exposure to Cd can cause various deleterious effects on cellular molecules, mainly due to oxidant-antioxidant imbalance [1]. Moreover, Cd has been implicated in the pathogenesis of many cancers, itai-itai disease, and cardiovascular diseases, inducing nephrotoxicity and osteotoxicity and impairing the function of the immune system [1,8].

Evaluating the contamination of cultivated soil with heavy metals can help judge whether the soil meets the standard and whether the pollution will threaten

human health and the ecological environment. In addition, it may provide a scientific basis for determining the heavy metals whose control needs to be a priority and managing the potential health risks.

Owing to the hazard of Cd, the presence of several anthropogenic activities that can release Cd into the environment near some cultivated lands, and the toxic effects that may result on human health and the environment, this study aimed to determine the concentration of Cd in several agricultural soils in Syria and to assess the extent of their contamination due to the spread of the metal pollution from waste dumpsites to these agricultural areas.

■ EXPERIMENTAL SECTION

Materials

The materials used in this study were concentrated nitric acid (Sigma-Aldrich), and concentrated hydrochloric acid (Sigma-Aldrich).

Instrumentation

The digestion was done in Anton Paar-Multiwave 3000 microwave (Scientific Instruments), and the Cd

concentration was measured using graphite furnace atomic absorption spectrometry (GF-AAS ZEEnit 700 P, Analytik Jena AG, Germany). Soil pH was measured by a pH meter (Boeco, BT-600, Germany).

Procedure

Study area

Six typical agricultural soils in Damascus and Homs were selected as the study areas. Deir Ali is a small town in southern Syria administratively subordinate to the Damascus countryside. Ibn Al-Nafees region is located in the north of Damascus and contains orchards, including those of Abu Jarash. Al-Mleha is a town in the Ghouta area of Damascus countryside, west of Jaramana. Qattinah is a village in central Syria, located south of Homs. Tall al-Shawr is a village located in the southwest of Homs. Finally, Hassia is an industrial city 40 km from Homs, as shown in Fig. 1.

Collection and treatment of soil samples

The top surface soil samples (0–25 cm deep) were collected randomly from the agricultural lands in self-locking polyethylene bags and transported to the laboratory. After collection, pebbles, and twigs were



Fig 1. Location map of the sampling points in the study area

removed. The samples were air-dried at room temperature, grounded, homogenized, and sieved through a 2 mm stainless steel sieve. Finally, fine powder was stored until analysis.

Sample preparation and analysis

Sixty soil samples were processed to assess the total concentration of Cd. To estimate the whole content of Cd, a 0.6 g dried soil sample was digested with acid mixture of concentrated nitric acid and concentrated hydrochloric acid (5 mL HNO₃ + 1 mL HCl) in the microwave digestion system for 15 min according to the US EPA method 3051A (the protocol followed in the laboratories of the Ministry of Local Administration and Environment), where it was put in heat and pressure resistant Teflon tube. The digested samples were then filtered through the filter paper.

The extracts of soil samples were digitized and ready to be read in graphite furnace atomic absorption spectrometry. The metal standards were prepared from a stock solution of 1000 ppm by successive dilutions to get the following solution concentrations of Cd (0, 0.2, 0.5, 1 ppm). All measurements were made in triplicates. Soil pH was conveniently measured in (1/2.5) soil/water suspensions using a pH meter.

Statistical analysis

Descriptive statistics, including maximum, minimum, mean, and standard deviation were calculated. Regression coefficients and ANOVA were used to identify the relationship between soil pH and Cd concentration.

RESULTS AND DISCUSSION

The pH is a main factor in assessing the mobility and retention of heavy metals in soils [10]. The range of pH values was from 1.3 to 8.1, indicating that the soil in the study areas was strongly acidic and slightly alkaline, Table 1. Changes in pH seem to be one of the most important factors affecting heavy metal content in soil. Soil acidity increases the absorption of heavy metals, while the alkalinity of the soil may reduce the retention of heavy metals. In other words, lower soil pH will increase the activity of heavy metal ions and enhance bioavailability [10-11]. Table 2 shows the study of the relationship between soil pH and Cd metal concentration by applying a regression coefficient ($P > 0.05$). So, this study found no linear correlation between pH soil and Cd content, Fig. 2. Although Cd is one of the most mobile heavy metals in the environment, this may be attributed to the physicochemical properties of soil and the surrounding anthropogenic activities that can affect the soil pH [12-13].

Table 1. Results of soil pH

Region	pH
Deir Ali	1.6
Ibn Al-Nafees Orchards	1.3–1.6
Al-Mleha	7.9–8.0
Tall Al-Shawr	7.7–7.9
Qattinah	7.3–7.5
Hassia	7.8–8.1

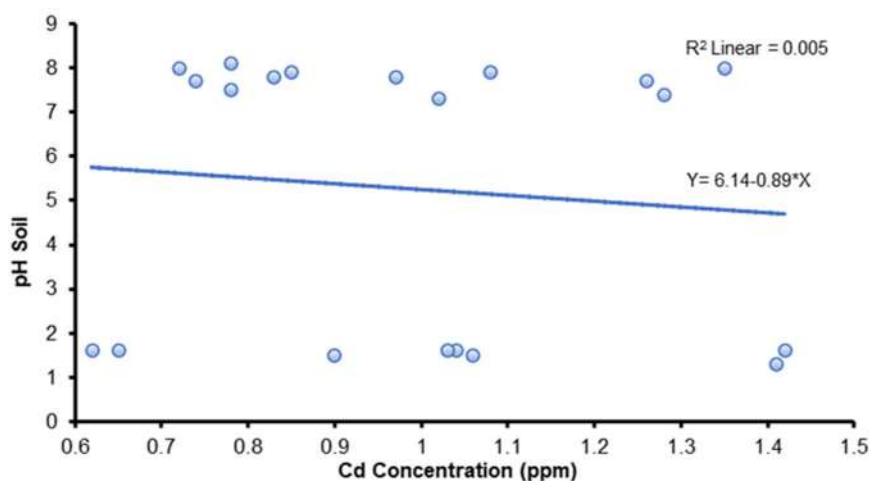


Fig 2. Correlation between pH and Cd concentration

Table 2. Regression coefficient and ANOVA results of pH with Cd concentration

Regression:						
Model	R	R Square	Adjusted R Square	Std. Error of the Estimate		
1	.067 ^a	.005	-.051	3.21173		
Predictors: (Constant), Cd Concentration						
ANOVA ^a						
Model		Sum of Squares	df	Mean Square	F	Sig.
1	Regression	.848	1	.848	.082	.778 ^b
	Residual	185.674	18	10.315		
	Total	186.522	19			
a. Dependent Variable: pH						
b. Predictors: (Constant), Cd Concentration						
Coefficients ^a						
Model		Unstandardized Coefficients		Standardized Coefficients	t	Sig.
		B	Std. Error			
1	(Constant)	6.141	3.123		1.967	.065
	Cd Concentration	-.889	3.099	-.067	-.287	.778

a. Dependent Variable: pH

b. Predictors: (Constant), Cd Concentration

The statistical tables showed (P > 0.05), So there is no linear correlation between soil pH and Cd concentration.

There is a growing environmental concern about Cd being one of the most ecotoxic metals, exhibiting highly adverse effects on soil health, biological activity, plant metabolism, and the health of humans and animals [14-15]. It is worth noting that the permissible limit of Cd, according to the Syrian standard, is 1 ppm.

The measurement results showed that the values of Cd concentration ranged between 0.60 and 1.48 ppm in the studied soil samples, and the highest measured value for Cd was in sample No. (7), which was taken from the orchards of Abu Jarash in the Damascus Ibn al-Nafees area, while the Cd's lowest value was in sample No. (3),

which was taken from the workers' housing for Deir Ali thermal station in Damascus countryside. Descriptive statistical characteristics of the soil Cd content are shown in Table 3 according to each area.

The results found that the highest value of the average Cd concentration was for the samples of Ibn Al-Nafees orchards, where the values exceeded 1 ppm in most points. In comparison, it was more dispersed in both Qattinah and Hassia Industrial City despite exceeding the value of 1 ppm at some points, then Tall Al-Shawr, and finally the Deir Ali thermal station and Al-Mleha, Fig. 3.

Table 3. Descriptive statistics of the soil cadmium content according to each area

	Sample number	Minimum value	Maximum value	Mean	Standard deviation	Median
Deir Ali	9	0.60	1.09	0.77	0.21	0.66
Ibn Al-Nafees Orchards	15	0.85	1.48	1.13	0.19	1.07
Al-Mleha	6	0.67	0.94	0.78	0.09	0.77
Tall Al-Shawr	12	0.66	1.33	0.98	0.22	0.94
Qattinah	6	0.74	1.47	1.03	0.31	0.94
Hassia	12	0.71	1.41	1.03	0.22	1.00

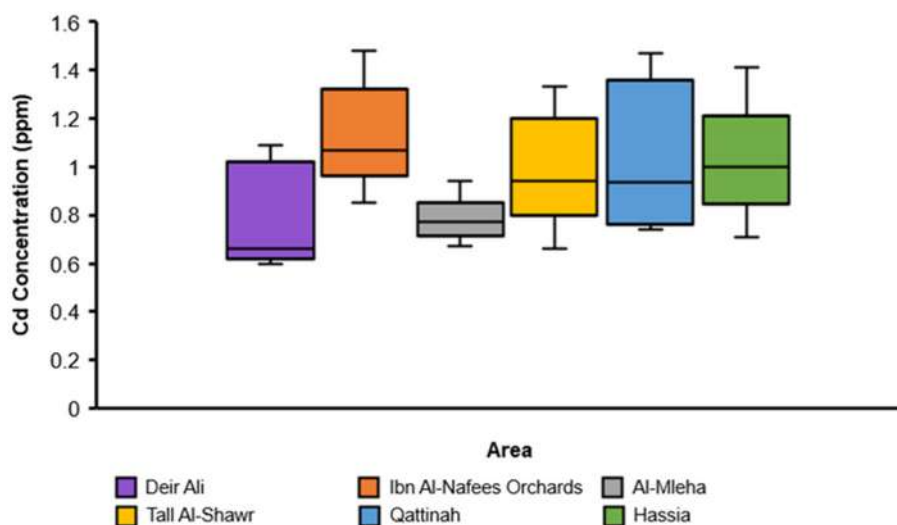


Fig 3. Quartile distribution of cadmium in the soil samples

Cd in Ibn Al-Nafees orchards may be attributed to the widespread use of cadmium in various industries near this area, such as battery production, tanning, and dyeing. This was consistent with the study of Amouei et al. [16] and Sor et al. [17], where the levels of metals, including Cd, are higher in industrial lands or near them than that in remote lands due to industrial human activities. Cd content in the samples of Abu Jarash orchards exceeded the upper acceptable limit as a result of the use of phosphate fertilizers and irrigation with polluted Yazid River water that directly exposed the soil to this metal, and this was supported by the study conducted by Maas et al. [18], where the percentage of Cd pollution was low, due to the non-use of phosphate fertilizers contaminated with it.

There was also observed dispersion in the values obtained in both the Qattinah and Hassia industrial areas, and the difference may be attributed to the presence of Cd in the samples of agricultural lands near the industrial facilities with higher concentrations than the samples of agricultural lands far from them. It must be pointed out that the population living in places close to sources of Cd pollution is exposed to severe damage, as chronic exposure to Cd leads to anemia, insomnia, high pressure, and renal disorders, as indicated by Rahman et al. and Yang et al. [19-20].

The agricultural lands in the Tall al-Shawr area were irrigated with a stream contaminated with the residues of

the fertilizer factory near this area, and the cultivation of vegetables like potatoes, cabbage, and sugar beet mainly prevails. Due to cadmium, metal has a high mobility in the soil, which makes it easy to pick up by plants. Therefore, it is recommended rainfed agriculture only in such areas.

In the Deir Ali region, the results were almost in agreement with the results of Kelmendi et al. [21], which showed elevated concentrations of Cd in the studied soils. The current study concluded that Cd contamination exceeded the permissible limits due to the proximity of the agricultural lands from which the samples were taken to the power plant, which was evident in this study in Sample No. (2) taken from agricultural land located at the drainage outlet of Deir Ali station. Since Cd reaches the atmosphere as a passive product of coal combustion processes in power plants, it settles in soil or water sources and then living organisms with toxic effects.

This study also found that Cd content was within the natural limits in Mleha samples due to the absence of industrial facilities surrounding the area, in addition to irrigating agricultural lands with pure well water. According to the governorates, the current study displayed that Cd value is higher than 1 ppm in each of the governorates of Damascus and Homs, while it is the lowest in Damascus countryside, with less dispersion, as shown in Fig. 4. This may be due to the multiplicity and

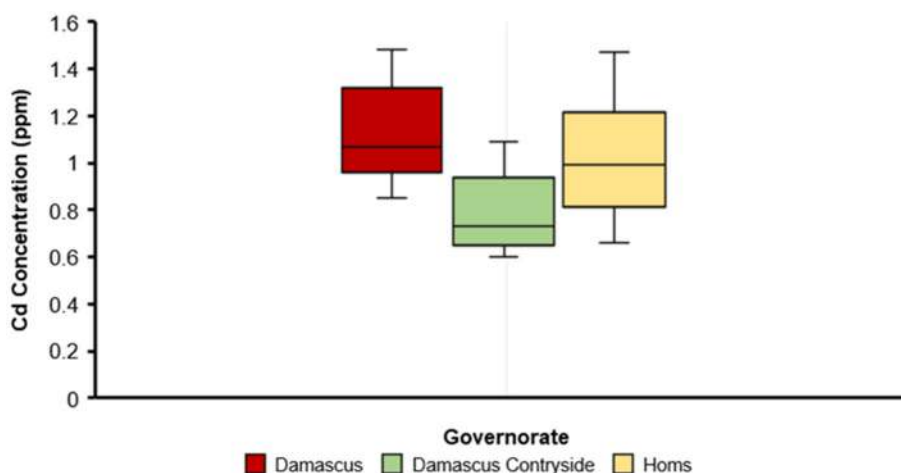


Fig 4. Quartile distribution of cadmium in the soil samples according to governorate

proximity of the sources of pollution to agricultural lands in Damascus and Homs than it is in the countryside of Damascus.

CONCLUSION

The results revealed that elevated concentrations of Cd were found in almost all the soil samples, indicating that the surrounding industrial activities greatly affect the soil in the contaminated areas. This may contribute to the pollution of water sources and the transformation of Cd from soil to vegetables and, consequently, human health risks. Thus, the present study provides a scientific basis for preventing and controlling soil heavy metal pollution to ensure local agricultural production safety and health risk management. However, further Research is required to assess the heavy metals in farmland soils, especially near industrial areas.

ACKNOWLEDGMENTS

The authors thank the Ministry of Local Administration and Environment for assistance in the lab analysis.

AUTHOR CONTRIBUTIONS

Ranim Ibrahim conceived and designed the experiments, collected the samples, performed the experiments, analyzed and interpreted the data, and wrote the paper. Sophie Barguil was the supervisor, also conceived and designed the experiments, contributed to interpreting the data, and reviewed the paper. Sondos

Hesenow contributed to conceiving and designing the experiments, analyzing and interpreting the data, and writing and reviewing the paper.

REFERENCES

- [1] Li, C., Zhou, K., Qin, W., Tian, C., Qi, M., Yan, X., and Han, W., 2019, A review on heavy metals contamination in soil: Effects, sources, and remediation techniques, *Soil Sediment Contam.: Int. J.*, 28 (4), 380–394.
- [2] Bayata, A., 2020, Assessment, accumulation, toxicity and importance of heavy metals in agricultural soil and living system - Review, *Am. J. Environ. Prot.*, 9 (6), 116–119.
- [3] Alengebawy, A., Abdelkhalek, S.T., Qureshi, S.R., and Wang, M.Q., 2021, Heavy metals and pesticides toxicity in agricultural soil and plants: Ecological risks and human health implications, *Toxics*, 9 (3), 42.
- [4] Hu, Z., Li, J., Wang, H., Ye, Z., Wang, X., Li, Y., Liu, D., and Song, Z., 2019, Soil contamination with heavy metals and its impact on food security in China, *J. Geosci. Environ. Prot.*, 7 (5), 168–183.
- [5] Wuana, R.A., and Okieimen, F.E., 2011, Heavy metals in contaminated soils: A review of sources, chemistry, risks and best available strategies for remediation, *ISRN Ecol.*, 2011, 402647.
- [6] Masindi, V., and Muedi, K.L., 2018, "Environmental Contamination by Heavy Metals" in *Heavy Metals*, Eds. Saleh, H.M., and Aglan, R.F., IntechOpen, Rijeka, Croatia, 115–133.

- [7] Alves, L.R., dos Reis, A.R., and Gratão, P.L., 2016, Heavy metals in agricultural soils: From plants to our daily life, *Científica*, 44 (3), 346-361.
- [8] Kubier, A., Wilkin, R.T., and Pichler, T., 2019, cadmium in soils and groundwater: A review, *Appl. Geochem.*, 108, 104388.
- [9] Arora, S., Jain, C.K., and Lokhande, R.S., 2017, Review of heavy metal contamination in soil, *Int. J. Environ. Sci. Nat Resour.*, 3 (5), 139–144.
- [10] Štofejová, L., Fazekas, J., and Fazekasová, D., 2021, analysis of heavy metal content in soil and plants in the dumping ground of magnesite mining factory Jelšava-Lubeník (Slovakia), *Sustainability*, 13 (8), 4508.
- [11] Li, G., Lu, N., Wei, Y., and Zhu, D., 2018, relationship between heavy metal content in polluted soil and soil organic matter and pH in mining areas, *IOP Conf. Ser.: Mater. Sci. Eng.*, 394, 052081.
- [12] Wen, J., Wu, C., Bi, X., Zhang, S., Ouyang, H., Ye, J., Ohnuki, T., and Yu, Q., 2023, Soil pH change induced by smelting activities affects secondary carbonate production and long-term Cd activity in subsoils, *Appl. Geochem.*, 152, 105663.
- [13] Zhang, J., Wu, Y., and Xu, Y., 2016, Factors Affecting the Levels of Pb and Cd Heavy Metals in Contaminated Farmland Soils, *Proceedings of the 2016 International Conference on Biological Engineering and Pharmacy (BEP 2016)*, Atlantis Press, 379–387.
- [14] Haider, F.U., Liqun, C., Coulter, J.A., Cheema, S.A., Wu, J., Zhang, R., Wenjun, M., and Farooq, M., 2021, Cadmium toxicity in plants: Impacts and remediation strategies, *Ecotoxicol. Environ. Saf.*, 211, 111887.
- [15] Asrari, E., 2014, *Heavy Metal Contamination of Water and Soil: Analysis, Assessment, and Remediation Strategies*, 1st Ed., Apple Academic Press, New York.
- [16] Amouei, A., Cherati, A., and Naghipour, D., 2018, Heavy metals contamination and risk assessment of surface soils of Babol in northern Iran, *Health Scope*, 7 (1), e62423.
- [17] Sor, A.L., Edori, O.S., Nwineewii, J.D., 2020, Concentrations of heavy metals in farmland soils from selected oil bearing communities in Gokana, Rivers State, Nigeria, *Int. J. Res. Sci. Innovation*, 7 (5), 173–180
- [18] Maas, S., Scheifler, R., Benslama, M., Crini, N., Lucot, E., Brahmia, Z., Benyacoub, S., and Giraudoux, P., 2010, Spatial distribution of heavy metal concentrations in urban, suburban and agricultural soils in a Mediterranean city of Algeria, *Environ. Pollut.*, 158 (6), 2294–2301.
- [19] Rahman, S.H., Khanam, D., Adyel, T.M., Islam, M.S., Ahsan, M.A., and Akbor, M.A., 2012, Assessment of heavy metal contamination of agricultural soil around Dhaka Export Processing Zone (DEPZ), Bangladesh: Implication of seasonal variation and indices, *Appl. Sci.*, 2 (3), 584–601.
- [20] Yang, J., Ma, S., Zhou, J., Song, Y., and Li, F., 2018, Heavy metal contamination in soils and vegetables and health risk assessment of inhabitants in Daye, China, *J. Int. Med. Res.*, 46 (8), 3374–3387
- [21] Kelmendi, M., Sadiku, M., Kadriu, S., Dobroshi, F., and Igrishita, L., Baruti, B., 2018, Research of heavy metals on the agricultural land in Bajgora region, Kosovo, *Acta Chem. Iasi*, 26, 105–122.